

# Satellite communication antenna technology : summer school, 1982, Technische Hogeschool Eindhoven: lectures

***Citation for published version (APA):***

Maanders, E. J., & Mittra, R. (Eds.) (1982). *Satellite communication antenna technology : summer school, 1982, Technische Hogeschool Eindhoven: lectures*. Technische Hogeschool Eindhoven.

***Document status and date:***

Published: 01/01/1982

***Document Version:***

Publisher's PDF, also known as Version of Record (includes final page, issue and volume numbers)

***Please check the document version of this publication:***

- A submitted manuscript is the version of the article upon submission and before peer-review. There can be important differences between the submitted version and the official published version of record. People interested in the research are advised to contact the author for the final version of the publication, or visit the DOI to the publisher's website.
- The final author version and the galley proof are versions of the publication after peer review.
- The final published version features the final layout of the paper including the volume, issue and page numbers.

[Link to publication](#)

***General rights***

Copyright and moral rights for the publications made accessible in the public portal are retained by the authors and/or other copyright owners and it is a condition of accessing publications that users recognise and abide by the legal requirements associated with these rights.

- Users may download and print one copy of any publication from the public portal for the purpose of private study or research.
- You may not further distribute the material or use it for any profit-making activity or commercial gain
- You may freely distribute the URL identifying the publication in the public portal.

If the publication is distributed under the terms of Article 25fa of the Dutch Copyright Act, indicated by the "Taverne" license above, please follow below link for the End User Agreement:

[www.tue.nl/taverne](http://www.tue.nl/taverne)

***Take down policy***

If you believe that this document breaches copyright please contact us at:

[openaccess@tue.nl](mailto:openaccess@tue.nl)

providing details and we will investigate your claim.

LSL 82 SAT bse

BIBLIOTHEEK

8 207411

T.H.EINDHOVEN

th e

Technische Hogeschool  
Eindhoven

# Summer School on Satellite Communication Antenna Technology

## Course directors:

Eduard J. Maanders, Associate Professor of Electrical Engineering,  
Eindhoven University of Technology, Netherlands  
and

Raj Mittra, Professor of Electrical Engineering,  
University of Illinois, USA.

## Lecturers:

Jens Arnbak, Professor of Electrical Engineering and Director of Tele-  
communications Division, Eindhoven University of Technology, Netherlands.

Peter J.B. Clarricoats, Professor of Electrical Engineering,  
Queen Mary College, London, U.K.

Giorgio Franceschetti, Professor of Electrical Engineering,  
Istituto Elettrotecnico, Università Napoli, Italy.

Flemming Holm Larsen, Research Associate, Technical University of  
Denmark, Lyngby, Denmark.

William A. Imbriale, Deputy Manager, RF and Microwave Subsystems,  
California Institute of Technology, Jet Propulsion Laboratory,  
Pasadena, CA, USA.

Raj Mittra, Professor of Electrical Engineering & Associate Director  
of the Electromagnetics Laboratory, University of Illinois,  
Urbana, IL, USA.

K.C. Lang, Section Head, Commercial Satellite Section,  
Hughes Aircraft Company, Space and Communications Group,  
El Segundo, CA, USA.

Douglas O. Reudink, Director Radio Research Laboratory,  
Bell Laboratories, Holmdel, N.J., USA.

Leon J. Ricardi, Group Leader, Antennas and Propagation,  
M.I.T. Lincoln Laboratory, Lexington MA, USA.

Alan W. Rudge, ERA Technology, Leatherhead, Surrey, U.K.

V.J. Vokurka, Associate Professor of Electrical Engineering,  
Eindhoven University of Technology, Netherlands.

August 23 - August 27, 1982

Eindhoven University of Technology, Department of Electrical Engineering  
Eindhoven, Netherlands, in cooperation with IEEE Benelux and the  
University of Illinois, USA.

## Contents

- Chapter 1. "Satellite Systems Background", by Jens Arnbak.
- Chapter 2. "Offset Reflector Antennas", by Alan Rudge.
- Chapter 3. "Feeds for Earth-Station and Spacecraft Antennas"  
by Peter Clarricoats.
- Chapter 4. "Design Aspects of Commercial Satellite Antennas",  
by K.C. Lang.
- Chapter 5. "Efficient Pattern Computation, Synthesis of Dual-Shaped  
Reflectors", by Raj Mittra.
- Chapter 6. "Adaptive and Multiple-Beam Antenna Systems",  
by Leon J. Ricardi.
- Chapter 7. "Phased Arrays for Satellites and the TDRSS Antenna",  
by William A. Imbriale.
- Chapter 8. "The Role of Antennas in Advanced Communication Satellites",  
by Douglas O. Reudink.
- Chapter 9. "Some Aspects of Antenna Measurements".
- 9.1. "Spherical Near-Field Scanning" by F. Holm Larsen.
  - 9.2. "The Role of Sampling Techniques in Antenna Measurements",  
by G. Franceschetti.
  - 9.3. "Compact Antenna Range" by V. Vokurka.

## 1. The Systems Background for Satellite Communication Antennas

by J.C. Arnbak.

*So soft and uncompounded is their essence pure ...  
In what shape they choose  
Dilated or condensed, bright or obscure  
Can execute their aery purposes*

John Milton: Paradise Lost.

### 1.1. Introduction

A modern satellite system combines very diverse technical aspects - e.g. a mission in space, a responsive service to all its users, and electromagnetic compatibility (EMC) with many other systems in need of access to the radio spectrum and the most attractive satellite orbits. As a result, many designers of satellite communication antennas feel expelled from the pure paradise of classical antenna theory and cursed with a heavy concern with more general system objectives to be achieved. Choice of any one antenna parameter is likely to affect several other system parameters both inside and outside the antenna subsystems of a satellite network. Such complex interactions indeed require the modern antenna engineer to consider various system questions of "why" - and not merely the component questions of "how" - at each development stage of a high-performance satellite system. Even the briefest glance at the increasingly prominent antenna farms of recent satellite designs suggests that the advanced electromagnetic engineer may be accused of having eaten from the tree of knowledge of good and poor system technology.

The spacecraft designed for the Tracking and Data Relay Satellite System (TDRSS) may serve as an example (Fig. 1). Located in their orbit some 36000 km above the Equator, these satellites will support a great variety of missions at lower orbital altitudes, including Space-Shuttle operations, earth observation satellites and space telescopes. They can also provide commercial service in a U.S. domestic communications network (Advanced WESTAR). This versatility, which is intended to reduce operational costs, is reflected in the very diverse antennas shown. Communication links with



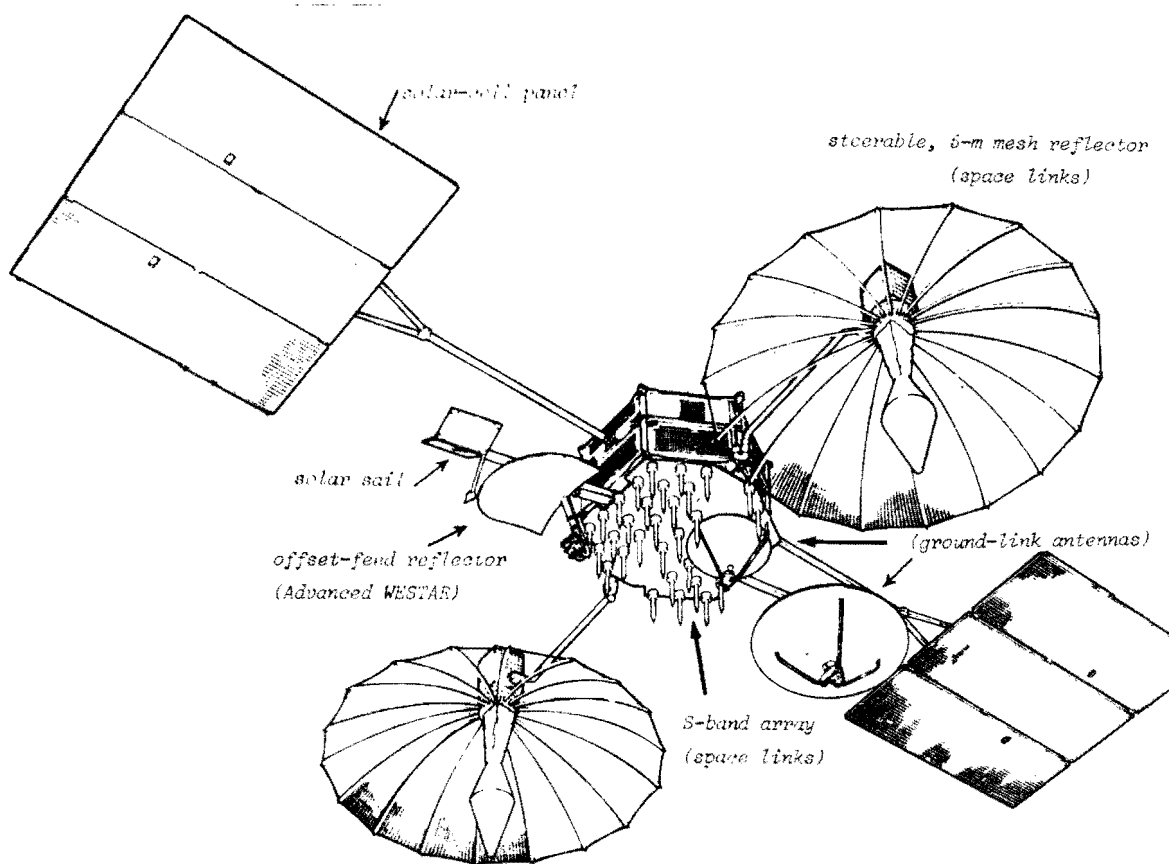


*Fig. 1: View of NASA's Tracking and Data Relay Satellite (TDRS), showing the diverse antenna types required to meet different system requirements.*

other space platforms can be supported either by the two large deployable mesh reflectors (both working in two frequency bands) or by the phased array of small S-band helices mounted on the face of the spacecraft body. Obviously, so different antennas are designed to different service requirements. The single narrow beam of a 5-m reflector antenna can be pointed mechanically to support the extremely high data rates characteristic of some remote sensing missions, Space-Shuttle payload releases or rendez-vous operations. However, simultaneous links to many widely separated orbiting platforms will be established through the phased array, which is capable of forming and scanning up to 20 separate beams. The beam gains and maximum data rates are necessarily lower than with the large mesh reflectors; in return, simultaneous tracking of several platforms relieves these of a need to store

data for long periods while out of coverage of a ground tracking antenna or one of the 5-m reflectors. Moreover, the adaptive beam forming from the ground control centre can also be used to discriminate between platforms and any localized source of radio interference. This is a matter of some importance in the S-band where high-power radars may also be operating.

These aspects of the TDRSS space-to-space links will be dealt with in much greater detail in a later Chapter. The present consideration of the related antennas, and comparison with the three other reflector antennas in Fig. 1 (which serve the various ground links) suffice to demonstrate the case in point here: there are always intimate connections between general system objectives on the one hand, and the specific antenna functions and designs on the other hand. Different mission requirements and orbit constraints are clearly seen to result in distinctly different antenna designs in Fig. 1. This illustrates the necessity for the modern antenna designer to distinguish different satellite services and describe spacecraft orbits and attitudes, as dealt with in the following sections of this Chapter.

Of course the antenna realisation impacts back on the entire system design, too. An example is the requirement for output RF power (and consequently for the solar cells generating the DC power in the spacecraft), which may be traded off for antenna gain. However, larger antennas and smaller solar panels would also change the mass distribution and the torques set up by incident sunlight and by radiated RF-power; hence, the attitude control of the spacecraft would be affected. The small solar sail mounted on the same boom as the D-shaped offset reflector seen in Fig. 1 just serves to balance these minute radiation torques, so that the antenna pointing can be maintained with minimum fuel expenditure for active attitude control.

Thus, as antennas deployed in modern satellite systems have steadily increased in size, complexity and number, this two-way linkage with systems engineering is now confronting the antenna designer and requiring from him an increasing grasp of system thinking. Seen in a more traditional perspective, any antenna was merely a transformer between guided and radiated waves. Classical design methods based on this physical distinction may actually, in the absence of consideration of the system context, attempt to

segregate (rather than link) the system functions of any antenna. Externally, it should direct incoming or outgoing radio waves in a certain way; internally, it should be a matched component of an electronic circuit. Viewed in this familiar way, the antenna was just a prescribed interface between dissociated physical realms in which separate design problems could be specified and solved - at their best rigorously. Classical examples of such separated problems are pattern synthesis, impedance matching, and power-handling capability.

In their purest academic form, the classical approaches to antenna design are based on the identification, solution and combination of highly idealized configurations (known as "canonical problems" in electromagnetic theory), which can serve as building blocks in the structuring of more involved antenna shapes. The geometrical theory of diffraction [1] and the method of moments [2] are presumably the best known examples of such building techniques for complex antennas. Far from abandoning these powerful combinations of deductive mathematical physics and modern computational power, modern satellite antenna engineering is exploiting them in the wider and more demanding context of system engineering.

The many facets of modern aerospace systems in general, and of satellite systems in particular, have increased the responsibility of the antenna designer to be very conscious of his own contributions to (and possible penalties imposed on) the functional performance and cost of a system in its operational environment. This Chapter will focus on major elements of this environment, in which any satellite system must function next to other man-made systems and subject to both the many laws of Nature and those of the national and international institutions regulating access to outer space and the radio spectrum. The definitions and formulae given are intended to provide general guidance and show major constraints relevant at all stages of antenna engineering for satellite systems. The reverse problem, that of the antenna influences on satellite systems and the associated optimum trade-off parameters, will be dealt with in Chapter 8.

### 1.2. The necessity of a consistent international terminology

Unfortunately, the terminology of satellite communications is not always consistently used. Examples are the frequent confusions between terms as

- (i) a spacecraft and a satellite
- (ii) (geo)synchronous and (geo)stationary
- (iii) the satellite itself and its related satellite service(s)
- (iv) a satellite system and a satellite network

which may be partly overlapping, but are never synonymous. Such inaccuracies may be troublesome in the study of the technical literature, and expensive if used in procurement specifications for new satellite communications equipment including antennas. More seriously, they may result in international misunderstandings in the registration, and in improper use, of satellite communications traffic. The International Telecommunication Union (ITU) and its International Radio Consultative Committee (CCIR) have therefore gone to great length in carefully defining a terminology for satellite communications. This has been included in the Radio Regulations [3], to which more than 150 nations are signatories. After all, telecommunications in general - and satellite communications in particular - are a trans-national affair, not only by transporting information across frontiers, but also by sharing the common radio spectrum and the common geostationary orbit. Setting up and adhering to the rules for technical exploitation and protection of such limited resources requires an agreed terminology. As the antenna engineer has considerable responsibility for providing the communication precisely where it is needed, and for avoiding any unnecessary losses of information or traffic capacity, he is well advised in taking good notice of and using the international terminology [3,4].

### 1.3. A few satellite terms and orbital definitions

A spacecraft is a man-made vehicle intended to go beyond the Earth's atmosphere. A communications satellite is a spacecraft with its operational orbit primarily and permanently determined by the gravitation of a (much heavier) primary body, normally the Earth, and intended to (re)transmit radiocommunication signals. It should be carefully noted that this internationally agreed definition excludes several space objects which might be

involved in communications, for instance

- deep space probes (the movements of which are normally determined by several celestial bodies or which may escape their attraction completely),
- launch vehicles and rockets (which are active transportation systems moving through the atmosphere while consuming internal energy),
- natural objects capable of scattering RF signals (the Moon, meteor bursts).

The unperturbed orbit of a satellite is the idealized path (relative to a specified coordinate system) described by its centre of gravity, when it is subject to only the central attraction of the primary body. In any specified reference coordinate system having origin in the centre of gravity of the primary body and axes fixed in relation to the stars (the reference frame), the unperturbed orbit is a conic section with the centre of gravity of the primary body in one of its foci (Kepler's first law). Since the kinetic energy of any satellite by definition is insufficient to escape the gravitational field of the primary body, its unperturbed orbit is periodic and closed. Thus, the conic section is an ellipse - including as a special case a circle. The period of revolution is determined by Kepler's third law in the reference frame

$$T = 2\pi \left[ \frac{a^3}{\mu} \right]^{\frac{1}{2}} \quad (1)$$

where  $a$  is the major semiaxis of the elliptic orbit, and  $\mu$  is constant for all orbits around a certain primary body\*. For the Earth, a currently accepted value is

$$\mu = 3.986032 \dots \times 10^{14} \text{ m}^3 \text{ s}^{-2} \quad (2)$$

A synchronous satellite has  $T$  equal to the sidereal period of rotation of its primary body,  $T_p$  (i.e., the period in any fixed reference coordinate system). It should be noted that for the Earth,  $T_p$  is not 24 hours (the so-called synodal period), because in one day, the Earth both rotates once around its polar axis and also completes  $1/365,24 \dots$  of the annual Earth

---

\*  $\mu$  equals the product of the mass of the primary body and the universal gravitation constant  $G$ . For a fuller treatment of classical Newtonian mechanics applied to satellites, see [5,6].

orbit around the Sun. Consequently, a geosynchronous satellite must have a period

$$\begin{aligned} T &= T_p = (1 - 1/365,24) \times 24h \\ &= 86163,44 \text{ s} \\ &\approx 23^h 56^m 4^s \end{aligned} \tag{3}$$

in any fixed coordinate system. If

$$T = nT_p \quad ; \quad n = 2, 3, 4 \dots \tag{4}$$

the satellite is called super-synchronous, whereas a sub-synchronous satellite has  $T$  and  $T_p$  interchanged in Eq. (4).

For an earth satellite, the reference frame is taken as a rectangular coordinate system (OXYZ) with origin O in the Earth's centre of gravity; the Z-axis coincides with the polar axis and is oriented towards the North\*. The XY-plane is thus the equatorial plane of the Earth; its angle  $i$  with the satellite orbit plane (of the conic section)\* is called the inclination and is defined in the interval  $(0^\circ < i < 180^\circ)$ .

A satellite orbit is equatorial, if the orbit plane coincides with the reference plane of the primary body ( $i = 0^\circ$ ). An orbit is polar, if the orbit plane contains the polar axis of the primary body ( $i = 90^\circ$ ). An orbit is inclined if it is neither equatorial nor polar.

Inclined or equatorial orbits in which the satellite's projection on the equator plane of the primary body revolves in the same direction as the primary body itself are known as direct orbits. They have inclinations less than  $90^\circ$ . Earth rotation is seen to assist the launching of satellites into direct orbits. Orbits for which  $i > 90^\circ$  are retrograde orbits.

A geostationary satellite is synchronous and, moreover, has an equatorial, circular and direct orbit. (Note again that synchronous is often confused with stationary: Polar and inclined orbits can be synchronous, but never stationary).

---

\* Fig. 5 on page 1.18 shows the general geometry.

From Eqs. 1 - 3, the geostationary orbit is therefore the unique circle in the Equator plane with radius

$$a = (T_p/2\pi)^{2/3} \mu^{1/3}$$

$$= 42164.04 \dots \text{ km} \quad (5)$$

and its centre in the Earth's centre of gravity (Fig. 2).

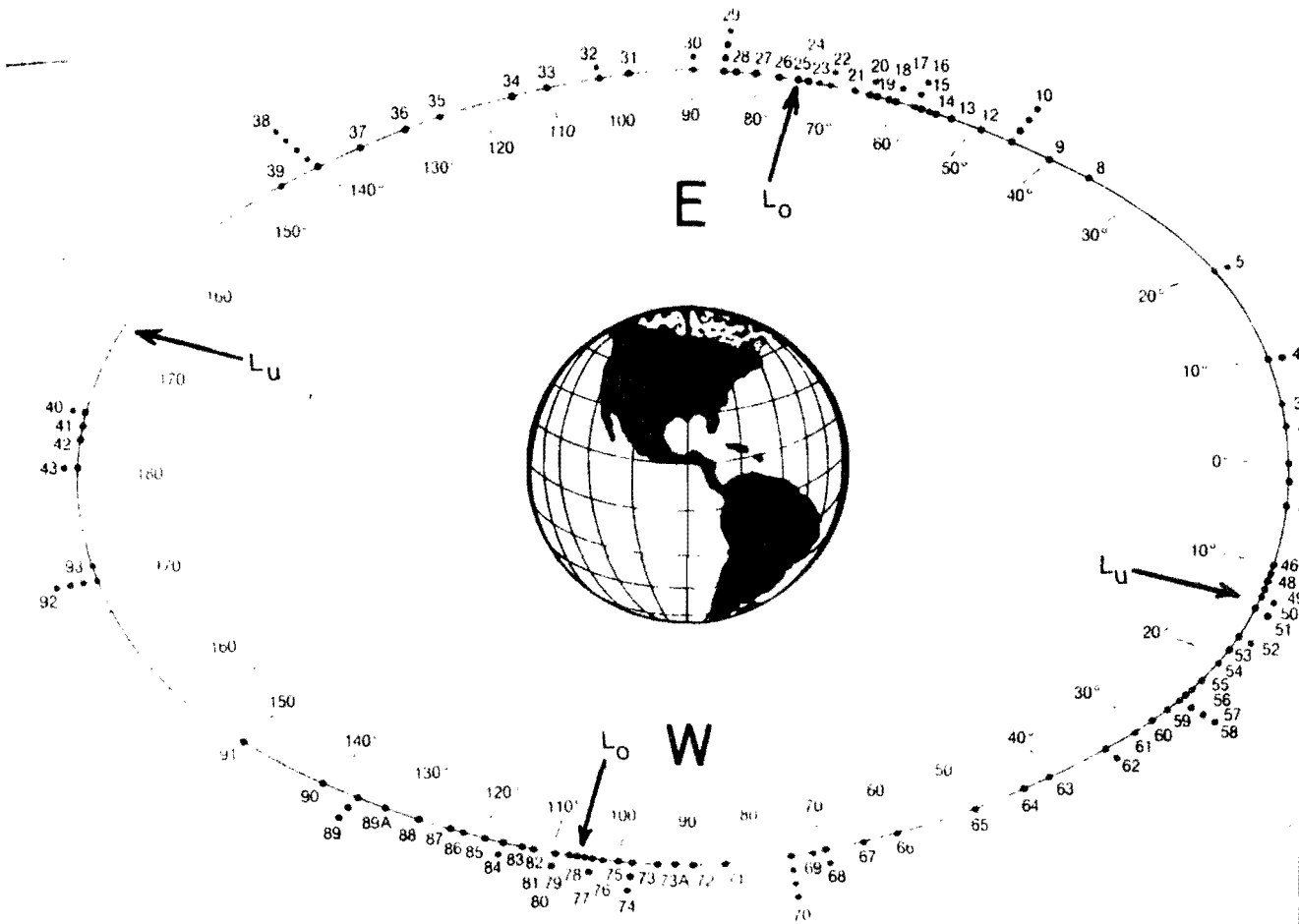


Fig. 2: Geostationary satellites planned or in service by 1980.  
 $L_0$  stable longitudinal equilibrium,  $L_u$  unstable longitudinal equilibrium.

The area on the Earth which is visible from a satellite is called its field of view (FOV). The FOV of a perfectly geostationary satellite is fixed; any observation point in its FOV will have constant range and observation angles to the geostationary satellite. Hence it is (relatively) easy for earth

antennas to acquire and track geostationary satellites.

It is obvious that the geostationary orbit is a limited natural resource. It should be used as efficiently as possible to reduce mutual interference between closely spaced satellites. The positions of greatest interest are midway over oceans (for intercontinental and maritime traffic) and over land (for regional or domestic traffic); this results in several satellite clusters in the geostationary orbit (Fig. 1). High antenna sidelobes of earth terminals is one limiting factor in the occupation of such clusters. Another is the inability to keep the satellites fixed relative to each other.

#### 1.4. Perturbations and stationkeeping in the geostationary orbit

Unfortunately, the geostationary orbit is a wishful idealization. Once placed there, a radio station onboard a satellite inevitably drifts away from its desired position due to several small, but significant perturbing forces, mainly

- (a) solar and lunar gravity and radiation pressures which, if left uncorrected, cause a natural inclination of the orbital plane between  $0.75^{\circ}$  and  $0.95^{\circ}$  in one year. This annual inclination increment has a long-term periodicity of 17 years, the next maximum occurring in 1987 ( $0.95^{\circ}/\text{year}$ ).
- (b) asymmetric Earth potentials, caused by the non-spherical and inhomogeneous Earth. There are two points of stable equilibrium in the geostationary orbit (at  $L_0 \sim 105^{\circ}$  W and  $L_0 \sim 75^{\circ}$  E longitude) and two unstable positions  $90^{\circ}$  away from these (Fig. 2); a satellite at any other position will start to drift along the Earth Equator\*.

The necessary compensation of these forces is obtained by accurate firing of reaction equipment (thrusters, microjets) onboard the satellite in order to keep it on station. Compensation of the inclination increments corresponds to N-S stationkeeping and requires a thrust impulse perpendicular to the

---

\* After their useful life, satellites may be 'buried' in one of the stable minima to avoid drifting 'ghost' spacecraft producing unnecessary radio interference and radar disturbances in the management of the geostationary orbit.



orbital plane. E-W stationkeeping (as well as quick relocation to a different satellite position in the geostationary orbit) are obtained by applying thrusts in the orbital plane.

The new Radio Regulations [3] require of ITU members that satellites in the geostationary orbit can be kept there with an E-W accuracy of better than  $\pm 0.1^\circ$ . This is a considerable tightening of the previous regulation; the reason may be guessed from a glance at the satellite congestions in Fig. 2. However, except for future satellites to broadcast audio or television directly to the general public, ITU does not demand N-S stationkeeping at present. As will be shown below, N-S corrections are considerably more costly in terms of fuel expenditure for the reaction equipment. Depending on the extra cost to the ground system of earth terminals with tracking antennas and receivers which are tolerant to the variations in transmission delay and Doppler frequency shift caused by moderate N-S movements, a satellite system planner may therefore prefer not to correct the annual change of inclination at all. Instead, the satellite is launched into a slightly inclined orbit such that the inclination first decreases from  $i_{\max}$  to zero, and then again increases to  $i_{\max}$ . If the planned lifetime of the satellite is  $T_L$  years, then approximately

$$i_{\max} \approx \frac{1}{2} i_{av} T_L \quad (6)$$

where  $i_{av}$  is the natural annual change of inclination averaged over the lifetime  $T_L$ . A typical value for long-lived satellites is  $i_{av} = 0.86^\circ$ .

In many modern satellite systems, N-S stationkeeping will be a requirement due to the use of low-cost terminals without full antenna tracking capabilities, or to problems with correct signal timing in digital networks. If the small inclination angle to be cancelled is  $\Delta i$  (radians), the required thrust impulse normal to the satellite orbital velocity vector  $\vec{V}$  should result in the change

$$\Delta V_{NS} = |\vec{V}| \tan \Delta i \approx V \Delta i \quad (7)$$

For a geostationary satellite, the orbital speed is

$$V = \frac{2\pi a}{T_p} = 3075 \text{ m/s} \quad (8)$$

If the planned useful lifetime of the satellite is  $T_L$ , the sum of all velocity increments for N-S stationkeeping manoeuvres through the planned operational life is

$$\Delta V_{NS} = V \int_0^{T_L} \Delta i = V T_L i_{av} \quad (9)$$

Assuming  $T_L = 10$  years and  $i_{av} = 0.86^\circ$  gives  $\Delta V \approx 460$  m/s, indeed no trivial velocity increase! This has implications for the extra fuel and mass at launch of a satellite with N-S stationkeeping.

Concerning the unavoidable E-W stationkeeping in the geostationary orbit, the most significant change of satellite longitude  $L$  due to Earth asymmetry is given by the equation of motion

$$\ddot{L} + k^2 \sin 2(L - L_0) = 0 \quad (10)$$

where the measured value of the perturbation constant for attraction to the nearest equilibrium (at  $L_0$ ) is  $k^2 = 4 \cdot 10^{-15} \text{ rad/s}^2$ . The dot operator denotes, as usual, a time derivative. Multiplying by  $2\dot{L}$  and integrating once, we find

$$(\dot{L})^2 - k^2 \cos 2(L - L_0) = C_1 \quad (11)$$

which gives the family of curves plotted in Fig. 3 for different values of the integration constant  $C_1$ . For  $C_1 > k^2$ , the drift rate  $\dot{L}$  of an uncontrolled satellite is too high for an oscillation trapped around the stable point  $L_0$ . Instead, the Earth is slowly encircled along the Equator, either eastwards ( $\dot{L} > 0$ ) or westwards ( $\dot{L} < 0$ ).

However, for  $|C_1| < k^2$ , there will be turning points in the orbit of an uncontrolled quasi-geostationary satellite, namely, where  $\dot{L} = 0$ . In this case, the satellite is trapped in an oscillation about the stable point of equilibrium ( $\theta = 0$ ), where

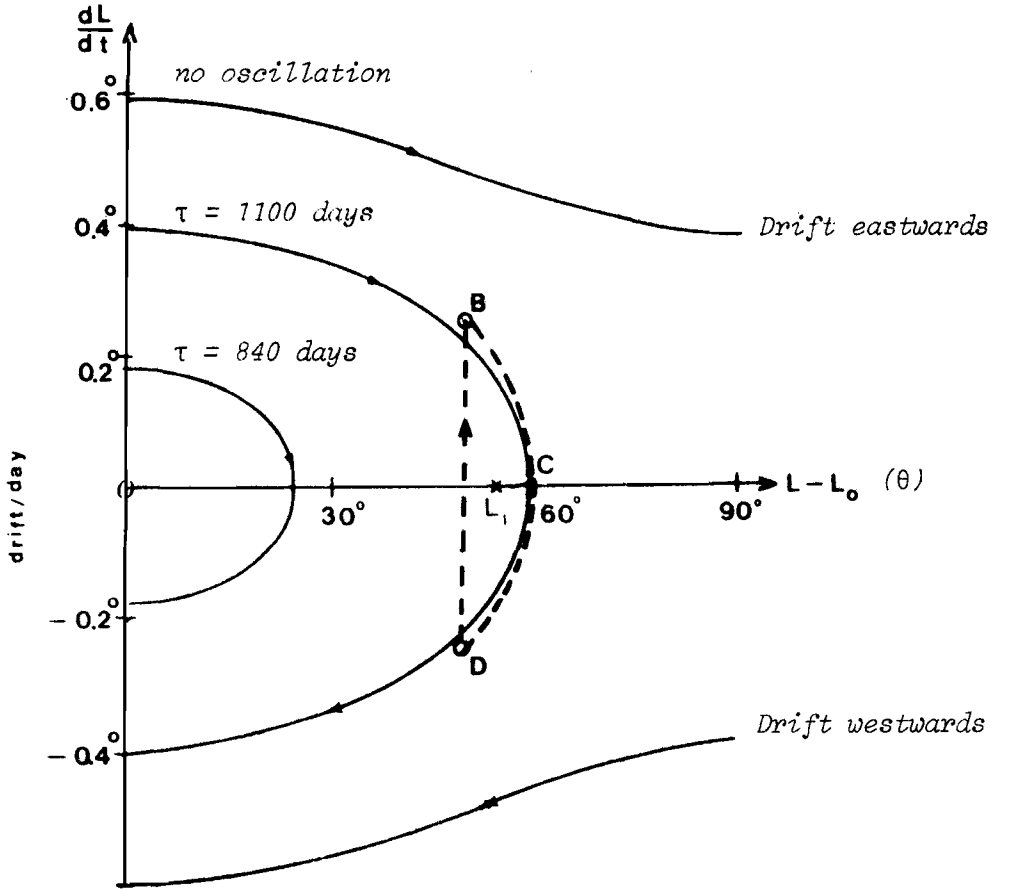


Fig. 3: Satellite drift rate ( $\dot{L}$ ) along the geostationary orbit as a function of angular spacing from nearest equilibrium ( $L_0$ ), with longitudinal oscillation period as a parameter. (Diagram extends symmetrically to negative values of  $\theta$ ).

$$\theta \triangleq L - L_0 \quad (12)$$

The corresponding differential equation is, rewriting (11)

$$\left(\frac{d\theta}{dt}\right)^2 + 2k^2 \sin^2 \theta = C_1 + k^2 \quad (13)$$

The satellite's turning points in the geostationary orbit are given by

$$\sin^2 \theta_{\max} = \frac{C_1 + k^2}{2k^2} \quad (14)$$

To find the oscillation period,  $\tau$ , combine (13) and (14) into the equation

$$\frac{dt}{d\theta} = \frac{1}{\sqrt{C_1 + k^2} \sqrt{1 - (\sin\theta/\sin\theta_{\max})^2}} \quad (15)$$

which can be integrated over one fourth of the complete period

$$\begin{aligned} \int_0^{\tau/4} dt &= \frac{1}{\sqrt{C_1 + k^2}} \int_0^{\theta_{\max}} \frac{d\theta}{\sqrt{1 - (\sin\theta/\sin\theta_{\max})^2}} \\ &= \frac{1}{\sqrt{2k^2}} \int_0^{\pi/2} \frac{dx}{\sqrt{1 - \sin^2 x \sin^2\theta_{\max}}} \end{aligned} \quad (16)$$

The last integral, known and tabulated as the complete elliptic integral  $F(\sin\theta_{\max}, \frac{\pi}{2})$ , was obtained by the substitution of variable

$$\sin x \triangleq \sin\theta/\sin\theta_{\max}$$

Consequently, the time to complete one complete oscillation induced on a nominally geostationary satellite by the most significant equatorial asymmetry of the Earth gravity is

$$\tau = \frac{2\sqrt{2}}{k} F(\sin\theta_{\max}, \frac{\pi}{2}) \quad (17)$$

This indicates how exceedingly weak this perturbing force is: the constant factor is of the order of 500 days, while the elliptic integral is never smaller than  $\frac{\pi}{2}$ .

Nevertheless, most communications satellites have to remain close to a prescribed longitude  $L_1$  (Fig. 2), say within an interval of width  $\Delta L_{\max}$ . Whenever  $L_1 \neq L_0$ , it is thus necessary to enforce a smaller oscillation around the point  $L_1$ , with an amplitude of  $\Delta L_{\max}$  (peak-to-peak). In general, this interval is determined by system considerations (such as the tracking ability or beamwidth of the ground antennas), within the bound laid down by the ITU Radio Regulations [3] already mentioned ( $\pm 0.1^\circ$ ).

In the phase space of Fig. 3, the E-W stationkeeping is achieved by letting the satellite move freely through this interval once (along the curve BCD) and then precisely reverse the drift rate at the point D by a thrust impulse sufficient to re-start this cycle at the point B. The corresponding calculations proceed as follows:

Writing  $L = L_1 + \Delta L$ ,  $2|\Delta L| \leq \Delta L_{\max}$ , Eq. (13) gives to first order in  $\Delta L$

$$(\dot{L})^2 + 2k^2 \Delta L \sin 2(L_1 - L_0) \approx C_1' \quad (18)$$

An exaggerated example of this parabolic approximation to (13) is shown stippled in Fig. 3. The new constant  $C_1'$  is determined at the point C, (where  $\dot{L} = 0$ , and  $\Delta L = \Delta L_{\max}/2$ ). Next, the required impulsive change of drift rate is determined, using (18) at the points B and D (where  $\Delta L = -\Delta L_{\max}/2$ ), to be

$$|\dot{L}_B - \dot{L}_D| = |2\dot{L}_B| \approx 2k \{2\Delta L_{\max} \sin 2|L_1 - L_0|\}^{\frac{1}{2}} \quad (19)$$

The actual sign, corresponding to the direction of the thrust, must be selected to counteract the attraction to the stable equilibrium  $L_0$ , as determined by the sign of  $L_1 - L_0$  in (18).

(The corresponding velocity change of the satellite is obtained by multiplying (19) by the orbit radius  $a$ ). This reversing thrust must be repeated with a period  $\tau_p$  found by integrating (18) from B to C in Fig. 3

$$\int_0^{\tau_p/2} dt \approx \frac{1}{k} \int_B^C \{(\Delta L_{\max} - 2\Delta L) \sin 2(L_1 - L_0)\}^{-\frac{1}{2}} dL$$

i.e., accounting also for the possibility  $L_1 - L_0 < 0$

$$\tau_p \approx \frac{2\sqrt{2}}{k} \left[ \frac{\Delta L_{\max}}{\sin 2|L_1 - L_0|} \right]^{\frac{1}{2}} \quad (20)$$

From (19) and (20), note that the sum of all satellite velocity changes required for E-W stationkeeping throughout the satellite lifetime  $T_L$

$$|\Delta V_{EW}| = |2a\dot{L}_B T_L / \tau_p| \approx k^2 a T_L \sin 2|L_1 - L_0| \quad (21)$$

to the first order is independent of the specified tolerance  $\Delta L_{\max}$ . E-W stationkeeping accuracy is therefore limited only by the precision of the reaction control equipment and by the period  $\tau_p$  between the firing commands, but not by the amount of fuel carried by the satellite for stationkeeping.

As an example, suppose that a nominally geostationary satellite has to be maintained at the longitude  $L_1 = 0^\circ \pm 0.1^\circ$  during a life of  $T_L = 10$  years. Noting that

$$\sin 2|L_1 - L_0| = \sin 150^\circ = 0.5$$

$$\Delta L_{\max} = 0.2^\circ = 0.00349 \text{ rad},$$

we find that by firing the thruster(s) every

$$\tau_p \approx 2 \left[ \frac{2 \times 0.00349}{0.5 \times 4.10^{-15}} \right]^{\frac{1}{2}} \text{ sec.} = 43 \text{ days} \quad (\text{from 20})$$

when the drift rate reaches a maximum of

$$\dot{L}_D = (4.10^{-15} \times 2 \times 0.00349 \times 0.5)^{\frac{1}{2}} \text{ rad/s} \quad (\text{from 19})$$

$$= 0.02^\circ/\text{day} \text{ (eastwards towards the nearest stable equilibrium)}$$

the satellite is kept inside the required interval. The total westward velocity impulses summed over the entire satellite lifetime

$$\Delta V_{EW} \approx -(4.10^{-15}) \times 42164.10^3 \times (10 \times 365 \times 24 \times 3600) \times 0.5$$

$$= -27 \text{ m/s} \quad (\text{using 21})$$

are seen to be much less than required for N-S stationkeeping (9). Thus, more than 90% of the thruster fuel for stationkeeping may be saved, when the ground network can tolerate complete absence of N-S corrections of the orbit of a nominally geostationary satellite. The extra useful payload onboard the satellite may be an attractive trade-off, but obviously involves careful consideration of the wider pointing or beamwidth margins of the antennas

required in the absence of N-S stationkeeping.

This summary treatment of the dominant N-S and E-W perturbations in the geostationary satellite orbit is intended to quantify those phenomena directly affecting microwave antenna designs and daily pointing alignments in a satellite communications network. It should not completely escape our attention that there are also weaker perturbation forces; these may potentially affect systems with very narrow beams, such as EHF and laser links. Fig. 4 shows the principle of a typical geodetic satellite experiment, intended to map the fine structure of Earth gravity by laser tracking of smaller satellites from a master satellite. Such measurements are desirable

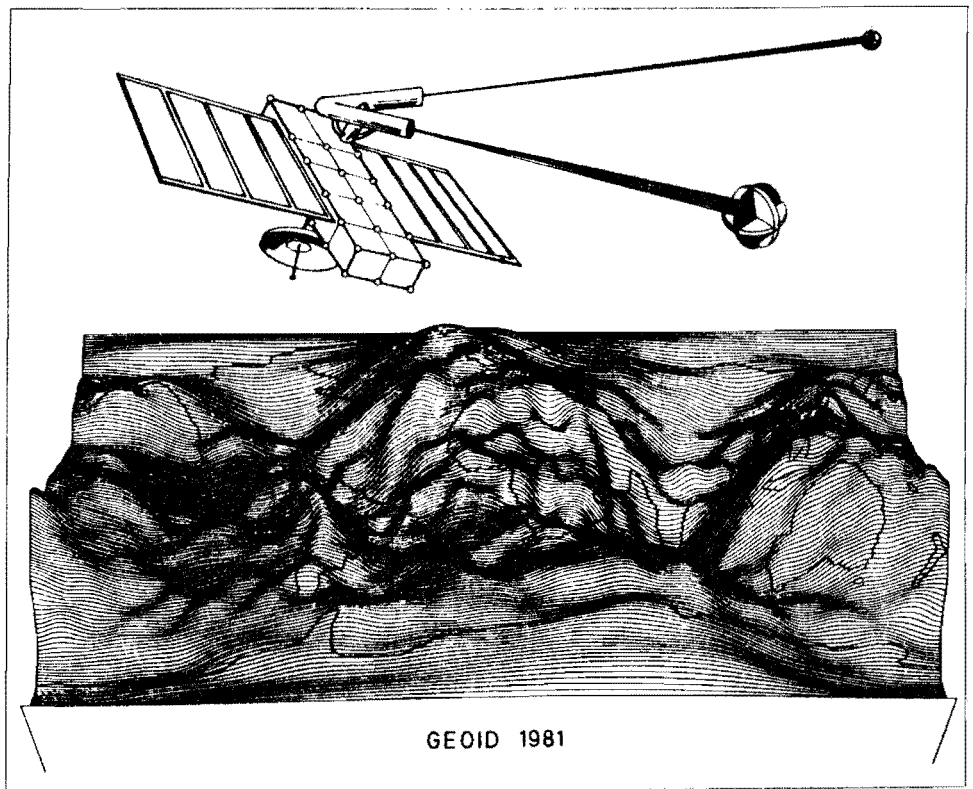


*Fig. 4: Geodetic satellite measurement of Earth gravity variations by intersatellite laser tracking (from S. Hieber, ESA Bulletin No. 28, Nov. 1981). The experiment demonstrates the potential significance of orbit perturbations on EHF and optical antenna pointing.*

for precise orbit determination required for navigation satellites and as remote sensing of Earth crust movements (earthquake early warning!) or hidden mineral deposits. As the wavelength and antenna beamwidth of future satellite systems decrease, satellite antenna technology may conceivably be confronted with such small-scale angular perturbations, too.

### 1.5. Antenna tracking on Earth-satellite links

After having briefly described dynamics and stationkeeping of orbiting satellites, it is now appropriate to change from the reference frame (fixed orientation in space) to geographical coordinates. This allows the pointing angles of earth terminals and coverage areas of satellite antennas to be described from our rotating Earth, which for this purpose can be considered spherical. (A more accurate approximation for calculation of path lengths and delays is Hayford's spheroid, for which the semi-axis to the North or South Pole is 6356.9 km, corresponding to a flattening at the poles of  $1/297$ . For local link descriptions, the actual heights above mean sea level may be required, e.g., in calculations of interference between an earth terminal and a terrestrial radio-relay antenna. These calculations are not our main concern here).

Fig. 5 shows a satellite S (in an inclined, direct orbit) at a distance  $KR_0$  from the Earth centre,  $R_0$  being the radius of the "spherical" Earth (6378.4 km), with the dimensionless parameter  $K > 1$ . An earth terminal J with geographical longitude  $l_j$  and latitude  $b_j$  tracks S with elevation angle  $\epsilon$  ( $0 \leq \epsilon \leq 90^\circ$ ) and azimuth  $A$  ( $0 \leq A < 360^\circ$ , measured from local N through E). The point  $S'$  ( $l_s, b_s$ ) is called the subsattellite point. The satellite passes the equatorial plane from the South in the point A (ascending node) at time  $t_0$ . As previously indicated, the inclination angle  $i$  ( $0 \leq i < 180^\circ$ ) is less than  $90^\circ$  for direct orbits and equals  $90^\circ$  for polar orbits. Geographical longitudes ( $-180^\circ < l \leq 180^\circ$ ) will be taken positive if east of Greenwich; latitudes ( $-90^\circ \leq b \leq 90^\circ$ ) will be taken negative if south of Equator. If the satellite is synchronous in a circular orbit, it is simple to determine the geographical coordinates of the subsattellite point  $S'$ . The angular velocity of the satellite is then constant and equal to





$$\omega_E = 2\pi/T_p = 7.29217 \times 10^{-5} \text{ rad/s} . \quad (22)$$

From the right-angled spherical triangle A'S'F', the geographical coordinates of S' are given by

$$\sin b_s = \sin i \sin \omega_E(t - t_0) \quad (23)$$

$$\tan\{l_s + \omega_E(t - t_{\text{ref}})\} = \cos i \tan \omega_E(t - t_0) . \quad (24)$$

Here,  $t_{\text{ref}}$  is the time when the Greenwich meridian plane ( $l = 0$ ) rotates through the ascending node (A), while  $t_0$  is the time when the satellite passes A.

In the important special case of a quasi-geostationary orbit,  $i$  is a small angle. Neglecting third-order and higher terms of  $i$  gives

$$b_s \approx i \sin \omega_E(t - t_0) \quad (25)$$

and

$$l_s + \omega_E(t - t_{\text{ref}}) \approx \text{Arctan} \left\{ \left(1 - \frac{1}{2} i^2\right) \tan \omega_E(t - t_0) \right\} .$$

Taylor-expansion of the Arctan-function results in

$$\begin{aligned} l_s &\approx -\omega_E(t_0 - t_{\text{ref}}) - \frac{1}{2} i^2 \frac{\tan \omega_E(t - t_0)}{1 + \tan^2 \omega_E(t - t_0)} \\ &= \omega_E(t_{\text{ref}} - t_0) - \frac{i^2}{4} \sin 2\omega_E(t - t_0) . \end{aligned} \quad (26)$$

Eqs. (25) and (26) show that the daily movement of the subsatellite point S' is an 8-shaped figure around the Equator point with longitude  $\omega_E(t_{\text{ref}} - t_0)$ . The maximum daily latitude variation is  $\pm i$ ; this is much more than the daily longitude variation ( $\pm i^2/4$ ), when  $i$  is small. Nevertheless, imperfect N-S stationkeeping ( $i \neq 0$ ) is seen to result in some diurnal E-W movements of S', even for a perfectly synchronous orbit. These E-W movements come in addition to the slower perturbations considered in Fig. 3, and to those caused by any residual eccentricity of the circular orbit [8].

Given the geographical coordinates of the subsatellite point S', we are now in a position to determine the pointing angles  $\epsilon$  and A, as well as the satellite range  $\rho = JS$ , for the earth terminal J. Using the plane triangle OJS (Fig. 6), the range and the elevation  $\epsilon$  are determined by

$$\rho^2 = R_0^2 (K^2 + 1 - 2K \cos d) \quad (27)$$

$$\epsilon = \text{Arcsin}\{(K \cos d - 1) / (K^2 + 1 - 2K \cos d)^{1/2}\} \quad (28a)$$

where d is the great-circle distance JS'. From spherical trigonometry (Fig. 7)

$$\cos d = \cos b_J \cos b_S \cos (l_J - l_S) + \sin b_J \sin b_S \quad (29)$$

$$\sin A = \frac{\cos b_S}{\sin d} \sin (l_S - l_J) \quad (30)$$

(Care should be taken to select the proper value of the azimuth angle A in the range  $0 \leq A < 360^\circ$ ). An alternative useful expression for the elevation is obviously

$$\epsilon = \text{Arctan}\{(\cos d - 1/K)/\sin d\} \quad (28b)$$

The theoretical field of view of the satellite is contained within the closed curve at the Earth at which  $\epsilon = 0$ . From (28) this curve is determined by having the great-circle distance

$$d_{\text{FOV}} = \text{Arccos } \frac{1}{K} \quad (31)$$

from the subsatellite point S'. In particular, for a geostationary satellite, K is constant and equal to

$$K = a/R_0 = 42164/6378 = 6.61$$

so that ideally

$$d_{\text{FOV}} = \text{Arccos } (1/6.61) = 81.3^\circ \quad (32)$$

Communication through geostationary satellites may thus take place from earth terminals up to about 9030 km from the (fixed) subsatellite point S'. In practice this is too optimistic due to terrain screening and the increased atmospheric refraction and attenuation at low elevation angles [7]. There is also a legal consideration: To reduce mutual interference with terrestrial systems, the ITU Radio Regulations [3] require elevation angles to be at least  $3^\circ$  for most operational terminals. The corresponding  $d_{\max}$  can be determined from (28). This equation obviously also allows families of curves for constant elevation to be drawn on a transparent sheet, which can then be translated along the Equator on a map to establish the acceptable geostationary satellite positions for a given network of terminals, or for a certain coverage area. The two arcs of the geostationary orbit, within which a given satellite (i) is seen above the local horizon ( $\epsilon \geq 0$ ) or (ii) can provide adequate service to all of its associated earth terminals and their users, are called its visible arc and its service arc, respectively. These two arcs are important in the initial assessment of potential mutual interference with existing radio systems (including earth terminals in other networks) following an international notification of a new satellite system [3].

Use of (27) allows the uplink and downlink transmission delay  $\rho/c$  (with  $c$  the speed of light) to be calculated for any given satellite link. This may be of interest, especially for two-way telephone circuits or for synchronization of digital links and satellite-switched spot beam antennas in time-division multiple access (SS-TDMA, described later in this Chapter) on p. 1.42).

The satellite range rate (the velocity away from J) is from (27), (29) and (23)

$$\begin{aligned} \dot{\rho} &= - \frac{KR_0^2}{\rho} \frac{d}{dt} (\cos d) \\ &\approx - \frac{i\omega_E KR_0^2}{\rho} \sin b_J \cos \omega_E(t - t_0) + \text{terms of order } i^2 \end{aligned} \quad (33)$$

In deriving (33), the earth terminal was assumed to be static ( $b_J$  and  $l_J$  constant), and not too near to the Equator ( $b_J \gg i$ ). For mobile terminals or terminals in the equatorial region, a more complete time derivative of

(29) is required. Expressions including orbit eccentricity are found in [8]. The frequency shift of a signal with frequency  $f$  due to Doppler effects is

$$\Delta f \approx -\dot{\rho}f/c \quad (34)$$

Thus microwave signals are shifted (and wideband signals stretched) in frequency by satellite range-rate effects.

Analytical formulas have been provided throughout this Section, rather than graphs, so that they can be included in computer software for antenna designs or assessments in a system context. The reader will also find it easy to use these formulas with a simple pocket calculator, as the following closing example shows.

An earth station at Eindhoven, the Netherlands, ( $l_J = 5.50^\circ$ ,  $b_J = 51.42^\circ$ ) tracks a quasi-geostationary satellite at  $l_S = 10^\circ$  with inclination  $i = 4.3^\circ$ . For  $t = t_0 + n\pi/\omega_E$ , there is an Equator crossing, so

$$b_S = 0 \quad (\text{from 23})$$

$$\cos d = \cos 51.42^\circ \cos 4.5^\circ = 0.6217 \quad (\text{from 29})$$

$$\rho = R_0 \{6.61^2 + 1 - 2 \times 6.61 \times 0.6217\}^{1/2} \quad (\text{from 27})$$

$$= 6.039 R_0 = 38519 \text{ km.}$$

$$\varepsilon = \text{Arcsin} \{(6.61 \times 0.6217 - 1) / 6.039\} = 30.99^\circ \quad (\text{from 28})$$

$$A = \arcsin \{\sin 4.5^\circ / \sin d\} = 174.25^\circ$$

(N.B.!  $A$  is greater than  $90^\circ$  for a terminal on the Northern hemisphere)

$$\dot{\rho} = \pm \frac{4.3 \times 7.292 \cdot 10^{-5} \times 6.61 \times 6378^2 \times \sin 51.42}{180 \times 38519} \text{ km/s}$$

$$= \pm 29.7 \text{ m/s (sign depending on } n)$$

An uplink signal at 30 GHz is shifted by

$$\Delta f = \pm 29.7 \times 30 \times 10^9 / 3 \times 10^8$$

$$= \pm 3 \text{ kHz}$$

An uplink bit stream at 34 Mbit/s is accelerated by  $\pm 3.366$  bits per second or about  $\pm 12$  kbits in an hour. Downlink shifts should be added to this. There are obvious consequences of these frequency effects in a digital network, whereas antenna designs proper are hardly affected. However,  $\epsilon$  and  $A$  will vary substantially during the day (try  $t = t_0 + (n + \frac{1}{2})\pi/\omega_E$ ). Therefore, the earth station should possess either a wide beam with moderate gain, or else a tracking antenna system. So if the latter is based on a narrowband phase-locked loop receiver, this must be able to follow the Doppler variations of the satellite beacon signal. Clearly, the satellite orbit influences the choice of antenna system technology!

Let the antenna gain on the main-beam axis ( $\phi = 0$ ) be  $G_{\max}$ . (For a circular aperture of diameter  $D$  and r.m.s. deviation from an ideal geometrical surface  $\delta$

$$G_{\max} = \eta_{\text{eff}} \left( \frac{\pi D f}{c} \right)^2 \exp \left\{ - \left( \frac{4\pi f \delta}{c} \right)^2 \right\} \quad (35)$$

where  $\eta_{\text{eff}} < 1$  is the antenna efficiency in the absence of surface errors). Any pointing error ( $\Delta\phi$ ) reduces the available gain in the direction of the satellite. Approximating the main-lobe pattern by an exponential pencil beam

$$G(\phi) = G_{\max} \exp \left( -k_1 \left( \frac{\phi}{\phi_{3\text{dB}}} \right)^2 \right) \quad (36)$$

we find  $k_1 = 2.764$  by identifying

$$G(\frac{1}{2}\phi_{3\text{dB}}) \triangleq \frac{1}{2} G_{\max} \quad (37)$$

Moreover, since the 3-dB beamwidth is inversely proportional to the antenna diameter  $D$  and to frequency

$$\phi_{3\text{dB}} = k_2 c / (fD) \quad (38)$$

where  $k_2$  is typically 65-70 degrees, Eqs. (36) - (38) give for the pointing loss

$$\Delta G(\Delta\phi) = -12 \left( \frac{\Delta\phi f D}{k_2 c} \right) \text{ dB} \quad (39)$$

Together with (35), this shows that for any given pointing error, there will be a maximum profitable antenna diameter  $D_{\max}$  (or frequency  $f_{\max}$ ) beyond which the achievable gain drops due to poor pointing. Neglecting static gravitational sags, and dynamic deformations by wind or temperature variations, the tracking error may be identified with the pointing error, i.e.,

$$\Delta\phi = \sqrt{(\Delta\epsilon)^2 + (\Delta A)^2} \quad (40)$$

Together with Eqs. (28), (30), (25) and (26), this can be used to determine the stepping times of a programme-tracked antenna system, given a maximum pointing loss (39).

#### 1.6. Earth-terminal off-axis limitations

The antenna parameter of greatest immediate interest to the system designer and link budget planner is the gain in the direction of the satellite (i.e.  $G_{\max}$  less the pointing loss  $\Delta G$ ). This figure defines the enhancement, relative to a fictitious isotropic radiator, of the power-flux density emitted (or received) by the earth terminal in the direction of the satellite. The product of the antenna input power and its transmit gain is called the equivalent isotropically radiated power (EIRP). On the other hand, the ratio of its receive gain and the equivalent satellite link noise temperature  $T^*$  is called the terminal operating figure-of-merit (G/T).

---

\*  $T$  is the noise temperature (in kelvin), referred to the output of the receiving antenna, corresponding to the RF noise power which produces the total observed noise at the output of the satellite link, excluding noise due to interference coming from satellite links using other satellites and from terrestrial systems. See Eq. (42) in Sect. 1.8.

Within a certain transmission system, the on-axis antenna gain can obviously be traded off for higher transmit power (or lower noise temperature, as appropriate). However, antenna gain at angles in the direction of geostationary orbit off the main-beam axis has a significant impact on interference caused to, or received from, other geostationary-satellite networks sharing the same frequency bands. This results in various minimum angular spacings between satellites (Fig. 2) which share frequency bands. Likewise, the earth terminal gain in any direction towards the local horizon may result in mutual interference with terrestrial radiocommunication services sharing the same frequency bands. The distance (on a given azimuth  $A$ ) from an earth terminal beyond which a terrestrial radio station sharing the same frequency band neither causes, nor is subject to, interference greater than a permissible level, is known as the coordination distance  $D$ . The contour  $D(A)$  around the earth terminal is known as the coordination contour; it encloses the coordination area, outside of which the risk of interference is reduced to a permissible level.

Interference between networks using adjacent geostationary satellites is assessed in accordance with an internationally agreed method set out in Appendix 29 to the Radio Regulations [3]. Similarly, terrestrial coordination contours around earth terminals are to be calculated in accordance with an internationally agreed method set out in Appendix 28 [3]. In these calculations, many different system parameters (modulation, power levels, required protection ratios, etc.) are relevant. Clearly, the off-axis radiation diagram  $G(\phi)$  of the earth terminal antenna is instrumental for providing sufficient isolation towards other space or terrestrial systems. As progressively more intensive use of the geostationary orbit and the radio spectrum is made, the CCIR is therefore showing increased interest in recommending lower sidelobes of earth terminal antennas. The present recommendation, Rec. 465-1, for a reference radiation pattern for interference calculations (Fig. 8)

$$G(\phi) \leq \begin{cases} 32 - 25 \log \phi \text{ (dB)}, & 1^\circ < \phi < 48^\circ \\ -10 \text{ (dB)}, & 48^\circ < \phi < 180^\circ \end{cases} \quad (41)$$



serves also as a design objective for large earth antennas ( $D/\lambda > 100$ ). At present, there are attempts to have the design objective for the maximum sidelobe level near the main beam tightened by 3 dB (that is, to  $29-25 \log \phi$ ). This could indeed allow increased use of the geostationary orbit, but also causes both objections from owners of existing antennas and additional capital costs for new earth terminals.

An alternative means of improving the orbit utilization is shown in Fig. 8. Instead of reducing the sidelobe level in general (thereby possibly decreasing the antenna aperture efficiency or removing blocking effects), it may be possible to exploit the tighter E-W stationkeeping tolerance required since January 1982 [3] - see page 1.10. In effect, this may allow suppression of specific sidelobes, instead of the present general design approach requiring control of (most) sidelobes as implied in CCIR Rec. 465-1. An auxiliary, defocused feed is used to scan a beam towards an adjacent satellite [9]; interferometric suppression of the sidelobe(s) in that specific direction may then be obtained by suitable cancellation networks [10]. Fig. 8 indicates that theoretically [11] it appears quite feasible to reduce the interference from (or to) a satellite nominally  $1.2^\circ$  away from the main-beam

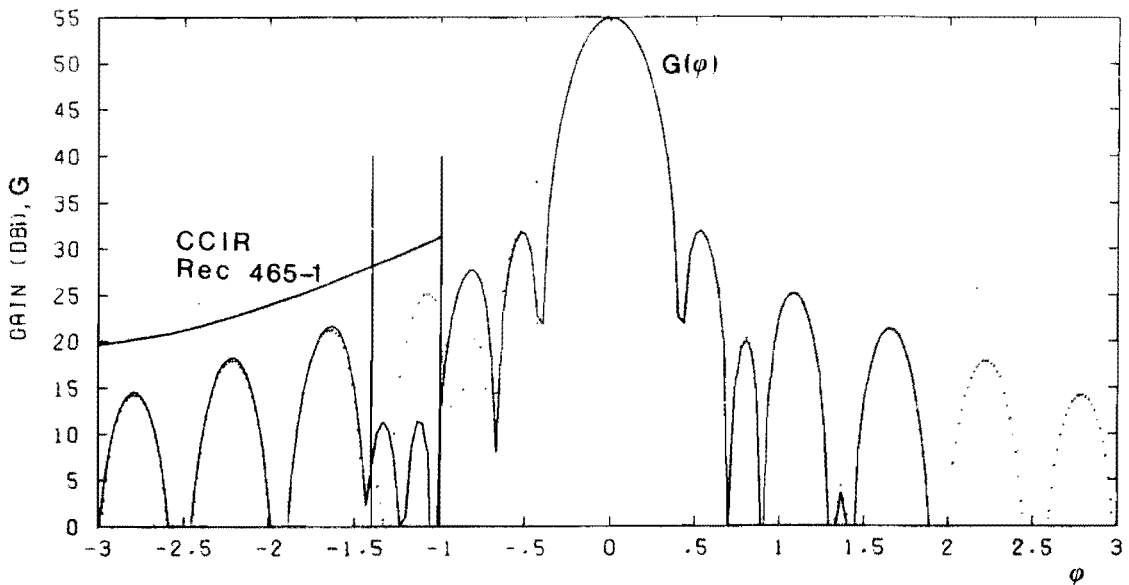


Fig. 8: Interferometric sidelobe suppression in earth terminal to increase intersystem isolation and geostationary-orbit utilization [11].

axis ( $\pm 0.2^\circ$  as arising from the combined maximum E-W tolerances of both satellites), down to the mutual isolation levels reached with present antennas at about  $4^\circ$  satellite spacing. A considerable enhancement in inter-system isolation may thus result, without invoking new reflector systems and with just a relatively simple retrofit of the many existing terminal facilities presently constraining the utilization of the geostationary orbit (Fig. 2). Further investigations towards future implementation of this isolation method may prove worthwhile.

While it will be in the natural interest of any system designer planning a satellite network to avoid harmful interference from other systems into his earth terminals, there is no immediate incentive for him to protect future systems against any interference to them from his system. Consequently, he might be tempted to seek the most cost-effective system trade-off of on-axis gain against transmit power, irrespective of any other potential users of the same bands and the geostationary orbit. (The off-axis gain limits recommended by CCIR (41) are not sufficient to avoid excessive power flux-densities, because the uplink transmit power may be raised indefinitely to meet the on-axis EIRP objective). This is obviously a situation requiring regulation by (international) law.

Harmful interference to other users has been limited by certain provisions laid down in the international Radio Regulations [3]; implicitly, they restrict the freedom in seeking antenna system options and should therefore be carefully studied by any earth antenna designer. Leaving aside some of the exceptions, the most significant technical earth-terminal restrictions can be summarized as follows (see Chapter VIII of the Radio Regulations [3]):

(a) the EIRP towards the horizon within frequency bands shared with equal rights with terrestrial radio services shall not exceed the following limits:

(i) between 1 GHz and 15 GHz

$$\text{EIRP} < \begin{cases} 40 \text{ dBW in any 4 kHz band, for } \theta_h \leq 0^\circ \\ (40 + 3\theta_h) \text{ dBW in any 4 kHz band, for } 0^\circ < \theta_h \leq 5^\circ \end{cases}$$

(ii) above 15 GHz

$$\text{EIRP} \leq \begin{cases} 64 \text{ dBW in any 1 MHz band, for } \theta_h \leq 0^\circ \\ (64 + 3\theta_h) \text{ dBW in any 1 MHz band, for } 0^\circ < \theta_h \leq 5^\circ \end{cases}$$

where  $\theta_h$  is the angle of elevation of the horizon viewed from the antenna radiation centre, measured in degrees as positive above the horizontal plane and negative below it.

- (b) the EIRP limits in (a) may be exceeded by not more than 10 dB. However, if the resulting coordination area enclosed by  $\mathcal{D}(A)$  extends into the territory of another country, such EIRP increase shall be subject to agreement by the Administration\* of that country.
- (c) the elevation angle  $\epsilon$  of a transmitting earth terminal shall not be less than  $3^\circ$ , except by agreement by administrations concerned and those whose services may be affected.

Reciprocally, Chapter VIII of the Radio Regulations also impose technical limitations on terrestrial radiocommunications services sharing frequency bands with satellite services above 1 GHz. These leave room for future introduction of satellite services without harmful interference from terrestrial systems already in use.

#### 1.7. A few definitions of communication satellite stations, systems and services

After having considered their possible path geometries (including terminal pointing), let us now deal with the terminology and operational services of communication satellites. A service involves the transmission, emission and/or reception of radio waves for specific telecommunication purposes. Frequently, these specific purposes are defined in terms of the involved

---

\* see definition in Sect. 1.7.

space stations\* or earth stations\*; the former are located beyond, the latter within, the major portion of the Earth's atmosphere. A satellite link is a radio link between a transmitting earth station and a receiving earth station through one space station onboard a satellite; it comprises one up-link and one down-link. On the other hand, a multi-satellite link comprises one up-link, one or more intersatellite links, and one down-link. A terminal is one end of a RF link. Terminals, stations, and services may be operated by many entities (international, national, as well as private). However, the ITU recognizes only governmental administrations as responsible for discharging the obligations undertaken in the Radio Regulations; all other entities must therefore conclude agreements with a suitable national administration in order to liaise with ITU, e.g. for international frequency coordination and management. In Europe, this is generally a PTT.

A satellite system is any group of cooperating earth stations using one or more earth satellites for specific purposes. A satellite network is a satellite system, or a part thereof, consisting of only one satellite and the cooperating earth stations.

The fixed-satellite service (FSS) is a radiocommunication service between earth stations at specified fixed points when one or more satellites are used. It may also include feeder links from an earth station at a specified fixed point to a satellite, or vice versa, conveying information for a space service other than for the FSS. (The up- and down-links between the TDRS - Fig. 1 - and its earth station are examples of feeder links conveying information for the space operation service, which is concerned exclusively with the operation of spacecraft, e.g. with tracking, telemetry and telecommand (TT&C)).

The broadcasting satellite service (BSS) is a radiocommunication service in which signals (re-)transmitted by space stations are intended for direct

---

\* ITU defines a station as one or more transmitters or receivers, or a combination thereof, including the accessory equipment, necessary at one location for carrying on a radiocommunication service (or radio astronomy).

reception by the general public, either by individual reception by simple domestic installations or by larger installations for community reception. (The BSS is frequently confused with the special use of the FSS allowed by Article 9, § 4 of the Radio Regulations for unilateral transmission from one specified fixed point to more specified fixed points, provided that such transmissions are not intended to be received directly by the general public. This use of the FSS is very widespread in both North America and the USSR for TV-programme distribution to local networks).

The mobile satellite service (MSS) is a radiocommunication service between mobile earth stations and one or more space stations, or between mobile earth stations via one or more space stations. It may include the necessary feeder links (i.e., from specified fixed earth terminals). The MSS can be subdivided in the land, maritime, and aeronautical mobile-satellite services, and may include emergency and distress operations.

The Earth-exploration satellite service (EESS) involves active or passive remote sensing of natural phenomena from earth satellites, the collection of information from airborne or Earth-based platforms, the distribution of this information to earth stations, platform interrogation, and any feeder links necessary. The meteorological-satellite service is a special EESS.

Why are these (and many other) legalistic service definitions contained in the Radio Regulations so significant to the antenna system designer? Because frequency bands have been allocated to each type of satellite service in the member states of the ITU; moreover, strict tolerances for antenna pointing accuracies, radiation patterns or power-flux densities are imposed on certain services. As illustrated by Eqs. (35) and (39) in the previous Section, frequency allocations and technical regulations restrict the design trade-offs available to the antenna engineer, who should always consult the Radio Regulations and the latest CCIR Recommendations [4] before embarking on design of any antenna for a space or earth station in any given satellite service.

### 1.8. Satellite link budgets

Communication antennas are intended to contribute to favourable performance

criteria for the links in a satellite network. In this Section, we shall formulate the performance budget for an individual RF link; earth terminal antennas are designed mainly with this in mind. While the performance of the satellite antennas on each individual link is of course equally significant, they must also satisfy collective requirements related to the shared use by several earth stations in the service area; this will be discussed in the following Section (1.9).

The RF link performance will be derived from a required circuit objective, for instance the performance criteria formulated by the CCIR [4] for the

- noise power in a demodulated TV-channel (Recs. 354-2, 567)
- noise power in a demodulated FDM telephone circuit (Rec. 353-2)
- bit-error rate (BER) in a demodulated PCM channel (Rec. 522).

Based on such general objectives given to the transmission engineer and his own choice of modulating and demodulating equipment, he can translate the circuit objective into a RF-terminal objective at the input to the demodulator. This is normally expressed as the carrier-to-noise density ratio  $(C/N_0)$  required to meet the above circuit objective with a certain margin at the demodulator input.

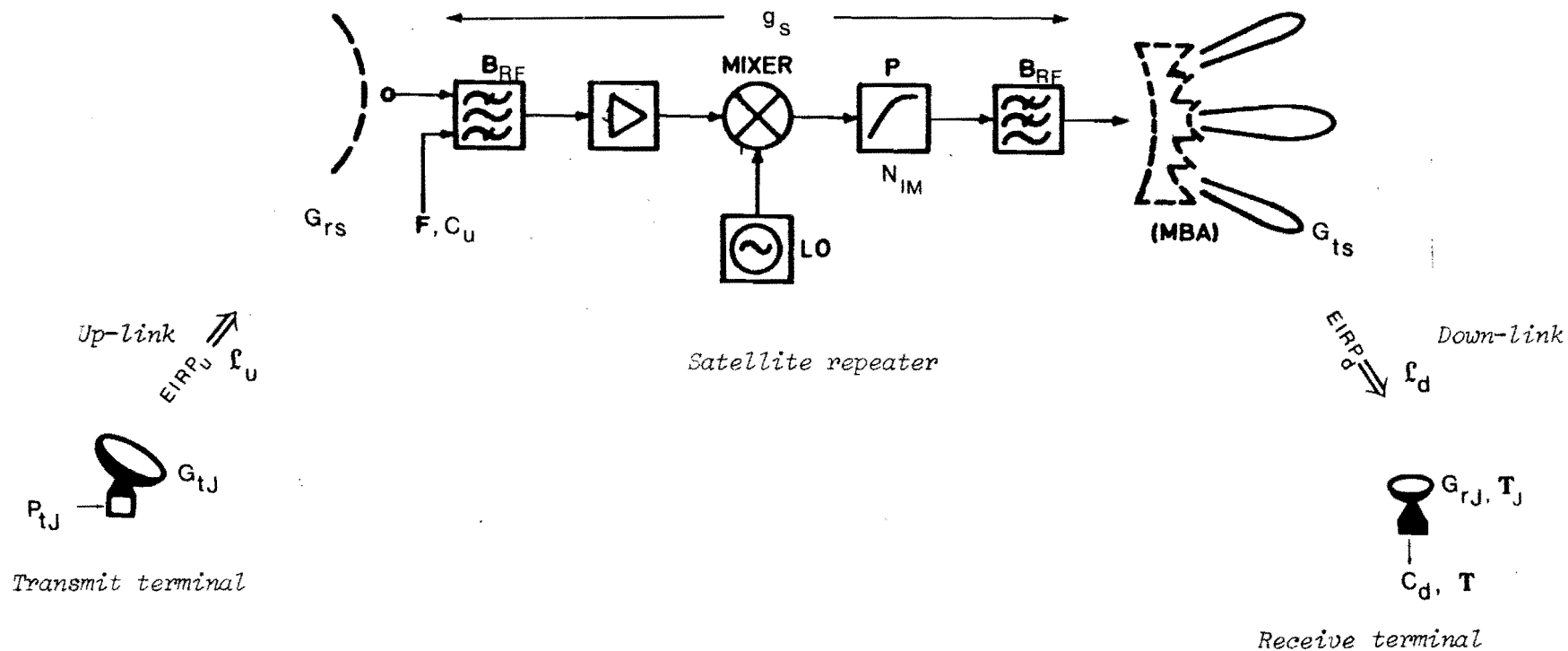
The various signal and noise contributions to this ratio are summarized in Fig. 9. The total noise power density at the receiver is

$$kT = kT_J + \{kT_S g_S + N_{IM}\} \frac{G_{ts} G_{rJ}}{L_d} \quad (42)$$

Note carefully that higher gains of the down-link antennas increase the noise contributions to the operating G/T from the satellite repeater. This is a reason to keep the gain  $g_S$  and noise figure  $F$  of the repeater low. If the satellite receive antenna looks at the "hot" Earth ( $T_0 = 290$  K), then

$$T_S \approx FT_0 \quad (43)$$

The intermodulation noise density  $N_{IM}$  is determined by the access plan and number of carriers sharing the repeater bandwidth simultaneously (Section 1.9). With pure time-division multiple access (TDMA),  $N_{IM} = 0$ ; repeater nonlinearities do not contribute additive satellite noise with TDMA. (Non-



$$\begin{aligned} \text{path loss } (\ell) &= \text{free-space loss} + \text{excess path loss} \\ &= 20 \log \{4\pi f \rho / c\} + \ell_{\text{rain}} \end{aligned}$$

(dB)

$$\text{received noise power density (kT)} = -198.6 \text{ dBm/Hz/k} + 10 \log\{T, \text{kelvin}\}$$

(dBm/Hz)

Fig. 9: Definition of signal and noise contributions to satellite link budget  
(additive noise and non-regenerative repeater assumed).

linearities do, however, contribute to carrier distortion [12]. This multiplicative effect must be separately accounted for in performance budgets and in any up-link power-control algorithms adopted in satellite networks).

The receiving system noise temperature  $T_J$  of an earth terminal at a given frequency is (CCIR Ref. 208-4 [4])

$$T_J = T_{RX} + T_{\text{ground}} + T_{\text{sky}} / \mathcal{L}_{\text{rain}} + (1 - 1/\mathcal{L}_{\text{rain}}) T_{\text{rain}} \quad (44)$$

where

- $T_{RX}$ : noise temperature of receiver (K), referred to the antenna output port
- $T_{\text{sky}}$ : (clear-)sky contribution to antenna noise temperature (K)
- $T_{\text{ground}}$ : ground contribution to antenna noise temperature (K)
- $\mathcal{L}_{\text{rain}}$ : rain attenuation (excess path loss)
- $T_{\text{rain}}$ : effective rain temperature (K)

The system noise temperature is a statistical, time- and location-dependent variable.  $T_{\text{sky}}$  and  $T_{\text{ground}}$  vary with elevation angle  $\epsilon$ , and  $\mathcal{L}_{\text{rain}}$  is also a function of the instantaneous local rain geometry.  $T_{\text{rain}}$  is not the (average) physical temperature of the rain medium [13]; it includes contributions of scattered thermal noise, e.g., from the (cold) sky and the (hot) ground. The empiric expression

$$T_{\text{rain}} = 1.12 T_{\text{ambient}} - 50 \text{ kelvin} \quad (45)$$

is sometimes adopted to allow use of the readily available ambient temperature at the terminal location.

Eqs. (42) - (45) show that the operating figure-of-merit of an earth terminal ( $G/T$  defined on p. 1.24) is smaller than the normally quoted radiometric figure of merit  $G/T_J$  measured in the absence of a satellite repeater, especially when the condition

$$F T_0 g_s G_{ts} / \mathcal{L}_d \ll T_J \quad (46)$$

is not satisfied. With any use of satellite transmit spot-beam antennas, the



satellite's repeater gain and front-end noise must consequently be lower than with Earth-coverage satellite antennas, to maintain a fixed earth-terminal degradation. (Another way of controlling additive noise from the satellite up-link, applicable only in the event of digital transmission, would be to demodulate and remodulate the signal in the satellite. Such a regenerative repeater [14] adds up-link and down-link BERs, rather than noise contributions as in Eq. (42)).

A second observation of major importance to the antenna system engineer concerns the complex influence of (excess) path losses on the G/T-ratios (see (42) and (44)). At the conventional FSS down-link frequencies (3.4 - 4.2 GHz), this is no practical problem because rain losses will be quite moderate for the 99.7% of any month invoked by CCIR performance criteria. For example, standard "A" and "B" earth stations approved by INTELSAT for its international FSS satellite system are merely required to meet one G/T-specification at clear-sky conditions, at elevation angles down to  $\epsilon = 10^0$ . Thus, with  $f$  in GHz

$$\begin{aligned} (G/T)_{\text{"A"}} &\geq 40.7 + 20 \log (f/4) \quad \text{dB/K} \\ (G/T)_{\text{"B"}} &\geq 31.7 + 20 \log (f/4) \quad \text{dB/K} \end{aligned} \tag{47}$$

However, the situation becomes altogether different for standard "C" earth stations working with INTELSAT-V space stations in the bands 10.95 - 11.2 GHz and 11.45 - 11.70 GHz. Due to the potentially much heavier rain losses, local propagation data, clear-sky temperatures and repeater usage must be taken into account in the approval process. The reason is, in INTELSAT's own words [15]: "To ensure the best utilization of the space segment, the aim is to achieve for the receiving system a gain-to-noise-temperature ratio (G/T) that is sufficient to ensure that CCIR performance criteria are met. This requires a consideration of long-term rainfall data and the associated attenuation and sky noise temperature data at each earth station. Considering the form in which propagation information is available, it is more convenient to express CCIR monthly noise criteria in terms of percentage-of-a-year relationships which are chosen to be equivalent to CCIR values. Annual noise criteria are given in terms of "nominal" performance requirements associated with 90% of the time in a year and degraded performance requirements associated with a small percentage of the time in a year".

Accordingly, the antenna system engineer is no longer permitted to consider, once and for all, the gain trade-off with the receiving system noise temperature in clear weather. He is now forced into much deeper individual station studies, as the following specifications show [15]:

- (i)  $G/T_1 - \mathcal{L}_1 \geq A + 20 \log (f/11.2) \quad \text{dB/K} \quad \text{for all but } P_1\% \text{ of the time}$   
(48)
- (ii)  $G/T_2 - \mathcal{L}_2 \geq B + 20 \log (f/11.2) \quad \text{dB/K} \quad \text{for all but } P_2\% \text{ of the time}$
- (iii) In the case of terminals in site diversity (arrangements to avoid the influence of concentrated rain storms) the above specifications apply to the figure of merit derived from the operating terminal at any given time.

In (48), the values of A, B,  $P_1$  and  $P_2$  shown in Table I apply. The term  $\mathcal{L}_i (i = 1, 2)$  is the predicted attenuation relative to a clear sky, at the frequency of interest, exceeded for no more than  $P_i (i = 1, 2)$  percent of the time\*, along the path to the satellite(s) with which operation is desired. The value of  $\mathcal{L}_i$  shall be that predicted on the basis of the statistical distribution of mean attenuation within periods of the order of 1 min. The term  $T_i (i = 1, 2)$  is the receiving system noise temperature, including noise contributions from the atmosphere at the frequency of interest, when the attenuation  $\mathcal{L}_i$  prevails. The terms  $G/T_i$  and  $\mathcal{L}_i$  are assumed to be given in decibel notation; f is the frequency of interest expressed in gigahertz.

Parameter	INTELSAT V Coverage in Which Earth Station is Located	
	West spot	East spot
A	39.0 dB	39.0 dB
B	29.5 dB	32.5 dB
$P_1^*$	10.0 %	10.0 %
$P_2^*$	0.017 %	0.017 %

Table I: Values of parameters specified for INTELSAT-V standard "C" earth stations [15]. Note that spot-beam coverage may be shifted to match traffic requirements.

\* The time period to which this percentage applies shall be that period for which statistics are available, preferably a minimum of 5 years.

Clearly, elaborate propagation studies are a pre-requisite for planning, designing and operating satellite services and earth stations above 10 GHz.

The down-link carrier level at the receiver input is

$$C_d = C_u \frac{g_s G_{ts} G_{rJ}}{L_d} = \text{EIRP}_d \times G_{rJ} / L_d \quad (49)$$

Combining (49) and (42) gives the satellite link carrier-to-noise density ratio

$$\frac{C}{N_o} = \frac{C_d}{kT} \triangleq \frac{1}{\left[ \frac{C_u}{kT_s} \right]^{-1} + \left[ \frac{C_u g_s}{N_{IM}} \right]^{-1} + \left[ \frac{\text{EIRP}_d}{k L_d} \left( \frac{G_r}{T} \right)_J \right]^{-1}} \quad (50)$$

in terms of the up-link carrier-to-noise density ratio

$$\frac{C_u}{kT_s} \triangleq \frac{P_{tJ} G_{tJ} G_{rs}}{k F T_o L_u} = \frac{\text{EIRP}_u}{L_u} \left( \frac{G_{rs}}{F} \right) \frac{1}{kT_o} \quad (51)$$

the repeater output carrier-to-IM density ratio, and the down-link EIRP, earth-station (radiometric) figure-of-merit, and down-link path loss.

As satellite repeaters are, as yet, down-link power-limited, most link budgets are set up to minimize the degradations due to up-link noise and IM noise in (50). This may require up-link transmit power control [16], to combat any fading on the up-link (see 51), and to maintain backed-off operation of the repeater so that any multiple-carrier IM noise will be kept within acceptable bounds [17]. The repeater gain  $g_s$  is selected to satisfy (46) as well as any multiple-access requirement for a back-off ( $\beta < 1$ ) of the total repeater output power shared by  $j$  carriers

$$\sum_j p_j \triangleq \sum_j C_{u,j} g_{s,j} = \beta P \quad (52)$$

below the saturated output level  $P$ . Note that, in general, the repeater gains for the different carriers in a nonlinear satellite will be different [18]. The influence of the various antenna gains is clear from Eqs. (49) - (51).

### 1.9. Multiple access and satellite antennas

A satellite repeater can obviously be shared by several individual signals, without first combining these into a single multiplexed signal. The separate carriers are instead allowed to access the repeater in accordance with a prescribed order, a protocol\* or multiple-access method. This organises the various signals in a known way designed to strike a desired balance between conflict-free sharing and flexible use of the (limited) satellite resources. Multiple access should thus not be confused with multiplexing.

Shared radio channels may be best known from the Citizens' Band at 27 MHz, where the limited common resource is the bandwidth. The multiple-access protocol is here a completely decentralized, self-ordered access based on user demand assignment via a control channel reserved for this single purpose. While a data bus approximates the virtual channel studied by many computer scientists and information theorists, Citizens' Band radio makes use of real channels; fading, interference and other transmission impairments establish significant extra limitations on channel efficiency.

An even more limited physical channel is the typical satellite channel established between distributed earth stations via a spaceborne repeater. Here, too, bandwidth is becoming a limitation due to traffic growth, but in addition the satellite repeater has limited transmit power (requiring relatively large earth stations). The repeater therefore becomes non-linear when efficiently used, producing intermodulation between any simultaneous accesses [17]. As seen in Eq. (50), the down-link antennas can be used to trade-off repeater power for antenna gain, EIRP being the significant figure. Consequently, satellite antenna engineering is closely linked with the multiple-access method adopted in a satellite network.

In general, a multiple-access network consists of  $N$  different users (stations)

---

\* Protocol: from Greek  $\pi\rho\omega\tau\omicron\varsigma$  (= first) and  $\kappa\omicron\lambda\lambda\alpha$  (= glue); originally a record glued to the entry of a document roll and stating its contents. Later the social hierarchy of the diplomatic or military service; official record of a meeting (minutes).

having a need to connect to each other via a common communications channel. If the required communications capacity from user  $i$  to user  $j$  is  $R_{ij}$  (given in bit/s, number of telephone channels, or another suitable unit), we may state the connectivity matrix (also called traffic matrix)

$$\underline{R} \triangleq \begin{pmatrix} R_{11} & R_{12} & \dots & R_{1N} \\ R_{21} & R_{22} & \dots & R_{2N} \\ . & & & . \\ . & & & . \\ R_{N1} & & & R_{NN} \end{pmatrix} \quad (53)$$

For widely separated earth stations in a satellite network, this matrix establishes the requirements for physical links and, by implication, also any possibilities to avoid mutual coverage of some stations. Both aspects are of major interest to the antenna designer, who is concerned with providing the (common) coverage (exactly) where it is needed.

Obviously, the elements of  $\underline{R}$  can either be functions of time, e.g., the varying telephone circuit requirements via an international satellite, or be the busy-hour capacity required to meet the maximum user requirements. Any flexible MA-method designed to respond to fluctuations of the elements is an example of demand assignment of traffic, whereas all fixed MA-methods based on permanent allocation of repeater capacity fall in the category of pre-assignment of traffic.

If row  $i$  is summed, we get the required total outgoing capacity from terminal  $i$

$$R_i \triangleq \sum_{j=1}^N R_{ij} \quad (54)$$

If this is physically combined into one up-link signal by multiplexing (followed by carrier modulation) the transmission is by a multi-destination signal intended for all those terminals  $k$  for which

$$R_{ik} \neq 0 .$$

(55)

A multi-destination signal should generally not be confused with a broadcast signal, for which all receiving terminals wish to receive the same information from terminal  $i$  and hence, in Eq. (54), should be represented by a single entry  $j = b$  so as not to count the same capacity requirement more than once within a given up-link feeding the down-link broadcast.

When the matrix elements from the terminal  $i$  are not combined into a single up-link transmission (54), but are individually sent over the channel, the transmission is a single-destination scheme. An obvious advantage of single destination is that each receiving terminal  $j$  does not need equipment to receive, demodulate and demultiplex the "irrelevant" information in (54) intended for other terminals. The main advantages of multi-destination are that the transmitting terminal  $i$  needs only one single sending chain (with multiplex, modulator, up-converter and RF amplifier), which can be shared by many individual traffic sources. Multi-destination may be preferable where the transmitting costs are relatively high and the up-link traffic is heavy (high-quality international satellite links), whereas single destination may be chosen in a network with many terminals of low cost and complexity (third-world or other thin-route satellite systems).

The diagonal elements in (53) represent "loop" requirements and should at first sight be zero, because a user should never need access to information which he himself has transmitted. However, in a distributed network and a physical channel with variable transmission delays, reception of apriori known information may be necessary to synchronize digital transmissions through the distant repeater (TDMA and CDMA) or to check that a random access has not been destroyed by a random access from another terminal (Aloha). This imposes additional requirements for joint antenna coverage for both the up-link and the down-link.

In order to saturate the satellite repeater without creating intermodulation between carriers, the transmitting earth terminals can be allowed to access the satellite repeater sequentially, one by one, by digital carriers in a burst mode. This is known as time-division multiple access (TDMA). Buffer

stores are required in TDMA earth terminals to translate individual continuous data-rate requirements  $R_{ij}$  into/from a (much higher) common burst-mode data rate  $R_{burst}$ . This can be chosen as large as allowed by the selected digital modulation method (e.g. QPSK) in the available repeater bandwidth  $B_{RF}$ .

The burst time of transmit terminal  $i$  required for its multi-destination carrier to the various receive terminals is given by (Fig. 10)

$$T_{burst,i} = T_{pre} + \sum_{j=1}^N R_{ij} T_{frame} / R_{burst} \quad (56)$$

with  $T_{frame}$  the period length of one complete frame (sequence of bursts from all  $N$  terminals).  $T_{pre}$  is the time occupied by the preamble of each burst and contains a margin for inaccurate synchronization for bursts, time for demodulator synchronization and time for address labels identifying the contents of the multi-destination carrier. An engineering service channel (order wire) to the receiving terminals for liaison and control may also be included. See Fig. 10.

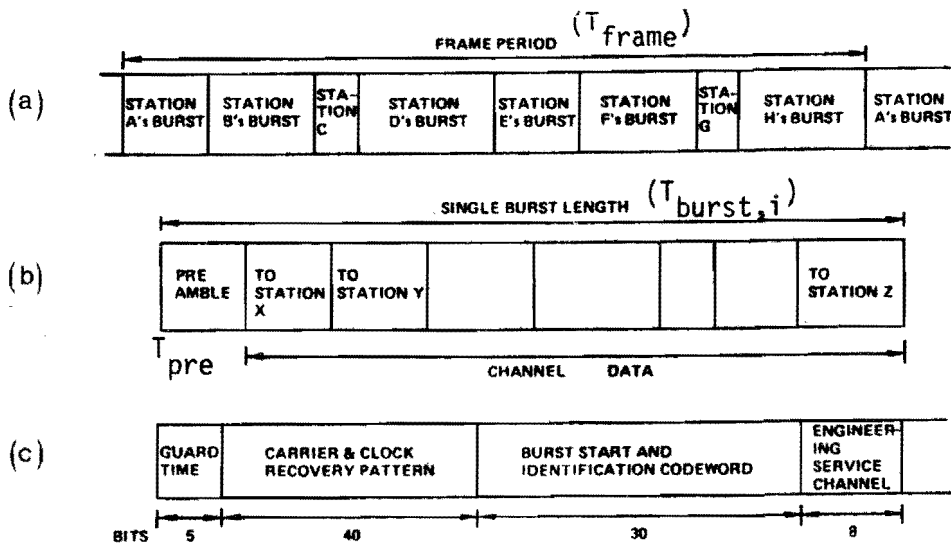


Fig. 10: Access structure in a typical TDMA network.

(a) Frame format. (b) Station burst format. (c) Preamble.

In TDMA networks carrying PCM telephony, the frame period  $T_{frame}$  is often a multiple of 125  $\mu\text{sec}$ .

The burst times within a given frame length are limited by

$$\sum_{i=1}^N T_{\text{burst},i} \leq T_{\text{frame}} \quad (57)$$

which together with (56) gives the bound

$$\sum_{i=1}^N \sum_{j=1}^N R_{ij}/R_{\text{burst}} \leq 1 - NT_{\text{pre}}/T_{\text{frame}} \quad (58)$$

This shows that with a long frame ( $T_{\text{frame}} \gg NT_{\text{pre}}$ ) the burst capacity is efficiently used. This requires big data buffers in the earth stations, as well as very precise terminal synchronization and fast-locking demodulators in order to keep the preamble short. The efficiency of TDMA is thus obtained by imposing high technical standards and a demanding common time discipline throughout the network. This is not at all a simple matter, when the common repeater is moving slightly around its nominal position in the geostationary orbit (Sect. 1.4). Despite the recognized principal advantages of TDMA, it is not yet in widespread operational use in multi-user civil satellite networks and still a subject of much R & D.

Synchronization is frequently governed by a master station, which will send a time reference to all other earth stations (the slaves) as part of its preamble. The slaves adjust their bursts through the satellite relative to this reference, using precise knowledge of their own (variable) transmission delay to the satellite. This can be measured by receiving their own burst as discussed in relation to the connectivity matrix ( $R_{ij} \neq 0$ , loop back), provided that the satellite transmit antenna covers each slave station during its burst.

This is not necessarily so, especially not when spot-beam satellite antennas are used. It was stated above that  $R_{\text{burst}}$  can, in principle, be chosen as large as allowed by the modulation scheme and the repeater bandwidth ( $B_{\text{RF}}$ ). However, the capacity can not be increased indefinitely just by increasing  $B_{\text{RF}}$ , because the satellite EIRP is also bounded and cannot support an arbitrarily high data rate without violating the minimum acceptable performance (BER) of the demodulator. This second bound is given by (50)



$$\left(\frac{C}{N_0}\right) \triangleq R_{\text{burst}} \left(\frac{E_b}{N_0}\right)_{\min} \leq \frac{\text{EIRP}_d}{k f_d} \left(\frac{G}{T}\right)_J \quad (59)$$

where the minimum bit-energy-to-noise-density ratio is determined by the acceptable bit-error rate. With a multi-destination carrier, the maximum achievable burst rate is therefore determined by the one earth terminal with the lowest operating figure of merit and/or the deepest fading. This may not be as efficient as suggested by (58), unless the burst times are adaptively allocated to take this into account [19].

With a single-destination carrier, the satellite antenna gain  $G_{ts}$  could be raised in a particular direction by using a narrow spot beam, and thus the  $\text{EIRP}_d$  could be made higher in (59). This, in turn, would allow a higher burst rate and more information to be transferred within a fixed burst time (56). However, the high antenna gain  $G_{ts}$  would then be required at different destinations for different bursts! In other words, the antenna spot beam should either be scanned over the receiving earth terminals in frame synchronism [20], or else a satellite-borne time-division switch should route the arriving bursts to the right fixed spot beam [21]. The latter solution is known as satellite-switched TDMA (SS-TDMA) and corresponds, in fact, to carrying a higher-order telephone trunk exchange onboard the satellite, which can therefore provide optimum routing of transmission trunks between various lower-order exchanges.

The experimental SS-TDMA repeater planned for ESA's L-Sat is seen in Fig. 11. The switch matrix is programmed by telecommand from a space-operation earth station and sequentially interconnects the transmit and receiver ports of the various spot-beam antennas seen in Fig. 11. The switch matrix must be clocked in synchronism with the TDMA frame format, thus translating the up-link rows in the connectivity matrix (53) into suitable down-link columns. Optimum framing and synchronisation for this is an interesting matrix problem.

If carriers cannot be operated in sequential synchronized bursts, such as in TDMA or SS-TDMA, they may be given different frequency assignments within the bandwidth  $B_{RF}$ . This is known as frequency-division multiple access (FDMA)

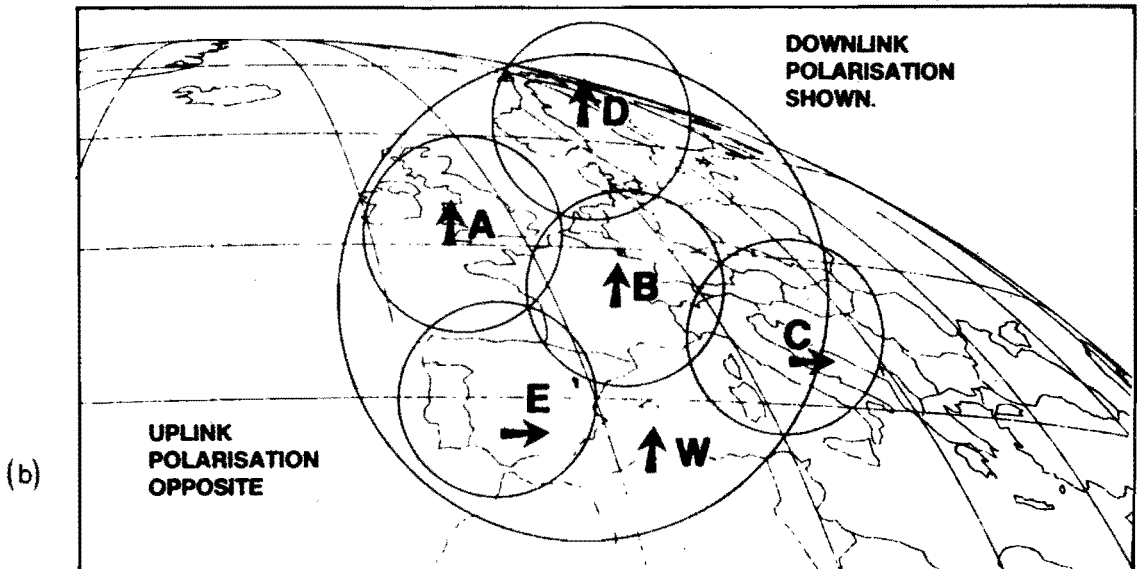
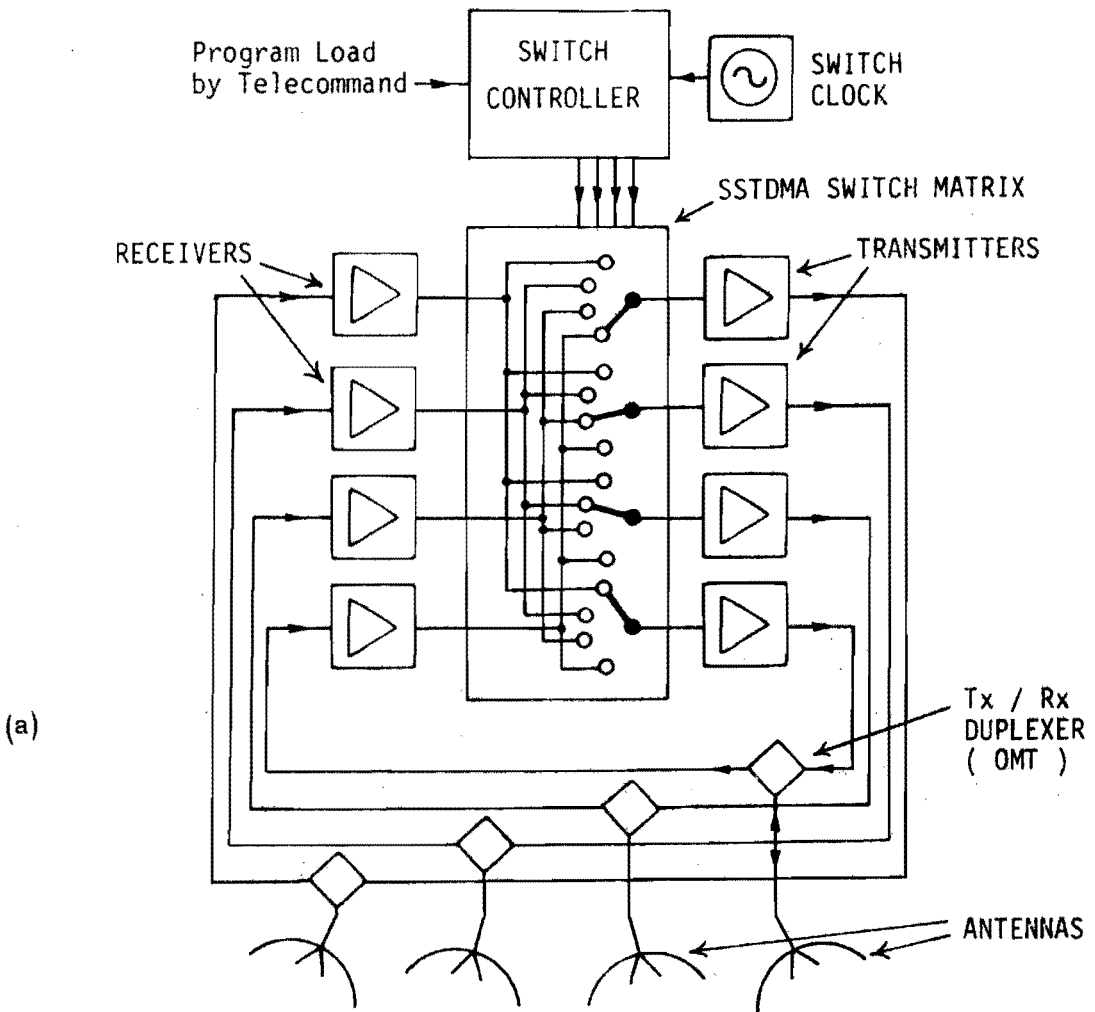


Fig. 11: L-Sat SS-TDMA payload (a), with associated coverage areas (b) over Europe. Note up-link/down-link isolation by dually polarised antennas [from ESA document CCF/25237, Feb. 1982].

and admits less complex digital modems and presence of analogue carriers (FM, etc.).

The capacity limits for single-destination digital FDMA carriers with bandwidth  $B_{ij}$  in a given satellite repeater are

$$\sum_{i=1}^N \sum_{j=1}^N B_{ij} \leq \gamma B_{RF} \quad (60)$$

$$\sum_{j=1}^N \left( \frac{E_b}{N_0} \right)_j \frac{k f_j}{G_{ts,j}} \left( \frac{G}{T} \right)_{J,j}^{-1} \sum_{i=1}^N R_{ij} \leq \beta P \quad (61)$$

where it is assumed that the receiving earth terminals may have different figures of merit and experience different down-link path losses. This allows consideration of traffic adaptation and down-link fading control using satellite multiple-beam antennas [22] with adjustable antenna gains  $G_{ts,j}$  in each down-link direction. In (60) and (61),  $\gamma$  is a parameter reflecting the need to provide some guard bandwidth between two adjacent carriers to avoid mutual interference whereas the back-off  $\beta$  reflects that it may be necessary to reduce the intermodulation products generated between the various carriers in a non-linear repeater (50). Adaptive allocation of capacity in an FDMA network [23] is therefore potentially more complex than the algebraic SS-TDMA problem, whereas the earth stations can be much simpler.

In the preceding, a relaxation has been made from highly disciplined multiple-access methods (TDMA) towards more loosely organized methods (FDMA) with lower efficiency and lower terminal complexity. Obviously, it is possible to relax the multiple-access discipline even further, if each user needs only a short information burst ("packet") from time to time. Then it does not pay to organize the sharing of the collective repeater; each user simply sends his packets off at random, whenever necessary. By receiving his own transmissions back via the repeater and a wide-coverage antenna (loop back,  $R_{ij} \neq 0$ ), any user within the service area can decide whether one of his packets has suffered contention from another overlapping transmission and should be repeated.

Such a random-access scheme becomes advantageous with a multitude of users, each having only short and infrequent needs to access the channel. It was

first investigated by the University of Hawaii for local-area computer networks (and is therefore sometimes referred to as an Aloha-system [24]), but it should also be considered whenever earth terminals must be kept as simple as possible. However, the repeater efficiency is not very high, due to the contentions between packets and the need for a total-coverage transmit antenna. In all events, the satellite capacity is thus inefficiently used (less than 20%). Higher efficiency (up to 37%) can be obtained by disciplining the users to send their packets only in given time slots of fixed length. Clearly, the users have to be synchronized to a common clock marking the slots. Still, contrary to TDMA, each user is free to send a packet in any slot. Thus, slotted Aloha does not depend on any particular sequencing of the terminals (as in Fig. 10), which explains its lower complexity and efficiency, and its higher flexibility.

In general, Aloha and other random-access protocols [24] experience congestion when the offered random traffic is high. It is therefore advantageous to reduce the burst length. This, in turn, is done by selecting the highest possible burst rate allowed by the repeater bandwidth  $B_{RF}$  and down-link EIRP, so that the messages are transmitted as fast as possible. The corresponding formula is identical to that for TDMA, namely (59). Note, however, that a total-coverage down-link antenna is essential for random-access satellite access, whenever some form of transmission control by users is to be maintained. Any use of satellite antennas with narrower coverage than the total service area implies either some form of centralized control or a pre-assigned multiple access method.

#### 1.10. Specification of satellite antennas

From Section 1.9, it is evident that the satellite antenna coverage area(s) must be defined after due consideration of the multiple-access method adopted for a given satellite network. Fig. 12 shows the principal problems: Which gains are required for separate beams in the direction of each earth station? Subsequently, must these various constituent antenna beams be assembled into larger coverage areas or rather remain separate spot beams, to be interconnected by microwave circuitry in the repeater? And do the terminal connectivity and the network capacity require dynamic antenna

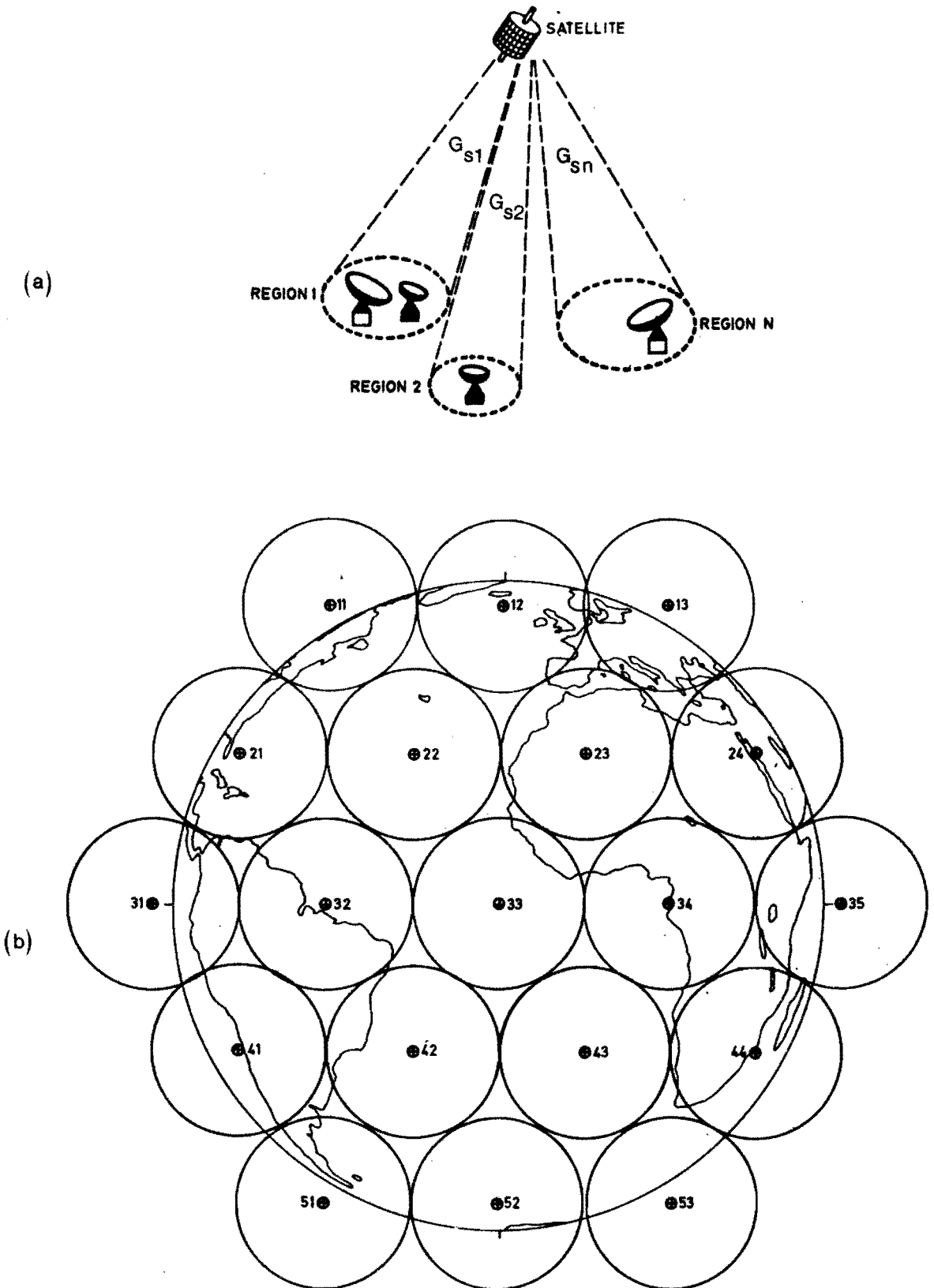


Fig. 12: Satellite coverage of individual regions with different gains (a), obtained by separate excitation of constituent beams (b) [from Ref. 23].

patterns adapting to the traffic pattern, or rather a static pattern for self-ordered access control or broadcast services? Such design questions come in addition to those for the earth station antenna, which is not normally intended to provide links to several(space)stations simultaneously.

However, pointing accuracy is again seen to be a major design constraint. Since the satellite antenna is an integral part of a dynamic platform in the difficult space environment, attitude- and thermal-control accuracies directly affect the ability to point the main lobe towards its earth station(s). Typical open-loop pointing capabilities for spacecraft antennas are of the order of  $\pm 0.1^\circ$  to  $\pm 0.2^\circ$  (r.m.s.). Eqs. (35) - (39) then show that the gain of any constituent beam serving a specific earth target is limited to some 50 dB on-axis, unless closed-loop RF-tracking is included. This extra complexity may be invoked to meet the stringent technical and legal demands on the broadcasting-satellite service in the 12 GHz band [3].

In the absence of sufficient N-S stationkeeping of geostationary satellites, there is also a need to "nod" the satellite antennas during the sidereal day in order to avoid a systematic alignment error of the main lobe over its coverage area. The nodding function can be readily calculated from the geometry shown in Fig. 5, using the formulas for the 8-shaped diurnal movement of the subsatellite point S' in Sect. 1.5.

The individual link budgets (Sect. 1.8) will normally require specification of the minimum satellite antenna gain within the service area. Assuming generating pencil-shaped constituent beams, this will normally apply at their edge-of-coverage (EOC), where the gain slope is greatest. Using (35) and (39) gives

$$G(\phi_{EOC}) = G_{\max} \Delta G(\phi_{EOC}) \quad (62)$$

However, (36) shows that for a given antenna type

$$G(\phi_{EOC}) = \exp \left( -k_1 \left( \frac{\phi_{EOC}}{\phi_{3dB}} \right)^2 \right)$$

with which the 3-dB beamwidth in a given plane can be eliminated in (36) to

give

$$G_{EOC} = -kst \times \Delta G_{EOC} \log_e (\Delta G_{EOC}) \quad (63)$$

The optimum value of this EOC gain loss (found by differentiation)

$$\Delta G_{EOC} = 1/e \sim -4.34 \text{ dB}, \quad (64)$$

giving maximum antenna gain at the edge of coverage, is not very critical.

Considering the cost savings by relaxing antenna pointing in space, the antenna designer may therefore well be tempted to accept broader main beams than (64), because of their attendant lower pointing losses at EOC. Obviously, this could prove very undesirable for other radio systems (to be) located outside the coverage area, because of the increased risk of intersystem interference. Therefore, the ITU has recently tightened the regulation on pointing of any satellite antenna with less than global coverage [3], requiring now a capability of maintaining this within

(a) 10% of  $\phi_{3dB}$  relative to the nominal pointing direction, or (65)

(b)  $0.3^\circ$  relative to the nominal pointing direction, whichever is greater. (In the event of a non-symmetrical main beam, the tolerance in any plane through the axis of maximum radiation shall be related to the  $\phi_{3dB}$  measured in that plane).

To further protect terrestrial radio systems from satellite interference, the ITU has also limited the maximum power flux densities produced at the Earth's surface under assumed free-space propagation conditions. These elaborate limits [3] apply also inside the coverage area of any satellite antenna, and must therefore be observed in all link budgets. In practical terms, they result in a lower bound on the earth-terminal G/T in Eq. (50) required to meet given service performance objectives. Once again, the antenna designer is confronted with the "external" system requirements and international regulations.

Finally, a promising way of designing satellite antennas for flexible use should be mentioned: the weighting together of many constituent beams

(Fig. 12) by an on-board beam-forming network (BFN) . A hard-wired BFN may realise the fixed, but complex coverage required for efficient direct-broadcasting services to a given country [25]. This may be far more attractive than (re-)designing different contoured-beam antennas by reflector shaping, let alone fitting the cruder elliptical beams assumed in [3], for each new national coverage. A time-switched BFN operated "on-off" in synchronism with the earth stations results in SS-TDMA (Fig. 11), with great inherent flexibilities in routing and capacity allocation. In an FDMA network with single-destination carriers, these may be individually enhanced or suppressed by a BFN acting as a lossless, variable power divider. Optimum settings of the beam weights in different operational contexts have been discussed recently in [26, 23] and result in an adaptive antenna pattern, with variable coverage area and variable gain inside the coverage area. The TDRS S-band phased array (Fig. 1) is an example of such an adaptive antenna.

In conclusion, we note the following trends in satellite communications antenna technology:

- (i) On the one hand, an increasing impact of general system requirements (including compliance with international regulations) on the specific design and operational exploitation of antennas in satellite systems
- (ii) As a consequence, on the other hand more emphasis on adaptive, flexible, or multi-purpose antenna systems, to avoid designs or operational situations constrained by unpredictable changes in the specific system requirements or by the substantial non-recurrent costs of developing any specific space antenna system.

Thus, despite the lost paradise of classical antenna theory uncompounded by all earthly desires, the human strive of the space system engineer has remained one for those shapes and patterns which whether

"dilated or condensed, bright or obscure  
can execute their aery purposes".



1.11. References and general literature

- [1] R.C. Hansen (Ed.): "Geometric Theory of Diffraction", IEEE Press, 1981 (ISBN 0-87942-149-5).
- [2] J.R. Mautz and R.F. Harrington: "Computational Methods for Antenna Pattern Synthesis", IEEE Trans., Vol. AP-23, pp. 507-512 (July 1975).
- [3] Radio Regulations, Edition of 1982, ITU, Geneva 1982 (ISBN 92-61-01221-3).
- [4] Recommendations and Reports of the CCIR, (XIVth Plenary Assembly, Kyoto, 1978), ITU, Geneva 1978. (To be updated in 1982).
- [5] A. Bohrmann: "Bahnen künstlicher Satelliten", B-I Hochschultaschenbücher 40/40a, Mannheim (1966).
- [6] H. Gropp: "Ein betriebsgerichtete Verfahren für die Berechnung von angenähert geostationäre Satelliten - Umlaufbahnen bei Erdefunkstellen", Der Fernmelde-Ingenieur, Vol. 25, No. 9, (Sept. 1971).
- [7] D.J. Fang et al.: "A Low Elevation Angle Propagation Measurement of 1.5-GHz Satellite Signals in the Gulf of Mexico", IEEE Trans., Vol. AP-30, pp. 10-15 (Jan. 1982).
- [8] V.J. Slabinsky: "Variation in Range, Range-Rate, Propagation Time Delay, and Doppler Shift for a Nearly Geostationary Satellite", in P.L. Bargellini (Ed.): "Communications Satellite Technology", MIT Press, Cambridge, MA (1974).
- [9] A.V. Mrstik: "Scan Limits of Off-Axis Fed Parabolic Reflectors", IEEE Trans., Vol. AP-27, pp. 647-651, (1979).
- [10] White, N. et al.: "The Application of Interference Cancellation to an Earth Station", Proc. Conf. Satellite Comm. Systems Technology, London, 7-10 April 1975, pp. 233-238 (IEE Conf. Publication No. 126).
- [11] M.J.S. van Ommeren et al.: "Improved Orbit Utilization by Interferometric Sidelobe Suppression", Electronics Lett., Vol. 16, pp. 937-938 (1980).
- [12] S. Murakami et al.: "Optimum Modulation and Channel Filters for Non-Linear Satellite Channels", IEEE Trans., Vol. COM-27, pp. 1810-1819 (Dec. 1979).
- [13] A.M. Zavody: "Effects of Scattering on Radiometer Measurements at Millimeter Wavelengths", Proc. IEE, Vol. 121, pp. 257-263 (April 1974).
- [14] A.B. Carlson: "Communication Systems", McGraw-Hill, 1975 (ISBN 0-07-009957X).

- [15] INTELSAT Doc. BG-28-72E M/6/77 entitled: "Standard C Performance Characteristics of Earth Stations in the INTELSAT-V System (14 and 11 GHz Frequency Bands)".
- [16] A.N. Ince et al.: "Power Control Algorithms for Satellite Communications Systems", IEEE Trans., Vol. COM-24, pp. 267-275, (Febr. 1976).
- [17] G.R. Stette: "Calculation of Intermodulation from a Single Carrier Amplitude Characteristic", IEEE Trans., Vol. COM-22, pp. 319-323 (March 1974).
- [18] P.Y. Chang and O. Shimbo: "Input Power Assignment of Multicarrier Systems from Given Output Power Levels", IEEE Trans., Vol. COM-27, pp. 1577-1583 (Oct. 1979).
- [19] J. Arnbak: "Adaptive Control of Satellite Resources", Proc. Symp. on Advanced Satellite Comm. Systems at 20 and 30 GHz, Genoa, Italy, Dec. 14-16, 1977, ESA-SP-138, pp.43-49.
- [20] D.O. Reudink and Y.S. Yeh: "A Scanning Spot Beam Satellite System", Bell System Technical Journal, Vol. 56, No. 8, Oct. 1977.
- [21] T. Muratani: "Satellite-Switched Time-Domain Multiple Access", Proc. IEEE Electron. & Aerospace Convention (EASCON), October 7-9, 1974, pp. 189-196.
- [22] A.P. Dekker and J. Arnbak: "Compensation of Rain Fading in 20/30 GHz FDMA Systems Using Satellite Multiple-Beam Antennas", Proc. Intern. Comm. Conf. (ICC-1981), Denver, Colorado, June 15-18, 1981, Paper 54.6 (5 pp.).
- [23] A.T. Alper and J.C. Arnbak: "Capacity Allocation and Reservation in Common-User Satellite Communications Systems with a Reconfigurable Multiple-Beam Antenna and a Nonlinear Repeater", IEEE Trans. Comm., Vol. COM-28, No. 9, pp. 1681-1692, (Sept. 1980).
- [24] N. Abramson: "The Throughput of Packet Broadcasting Channels", IEEE Trans., Vol. COM-25, No. 1, pp. 117-128, (Jan. 1977).
- [25] L.M. Keane (Ed.): "A Direct Broadcast Satellite System for the United States", COMSAT Techn. Rev., Vol. 11, pp. 195-266 (Fall 1981).
- [26] J.T. Mayhan: "Nulling Limitations for a Multiple-Beam Antenna", IEEE Trans., Vol. AP-24, pp. 769-779 (Nov. 1976).

General Literature

G. Brussard and B. Battrick (Eds.): "ATS-6 Propagation Experiments in Europe", ESA SP-131, October 1977. (Conference on the first 20/30-GHz propagation measurement programme in Europe).

D.C. Cox and H.W. Arnold: "Results from the 19- and 28-GHz COMSAT Satellite Propagation Experiments at Crawford Hill", Proc. IEEE, Vol. 70, pp. 458-489 (May 1982) (Review of an extensive North-American propagation-measurement programme near the 20/30 GHz bands).

J. Dijk et al.: "Antenna Noise Temperature", Proc. IEE, Vol. 115, pp. 1403-1410 (Oct. 1968) (A classical review of the contributions to  $T_j$ ).

A.W. Lowe (Ed.): "Reflector Antennas", IEEE Press, 1978 (ISBN 0-87942-104-5). (Selected reprints on progress of large reflector systems).

A.G. Lubowe: "Path length variations in a Synchronous Satellite Communications Link", Bell System Techn. Journal, Vol. 47, pp. 2139-2144 (Dec. 1968).

L.J. Ricardi: "Communication Satellite Antennas", Proc. IEEE, Vol. 65, pp. 356-369 (March 1977). (Classical review of adaptive satellite antennas).

H. v. Trees (Ed.): "Satellite Communications", IEEE Press, 1979 (ISBN 087942-121-5). (Selected reprints on systems and technology).

## 2. Offset Parabolic Reflector Antennas\*

by A W Rudge

### 2.1 Introduction

#### A Fundamental Advantages and Disadvantages

The offset-parabolic reflector has found applications as an antenna for many years and was certainly receiving some attention during the 1940's. However, it is only in comparatively recent times that analytical and numerical models have been developed for this device which can provide reliable predictions of its electrical properties. Although the basic analytical techniques were available at the end of the second World War, the offset-reflector geometry did not readily lend itself to analysis without the aid of a digital computer. Hence, it was not until the 1960's that development in digital-computer technology provided a readily reliable and convenient means for accurate modelling and optimisation of the offset antenna's electrical performance.

Since the offset-parabolic reflector is a somewhat more complicated structure to deal with both structurally and analytically, it will be as well to briefly review its principal advantages and disadvantages as an antenna. First and foremost, the offset-reflector antenna reduces aperture-blocking effects. This fact, which is illustrated in Fig.2.1, represents a very significant advantage for the offset configuration over comparable axisymmetric counterparts. Aperture blocking by a primary-feed or a subreflector, with their supporting struts, leads to scattered radiation which results in a loss of system gain on the one hand and a general degradation in the suppression of sidelobe and cross-polarized radiation on the other. These latter effects are becoming increasingly important as antenna spurious radiation specifications tighten and frequency re-use requirements demand higher levels of isolation between orthogonal hands of polarization.

---

\*Extracted from 'The Handbook of Antenna Design' by Rudge et al, to be published by Peter Peregrinus, 1982.

A second major advantage of the offset configuration is that the reaction of the reflector upon the primary-feed can be reduced to a very low order. The excellent isolation between reflector and primary-feed which can be achieved implies that the primary-feed VSWR can be made to be essentially independent of the reflector. When multiple-element or dual-polarized primary-feeds are to be employed, the mutual coupling occurring between feed elements via the reflector can be reduced to an insignificant level.

Compared to an axisymmetric paraboloid, the offset configuration leads to the use of larger focal-length to diameter ratios ( $F/d$ ) while maintaining an acceptable structural rigidity. As a consequence, the offset-reflector primary-feeds employ relatively larger radiating apertures which, in the case of multiple-element primary-feeds, will result in lower direct mutual coupling between adjacent feed elements. The use of larger aperture primary-feed elements in certain cases can also provide an opportunity for improved shaping of the primary-feed radiation pattern and better suppression of the cross-polarized radiation emanating from the feed itself.

The offset-reflector configuration also has its disadvantages. When illuminated by a conventional linearly polarized primary-feed, the offset reflector will generate a cross-polarized component in the antenna radiation field. When circular polarization is employed, the reflector does not depolarize the radiated field, but the antenna beam is squinted from the electrical boresight. For small offset reflectors this squinting effect has also been observed with linear polarization.

Structurally the asymmetry of the offset reflector might be considered as a major drawback, although there are many applications where its structural peculiarities can be used to good advantage. In the design of spacecraft antennas, for example, an offset configuration can often be accommodated more satisfactorily than an axisymmetric design, particularly when it is necessary to deploy the reflector after launching. Nevertheless, it is clear that the offset geometry is more difficult to deal with and generally more costly to implement. For these reasons its use in the past has tended to be restricted to applications where electrical performance specifications have been severe. The rapid growth in the use of offset antenna systems in more recent times is an indication of the increasing demands being made upon antenna performance.

## B Single and Dual-Reflector Systems

As for its axisymmetric counterpart, the offset-parabolic reflector can be utilised as a single-reflector fed from the vicinity of its prime-focus, or arranged in a dual-reflector system where the main offset reflector is illuminated by the combination of a primary-feed and subreflector. By this means offset Cassegrainian and offset Gregorian systems can be designed. A further dual-reflector system will be dealt with here in which the primary-feed illuminates an offset section of a hyperboloid, and the combination feed an offset parabolic reflector. The geometry of this configuration can be adjusted such that no blocking of the optical path occurs either by the primary-feed or the subreflector. The primary-feed in this case is located below the main parabolic reflector. This arrangement contrasts with the open Cassegrainian configuration originated by Bell Laboratories in which the primary-feed protrudes through the main reflector. To distinguish between these configurations, the no-blocking case will be termed a double-offset reflector antenna, while the general case will be referred to as dual-reflector offset antennas. Figure 2.2 illustrates some of the configurations which are of particular interest.

## C Background

Much of the initial difficulty in dealing with the offset-parabolic reflector can be attributed to its asymmetric geometry. This geometry is the key to the analysis of the offset antenna and to ultimately understanding its electrical properties. One of the best analyses of the offset-reflector geometry can be found in a monograph issued by the Bell Telephone System [1]. This work by Cook et al, which was concerned with the analysis of a dual-reflector open Cassegrainian system, was published in 1965 [1]. Much of the subsequent analysis of the offset reflector either makes use of this geometry or, if performed independently, follows a similar approach to that established by these authors [2].

The depolarization properties of asymmetric antennas have deservedly received considerable attention in the literature. While the polarization characteristics of the offset reflector were subject to the independent study of a

number of authors, including the original work by Cook et al [1,2], Chu and Turrin [3] first published detailed graphical data and provided a clear insight into the beam-squinting properties of the circularly polarized prime-focus-fed offset reflector. The radiation properties of offset-reflector antennas with off-axis feeds were studied by Rudge et al [4-7], while Dijk et al [8,9] performed an in-depth analysis of the polarization losses of offset paraboloids. The low cross-polar radiation achievable with large  $F/d$  ratio offset reflectors was confirmed by Gans and Semplak [10].

The optimisation of the geometry of dual-reflector offset antennas to reduce or eliminate cross-polarized radiation was first demonstrated by Graham [11] and confirmed theoretically by Adatia [12] in the UK. Working independently, Tanaka and Mizusawa [13] established a simple geometric-optics-based formula for this optimisation process.

The reduction of offset reflector cross polarization by use of a field-matching primary-feed technique was proposed and demonstrated by Rudge and Adatia [14,15]. Jacobsen [16] has made the point that, in principle, similar results could be achieved with an array of Huygen sources directed toward the vertex of the parent paraboloid and phased to direct the energy into the cone of angles subtended by the offset portion of the reflector. A comparison of the radiation pattern and impedance properties of offset-Cassegrainian and offset-Gregorian antennas with their symmetrical counterparts has been performed by Dragone and Hogg [17]. Their results confirm the anticipated advantages of the offset structures with regard to both sidelobe radiation levels and VSWR. The use of offset-reflector antennas in applications where very low sidelobe radiation is mandatory has also received attention [18,36].

The avoidance of aperture blockage implies that offset reflectors should offer good potential as multiple-beam antennas. This possibility has been investigated by a number of workers. Rudge et al [4-7,19,20] have studied the use of small clusters of feed elements, both linearly and circularly polarized, in conjunction with single offset reflectors. Ingerson [21] has also investigated the off-axis scan characteristics of offset reflectors, and Kaufmann and Croswell [22] have considered the effect of large axial displacements of the offset-reflector primary-feed. Ohm [23] has analysed a

proposed multiple-beam earth station based upon a dual-reflector offset system.

The use of offset-reflector systems to provide shaped or contoured beams for satellite communications has also received attention. Shaped beams have been achieved either by deforming the offset-reflector surface, as described by Wood et al [24], or by the use of a weighted array or primary-feed elements, as favoured by Han [25] and his colleagues for the Intelsat V communications satellite.

Although their low sidelobe potential makes offset-reflector antennas attractive for many radar applications, difficulties were experienced in the past when a precision tracking capability was required. These difficulties, which arise as a result of the offset-reflector depolarization, are now well understood, and the means of compensating for these effects by use of improved monopulse primary-feeds have been recently demonstrated [26].

## 2.2 Single Offset-Reflector Analysis

### A Basic Techniques

Either the surface-current [Ref.29, Section 5.7] or aperture-field [Ref.29, Section 5.11] version of physical optics may be used to determine the radiated field. In the former case, the geometrical-optics approximation of the surface-current density is integrated over the reflecting surface  $S_1$  (see Fig.2.3); in the latter, the geometrical-optics approximation of the aperture field is integrated over the projected aperture  $S_2$ . For projected aperture diameters exceeding 20 wavelengths, the two techniques provide virtually identical predictions for the co-polarized fields over the main lobe and first four or five sidelobes. At wide angles from the boresight, the predictions differ and these differences tend to increase with increasing reflector curvature. For the cross-polarized radiation, the two methods differ significantly only when the peak levels of this radiation are very low (i.e. less than -50 dB relative to the peak value of the main beam co-polarized field). The electric-current method is generally considered to be the more accurate of the two methods, but for most practical purposes the differences



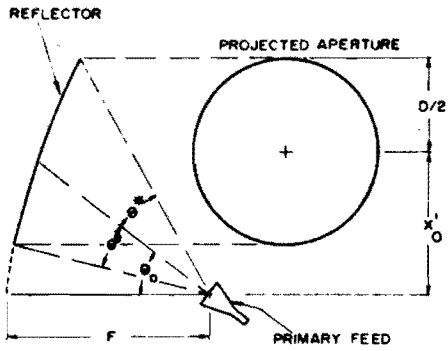


Fig. 2.1 Basic single-offset-reflector configuration.

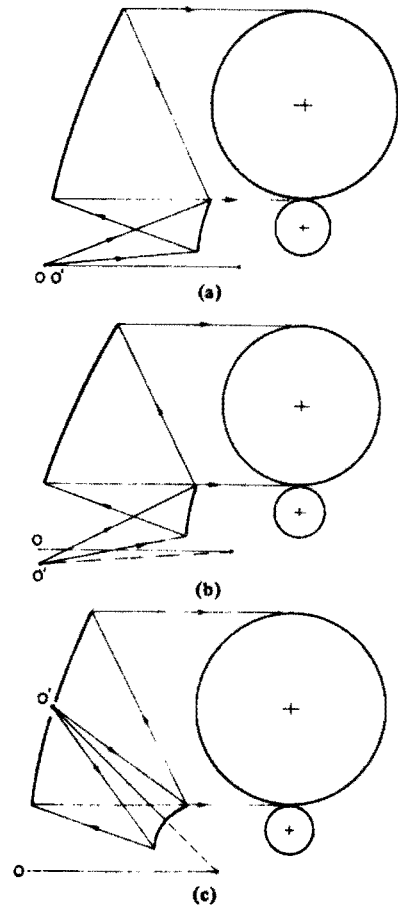


Fig. 2.2 Dual-offset-reflector configurations. (a) Double-offset system. (b) optimized double offset. (c) Open Cassegrainian system. Paraboloid vertex at  $O$  and feed phase center located at  $O'$ .

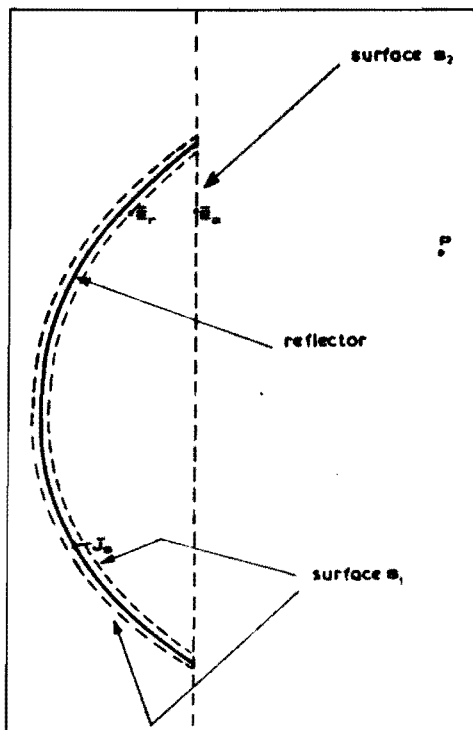


Fig. 2.3 Surfaces of integration for surface-current current technique ( $S_1$ ) and aperture-field method ( $S_2$ ).

between the predictions tend to be insignificant. For small offset parabolic reflectors (i.e. projected aperture diameters of less than 20 wavelengths) the discrepancies between the predictions of the techniques become more discernible.

Boswell and Ashton [27] have shown that a beam-squinting effect can occur with small linearly polarized offset reflectors. This effect is predictable using the surface-current technique but not with aperture fields. In their example a beam squint of 0.03 of a beamwidth occurred with a reflector of 6-wavelengths diameter. This result is particularly interesting in that it is a comparatively rare example of experimental confirmation of the accuracy of the surface-current technique for small parabolic reflectors.

In dealing with the radiation from large offset-parabolic-reflector antennas in a moderate cone of angles about the antenna boresight and over a dynamic range of the order of 50-60 dB, there is, for most practical purposes, little significant variation between the predictions obtained by the two methods. Under these circumstances the technique which is more convenient analytically and computationally can be employed. On this basis the aperture-field method, which involves an integration over a planar surface, results in generally more simple mathematical expressions and thus offers some saving in computational effort.

#### B Offset-Reflector Geometry

The geometry of a single-offset-parabolic reflector is shown in Fig.2.4. The basic parameters of the reflector are shown as the focal length  $F$  of the paraboloid, the offset angle  $\theta_0$ , and the half angle  $\theta^*$  subtended at the focus by any point on the reflector rim. With  $\theta^*$  maintained constant, a rotation about the inclined  $z$  axis will generate a right circular cone with its apex at the reflector geometric focus. If the boundary of the parabolic surface is defined by its intersection with the cone, then the resultant reflector will have an elliptical contour, while the projection of this contour onto the  $x'y'$  plane will produce a true circle.

To deal with this offset geometry it is desirable to obtain a coordinate transformation from the primary spherical coordinate system of the symmetrical parent paraboloid to an offset spherical coordinate system about the inclined  $z$  axis. The reflector parameters which are readily expressed in terms of the symmetrical primary coordinates can then be transformed into the offset coordinate system. If the symmetrical coordinates are defined conventionally as  $\rho'$ ,  $\theta'$ ,  $\phi'$  with associated Cartesian coordinates  $x'$ ,  $y'$ ,  $z'$ , then their relationships to the unprimed offset coordinates  $\rho$ ,  $\theta$ ,  $\phi$  and  $x$ ,  $y$ ,  $z$  are obtained by simple geometry as:

$$\rho' = \rho \quad (2.1a)$$

$$\cos \theta' = \cos \theta \cos \theta_0 - \sin \theta \sin \theta_0 \cos \phi \quad (2.1b)$$

$$\sin \theta' \sin \phi' = \sin \theta \sin \phi \quad (2.1c)$$

$$\sin \theta' \cos \phi' = \sin \theta \cos \theta_0 \cos \phi + \cos \theta \sin \theta_0 \quad (2.1d)$$

$$\tan \phi' = \sin \theta \sin \phi / (\cos \theta \sin \theta_0 + \sin \theta \cos \theta_0 \cos \phi) \quad (2.1e)$$

and these equations provide the basis for the transformations. Applying the transformations, the distance from the reflector focus to a point on the parabolic surface ( $\rho$ ) is given by:

$$\begin{aligned} \rho &= 2F/(1 + \cos \theta') \\ &= 2F/(1 + \cos \theta \cos \theta_0 - \sin \theta \sin \theta_0 \cos \phi) \end{aligned} \quad (2.2)$$

The diameter of the projected aperture of the offset reflector ( $d$ ) is:

$$d = 4F \sin \theta^*/(\cos \theta_0 + \cos \theta^*) \quad (2.3)$$

Similarly the distance ( $x'_0$ ) from the axis of the parent paraboloid to the centre of the projected apertures is:

$$x'_0 = 2F \sin \theta_0 / (\cos \theta_0 + \cos \theta^*) \quad (2.4)$$

Distances from the reflector focus in the  $z' = 0$  plane can be written:

$$x' = \rho (\cos \theta_0 \sin \theta \cos \phi + \sin \theta_0 \cos \theta) \quad (2.5a)$$

$$y' = \rho \sin \theta \sin \phi \quad (2.5b)$$

The Jacobian for a surface element  $dx' dy'$  can be obtained from the equations given as:

$$\begin{aligned} dx' dy' &= \rho^2 \sin \theta' d\theta' d\phi' \\ &= \rho^2 \sin \theta d\theta d\phi \end{aligned} \quad (2.6)$$

The unit normal to the reflector parabolic surface ( $\hat{a}_n$ ) is given by:

$$\begin{aligned} \hat{a}_n &= - \sqrt{(\rho/4F)} (\sin \theta \cos \phi - \sin \theta_0) \hat{a}_x + \\ &\sin \theta \sin \phi \hat{a}_y + (\cos \theta + \cos \theta_0) \hat{a}_z \end{aligned} \quad (2.7)$$

### C Co-polar and Cross-polar Definitions

The radiation fields from an antenna can be completely specified in terms of two vector components. The definition of the two components at a point in space and their identification in terms of a co-polarized and cross-polarized component is somewhat arbitrary. Ludwig [28] clarified and discussed some of the popular choices in his 1973 paper. For offset-reflector antennas which are operated in a predominantly linearly polarized mode, the definition which is preferred by the author is the third definition presented by Ludwig in the

referenced paper. With this choice, the principally polarized or co-polar field is that which would be measured by a conventional antenna-range technique with the polarization of the distant source initially aligned with that of the test antenna on boresight, and remaining fixed while the test antenna is rotated in the normal way to produce the measured radiation patterns (e.g. see Ref.29, Chapter 15). If the polarization of the distant source antenna is then rotated through  $90^\circ$ , and the radiation-pattern measurements repeated, then the recorded data represents a measurement of the cross-polar field distribution.

In the primary spherical coordinate system  $\rho, \theta, \phi$  shown in Fig.2.4, the primary-feed spherical-coordinate fields will be defined as  $E_\theta, E_\phi$ . If the primary-feed antenna has its principal electric vector along the y axis then the feed co-polar measured-field component ( $e_p$ ) and the cross-polar component ( $e_q$ ) can be simply defined by [7,28]:

$$\begin{bmatrix} e_p \\ e_q \end{bmatrix} = \begin{bmatrix} \sin \phi & \cos \phi \\ \cos \phi & -\sin \phi \end{bmatrix} \begin{bmatrix} E_\theta \\ E_\phi \end{bmatrix} \quad (2.8)$$

Similarly, in terms of the secondary coordinate system,  $r, \psi, \phi$ , the overall radiation fields from the antenna will be defined as  $E_\psi, E_\phi$  and the co-polar ( $E_p$ ) and cross-polar ( $E_q$ ) can be obtained from the right-hand side of (2.8) with  $\psi, \phi$ , replacing  $\theta, \phi$ , respectively.

It is worth noting that a zero cross-polarization primary-feed by the definition of (2.8) will produce a purely linearly polarized field in the projected aperture plane of an axisymmetric paraboloidal reflector. This condition will in turn result in a low level of cross-polarized radiation in the overall antenna far-field, providing that the reflector aperture is large with respect to the wavelength and that the blockage effects are small. However, the field distribution in the mouth of the primary-feed will not be purely linearly polarized but must exhibit some field-line curvature to establish this desired radiation condition [30].

### D Projected-aperture Fields

The tangential electric-field distribution in the aperture plane of the off-set reflector ( $\bar{E}_a$ ) can be approximated by assuming an optical reflection of the incident primary-feed fields. If the incident primary field at the reflector is taken as the radiation field of the primary-feed, then this can be expressed as:

$$\bar{E}_i = \frac{1}{\rho} [A_\theta(\theta, \phi) \hat{a}_\theta + A_\phi(\theta, \phi) \hat{a}_\phi] \exp(-jk\rho) \quad (2.9)$$

where  $A_\theta$ ,  $A_\phi$  are the normalised spherical coordinate components of the primary-feed radiation pattern and  $k = 2\pi/\lambda$ . Optical reflection then yields the offset-reflector projected-aperture electric-field distribution expressed in Cartesian components ( $E_{ax}$ ,  $E_{ay}$ ):

$$\begin{bmatrix} E_{ay}(\theta, \phi) \\ E_{ax}(\theta, \phi) \end{bmatrix} = K \begin{bmatrix} -S_1 & C_1 \\ C_1 & S_1 \end{bmatrix} \begin{bmatrix} A_\theta(\theta, \phi) \\ A_\phi(\theta, \phi) \end{bmatrix} \quad (2.10)$$

where:

$$S_1 = (\cos \theta_0 + \cos \theta) \sin \phi \quad (2.11a)$$

$$C_1 = \sin \theta \sin \theta_0 - \cos \phi (1 + \cos \theta \cos \theta_0) \quad (2.11b)$$

$$K = \exp(-j2kF)/2F \quad (2.11c)$$

For a circularly polarized primary-feed:

$$\begin{bmatrix} E_{aR}(\theta, \phi) \\ E_{aL}(\theta, \phi) \end{bmatrix} = \frac{2FK}{\rho} \begin{bmatrix} \exp(j\Omega) & -j\exp(j\Omega) \\ \exp(j\Omega) & j\exp(-j\Omega) \end{bmatrix} \begin{bmatrix} A_\theta(\theta, \phi) \\ A_\phi(\theta, \phi) \end{bmatrix} \quad (2.12)$$

where  $E_{aR}$  and  $E_{aL}$  are the right-hand and left-hand components respectively and,

$$\Omega(\theta, \phi) = \arctan S_1/C_1 \quad (2.13)$$

If the circularly polarized primary-feed has a normalised radiation-pattern of the form:

$$\bar{A}_n(\theta, \phi) = [A_\theta(\theta) \hat{a}_\theta - jA_\phi(\theta) \hat{a}_\phi] \exp(-j\phi) \quad (2.14)$$

where the functions  $A_\theta$  and  $A_\phi$  are independent of  $\phi$ , then the offset-reflector aperture-plane fields have the form:

$$E_{aM} = \frac{2FK}{\rho} [A_\theta(\theta) \pm A_\phi(\theta)] \exp[j(\phi \pm \Omega)] \quad (2.15)$$

where M is either R or L and L takes the upper sign. Equation (2.15) can be satisfied by many practical types of circularly polarized conical horns including fundamental mode, dual mode (Potter), and corrugated types [30,31]. It is apparent that when  $A_\theta(\theta) = A_\phi(\theta)$ , which is the condition for zero cross-polarized radiation from the conical feed, then the reflector aperture plane will be purely co-polarized with a beam-squinting phase distribution given by  $\phi + \Omega$ . This can be contrasted with the linearly polarized case in which the introduction of a zero cross-polarized primary-feed fails to reduce the projected-aperture field to a single linear polarization, unless the offset angle  $\theta_0$  is put to zero.

#### E The Off-focus Primary-feed

When the phase centre of the primary-feed is coincident with the reflector geometric focus, the incident electric fields at the reflector are described by (2.9). This equation assumes that the reflector is in the far-field of the primary-feed. In general, movements of the primary-feed can be accounted for by means of a suitable coordinate transformation between a set of coordinates employed to define the feed radiation and a set describing the offset

reflector surface. However, if the primary-feed offsets are to be small relative to the reflector-to-feed dimension ( $\rho$ ), then the variation in the amplitude terms in (2.9) will be small, and the effect of such amplitude changes upon the predicted radiation fields of the overall antenna will be negligible for most practical purposes. Similarly, providing the orientation of the principal polarization vector remains aligned with one of the principal axes of the focal plane, the depolarizing effects of the feed offset will also be negligible. However, the off-focus location of the primary-feed phase centre will modify the phase terms in (2.9) and this will significantly change the overall radiation fields.

Referring to Fig.2.5, the location of an offset primary-feed phase centre can be described in the offset coordinate system  $x,y,z$  by the vector  $\bar{A}$  or the cylindrical coordinates  $\Delta_t, \Delta_z$  and  $\phi_0$ , where  $\Delta_t$  is a small transverse offset,  $\Delta_z$  a small axial offset, and  $\phi_0$  the polar angle to the  $x$  axis in the  $x,y$  plane. Employing this geometry, a compensating phase term can be derived which, when used as a multiplying term on (2.9), effectively corrects the phase characteristics for the off-axis feed location.

Thus, assuming  $\lambda^{2/\rho^2} \ll 1$ ,  $\Delta_t/\rho < 1$ , and  $\Delta_z/\rho < 1$ , the field of the feed can be assumed to be:

$$\bar{E}_1 = \frac{1}{\rho} [A_\theta(\theta, \phi) \hat{a}_\theta + A_\phi(\theta, \phi) \hat{a}_\phi] \exp [jk (R_1 - \rho)] \quad (2.16)$$

where:

$$R_1(\theta, \phi) = \Delta_t \sin \theta \cos (\phi - \phi_0) + \Delta_z \cos \theta \quad (2.17)$$

Similarly, the electric field in the offset reflector projected aperture plane can be simply modified to account for the off-axis feed by multiplying (2.11c) and (2.12).

Imbriale et al [32] have compared the predictions obtained from a scalar equation for the far-field radiation of a paraboloid (which included a phase compensation term similar to (2.17)) with a complete vector formulation



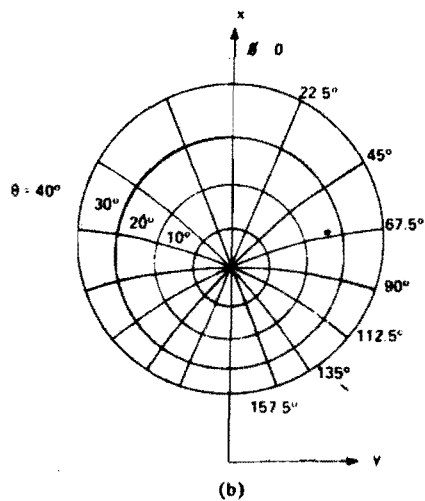
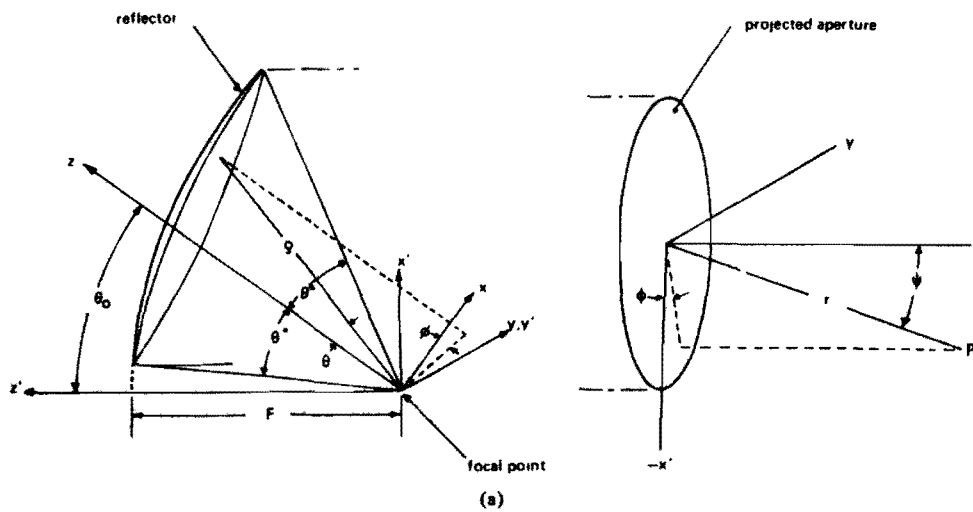


Fig. 2.4 (a) Single-offset-reflector coordinate system. (b) Constant  $\theta, \phi$  contours on projected-aperture plane.

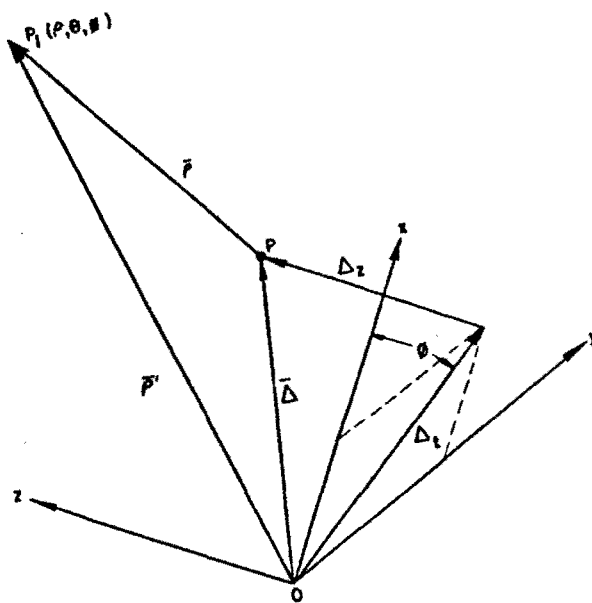


Fig. 2.5 Coordinate geometry for offset primary-feed.  $P_1$  is a point on the reflector surface and  $P$  a point in the vicinity of the reflector geometric focus ( $O$ ).

employing coordinate transformations. Their results support this author's experience that for small feed offsets, at least up to the point where the radiation-pattern degradation would be unacceptable for most practical applications, the quality of the approximate expression is very good. The use of (2.16) and (2.17) in a vector formulation of the type shown here thus offers a very reasonable compromise between accuracy and analytical and computational simplicity.

### F The Field Integrals

Making use of the physical-optics approximation and well-established vector-potential methods, mathematical models can be established for offset-reflector antennas. For example, employing the tangential aperture-field approach, the normalised co-polar ( $E_{pn}$ ) and cross-polar ( $E_{qn}$ ) radiation patterns of a linearly polarized offset-reflector antenna can be expressed as:

$$\begin{bmatrix} E_{pn}(\psi, \phi) \\ E_{qn}(\psi, \phi) \end{bmatrix} = \frac{1 + \cos \psi}{2F_p(0,0)} \begin{bmatrix} 1 - t^2 \cos 2\phi & t^2 \sin 2\phi \\ t^2 \sin 2\phi & 1 + t^2 \cos 2\phi \end{bmatrix} \cdot \begin{bmatrix} F_p(\psi, \phi) \\ F_q(\psi, \phi) \end{bmatrix} \quad (2.18)$$

where  $F_p, F_q$  are the spatial Fourier transforms of the co-polar and cross-polar tangential electric-field distribution in the projected-aperture plane of the offset-reflector, and  $t = \tan \psi/2$ .

Similarly, for a circular polarized antenna, the far-field radiation pattern can be expressed in terms of its normalised right- and left-hand components by:

$$\begin{bmatrix} E_{Rn}(\psi, \phi) \\ E_{Ln}(\psi, \phi) \end{bmatrix} = \frac{1 + \cos \psi}{2F_R(0,0)} \begin{bmatrix} 1 & t^2 \exp(j2\phi) \\ t^2 \exp(-j2\phi) & 1 \end{bmatrix} \cdot \begin{bmatrix} F_R(\psi, \phi) \\ F_L(\psi, \phi) \end{bmatrix} \quad (2.19)$$

where  $F_R$  and  $F_L$  are the spatial Fourier transformations of the right- and left-hand components of the projected-aperture tangential electric field.

The general form of the transform in terms of the geometrical parameters specified in (2.3) to (2.7) is given by:

$$F = \iint_{x',y} E_a(x',y) \exp jkR'(x',y,\psi,\phi) dx' dy \quad (2.20)$$

where:

$$R'(x',y,\psi,\phi) = (x'_0 - x) \sin \psi \cos \phi + y \sin \psi \sin \phi \quad (2.21)$$

and  $E_a$  is the tangential aperture field as specified by either (2.10) or (2.12).

To predict the offset antenna radiation pattern it is necessary to set values for the reflector parameters ( $F$ ,  $\theta_0$ , and  $\theta^*$ ), to specify the primary-feed radiation fields at the reflector ( $E_\theta, E_\phi$ ), to compute the two-dimensional transform integrals, and finally to evaluate (2.18) or (2.19). For accurate predictions, the choice of primary-feed model is critical, while the evaluation of the two-dimensional integrals clearly represents the crux of the computational problem.

#### G Primary-feed Models

Techniques for theoretically modelling parabolic reflectors have received considerable attention in the literature in the past [2-7]. The need for accurate yet mathematically simple models for the primary-feed radiation has tended to be somewhat overlooked. However, this aspect of reflector-antenna modelling is critical and can raise more difficulties and produce more serious discrepancies than many of the differences observed between reflector-modelling techniques. The accuracy of primary-feed models becomes particularly critical when predictions of cross-polarized radiation are of concern.

For prediction of radiation fields from microwave horns it has been found that analytical models based upon an assumed tangential electric-field distribution in the horn mouth can provide reasonable predictions of both the co-polar and cross-polar radiation fields over the range of angles subtended by a typical reflector [4,30,34]. In its simplest form this approach, which has been termed the E-field model, essentially involves an assumption that the horn mouth is surrounded by an infinite flange. The expressions for the model in this form are identical to (2.18) or (2.19) with  $\Psi, \Phi$  replaced by the primary coordinates  $\theta, \phi$ . The tangential aperture fields in this case can be taken as the waveguide modes in a cross-section of an infinite waveguide, and the model can be improved for larger horns by multiplying the aperture-field expression by a phase distribution function to account for the sphericity of the phase front in the horn mouth.

For small flare-angle feed horns, where the fundamental mode tangential electric field distribution in the horn mouth is an acceptable approximation, the following expressions can be derived for the normalised radiation-pattern field components ( $A_\theta, A_\phi$ ). In each case the principal polarization vector of the horn is assumed to be aligned with the y-axis of the primary coordinate system of Fig.2.4.

(i) Rectangular waveguide horn ( $TE_{10}$  mode)

With aperture dimensions of  $2a$  in the magnetic plane and  $2b$  in the electric plane, the expressions can be written:

$$A_\theta(\theta, \phi) = A(\theta, \phi) \sin \phi \quad (2.22a)$$

$$A_\phi(\theta, \phi) = A(\theta, \phi) \cos \theta \cos \phi \quad (2.22b)$$

where:

$$A(\theta, \phi) = \frac{\pi}{4} \left[ \frac{\cos (ka \sin \theta \cos \phi)}{1 - \left( \frac{2ka \sin \theta \cos \phi}{\pi} \right)^2} \right] \left[ \frac{\sin (kb \sin \theta \sin \phi)}{kb \sin \theta \sin \phi} \right] \quad (2.23)$$

(ii) Cylindrical waveguide horn ( $TE_{11}$  mode)

With an aperture diameter of  $2b$  the expressions for the conical horn can be written:

$$A_{\theta}(\theta, \phi) = \frac{2J_1(kb \sin \theta) \sin \phi}{kb \sin \theta} \quad (2.24a)$$

$$A_{\phi}(\theta, \phi) = \frac{J_1'(kb \sin \theta) \cos \theta \cos \phi}{1 - \left(\frac{kb \sin \theta}{u'}\right)^2} \quad (2.24b)$$

where  $J_1'(u) = dJ_1(u)/du$  and  $u'$  is the first root of  $J_1'(u') = 0$ , i.e.  $u' \approx 1.841$ .

Studies have shown that, for horns having aperture dimensions exceeding about one wavelength, good correlation can be obtained between the E-field model and horns with finite flanges. Some typical results are shown in Figs. 2.6-2.8. It is noteworthy that the E-field model provides improved predictions over the method due to Chu [29] when applied to flanged rectangular or conical horns of either the smooth-walled or corrugated varieties [30]. The differences between the predictions obtained from the two methods can be very significant when cross polarization is of interest.

For horns having aperture dimensions of less than one wavelength, the radiation pattern becomes increasingly flange-dependent, and for small or non-existent flanges the E-field model is not reliable. However, its validity can be extended into this region by using the E-field model in conjunction with the geometric theory of diffraction (GTD). The GTD can be applied to predict the additional contribution of the finite flanges to the radiation field, and this hybrid model can provide significantly improved predictions for the vector radiation fields from small horns. A more rigorous solution for the vector radiation from small waveguide horns can be obtained by an application of the method of moments [35]. However, this technique is more appropriate

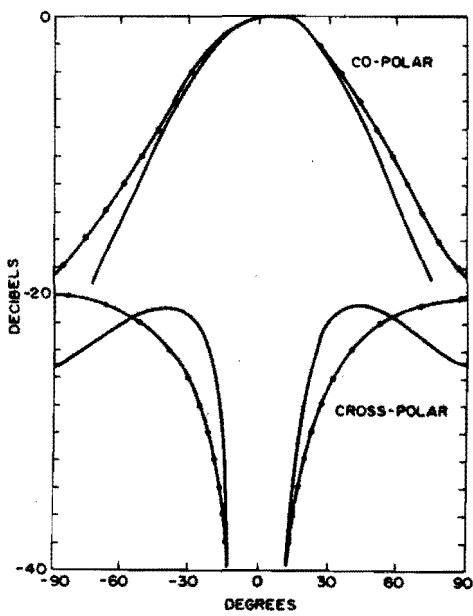


Fig. 2.6 Radiation patterns in diagonal plane for  $0.92 \lambda \times 1.11 \lambda$  pyramidal horn. Measured —. Predicted —●—.

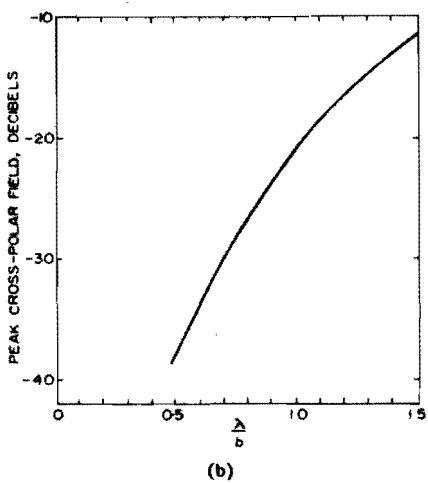
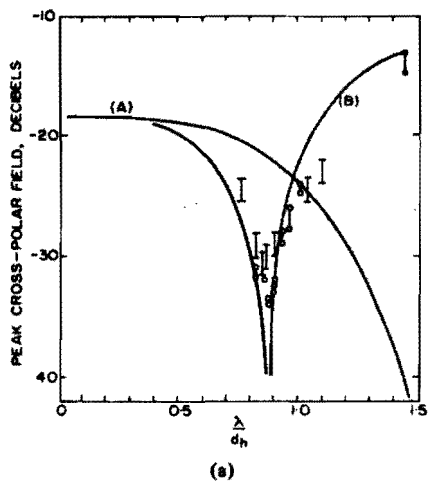


Fig. 2.8 (a) Peak cross-polar levels occurring in diagonal planes of fundamental-mode conical horns of diameter  $d_h$ . (A): Predicted Chu model. (B): Predicted  $E$ -field model with superimposed measured data from a variety of conical horns. (b) Peak radiated cross-polar level in the diagonal plane of a fundamental-mode square-aperture waveguide horn with side dimensions  $b$  wavelengths.

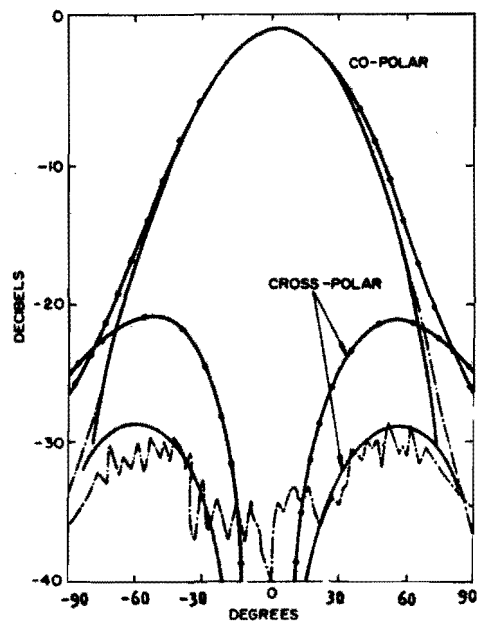


Fig. 2.7 Copolar and cross-polar radiation fields from a circularly polarized fundamental-mode conical horn with aperture diameter of  $1.25 \lambda$ . — Predicted ( $E$ -field model). —●— Predicted (Chu model). - - - Measured data.

for the analysis of electrically small waveguide horns alone, rather than in conjunction with an offset main reflector, when the combined computational effort may become excessive.

In performing initial design studies and establishing limiting conditions, the use of idealised primary-feed devices can be convenient. Simple mathematical expressions for the radiation characteristics of several such devices are given below:

(i) Small electric dipole (aligned with y axis)

$$A_{\theta} = \cos \theta \sin \phi \quad (2.25a)$$

$$A_{\phi} = \cos \phi \quad (2.25b)$$

(ii) Small magnetic dipole (aligned with x axis)

This theoretical device provides a useful model for the radiation from a short radiating slot in a groundplane, when the slot is aligned with the x axis.

$$A_{\theta} = \sin \phi \quad (2.26a)$$

$$A_{\phi} = \cos \theta \cos \phi \quad (2.26b)$$

(iii) Huygen source

The Huygen source comprises a spatially-orthogonal combination of an electric and magnetic dipole. The device forms an ideal primary-feed in the sense that it is rotationally symmetric and contains zero radiated cross-polar energy. However, no pattern-width control is available with this model. For this case:

$$A_{\theta} = (1 + \cos \theta) \sin \phi \quad (2.27a)$$

$$A_{\phi} = (1 + \cos \theta) \cos \phi \quad (2.27b)$$

(iv) Uniform distribution of Huygen sources in a circular aperture

To overcome the fixed pattern-width limitations of the single Huygen source, an idealised model can be employed which incorporates a circular aperture horn with 100% aperture efficiency and zero cross-polarized radiation. Pattern-width control is available via the horn diameter (2b). The equations for this device are:

$$A_{\theta}(\theta, \phi) = (1 + \cos \theta) \frac{J_1(kb \sin \theta)}{kb \sin \theta} \sin \phi \quad (2.28a)$$

$$A_{\phi}(\theta, \phi) = (1 + \cos \theta) \frac{J_1(kb \sin \theta)}{kb \sin \theta} \cos \phi \quad (2.28b)$$

(v) Idealised dual-mode and corrugated conical horns

The dual-mode (Potter) horn combines the  $TE_{11}$  and  $TM_{11}$  cylindrical waveguide modes to produce a radiation-pattern with good rotational symmetry over its main beam. Cross-polar radiation can be suppressed below -30 dB over a narrow band (i.e. approximately 5%). The conical corrugated horn provides even better symmetry and lower cross-polar radiation over a wider bandwidth. With the assumption that the cross-polar radiation from these devices is essentially zero, the radiation fields from either device with a diameter of 2b can be modelled approximately by:

$$A_{\theta}(\theta, \phi) = \frac{J_1'(kb \sin \theta)}{1 - \left(\frac{kb \sin \theta}{u'}\right)^2} \sin \phi \quad (2.29a)$$

$$A_{\phi}(\theta, \phi) = \frac{J_1'(kb \sin \theta)}{1 - \left(\frac{kb \sin \theta}{u'}\right)^2} \cos \phi \quad (2.29b)$$



## 2.3 Electrical Performance Of The Single Offset-Reflector Antenna

### A Linear Polarization

The literature provides evidence of a number of analytical models, largely based upon physical-optics techniques, which have been applied to study the radiation characteristics of the offset parabolic reflector. Precise experimental data is somewhat more sparse, but sufficient material has been published to validate the main conclusions from the analytical studies.

When fed by a purely linearly polarized primary-feed, as defined by (2.8), the offset-parabolic reflector exhibits a characteristic de-polarizing effect which results in the generation of two principal cross-polarized lobes in the plane of asymmetry (i.e. the  $yz'$  plane or  $\phi = \pi/2$  plane) in the coordinate system of Fig.2.4. Figure 2.9 shows measured data obtained with a precisely machined offset reflector fed by a fundamental-mode rectangular horn with a 12 dB illumination taper at the reflector rim [5,7]. Predicted data obtained from a numerical model has been superimposed and, in general, an excellent correlation is observed. The cross-polar correlation is slightly inferior; and, in fact, better correlation was observed with later unpublished results. These radiation patterns are characteristic of the linearly polarized offset reflector, and similar results have been published by Cook et al [1,2], Chu and Turrin [3] and others. The cross-polar lobes which arise as a consequence of the reflector asymmetry have peak values in the vicinity of the -6 dB contour of the main co-polarized beam, and the next subsidiary lobes are typically a further 20 dB down below the peaks. The co-polar sidelobe radiation has the form of a well-defined diffraction pattern, with a comparatively rapid decay of sidelobe levels with increasing angle from boresight. Numerical models of the type discussed above reproduce these characteristics reliably and can be used profitably in performing parameter studies. For example, Fig.2.10 illustrates some general sidelobe trends for fully offset antennas in which the reflector parameters are chosen such that the primary-feed hardware does not protrude into the projected aperture of the reflector.

It is evident from Fig.2.10 that the peak value of the reflector cross polarization is dependent very largely upon the parameters  $\theta_0, \theta^*$  and is

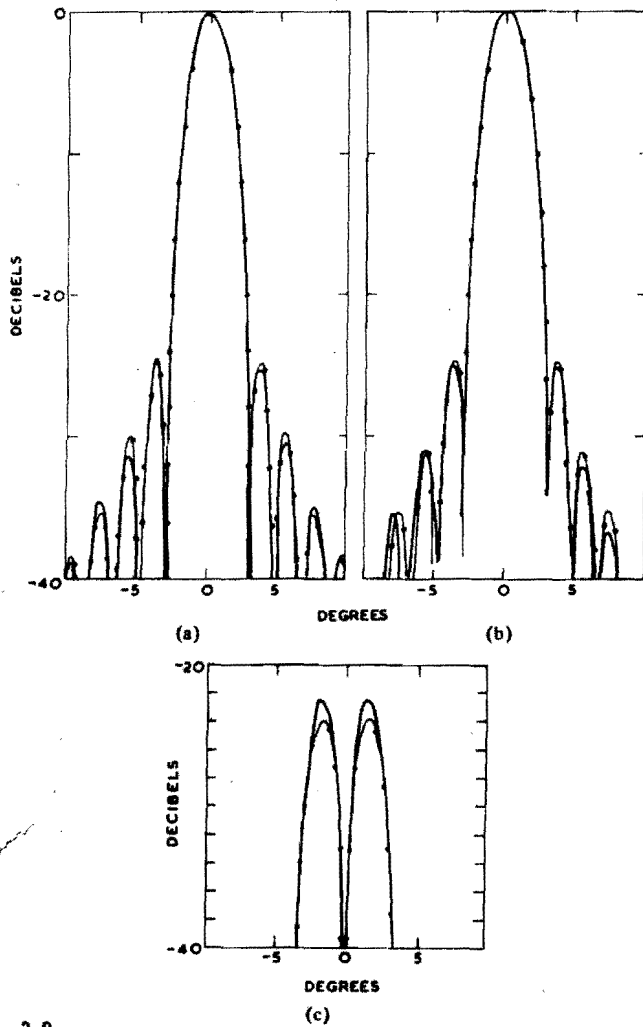


Fig. 2.9 Radiation fields from a K-band offset-reflector antenna. Copolar radiation in (a) plane of asymmetry ( $\Phi = \pi/2$ ) and (b) plane of symmetry ( $\Phi = 0$ ). Cross-polar radiation in (c) plane of asymmetry. Measured——. Predicted—•—.

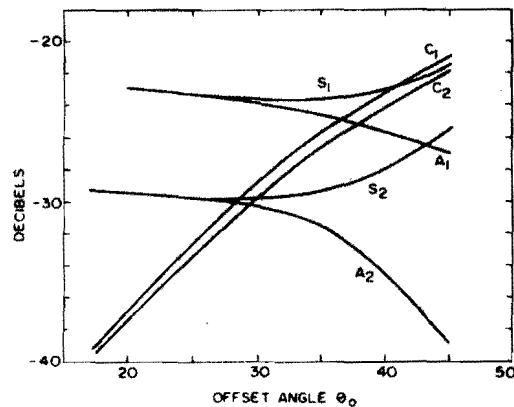


Fig. 2.10 Peak copolar sidelobe levels in planes of symmetry ( $S$ ) and asymmetry ( $A$ ) for offset reflectors with  $\theta_0 = \theta^* + 5^\circ$ , fed by uniformly illuminated circular aperture feeds producing -10-dB (subscript 1) and -20-dB (subscript 2) illumination tapers at  $0 = \theta^*$ . Peak cross-polar levels ( $C$ ) occurring in plane of asymmetry are also indicated.

relatively insensitive to the feed-imposed illumination taper. It is also clear that large values of  $\theta_0$  and  $\theta^*$  result in higher peak levels of co-polar and cross-polar radiation. However, these results should not be assumed to indicate the low-sidelobe limitations of the offset system, since at low levels this is strongly dependent upon the illumination taper introduced by the primary-feed antenna. In the sample shown, the primary-feed comprises a uniformly excited circular aperture which does not produce a good illumination characteristic when low sidelobes are a major concern.

The loss of aperture efficiency, arising from offset-reflectors' depolarization, tends to be small for values of  $\theta_0, \theta^*$ , less than  $45^\circ$ , but can become significant for larger angles. Some computer data due to Dijk et al [8,9] are shown in Fig.2.11.

Figure 2.12 shows the predicted and measured radiation patterns of a linearly polarized offset reflector fed by an off-axis primary-feed [4,7]. These results provide further confidence in the quality of the analytical predictions and also serve to illustrate the comparative insensitivity of the peak cross-polar lobes to small transverse offsets in the primary-feed location. The formation of the co-polarized coma lobe is the most evident source of pattern degradation. Studies have shown that the loss of gain suffered by an offset-reflector antenna with offset feed is essentially independent of the transverse plane in which the feed is offset. However, the general radiation pattern deterioration appears to be more pronounced when feeds are offset in the plane of symmetry rather than the plane of asymmetry [19-21]. Some relevant computed data on gain and sidelobe performance is shown in Fig.2.13 [19], but no distinction as to the plane of offset is made for this data. The off-axis performance of an offset-reflector antenna is dependent upon the offset angle  $\theta_0$  and is inferior to an ideal (unblocked) axisymmetric antenna with the same semi-angle  $\theta^*$ . Approximate formulae for the beam deviation characteristics of offset reflectors have been derived, which illustrate the role played by the offset angle  $\theta_0$  [19-22].

The cross-polar characteristics of the offset-parabolic reflector are not unduly sensitive to small reflector profile errors. Small profile errors do not themselves generate a significant cross-polarized contribution to the

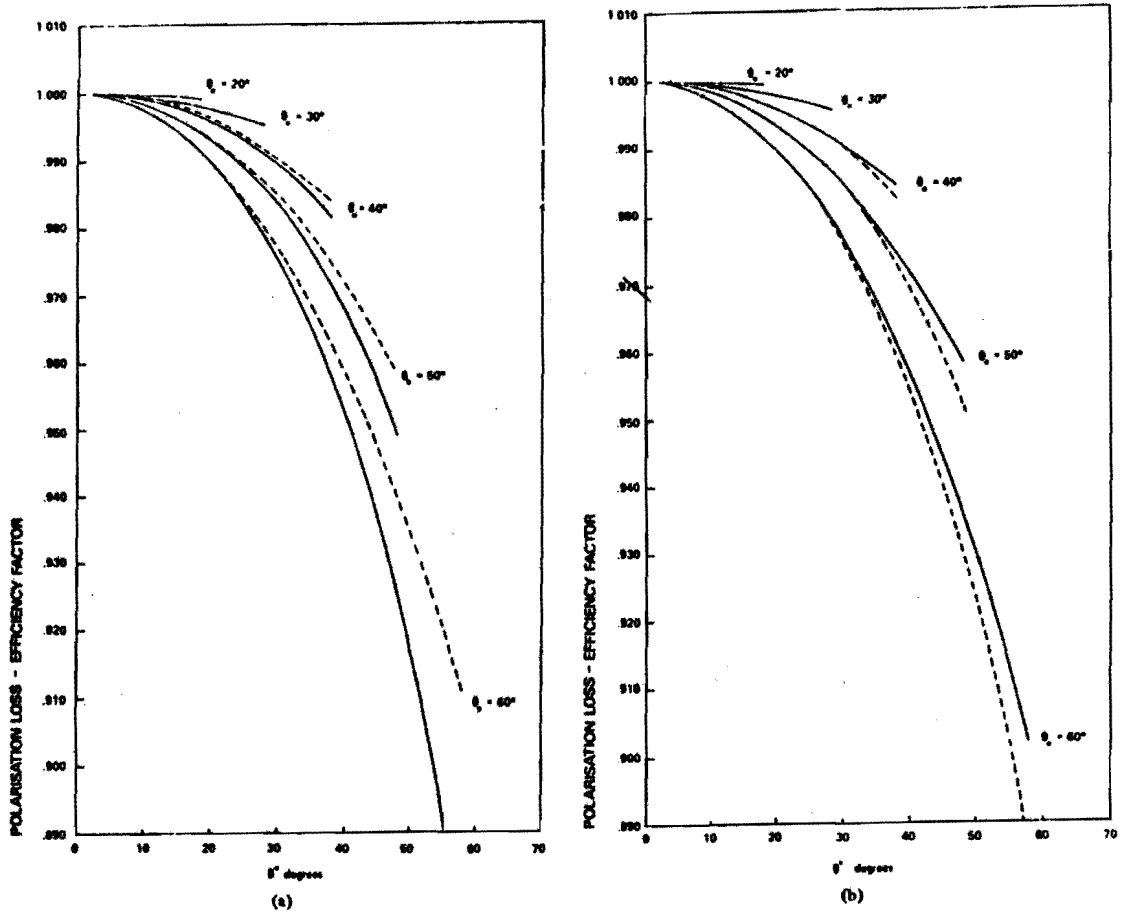


Fig. 2.11 (a) Polarization loss-efficiency factor of offset paraboloid reflector, offset angle  $\theta_0$  being a parameter, illuminated by ——— electric dipole oriented along  $x'$  axis and Huygens source and - - - - electric dipole oriented along  $y'$  axis. (b) Polarization loss-efficiency factor of open Cassegrain antenna, offset angle  $\theta_0$  being a parameter, illuminated by ——— electric dipole oriented along  $x'$  and  $y'$  axis and - - - - Huygens source.

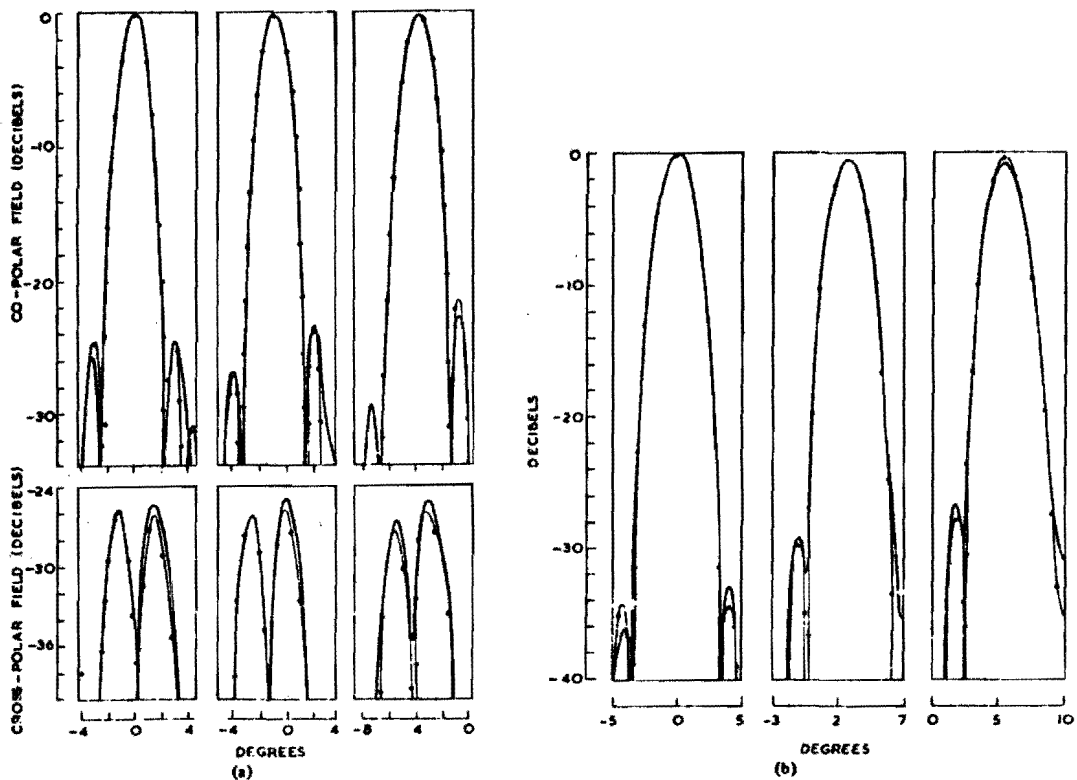


Fig. 2.12 (a) Radiation fields from offset reflector ( $F = 30.4 \lambda$ ,  $\theta_0 = 35^\circ$ ,  $\theta' = 30^\circ$ ) with linearly polarized pyramidal-horn primary feed offset transversely along  $y$  axis by 0, 0.82  $\lambda$ , and 2.5  $\lambda$ , respectively. (b) Copolar radiation field from circularly polarized offset reflector ( $F = 22.7 \lambda$ ,  $\theta_0 = 44^\circ$ ,  $\theta' = 30^\circ$ ) with scalar-horn feed offset transversely by 0, 1.4  $\lambda$ , and 2.8  $\lambda$ , respectively. ——— Measured. —●— Predicted.

radiated field but rather act as a phase-error distribution in the reflector aperture plane. As such, these errors will redistribute the existing co-polar and cross-polar radiation in the far field of the antenna. However, like the main co-polar lobe, the two main lobes of the cross-polarized field are relatively insensitive to the effects of small phase errors and, although some increase in levels will occur in the subsidiary cross-polar lobes, the peak lobes will remain substantially unchanged [37].

The principal cross-polarized lobes radiated from a linearly polarized offset-reflector antenna are in phase quadrature with the main co-polar beam and are essentially contained within the co-polar beam envelope. The polarization over the main beam varies from linear at the beam centre to an elliptical polarization in the region of the cross-polarized lobes. In some applications this will not constitute a serious drawback; but, if linear polarization is required over the main beam region, then the inherent limitations of an offset parabolic antenna with a conventional primary-feed are obvious. The peak levels of the cross-polarized lobes can be reduced to low levels (i.e. below -35 dB), if the offset angle is made very small. This is evident from examination of Fig.2.14 and Gans and Semplak [10] have described an antenna of this type with peak cross-polar levels of below -37 dB. However, if aperture blocking is to be avoided, then  $\theta^* < \theta_0$ , and this implies a long reflector structure which may be impractical in many cases.

It is worth noting, however, that a dual linearly polarized offset antenna can radiate two orthogonal elliptically polarized signals which are resolvable into their orthogonal components by a suitably elliptically polarized receiving antenna [38]. Hence frequency re-use by polarization diversity is feasible even with a conventionally fed offset parabolic reflector. However, the pointing accuracy of the antenna must be maintained to a high order of accuracy if the use of a fast-operating adaptive polarizer is to be avoided.

#### *B    Circular Polarization*

With a purely circular polarized primary-feed illumination, the offset parabolic reflector does not depolarize the signal. On reflection, each of the linearly polarized components of the incident wave effectively generates a

cross-polarized component. However, when the phase-quadrature relationship is introduced between the linear components it is found that the combination of the two orthogonal co-polarized vectors and the phase-asymmetric pair of cross-polarized vectors have the same direction of rotation. Hence the sum of these two signals results in a purely circularly polarized radiation, but the sum of the symmetric and asymmetric components results in a squinting of the radiation pattern from its boresight axis. The beam-squint effect acts to move the beam either forward or away from the axis of symmetry. The direction of the movement is dependent upon the hand of polarization.

Chu and Turrin [3] first published computed graphical data showing the effect of the reflector parameters  $\theta_o, \theta^*$  upon the magnitude of the beam-squint, and some key results are shown in Figs. 2.15 and 2.16. Adatia and Rudge [39] have derived an approximate formula which gives the beam-squint angle ( $\Psi_s$ ) simply as:

$$\Psi_s = \arcsin \frac{(\lambda \sin \theta_o)}{4\pi F} \quad (2.30)$$

This formula has been tested against computed and measured data and has been found, in all cases, to be accurate with 1.0 per cent of the antenna half-power beamwidth.

### C Practical Applications

The fully offset parabolic reflector is attractive for many applications, in that it offers the possibility of improved sidelobe performance and higher aperture efficiency. Some typical applications are considered below. In these cases, unless stated otherwise, the primary-feed has been assumed to be of conventional design and with good polarization properties.

#### (i) Point-to-point communications

With circular polarization the boresight gain reduction arising from beam-squinting effects need not be a major problem. For systems employing a single hand of polarization the beam-squint is simply compensated in the antenna

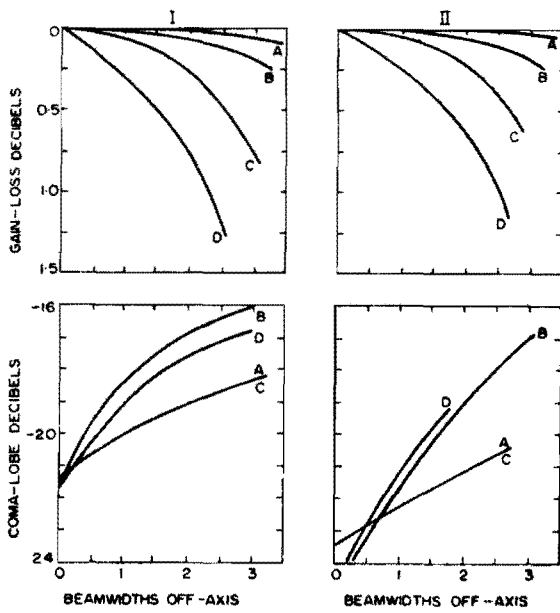


Fig. 2.13 Beam-scanning gain loss and coma-lobe levels. Illumination tapers of -6 dB (column I) and -10 dB (column II). (A):  $\theta^* = 30^\circ$ ,  $\theta_0 = 0$ . (B):  $\theta^* = 45^\circ$ ,  $\theta_0 = 0$ . (C):  $\theta^* = 30^\circ$ ,  $\theta_0 = 45^\circ$ . (D):  $\theta^* = 45^\circ$ ,  $\theta_0 = 45^\circ$ .

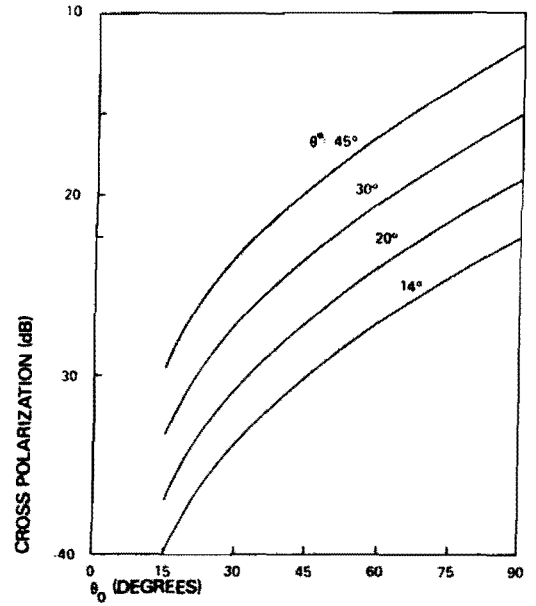
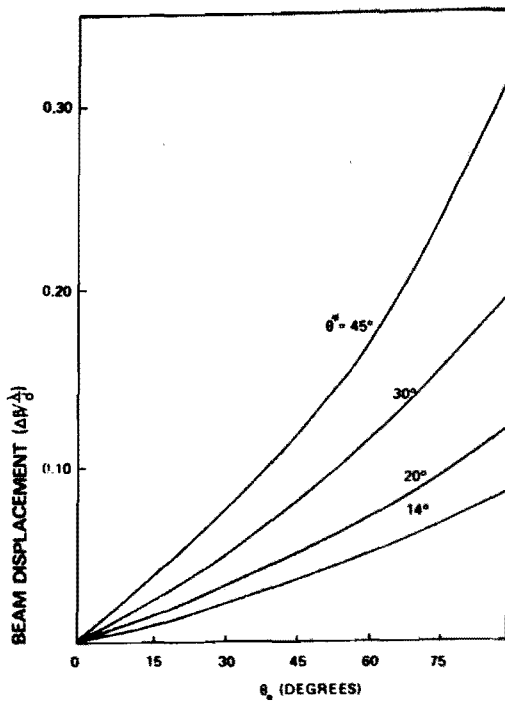


Fig. 2.14 Peak cross-polar levels radiated in the plane of asymmetry ( $\Phi = \pi/2$ ) as a function of the offset-reflector parameters  $\theta_0$  and  $\theta^*$ .



2.15 Beam displacement as a function of the offset-reflector parameters  $\theta_0$  and  $\theta^*$ .  $\Delta\beta$  is the angular squint of the beam in radians.

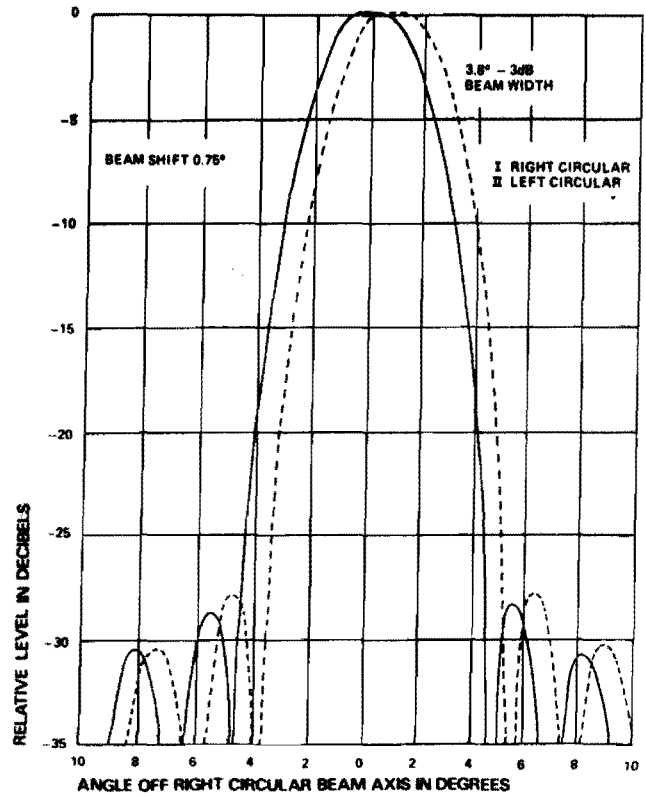


Fig. 2.16 Measured radiation patterns of an offset-reflector antenna operated with circular polarization at 18.5 GHz ( $F = 9.4 \lambda$ ,  $\theta_0 = 45^\circ$ ,  $\theta^* = 45^\circ$ ).

alignment. For dual-polarized applications, where the direction of squint is reversed for opposite hands of polarization, the boresight-gain loss can be readily reduced to less than 0.03 dB per beam by suitable choice of the reflector parameters. This loss corresponds to a beam-squint angle of less than 10 per cent of the antenna half-power beamwidth.

With linear polarization, a very exact alignment of the radiated beam is called for to remain within the boresight null of the cross-polarized radiation pattern. Practical dual-polarized operation, therefore, demands the use of a moderately large reflector  $F/d$  ratio [10]. Alternatively, good cross-polarization suppression can be achieved for a single linear polarization by use of a polarization-selective grid, either in the aperture plane or at the surface of the reflector [40,41]. A dual-polarized system can then be formed by interleaving two orthogonal polarization-sensitive reflector surfaces with separate foci. This is illustrated in Fig.2.17 [40,42].

(ii) Shaped or contoured beams

For certain spacecraft applications, where circularly polarized area coverage is required, even a 5 per cent beam-squint can produce significant changes in the gain at the edge of the coverage zone. This problem is simply overcome for a single hand of circular polarization, but for dual-polarized applications, the  $F/d$  of the reflector must be made as large as possible, consistent with the volumetric constraints. When the offset-reflector profile is deformed to provide a shaped or contoured beam, the beam-squint compounds the design difficulty; numerical techniques are virtually essential to achieve a desired beam-shape.

Wood et al [24] described the design and evaluation of a dual circularly polarized offset antenna intended for the European Communication Satellite System. The reflector surface was deformed in one plane to provide an elliptical coverage pattern of  $8.6^\circ \times 4.9^\circ$ . A co-polar/cross-polar ratio of better than 33 dB was predicted over the coverage zone. Limitations in the corrugated-horn primary-feed performance reduced this figure to 30 dB over 95 per cent of the zone on the experimental model. The tolerances upon the reflector profile and the location of the primary-feed are also likely to be



more critical in these designs and the beam shape and gain can be very sensitive to small feed misalignments [43]. For example, Fig.2.18, which is taken from [43], shows the variations in the peak gain of an offset reflector with small primary-feed displacements. This reflector has an  $F/d$  ratio of 0.52 and is shaped in the plane of asymmetry to provide an elliptical beam with an aspect ratio of approximately 1.8 : 1.

For linear polarization, the effective phase error introduced by the departure of the shaped reflector from true parabolic, results in a spatial redistribution of the cross-polar lobes generated by the reflector. Unless the reflector offset angle is made small, the antenna will exhibit very poor polarization purity in the coverage zone. Fasold [44] has described a linearly polarized offset-reflector system in which the perimeter of the reflector was contoured to provide an elliptical beam shape. However, the cross-polarization from this antenna was predictably high, with peak levels close to -20 dB. For a single linear polarization, good polarization purity can be restored by use of polarization-sensitive grids; for dual polarization, a larger  $F/d$  ratio is necessary.

Contoured beam shapes can also be achieved by the use of offset parabolic reflectors with multiple-element feed clusters. The feed elements are combined in amplitude and phase to generate a desired footprint over the coverage zone. Ultimately this technique offers considerably more flexibility in that the beam can be reconfigured to a variety of coverage patterns by changing the relative excitation coefficients of the feed array. The implications on the offset-reflector design are as for the previous cases, and a relatively large  $F/d$  ratio must be employed for dual-polarized applications. For applications demanding good polarization purity there are additional complications in that the feed array must itself exhibit good polarization properties. The combining network for the multiple elements will also be complex and is likely to be a critical feature of any practical design.

A multiple-feed offset antenna of this class has been developed for the Intelsat V spacecraft. The circularly polarized system described by Han [25] employs an offset parabolic reflector with an  $F/d$  ratio of approximately unity. The feed cluster has 78 square waveguide horns and produces

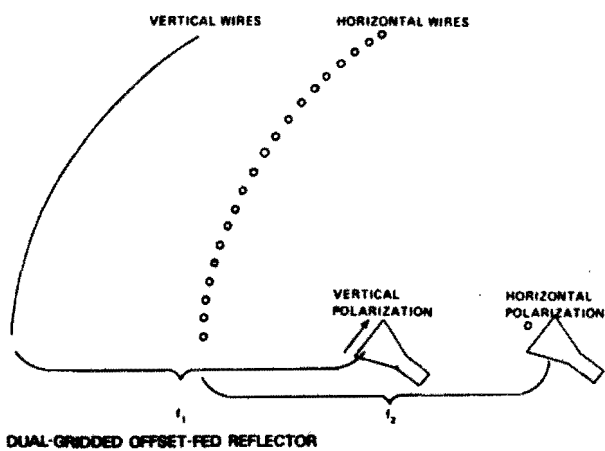


Fig. 2.17 Illustrating a dual-polarized offset-reflector antenna employing polarized grids.

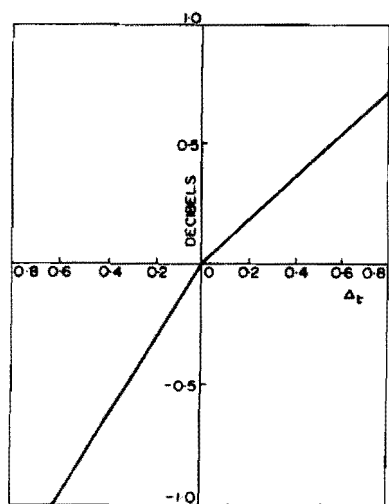


Fig. 2.18 Variations in the peak gain of the offset antenna ( $F/d = 0.52$ ) with primary-feed displacement by  $\Delta_t$  wavelengths along the  $y$  axis.

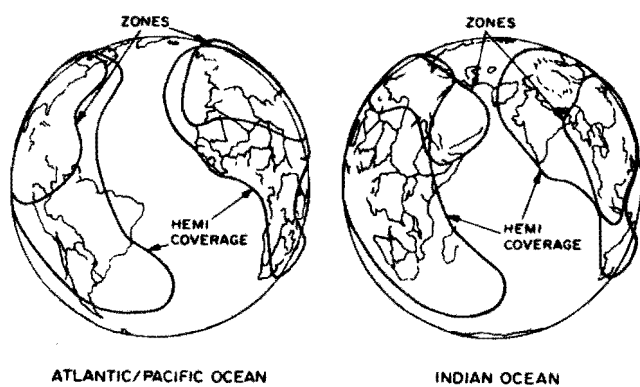


Fig. 2.19. Required coverages for Intelsat V hemi/zone antenna

4 hemispheric-shaped beams, two having right-hand and two left-hand polarization. The axial ratio of these beams within their respective coverage zones is less than 0.75 dB and the isolation between beams is better than 27 dB. The power distribution networks for each beam employ low-loss air stripline with switches to provide some reconfiguration of the beams for different subsatellite locations. Figure 2.19 illustrates a contour plot of the required coverage zones to be provided by this antenna.

(iii) Multiple spot beams

The performance of the single offset reflector as a multiple-spot-beam antenna was studied in some detail by Rudge et al [19,20]. In this investigation a three-beam circularly polarized configuration was designed and optimised using numerical techniques, and a detailed experimental evaluation was performed on a precisely made breadboard model. Since frequency re-use within each beam was not required, the antenna design made use of the beam-squint effect to reduce the beam spacing between the most closely spaced pair of beams. These beams were orthogonally polarized and had a minimum beam spacing of 1.1 HPBW with a beam efficiency of 60 per cent. The feed elements were conical-horn elements with optimum dimensions for cross-polar suppression (see Fig.2.8) and exhibited an isolation between beamports of better than 40 dB. Figure 2.20a shows the predicted and measured radiation patterns for the two beams. Figure 2.20b shows the radiation characteristics of the third beam. A beam to beam isolation of better than 30 dB in the coverage zone was achieved for this antenna. A means of achieving an outline design of antennas of this type is described in Section 2.4.

(iv) Monopulse tracking radars

This application, in particular, is one in which the offset-reflector depolarization can be a serious handicap. The predicted co-polar and cross-polar radiation fields of an offset reflector fed by a 4-horn static split monopulse feed in its tracking mode are illustrated in Fig.2.21. The cross-polar field can be seen to have a peak on the boresight axis. Randomly polarized signals from a radar target will result in an output from the tracking channel in which the boresight location appears to shift

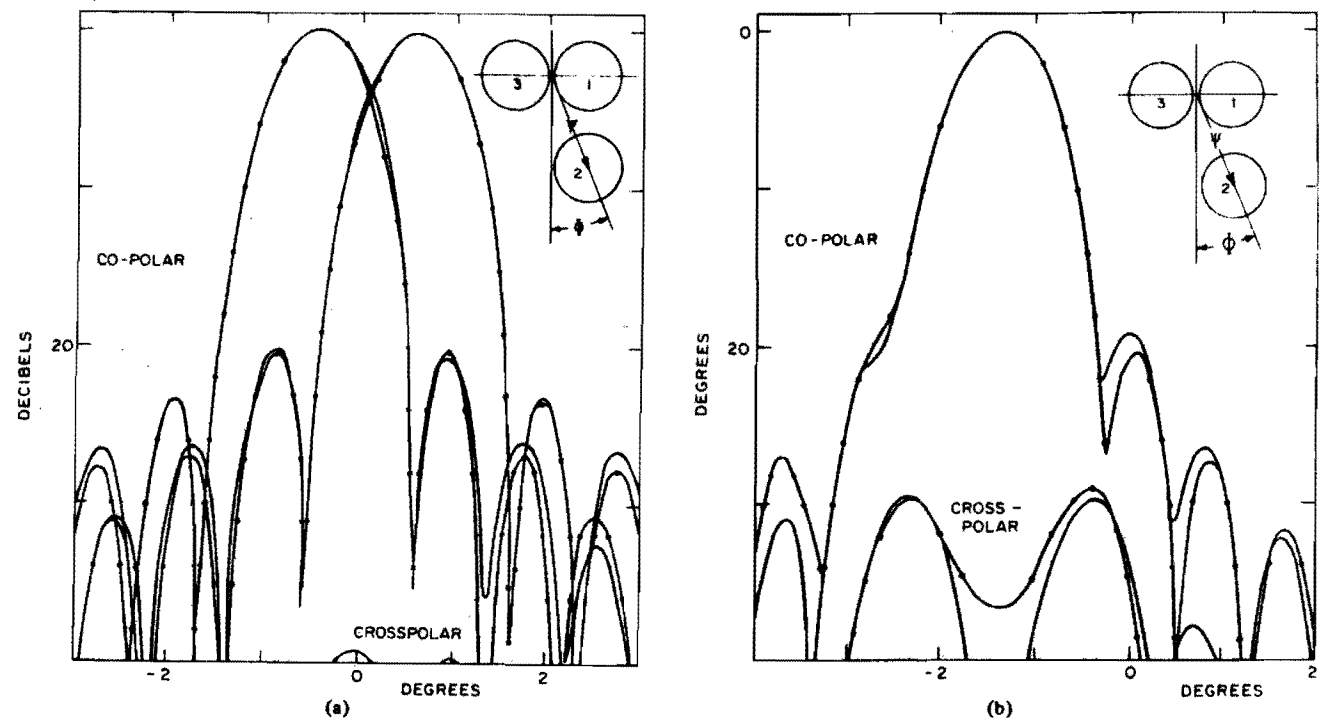


Fig. 2.20

Copolarized and cross-polarized radiation patterns of multiple-spot-beam antenna at 30 GHz. Measured ———. Predicted —●—. (a) Cut through beams 1 and 3:  $\Phi = 90^\circ$ . (b) Cut through beam 2:  $\Phi = 23.5^\circ$ .

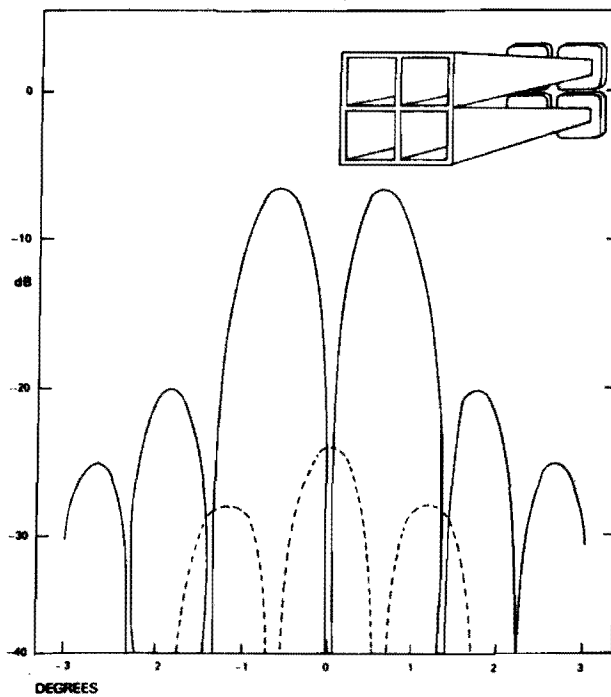


Fig. 2.21 Radiation pattern of a single-offset reflector fed by a 4-horn static-split monopulse feed (shown inset) in its tracking mode. Copolar ———. Cross-polar - - - - -.

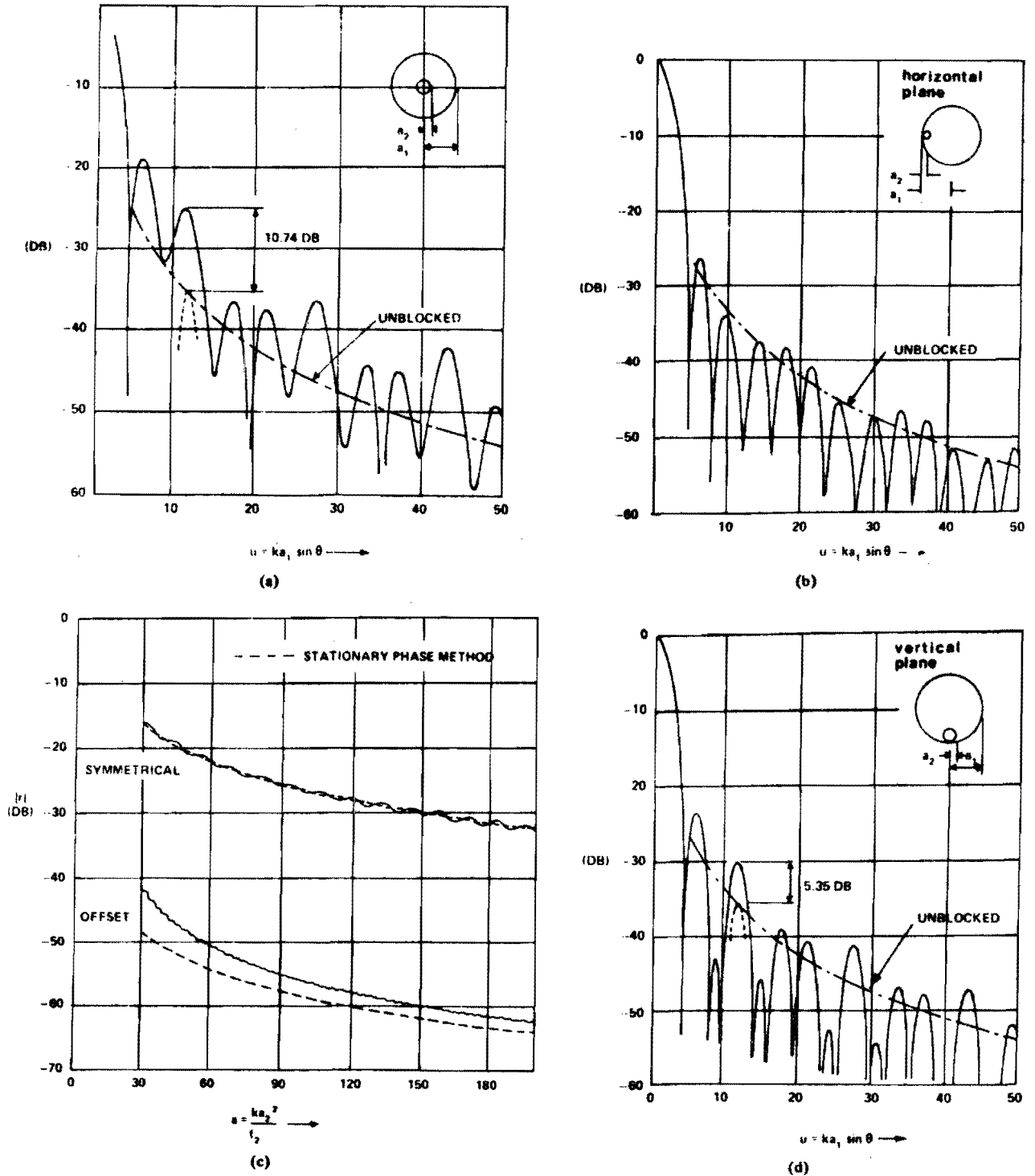


Fig. 2.22 Effects of aperture blockage on the radiated sidelobe levels and the reflection coefficient at the primary-feed for symmetrical and offset antennas. (a) Radiation pattern of blocked aperture ( $a_2/a_1 = 0.2$ ). (b) Radiation pattern for marginally blocked aperture ( $a_2/a_1 = 0.2$ ) in horizontal and vertical planes. (c) Reflection coefficients for illumination taper of 13 dB at subreflector edge. (d) Radiation pattern for marginally blocked aperture ( $a_2/a_1 = 0.2$ ) in horizontal and vertical planes.

sporadically. Its precise location at any time will be dependent upon the relative magnitudes of the orthogonally polarized components in the returning signal. This boresight uncertainty, which is sometimes termed boresight jitter, can impose serious limitations upon radar tracking accuracies.

Since the cause of boresight-jitter is the reflector de-polarization, one cure (with conventional feeds) is to employ larger  $F/d$  ratio reflectors. Alternative approaches are discussed in Section 2.5.

(v) Low-sidelobe antennas

One of the major attractions of the offset reflector antenna is the possibility of lower sidelobe radiation. This feature has become increasingly important in recent years as a consequence of the pressure upon the available frequency spectrum and the need to avoid interference from both friendly and unfriendly sources.

Dragone and Hogg [17] have shown theoretically that the fully offset parabolic reflectors offer significant advantages over their (blocked) axisymmetric counterparts. Improvements of up to 10 dB in near-in side-lobe levels can be inferred from their results given in Fig.2.22. The data shown in Fig.2.10 indicates that first sidelobe levels of the order of -30 dB can be realised with illumination tapers of the order of -20 dB. In fact, more favourable tapers than those provided by the feed employed in Fig.2.10 can reduce these levels considerably. Using corrugated horn feeds, pencil beams can be produced with first sidelobes at the -33 dB level coupled with aperture efficiencies of 70 per cent. An example of an antenna with this order of performance is shown in Fig.2.23. Lower sidelobes are also feasible with a more sophisticated primary-feed design, although some reduction in aperture efficiency will be implied. Elliptical beams can be generated by offset antennas in which the first sidelobes in a specified critical plane can be suppressed below the -40 dB level [36].

The illumination asymmetry in the principal plane of the offset reflector does introduce an undesirable shoulder on the beam when larger offset angles are used. This effect can be detected on the data shown in Fig.2.10 and cannot be

completely obviated except by the use of larger  $F/d$  ratios or more sophisticated primary-feeds.

Linearly polarized offset antennas will, of course, generate significant levels of cross-polar radiation unless the reflector has a large  $F/d$  ratio. However, for most applications it is found that the reflector de-polarization lies below the co-polarized sidelobe envelope. Hence, the offset reflector de-polarization does not preclude the use of this antenna in a low sidelobe role. For smaller offset reflectors, primary-feed spillover constitutes the main limitation on the overall sidelobe performance. These effects can be alleviated by good primary-feed design and some use of shields or blinders about the antenna aperture.

## 2.4 Design Procedure for Multiple Spot-Beam Antennas

### *A      Introduction*

In the electrical design of a multiple spot-beam offset-reflector antenna a large number of parameters must be taken into account and a considerable degree of interaction must be anticipated between these parameters. To achieve an optimised design it is obviously desirable to make use of numerical techniques to model the antenna configuration. However, even when sophisticated numerical models are available, a case can still be made for a more prosaic design procedure to produce an outline design. By this means the ranges of the parametric variables in the computations can be reduced and a better understanding obtained of the trade-offs and compromises involved.

To illustrate this process a step-by-step procedure will be described which can be employed to establish the outline design of a circularly-polarized offset reflector with multiple spot beams. A single spot beam can be designed using this process but the graphical data will not be accurate for very low sidelobe designs. The design of a linearly-polarized antenna follows a similar procedure but in this case the asymmetric reflector will not generate a beam-squint and the usual cross-polar lobes will appear in the plane of asymmetry. For linearly-polarized antennas the peak value of these lobes can be obtained from Fig.2.14.

## B The Design Parameters

The step-by-step procedure takes as its starting point a required beam-coverage specification for a set of  $n$  circularly polarized beams. The beam-coverage specification is expressed as the half-power beamwidth ( $\Psi_{0n}$ ) of each beam with its associated beam-pointing angles ( $\Psi_n, \phi_n$ ). These angles refer to fixed values in the secondary coordinate system of Fig.2.4. Since the maximum dimensional requirements of the antenna system are often an important parameter in a practical design, a volumetric constraint in the form of a bounding cylinder has been assumed. The bounding cylinder, which is described by its diameter  $D$  and height  $h_c$ , is assumed to contain both the reflector and its primary-feed system. The general configuration is illustrated in Fig.2.24. Other geometric constraints are obviously possible and could be treated similarly by a suitable geometric analysis.

Referring to Fig.2.24, the defining parameters of the offset reflector antenna to be specified by the design procedure are the focal length of the parent paraboloid ( $F$ ), the offset angle ( $\theta_0$ ) and the maximum semi-angle subtended by the reflector at the focus. Two secondary parameters, which are of particular interest here, are the diameter of the offset reflector projected aperture ( $d$ ) and the clearance ( $d_c$ ) between the parent paraboloid axis and the lower edge of the projected aperture.

The primary-feed is defined by type, diameter ( $2b$ ) and length ( $\ell$ ). Three feed types are considered here; the conical corrugated horn, the dual-mode (Potter) horn and the fundamental-mode conical horn. The locations of the primary-feed phase centres, to satisfy the desired beam-pointing criteria, are given in polar coordinates ( $\Delta_{tn}, \phi_n$ ) in the  $xy$  plane (see Fig.2.4) with origin at the reflector focus. The polar angle  $\phi_n$  is measured from the  $x$  axis.

Having established values for each of the parameters given above, data can be extracted from the graphs provided in this section to obtain an outline performance estimate for each beam. In addition to the achievable beam-pointing specification, which may differ from that desired initially, estimates can be made of the peak coma-lobe level, the gain loss due to off-



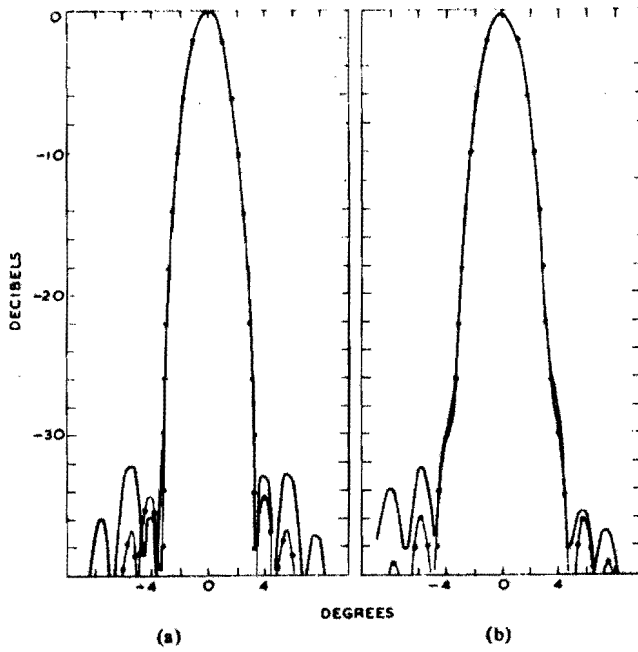


Fig. 2.23 Radiation patterns in principal planes for an offset reflector ( $F = 22.7 \lambda$ ,  $\theta_0 = 44^\circ$ ,  $\theta^* = 30^\circ$ ) fed by a circularly polarized corrugated horn with a -18-dB illumination taper at  $\theta = \theta^*$ . Frequency = 30 GHz. Antenna efficiency 70 percent neglecting ohmic losses. (a)  $\Phi = \pi/2$  (b)  $\Phi = 0$ . Measured —, Predicted —•—.

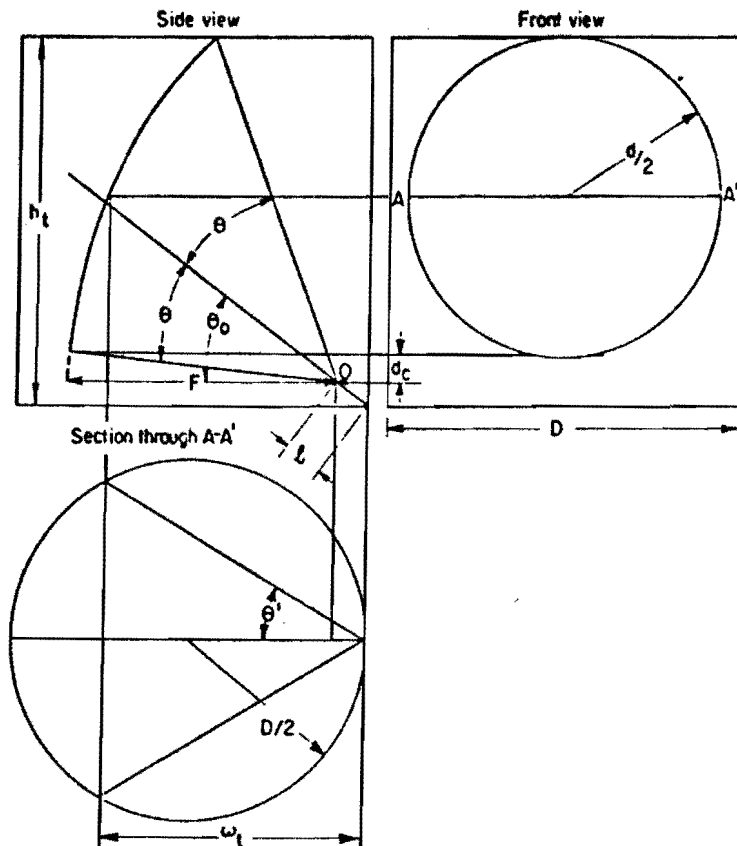


Fig. 2.24. Geometry of the bounding cylinder

axis feed locations, the spillover loss and the peak levels of the cross-polarized lobes. In Table 2.1 the input, output and performance parameters are summarised.

Table 2.1

Step by step design parameters

<u>Input Data</u>	
(i)	<u>Desired beam-coverage specification</u>
	$\psi_{on}$ = half-power beamwidth of nth beam
	$\psi_n$ = boresight pointing-angle of nth beam
	$\phi_n$ = azimuthal pointing-angle of nth beam
(ii)	<u>Volumetric constraints</u>
	D = diameter of bounding cylinder
	$h_t$ = height of bounding cylinder
<u>Output Data</u>	
(i)	<u>Basic reflector parameters</u>
	F = focal length of parent paraboloid in wavelengths
	$\theta_o$ = offset angle
	$\theta^*$ = semiangle subtended by reflector rim from focus
(ii)	<u>Secondary reflector parameters</u>
	d = diameter of reflector projected aperture
	$d_c$ = clearance distance reflector-to-feed
(iii)	<u>Feed parameters</u>
	Feed } = hybrid-mode, dual-mode or fundamental-mode conical type } horn
	2b = feed horn aperture diameter
	l = overall length of feed system
(iv)	<u>Feed phase-centre location in xy plane</u>
	$\Delta_{tn}$ = radial distance from geometric focus
	$\phi_n$ = polar angle from x-axis
(v)	<u>Performance parameters</u>
	Achievable beam-coverage specification
	Peak coma-lobe levels
	Off-axis gain loss
	Spillover loss
	Peak cross-polarized lobe level

### C The Design Procedure

The design procedure commences from a given beam-coverage specification and the dimensions of the bounding cylinder about the antenna. The procedure is outlined in Table 2.2. For circularly polarized offset reflector antennas, the primary-feed location must account for the beam-squinting effects introduced by the asymmetric geometry. This has been dealt with here by use of a modified 'beam deviation factor' derived in the text.

Table 2.2

Design procedure

Step	Operation	Output
1	Specify projected aperture diameter	$d$
2	Specify reflector parameters	$F, \theta_o, \theta^*$
3	Specify primary-feed parameters	$b_n, \ell$
4	Determine primary-feed locations	$\Delta_{tn}, \phi_n$
5	Test for feed spacing	
6	Outline performance estimate	half-power beamwidth beam-pointing angles coma-lobe level off-axis gain loss spillover loss cross- polar lobe level

#### Step 1: Reflector projected aperture

The minimum half-power beamwidth ( $\psi_{\min}$ ) required to satisfy a given antenna specification will define the minimum projected-aperture area which must be made available. For a moderate degree of sidelobe suppression (i.e. maximum sidelobe levels below -20 dB) a minimum projected-aperture diameter of the order of  $1.1 \lambda / \psi_{\min}$  will be necessary. To achieve a sidelobe specification of the order of -30 dB a minimum projected-aperture diameter of at least

$1.2 \lambda / \Psi_{\min}$  will be required. The minimum beam-spacing which can be achieved with a simple primary-feed configuration is of the order of one half-power beamwidth, and to achieve this limit with a single reflector implies a compromise with regard to both the maximum sidelobe levels and the spillover loss, which can be tolerated. To provide some guide to this trade-off, note that to achieve a beam-spacing approaching one beamwidth implies sidelobe levels of the order of -20 dB for a beam close to the antenna boresight, and a corresponding spillover loss of the order of 1.5 to 2.0 dB. From the data and trends indicated, an initial value for the projected-aperture  $d$  can be selected.

### Step 2: Reflector parameters

In many practical applications the volumetric constraints upon the overall antenna structure will impose significant constraints upon the range of the reflector parameters,  $F$ ,  $\theta_0$ , and  $\theta^*$ . In the procedure established here the bounding surface of the antenna structure is taken as a cylinder of height  $h_t$  and diameter  $D$ . The geometry is illustrated in Fig.2.24. The diameter of the projected-aperture of the offset reflector is related to the other parameters by (2.3) and from the geometry we find:

$$h_t = 2F \tan \left( \frac{\theta_0 + \theta^*}{2} \right) + \ell \sin \theta_0 \quad (2.31)$$

$$D = \frac{d^2/4 + W_t^2}{W_t} \quad (2.32)$$

where:

$$W_t = F \left[ 1 - \left( \frac{\sin \theta_0}{\cos \theta_0 + \cos \theta^*} \right)^2 \right] + \ell \cos \theta_0 \quad (2.33)$$

The feed clearance distance ( $d_c$ ) is given by:

$$d_c = 2F \tan \left( \frac{\theta_0 - \theta^*}{2} \right) \quad (2.34)$$

To avoid aperture-blocking effects and to minimise the reflector reaction upon the primary-feed, it is desirable that  $d_c$  be large enough to provide clearance for the primary-feed hardware.

When illuminated with circularly-polarized radiation, the offset reflector will produce a beam-squinting effect, the magnitude of which is a function of the reflector parameters. With respect to the offset reflector axis of symmetry, the direction of the squint is toward the left for right-handed circular polarization and toward the right for left-handed polarization<sup>+</sup>. In certain cases it may be desirable to maximise this effect, with the objective of squinting two orthogonally-polarized beams toward each other. In other cases it may be necessary to minimise the effect to prevent movement of a beam which is said to be used simultaneously for two hands of polarization. From (2.30) the angle squinted through ( $\psi_g$ ) can be obtained to an accuracy of better than  $0.01 \lambda/d$ .

Having established an initial value for  $d$  from Step 1, the equations (2.30-2.34) can be employed to tabulate the values of  $h_t$ ,  $D$ ,  $d_c$  and  $\psi_g$  as a function of only  $\theta_0$  and  $\theta^*$ . An initial value of between 5 and 10 wavelengths should be allowed for the feed length  $\ell$ . To provide an example, Fig.2.25 shows these values for a constant projected-aperture ( $d$ ) of  $70\lambda$  and  $\ell = 10\lambda$ . Given the volumetric constraints in terms of  $h_t$  and  $D$ , a range of acceptable parameter combinations may be obtained from these data. The range can be expressed, for example, as the combination which maximises  $\theta_0$  and that which minimises  $\theta_0$  while satisfying the volumetric constraints and providing an acceptable feed-clearance distance  $d_c$ . Initial values for  $F$ ,  $\theta_0$  and  $\theta^*$  can thus be established as one, or both, of the limiting values of this range or, alternatively, a combination which corresponds to a suitable mid-point in the  $\theta_0$  spread. In making this choice the following comments may be found useful:

---

<sup>+</sup> A wave receding from an observer having clockwise rotation of the electric field is taken as right-handed circular polarization.

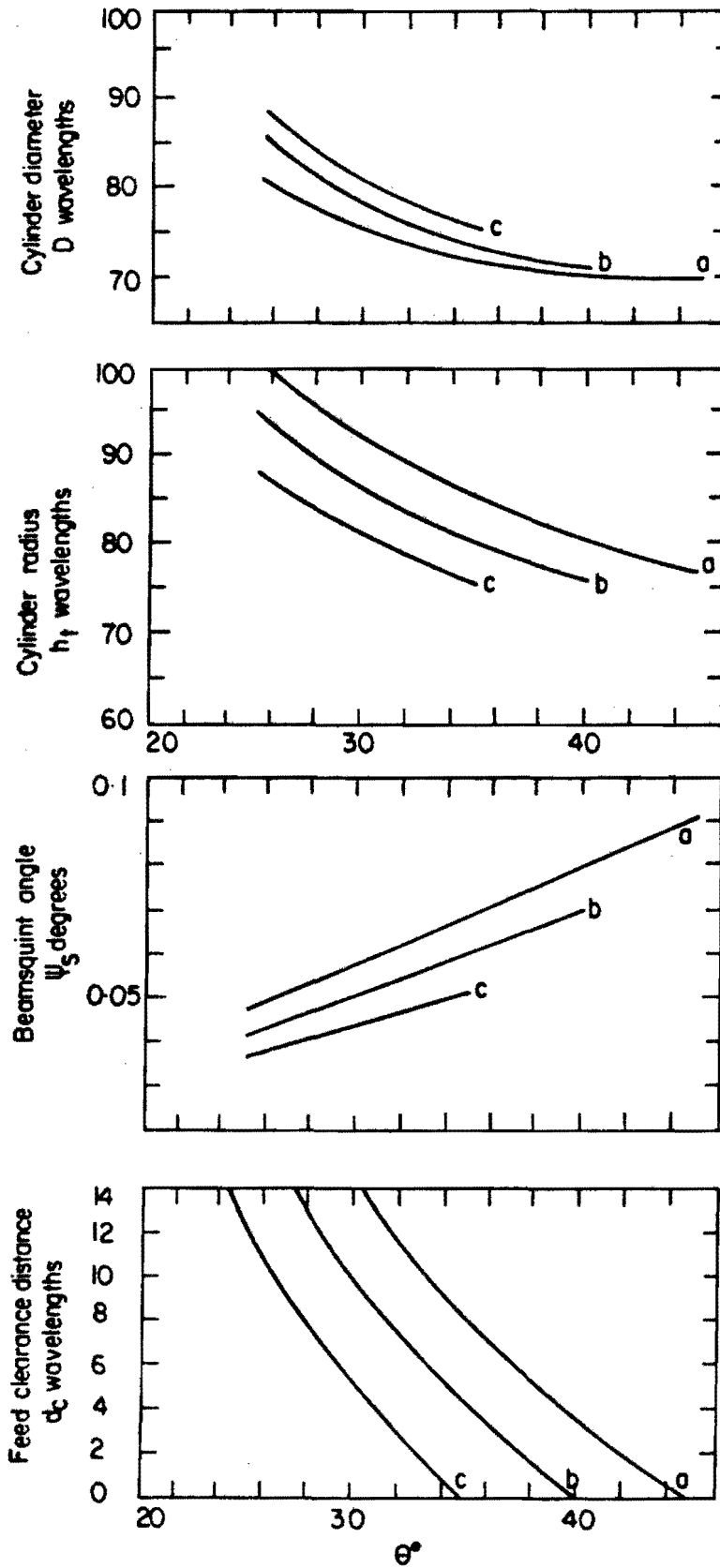


Fig. 2.25 Parameters for an offset reflector with diameter  $70\lambda$  and feed length  $10\lambda$ , contained within a cylinder  
 (a)  $\theta_0 = 45^\circ$ , (b)  $\theta_0 = 40^\circ$ , (c)  $\theta_0 = 35^\circ$

If two polarizations are to be employed on a single-beam  $\Psi_s$  should be made as small as possible. If dual polarization on a single beam is not contemplated and two orthogonally polarized beams are to be closely spaced, then the beam-squint effect may be utilised usefully to reduce the spacing of the beams.

Large values of  $\theta_0 + \theta^*$  tend to produce increased distortion of off-axis beams and some disparity in the sidelobe performance in the two principal planes. Figure 2.10 presents some computed data showing the sidelobe trend for on-axis beams.

### Step 3: Primary-feed parameters

Three practical primary-feed types are considered here as suitable feed elements for an offset reflector antenna:

- (i) The corrugated or hybrid-mode conical horn,
- (ii) The 'Potter' or dual-mode conical horn,
- (iii) The fundamental mode ( $TE_{11}$ ) conical horn.

Both the hybrid-mode and dual-mode horns can be considered to be high performance feeds for the circularly-polarized offset-reflector antenna. The cross-polarization generated by these devices is of a very low level (i.e.  $< -30$  dB) and the co-polarized beam is rotationally symmetric with low side-lobe radiation; VSWRs in both cases can be made very low (i.e.  $< 1.1 : 1$ ). The dual mode horn is a somewhat narrow-band device with a bandwidth of the order of 5%. The hybrid-mode feed can be operated over significantly larger bandwidths and its drawbacks in the multiple-beam application are largely a function of its higher mass and that the corrugations make its outer dimensions significantly larger than its radiating aperture area. In addition, both the corrugated horns and the dual-mode horn have a tapered aperture-illumination which implies a lower gain for a given aperture diameter. This feature can be very undesirable when closely spaced beams are required.

The small flare-angle fundamental-mode conical-horn will operate over a reasonably wide bandwidth and has an aperture diameter which is approximately 11% smaller than that of either the hybrid-mode or dual-mode horn for approximately the same shape main-beam illumination characteristics. The fundamental-mode horn generates a cross-polar component, however, which has a minimum value when the horn aperture is 1.14 wavelengths in diameter. The cross-polar characteristics of the horn are summarised in Fig.2.8a. The effect of the horn cross-polar radiation is illustrated in Fig.2.26 which shows typical values of radiated cross-polarization peaks from offset reflector antennas fed by  $TE_{11}$  mode horns of diameter  $2b$ . The peak values occur in a crest around the main co-polar beam, at points corresponding to the -10 to -20 dB level of the main co-polar beam and are theoretically similar in any plane.

Either a hybrid-mode horn or a dual-mode horn is generally preferable from the point of view of illumination characteristics. However, for closely-spaced beams it may be necessary to employ the physically smaller, higher gain, fundamental-mode horn.

Having established values for  $\theta_0$  and  $\theta^*$  in Step 2, the aperture radius ( $b$ ) of either a hybrid-mode, dual-mode or fundamental-mode horn can be determined to provide a specified sidelobe performance for an on-axis beam. From Fig.2.27 the necessary aperture-illumination taper ( $T$ ) to produce a given sidelobe level is illustrated for several values of  $\theta^*$ . The illumination taper on an asymmetrical reflector differs in its principal planes and this is accounted for in Figs.2.28 and 2.29. The illumination taper  $T$  is composed of a symmetrical component  $G$ , which is a function of the feed aperture diameter ( $2b$ ), plus a space-factor  $S$  which is dependent upon  $\theta_0$  in the plane of symmetry ( $S_s$ ) but essentially independent of  $\theta_0$  in the plane of asymmetry ( $S_a$ ). The decibel sum of either  $G + S_s$  or  $G + S_a$  provides an effective illumination taper  $T$  for each principal plane which is related to the first sidelobe levels in these planes in Fig.2.27. The illumination taper  $G + S_a$  is in fact the mean value of the edge illumination, which varies around the reflector periphery. The taper  $G + S_s$  corresponds to the minimum taper value and the correspondence between this factor and the resultant sidelobe prediction has been tested



against computed data and found to be accurate within 1 dB for illumination tapers of not more than 10 dB.

While employing Figs.2.27-2.29 to select a suitable feed diameter, it may also be desirable to be aware of the beam-broadening effect of the edge illumination taper upon the radiated beam. In Fig.2.30 a beam-width factor  $N$  is shown as a function of the illumination taper  $T$ . The half-power beam-width of the radiated beam in question can be obtained from:

$$\psi_{on} = \frac{N\lambda}{d} \quad (2.35)$$

The length of the primary-feed elements can then be estimated by assuming a typical flare for the feed of the order of 10 degrees semi-angle. Having determined the aperture radius  $b$ , the feed length can be simply derived, but on specifying  $l$  an additional allowance must be made for the location of such components as polarizers, orthomode transducers or transitions if they are to be employed.

#### Step 4: Primary-feed location

Since the offset reflector antenna is an asymmetric structure, some decision must be taken with regard to the relative alignment of the reflector axis of symmetry and the beam-cluster to be generated. In certain cases this decision may be dictated by other considerations but, where a freedom of choice exists, the following general points are worthy of consideration:

Gain loss due to off-axis beam locations is virtually independent of the plane of offset;

The beam-squint effect can best be used to squint beams together, or apart, by locating orthogonally polarized beams on opposite sides of the reflector axis of asymmetry (i.e. about the plane  $\phi = 0^\circ$ ).

The quality of the radiation pattern appears to be best maintained by locating off-axis beams in the plane of asymmetry ( $\phi = 90^\circ$ ). Off-axis beams in the

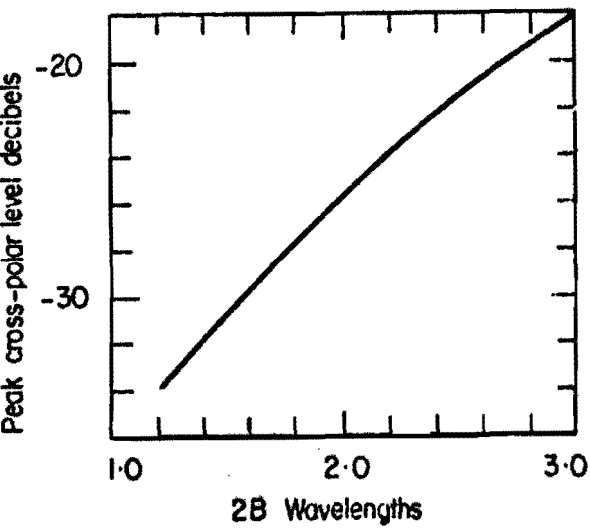


Fig. 2.26 Computed radiated cross-polar peaks from offset reflector antennas with  $\theta_0$  values in range 40-45 degrees and  $\theta^0$  values in the range 30-35 degrees when fed by circularly-polarised fundamental-mode conical horns of diameter  $2B$ .

Fig. 2.27 First radiated sidelobe levels from reflectors, as a function of reflector illumination taper  $T$ .

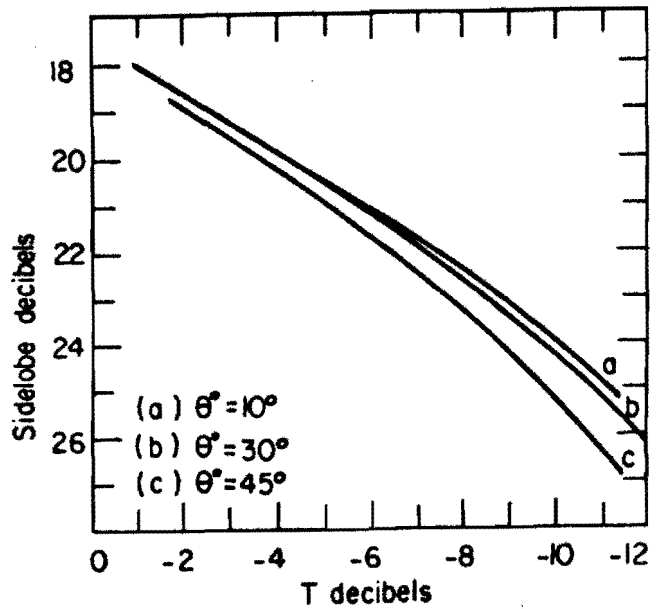
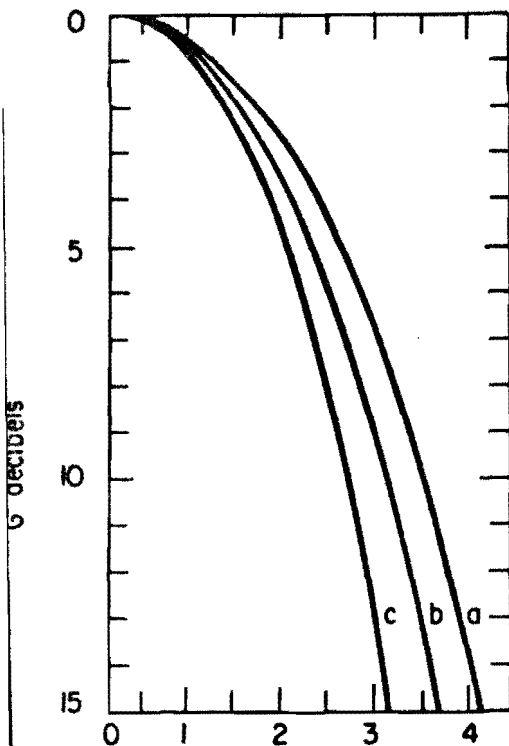


Fig. 2.28 Illumination taper due to predominant terms of feed directivity as a function of  $u = 2\pi b \sin \theta^*$ , where  $b$  is the feed aperture radius.

- (a) Hybrid-mode or dual-mode feeds
- (b) Circularly-polarised fundamental-mode feed
- (c) Uniformly illuminated circular-aperture feed - for comparative purposes



plane of symmetry ( $\phi = 0$ ) tend to exhibit a 'shoulder' on the main beam for relatively small off-axis shifts.

Having aligned the reflector axis of symmetry with the required beam cluster, beam locations can be specified in terms of their pointing angles  $\psi_n, \phi_n$ . From Steps 1-3 initial parameter values have been assigned for both the reflector and the primary-feed. The primary-feed aperture radius for any specified beam ( $b_n$ ) has been selected initially purely on the desired illumination characteristics for an on-axis beam. When several beams are to be generated from a single reflector, this initial value may well be modified.

From a knowledge of the initial estimate of the feed radius ( $b_n$ ) Figs.2.28 and 2.29 can be employed to determine the mean illumination taper ( $G + S_a$ ) dB. This illumination taper can then be applied in Fig.2.31 to obtain the relevant beam deviation factor ( $B_{df}$ ) for this reflector and feed configuration.

Given the beam-pointing coordinates ( $\psi_n, \phi_n$ ), the location of the primary-feed phase-centre is to be specified in terms of the focal region coordinates ( $\Delta_{tn}, \phi_n$ ). The derivation of  $\Delta_{tn}, \phi_n$  is complicated by the beam-squint effect, but this effect has been accounted for in the following equations. The direction of the squint is a function of the hand of polarization and in (2.36) and (2.37) the choice of the upper sign implies a beam-squint toward the axis of symmetry of the antenna ( $\phi = 0$ ) while the lower sign should be taken for a squint away from the symmetry axis. The equations provided have been tested against computed data for high gain offset-reflector antennas ( $d$  greater than 20 wavelengths) and found to produce good results for off-axis beams within 10 degrees of the antenna boresight, providing that the comatic distortion of the radiation pattern is not excessive.

To determine  $\Delta_{tn}, \phi_n$ , the following procedure is followed:

The beam-squint angle ( $\psi_s$ ) can be obtained from (2.30).

The azimuthal feed-location angle ( $\phi_n$ ) is then given by:

$$\phi_n = \arctan \left[ \frac{\sin \psi_n \sin \phi_n \pm \sin \psi_s}{\sin \psi_n \cos \phi_n} \right] . \quad (2.36)$$

The effective focal-length for the offset reflector is given by:

$$F_e = F \left( \frac{1 + \cos \theta^*}{\cos \theta_0 + \cos \theta^*} \right) \quad (2.37)$$

and the radial feed location distance  $\Delta_{tn}$  is then given by:

$$\Delta_{tn} = \frac{F_e}{B_{df}} \sqrt{\left( \sin^2 \psi_n + \sin^2 \psi_s \pm 2 \sin \psi_n \sin \psi_s \sin \phi_n \right)} \quad (2.38)$$

#### Step 5: Test for feed-spacing

Having followed Steps 3-4 for the beam-pointing angles of interest, a test must be carried out to ensure that the feed aperture-dimensions and the feed locations are physically compatible. In the event that the configuration fails this test, the dimensions of one or more of the feeds must be reduced and Steps 3-5 reiterated until an acceptable compromise is reached.

#### Step 6: Outline electrical performance

The outline electrical performance of the multiple-beam antenna configuration derived from Steps 1-5 can be estimated by reference to the data provided here. Commencing with the primary-feed radius for the  $n$ th beam ( $b_n$ ), Figs. 2.28 and 2.29 can be employed to determine the feed mean illumination taper  $T$ , given by  $(G + S_a)$  dB. From Fig. 2.30 the half-power beamwidth for the beam can then be obtained. Although this data was computed for on-axis beams, it has been found that the half-power beam-broadening effect due to a small shift from the focus is small for offset-reflectors with  $\theta^*$  not greater than

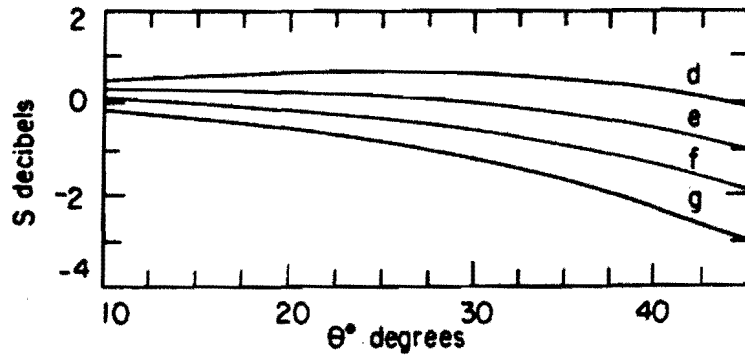


Fig 2.29 Space attenuation factor for offset reflectors, including additional  $\frac{1}{2}(1+\cos\theta^2)$  term from feed expression. For plane of symmetry use (d)  $\theta = 45^\circ$  (e)  $\theta = 40^\circ$  (f)  $\theta = 35^\circ$ . For plane of asymmetry use curve (g) for any offset angle.

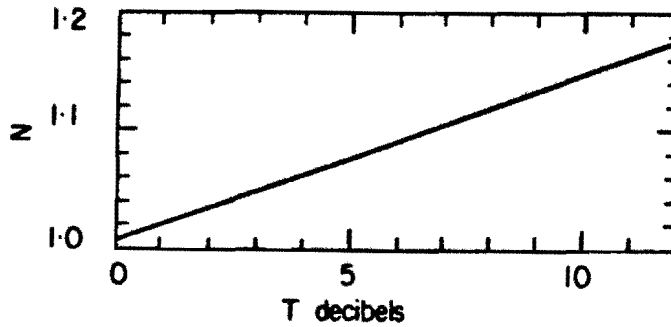


Fig. 2.30 Beamwidth factor  $N$  as a function of reflector illumination taper.

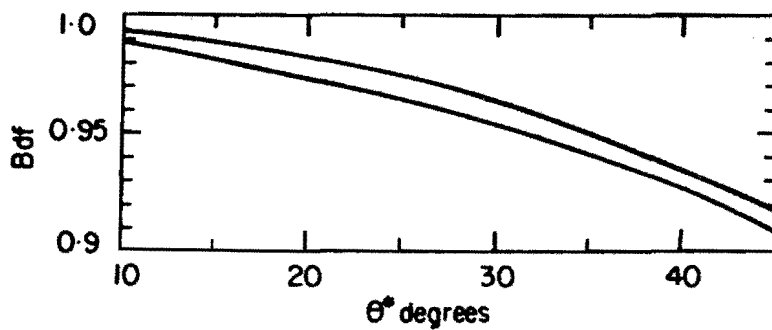


Fig. 2.31 The Beam Deviation Factor with mean reflector illuminations of (a) -10dB and (b) -6dB

45°. An estimate of the spillover loss for this combination of feed and reflector can be obtained from Fig.2.32. For a fundamental-mode conical horn a guide to the peak cross-polarization level in the antenna far-field can be obtained from Fig.2.26 which was compiled from computed data for offset reflectors with offset angles in the range 35-45° and  $\theta^*$  in the range 30-35°. The E-field model for the radiation from an open-ended circular waveguide was employed in the computations and it was found that the predicted levels were, to a first order accuracy, independent of the reflector parameters over the range indicated. It has also been noted that the peak levels of the cross-polarized radiation are relatively insensitive to small beam offsets.

Finally, the curves provided in Fig.2.13 give some indication of the reduction in gain which can be anticipated for an off-axis beam and the level of the peak coma-lobe. Interpolation between these computed characteristics will provide an indication of the antenna performance, but extrapolation should be applied with caution, since radiation patterns which involve significant gain losses due to off-axis beams may also exhibit other distortions than the coma-lobe characteristic indicated. Any significant discrepancies between the desired antenna performance and that realised, will demand a reiteration of the process from the relevant step in the procedure.

#### *D    A Beam Deviation Factor For Offset Reflector Antennas*

For an axisymmetric parabolic reflector, given a beam-pointing specification  $(\psi', \phi')$  the corresponding primary-feed location can be expressed in terms of focal plane polar coordinates  $\Delta_{tn}, \phi_n$ , as in [63].

$$\Delta_{tn} = \frac{F' \sin \psi'}{B_{df}} \quad (2.39a)$$

$$\phi_n = \phi' \quad (2.39b)$$

where  $B_{df}$  is termed the Beam Deviation Factor and is a function of the reflector curvature and the feed illumination taper, and  $F'$  is the focal length of the axisymmetric paraboloid.

For offset reflector antennas with offset angles not exceeding  $45^\circ$  it has been found that, in the absence of beam-squinting effects, the relationships expressed by the above equations can provide useful results by applying a concept of an 'equivalent' symmetrical reflector.

Equivalence is taken here to imply a symmetrical reflector which subtends the same semi-angle  $\theta^*$  and has the same value of projected-aperture diameter as the offset reflector of interest. Equating projected-apertures for offset and symmetrical reflectors of the same semi-angle  $\theta^*$ , we find that the focal-length of the equivalent reflector is given by:

$$F_e = \frac{(1 + \cos \theta^*)}{\cos \theta_0 + \cos \theta^*} F \quad (2.40)$$

where  $F$  is the focal length of the offset reflector as defined in Fig.2.1. The dimension  $F_e$ , which will be a constant for any given offset reflector, could also be interpreted as the effective focal length of the offset reflector.

Substitution of the effective focal length for  $F'$  in (2.39a) will provide a relationship between the primary-feed location and the resultant beam-pointing direction, which is valid for offset reflectors in the absence of beam-pointing effects. From an examination of the beam-squint phenomenon in high-gain offset reflector antennas, it has been observed that, within the small cone of angles of interest here, the beam-squint acts similarly on every radiated beam to either shift this beam toward or away from the axis of symmetry of the reflector. On a contour plot of the antenna beam coverage (in  $\sin \psi$  space) the direction of this shift is thus perpendicular to the  $\phi = 0$  axis, with a magnitude given by  $\sin \psi_s$ . This is illustrated in Fig.2.33 where the primed coordinates  $\psi', \phi'$  indicate the position of the beam prior to the action of the beam-squint effect and  $\psi_n \phi_n$  denotes the final location of

the beam. In the case illustrated the hand of polarization has been chosen to squint the beam toward the antenna axis of symmetry. Use of the opposite hand of polarization would result in a squint of the same magnitude, still acting perpendicular to the axis of symmetry, but acting in the opposite sense to that shown and thus leading to  $\psi_n > \psi'$  and  $\phi_n > \phi'$ .

Making use of (2.30) and the geometry of Fig.2.33 the relationship between the unsquinted and the squinted locations of the radiated beams can be resolved into radial and azimuthal components as follows:

$$\sin \psi' = \sqrt{\left( \sin^2 \psi_n + \sin^2 \psi_s \pm 2 \sin \psi_n \sin \psi_s \sin \phi_n \right)} \quad (2.41a)$$

$$\tan \phi' = \frac{\sin \psi_n \sin \phi_n \pm \sin \psi_s}{\sin \psi_n \cos \phi_n} \quad (2.41b)$$

where a choice of the upper sign implies a shift toward the axis of symmetry and the lower sign indicates a shift away from this axis. Substitution of (2.41) in (2.39) provides an approximate offset reflector beam-deviation factor, inclusive of beam-squint effects.

## 2.5 Primary Feeds For Offset-Reflector Antennas

### A Offset-reflector Focal-plane Fields

The offset parabolic reflector has many obvious advantages, but the depolarizing beam-squinting phenomena clearly represent a major limitation in many applications. However, since analytical insight has provided a good understanding of the casual factors, it can also indicate the necessary cure. To follow this vein, it will be useful to consider the form of the electromagnetic fields set up in the focal region of the offset reflector when a plane wave is normally incident upon the reflector aperture plane.

Bem [45] has performed an analysis of the focal-plane fields which, although limited to normally incident waves, has the particular merit that the trans-



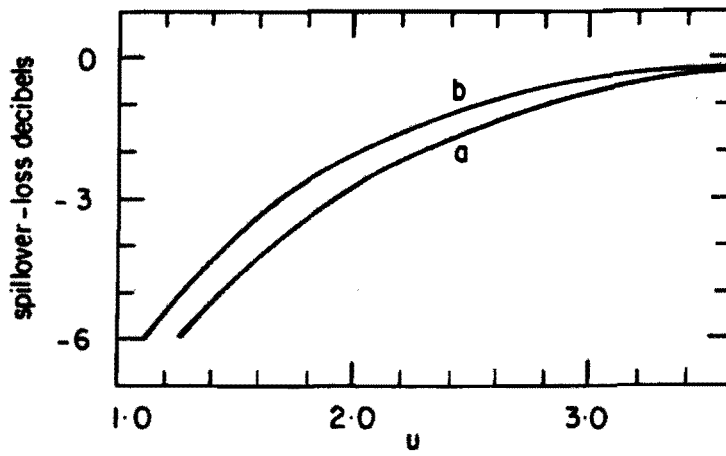


Fig. 2.32 Feed spillover loss. (a) Hybrid-mode or dual-mode feeds. (b) Fundamental-mode conical feeds (circularly-polarised).

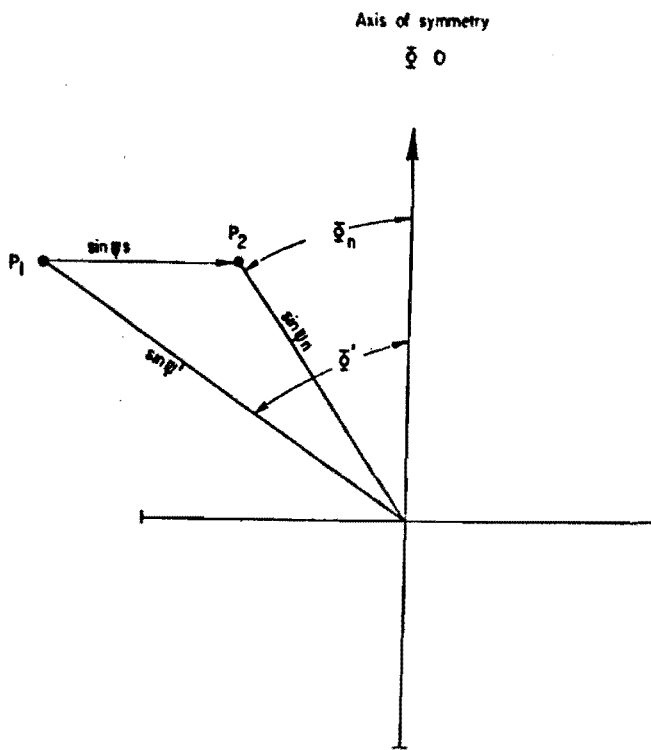


Fig 2.33 Beam squint diagram, where  $P_2$  and  $P_1$  refer to the location of the beam centre with and without the beam-squint effect.

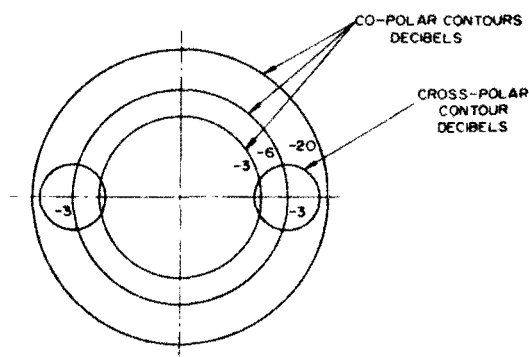


Fig. 2.34 Approximate contour plot of typical focal-plane field distribution of an offset parabolic reflector uniformly illuminated from a distant linearly polarized source.

verse focal-plane fields  $E_x$ ,  $E_y$  can be expressed approximately in a simple closed form. Valentino and Toullos [46] confirmed Bem's results by extending them to include incident waves making small angles with the reflector bore-sight and comparing their results with measured data. Ingerson and Wong [47] have also employed a focal-region field analysis to determine beam-deviation factors for offset-reflector antennas. For offset-reflectors with long focal length and polarized in the plane of symmetry, we have from Bem's analysis:

$$E_x(u, \phi_0) = \frac{2J_1(u)}{u} + \frac{jd \sin \theta_0}{F} \frac{J(u)}{u} \cos \phi_0 \quad (2.42a)$$

$$E_y(u, \phi_0) = \frac{-jd \sin \theta_0}{F} \frac{J_2(u)}{u} \sin \phi_0 \quad (2.42b)$$

where  $r', \phi_0$  are polar coordinates in the reflector focal plane with origin at the geometric focus,  $u(r')$  is a normalised parameter representing the distance  $r'$  to a point in the focal plane and all multiplying constants have been suppressed.  $J_n(u)$  is the Bessel function of order  $n$ . The solutions for the wave polarized in the plane of asymmetry is achieved from (2.42) by interchanging  $x$  and  $y$  and replacing  $\phi_0$  by  $2\pi - \phi_0$ .

Inspection of (2.42) reveals that the cross-polar component ( $E_x$ ) is an axisymmetric function with a magnitude increasing with the offset angle  $\theta_0$  and in phase quadrature with the principal axisymmetric co-polar component. The axisymmetric co-polar term is also modified by the presence of a quadrature component which is identical to the cross-polar term in all but its dependence upon  $\phi_0$ . Figure 2.34 shows an idealised contour plot of the amplitude of the focal-plane field in the vicinity of the geometric focus.

#### B The Offset-reflector Matched-feed Concept

If the primary-feed is to provide an optimum conjugate match to the incoming field, then its aperture fields must exhibit similar polarization characteristics. Conventional high performance axisymmetric feeds (such as the corrugated horn) provide a conjugate match to the co-polar component

only, which results in the apparently poor polarization properties of the offset reflector.

The focal-plane field distributions described by (2.42) can be matched very effectively by making use of higher order asymmetric waveguide modes. Rudge and Adata [14,15,26] have proposed a class of new primary-feed designs employing mode combinations in cylindrical, rectangular and corrugated waveguides. To illustrate the general principle of this approach, Fig.2.35a illustrates the nature of the symmetric and asymmetric components which make up the offset-reflector focal-plane fields for two linear polarizations. To adequately match this characteristic in a smooth-walled cylindrical waveguide, the required asymmetric mode is the  $TE_{21}$ . Figure 2.35b shows the field distribution in the conical-horn mouth for the two orthogonal  $TE_{21}$  modes which, for convenience, are designated  $TE_{21}^1$  and  $TE_{21}^2$ . The transverse field components of these modes ( $E_x^1, E_y^1, E_x^2, E_y^2$ ) can be readily derived from the solution of the vector wave equation in the cylindrical guide [29]. In terms of a normalised distance parameter  $u'$  and a polar angle  $\phi_0$  and omitting multiplying constants, these components can be expressed as:

$$E_x^1(u', \phi_0) = K' [J_1(u') \cos \phi_0 + J_3(u') \cos 3\phi_0] \quad (2.43a)$$

$$E_y^1(u', \phi_0) = -K' [J_1(u') \sin \phi_0 - J_3(u') \sin 3\phi_0] \quad (2.43b)$$

$$E_x^2(u', \phi_0) = K'' [J_1(u') \sin \phi_0 + J_3(u') \sin 3\phi_0] \quad (2.44a)$$

$$E_y^2(u', \phi_0) = K'' [J_1(u') \cos \phi_0 - J_3(u') \cos 3\phi_0] \quad (2.44b)$$

where  $K'$  and  $K''$  are constant factors proportional to the complex coefficients of the two  $TE_{21}$  modes.

In the principal planes ( $\phi_0 = 0$  and  $\pi/2$ ), Equations (2.44) reduce to:

$$E_x^1(u', 0) = 4K'J_2(u')/u' \quad (2.45a)$$

$$E_y^1(u', 0) = 0 \quad (2.45b)$$

$$E_x^1(u', \pi/2) = 0 \quad (2.45c)$$

$$E_y^1(u', \pi/2) = 4K'J_2(u')/u' \quad (2.45d)$$

Comparing (2.45) with the asymmetric terms in (2.42) it can be seen that the coefficient of the  $TE_{21}^1$  mode can be selected to provide a perfect match to both the co-polar and cross-polar asymmetric components when the reflector is polarized in the plane of symmetry (ie along the  $-x$  axis). For operation with the principal polarization along the  $y$  axis (plane of asymmetry) from (2.44), the  $TE_{21}^2$  mode gives in the principal planes:

$$E_x^2(u', 0) = 0 \quad (2.46a)$$

$$E_y^2(u', 0) = 2K''J_2'(u') \quad (2.46b)$$

$$E_x^2(u', \pi/2) = 2K''J_2'(u') \quad (2.46c)$$

$$E_y^2(u', \pi/2) = 0 \quad (2.46d)$$

where:

$$J_2'(u') = dJ_2(u')/du'$$

Equations (2.46) can be compared with the asymmetric components of the reflector focal-plane field for a wave polarized in the plane of asymmetry. Making the necessary simple transformations in (2.42) the asymmetric components ( $E^a$ ) are given by:

$$E_x^a(u,0) = 0 \quad (2.47a)$$

$$E_y^a(u,0) = \frac{jd \sin \theta_0}{2F} \frac{J_2(u)}{u} \quad (2.47b)$$

$$E_x^a(u,\pi/2) = \frac{jd \sin \theta_0}{2F} \frac{J_2(u)}{u} \quad (2.47c)$$

$$E_y^a(u,\pi/2) = 0 \quad (2.47d)$$

Comparison of (2.46) with (2.47) indicates a non-ideal match. However, the Bessel differential functions  $J_2'(u)$  have very similar general characteristics to the  $J_2(u)/u$  distribution; and, by judicious choice of the constant  $K''$ , the two functions can be closely matched over the aperture of the feed horn.

The differences in the principal-plane distributions of the orthogonal  $TE_{21}$  modes is a consequence of the boundary conditions imposed by the smooth-walled cylindrical structure. The boundary conditions have similar implications with regard to the lack of axisymmetry in the co-polarized radiation arising from the fundamental  $TE_{11}$  mode. To achieve axisymmetry in the co-polarized radiation it is necessary to add a component of the  $TM_{11}$  mode. This technique is well-established and forms the basis of the well known dual-mode horn or

Potter horn [31]. For cylindrical corrugated structures in which the fields satisfy anisotropic boundary conditions, it can be shown that the corresponding  $HE_{21}$  hybrid modes have identical distributions in the principal planes. Combined with the fundamental  $HE_{11}$  mode, these structures can provide a close to ideal match to the offset reflector focal fields in both principal polarizations.

In Table 2.3 the modes required to provide focal-plane matching with three different feed structures are summarised. The cylindrical structures are also suitable for use with two hands of circular polarization. The corrugated rectangular case, although equally feasible, is not shown since the mode designations for this structure are not standardised.

Table 2.3

Waveguide modes for offset reflector focal-plane matching

Feed structure	Waveguide modes	
	Principal polarization	
	Plane of symmetry (-x)	Plane of asymmetry (y)
Smooth-walled cylindrical*	$TE_{11}^1 + TM_{11}^1 + TE_{21}^1$	$TE_{11}^2 + TM_{11}^2 + TE_{21}^2$
Corrugated cylindrical*	$HE_{11}^1 + HE_{21}^1$	$HE_{11}^2 + HE_{21}^2$
Smooth-walled rectangular	$TE_{10} + TE_{11}/TM_{11}$	$TE_{01} + TE_{20}$

Efficiency optimisation techniques, such as those described in a recent review paper by Clarricoats and Poulton [31], can be applied to optimise the performance of the offset antenna. If  $\bar{E}_1$ ,  $\bar{H}_1$  are the offset-reflector focal-

plane fields and  $\bar{E}_2, \bar{H}_2$  the fields created at the aperture of the primary-feed when unit power is transmitted, then the efficiency can be obtained from an integration of these fields over the aperture plane of the feed(s).

$$\eta = \frac{1}{2} \int_S \left( \bar{E}_1 \times \bar{H}_2 + \bar{H}_1 \times \bar{E}_2 \right) \cdot d\bar{S} \quad (2.48)$$

Optimisation of this  $\eta$  parameter will lead to the optimum values of the mode coefficients, but the optimum efficiency condition will not be the desired condition for all applications.

Alternatively and more simply in this case, the antenna co-polar performance can be optimised independently to whatever criterion is relevant and the cross-polar performance simply optimised by choice of the higher order mode coefficients. The interaction with the co-polar characteristic will be small and generally favourable in that the higher order modes which cancel the offset reflector cross-polar lobes will also act to compensate for the asymmetric space-attenuation factor introduced by the offset geometry.

The optimum values of the complex coefficients of the modes can be determined by using the mathematical techniques described in the early sections, with the desired higher order modes included in the primary-feed models. By examining the cross-polar radiation pattern of the offset antenna, for a range of values of the mode coefficients, the optimum characteristics can be readily determined. The close correlation between the value of the first cross-polar lobe peaks and the required level of the higher order mode coefficient in the primary-feed will be found to be an excellent guide in most cases.

Trimode devices based upon the matched-feed principle have been constructed in smooth-wall cylindrical guides and dual-mode rectangular feeds have also been demonstrated. These prototype devices were constructed for operation with a single linear polarization. A fully dual-polarized version of the trimode cylindrical structure has been recently developed and corrugated hybrid-mode versions have also been studied [48]. The practical aspects of the matched-feed approach can best be realised by examining the design of the

prototype trimode device introduced in 1975 [14]. The basic configuration is illustrated in Fig.2.36.

### C Prototype Trimode Matched-Feed

The trimode primary-feed is essentially a small flare-angle conical horn with two steps or discontinuities. The first step region ( $d_3/d_2$ ) is asymmetric and generates the  $TE_{21}$  mode. The diameter  $d_2$  cuts off all higher modes. The second step ( $d_2/d_1$ ) is axisymmetric and the guide dimensions cut off all modes above the  $TM_{11}$ . The symmetry of this discontinuity avoids the further generation of the  $TE_{21}$  mode. The amplitudes of the modes are governed by the ratios  $d_3/d_2$  and  $d_2/d_1$  and the relative phases of the modes are adjusted by the constant-diameter phasing section which follows each discontinuity. The mode amplitudes required are a function of the offset angle  $\theta_0$  and the semi-angle  $\theta^*$  of the offset reflector. Typically, the required mode amplitudes lay in the range 20-30 dB below the fundamental. The diameter of the primary-feed aperture is selected in the usual way to satisfy the illumination requirements of the reflector. The overall length of the feed is between 0.25 and 1.0 wavelengths greater than a conventional axisymmetric dual-mode feed of the Potter type.

Predicted and measured radiation characteristics of this feed are shown in Fig.2.37. The feed has an aperture diameter of  $2.8 \lambda$  and the measurements are made at 30 GHz. When used with a precision offset reflector with parameters  $F = 22.7 \lambda$ ,  $\theta_0 = 44^\circ$  and  $\theta^* = 30^\circ$ , the matched-feed provides a significant improvement in cross-polar suppression over a conventional feed. Typically, feeds of this particular design can provide a minimum of 10 dB additional suppression of the reflector cross-polarization (relative to a conventional primary-feed) over a 4-5 per cent bandwidth. At mid-band the additional cross-polar suppression can approach 20 dB. Typical radiation pattern and bandwidth characteristics are shown in Figs.2.38 and 2.39. These characteristics should not be interpreted as defining the fundamental bandwidth limitations of multimode matched-feed devices. A number of techniques can be applied to improve the bandwidth of the feeds. For example, dual-mode corrugated horn devices should offer significantly improved performance in this respect [48].



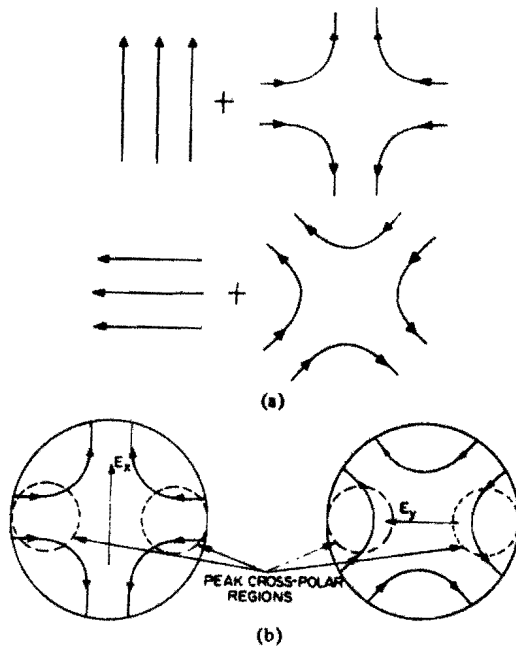


Fig. 2.35 (a) Field configurations of symmetric and asymmetric components of the offset-reflector focal-plane fields with the incident wave polarized in the plane of symmetry and in the plane of asymmetry. (b) Required field configuration in the aperture of a circular horn for focal-plane field matching in the orthogonal linear polarizations.

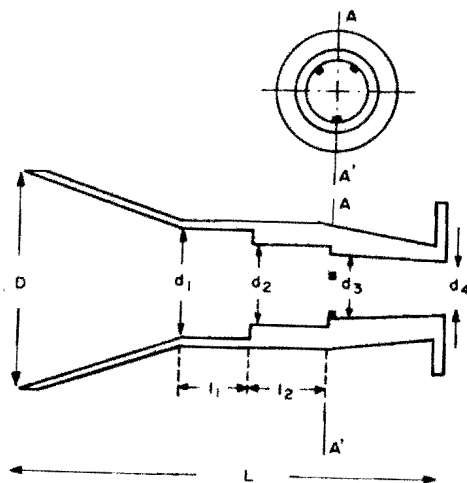


Fig. 2.36 Prototype trimode offset-reflector matched-feed device.

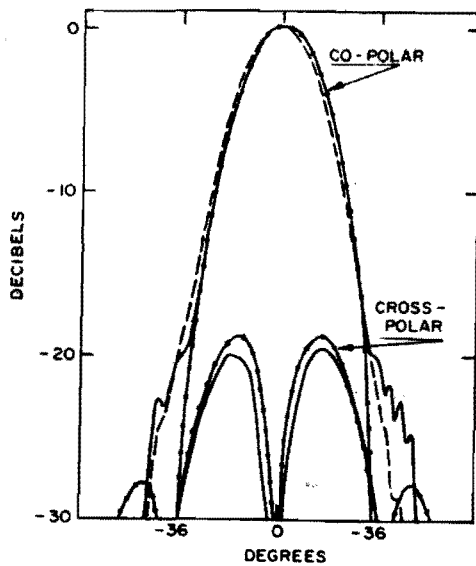


Fig. 2.37 Predicted and measured radiation characteristics for the 30-GHz prototype matched feed. Predicted ( $H$  plane) —•—, Measured ( $H$  plane) ———, ( $E$  plane) - - - -.

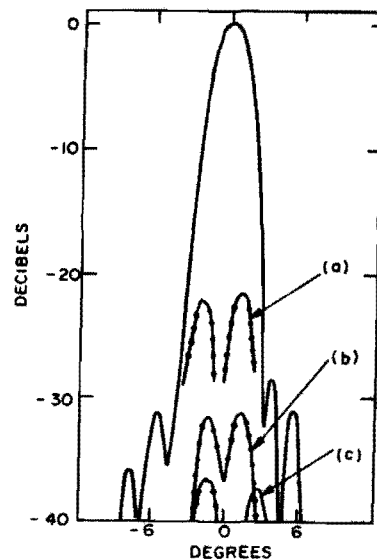


Fig. 2.38 Measured radiation patterns in plane of asymmetry for off-set-reflector antenna ( $F = 22.7 \lambda$ ,  $\theta_0 = 44^\circ$ ,  $\theta^* = 30^\circ$ ). (a): Conventional Potter-horn feed. (b): Matched feed (initial measurement) (c): Optimized matched feed. Copolar ———. Cross-polar —•—.

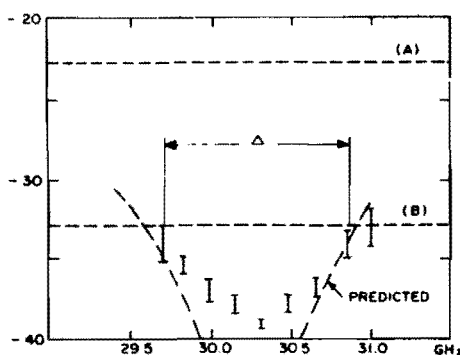


Fig. 2.39 Measured cross-polar suppression bandwidth of K-band trimode matched feed (I). (A): Nominal cross-polar level with conventional feed (reflector with  $\theta_0 = 44^\circ$ ,  $\theta^* = 30^\circ$ ). (B): 10-dB improved suppression level, defining bandwidth  $\Delta$ .

## D Matched-Feed for Monopulse Radars

The undesirable effect of offset-reflector de-polarization upon precision tracking monopulse radars has been mentioned. Rudge and Adatia [15,26] proposed that the matched-feed principle could be applied to this problem by incorporating the necessary higher order modes in a 4-horn static split feed. The questionable features of this application were identified as:

- (i) the level of cross-polar suppression which could be achieved by an essentially off-axis rectangular feed element, and
- (ii) whether the matched-feed condition could be maintained for both sum and difference excitations of the mono-pulse feed.

The proposal was investigated by mathematical modelling of the offset reflector with its multimoded feed elements and the construction and evaluation of one element of the 4-horn feed. Figure 2.40 shows the computed cross-polar levels for a 4-horn matched-feed and a conventional 4-horn device. The difference channel radiation pattern in the principal plane ( $\phi = 0$ ) has zero cross-polar radiation and is not shown in the figure. Figure 2.41 shows the rectangular feed element and Fig.2.42 summarises the measured radiation pattern and VSWR bandwidth performance of this K-band device. It was concluded that significant reductions in boresight jitter can be achieved by matched-feed techniques.

## 2.6 Dual-Reflector Offset Antennas

### A The Open Cassegrainian Antenna

For applications involving complex primary-feed structures, the use of a Cassegrainian feed system has some obvious advantages. In particular, the Cassegrainian configuration allows the feed elements and the associated circuitry to be located close to the main reflector surface, possibly avoiding long RF transmission paths and the need for extended feed support structure, while the forward-pointing feed format can be a desirable attribute for applications requiring low-noise performance.



Of the variety of offset Cassegrainian systems proposed in the literature, perhaps the best known is the open Cassegrainian antenna introduced in 1965 by the Bell Telephone Laboratories [1,2]. The antenna, shown in Fig.2.2 comprises an offset section of a paraboloid and an offset hyperboloid subreflector, fed by a primary feed which protrudes from an aperture in the main reflector surface. With this configuration it is possible to design the antenna such that the subreflector does not block the aperture of the main reflector. However, as a direct consequence of the positions of the primary-feed, some aperture blockage due to the feed system is unavoidable.

The analysis of the complete antenna can be performed by means of the physical-optics-based current distribution technique for the subreflector and the aperture-field integration method for the main reflector (see Fig.2.43). Expressed in spherical coordinate components ( $E_\theta$ ,  $E_\phi$ ), the subreflector fields thus obtained can be inserted into (2.10) and (2.12) to determine the tangential aperture fields of the main reflector and, hence, via (2.18) or (2.19) to determine the far fields of the overall antenna. Thus the analysis essentially involves the evaluation of four two-dimensional diffraction integrals at each field point. Under certain circumstances, use can be made of the axes of symmetry afforded by the subreflector geometry to eliminate the azimuthal dependent integrals, thereby alleviating the computational problem. Tierley and Zucker [49] have also described a technique for reducing the double integrals associated with the main reflector into a more convenient one-dimensional form. The technique, which is based upon an application of the stationary-phase approximation in the azimuthal part of the integral, allows more economical predictions of both the near-in and the far-out sidelobe performance of the open Cassegrainian antenna.

In general, the basic radiation characteristics of the open Cassegrainian antenna do not differ significantly from those of an equivalent single-offset-reflector antenna. To avoid aperture blockage, the open Cassegrainian antenna must employ large offset angles and, when fed by conventional primary-feeds, exhibits beam squinting and de-polarizing characteristics which are similar to the single offset reflector. However, for applications where these particular performance parameters are not of major concern, the open

Cassegrainian configuration offers excellent potential for realising high overall efficiency and low wide-angle sidelobe radiation. Figure 2.44 shows an open Cassegrainian antenna of the Bell Laboratories design located at the University of Birmingham in England. Figure 2.45 shows measured and predicted data made on a precision model of this design at the Bell Laboratories. This antenna had a computed efficiency of better than 65 per cent (including spillover and scattering losses, but not ohmic loss).

#### *B    The Double-Offset-Reflector Antenna*

An alternative dual-offset-reflector configuration, which offers a number of attractive features, is the so-called double-offset antenna shown in Fig.2.2. This antenna, which was first implemented by Graham [11], provides a convenient location for the primary-feed hardware by use of an offset section of a hyperboloidal subreflector in a Cassegrainian arrangement. Two variations of the double offset are illustrated in the figure. A Gregorian version, in which the subreflector comprises an offset portion of an ellipsoidal reflector, is also feasible and has been considered by Mizugutch et al [50]. For either of the versions shown, the overall antenna geometry can be designed to be completely free of aperture blockage.

Analyses performed by several workers [12,13,50,52] have shown that the double-offset antenna can be designed such that, when fed by a conventional linearly polarized primary-feed, the de-polarization arising from the two offset reflectors can be made to cancel, thus providing an overall low cross-polar characteristic. This performance is achieved by matching the scattered radiation fields from the subreflector to the main reflector.

The principle is essentially similar to the matched-feed approach previously described for single offset reflectors and, in theory, the technique offers a greater potential for broadband performance.

Approximate techniques based upon the use of geometric optics [13,50,51] indicate that a perfect match can be achieved (i.e. giving zero cross-polar fields in the main reflector aperture) when the axis of the parent sub-reflector surface is depressed by an angle ( $\alpha$ ) from the axis of the parent

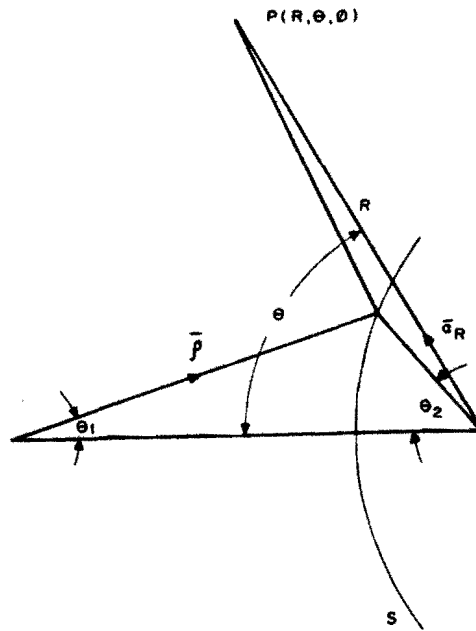


Fig. 2.43 Subreflector geometry.

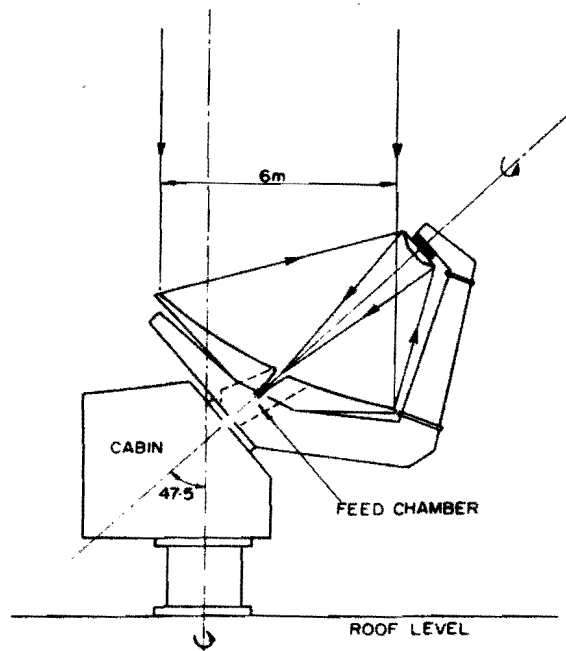


Fig. 2.44 6-m open Cassegrainian antenna located at the University of Birmingham, England.

paraboloid. This condition is illustrated in Fig.2.2. A mathematical expression relating the depression angle  $\alpha$  to the parameters of the subreflector has been derived by Mizugutch et al [50]. In its simplified form this can be expressed as:

$$\tan \frac{\alpha}{2} = \frac{1}{M} \tan \frac{\psi_0}{2} \quad (2.49)$$

where  $M = (1 + e)/(1 - e)$  and  $e$  is the eccentricity of the subreflector,  $\psi_0$  is the feed offset angle, and the geometry is illustrated in Fig.2.46.

Structurally, the optimised geometry is not very compact and this can be a drawback for applications where the volumetric constraints are severe. Earlier experimental results described by Graham [11] and the rigorous diffraction analysis performed by Adatia [12] confirmed the general validity of the optimisation formula, although the level of cross-polar suppression is not independent of the subreflector dimensions and curvature. Later results obtained by Adatia [52] indicated that the major limiting factor in the realisation of polarization purity with double-offset antennas is the diffraction effects introduced by the finite-sized subreflector. Diffraction analysis shows that the magnitude of the diffraction-generated cross-polar field component is primarily a function of the transverse dimensions of the subreflector in wavelengths, the eccentricity of the subreflector surface and the primary-feed illumination taper. For good cross-polar suppression, subreflectors with large transverse dimensions and high values of eccentricity are favoured.

In Fig.2.47 the co-polar and cross-polar components of the fields scattered from an offset subreflector with a diameter of  $10 \lambda$  are shown for the plane of asymmetry. The associated differential phase characteristics are shown in Fig.2.48. The deviation from the ideal in-phase characteristics is a consequence of the non-optical scattering by the finite subreflector. This phase deviation essentially limits the polarization purity of the overall antenna, since the cancellation of the de-polarized field generated at the main reflector is impaired. This is apparent in Fig.2.47 which also shows the



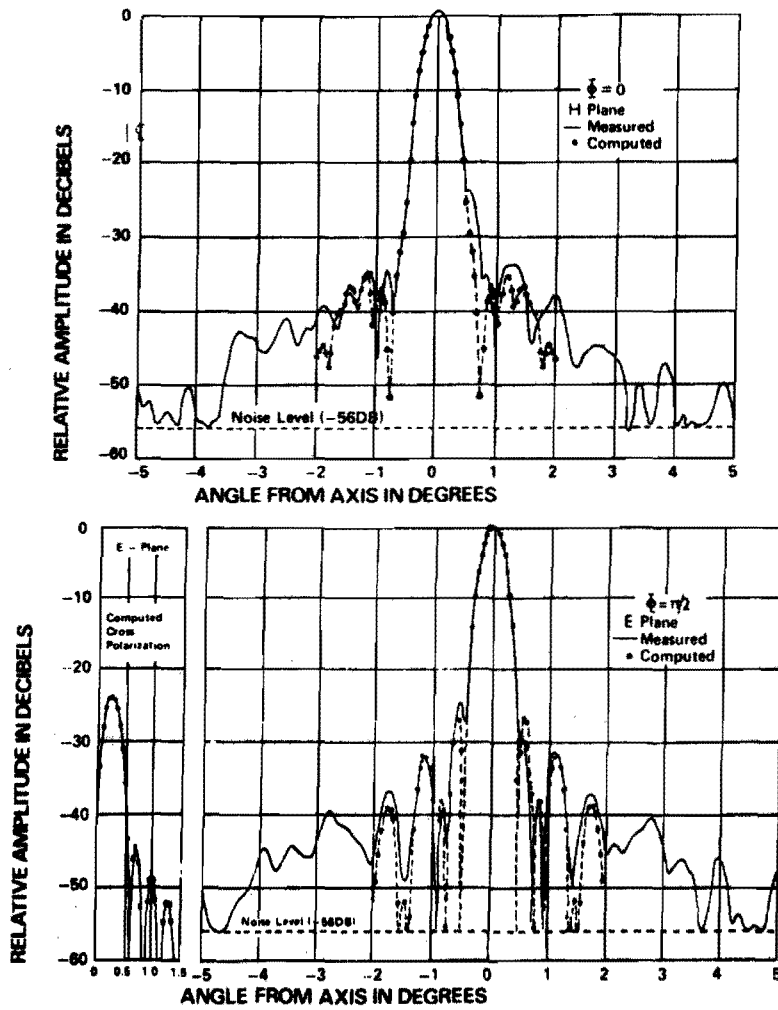


Fig. 2.45 Radiation patterns of a 60-GHz experimental model of the Bell open Cassegrainian antenna with parameters  $F = 152 \lambda$ ,  $\theta_0 = 47.5^\circ$ ,  $\theta^* = 30.5^\circ$ ,  $\theta_1 = 7.5^\circ$ , and a subreflector diameter of  $40 \lambda$ .

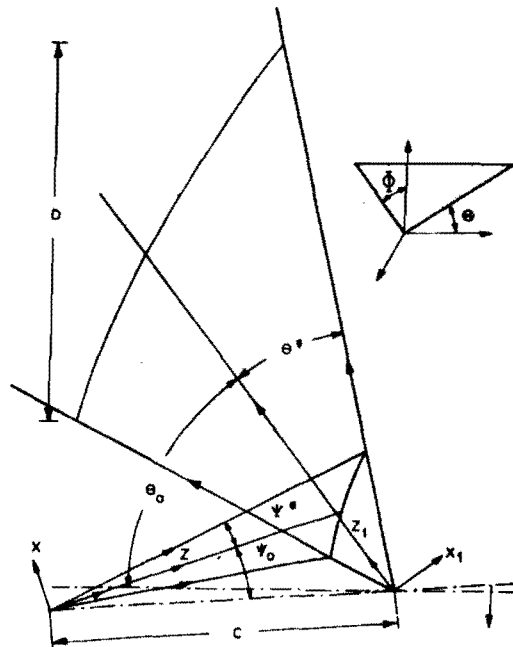


Fig. 2.46 The double-offset antenna geometry and parameters.

residual cross-polar field distributions in the main offset-reflector projected aperture. The multilobe structure of this distribution is directly attributable to the non-uniform phase distributions of the subreflector fields. Figure 2.49 shows the predicted secondary field characteristics in the principal planes for a double-offset antenna with the parameters given in Table 2.4 and a subreflector diameter of  $10 \lambda$ . The cross-polar fields are well above the levels indicated by geometric optics and can be reduced to below -40 dB only by use of a subreflector diameter of greater than  $25 \lambda$ .

Table 2.4

Parameters of a dual offset reflector antenna with geometry optimised for optimum cross-polar cancellation

Main offset reflector	Subreflector
$\theta_o = 53.3^\circ$	$\bar{\Psi}_o = 16^\circ$
$\theta^* = 24.8^\circ$	$\Psi^* = 8^\circ$
$d = 36 \lambda$	$\alpha = 4^\circ$
Magnification $M = 4.03$	

An alternative approach to the elimination of cross-polarization from dual-offset reflector systems has been followed by Albertsen [53,54]. In this approach the two reflecting surfaces are shaped to provide the desired aperture-field conditions in the main reflector. The mathematical approach involves the solution of simultaneous partial differential equations with certain specified initial conditions. The solutions provide the profiles of the two reflector surfaces under constraints which provide for an in-phase cross-polar free-field distribution in the projected aperture of the main reflector. One of the principal attractions of this general approach is that the problem may be formulated for any prescribed position of the main and sub-reflector surfaces. Hence, at least in principle, highly compact dual-offset configurations can be realised, although subreflector diffraction effects will still limit the cross-polar performance when small subreflectors are

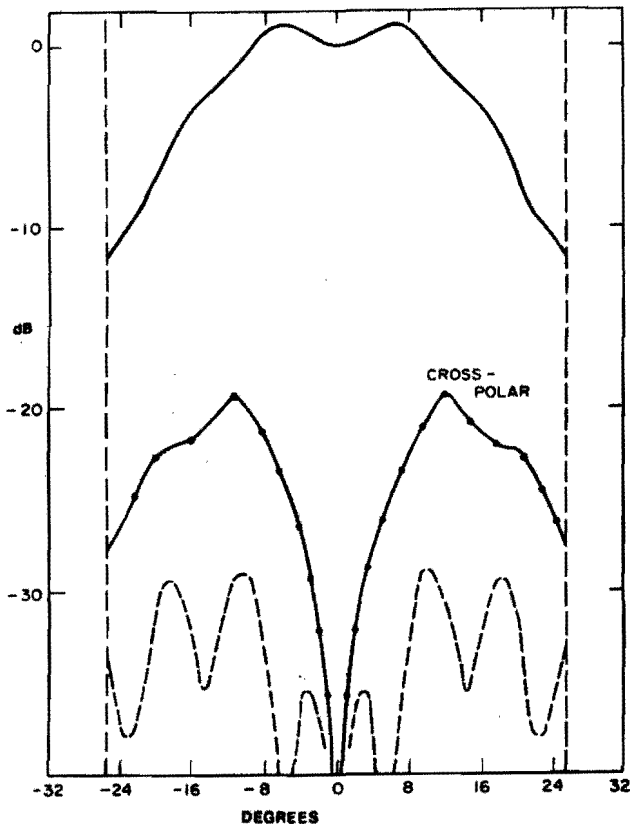


Fig. 2.47 Scattered radiation fields from the offset subreflector in the plane of asymmetry. The broken curve shows the cross-polar distribution in the aperture of the main reflector.

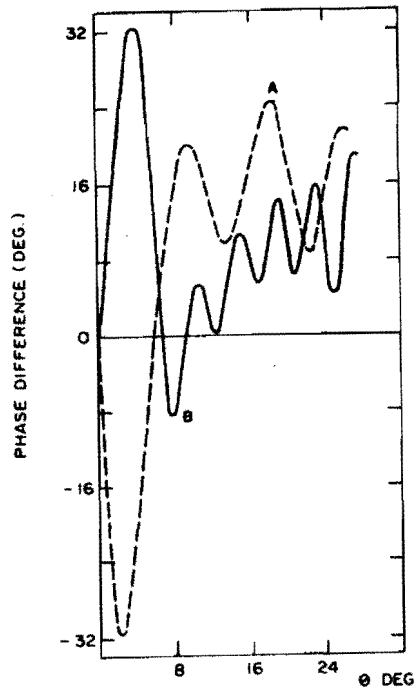


Fig. 2.48 Differential phase between the copolar and the cross-polar components of fields scattered from the offset subreflector (A) subreflector diameter  $10\lambda$ . (B) subreflector diameter  $20\lambda$ .

employed. An additional advantage is that, by appropriate choice of initial conditions, the method can provide solutions for elliptically contoured beams of any aspect ratio. Hence, state-of-the-art axisymmetric low cross-polar primary-feeds, such as the cylindrical corrugated horn, could be employed to efficiently illuminate a dual-reflector system generating an elliptical main beam with good polarization purity. However, the full implications of this approach have yet to be investigated and confirmed experimentally.

A further variation of the double-offset-reflector configuration was considered by Cha et al [55]. In this work the offset subreflector was designed as a frequency selective filter. The double-offset antenna was thus fed from both the prime focus of the main reflector and via the subreflector, which comprised an array of conformal printed-circuit crossed dipoles. The Cassegrainian geometry was utilised in the resonant band of the subreflector surface. An overall efficiency of 50 per cent was estimated for the Cassegrainian system, but the sidelobe performance was poor.

### C Applications

Dual-offset-reflector antennas can be designed to avoid (or minimise) aperture-blockage effects and thereby offer a good range of compromise between high efficiency and low sidelobes. The use of a subreflector provides a mechanical advantage for some applications in that the antenna system can be folded to locate the primary-feed either within or below the main reflector. Electrically the dual-reflector system offers the designer some additional degrees of freedom, which can be employed to compensate for the depolarization effects introduced by the asymmetric reflectors. However, in this optimised configuration the dual-offset system is not especially compact. In addition, the very low cross-polar performance (i.e. below -40 dB) which is predicted by geometric optics, can only be achieved if the subreflector dimensions are greater than about 20 wavelengths. Hence, when good polarization purity is desired, dual offset reflector systems are best suited for applications where their dimensions can be made large with respect to the operating frequency. Earth stations, radio telescopes, terrestrial communications and ground radar systems are likely examples.

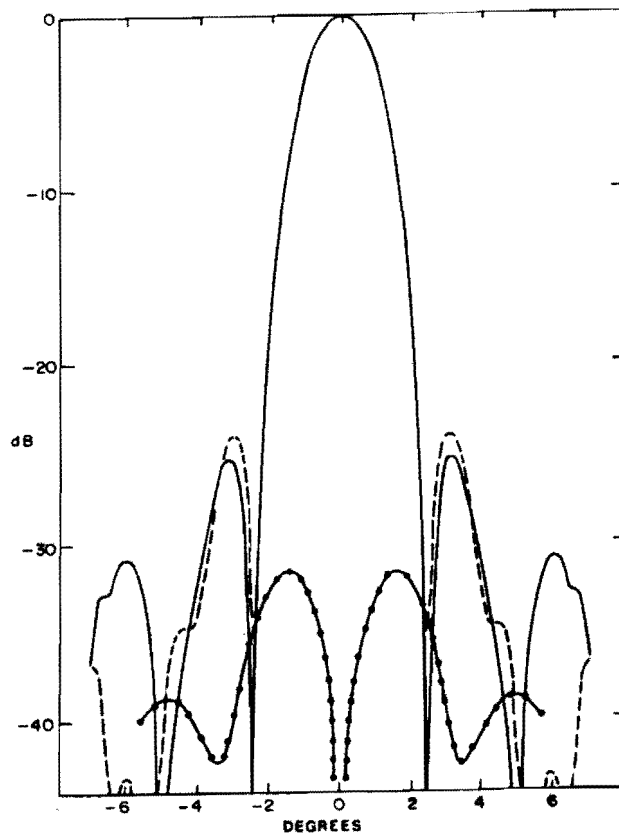


Fig. 2.49 The radiation fields from the double-offset-reflector antenna.  
 — Copolar ( $\Phi = 90^\circ$ ). —•— Cross-polar ( $\Phi = 90^\circ$ ). - - -  
 Copolar ( $\Phi = 0^\circ$ ).

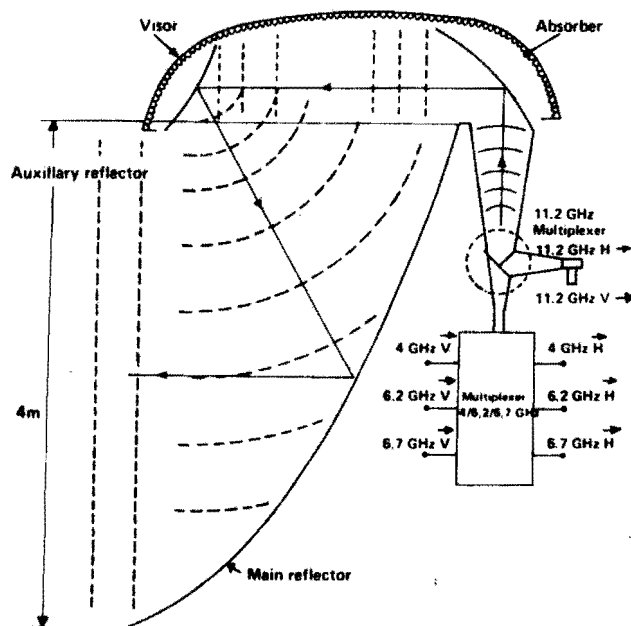


Fig. 2.50

Schematic diagram of a four-band offset Cassegrainian antenna.

The Bell System open Cassegrainian design has been implemented with a 6 m main reflector and has been used in satellite communication experiments with the UK Post Office and the University of Birmingham (UK). The design has operated successfully although it exhibits the predictably poor cross-polar performance. Magne and Bui-Hai [56] have described a 4-band dual-polarized double-offset antenna for terrestrial microwave links. Their design is illustrated in Fig.2.50. Mizusawa et al [57] have described the geometric-optics design and experimental modelling at 24 GHz of a dual-shaped reflector configuration for a circular-polarized shaped-beam antenna. The design was intended for a search radar and provided a very narrow beam in the azimuth plane with a cosecant-squared beam in the elevation plane. This fully offset antenna incorporated an axisymmetric primary-feed illumination which was converted by the shaped subreflector to feed the main elliptically contoured, shaped main reflector. The measured azimuthal-plane sidelobes of this antenna were only -18 dB down and the axial ratio of the circular polarization was also poor. Both performance parameters were attributed to a non-optimum primary-feed horn design.

Semplak [58] has described measurements (at 100 GHz) on a multiple-beam offset antenna which employs an interesting three-reflector configuration. Although the author indicates that the design is suitable for both satellites and earth stations, the structure has a projected-aperture diameter of more than 200 wavelengths with an  $F/d$  ratio of 1.9. Without deployment this would be difficult to accommodate on a satellite for frequencies lower than the 30 GHz possibility mentioned in the text. The three-reflector design exhibits good wide-angle beam performance.

Much of the analysis of the dual-offset reflector antenna has been performed in connection with either future earth-station antennas [13,50,51] or spacecraft applications [52-54]. The spacecraft application tends to be limited by the volumetric constraints imposed by the launcher. Without deployment, the cross-polar performance of the antenna tends to be limited by diffraction effects arising from the relatively small subreflector. As an earth-station antenna, however, the electrical performance of the optimised double offset reflector antenna is very attractive. The increasing demands made upon the radiation performance of earth-station antennas and particularly the sidelobe

and cross-polar specifications, suggest that optimised double-offset reflector antennas may well be necessary to satisfy the electrical requirements of the next generation of large earth stations.

The more general application of the dual offset reflector antenna may be hampered by the considerable computational effort which is involved in performing design and optimisation with physical-optics techniques. Approximate techniques, based upon geometric optics and the GTD, are adequate for large reflectors, but subreflector diffraction must be accurately modelled for other cases. Analytical techniques of the type recently introduced by Galindo-Israel and Mittra [59-61] or the GTD methods under development by Pontoppidan [62] are likely to be useful here, while the exact analytical solutions offered by the methods of Westcott and Brickhill [64] could result in very significant advantages. As an interim step it is worth noting that much of the dual-offset reflector optimisation can be performed by examining the vector fields in the aperture plane of the main offset reflector and thus minimising the need for the second (and costly) two-dimensional integration over the reflector surface.

## 2.7 References

- 1 Cook, J S; Elam, E M et al: 'The open Cassegrain antenna', Bell Telephone Syst. Tech. Publ., Monograph 5051, 1965. Also published in the Bell Syst. Tech. J., Vol.44, pp.1255-1300, 1965.
- 2 Rudge, A W and Adatia, N A: 'Offset parabolic-reflector antennas: A review'. Proc. IEEE, Vol.66, pp.1592-1618, December 1978.
- 3 Chu, T S and Turrin, R H: 'Depolarization properties of offset reflector antennas', IEEE Trans. Antennas Propagat., Vol.AP-21, pp.339-345, May 1973.
- 4 Rudge, A W and Shirazi, M: 'Multiple beam antennas: Offset reflectors with offset feeds', Univ. Birmingham, England, Final Report ESA Contract 1725/72PP, July 1973.
- 5 Rudge, A W; Pratt, T and Shirazi, M: 'Radiation-fields from offset reflector antennas', in Proc. European Microwave Conf. (Brussels, Belgium), Vol.C3.4, pp.1-4, 1973.
- 6 Rudge, A W: 'Multiple-beam offset reflector antennas for spacecraft', in Proc. Inst. Elec. Eng. Int. Conf. on Antennas for Aircraft and Spacecraft (London, England), Conf. Publ.128, pp.136-141, 1975.
- 7 Rudge, A W: 'Multiple-beam antennas: Offset reflectors with offset feeds', IEEE Trans. Antennas Propagat., Vol.AP-23, pp.317-322, May 1975.
- 8 Dijk, J; van Diepenbeek, C T W et al: 'The polarisation losses of offset antennas', Eindhoven Univ. Tech., The Netherlands, TH Rep 73-E-39, June 1973.
- 9 Dijk, J and van Diepenleek, C T W et al: 'The polarisation losses of offset paraboloid antennas', IEEE Trans. Antennas Propagat., Vol.AP-22, pp.513-520, July 1974.
- 10 Gans, M J and Semplak, R A: 'Some far-field studies of an offset launcher', Bell Syst. Tech. J., Vol.54, pp.1319-1340, 1975.
- 11 Graham, R: 'The polarisation characteristics of offset Cassegrain aeriels', in Proc. Inst. Elec. Eng. Int. Conf. on Radar Present and Future, Conf. Publ.105, pp.23-25, 1973.
- 12 Adatia, N A: 'Cross-polarisation of reflector antennas', Ph.D. dissertation, Univ. Surrey, England, December 1974.
- 13 Tanaka, H and Mizusawa, M: 'Elimination of cross-polarisation in offset dual reflector antennas', Elec. Commun. (Japan), Vol.58, pp.71-78, 1975.
- 14 Rudge, A W and Adatia, N A: 'New class of primary-feed antennas for use with offset parabolic-reflector antennas', Inst. Elec. Eng. Electron. Lett., Vol.11, pp.597-599, 1975.



- 15 Rudge, A W and Adatia, N A: 'Matched-feed for offset parabolic reflector antennas', in Proc. 6th European Microwave Conf. (Rome, Italy), pp.143-147, September 1976.
- 16 Jacobsen, J: 'On the cross polarisation of asymmetric reflector antennas for satellite applications', IEEE Trans. Antennas Propagat., Vol.AP-25, pp.276-283, March 1977.
- 17 Dragone, C and Hogg, D C: 'The radiation pattern and impedance for offset and symmetrical near-field Cassegrainian and Gregorian antennas', IEEE Trans. Antennas Propagat., Vol.AP-22, pp.472-475, May 1974.
- 18 Coleman, H P et al: 'Paraboloidal reflector offset feed with a corrugated conical horn', IEEE Trans. Antennas Propagat., Vol.AP-23, pp.817-819, November 1975.
- 19 Rudge, A W; Foster, P R et al: 'Study of the performance and limitations of multiple-beam antennas', ERA (RF Technology Centre, England), Rep. ESA Con.2277/74HP, September 1975.
- 20 Rudge, A W and Williams, N: 'Offset reflector spacecraft antennas: Design and evaluation at 30 GHz', in Proc. Symp. on Advanced Satellite Communication Systems (Genoa, Italy), ESA Publ. SP-138, pp.105-113, December 1977.
- 21 Ingerson, P G: 'Off-axis scan characteristics of offset fed parabolic reflectors', in IEEE Int. Symp. Digest AP-S (Urbana, Illinois), pp.382-383, June 1975.
- 22 Kaufmann, J F and Croswell, W F: 'Off-focus characteristics of the offset fed parabola', in IEEE Int. Symp. Digest AP-S (Urbana, Illinois), pp.358-361, June 1975.
- 23 Ohm, E A: 'A proposed multiple-beam microwave antenna for earth stations and satellites', Bel Syst. Tech. J., Vol.53, pp.1657-1665, October 1974.
- 24 Wood, P; Boswell, A G P et al: 'Elliptical beam antenna for satellite applications', in Proc. Inst. Elec. Eng. Int. Conf. on Antennas for Aircraft and Spacecraft (London, England), Conf. Publ.128, pp.83-94, June 1975.
- 25 Han, C C: 'A multifeed offset reflector antenna for the Intelsat V Communications Satellite', in Proc. 7th European Microwave Conf. (Copenhagen, Denmark), pp.343-347, September 1977.
- 26 Rudge A W and Adatia, N A: 'Primary-feeds for boresight-jitter compensation of offset-reflector radar antennas', in Proc. Inst. Elec. Eng. Int. Conf. on Radar 77 (London, England), Conf. Publ.155, pp.409-413, October 1977.
- 27 Boswell, A G P and Ashton, R W: 'Beam squint in a linearly polarised offset reflector antenna', Inst. Elec. Eng. Electron. Lett., Vol.12, pp.596-597, October 1976.

- 28 Ludwig, A C: 'The definition of cross polarisation', IEEE Trans. Antennas Propagat., Vol.AP-21, pp.116-119, January 1973.
- 29 Silver, S: Microwave Antenna Theory and Design, New York: McGraw-Hill, 1949.
- 30 Adatia, N A; Rudge, A W and Parini, C: 'Mathematical modelling of the radiation fields from microwave primary-feed antennas', in Proc. 7th European Microwave Conf. (Copenhagen, Denmark), pp.329-333, September 1977.
- 31 Clarricoats, P J B and Poulton, G T: 'High efficiency microwave reflector antennas - A review', Proc. IEEE, Vol.65, pp.1470-1504, October 1977.
- 32 Imbriale, W A et al: 'Large lateral feed displacements in a parabolic reflector', IEEE Trans. Antennas Propagat., Vol.AP-22, pp.742-745, 1974.
- 33 Ludwig, A C: 'Calculation of scattered patterns from asymmetrical reflectors', Jet Propulsion Lab., (Pasadena, CA), Tech. Rep.32-1430, 1970.
- 34 Rudge, A W; Pratt, T and Fer, A: 'Cross-polarised radiation from satellite reflector antennas', in Proc. AGARD Conf. on Antennas for Avionics (Munich, Germany), Vol.16, pp.1-6, November 1973.
- 35 Hansen, J E and Shafai, L: 'Cross-polarised radiation from waveguides and narrow-angle horns', Inst. Elec. Eng. Electron. Lett., pp.313-315, May 1977.
- 36 Foster, P R and Rudge, A W: 'Low sidelobe antenna study: Part 1: Literature survey and review', ERA RF Technology Centre, England, Rep.190476/1, October 1975.
- 37 Adatia, N A; Foster, P R and Rudge, A W: 'A study of the limitations in RF sensing signals due to distortions of large spacecraft antennas', ERA (RF Technology Centre, England), Rep. ESA Con. 2330/74 AK, September 1975.
- 38 DiFonzo, D F; English, W J and Janken, J L: 'Polarisation characteristics of offset reflectors with multiple-element feeds', in IEEE Int. Symp. Digest PGAP (Boulder, Colorado), pp.302-305, 1973.
- 39 Adatia, N A and Rudge, A W: 'Beam-squint in circularly-polarised offset reflector antennas', Int. Elec. Eng. Electron. Lett., pp.513-515, October 1975.
- 40 Gruner, R W and English, W J: 'Antenna design studies for a US domestic satellite', Comsat Tech. Rev., Vol.4, 2, pp.413-447, Fall 1974.
- 41 Raab, A R: 'Cross-polarisation performance of the RCA Satcom frequency re-use antenna', IEEE Int. Symp. Digest APS (Amherst, MA), pp.100-104, October 1976.

- 42 Lang, K C; Eick, M K and Nakatani, D T: 'A 6/4 and 30/20 dual foci offset paraboloidal reflector antenna', in IEEE Int. Symp. Digest AP-S (Urbana Illinois), pp.391-395, June 1975.
- 43 Adatia, N A and Rudge, A W: 'High performance offset-reflector spacecraft antenna development study', ERA RF Technology Centre, England, Ref. ESA Con. 2654/76/NLSW, June 1976.
- 44 Fasold, D: 'Rechnergestützte Optimierung und Realisierung einer Offset-Reflektorantenne für Satelliten', NTG-Fachber, Germany, Vol.57, pp.124-133, 1977.
- 45 Bem, D J: 'Electric field distribution in the focal region of an offset paraboloid, Proc. Inst. Elec. Eng., Vol.116, pp.579-684, 1974.
- 46 Valentino, A R and Toullos, P P: 'Fields in the focal region of offset parabolic reflector antennas', IEEE Trans. Antennas and Propagat., Vol.AP-24, pp.859-865, November 1976.
- 47 Ingerson, P G and Wong, W C: 'Focal region characteristics of offset fed reflectors', in IEEE Int. Symp. AP-S (Georgia), pp.121-123, 1974.
- 48 Watson, B K; Rudge, A W and Adatia, N: 'Dual-polarised mode generator for cross-polar compensation in offset parabolic reflector antennas', presented at 8th European Microwave Conf., Paris, France, September 1978.
- 49 Ierley, W H and Zucker, H: 'A stationary phase method for computation of the far-field of open Cassegrain antennas', Bell Syst. Tech. J., Vol.49, pp.431-454, March 1970.
- 50 Mizugutch, Y; Akagawa, M and Yokoi, H: 'Offset dual reflector antenna', in IEEE Int. Symp. AP-S (Amherst, MA), pp.2-5, October 1976.
- 51 Mizusawa, M and Katagi, T: 'The equivalent parabola of a multi-reflector antenna and its application', Mitsubishi Elec. Eng., No.49, pp.25-29, September 1976.
- 52 Adatia, N A: 'Diffraction effects in dual offset Cassegrain antenna', to be presented at IEEE Int. Symp. AP-S, Washington, DC, May 1978.
- 53 Albertsen, N C: 'Shaped-beam antenna with low cross-polarisation', in Proc. 7th European Microwave Conf. (Copenhagen, Denmark), pp.339-342, September 1977.
- 54 'Dual offset reflector antenna shaped for low cross polarisation', TICRA (Copenhagen, Denmark), Rep.S-53-01, March 1977.
- 55 Cha, A G; Chen, C C and Nakatani, D T: 'An offset Cassegrain reflector antenna system with frequency selective subreflector', in IEEE Int. Symp. Digest AP-S (Urbana, Illinois), 1975.

- 56 Magne, P and Bui-Hai, N: 'A modular offset Cassegrain antenna operating simultaneously in four frequency bands', in IEEE Int. Symp. Digest AP-S (Amherst Mass.), pp.10-19, October 1976.
- 57 Mizusawa, M; Betsudan, S et al: 'The dual doubly-curved reflectors for circularly polarised shaped-beam antennas', IEEE Int. Symp. Digest AP-S (Georgia), pp.249-252, 1974.
- 58 Semplak, R A: '100-GHz measurement on a multiple-beam offset antenna', Bell Syst. Tech. J., Vol.56, pp.385-398, March 1977.
- 59 Galindo-Israel, V and Mittra, R: 'A new series representation for the radiation integral with application to reflector antennas', IEEE Trans. Antennas Propagat., Vol.AP-25, pp.631-641, September 1977.
- 60 Galindo-Israel, V and Mittra, R: 'Synthesis of offset dual shaped reflectors with arbitrary control of phase and amplitude', in Proc. IEEE Int. Symp. Digest AP-S (California), 1977.
- 61 Galindo-Israel, V and Mittra, R: 'New approaches to the analysis and synthesis of reflector antennas', in Proc. Symp. on Advanced Satellite Commun. Syst. (Genoa, Italy), ESA Publ.SP-138, pp.75-79, December 1977.
- 62 Pontoppidan, K: 'General analysis of dual-offset reflector antennas', TICRA AP-S (Denmark), Final Rep.S-66-02, October 1977.
- 63 Ruze, J: 'Lateral feed displacement in a paraboloid', IEEE Trans. AP-13, pp.660-665, 1965.
- 64 Westcott, B S and Brickhill, F: 'Compensation for feed cross-polarisation in shaped dual offset reflectors', Electronic Letters, 18, pp.126-127, 1982.

### 3. Feeds for Earth-Station and Spacecraft Antennas

by P.J.B. Clarricoats

#### 3.1. Introduction

The performance of a satellite system, be it for communication or broadcast, depends critically on the performance of both spacecraft-and earth-station-antennas. In turn, they depend critically on soundly-based feed design and this chapter is concerned with some of their underlying principles. Two texts [1][2] dealing with feeds are to appear shortly and reference to these should be made by readers seeking more information.

Fig. 3.1 establishes the main types of reflector antenna and feed; it originated in a 1974 review paper [3] and since that time one new category of feed has risen in importance; namely the array-feed.

With spacecraft antennas in mind, we identify in Fig. 3.1 both pencil-beam and shaped-beam patterns as relevant classes. Shaped-beams feature in both communication and broadcast applications and dual-polarisation is becoming mandatory for both. Early spacecraft antennas used prime-focus symmetric paraboloids but off-set reflectors offer significant performance advantages and are now essential when large complex feed systems are used. Both single-reflector and dual-reflector designs feature in current earth-station and spacecraft systems. Corrugated feeds supporting hybrid-modes are used when a single element suffices as in an earth-station antenna, but, when a complex pattern is required, leading to an array-feed, the pure-mode element has proved the norm so far. However, when close element spacing and high feed-gain is required surface-wave feeds offer potential and the disc-on-rod radiator is one example.

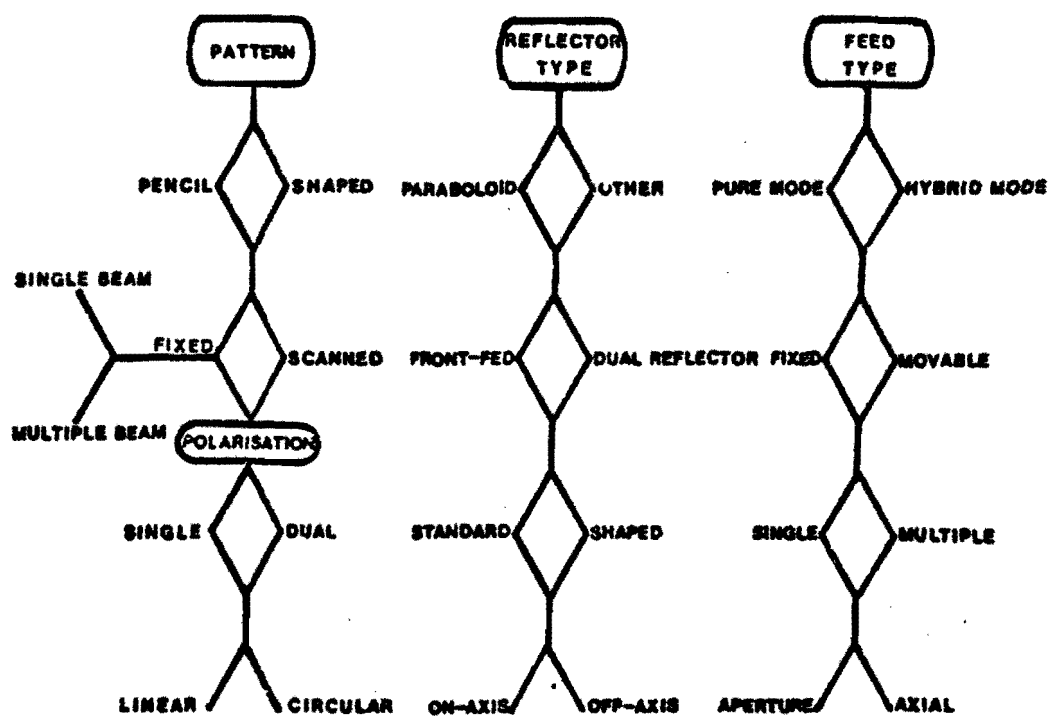


Fig. 3.1.  
Antenna Classification

Satellite-communication systems operate with typically a 1:1.5 ratio between up-link and down-link frequencies, thus establishing a minimum bandwidth specification. Broadcast satellites have beacon frequencies separated by a somewhat wider ratio and considerable ingenuity has been required to satisfy these demands. Slots with periodic changes in depth provide one technique for increasing the bandwidth of corrugated horns.

This Chapter begins with an examination of the focal-region fields of reflector antennas since this affords insight into the choice of an optimum feed. From this study, the hybrid feed emerges as an optimum choice. When the reflector is symmetric, a hybrid feed supporting the  $HE_{11}$  mode provides a good match to the focal field but in an off-set paraboloid we must turn to multimode feeds for the optimum prime-focus solution. Multimode feeds also feature in designs where tracking is needed in addition to a signal channel. Following a study of focal-fields, the propagation and radiation properties of corrugated feeds is next considered in both their single-mode and multimode form. Pure-mode feeds are then discussed briefly as a prelude to a discourse on array-feeds which use pure-mode elements. Finally, the disc-on-rod surface-wave radiator is discussed.

## 3.2 Fields in the Focal Region of a Reflector Antenna

### 3.2.1 Derivation of Focal Region Fields

Our aim is to determine the focal region field of a paraboloidal antenna when a plane wave is incident along the reflector axis. The method is readily extended to other surfaces with axial symmetry.

The incident plane wave is assumed to have its electric field polarised in the  $\hat{x}$  direction

The magnetic field

$$H_i = -H_0 \hat{y} e^{-jkr_0 \cos\theta}$$

The electric field in the focal region (see figure 3.2.1) is given by

$$\underline{E} = \frac{j\omega\mu_0}{4\pi} \int_S \{ \underline{K} - (\underline{K} \cdot \underline{\hat{r}}) \underline{\hat{r}} \} \frac{e^{-jkr}}{r} dS$$

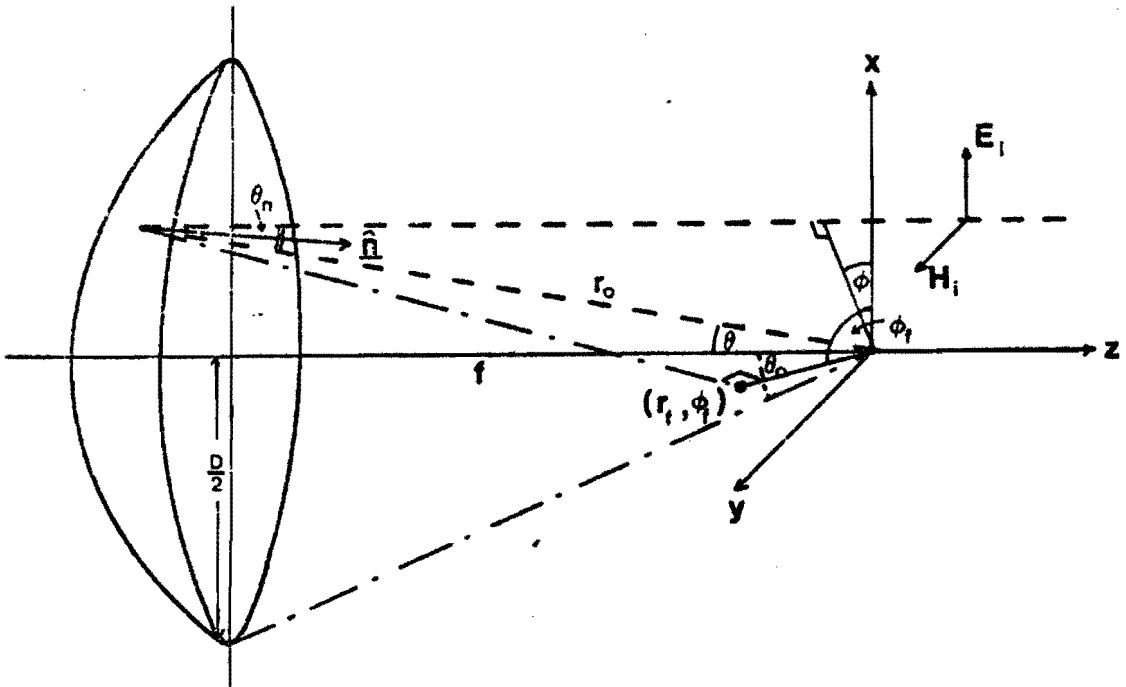


Fig. 3.2.1



Since  $\underline{K} = 2\hat{n} \times \underline{H}_i$ , where  $\hat{n}$  is the unit normal at a point on the reflector surface, the total phase  $\phi$  is given by

$$\phi = -k(r+r_0 \cos \theta)$$

where

$$r = r_0 - r_f \sin \theta \cos(\phi - \phi_f) + \text{higher order terms}$$

We next evaluate the amplitude term using the physical optics approximation

$$\underline{K} = 2\hat{n} \times \underline{H}_i$$

where

$$\hat{n} = -\hat{x} \sin \theta_n \cos \phi - \hat{y} \sin \theta_n \sin \phi + \hat{z} \cos \theta_n$$

$\theta_n$  is the angle which the normal makes with the  $\hat{z}$  axis

Thus,

$$\begin{aligned} \underline{K} &= 2\hat{n} \times \underline{H}_i \\ &= 2H_0 \{ \hat{x} \cos \theta_n + \hat{z} \sin \theta_n \cos \phi \} \end{aligned}$$

In the zeroth order approximation

$$\begin{aligned} \underline{r} &= \underline{r}_0 \\ &= \hat{x} r_0 \sin \theta \cos \phi + \hat{y} r_0 \sin \theta \sin \phi - \hat{z} r_0 \cos \theta \end{aligned}$$

$$(\underline{K} \cdot \underline{r}) = 2H_0 \sin(\theta - \theta_n) \cos \phi$$

$$\begin{aligned} \underline{K} \cdot (\underline{K} \cdot \hat{r}) \hat{r} &= 2H_0 \{ \hat{x} [\cos \theta_n - \sin \theta \sin(\theta - \theta_n) \cos^2 \phi] + \\ &\quad \hat{y} [-\sin \theta \sin(\theta - \theta_n) \sin \phi \cos \phi] + \\ &\quad \hat{z} [\sin \theta_n \cos \phi + \cos \theta \sin(\theta - \theta_n) \cos \phi] \} \end{aligned}$$

For a paraboloid  $\theta_n = \theta/2$ . Then with simplification we obtain

$$\begin{aligned}\underline{K} - (\underline{K} \cdot \underline{\hat{r}}) \underline{\hat{r}} &= 2H_0 \{ \underline{\hat{x}} [\cos^3 \theta_n - \sin^2 \theta_n \cos \theta_n \cos 2\phi] \\ &\quad - \underline{\hat{y}} \sin^2 \theta_n \cos \theta_n \sin 2\phi \\ &\quad + \underline{\hat{z}} 2 \sin \theta_n \cos^2 \theta_n \cos \phi \}\end{aligned}$$

In order to carry out the integration over the surface S we note that

$$dS = \frac{r_0^2 \sin \theta}{\cos(\theta - \theta_n)} d\theta d\phi$$

For a paraboloid since  $\theta_n = \theta/2$

$$dS = 2r_0^2 \sin \theta_n$$

The  $\phi$  integration can be made using

$$\int_0^{2\pi} \frac{\sin}{\cos} m\phi e^{jM \cos(\phi - \phi_f)} d\phi = 2\pi j^m J_m(u) \frac{\sin}{\cos} m\phi_f$$

The total expression for the E field is

$$\begin{aligned}\underline{E} &= \frac{j\omega\mu_0}{2\pi} H_0 \int_0^{\theta_0} \int_0^{2\pi} \{ \underline{\hat{x}} [\cos^3 \theta_n - \sin^2 \theta_n \cos \theta_n \cos 2\phi] - \underline{\hat{y}} \sin^2 \theta_n \cos \theta_n \sin 2\phi \\ &\quad + \underline{\hat{z}} 2 \sin \theta_n \cos^2 \theta_n \cos \phi \} e^{-j\phi_0 - jkr_f \sin \theta \cos(\phi - \phi_f)} 2r_0 \sin \theta_n d\phi d\theta \\ &= 2j\omega\mu_0 H_0 \int_0^{\theta_0} r_0 \sin \theta_n e^{-j\phi_0} \{ \underline{\hat{x}} [\cos^3 \theta_n J_0(u_1) + \sin^2 \theta_n \cos \theta_n J_2(u_1) \cos 2\phi_f] \\ &\quad + \underline{\hat{y}} \sin^2 \theta_n \cos \theta_n J_2(u_1) \sin 2\phi_f \\ &\quad + \underline{\hat{z}} 2j \sin \theta_n \cos^2 \theta_n J_1(u_1) \cos \phi_f \} d\theta\end{aligned}$$

where

$$u_1 = kr_f \sin \theta$$

Finally we have

$$\underline{E} = j\omega\mu_0 H_0 \{ \hat{x}(I_1 + I_2 \cos 2\phi_f) + \hat{y} I_2 \sin 2\phi_f + \hat{z} j I_3 \cos \phi_f \}$$

$$\underline{H} = j\omega\mu_0 Y_0 H_0 \{ \hat{x} I_2 \sin 2\phi_f + \hat{y}(I_1 - I_2 \cos 2\phi_f) + \hat{z} j I_3 \sin \phi_f \}$$

$$I_1 = 2 \int_0^\theta r_0 \sin \theta_n \cos^3 \theta_n J_0(u_1) \epsilon^{-j\phi_0} d\theta$$

$$I_2 = 2 \int_0^\theta r_0 \sin^3 \theta_n \cos \theta_n J_2(u_1) \epsilon^{-j\phi_0} d\theta$$

$$I_3 = 4 \int_0^\theta r_0 \sin \theta_n \cos^2 \theta_n J_1(u_1) \epsilon^{-j\phi_0} d\theta$$

For a paraboloid

$$r_0 = \frac{f}{\cos^2 \theta_n} \quad \text{and} \quad \theta_n = \frac{\theta}{2}$$

Then

$$I_1 = f \int_0^\theta \sin \theta J_0(u_1) \epsilon^{-j\phi_0} d\theta$$

$$I_2 = f \int_0^\theta \sin \theta \tan^2 \frac{\theta}{2} J_2(u_1) \epsilon^{-j\phi_0} d\theta$$

$$I_3 = 4f \int_0^\theta \sin^2 \frac{\theta}{2} J_1(u_1) \epsilon^{-j\phi_0} d\theta$$

If we refer the phase to a fixed reference distance  $z$  from the focal point, the phase factor becomes  $\epsilon^{-jk(2f+z)}$  and in the focal plane where  $z = 0$  the phase factor is a constant  $\epsilon^{-j2kf}$ .

The above expressions then compare directly with those presented by Minnett and Thomas [4] noting that their  $z$  direction is opposite to that above and

because of the rotation of axes, their electric field is y polarised.

To interpret the figures taken from the paper by Minnett and Thomas we note that

$$A(U) = \frac{1}{2} \operatorname{cosec}^2 \frac{\theta_0}{2} I_1$$

$$B(U) = \frac{1}{2} \operatorname{cosec}^2 \frac{\theta_0}{2} I_2$$

$$C(U) = \frac{1}{8} \operatorname{cosec}^2 \frac{\theta_0}{2} I_3$$

$$U = kr_f \sin \theta_0$$

$$\rho = r_f$$

$$\xi = \phi$$

The functions  $A(U)$  and  $B(U)$  are plotted below for antennas with different values of  $\theta_0$ . For guidance, the Max Planck radio telescope has  $F/D = 0.3$ ,  $\theta_0 = 80^\circ$ , while the Australian Parkes radio telescope has  $F/D = 0.4$ ,  $\theta_0 = 63^\circ$ . Typical front-fed microwave communication antennas have  $F/D$  between 0.25,  $\theta_0 = 90^\circ$  (focal plane reflector) and  $F/D = 0.4$ .

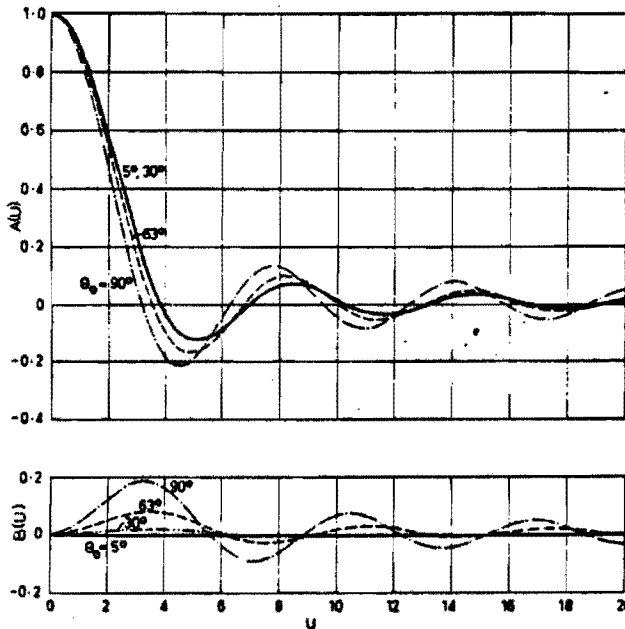


Fig. 3.2.2

Functions  $A(U)$  and  $B(U)$  for paraboloid subtending semi-angle  $\theta_0$  at focus

In general the integrals above are complex. However, in the focal plane where  $z=0$  they are real and if,  $\theta_0$  is small corresponding to an antenna with long focal length,

$$A(U) = 2 \frac{J_1(U)}{U}, \quad B(U) = 0, \quad C(U) = \frac{\theta_0}{2} \frac{J_2(U)}{U}$$

Under these conditions

$$E_x = 2E \left( \frac{\pi D^2}{4f\lambda} \right) \frac{J_1(kr_f \theta_0)}{kr_f \theta_0}$$

### 3.2.3 Properties of Focal Fields

The above equation is the scalar solution obtained by Airy for distribution of light in the focal region of a lens. The dark rings occur on the circles where  $J_1(U) = 0$  and the polarisation is transverse and parallel to the incident field. Even when the above constraint on  $\theta_0$  is no longer obeyed figure 3.2.3 shows that the field in the central region of the focal field is nearly linearly polarised and the distribution matches quite well the field produced in a hybrid mode waveguide under balanced hybrid conditions, as discussed in section 3.3.

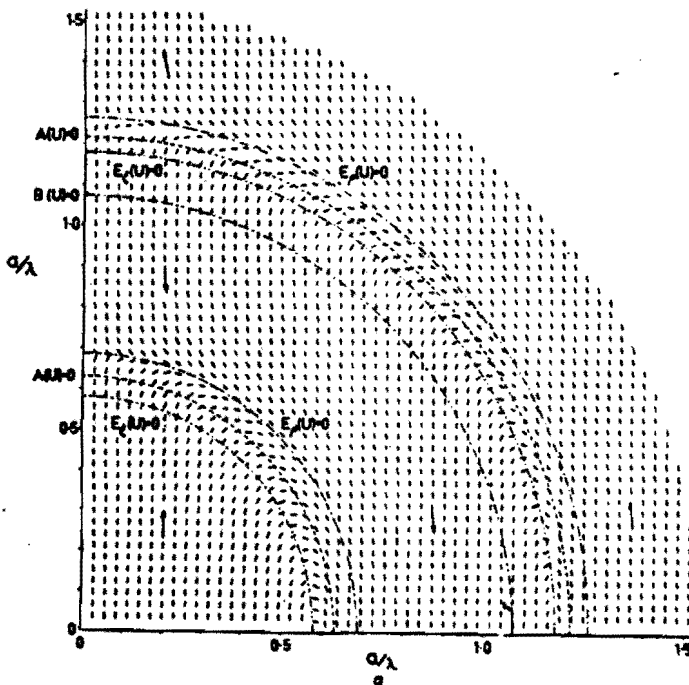


Fig. 3.2.3

Field distribution in focal plane of paraboloid with  $\theta_0 = 63^\circ$

(a) Polarisation of E field

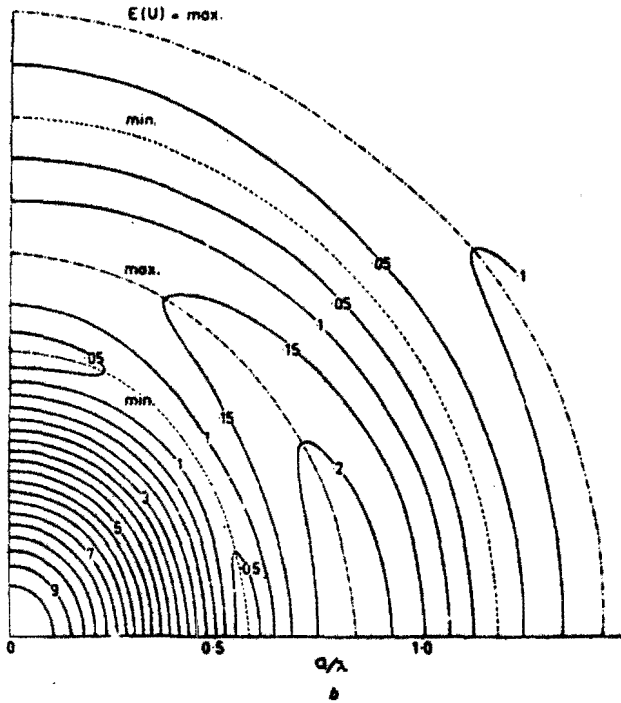


Fig. 3.2.3

Field distribution in focal plane of paraboloid with  $\theta_0 = 63^\circ$

(b) Contours of amplitude  $E(U)$

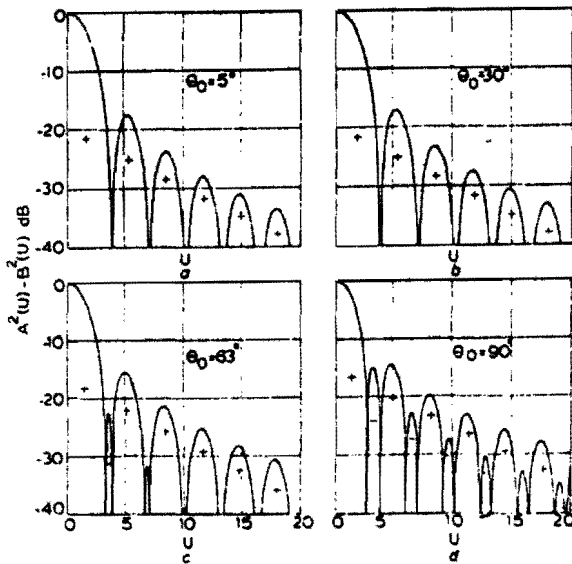


Fig. 3.2.4

Intensity functions in focal plane of paraboloid; (a)  $\theta_0 = 5^\circ$ ; (b)  $\theta_0 = 30^\circ$ ; (c)  $\theta_0 = 63^\circ$ ; (d)  $\theta_0 = 90^\circ$ .

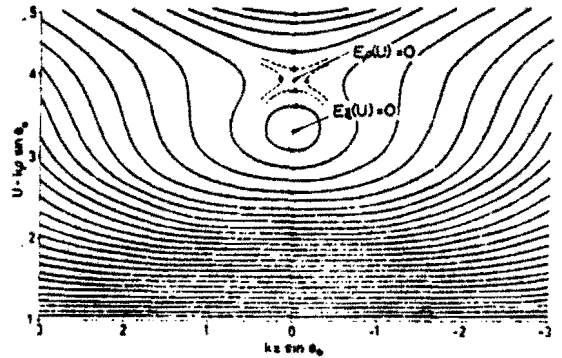


Fig. 3.2.5

Direction of energy flow across the focal plane near first dark ring ( $U = 3.25$ ) of paraboloid with  $\theta_0 = 63^\circ$

Figures 3.2.3 - 3.2.5, taken from the paper by Minnett and Thomas, show the field distribution in the focal region of a paraboloid with  $\theta_0 = 63^\circ$ , corresponding to the Parkes radio telescope, the intensity functions in the focal plane and the energy flow diagram for the case  $\theta_0 = 63^\circ$ . The role of the function  $B(U)$  is apparent. For other than very small values of  $\theta_0$ , there is a significant cross-polar contribution to the focal field which is manifested in the  $45^\circ$  plane. However, it occurs at a radius where the  $\phi$  independent part of transverse H and E fields experience a null and the Poynting vector is reversed. This is important for it implies that there is no coupling of the cross-polar field to a waveguide supporting a balanced hybrid mode.

The average rate of energy flow in a given direction  $\bar{S}$  is determined by the real part of the component of the complex Poynting vector in that direction. The power flowing in the z direction is given by

$$\bar{S}_z = -\frac{2}{Z_0} (kfE)^2 \sin^4 \frac{\theta_0}{2} \{|A|^2 - |B|^2\}$$

If we integrate  $S_z$  over an aperture in the focal plane we obtain the total energy P passing through a cylindrical region as shown in figure 3.2.6.

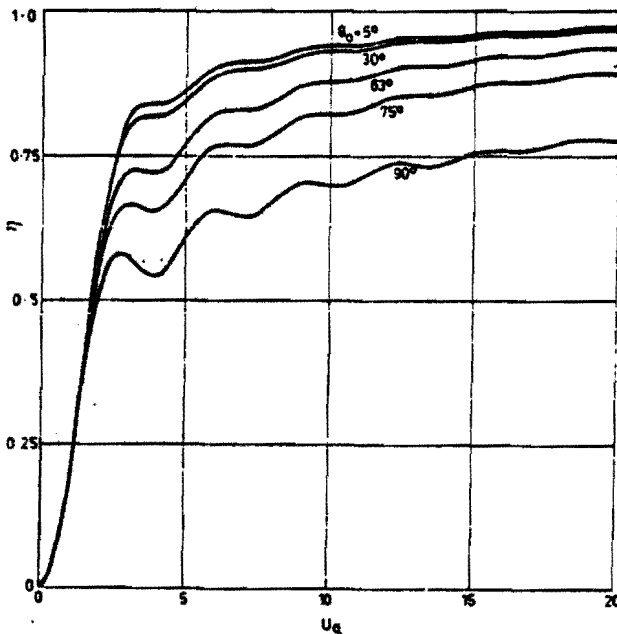


Fig. 3.2.6

Aperture efficiency  $\eta$  of paraboloid with semiangle  $\theta_0$  and optimum aperture-type feed of radius  $a$

The power incident on the aperture of the paraboloid is

$$P_0 = 2\pi(f \tan \frac{\theta_0}{2})^2 \frac{E^2}{Z_0}$$

Thus, the quantity  $\frac{P}{P_0}$  represents the fraction of the total power which passes through a region of radius  $a$ ,

$$\eta = \frac{P}{P_0} = \frac{1}{2} \int_0^{U_a} \{A^2(U) - B^2(U)\} U dU$$

$$U_a = k a \sin \theta_0$$

For small  $\theta_0$ ,  $U = k a \theta_0$ , then

$$\eta = 1 - J_0^2(U_a) - J_1^2(U_a)$$

a formula derived originally by Lord Rayleigh.

### 3.2.3 Optimum Feeds for Paraboloidal Reflectors

Figure 3.2.6 above, shows  $\eta$  as a function of  $U_a$ . The oscillatory form mainly arises from the function  $B(U)$ . For this reason the value of  $\eta$  decreases with increasing  $\theta_0$  at a given radius. Minnett and Thomas assume that  $\eta$  represents the maximum efficiency obtainable with an optimum feed. Clearly, it does not represent the power transferred to a mode in a waveguide and we can ask the question: Is there a form of waveguide which would respond only to the (A) type linearly polarised field? The answer appears to be yes, a balanced hybrid mode as obtained in an 'ideal' corrugated waveguide. Under this condition the electric and magnetic fields are in the ratio  $Z_0$ . The term ideal is introduced, recognising that the inevitable presence of a flange will prevent the optimum balanced hybrid condition from being achieved in practice. Actually the field in the ideal waveguide aperture has a dependence of the form  $J_0(kr)$  while that of the (A) type field is of the form  $\frac{J_1(u)}{u}$ . Nevertheless, if  $K = k \sin \theta_0$  the two functions



are quite closely matched over the central region of the focal field.

We shall next demonstrate that an ideal feed couples only to an (A) type field.

To calculate the power coupled into the waveguide, we use a theorem based on reciprocity. If  $\eta$  is now the efficiency of power coupling

$$\eta = \left| \frac{1}{2} \int_S (\underline{E}_1 \times \underline{H}_2 + \underline{H}_1 \times \underline{E}_2) \cdot d\underline{S} \right|^2$$

where the fields in the focal region  $\underline{E}_1$  and  $\underline{H}_1$  arise from unit incident power in the plane wave at the reflector aperture while those in the feed aperture  $\underline{E}_2$ ,  $\underline{H}_2$  arise from unit power in the feed. Now, as previously noted, we can resolve the focal region transverse fields into two types

$$(A) \quad \underline{E}_A \propto \hat{x} I_1 \quad ; \quad \underline{H}_A \propto \hat{y} I_1$$

$$(B) \quad \underline{E}_B \propto \hat{x} I_2 \cos 2\phi + \hat{y} I_2 \sin 2\phi \quad ; \quad \underline{H}_B \propto -\hat{y} I_2 \cos 2\phi + \hat{x} I_2 \sin 2\phi$$

Furthermore, we assume that

$$\underline{E}_2 = \hat{x} F(r, \phi) \quad \underline{H}_2 = -\hat{y} F(r, \phi) Y_0$$

corresponding to a balanced hybrid mode travelling in the negative  $z$  direction. We can substitute for the fields in the equation for  $\eta$ . Thus,

$$\begin{aligned} \eta &= \left| \frac{1}{2} \int_0^{2\pi} \int_0^a (E_{1x} H_{2y} - H_{2x} E_{1y} + H_{1x} E_{2y} - E_{2x} H_{1y}) r dr d\phi \right|^2 \\ &= \int_0^{2\pi} \int_0^a \{ -(I_1 + I_2 \cos 2\phi) Y_0 F(r, \phi) - Y_0 (I_1 - I_2 \cos 2\phi) F(r, \phi) \} r dr d\phi \\ &= - \int_0^{2\pi} \int_0^a 2 Y_0 I_1(\rho) F(r, \phi) r dr d\phi \end{aligned}$$

We observe that the contribution from the (B) type field disappears.

From the above, the efficiency factor for an optimum feed is given by

$$\eta = \frac{1}{2} \int_0^a A^2(U) U dU$$

corresponding to a feed which provides a conjugate match to an (A) type focal field. This observation was first made by Poulton who also recognised that  $\eta$  as given by the above expression exceeds unity if the radius  $a$  is very large. One may conclude that in a practical situation it is impossible to realise a feed which will provide a match to the (A) field over an aperture large enough to create an  $\eta$  value exceeding unity.

#### 3.2.4 Non-uniform Aperture Distribution

The focal field distribution derived in section 3.2.1 corresponds to a reflector aperture which is illuminated by a plane wave. Conversely it provides the focal-field distribution necessary to create a uniform distribution over the reflector aperture.

If the aperture distribution is weighted by a function  $g(s)$  where

$$g(s) = g\left(\frac{\theta}{\theta_0}\right)$$

the corresponding focal field is obtained on multiplying the integrands of  $I_{1,2,3}$  by  $g(s)$ . For a long focal-length antenna (as might be realised in practice with a Cassegrain configuration) the focal-plane distribution then becomes

$$|E_x| = E_0 \frac{D^2}{4f\lambda} 2\pi \int_0^1 g(s) J_0(2\pi qs) s ds$$

where

$$q = \frac{r}{\lambda} \theta_0$$

$$\theta_0 \sim \frac{D}{2f}$$

The integration can be completed in closed form when  $g(s)=1$  and for specific functional forms of  $g(s)$ . When  $g(s)=1$

$$|E_x| = 2E_0 \left(\frac{\pi D}{4f\lambda}\right)^2 \frac{J_1(kr\theta_0)}{(kr\theta_0)}$$

as demonstrated by Minnett and Thomas [4]. However, since  $g(s)=0$  for  $s>1$  we can extend the integration range so that

$$|E_x(q)| = E_0 \left(\frac{D^2}{4f\lambda}\right) 2\pi \int_0^\infty g(s) J_0(2\pi qs) s ds$$

The equation reminds us that the aperture and focal plane distributions are related by Hankel-transform pairs. The above equation can be integrated in closed form when  $g(s) = e^{-p^2 s^2}$ . Then,

$$|E_x(q)| = E_0 \left(\frac{D^2}{4f\lambda}\right) \frac{1}{p^2} e^{-\pi^2 q^2 / p^2}$$

Thus for the special case of a gaussian aperture distribution, the focal region field has a gaussian form. In section 3 we find that the field in the aperture of an ideal hybrid mode waveguide under balanced hybrid conditions has a  $J_0(kr\theta)$  form which for values of  $kr\theta < 1$ , closely approximate a gaussian function.

### 3.2.5 Focal Fields of a Spherical Reflector Antenna

Thomas, Minnett and Vu [5] have extended the theory developed in section 3.2.1 to the case of the spherical reflector of radius of curvature  $R$  (shown as  $R_0$  in certain figures). Such reflector shapes permit beam scanning by feed movement. The functions  $A(U)$  etc. of 3.2.1 then become

$$\frac{A(U)}{B(U)} = \frac{1}{2} \operatorname{cosec}^2 \theta_0 \int_0^{\theta_0} \kappa(\theta) (1 \pm r) J_0(u) e^{-j\phi} d\theta$$

$$C(U) = \frac{1}{2} \operatorname{cosec}^2 \theta_0 \int_0^{\theta_0} \frac{\sin \theta}{r} \kappa(\theta) J_1(u) e^{j\phi} d\theta$$

where

$$U = \frac{krs \sin \theta}{\zeta}$$

$$\kappa(\theta) = \frac{\sin \theta}{\zeta^2} \left[ 1 - \left( \frac{z}{R} \right) \cos \theta \right]$$

$$r = \frac{\cos \theta - z/R}{\zeta}$$

$$\zeta = \left[ 1 - \frac{2z}{R} \cos \theta + \left( \frac{z}{R} \right)^2 \right]^{\frac{1}{2}}$$

The phase  $\phi$  is taken relative to the phase of the incident wave at the plane  $z = 0$ . (Note that the above authors have the  $z$  axis pointing towards the reflector).

$$\phi = kR(\cos \theta + \zeta)$$

The focal field equations are normalised so that  $A(U) = 1$  at the paraxial focus  $F$ , see figure 3.2.6.

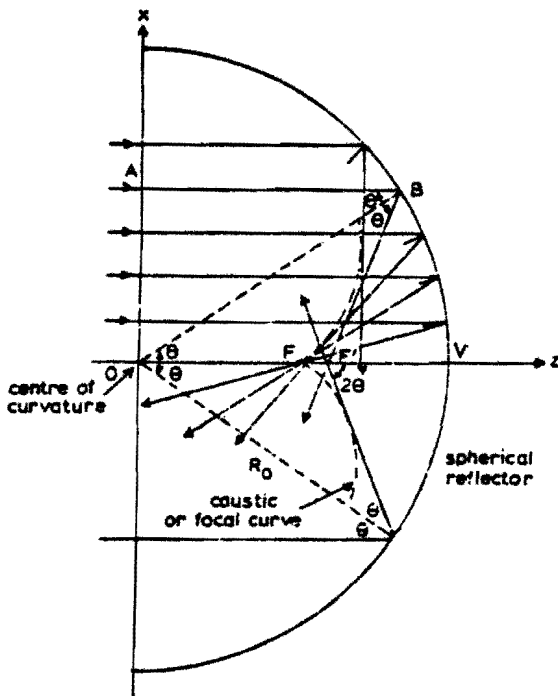


Fig. 3.2.6

Geometrical reflection by a spherical reflector

$R_0$  = radius of curvature

$F$  = paraxial focus =  $OF = FV$   
 $= R_0/2$

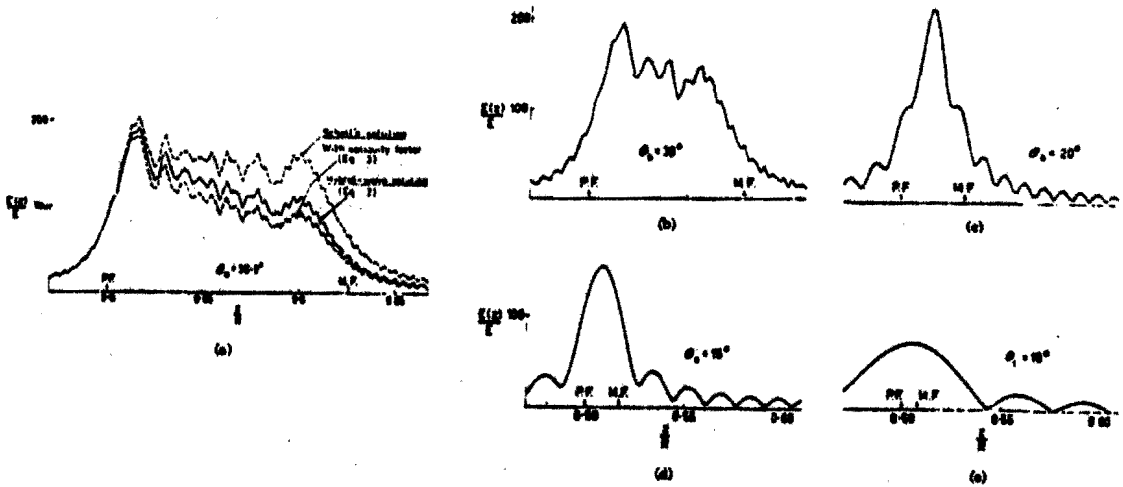


Fig. 3.2.7

Normalised field along axis of a spherical reflector,  $R/\lambda = 400$  for various values of  $\theta_0$ . Computation interval 0.002 in  $z/R$ . P.F. - paraxial focus; M.F. - marginal focus.

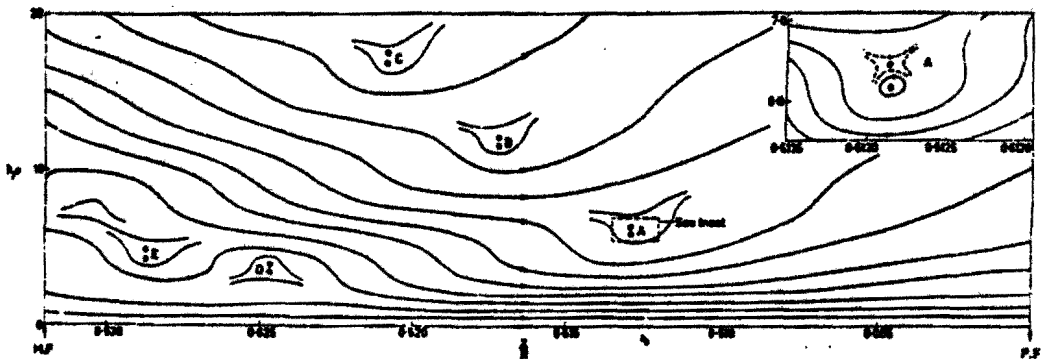


Fig. 3.2.8

Direction of energy flow in focal region of a spherical reflector,  $\theta_0 = 20$  degrees,  $R/\lambda = 400$

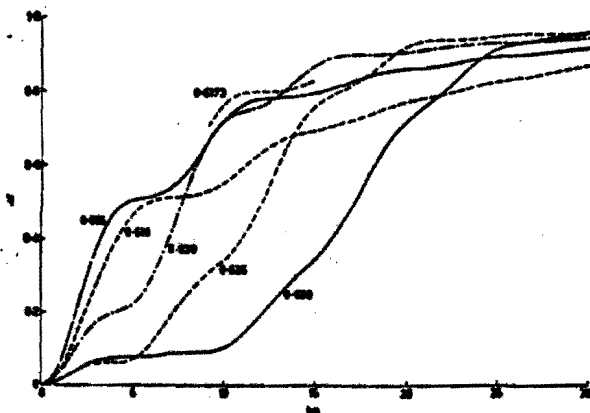


Fig. 3.2.9

Efficiency  $\eta$  of a spherical reflector,  $\theta_0 = 20$  degrees  $R/\lambda = 400$ , with  $z/R$  as parameter.

Figure 3.2.7 due to Thomas, Minnett and Vu, shows normalised longitudinal field along the axis of a spherical reflector with  $\frac{R}{\lambda} = 400$  and various values of  $\theta_0$ . Only for  $\theta_0$  small (when the spherical surface approximates a paraboloid) is the distribution appreciably confined. This situation might be anticipated by examination of the geometric optics rays. The above mentioned authors have also calculated the direction of energy flow in the focal region, Fig. 3.2.8 and the efficiency factor  $\eta$ , Fig. 3.2.9, discussed in section 3.2.1.

Figure 3.2.8 shows that several regions of circulation of energy exist as with the paraboloid, although there they are centred in the focal plane near the dark rings of the Airy pattern. The axial power flow is greatest near  $\frac{z}{R} = 0.515$  (for  $\theta_0 = 20^\circ$ ) as revealed by the calculation of  $\eta$  which shows that 90% of the energy passes through an aperture with  $ka = 16$ . Little advantage is obtained by making  $ka$  larger.

Thomas et al [5] compare these results with the geometric optics 'circle of least confusion' (the smallest circle of radius  $r_c$  through which all the rays pass)

$$kr_c = 0.77 \frac{R}{\lambda} \tan^3 \theta_0$$

For  $\theta_0 = 20^\circ$ ,  $kr_c = 0.037 R/\lambda$ . It occurs when  $z/R = 0.56$ . If  $R/\lambda = 400$   $kr_c = 15$ , then reference to figure 3.2.8 shows that 70% of energy flows through a circle of this diameter in this longitudinal position which is less than the maximum. Geometric optics thus serves only as a guide to transverse feed design.

The investigation by the above authors was aimed at the production of a multimode hybrid waveguide feed for a spherical reflector radio telescope. The diameter of the waveguide was chosen to correspond to a null of the focal region field and the transverse distribution was synthesised using a number of modes. The amplitudes of these modes were determined using a mode matching procedure on a computer graphics terminal. For three modes and with  $z/R = 0.5208$  and  $ka = 17.2$  ( $a/\lambda = 2.74$ ) they obtained  $\eta = 0.86$ .

As far as is known, a transverse feed for a spherical reflector antenna has yet to be installed. The Arecibo spherical reflector utilises a line feed which was designed by A.W. Love so as to receive rays converging on the axis at the appropriate angle which, as Fig. 3.2.6 shows, depends upon  $z/R$ . The feed could be scanned by rotation about the centre of curvature as shown in Fig. 3.2.10. An aperture efficiency exceeding 80% was achieved with this design.

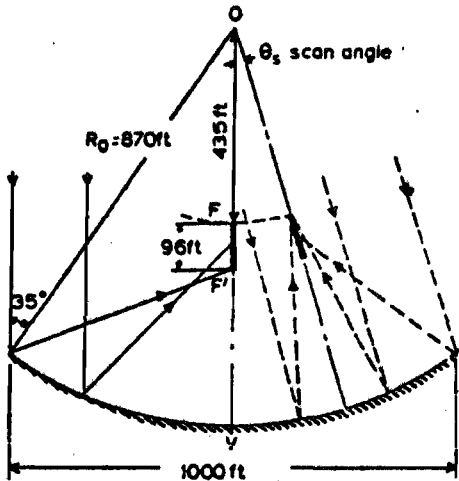


Fig. 3.2.10  
Spherical reflector with line feed.

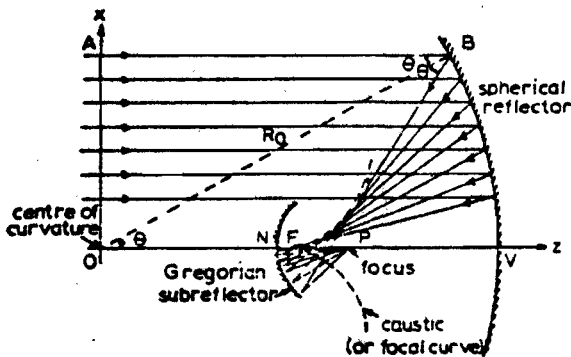


Fig. 3.2.11  
Spherical reflector with Gregorian reflector

An alternative design shown in Fig. 3.2.11 was investigated by Phillips and Clarricoats [6] and later designed and tested by Masterman. A gregorian subreflector causes rays to be brought to a point focus on the reflector axis. Table 3.2.1 gives the oaramaters for maximum efficiency. Masterman's experiments generally confirm the accuracy of the predictions although

recognisable discrepancies caused a measured gain loss of approximately 1dB. The principal disadvantage of the spherical reflector with gregorian corrector is the large diameter of the latter, giving rise to significant aperture blockage and high side-lobes. A reduction in the size of the gregorian corrector can be achieved if the main reflector shape is made intermediate between that of a sphere and paraboloid. A reduction in scan angle must be accepted.

Table 3.2.1

Parameters for maximum overall efficiency of a spherical reflector with a Gregorian subreflector for a scan angle  $\theta_s = \pm 7^\circ$

	Feed 1	Feed 2	Feed 3
20dB beamwidth of feed pattern, deg	60	86	111
Subreflector-vertex position	$0.475 R_0$	$0.470 R_0$	$0.465 R_0$
Focus position	$0.88 R_0$	$0.85 R_0$	$0.78 R_0$
Gain factor $G_{max}$	0.84	0.83	0.84
Optimum angular aperture $\theta_{op}$ , deg	37.0	40.0	41.5
$R_0/D = 1/2 \sin \theta_{op}$	0.83	0.78	0.75
Aperture efficiency $\eta_{ap}$	0.75	0.77	0.78
Overall efficiency $= G_{max} \eta_{ap}$	0.63	0.64	0.65
3dB beamwidth of far-field pattern ( $D/\lambda = 100$ ), deg	0.55	0.55	0.55
First side-lobe level ( $D/\lambda = 100$ ), dB	-11.8	-11.5	-11.3

Table 3.2.2

Principal feed parameters

Feed	Cylindrical corrugated waveguide propagating a balanced $HE_{11}$ hybrid mode <sup>23</sup>			20 dB beamwidth
	$a/b$	$ka$	$\beta_{11a}$	
1	0.8500	9.2453	8.9310	60°
2	0.8000	6.6356	6.1953	86°
3	Scalar horn with 120° flare angle propagating a balance $HE_{11}$ spherical hybrid mode. Approximate pattern factor <sup>24</sup>			111°



### 3.2.6 Focal Fields of an Off-set Paraboloid

Similar techniques to those described in section 3.2.1 can be used to derive the fields in the focal-region of an off-set paraboloid. If the reflector has a feed off-set angle  $\Psi$  and a long focal-length to diameter ratio  $f/D$ , then Bem [7] has shown that for polarisation in the plane of symmetry and to within a constant factor,

$$E_x = \frac{2J_1(U)}{U} + j \frac{D}{f} \sin\Psi \frac{2J_2(U)}{U} \cos\phi_f$$

$$E_y = -j \frac{D}{f} \sin\Psi \frac{J_2(U)}{U} \sin\phi_f$$

To obtain the electric fields for the orthogonal polarisation  $\phi_f$  is replaced by  $2\pi - \phi_f$ .

The equations show that the cross-polar field is an asymmetric function of  $\phi_f$ , in contrast with the symmetric paraboloidal case, it is also in quadrature with the principal co-polar component of field. For typical reflector parameters the cross-polar component of the focal-field is much stronger than in the symmetric case and the corresponding radiation pattern of an off-set paraboloid antenna, fed with a simple feed, exhibits strong cross-polarisation in the principal-plane which contains the off-set asymmetry.

The effect may be compensated by a multimode feed, as proposed by Rudge and Adatia [8] and discussed in section 3.3, or by the use of an appropriately positioned subreflector.

### 3.3 Propagation and Radiation Characteristics of Corrugated Waveguides

#### 3.3.1 Derivation of Characteristic Equation

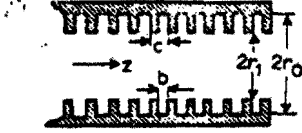


Fig. 3.3.1

Consider the corrugated waveguide shown in the figure 3.3.1. In the region  $r < r_1$ ,

$$\nabla_t^2 \frac{H_z}{E_z} + K_N^2 \frac{H_z}{E_z} = 0$$

$$E_z = \sum_{N=-\infty}^{N=+\infty} A_N J_m(K_N r) e^{-j\beta_N z} \cos m\phi$$

$$\beta_N = \beta_0 + \frac{2\pi N}{c}$$

If higher space harmonics are neglected

$$E_z = a_{mn} J_m(Kr) e^{-j\beta z} \cos m\phi$$

$$H_z = b_{mn} J_m(Kr) e^{-j\beta z} \sin m\phi$$

For convenience in analysis we drop the  $z$  dependence and write

$$E_z = a_m J_m(x) e^{jm\phi} \quad \text{where } x = Kr$$

$$H_z = -a_m j y_0 \bar{\Lambda} J_m(x) e^{jm\phi}$$

$\bar{\Lambda}$  is the hybrid factor and  $y_0 = (\epsilon_0/\mu_0)^{1/2}$

$$E_{\phi} = a_m \frac{x'}{x^2} J_m(x) \{m\bar{\beta} + \bar{\Lambda} F_m(x)\} e^{jm\phi} \quad x' = kr$$

$$H_{\phi} = -a_m j y_0 \frac{x'}{x^2} J_m(x) \{m\bar{\beta}\bar{\Lambda} + F_m(x)\} e^{jm\phi} \quad F_m(x) = \frac{x J'_m(x)}{J_m(x)}$$

For  $r_0 > r > r_1$  we have TE and TM standing waves in the slots. The lowest order wave is the  $TM_{m1}$  mode and if only this mode is included

$$E_z = \frac{a'_m}{Y_m(x'_0)} \{J_m(x') Y_m(x'_0) - Y_m(x') J_m(x'_0)\} e^{jm\phi} \quad x'_0 = kr_0$$

$$H_{\phi} = -\frac{a'_m j y_0}{Y_m(x'_0)} \{J_m(x') Y_m(x'_0) - Y_m(x') J_m(x'_0)\} e^{jm\phi}$$

As the lowest order TE mode is assumed to be unsupported in the slot

$$E_{\phi} = 0 \text{ at } r = r_1 \quad \text{Thus } m\bar{\beta} = -\bar{\Lambda} F_m(x_1)$$

The characteristic equation for  $\bar{\beta}$  is obtained by matching  $\frac{H_{\phi}}{E_z}$  at  $r = r_1$ .

$$F_m(x_1) - \frac{(m\bar{\beta})^2}{F_m(x'_1)} = \left(\frac{x_1}{x'_1}\right)^2 S_m(x'_1, x'_0)$$

where

$$S_m(x, y) = x \frac{J'_m(x) Y_m(y) - Y'_m(x) J_m(y)}{J_m(x) Y_m(y) - Y_m(x) J'_m(y)}$$

The condition  $S_m(x'_1, x'_0) = 0$  yields

$$(\bar{\Lambda})^2 = 1 \quad \text{where } \bar{\Lambda} = +1 \text{ corresponds to the } HE_{1m} \text{ mode and} \\ \bar{\Lambda} = -1 \text{ to the } EH_{1m} \text{ mode}$$

a condition known as "balanced hybrid" since  $\left| \frac{E_z}{H_z} \right| = \left( \frac{\mu_0}{\epsilon_0} \right)^{\frac{1}{2}}$  and the appropriate longitudinal components of the hybrid mode are then in the ratio of the free space wave impedance.

For large values of  $r_1$

$$S_m(x'_1, x'_0) \rightarrow -x'_1 \cot[k(r_0 - r_1)]$$



### 3.3.2 Fields Under Balanced Hybrid Conditions

As we shall see, for the simple feed model, the condition  $\bar{\Lambda} = \pm 1$  is of significance when we consider radiation characteristics.

For  $\bar{\Lambda} = \pm 1$

$$E_r = -f(x)\{\bar{\beta}F_m(x) \pm m\} \cos m\phi \quad f(x) = ja_m \frac{x'}{x} \frac{J_m(x)}{x}$$

$$\frac{H_r}{y_0} = \mp f(x)\{\bar{\beta}F_m(x) \pm m\} \sin m\phi$$

$$E_\phi = f(x)\{m\bar{\beta} \pm F_m(x)\} \sin m\phi$$

$$\frac{H_\phi}{y_0} = f(x)\{m\bar{\beta} \pm F_m(x)\} \cos m\phi$$

If  $E_r = \epsilon_r \cos m\phi$ ,  $H_r = h_r \sin m\phi$  etc.

$$y_0 \epsilon_T = \pm h_T$$

Rumsey [9] was first to show this to be a necessary condition if the radiation pattern arising from the field is to be everywhere linearly polarised (assuming a linearly polarised input).

Figure 3.3.5 shows transverse field patterns under balanced hybrid conditions. The resemblance of the patterns of the  $HE_{11}$  and  $HE_{12}$  modes to the focal fields shown in Fig. 3.2.3 is evident.

If  $kr_1 \gg 1$   $\bar{\beta} \rightarrow 1$  under balanced hybrid conditions at least for the  $HE_{11}$  mode. Also, as

$$F_m(x) \pm m = \pm x \frac{J_{m+1}(x)}{J_m(x)}$$

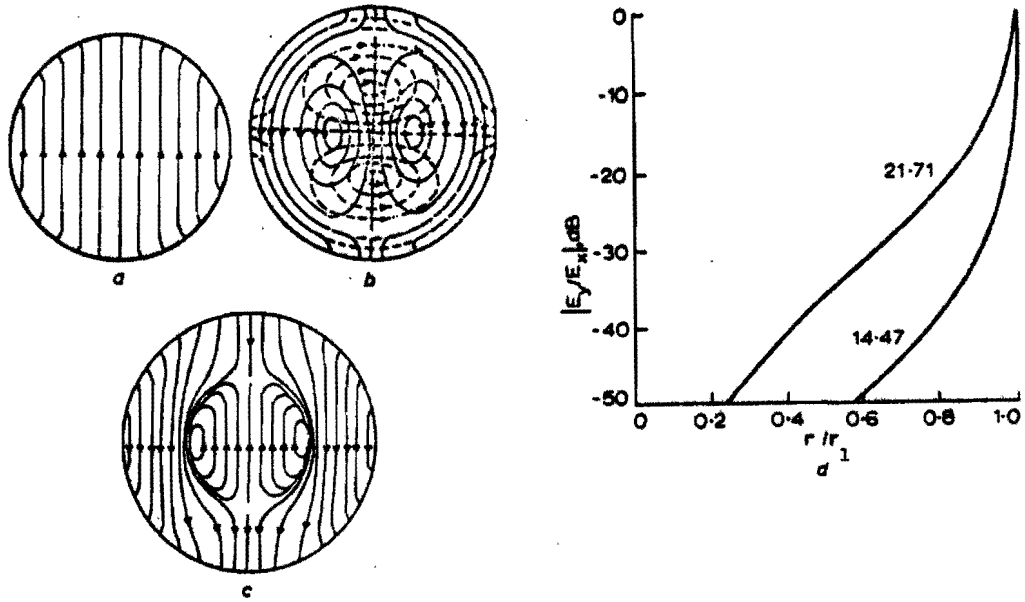


Fig. 3.3.5

Transverse field patterns for corrugated waveguides in region  $r \leq r_1$

- (a) Transverse electric-field pattern of  $HE_{11}$  mode under balanced hybrid conditions for  $r_1/r_0 = 0.9$
- (b) Transverse electric- and magnetic-field pattern of  $EH_{12}$  mode under balanced hybrid conditions for  $r_1/r_0 = 0.9$
- (c) Transverse electric-field pattern of  $HE_{12}$  mode under balanced hybrid conditions for  $r_1/r_0 = 0.9$
- (d) Cross-polarised component of  $HE_{11}$  mode as a function of  $r/r_1$  in corrugated circular waveguide for  $r_1/r_0 = 0.9$  and plane  $\psi = 45^\circ$ .  
Parameter  $x_1'$

then,

$$E_r = \bar{r} f(x) \times \frac{J_{m+1}(x)}{J_m(x)} = \bar{r} j a_m \frac{x'}{x} J_{m+1}(x) \cos m\phi$$

and

$$E_\phi = \pm f(x) \times \frac{J_{m+1}(x)}{J_m(x)} = \pm j a_m \frac{x'}{x} J_{m+1}(x) \sin m\phi$$

For the  $HE_{11}$  mode  $m = 1$

$$E_r = - j a_1 \frac{k}{K} J_0(Kr) \cos \phi$$

$$E_\phi = j a_1 \frac{k}{K} J_0(Kr) \sin \phi$$

Thus

$$E_x = E_r \cos \phi - E_\phi \sin \phi$$

$$= - j a_1 \frac{k}{K} J_0(Kr)$$

and

$$E_y = E_r \sin \phi + E_\phi \cos \phi$$

$$= 0$$

The field in  $r < r_1$  is thus linearly polarised. The extent to which this condition is actually achieved is shown in the previous figure. However, it is important to recognise that the present analysis has neglected the contribution from space-harmonics also, we shall see later that the flange of the waveguide is significant when a corrugated waveguide radiates.

### 3.3.3 General Expressions for the Field Components in a Hybrid Mode Waveguide

The following equations refer to a condition where  $\bar{\Lambda}$  is not unity

$$E_z = a_1 J_1(x) \cos \phi$$

$$H_z = a_1 \bar{\Lambda} J_1(x) \sin \phi$$

$$E_r = -ja_1 \frac{x'}{x} \{ \bar{\beta} J_1'(x) + \bar{\Lambda} \frac{J_1(x)}{x} \} \cos \phi$$

$$E_\phi = ja_1 \frac{x'}{x} \{ \bar{\beta} \frac{J_1(x)}{x} + \bar{\Lambda} J_1'(x) \} \sin \phi$$

$$\frac{H_r}{y_0} = -ja_1 \frac{x'}{x} \{ \bar{\beta} \bar{\Lambda} J_1'(x) + \frac{J_1(x)}{x} \} \sin \phi$$

$$\frac{H_\phi}{y_0} = -ja_1 \frac{x'}{x} \{ \bar{\beta} \bar{\Lambda} \frac{J_1(x)}{x} + J_1'(x) \} \cos \phi$$

If we use the Bessel function recurrence relation

$$J_1' = \frac{1}{2}(J_0 - J_2) \quad \text{and} \quad \frac{J_1}{x} = \frac{1}{2}(J_0 + J_2)$$

the above equations may be re-written abbreviating  $J_0(x)$  to  $J_0$  etc.,

$$E_r = -\frac{ja_1}{2} \frac{x'}{x} \{ (\bar{\beta} + \bar{\Lambda}) J_0 + (\bar{\Lambda} - \bar{\beta}) J_2 \} \cos \phi$$

$$E_\phi = \frac{ja_1}{2} \frac{x'}{x} \{ (\bar{\beta} + \bar{\Lambda}) J_0 - (\bar{\Lambda} - \bar{\beta}) J_2 \} \sin \phi$$

$$E_x = -\frac{ja_1}{2} \frac{x'}{x} \{ (\bar{\beta} + \bar{\Lambda}) J_0 + (\bar{\Lambda} - \bar{\beta}) J_2 \} \cos 2\phi$$

$$E_y = -\frac{ja_1}{2} \frac{x'}{x} (\bar{\Lambda} - \bar{\beta}) J_2 \sin 2\phi$$

Let us now resolve the propagation vector  $\underline{k}$  along the  $z$  and  $r$  directions.

$$k \cos \theta = \beta$$

$$k \sin \theta = K$$



On recalling that  $\bar{\beta} = \frac{\beta}{k}$

$$E_r = -\frac{ja_1}{2} \operatorname{cosec}\theta \cos^2\frac{\theta}{2} \{J_0 + \tan^2\frac{\theta}{2} J_2\} \cos\phi$$

$$E_\phi = \frac{ja_1}{2} \operatorname{cosec}\theta \cos^2\frac{\theta}{2} \{J_0 - \tan^2\frac{\theta}{2} J_2\} \sin\phi$$

and

$$E_x = -ja_1 \operatorname{cosec}\theta \cos^2\frac{\theta}{2} \{J_0 + \tan^2\frac{\theta}{2} J_2 \cos 2\phi\}$$

$$E_y = -ja_1 2 \operatorname{cosec}\theta \cos^2\frac{\theta}{2} J_2 \sin 2\phi$$

If we introduce the normalisation  $2kfE \sin^2\frac{\theta}{2} = a_1$

$$E_x = -jkf \sin\theta \{J_0 + \tan^2\frac{\theta}{2} J_2 \cos 2\phi\}$$

$$E_y = -jkf \sin\theta \{J_2 \sin 2\phi\}$$

$$E_z = 4kfE_0 \sin^2\frac{\theta}{2} J_1 \cos\phi$$

The total field is now

$$\underline{E} = -jkZ_0 H_0 \{(\bar{I}_1 + \bar{I}_2 \cos 2\phi) \hat{x} + \bar{I}_2 \sin 2\phi \hat{y} + \hat{z} \bar{I}_3 \cos\phi\}$$

On comparing this expression with that given for the focal field in section 2 and noticing that  $u_1 = x$ , we see that  $\bar{I}_1$ ,  $\bar{I}_2$  and  $\bar{I}_3$  are the kernels of the integrals  $I_1$ ,  $I_2$  and  $I_3$ . The field in the focal region is now recognised as an angular spectrum of hybrid waves.

### 3.3.4 Power Flow and Attenuation in a Hybrid Mode Waveguide

To obtain the Poynting vector we require the magnetic field components  $H_x$  and  $H_y$  which are readily obtained from

$$\frac{H_{r,\phi}}{y_0} = - \frac{ja_1}{2} \frac{x'}{x} \{ \bar{\beta} \bar{\Lambda} (J_0 - J_2) + (J_0 \pm J_2) \} \frac{\sin \phi}{\cos \phi} = C \{ J_0 (1 + \bar{\beta} \bar{\Lambda}) \pm J_2 (1 - \bar{\beta} \bar{\Lambda}) \} \frac{\sin \phi}{\cos \phi}$$

where the + sign and sin designation refers to  $H_r$ . Then

$$\frac{H_x}{y_0} = C J_2 (1 - \bar{\beta} \bar{\Lambda}) \sin 2\phi$$

$$\frac{H_y}{y_0} = C \{ J_0 (1 + \bar{\beta} \bar{\Lambda}) - J_2 (1 - \bar{\beta} \bar{\Lambda}) \cos 2\phi \}$$

$$S_z = E_x H_y - H_x E_y$$

$$= \frac{a_1^2}{4} y_0 \frac{k^2}{K^2} [ \bar{\beta} (1 + \bar{\Lambda}^2) \{ J_0^2 + J_2^2 \} + \bar{\Lambda} (1 + \bar{\beta}^2) \{ J_0^2 - J_2^2 \} - 2 \bar{\beta} (1 - \bar{\Lambda}^2) J_0 J_2 \cos 2\phi ]$$

The above expression shows that when  $\bar{\Lambda} = \pm 1$  the energy flow distribution is circularly symmetric.

The total power flow is obtained by integration over the waveguide cross-section  $r < r_1$  to give in general

$$P_T = a_m^2 \frac{(x_1^2 r_1^2) \pi}{x_1^4} y_0 J_m^2(x_1) [ \bar{\beta} (1 + \bar{\Lambda}^2) \{ \frac{1}{2} F_m^2(x_1) + F_m(x_1) + \frac{1}{2} (x_1^2 - m^2) \} + m \bar{\Lambda} (1 + \bar{\beta}^2) ]$$

when  $m = 1$ , the quantity in square brackets simplifies to

$$\bar{\beta} (1 + \bar{\Lambda}^2) \{ \frac{1}{2} (F+1)^2 + (\frac{x_1^2}{2} - 1) \} + \bar{\Lambda} (1 + \bar{\beta}^2)$$

Under balanced hybrid conditions  $F = \mp \bar{\beta}$  when  $\bar{\Lambda} = \pm 1$

Furthermore if  $\bar{\beta} \rightarrow 1$  under this condition then for the  $HE_{11}$  mode

$$P_T = a_1^2 \pi \frac{x_1'^2 r_1^2}{x_1^2} y_0 J_1^2(x_1)$$

The above result is for a circularly polarised wave; for a linearly polarised wave the value is halved.

If space-harmonics and higher-order slot modes are neglected, a simple expression for the attenuation coefficient  $\alpha$  in a corrugated waveguide can be obtained following fairly considerable algebraic manipulations.

$$\alpha = \frac{P_L}{2P_T b}$$

where  $b$  is the width between corrugations which are assumed to have negligible thickness.  $P_T$  has been given above and

$$P_L = P_{L_1} + P_{L_2}$$

where

$$P_{L_1} = a_m^2 \frac{2\pi}{k^2} R_s y_0^2 J_m^2(x_1) \left[ \frac{1}{2}(m^2 - x_1'^2) + \frac{2}{(\pi S_m^D(x_1', x_0'))^2} - S_m(x_1', x_0') - \frac{1}{2} S_m^2(x_1', x_0') \right] \dots \text{(side walls)}$$

$$P_{L_2} = a_m \frac{4R_s b}{\pi k^2 r_0} y_0^2 \frac{J_m^2(x_1)}{[S_m^D(x_1', x_0')]^2} \dots \text{(base)}$$

The superfix  $D$  denotes the denominator of the  $S$  function (defined in section 3.3.1). Attenuation characteristics corresponding to the dispersion curves of Fig. 3.3.2, are shown in Fig. 3.3.6.

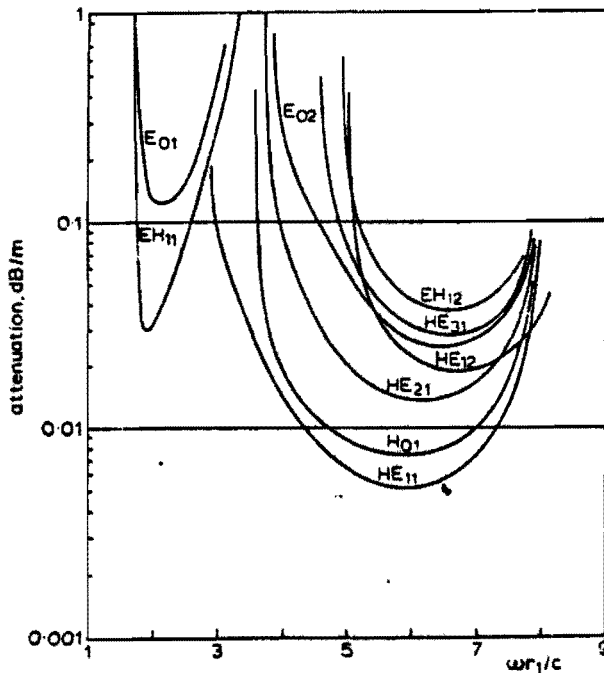


Fig. 3.3.6

Attenuation characteristics  
corresponding to Fig. 2.3.2.  
Conductivity of metal  
 $\sigma = 5.8 \times 10^7$  S/m

The results displayed there have been obtained by Clarricoats, Olver and Chong [10] using a complete space-harmonic and slot mode formulation, although in their general form they are similar to those obtained from the above expressions. In that simple case there is an obvious simplification under balanced hybrid conditions since  $S_m(x'_1, x'_0)$  is then zero corresponding to the condition  $H_\theta = 0$  at  $r = r_1$ . One might anticipate that under this condition the attenuation in a corrugated waveguide would be a minimum, actually the minimum is shifted to higher frequencies when space-harmonics and higher-order slot modes are included but the broad principle remains approximately correct.

One notices that the  $HE_{11}$  mode attenuation is lower than that of the  $H_{01}$  mode. The reason follows in part from the uniform power distribution about the axis for the former mode as compared to the ring like distribution for the latter. For a given power flowing in the waveguide, the field intensity near the walls is lower for the  $HE_{11}$  mode compared to that for the  $H_{01}$  mode. Also, only in the hybrid mode waveguide is it possible to achieve the condition that all magnetic field components tangential to metal surfaces, have a direct dependence on the strength of the longitudinal magnetic field. It will be recalled that therein lies the

explanation for low attenuation in the  $H_{01}$  mode in a conventional smooth wall waveguide since for a given power flow, the  $H_z$  components decrease indefinitely with frequency.

### 3.3.5 Radiation from Corrugated Waveguides

Two methods have been used to determine the radiation pattern of a corrugated waveguide: (a) Kirchhoff-Huygen (applied by L J Chu to small horns and usually described by his name), (b) Fourier Transform. Method (a) requires  $\underline{E}$  and  $\underline{H}$  to be specified over the aperture and zero elsewhere in the aperture plane, method (b) specifies  $\underline{E}$  over the aperture and requires only that  $\underline{E}$  should vanish elsewhere in the aperture plane. For large apertures the methods agree but for small apertures where the effect of the waveguide flange is more pronounced method (b) has been found to give results in better agreement with experiment. We shall now develop expressions for the radiation components of field using method (b).

The cartesian components of the electric field radiated from the aperture of the corrugated waveguide are given by

$$E_{xp} = A \int_0^{2\pi} \int_0^{r_1} E_x e^{jkrs \sin \theta \cos(\phi - \phi')} r dr d\phi' \quad \text{since } E_x = 0 \text{ } r > r_1$$

$$A = \frac{jk\epsilon}{2\pi R} e^{-jkR} \cos \theta$$

On substituting for the cartesian components of electric field in the aperture, the integral may be evaluated

$$E_{xp} = AB\{(\beta + \lambda) N_0 + (\lambda - \beta) N_2 \cos 2\phi\}$$

$$E_{yp} = AB\{(\lambda - \beta) N_2 \sin 2\phi\}$$

$$B = -ja \frac{k}{R} \pi$$

$$N_k = \frac{r_1^2}{v^2 - u^2} \{v J_k(u) J_1(v) - u J_k(v) J_1(u)\} \quad \begin{aligned} u &= kr_1 \\ v &= kr_1 \sin \theta \end{aligned}$$

To obtain the copolar and crosspolar radiated fields we use

$$E_{co} = E_{xp}(\cos^2 \frac{\theta}{2} - \sin^2 \frac{\theta}{2} \cos 2\phi) - E_{yp} \sin^2 \frac{\theta}{2} \sin 2\phi$$

$$E_{cp} = -E_{xp} \sin^2 \frac{\theta}{2} \sin 2\phi + E_{yp}(\cos^2 \frac{\theta}{2} + \sin^2 \frac{\theta}{2} \cos 2\phi)$$

On substituting for  $E_{xp}$

$$E_{co} = AB\{(\bar{\beta} + \bar{\lambda})N_0 + (\bar{\lambda} - \bar{\beta})N_2 \cos 2\phi\}$$

if terms in  $\sin^2 \frac{\theta}{2}$  are neglected, an assumption valid near to boresight.

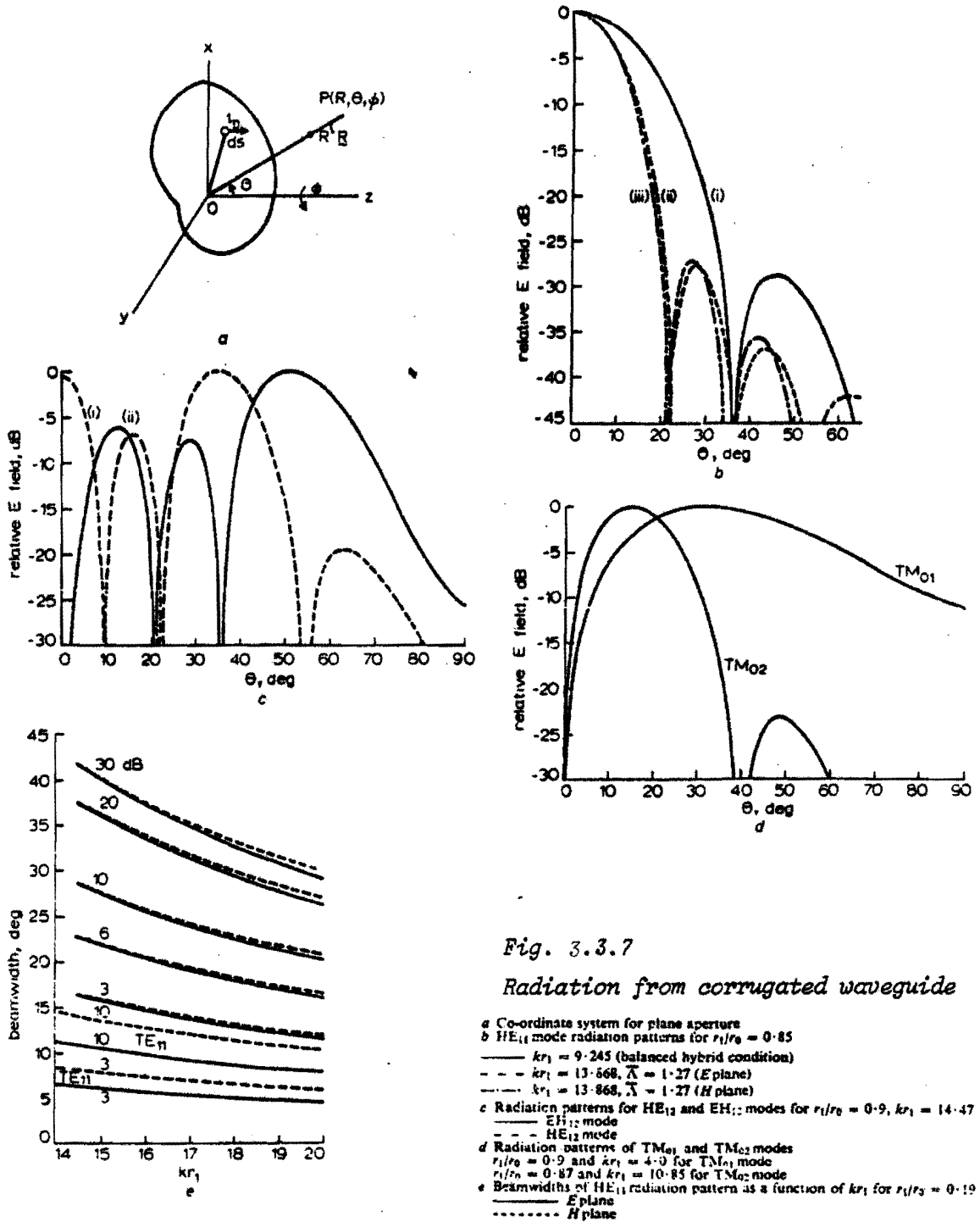
Similarly

$$E_{cp} = AB(\bar{\lambda} - \bar{\beta})N_2 \sin 2\phi$$

The above equation for  $E_{cp}$  must be used with caution because the maximum of the crosspolar pattern occurs generally at values of  $\theta$  such that neglect of terms in  $\sin^2 \frac{\theta}{2}$  is invalid. However, in the  $45^\circ$  planes we obtain generally that

$$E_{cp} = AB\{(\bar{\beta} + \bar{\lambda})N_0 \sin^2 \frac{\theta}{2} + (\bar{\lambda} - \bar{\beta})N_2 \cos^2 \frac{\theta}{2}\}$$

From this equation we can see that the condition  $\bar{\lambda} = \bar{\beta}$  is no longer the one for a crosspolar null, in fact the frequency is shifted to a higher value than the balanced hybrid value  $\bar{\lambda} = 1$ .



### 3.3.6 A Corrugated Waveguide Feed for a Paraboloidal Reflector Antenna

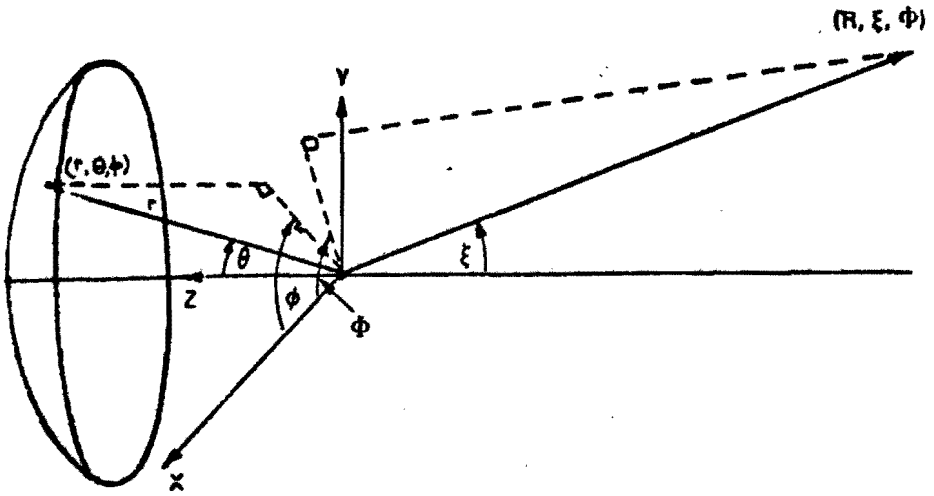


Fig. 3.3.8

Fig. 3.3.8 shows the coordinate system appropriate to a parabolic reflector antenna with a feed at the focus which is also the origin. The expression for the far-field may be obtained from the current distribution over the reflector surface in a manner similar to the focal field calculation of section 3.2.1. Thus

$$\begin{aligned} \underline{E}_p = \frac{-j k f}{\pi R} \int_0^{2\pi} \int_0^{\theta} & [\hat{x}(\bar{E}_\theta \sin^2 \phi - \bar{E}_\phi \cos^2 \phi) + \hat{y} \frac{1}{2}(\bar{E}_\theta + \bar{E}_\phi) \sin 2\phi \\ & - \hat{z} \bar{E}_\theta \sin \phi \tan \frac{\theta}{2}] \tan \frac{\theta}{2} e^{-j k f \sec^2 \frac{\theta}{2} \{1 + \cos \xi \cos \theta - \sin \theta \sin \xi \cos(\phi - \Phi)\}} d\theta d\phi \end{aligned}$$

where the feed is polarised with electric field in the  $\hat{x}$  direction so that the incident field at the reflector surface is

$$\underline{E}_i = \hat{i}_\theta \bar{E}_\theta \cos \phi - \bar{E}_\phi \sin \phi \hat{i}_\phi$$



On application of the Fourier-Bessel identity the equation for  $\underline{E}_p$  becomes

$$\begin{aligned} \underline{E}_p(R, \xi, \phi) = & -\frac{jkf}{R} \int_0^\theta \{ [\hat{x}(\bar{E}_\theta - \bar{E}_\phi) J_0(U_1) + (\bar{E}_\theta + \bar{E}_\phi) J_2(U_1) \cos 2\phi] \\ & + \hat{y}(\bar{E}_\theta + \bar{E}_\phi) J_2(U_1) \sin 2\phi - \hat{z} j 2 \bar{E}_\theta J_1(U_1) \tan \frac{\theta}{2} \sin \phi \} e^{-j U_2 \tan \frac{\theta}{2}} d\theta \end{aligned}$$

where

$$U_1 = 2kf \tan \frac{\theta}{2} \sin \xi$$

$$U_2 = kf \sec^2 \frac{\theta}{2} (1 + \cos \xi \cos \theta)$$

In the above,  $\bar{E}_\theta$  and  $\bar{E}_\phi$  are the  $\theta$  dependent pattern functions of the feed. Reference to section 3.3.5 shows for a corrugated waveguide, that when  $\bar{A}=1$ ,  $\bar{E}_\theta = -\bar{E}_\phi$ . Under this condition the co-polar secondary pattern is symmetric and the cross-polar pattern vanishes for all observation angles  $\xi$ .

### 3.3.7 Gain Factor of Corrugated Waveguide Feed

Under balanced hybrid conditions when the radiation pattern is symmetric, the feed gain factor is given by

$$G(\theta') = \frac{2|F(\theta')|^2}{\int_0^\pi |F(\theta)|^2 \sin \theta d\theta}$$

Table 3.3.1 shows the axial gain as a function of  $kr_1$  with  $r_1/r_0$  selected to maintain balanced hybrid conditions. The horn gain factor lies between 65% and 70% over the range. This figure is less than that obtained for a paraboloid antenna when the waveguide is used as a prime feed. The explanation is that the focal-plane field of the paraboloid is more closely matched than a uniform field to the  $J_0(x)$  distribution of the corrugated waveguide.

$r_1/r_0$	$kr_1$	Gain
		dB
0.70	4.0300	10.74
0.75	5.0728	12.68
0.80	6.6356	14.94
0.81	7.0473	15.44
0.82	7.5050	15.98
0.83	8.0167	16.55
0.84	8.5925	17.15
0.85	9.2453	17.77
0.86	9.9916	18.43
0.87	10.8530	19.15
0.88	11.8580	19.90
0.89	13.0470	20.75
0.90	14.4730	21.64
0.91	16.2160	22.65

Table 3.3.1

Gain of corrugated circular waveguide  
with balanced  $HE_{11}$  mode at the aperture

### 3.3.8 Gain Factor of Paraboloid Reflector with Corrugated Waveguide Feed

When a corrugated waveguide is employed as a prime feed for a paraboloid reflector, the axial gain factor under balanced hybrid conditions is

$$G_f = \frac{2 \cot^2 \Psi / 2 \left| \int_0^\Psi F(\theta) \tan \frac{\theta}{2} d\theta \right|^2}{\int_0^\pi |F(\theta)|^2 \sin \theta d\theta}$$

where  $\Psi$  = semiangular aperture of paraboloid and  $\cot \Psi/2 = 4f/D$ . In Fig. 3.3.9, we show  $G_f$  as a function of  $\Psi$  for different  $kr_1$  and  $r_1/r_0$  chosen from Table 3.3.1. We note that the maximum value of  $G_f$  increases slightly with decreasing  $\Psi$ , and we recall that the optimum angular aperture represents a compromise between spillover of the feed energy and aperture efficiency. At small angular aperture, it is possible to illuminate the aperture more uniformly, but, to avoid a long-focal-length system, a Cassegrain configuration must be used. However, diffraction by the sub-reflector and blockage will then deteriorate the gain, and a significant advantage is apparent only with shaped-reflector systems. The maximum gain factor for the paraboloid with a corrugated waveguide feed is about 84% and similar figures are also obtained with a wide-angle conical corrugated feed horn. An identical figure has been obtained by Phillips and Clarricoats [6] for spherical reflectors. The limitation is readily understood in terms of the

focal-plane field distribution. Unless we employ higher-order hybrid modes to synthesise the second lobe in addition to the main lobe, the best compromise is obtained when the feed-horn diameter just encloses the central region of illumination. For the front-fed paraboloid or conventional Cassegrain antenna, the efficiency is then given by

$$\eta = 1 - J_0^2(x_1')$$

and, with  $x_1' = 3.383$ ,  $\eta = 84\%$ . By using a shaped subreflector, the energy contained in the central region is appreciably increased.

We conclude this section by noting that the problem of optimising the gain factor of an antenna using a corrugated waveguide feed is very similar to that of optimising the efficiency of excitation of the  $HE_{11}$  mode on a cored-fibre optical waveguide by means of a focusing lens. The problem was first considered by Snyder, who obtained the same maximum excitation efficiency as above when the illumination was from a focused plane wave.

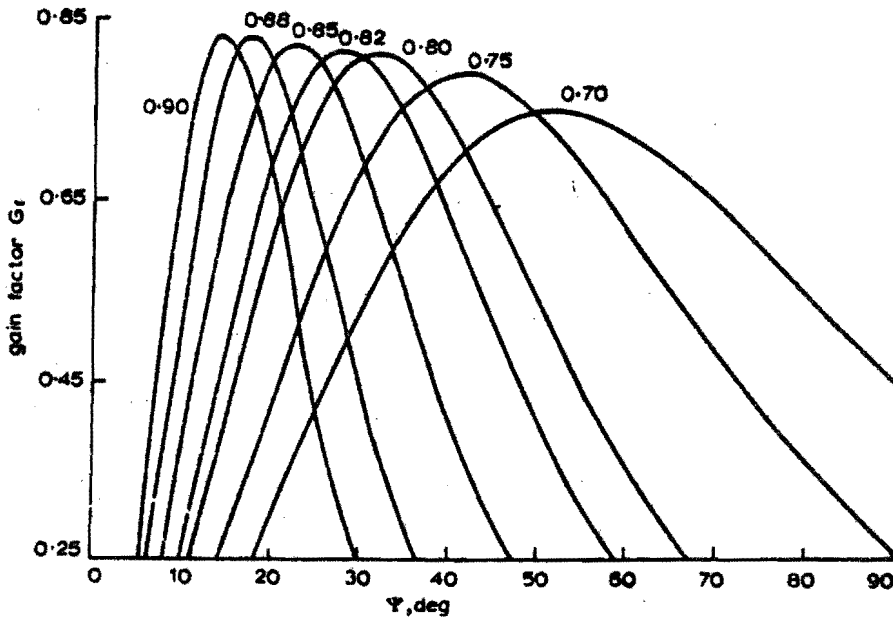


Fig. 3.3.9

Gain factor as function of semiangular aperture for parabolic reflector fed with corrugated circular waveguide feed

Parameter  $r_1/r_0$

### 3.4 Propagation and Radiation Characteristics of Corrugated Conical Horns

#### 3.4.1 Determination of Horn-aperture Fields

Figure 3.4.1(a) shows a section through a conical horn excited by a circular waveguide. We shall assume that the field in the interior of the horn may be described in terms of a single spherical hybrid mode, also that the impedance looking into the slots is independent of  $R$  in the vicinity of the horn aperture. In order to predict the radiation pattern the aperture fields must first be determined in a manner analogous to the corrugated waveguide of section 3.3.1. Consider the electric and magnetic scalar potentials

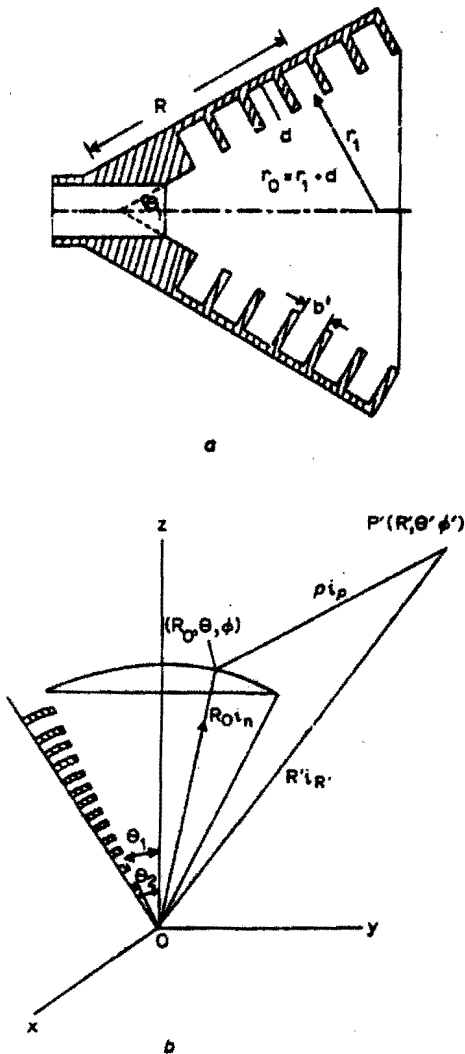


Fig. 3.4.1

Corrugated conical horn

(a) Section through  
corrugated conical horn

(b) Co-ordinate system for  
conical-horn analysis

$$A_R = A H_{\nu}^{(2)}(kR) P_{\nu}^m(\cos\theta) e^{jm\phi}$$

$$F_R = B H_{\nu}^{(2)}(kR) P_{\nu}^m(\cos\theta) e^{jm\phi}$$

The coefficients A and B depend on the excitation of the mode and are related through the equation

$$\frac{B}{A} = -j\eta_0 \bar{A}$$

where  $\eta_0 = (\mu_0/\epsilon_0)^{1/2}$  and the coefficient  $\bar{A}$  depends on the boundary conditions.  $\hat{H}_{\nu}^{(2)}(x) = kR h_{\nu}^{(2)}(kR)$ , where  $h_{\nu}^{(2)}(kR)$  is a spherical Hankel function of the 2nd kind, and henceforth the superscript (2) will be omitted.

$P_{\nu}^m(\cos\theta)$  is an associated Legendre function of order  $\nu$  which, in general, is noninteger.  $P_{\nu}^m(\cos\theta)$  is real provided  $-1 < \cos\theta < +1$ . This is always so in our investigation. The azimuthal dependence,  $e^{jm\phi}$ , corresponds to a circularly polarised form when  $m=1$  as in the present analysis. Later, we introduce a linearly polarised form to distinguish phase factors more clearly. A time dependence of the form  $e^{j\omega t}$  is assumed throughout and is suppressed for convenience, so that the corresponding outward travelling spherical wave has a radial dependence  $e^{-jkR}$ . In general,  $\hat{H}_{\nu}(x)$  is a complex function, although, when  $x \gg 1$ ,  $\hat{H}_{\nu}(x) \rightarrow j^{\nu+1} e^{+jx}$  and the radial dependence becomes that of a spherical wave. The equations for  $A_R$  and  $F_R$  are the consequence of separating the variables in the spherical-wave equation: a procedure which is only justified if the boundary conditions on the surface  $\theta = \theta_1$  are independent of  $R$  and  $\phi$ . In practice, the boundary conditions depend on  $R_1$ , but, near the horn aperture, the dependence is slight and the assumption is well justified.

The field components in spherical coordinates are obtained as follows, where, for convenience, the functions  $\hat{H}_{\nu}(kR)$  and  $P_{\nu}^m(\cos\theta)$  are abbreviated and the factor  $e^{jm\phi}$  omitted:

$$E_R = A \eta_0 \nu \frac{(\nu+1)}{j k R^2} \hat{H}_{\nu} P_{\nu}^m$$

$$H_R = -A\bar{\lambda}v \frac{(v+1)}{kR^2} \hat{H}_v P_v^m$$

$$E_\theta = -\eta_0 A \left[ \frac{m\bar{\lambda}}{R \sin\theta} \hat{H}_v P_v^m + \frac{j}{R} \hat{H}'_v \frac{dP_v^m}{d\theta} \right]$$

$$E_\phi = \eta_0 A \left[ -\frac{j\bar{\lambda}}{R} \hat{H} \frac{dP_v^m}{d\theta} + \frac{m}{R \sin\theta} \hat{H}'_v P_v^m \right]$$

$$H_\theta = A \left[ \frac{jm\hat{H}_v}{R \sin\theta} P_v^m - \bar{\lambda} \frac{\hat{H}'_v}{R} \frac{dP_v^m}{d\theta} \right]$$

$$H_\phi = -A \left[ \frac{\hat{H}_v}{R} \frac{dP_v^m}{d\theta} + j \frac{\bar{\lambda}m\hat{H}'_v}{R \sin\theta} P_v^m \right]$$

Let

$$p_v^m(\theta) = \frac{dP_v^m}{d\theta}(\cos\theta)/P_v^m(\cos\theta)$$

and

$$h_v(kR) = \frac{\hat{H}'_v(kr)}{\hat{H}_v(kr)} \rightarrow -j \text{ as } kR \gg 1$$

Then

$$\frac{E_\phi}{H_R} = \frac{jkR\eta_0}{v(v+1)} \left[ p_v^m(\theta) + \frac{jm h_v}{\bar{\lambda} \sin\theta} \right]$$

and

$$\frac{H_\phi}{E_R} = \frac{-jkR\eta_0}{v(v+1)} \left[ p_v^m(\theta) + \frac{j\bar{\lambda}m h_v}{\sin\theta} \right]$$

Provided that  $kb' < 2\pi$ , no TE spherical mode can be supported within the slots. Usually  $kb' \approx 1$ , and we are then justified in placing  $E_\phi/H_R=0$  at  $\theta = \theta_1$ . If, in general,  $H_\phi/E_R = Y$  at  $\theta = \theta_1$ , we obtain a characteristic equation for  $v$  in terms of  $\theta_1$  and  $R$ :

$$p_v^m(\theta_1) \left[ Y + \frac{jkR\eta_0}{v(v+1)} p_v^m(\theta_1) \right] = \frac{-jm^2kR\eta_0(h_v)^2}{v(v+1)\sin^2\theta_1}$$

If

$$\bar{Y} = \frac{-jY}{Y_0} \frac{v(v+1)}{kR}$$

where

$$Y = jy_0 \left( \cot kd + \frac{1}{2kr_1} \right)$$

$$p_v^m(\theta_1) \{ \bar{Y} + p_v^m(\theta_1) \} = \frac{-m^2}{\sin^2 \theta_1} (h_v)^2$$

In our studies of the frequency dependence of corrugated horns, we have neglected the second term in the equation for  $Y$ . Thus  $Y = 0$  when  $Kd = \pi/2$ .

When  $Y \neq 0$ , the characteristic equation depends on  $R$  as  $1/R$  since

$$\bar{Y} = \frac{\cot kd (v+1)v}{kR}$$

In practice,  $kR \gg 1$  at the mouth of a horn, and it is reasonable to assume that  $\bar{Y}$  is independent of  $R$  when calculating aperture fields.

The particular case  $\bar{Y} = 0$  is of special interest, since, under this condition the radiation pattern of the feed horn is circularly symmetric and the cross-polarisation component is zero. When  $\bar{Y} = 0$ ,

$$\sin^2 \theta_1 \{ p_v^m(\theta_1) \}^2 = m^2$$

where we have assumed  $h_v(x) = -j$ .

In Fig. 3.4.2 we show solutions of the equation for  $m = 1$  in the range  $0 < \theta_1 < 90^\circ$  and  $v < 12$ .

When  $\theta_1$  is small,  $\sin \theta_1 = \theta_1$  the characteristic equation becomes

$$(\alpha \theta_1)^2 \left[ \frac{J'_m(\alpha \theta_1)}{J_m(\alpha \theta_1)} \right]^2 = m^2 \left[ 1 - \left( \frac{\alpha}{kR_1} \right)^2 \right]$$

If we identify  $\alpha = \sqrt{v(v+1)}$  with  $KR_1$ , where  $K$  is the transverse (to  $z$ ) wavenumber of section 3.3.1 the equation becomes

$$F_m^2(Kr_1) = (m\bar{\beta})^2$$

where  $\bar{\beta} = \beta/k$  and  $K^2 = k^2 - \beta^2$ . This is the characteristic equation for the corrugated waveguide derived in section 3.3.1 by means of a cylindrical mode analysis.

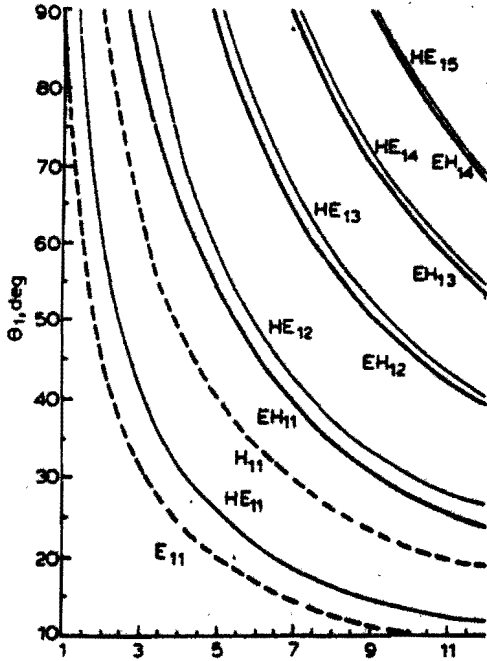


Fig. 3.4.2  
Solutions of characteristic equation for  $HE_{1N}$  and  $EH_{1N}$  modes in corrugated conical horn.  
---- modes in uncorrugated horn

### 3.4.2 Aperture Fields Under Balanced Hybrid Conditions

The boundary conditions on  $E_\phi$  and  $H_\phi$  lead to the expressions for the hybrid factor  $\bar{\Lambda}$ .

$$\bar{\Lambda} = \frac{-m}{p_v^m(\theta_1) \sin \theta_1}$$

$$\bar{\Lambda} = - (p_v^m(\theta_1) + \bar{Y}) \frac{\sin \theta_1}{m}$$

When  $Y = Q$ , we have  $\bar{\Lambda} = \pm 1$  and we call this the balanced hybrid condition since the components  $E_R$  and  $H_R$  are then in the ratio of the free-space wave impedance. The positive sign corresponds to HE modes, the negative to EH modes.



We have, when  $h_v = -j$ ,

$$E_\theta = -n_0 \frac{A\hat{H}_v}{R} \left( \frac{m\bar{\lambda}P_v^m}{\sin\theta} + \frac{dP_v^m}{d\theta} \right) \cos m\phi = \frac{A\hat{H}_v}{R} e_\theta \cos m\phi$$

$$E_\phi = n_0 \frac{A\hat{H}_v}{R} \left( \frac{\bar{\lambda}dP_v^m}{d\theta} + \frac{mP_v^m}{\sin\theta} \right) \sin m\phi = \frac{A\hat{H}_v}{R} e_\phi \sin m\phi$$

In general,

$$H_\theta = -y_0 E_\phi$$

$$H_\phi = y_0 E_\theta$$

If  $m = 1$ , under balanced hybrid conditions with  $\bar{\lambda} = \pm 1$   $e_\theta = \mp e_\phi$ ,  
 $h_\theta = \pm y_0 e_\theta$  and  $h_\phi = \mp y_0 e_\phi$ .

In Fig. 3.4.3, we show the function  $f_{v+}^1(\theta) = (P_v^1/\sin\theta) + (dP_v^1/d\theta)$  as a function of  $\theta$  for four values of  $\theta_1$ . We have normalised the curves by plotting  $f_{v+}^1/v(v+1)$ , since  $f_{v+}^1(0) = v(v+1)$ .

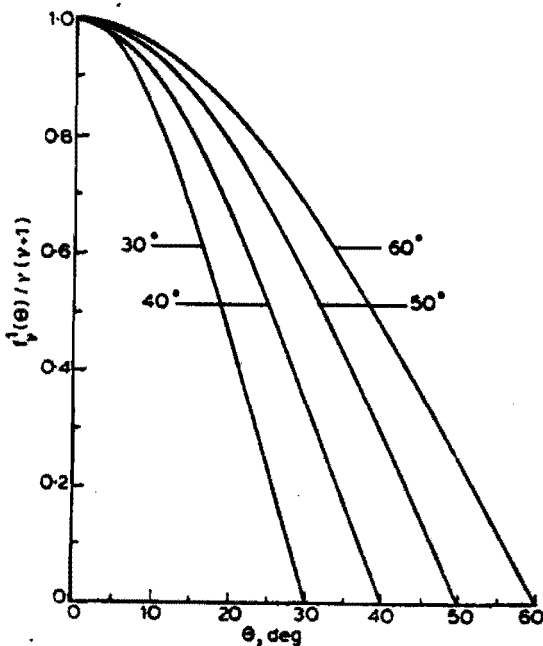


Fig. 3.4.3

Normalised aperture-field distribution for corrugated horn.

Parameter denotes horn semi-angle  $\theta_1$ .

### 3.4.3 Radiation from Corrugated Horn

#### 3.4.3.1 Kirchhoff-Huygen method

Now that the aperture field at the surface  $R = R_0$  of Fig. 2.4.1(b) is known, the radiation field  $E_p$  may be determined by a Kirchhoff-Huygen integration over the cap  $R = R_0$ ,  $-\theta_1 < \theta \leq \theta_1$ ,  $0 < \phi < 2\pi$ . From Silver [11],

$$\underline{E}_p(R', \theta', \phi') = \frac{jk \exp(-jkR')}{4\pi R'} \hat{i}_{R'} \times \int_S \{ \hat{i}_n \times \underline{E}_{\text{tang}} - z_0 \times (\hat{i}_n \times \underline{H}_{\text{tang}}) \} \exp(jkR_0 \hat{i}_{R'} \cdot \underline{\hat{i}}_R) dS$$

$\hat{i}_{R'}$ ,  $\hat{i}_n$  are unit vectors and the fields  $\underline{E}_{\text{tang}}$ ,  $\underline{H}_{\text{tang}}$  are tangential to the surface of the spherical cap. On replacing the factor outside the integral by  $c$ , we obtain, after some algebraic manipulation,

$$\begin{aligned} E_{p\theta}(\theta', \phi') &= c \int_0^{2\pi} \int_0^{\theta_1} [-E_\theta \cos(\phi' - \phi) - E_\phi \cos\theta \sin(\phi' - \phi) \\ &\quad + z_0 H_\theta \cos\theta' \sin(\phi' - \phi) - z_0 H_\phi (\sin\theta \sin\theta' \\ &\quad + \cos\theta \cos\theta' \cos(\phi' - \phi))] \exp[jkR_0 \{\cos\theta \cos\theta' \\ &\quad + \sin\theta \sin\theta' \cos(\phi' - \phi)\}] \sin\theta d\theta d\phi \\ E_{p\phi}(\theta', \phi') &= c \int_0^{2\pi} \int_0^{\theta_1} [E_\theta \cos\theta' \sin(\phi' - \phi) - E_\phi \{\sin\theta \sin\theta' \\ &\quad + \cos\theta \cos\theta' \cos(\phi' - \phi)\} + z_0 H_\theta \cos(\phi' - \phi) \\ &\quad + z_0 H_\phi \cos\theta \sin(\phi' - \phi)] \exp[jkR_0 \{\cos\theta \cos\theta' \\ &\quad + \sin\theta \sin\theta' \cos(\phi' - \phi)\}] \sin\theta d\theta d\phi \end{aligned}$$

Let  $a = kR_0 \cos\theta'$  and  $b = kR_0 \sin\theta'$ , and let

$$E_\theta(\theta, \phi) = -g(\theta)C \cos m\phi$$

$$E_\phi(\theta, \phi) = h(\theta)C \sin m\phi$$

On substituting for  $E_\theta$  and  $E_\phi$ , we obtain, after performing the integration and combining the constants,

$$E_{p\theta}(\theta', \phi') = D \cos m\phi' \int_0^{\theta_1} [2jg(\theta)J_m(b\sin\theta)\sin\theta\sin\theta' \\ + (j)^{m+1}J_{m+1}(b\sin\theta)\{g(\theta)(1+\cos\theta\cos\theta') \\ \mp h(\theta)(\cos\theta+\cos\theta')\} + j^{m-1}J_{m-1}(b\sin\theta) \\ \{g(\theta)(1+\cos\theta\cos\theta') \pm h(\theta)(\cos\theta+\cos\theta')\}] e^{(j\cos\theta)\sin\theta d\theta}$$

The integral for  $E_{p\phi}(\theta', \phi')$  is similar to that for  $E_{p\theta}$  except that  $g(\theta)$  and  $h(\theta)$  are interchanged and  $\cos m\phi'$  is replaced by  $-\sin m\phi'$ . When  $\bar{\Lambda} = +1$ , we have

$$g(\theta) = h(\theta) = f_{v+}^m(\theta) = \frac{mP_v^m}{\sin\theta} + \frac{dP_v^m}{d\theta} \quad \text{and when } \bar{\Lambda} = -1$$

$$g(\theta) = -h(\theta) = f_{v-}^m(\theta) = \frac{dP_v^m}{d\theta} - \frac{mP_v^m}{\sin\theta}$$

$$\text{Formal } E_{p\theta} = \pm \{F_r(\theta') + jF_i(\theta) \cos\phi' \\ \sin\phi\}$$

$$\text{where } F_{ri}(\theta') = D \int_0^{\theta} f_{v\pm}^1(\theta) G_{ri}(\theta, \theta') d\theta$$

$$G_{ri}(\theta', \theta') = \{(1+\cos\theta)(1+\cos\theta')\sin\theta \frac{\cos}{\sin} (a\cos\theta)J_0(b\sin\theta)\} \\ - \{(1-\cos\theta)(1-\cos\theta')\sin\theta \frac{\cos}{\sin} (a\cos\theta)J_2(b\sin\theta)\} \\ \mp \{2\sin\theta'\sin^2\theta \frac{\sin}{\cos} (a\cos\theta)J_1(b\sin\theta)\}$$

From the above equation, we observe that, under balanced hybrid conditions, pattern symmetry exists about the axis  $\theta' = 0$ . A maximum in the boresight direction  $\theta' = 0$  occurs for  $HE_{1n}$  modes, while for  $EH_{1n}$  modes there is a null on the boresight, and similarly for all modes with  $m > 1$ . There is no cross-polarised component of radiated field if the aperture field is linearly polarised.

### 3.4.3.2 Modal-expansion method for Copolar Radiation

In an alternative approach to the computation of the far-field of a corrugated conical horn, we use an expansion of the horn-aperture electric field in terms of the spherical modes of free space. To determine the excitation coefficients of these modes, we invoke the orthogonality properties of the Legendre functions over the spherical surface  $R = R_0$  and assume that the field producing the excitation is zero outside the horn where  $\theta > \theta_1$ .

For convenience, we begin our analysis with the case  $m = 1, |\bar{\Lambda}| = 1$ , for which the horn-aperture electric field is given by

$$E(R_0, \theta, \phi) = \frac{\exp(-jkR_0)}{R_0} f_v^1(\theta) (\hat{i}_\theta \cos\phi - \hat{i}_\phi \sin\phi)$$

We have set a multiplying constant equal to unity as we are concerned with radiation patterns rather than the absolute far-field intensity. The subscript  $\pm$  has also been omitted from the  $f_v^1(\theta)$  function, the choice of sign depending on the sign of  $\bar{\Lambda}$ . Let the electric far-field be represented in terms of a combination of TE and TM spherical modes which exist in  $R > R_0$ . For  $R = R_0$

$$E(R_0, \theta) = \sum_{n=1}^N C_n h_n^{(2)}(kR_0) f_n^1(\theta)$$

where  $f_n^1(\theta) = (dP_n^1/d\theta) \pm (P_n^1/\sin\theta)$ , the sign depending on the sign in  $f_v^1(\theta)$ . For  $N > kR_0$ , the coefficients  $C_n$  have negligible values and we may truncate the series at or near that value. On using well known orthogonality relationships,  $C_n$  is obtained as

$$C_n = \frac{\exp(-jkR_0)}{R_0} \frac{2n+1}{2n^2(n+1)^2 h_n^{(2)}(kR_0)} \int_0^{\theta_1} f_v^1(\theta) f_n^1(\theta) \sin\theta d\theta$$

Now that the intensity of excitation of the TE and TM spherical mode combinations are known, the far-field of the horn is obtained directly. On making use of the asymptotic expression for the spherical Hankel function, the normalised far-field pattern is given by

$$\left| \frac{E(\theta)}{E(0)} \right| = \left| \frac{\sum_{n=1}^N \frac{C_n j^{n+1}}{h_n^{(2)}(x'_0)} f_n^1(\theta)}{\sum_{n=1}^N \frac{C_n j^{n+1}}{h_n^{(2)}(x'_0)} f_n^1(0)} \right|$$

In Fig. 3.4.4, we compare radiation patterns predicted by the Kirchhoff-Huygen and modal expansion methods for  $\theta_1 = 50^\circ, 60^\circ$  and  $70^\circ$ ; the agreement is excellent. We have studied the convergence of the series and have found that for various observation angles, the pattern converges to within 1% when  $N = kR_0$ . A good approximation to the final pattern is also obtained with only about six terms in the series, especially for wide-flare-angle horns. It is also possible to use the above method to determine the near-field of corrugated horns as shown.

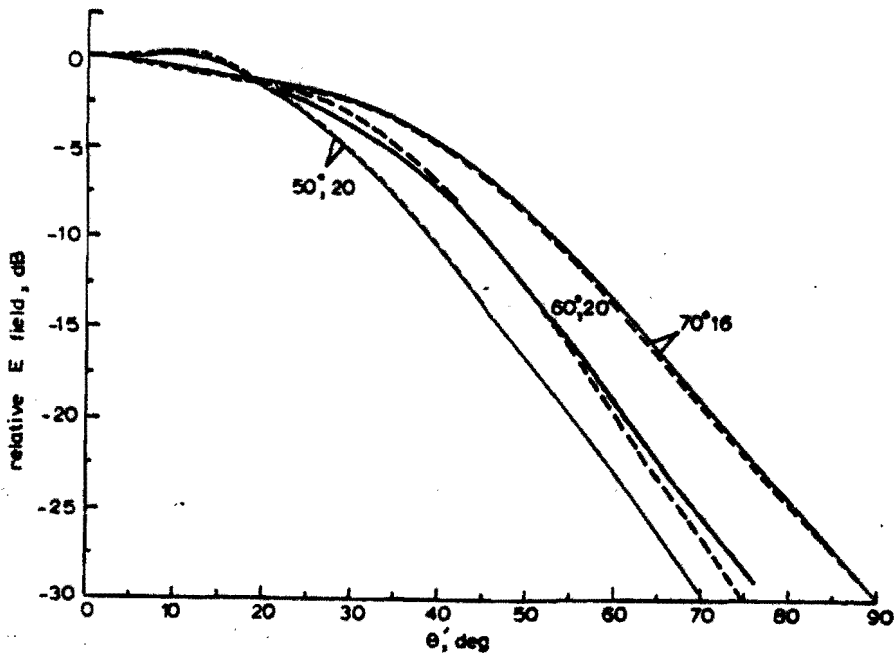


Fig. 3.4.4

*E plane radiation pattern for corrugated horn*

- modal expansion method
- Kirchhoff-Huygen method, parameters  $\theta_1, kR_0$

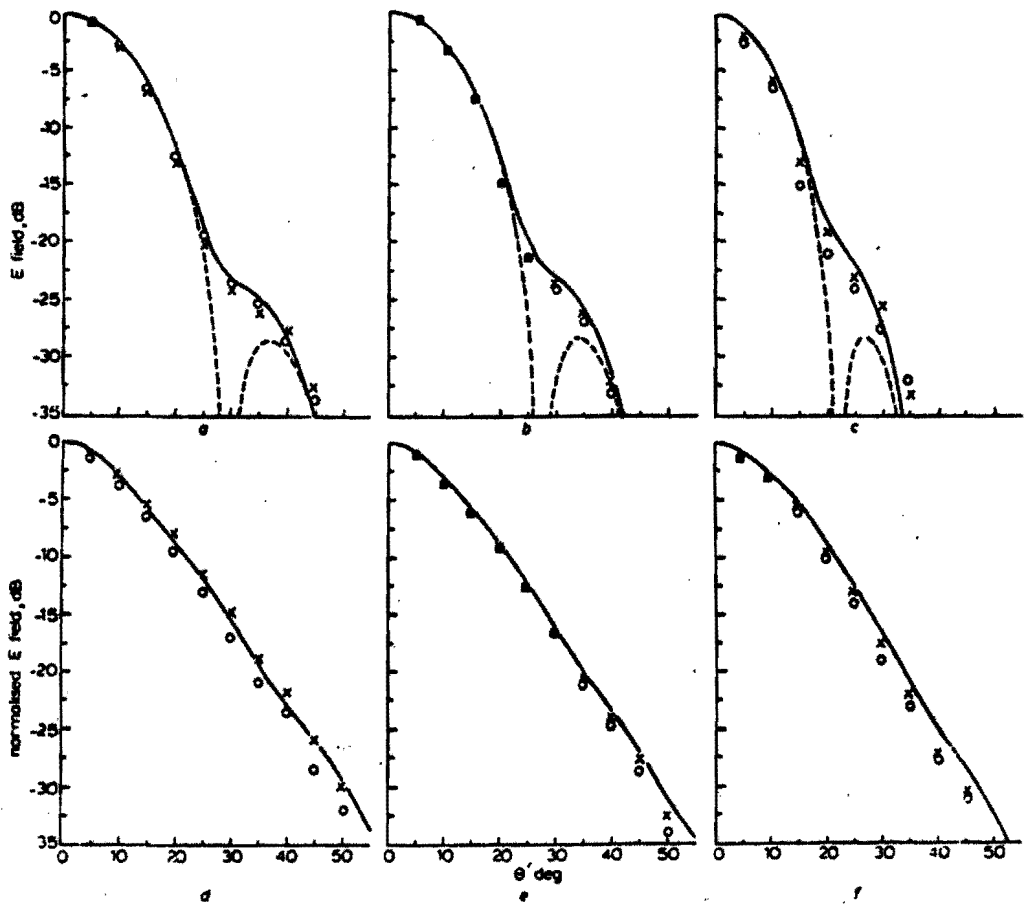


Fig. 3.4.5

*Theoretical and experimentally measured radiation patterns*

x H plane experimental points

o E plane experimental points

— theoretical average of E and H plane values obtained by spherical-mode analysis

----- obtained by cylindrical-mode analysis assuming constant phase over plane aperture

(a)-(c)  $\theta_1 = 12^\circ$

(a)  $F = 8.5$  GHz

(b)  $F = 9.0$  GHz

(c)  $F = 11.0$  GHz

(d)-(f)  $\theta_1 = 30^\circ$

(d)  $F = 8.5$  GHz

(e)  $F = 9.0$  GHz

(f)  $F = 11.0$  GHz

### 3.4.3.3 Modal Expansion Method For Cross-Polarisation

When  $\bar{\Lambda} \neq 1$ , neglecting constants,

$$E_{co} = \{ \frac{1}{2}(1+\bar{\Lambda})f_{v+}(\theta) + \frac{1}{2}(1-\bar{\Lambda})f_{v-}(\theta)\cos 2\phi \}$$

and

$$E_{xp} = \frac{1}{2}(1-\bar{\Lambda})f_{v-}(\theta)\sin 2\phi$$

Here we write,

$$\bar{\Lambda} = \frac{H_R}{E_R} y_0$$

$$f_{v\pm}(\theta) = \frac{dP_v^1(\cos\theta)}{d\theta} \pm \frac{P_v^1(\cos\theta)}{\sin\theta}$$

Figure 3.4.6 shows the normalised cross-polar aperture field in the diagonal plane corresponding to  $\phi = 45^\circ$  and with the semi flare-angle  $\theta$ , as parameter. In contrast with the copolar aperture field, the crosspolar field is a maximum at the horn boundary.

To predict the radiation pattern one may either use a Kirchoff-Huygens integration, or the spherical-wave expansion (SWEX) technique. SWEX has the advantage of mathematical simplicity and the near-field can be calculated as readily as the far-field. Interest in the near-field arises in certain measurement methods and in some types of Cassegrain antenna.

$$E_{co} = \frac{1}{2}(1+\bar{\Lambda})\sum_{n=1}^N C_{n+} f_{n+}(\theta)G(kR_0) + \frac{1}{2}(1-\bar{\Lambda})\sum_{n=1}^N C_{n-} f_{n-}(\theta)G(kR_0)\cos 2\phi$$

$$E_{xp} = \frac{1}{2}(1-\bar{\Lambda})\sum_{n=1}^N C_{n-} f_{n-}(\theta)G(kR_0)\sin 2\phi$$

$$C_{n\pm} = \frac{2n+1}{2n^2(n+1)^2} \int_0^{\theta_1} f_{v\pm} f_{n\pm} \sin\theta d\theta$$

$$G(kR_0) = \frac{j^{(n+1)}}{h_n^{(2)}(kR_0)}$$

Figure 3.4.7, a) and b), show for the  $HE_{11}$  mode, measured and predicted far-field copolar and crosspolar radiation patterns (the latter taken in the  $45^\circ$  plane) for two horn semi-flare-angles.

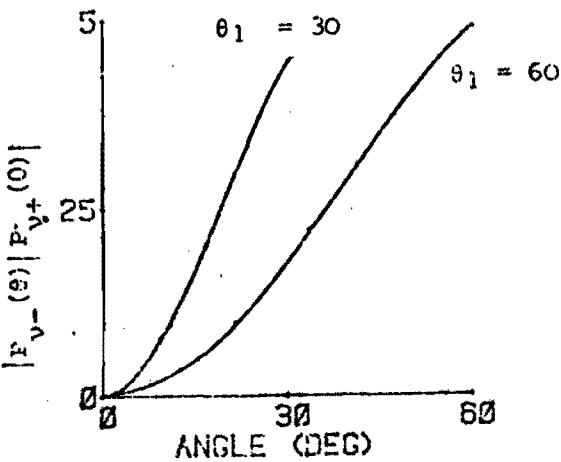


Fig. 3.4.6  
Cross-polar aperture field

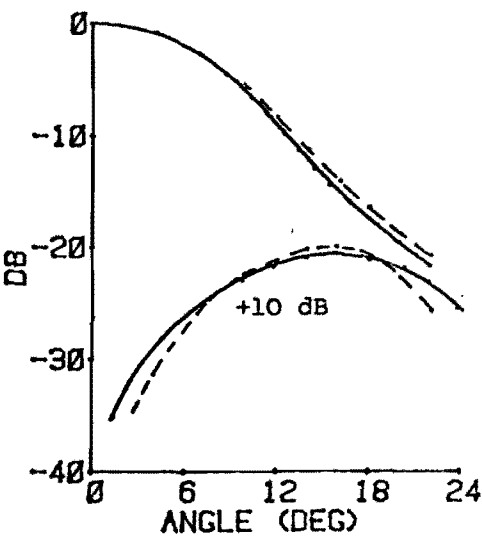


Fig. 3.4.7 (a)  
Measured —  
and predicted ---  
45° co and cross-polar patterns  
 $\theta_1 = 12^\circ$   $kR_0 = 77.4$



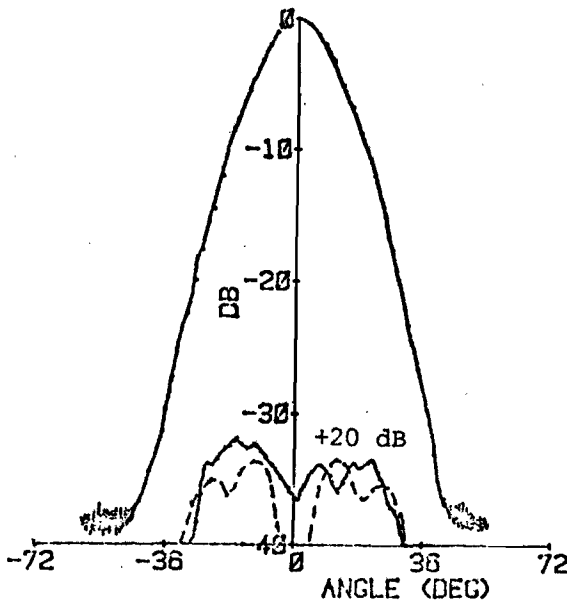


Fig. 3.4.7 (b)

$$\theta_1 = 30^\circ \quad kR_0 = 34$$

### 3.5 Excitation and Mode Conversion

Thus far we have considered only the propagation and radiation characteristics of individual modes. To complete our study we must consider in addition, the excitation of hybrid-modes at the entrance to the feed and mode conversion, if any, along the feed.

In respect of excitation, when both waveguides are cylindrical we are concerned with a discontinuity problem of the kind shown in the insert to Fig. 3.5.1. A transverse discontinuity in a closed structure can be readily solved using modal matching methods along lines described by Clarricoats and Slinn [12], Masterman and Clarricoats [13] among others. The basis for the technique relies on an expansion of the transverse-electric and transverse-magnetic fields in the common aperture of the two waveguides, leading on the application of orthogonality principles, to a set of infinite equations for the excitation coefficients. These can be reduced to finite matrix equations when the terms are truncated. They are readily solved numerically.

Clarricoats and Saha [14] were first to approach this problem for  $HE_{11}$  mode when a  $TE_{11}$  mode is incident in a smooth-wall circular waveguide. Later Cooper [15] considered a step discontinuity in a corrugated waveguide while much later Dragone [16] reconsidered the basic excitation problem and obtained a useful approximate result described below. In all of these cases, the surface-impedance model was used to represent the fields in the corrugated waveguide. This procedure is reasonable when the number of slots per wavelength is equal to or larger than five but the accuracy of the solution will deteriorate if the number is reduced significantly below that figure. An alternative procedure would be include space-harmonics to represent the field in the corrugated waveguide or to adopt the technique advanced by James [17]. He considers the practical case of a transition between the smooth-wall and uniform corrugated-waveguide in which the slot-depth varies between about  $\lambda/2$  and about  $\lambda/4$ , see Fig. 3.5.2. The discontinuity model for the corrugated waveguide comprises a change between successive circular waveguides with diameters equal to the inner and outer diameters of the corrugated waveguide. Matrices are established representing the standing-waves in these regions. Figure 3.5.1 due to Clarricoats and Saha compares with curve (i) of Figure 3.5.3 due to James and with Figure 3.5.4 due to Dragone (note that for parameters  $r_1/r_o = 0.5$  and  $r_1/r_h = 1.0$  the null in Figure 3.5.1 corresponds to  $\omega/\omega_c = 1$  in Figure 3.5.4). Dragone also shows that a very simple formula for the reflection coefficient  $\rho$  given below is very accurate

$$\rho = - \frac{\beta_1 - \beta_2}{\beta_1 + \beta_2}$$

where  $\beta_{1,2}$  are the propagation coefficients of the modes in the respective waveguides.

We turn now to the problem of mode conversion: this can occur both at the above discontinuity and along the feed if either the corrugation depth varies or the diameter increases as in a horn (or both). Dragone [16] and also Mahmoud and Clarricoats [18] have made a detailed study of this problem, the latter authors by extending the technique developed by Dragone [16] for narrow flare-angle horns. In a dominant mode horn, the most significant mode conversion effects are those which involve conversion from the  $HE_{11}$

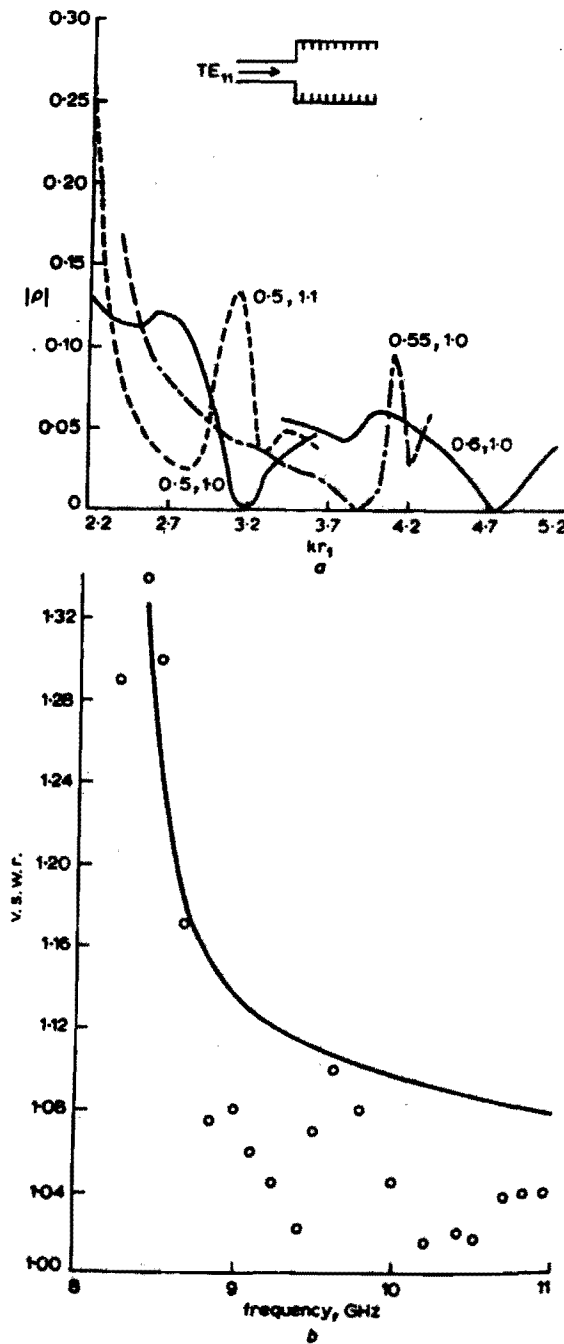


Fig. 3.5.1

- Reflection coefficient of TE<sub>11</sub> mode incident from a homogeneous circular waveguide on a junction with a corrugated circular waveguide. Parameters  $r_1/r_0$  and  $r_1/r_h$ .
- Experimental v.s.w.r. as a function of frequency measured at the throat of a narrow-flare-angle horn with  $\theta_1 = 12^\circ$  and theoretical curve for  $r_1/r_0 = 0.55$ ,  $r_1/r_h = 1.1$ .

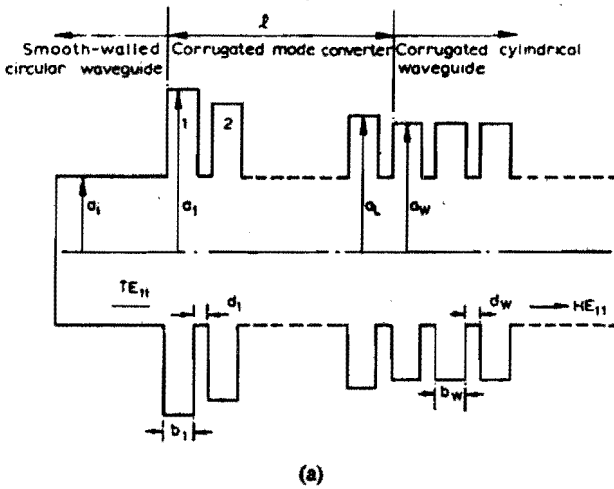


Fig. 3.5.2

Cross-sectional view of circular waveguides.

- (a) Corrugated mode converter section at the junction between a smooth-walled and corrugated waveguide.
- (b) Junction between two smooth-walled waveguides of differing radius.

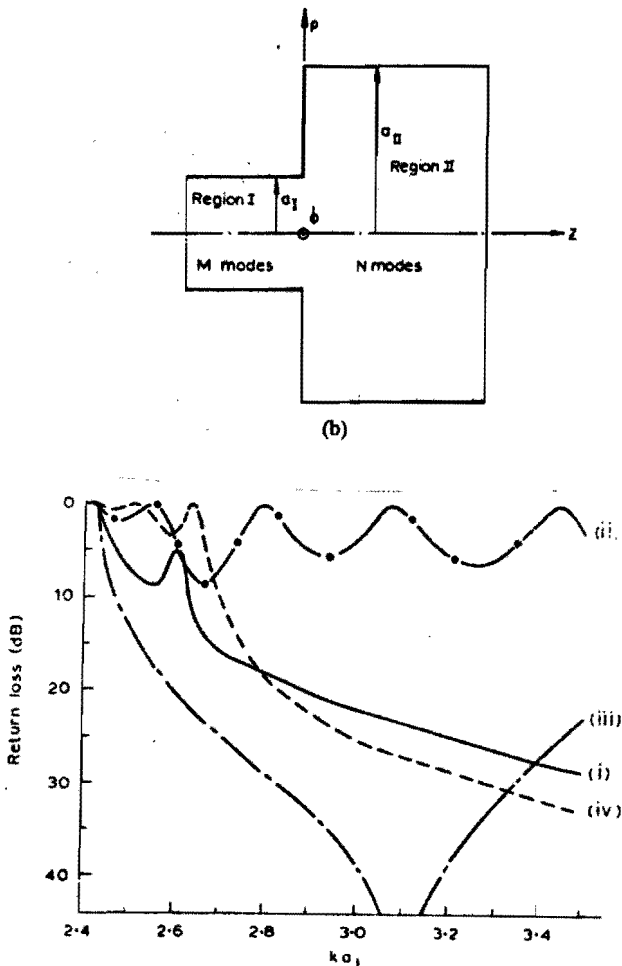


Fig. 3.5.3 Theoretical return-loss of a seven-slot corrugated waveguide

- (i) Return-loss without the converter section.
- (ii) Converter with slot depths increasing from zero.
- (iii) Converter with decreasing slot depths, beginning with  $\lambda_0/2$  at the input ( $f_0$  is the centre frequency where  $ka_1 = 2.9$ ).
- (iv) Converter with constant slot depth but with variable  $\delta$ .

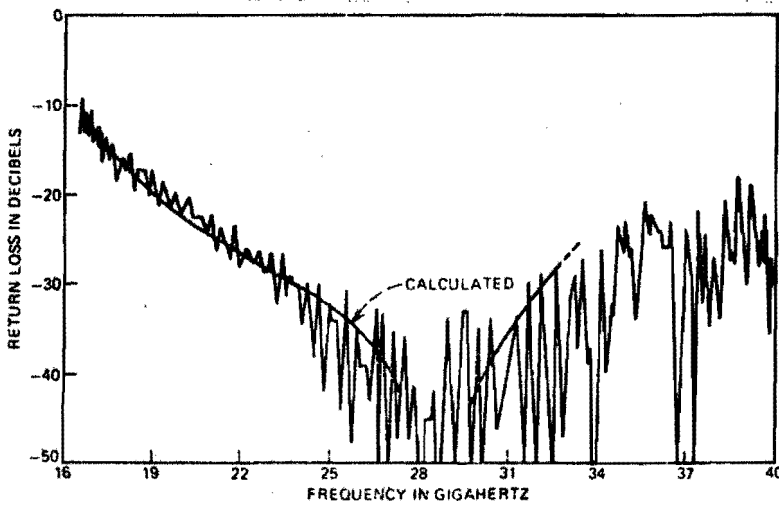


Fig. 3.5.4

Return-loss of  
corrugated horn with  
semi-flare-angle of  
 $4^\circ$  and aperture  
radius 3.14cm

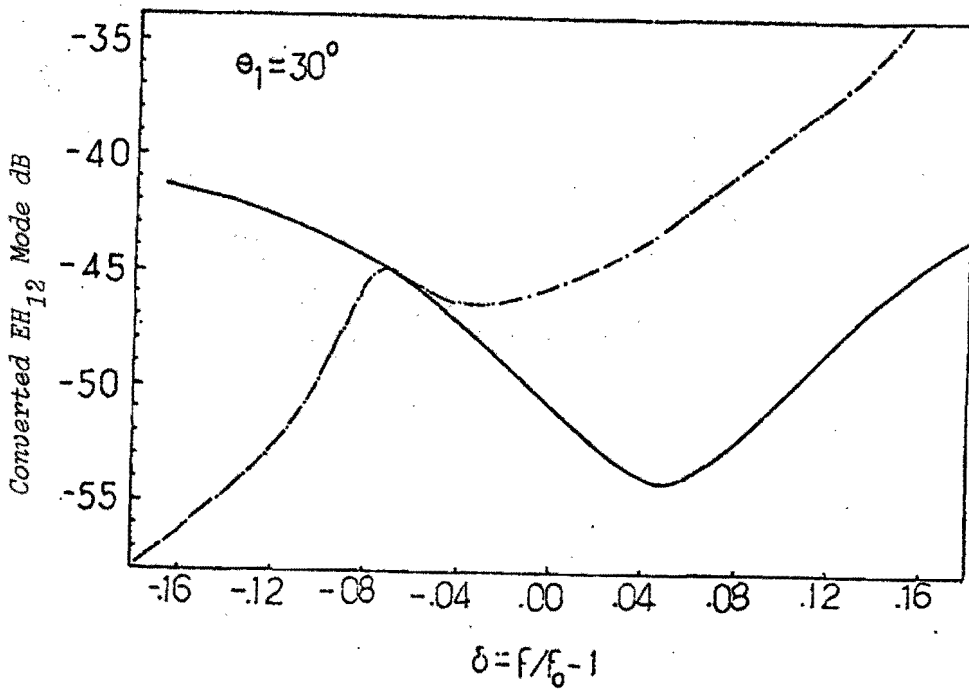


Fig. 3.5.5

$EH_{12}$  mode amplitude at the horn's mouth due to:

- (i) Mode generated at the throat (broken curve) and
- (ii) Mode converted along the horn.  $k_o a_{th} = 3$ ,  $k_o a_m = 15$ .

mode to the  $HE_{12}$  mode, since this latter mode is rich in cross-polar radiated field when the aperture conditions approximate balanced-hybrid.

By considering mode conversion in a small interval along the horn between  $R$  and  $R+dR$ , Mahmoud and Clarricoats [18] show that the differential change in the amplitude of the  $EH_{12}$  mode in a horn of semi-flare-angle  $\theta_1$  is given by

$$\frac{x_1 x_2 (\theta_1 \sin \theta_1)^{-\frac{1}{2}}}{x_2^2 - x_1^2 \frac{\theta_1}{\sin \theta_1}} d\bar{Y}$$

where  $d\bar{Y}$  is the change in the normalised surface-admittance. When the slot-depth is constant  $d\bar{Y}$  is nearly linearly proportional to  $1/kR_1$  which in turn is proportional to  $\sin \theta_1$ , assuming that the dimensions of the aperture are held constant as  $\theta_1$  changes. Figure 3.5.5 shows for a horn with  $\theta_1 = 30^\circ$ , how mode conversion along a horn with constant slot depth influences the radiated cross-polar level of the  $HE_{11}$  mode. The components of cross-polarisation due to mode conversion at the throat and the intrinsic  $HE_{11}$  crosspolar also contribute to the overall level.

### 3.6 Multimode Corrugated Feeds

The feeds considered above are designed to support one mode of propagation and a higher-order mode is present only as an undesirable feature. This situation contrasts with the multimode feed where the presence of the higher-order mode is an essential and desirable aspect of the design. Multimode feeds can be designed using smooth-wall waveguide but in general their features are similar to those of multimode corrugated feeds, with one exception. The exception is the so-called Potter horn where a hybrid field is synthesised by the excitation of a  $TE_{11}$  and  $TM_{11}$  mode in correct amplitude and phase. Such a feed emulates the  $HE_{11}$  mode of a corrugated feed, but over a limited bandwidth. Returning to multimode corrugated feeds per se, two principal applications exist, in one, higher-modes are present to improve efficiency; in another, they provide tracking information. An example of the first kind is the feed combining the  $HE_{11}$  and  $HE_{12}$  modes which was

developed as a prime-focus feed for the Parkes radio-telescope by Vu and others [19]. Another example in this class, is the feed combining  $HE_{11}$  and  $HE_{21}$  modes proposed by Rudge [8] to synthesise the focal-field of an off-set reflector antenna. In the second class lies the multimode feed shown in Figure 3.6.1 together with corresponding modal fields. The  $HE_{11}$  mode provides the signal channel while combinations of orthogonal  $HE_{21}$  modes with respectively  $H_{01}$  and  $E_{02}$  modes provide azimuth and elevation outputs. A feed of this kind has the advantage over a pure-mode equivalent, in that it affords polarisation purity and the concomitant opportunity to extract polarisation information in sum and difference channels.

The feed is operated at a frequency such that the normalised propagation coefficient of all three of the tracking modes are nearly degenerate and lie close to the condition  $\bar{\beta} = \bar{\lambda}$ .

General expressions for the fields are as follows.

$HE_{11}$  mode (sum channel)

$$E_x = -j \frac{a_{11}}{2} \frac{k}{K} \{ (\bar{\beta} + \bar{\lambda}) J_0(Kr) + (\bar{\lambda} - \bar{\beta}) J_2(Kr) \cos 2\phi \}$$

$$E_y = -j \frac{a_{11}}{2} \frac{k}{K} \{ (\bar{\lambda} - \bar{\beta}) J_2(Kr) \sin 2\phi \}$$

The form of the equation  $E_y$  shows that the aperture field becomes perfectly linearly polarised when  $\bar{\lambda} = \bar{\beta}$ . However other than for very large apertures, the condition for zero crosspolarisation of the radiated field occurs at a frequency slightly above that at which  $\bar{\lambda} = 1$ . This latter condition is referred to as balanced hybrid, and when it occurs the corrugation depth of a waveguide with  $kr_1 > 1$  is approximately  $\lambda/4$ .

$H_{01}$  mode (contributor to the azimuth-difference channel)

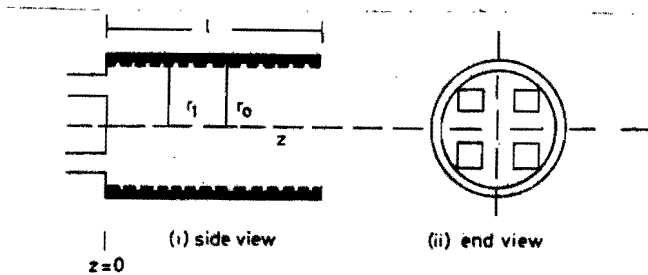
$$E_x = jnb_{01} \frac{k}{K} J_1(Kr) \sin \phi$$

$$E_y = -jnb_{01} \frac{k}{K} J_1(Kr) \cos \phi$$

$E_{02}$  mode (contributor to the elevation-difference channel)

$$E_x = ja_{02} \frac{k}{K} \bar{\beta} J_1(Kr) \cos \phi$$

$$E_y = ja_{02} \frac{k}{K} \bar{\beta} J_1(Kr) \sin \phi$$



schematic diagram of waveguide junction geometry

Channel	Aperture Distribution	Constituent modes
sum		$HE_{11}$
azimuthal difference		$H_{01}$ + $HE_{21}^*$
elevation difference		$E_{02}$ + $HE_{21}$

Fig. 3.6.1

Corrugated monopulse feed  
and monopulse mode patterns

$HE_{21}$  (contributor to the elevation-difference channel)

$HE_{21}^*$  (contributor to the azimuth-difference channel - Asterisk denotes orthogonal polarisation)

$$E_x = -j \frac{a_{21}}{2} \frac{k}{K} [(\bar{\beta} + \bar{\Lambda}) J_1(Kr) \cos \phi + (\bar{\Lambda} - \bar{\beta}) J_3(Kr) \cos 3\phi]$$

$y^*$



$$E_{y_{x^*}} = \pm j \frac{a_{21}}{2} \frac{k}{K} \{ (\bar{\beta} + \bar{\Lambda}) J_1(Kr) \sin \phi + (\bar{\Lambda} - \bar{\beta}) J_3(Kr) \sin 3\phi \}$$

In contrast with the  $HE_{11}$  mode, the equation above shows that for the  $HE_{21}$  mode, even if the term in  $(\bar{\Lambda} - \bar{\beta})$  is negligible, the field has equal copolar and crosspolar components. But, assuming mode degeneracy, a judicious choice of the ratio of coefficients  $a_{02}$  and  $a_{21}$  ensures, provided the fields are combined in-phase, that the crosspolar component of the total field vanishes. Then the linearly-polarised aperture field under nearly balanced-hybrid conditions generates an almost linear-polarised far field. Similar arguments apply for the  $H_{01}$  and  $HE_{21}^*$  modes.

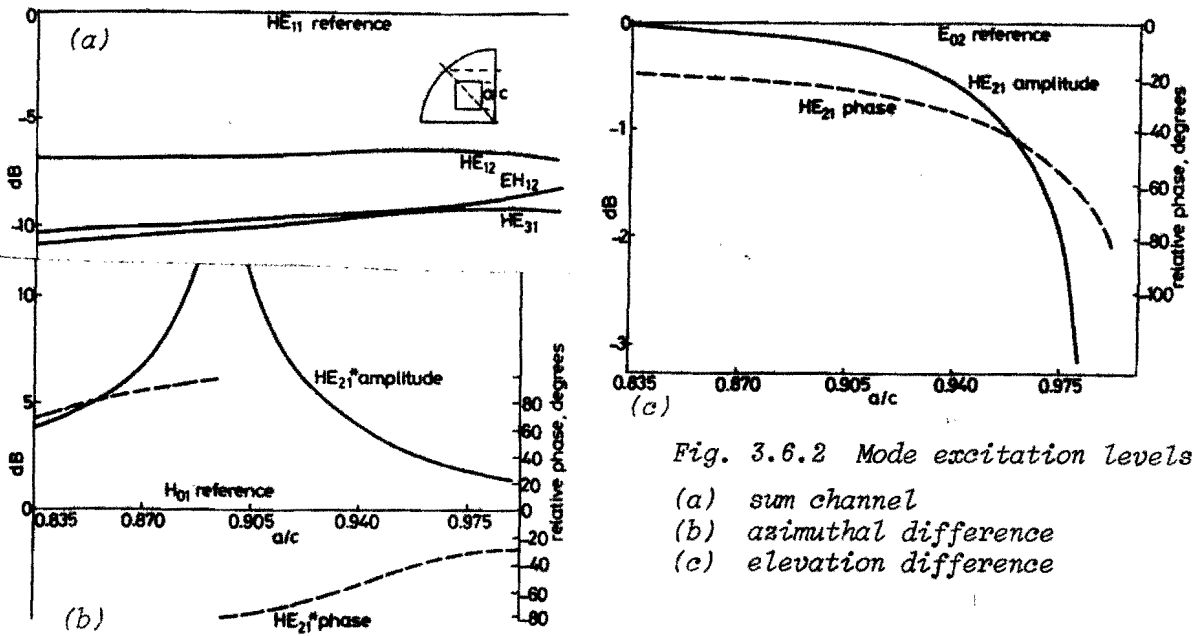


Fig. 3.6.2 Mode excitation levels

- (a) sum channel
- (b) azimuthal difference
- (c) elevation difference

In summary, the contributions to  $E_y$  from the  $H_{01}$ ,  $E_{02}$  and two types of  $HE_{21}$  modes cancel when the terms in  $(\bar{\Lambda} - \bar{\beta})$  are neglected, then the aperture fields of the difference channels have the form.

$$E_x = C_1 J_1(Kr) \cos \phi \text{ (elevation)}$$

$$E_x = C_2 J_1(Kr) \sin \phi \text{ (azimuth)}$$

As noted previously, any departure from the correct amplitude or phase of the combination will introduce corosspolarisation, as also will a significant departure from the condition that  $(\bar{\Lambda} - \bar{\beta})$  is negligible for the  $HE_{21}$  mode.

Clarricoats and Elliot [20] have made a detailed analysis of a feed of the kind shown in Figure 3.6.1 and have examined how the excitation coefficients depend on the size and location of the square input waveguides. Typical results are shown in Figure 3.6.2. From their parametric study they conclude that a cluster of square waveguides close to the centre of the feed is best to achieve appropriate excitation of all the modes, although they also demonstrate the need for a mode-selective phase-shifter in order to produce the correct phase characteristics in the feed aperture.

A similar multimode feed which just uses the  $HE_{11}$ ,  $HE_{21}$  and  $E_{02}$  modes has been developed by Watson, Dang and Ghosh [21]. In this feed the azimuth and elevation channels are extracted from a sum and difference of the latter mode pair. Their feed system was developed for use in a spacecraft where accurate alignment of the antenna with respect to a point on earth, is an essential requirement for efficient transmission.

### 3.7 Radiation Characteristics of Pure Mode Feeds

Feeds with smooth metallic walls can support both TE and TM modes. However, the simplest class are designed so that only the lowest order TE mode is excited. For feeds with circular and rectangular cross-section, their propagation and radiation characteristics are well documented; also appropriate expressions can be obtained as special cases of the hybrid-mode results of section 3.3. The radiation pattern of these simple feeds can be predicted using the Fourier Transform method and below are the Cartesian components of the radiated electric field for a number of feed types. The corresponding copolar and crosspolar fields can be obtained using the expressions given in section 3.3.

Rectangular Waveguide (Cross-section  $2a \times 2b$ ) with  $TE_{01}$  mode y-polarised

$$E_{yp} = E_0 \frac{\pi}{4} \left[ \frac{\cos ka \sin \theta \cos \phi}{1 - \frac{(2ka \sin \theta \cos \phi)^2}{\pi}} \right] \left[ \frac{\sin(kb \sin \theta) \sin \phi}{kb \sin \theta \sin \phi} \right]$$

$$E_{xp} = 0$$

Circular Waveguide (radius  $r_1$ ) with  $TE_{11}$  mode y-polarised

$$E_{yp} = \frac{2J_1(kr_1 \sin \theta)}{(kr_1 \sin \theta)} \sin^2 \phi + \cos \theta \frac{J'_1(kr_1 \sin \theta)}{1 - \frac{(kr_1 \sin \theta)^2}{(1.841)^2}} \cos^2 \phi$$

$$E_{xp} = \frac{1}{2}[f_1(\theta) - f_2(\theta)] \sin 2\phi$$

where  $f_1$  and  $f_2$  are the functions in the first and second terms of  $E_{yp}$ .

### Horns

For both rectangular and circular cross-section horns of narrow flare-angle, the radiation patterns can be evaluated numerically also using the Fourier Transform method only with the addition of a multiplicative phase-factor of the form  $\exp\{-\frac{j\mathbf{k}}{2}(\frac{x^2}{L_x} + \frac{y^2}{L_y})\}$  or  $\exp\{-\frac{jkr^2}{2R_0}\}$  respectively, where  $L_x$ ,  $L_y$  and  $R_0$  are the appropriate horn slant-lengths.

### Polygonal Feeds

The radiated fields of rectangular and circular cross-section horns and waveguides have crosspolar components which are unacceptably high for many satellite applications. However, on examining the expression for  $E_{cp}$  in section 3.3, we see that in the  $45^\circ$  plane where crosspolar radiation is generally a maximum, and for angles not too close to boresight,  $E_{cp}$  becomes zero if

$$\frac{E_{yp}}{E_{xp}} = \tan^2 \frac{\theta}{2}$$

To achieve this condition in the radiated field components  $E_{yp}$  and  $E_{xp}$ , both x and y components of field must be present in the radiating aperture. Thus, the optimum aperture electric field must have curved field lines and recognition of the need for field curvature led Rudge et al [22] to propose the use of polygonal horns as low crosspolar feed elements. The aperture field characteristics can be determined by numerical methods such as the Finite-Element technique and the radiation field by means of the Fourier Transform.

The amount of field curvature in a dominant mode feed depends both on the electrical size and shape of the feed. Figure 3.7.1 shows an 8-sided feed horn investigated by the above authors while Figure 3.7.2 shows the cross-polar performance. Very low crosspolarisation over a reasonable band occurs when the ratio  $\frac{a}{b} = 0.4$  and  $\frac{d}{\lambda} = 1.25$ . Because of the feed asymmetry the horn is unsuitable for dual-polarisation applications and for this reason the hexagonal feed with  $\frac{a}{b} = 0.5$  is generally preferred. Such horns are physically compact and are ideally suited as elements for an array feed where they permit closer packing than conical elements. The latter have been used for

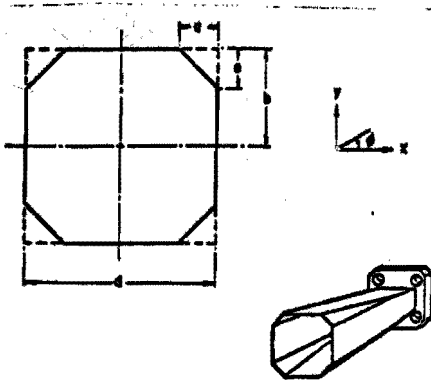


Fig. 3.7.1  
8-sided primary-feed horn.  
Dimensions in wavelengths ( $\lambda$ ).

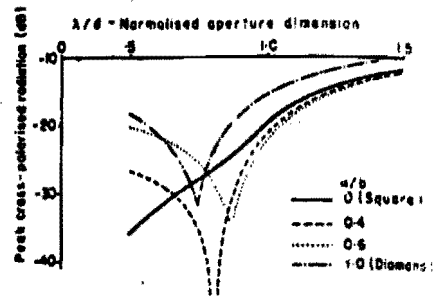


Fig. 3.7.2  
Predicted peak far-field cross-polar level in diagonal plane of 8-sided horn.

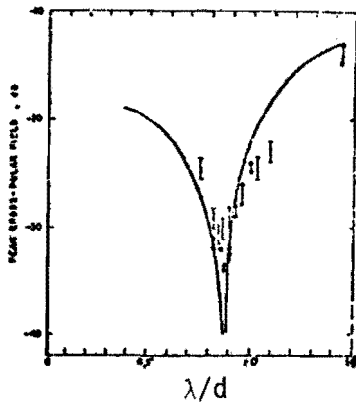


Fig. 3.7.3  
Peak cross-polar radiation from fundamental conical horns of diameter  $d$  wavelengths.

arrays and as Figure 3.7.3 due to Adatia et al [23] shows, they too exhibit low cross-polarisation for about the same aperture dimensions.

### 3.8 Array Feeds

As explained in 3.1 array-feeds are essential for advanced spacecraft antennas where either sophisticated contour-beams or multiple-beams are

required. Exceptionally high performance is possible when more than one element contributes to a given beam although the problem of array excitation can be formidable.

The elementary theory of arrays separates the array-factor and the element-factor. However, mutual-coupling causes the element factor to change with element spacing. Bird [24] has given detailed consideration to the multi-element circular waveguide array as shown in Figure 3.7.4. He uses a method originally proposed by Hockham in order to determine the effects of mutual coupling and a brief resume of his analysis follows.

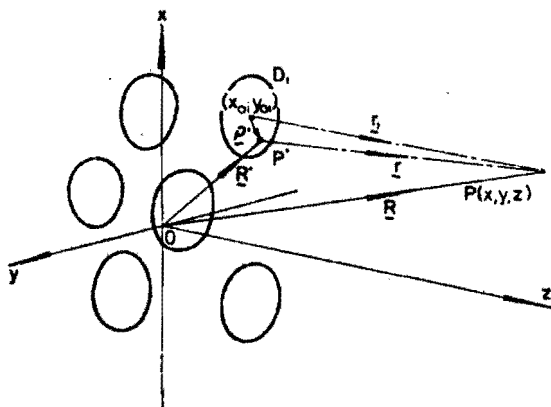
In Figure 3.7.4 the waveguides are assumed to be identical and in general they may be dielectric loaded and arbitrarily located in the ground plane.

The magnetic-field components at a distance  $R$  from the origin in a plane transverse to the  $z$ -direction are related to the aperture electric field through the identity

$$H_t(R) = \frac{j}{2\pi\omega\mu_0} (k_0^2 + \nabla_t \cdot \nabla_t) \cdot \hat{z} \times \int_{-\infty}^{\infty} \int_{-\infty}^{\infty} dS' E_t(K', 0) G(|R - R'|)$$

Fig 3.7.4

Planar array with the radiation field point  $P$  and the source point  $P'$  in the waveguide aperture.



where  $|R - R'| = \sqrt{(x - x')^2 + (y - y')^2 + z^2}$

$G(R) = \exp(-jk_0 R)/R$  is the free-space Green's function and  $\nabla_t$  is the transverse gradient operator.  $k_0 = \omega/c$  is the wave propagation constant in free-space. As  $E_t$  vanishes on the ground plane, the infinite integral

reduces to a sum of integrals over the N waveguide apertures  $D_i$  ( $i = 1, 2, \dots, N$ ).

In waveguide i the tangential fields are given approximately by the M mode expansions

$$H_t^{(i)} = \sum_{m=1}^M [a_m^{(i)} e^{-j\gamma_m z} - b_m^{(i)} e^{j\gamma_m z}] h_m$$

$$E_t^{(i)} = \sum_{m=1}^M Z_m [a_m^{(i)} e^{-j\gamma_m z} + b_m^{(i)} e^{j\gamma_m z}] h_m \times \hat{z}$$

where  $h_m$ , the transverse magnetic field of mode m and  $Z_m$  is the wave impedance of mode m which is given by

$$Z_m = \zeta_0 \begin{cases} k_0 / \gamma_m & \text{TE modes} \\ \gamma_m / k_0 \epsilon_r & \text{TM modes} \end{cases}$$

$\zeta_0$  is the intrinsic wave impedance of free-space and  $\epsilon_r$  is the dielectric constant of the waveguide filling.  $\gamma_m = \beta_m - j\alpha_m$  is the propagation constant of mode m. Mode m is the mode with the mth highest transverse wavenumber  $\lambda_m$ , or eigenvalue, when the wavenumbers of the TE and TM modes are arranged in order of ascending magnitude.

When the field point lies on the plane  $z = 0$ , the equation in Figure 3.7.4 becomes an integral equation in the field components tangential to the array aperture. This equation is a constraint upon all possible trial solutions to the aperture fields. One possible set of trial solutions are the fields inside the waveguides. Although these do not satisfy the edge condition at the mouth of the waveguides they are suitable trial solutions in many applications.

By the Galerkin procedure of projecting the vectors  $h_m$  onto the resulting equation throughout the domain  $D_i$ , a relation between  $A_m^{(i)}$  and  $B_m^{(i)}$  is obtained as  $B_m^{(i)} = C_{mn}^{(ij)} A_n^{(j)}$  where

$$A_m^{(i)} = a_m^{(i)} + b_m^{(i)} \quad \text{and} \quad B_m^{(i)} = a_m^{(i)} - b_m^{(i)}$$

and

$$C_{mn}^{(ij)} = \frac{j}{2\pi\omega\mu_0} \frac{Z_n}{N_m} \left[ \iint_{D_i} dS h_m \cdot (k_0^2 + \nabla_t^2) \cdot \iint_{D_j} dS' h_n' (G(|R-R'|)) \right]$$

This gives the coupling between mode m in waveguide i and mode n in waveguide j.

The operator  $\nabla_t$  acts only on the unprimed co-ordinates inside the integral over  $D_j$ . By means of Green's theorem it can be shown that the second term involving  $\nabla_t$  originates from an axially directed component. This enables the above equation to be more conveniently written as

$$C_{mn}^{(ij)} = \frac{j\omega\epsilon_0}{2\pi} \frac{Z_n}{N_m} \left[ \iint_{D_i} dS \psi_m \iint_{D_j} dS' \psi_n' G(|R-R'|) \right]$$

where the vector  $\psi_m$  is defined by

$$\psi_m = h_m + \frac{\gamma_m}{k_0} h_{zm} \hat{z}$$

$h_{zm}$  is the longitudinal magnetic field component of mode m.

Everywhere in the plane  $z = 0$  the Green's function can be represented by a contour integral in the complex frequency plane  $w$ . That is

$$G(|R-R'|) = G(|\rho-\rho_j|) = -jk_0 \sum_{s=0}^{\infty} \epsilon_{0s} \cos[s(\phi-\phi_j)] \int_0^{\infty} \frac{w J_s(k_0 \rho w) J_s(k_0 \rho_j w)}{\sqrt{1-w^2}} dw$$

where  $\rho$  and  $\phi$  are the co-ordinates of P relative to the centre of waveguide j. By means of the equation it is possible to complete all the integrals over the apertures. However, the contour integral in the  $w$ -plane remains and must be evaluated numerically. When the apertures are separate, the Green's function can be expanded asymptotically in terms of the separation distance and, therefore, contour integrals are not required.

Bird [24] gives numerical results for separated apertures which are valid provided the separation is large compared to the waveguide diameter and

provided the neglect of higher modes in the coupled waveguides is valid. Recently Tun and Clarricoats [25] have removed these restrictions in the case of a 7-element cluster. Prior to this theoretical work, experimental measurements were conducted by Adata, Claydon and Brain [26] with both conical and hexagonal elements in a 7-element cluster.

In contoured beam or multiple beam applications the reflector intercepts the element pattern of the array at the 3-4 dB level of the copolar radiation. Since dual-polarised operation is mandatory it is the crosspolar level within the corresponding angular domain which is of interest. Figures 3.7.5 a) and b) show experimental patterns [26] for two orientations of the  $TE_{11}$  mode electric vector in the conical horn aperture. The copolar plots clearly show distortion which Tun and Clarricoats [25] have found to be associated with the excitation of the  $TE_{21}$  mode in the elements of the array. This also explains the high level of crosspolarisation especially for vertical polarisation. The experimental work also showed increasing distortion with increasing frequency again attributable to the higher level of  $TE_{21}$  mode excitation. In practice, the array factor significantly reduces the undesirably high level of crosspolarisation but the importance of higher mode excitation in array feeds is apparent.

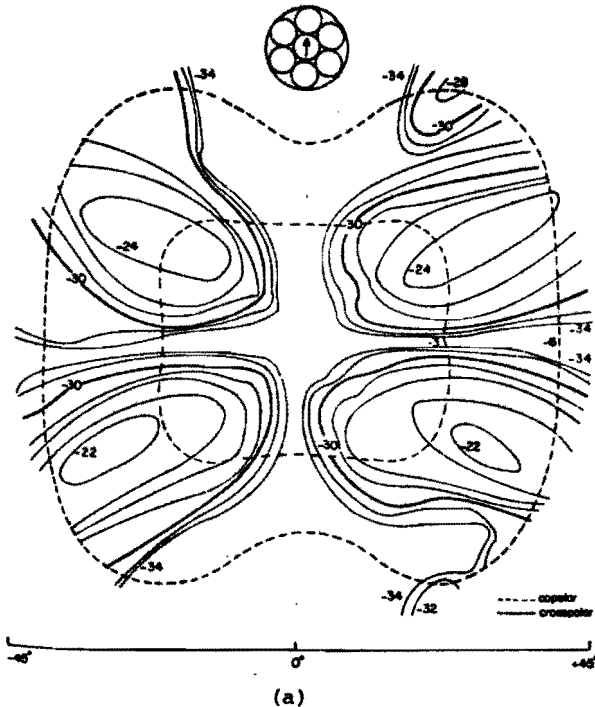


Fig. 3.7.5 (a)  
Linearly polarised radiation  
fields from immersed conical  
element.

Vertical polarisation



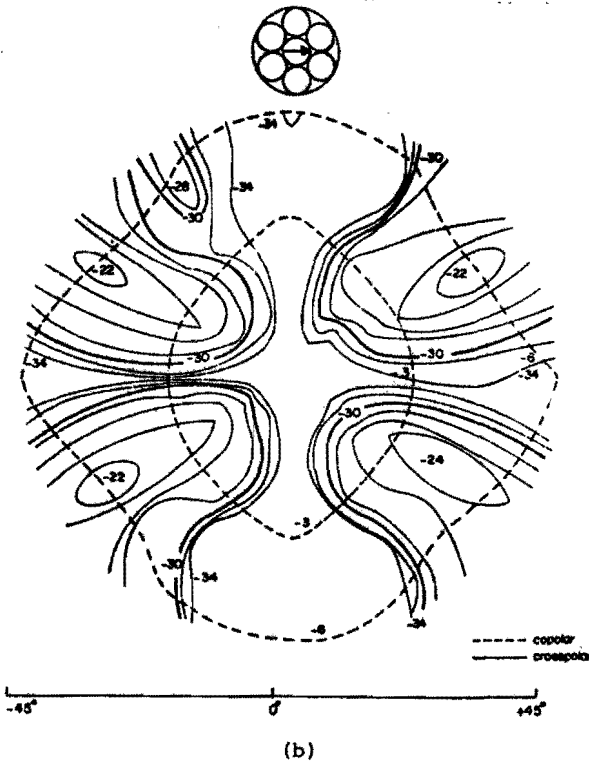


Fig. 3.7.5 (b)

Linearly polarised radiation fields from immersed conical element.

Horizontal polarisation

### 3.9 Surface-Wave Feeds

In situations where a number of high gain feeds are required in a close-packed array, the surface-wave feed element commends consideration. Several types of surface-wave element have been studied including the dielectric rod- and the disc-on-rod-antenna. As dielectric materials are not preferred for spacecraft applications we confine attention here to the disc-on-rod structure. Figure 3.9.1 shows the prototype where the region of width  $l$  may in general be dielectric filled although in the present case the relative permittivity of the dielectric is assumed to be unity; in the launcher region the disc-on-rod is surrounded by a perfectly conducting circular waveguide. In the radiating region the disc-on-rod structure is unshielded.

As with the analysis of the corrugated waveguide, the radiation properties are obtained after first solving the characteristic equation and obtaining the transverse aperture field. Because the structure is periodic the field must be represented in terms of space-harmonics leading to the following

characteristic equation for the normalised propagation coefficient  $\bar{\beta}_N$  of the Nth space-harmonic of the nth azimuthally dependent mode given by

$$\frac{S_n(x_1, x_2)}{x_1^2} = \frac{b}{d} \sum_{N=-\infty}^{N=+\infty} \left\{ \frac{S_n(Y_{N1}, Y_{N0})}{Y_{N1}^2} - \frac{(n\bar{\beta}_N)^2}{Y_{N1}^2 R_n(Y_{N1}, Y_{N0})} \right\} \left( \frac{\sin \Delta}{\Delta} \right)^2$$

where  $Y_N = k(\bar{\beta}_N^2 - 1)^{\frac{1}{2}} r_1$        $\bar{\beta}_N = \beta_0 + \frac{2\pi N}{d}$        $\Delta = \frac{\beta_N b}{2}$

Other functions have been defined previously. Figure 3.9.2 due to Olver and Dubrovka [27], shows  $1/\bar{\beta}_0 = C/V$  as a function of normalised wavelength for the  $HE_{11}$  mode. Comparison with experimental results (curve A) shows the need to include the first pair of space-harmonics in addition to the fundamental (curve C), in order to obtain results valuable in design. Curve B is the result obtained when space-harmonics are not included.

When the shield is removed to infinity the S and R functions in the characteristic-equation become identical and the bracketed term becomes

$$\left\{ \frac{M_n(y)}{y^2} - \frac{(n\bar{\beta}_N)^2}{y^2 M_n(y)} \right\} \quad \text{where} \quad M_n(y) = y \frac{K'_n(y)}{K_n(y)}$$

The transverse aperture field of the  $HE_{11}$  mode is given by

$$\underline{E}_T = A \{ K_0(y) \underline{i}_x - \frac{\bar{\Lambda} - \bar{\beta}}{\bar{\Lambda} + \bar{\beta}} K_2(y) [\cos 2\phi \underline{i}_x + \sin 2\phi \underline{i}_y] \}$$

Where  $K_0(y)$  and  $K_2(y)$  are Bessel functions of the third kind and of order zero and two.

The radiation pattern of the disc-on-rod antenna can be obtained by taking the Fourier Transform of the aperture field. The  $\phi$ -independent radiated field can be readily obtained from the Hankel Transform of  $K_0(y)$  if the integration interval over  $r$  is taken to lie between 0 and  $\infty$ . Then,

$$E_{xp} \approx \frac{1}{y_1^2 + (kr_1 \sin \theta)^2}$$

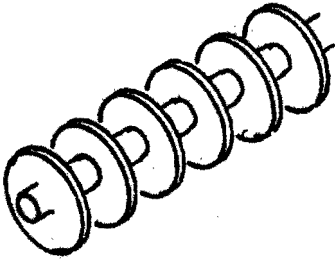


Fig. 3.9.1

Open corrugated waveguide

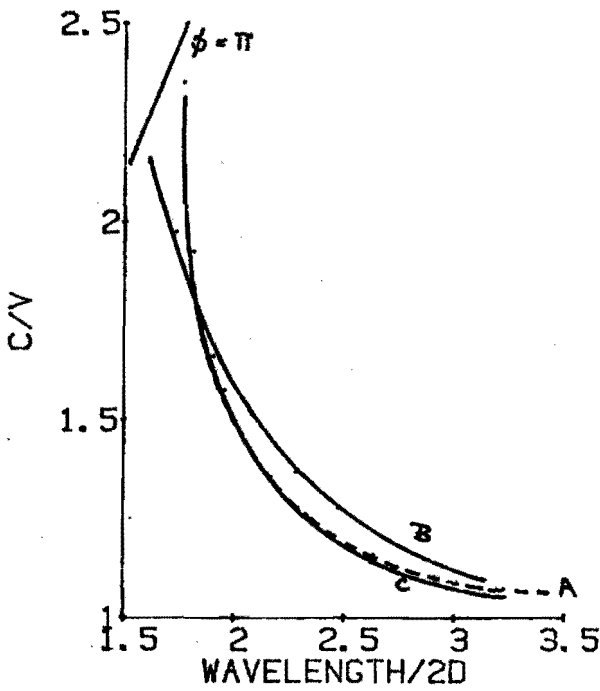
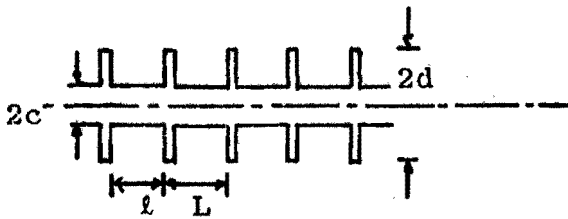


Fig. 3.9.2

Measured and computed  
propagation characteristics

In practise, the truncation of the aperture field at  $r = r_1$  will modify the above result and furthermore direct radiation from the launcher will add to the complexity of the radiation pattern.

Inspection of the equation for  $E_T$  once again shows that cross-polarisation vanishes if  $\bar{\alpha} = \bar{\beta}$ , a condition which occurs when  $S_n(x_1, x_2) = 0$ .

### 3.10 References

- 1) Rudge, A., Milne, K., Olver, A.D., Knight, P. (Editors). "The Handbook of Antenna Design: Chapter 4". To be published in 1982 by Peter Perigrinus Ltd (IEE).
- 2) Clarricoats, P.J.B. and Olver, A.D., "Theory and Design of Corrugated Feeds". To be published by Peter Perigrinus Ltd in 1983.
- 3) Clarricoats, P.J.B., "Improved Feed Systems for Microwave Antennas", Proceedings, 4th European Microwave Conference, 1974, pp153-162.
- 4) Minnett, H.C. and MacThomas, B., "Fields in the image space of symmetrical focussing reflectors", Proceedings IEE, 115, 10 October 1968, p1419.
- 5) MacThomas, B., Minnett, H.C. and Vu, T.B., "Fields in the focal region of a spherical reflector", IEE Trans. 1969, AP-17, p229.
- 6) Phillips, C.J.E. and Clarricoats, P.J.B., "Optimum design of a - Gregorian corrected spherical reflector antenna", Proc. IEE, April, 1970.
- 7) Bem, D.J., "Electric Field Distribution in the Focal Region of an Off-set Paraboloid", Proc. IEE, 116, 1974, pp579-584.
- 8) Rudge, A.W., Adatia, N.A., "New Class of Primary-Feed Antennas for use with Off-Set Parabolic Reflector Antennas", Electronics Letters, Vol. 11, 1975, pp597-599.
- 9) Rumsey, V.H., "Horn antennas with uniform power patterns around their axes", IEEE Trans., 1966, AP-14, pp656-658.
- 10) Clarricoats, P.J.B., Olver, A.D. and CHONG, S.L., "Attenuation in corrugated circular waveguides - Part I: Theory; Part II: Experiment", Proc. IEE, Vol. 122, No. 11, November 1975, pp1173-1186.

- 11) Silver, S., "Microwave Antenna Theory and Design", MIT Radiation Lab. Series 12, McGraw Hill Book Co., 1949.
- 12) Clarricoats, P.J.B. and Slinn, K.R., "Numerical solution of waveguide-discontinuity problems", Proc. IEE, 1967, 114, (7), pp878-886.
- 13) Masterman, P.H. and Clarricoats, P.J.B., "Computer field-matching solution of waveguide transverse discontinuities", *ibid.*, 1977, 118, (1), pp51-63.
- 14) Clarricoats, P.J.B., Saha, P.K., "Propagation and Radiation Behaviour of Corrugated Feeds", Parts 1 and 2, Proc. IEE, Vol. 118, 1971, pp1167-1186.
- 15) Cooper, D.N., "Complex propagation coefficients and the step discontinuity in corrugated cylindrical waveguide", Electronics Letters, 1971, 7, pp135-136.
- 16) Dragone, C., "Reflection Transmission and Mode Conversion in a Corrugated Feed", Bell System Technical Journal, Vol. 56, 1977, pp835-868.
- 17) James, G.L., "Analysis and Design of  $TE_{11}$ -to- $HE_{11}$  Corrugated Cylindrical Waveguide Mode Convertors", IEEE Trans. MTT-29, October 1981, pp1059-1065.
- 18) Mahmoud, S.F. and Clarricoats, P.J.B., "Radiation from Wide Flare-Angle Corrugated Conical Horns", IEE Proc. Part H, Microwaves, Optics and Antennas. To be published.
- 19) Vu, T.B. and VU, Q.H., "Optimum feed for large radiotelescopes: experimental results", Electronics Letters, 1970, 6, pp159-160.
- 20) Clarricoats, P.J.B. and Elliot, R.D., "Multimode corrugated Waveguide Feed for Monopulse Radar", IEE Proc., Vol. 128, Part H, Microwaves, Optics and Antennas, April 1981, pp102-110.
- 21) Watson, B.K., Dang, N.D. and Ghosh, S., "A Mode Extraction Network for RF Sensing in Satellite Reflector Antenna", IEE Conference Publication 195, 1981, pp323-327.
- 22) Rudge, A.W., Philippou, G.Y., and Williams, N., "Low Cross-Polar Waveguide Horns for Multiple-Feed Reflector Antennas", Proc. International Conference on Antennas and Propagation, 1978, IEE Conference Publication No. 169, pp360-363.
- 23) Adatia, N.A., Balling, P., Claydon, B., Ingvarson, P. and Roederer, A.,

- "A European Contoured Beam Reflector Antenna Development", Proc. 10th European Microwave Conference, 1980, pp95-99.
- 24) Bird, T.S., "Mode Coupling in a Planar Circular Waveguide Array", Proc. IEE Part H, 1979, pp172-180.
  - 25) Tun, S.M. and Clarricoats, P.J.B., "Radiation Patterns of Circular Horn Arrays". To be published.
  - 26) Adata, N.A., Claydon, B. and Brain, D., "Primary-Feed Elements for Multiple and Contoured Beam Satellite Antennas", IEE Conference Publication No. 195, 1981, pp98-103.
  - 27) Olver, A.D. and Dubrovka, F.F., "Propagation Characteristics of Open Cylindrical Corrugated Waveguides". To be published.

#### 4. Design Aspects of Commercial Satellite Antennas

by K.C. Lang and F.A. Taormina

##### 4.1. Historical background

Worldwide communications via commercial satellites was initiated in 1965 with the successful launch of the spin stabilized Early Bird (Intelsat I) satellite into synchronous orbit. Its high gain antenna consisted of an array of colinear dipoles providing a toroidal beam for earth coverage. Its capacity was 240 two-way telephone circuits.

In 1967 the first Intelsat II satellite was launched. Increased communications capacity over the Early Bird was achieved with additional spacecraft power, coupled with a directive beam from an electronically despun phased array. Each Intelsat II satellite provided 240 two-way telephone circuits and two-way television capability.

The Intelsat III series was launched in 1968 through 1969, each satellite providing 1200 two-way telephone circuits or four television channels. The mechanically despun antenna consisted of a horn and reflecting plate to provide an earth coverage beam.

The weights of these Intelsat series satellites increased progressively: 85 pounds for Intelsat I, 192 pounds for Intelsat II, and 322 pounds for Intelsat III. The next generation, Intelsat IV, was a giant by comparison. Launch weight swelled to 3058 pounds and communications capacity increased to 5000 two-way telephone circuits, 12 simultaneous color television channels, or any combination of transmissions to include telegraphy, data, and facsimile. The antenna system consisted of four earth coverage horns, two front fed reflectors (50 inches in diameter) providing spot beam coverages, and two bicones for telemetry and command. The first of this series was launched in 1970.

Increasing traffic of worldwide satellite communications created a demand for satellites with even higher communication capacity. Almost doubling the Intelsat IV capacity, the current Intelsat IVA satellite reuses the

available 500 MHz spectrum at the 6/4 GHz frequency bands. Each antenna provides an east and west hemispheric coverage shaped beams which are spatially isolated to allow frequency reuse. The first of the Intelsat IVA series was launched in September 1975, weighing 3335 pounds.

The world's first domestic satellite communications system using satellites in synchronous orbit was the Telesat (Anik A) series of Canada. Launched in 1972 with a weight of 1242 pounds, it has a communications capacity of 5760 telephone circuits. The first domestic synchronous orbit satellite of the United States is the Westar series, owned and operated by Western Union. Launched in 1975, it is a modified version of the Telesat satellite with the antenna beams reshaped for coverage of the continental United States (CONUS), Alaska, and Hawaii. The third domestic satellite system, Palapa A, for the Indonesian national was also a derivative of Telesat design with the antenna beam reshaped to provide coverage over Indonesia, Thailand, Malaysia, Singapore, and Phillipines and was launched in 1976.

The first domestic communication satellite system that has design techniques developed for beam shaping on the antenna, the Comstar series, utilized frequency reuse for increased communication capacity. This satellite reuses the frequency band via independent orthogonally polarized beams which are shaped for efficient illumination of continental United States, Alaska, Hawaii, and Puerto Rico. Launched in 1976, this satellite weighs 3255 pounds and has a communications capacity of 28,800 telephone circuits. The RCA Satcom satellite is similar to Comstar I in communications capacity. It uses elliptically shaped beams to provide coverage over CONUS and Alaska.

From the antenna technology viewpoint, the key features of commercial communication satellite antennas lie in (1) beam shaping for efficient illumination of designated coverage area, as demonstrated by the Telstar, Westar, and Palapa antenna designs and in (2) frequency reuse through spatial isolation or polarization diversity, as demonstrated by the Intelsat IVA, Comstar, and RCA Satcom antenna designs. Enhancement of these features helps to increase the communications capacity, and is demonstrated by the Intelsat V antenna design which provides almost a four-time increase in communications capacity over Intelsat IV through frequency reuse via the



spatial isolation technique demonstrated by Intelsat IVA and frequency reuse via polarization diversity. The first Intelsat V spacecraft was launched in 1981. Detailed discussion of the Intelsat V antenna design can be found in a paper by Han, et al.[1].

To date the most advanced commercial communication satellite antenna design is represented by the Intelsat VI antenna system being developed by Hughes Aircraft Company. It will provide a six-fold frequency reuse via two spatially isolated hemispheric beams and spatially isolated spot beams within each hemispheric beam, plus polarization between spot beams between the hemispheric beam. Each Intelsat VI will weigh 4000 pounds and will be able to carry 33,000 two-way telephone circuits and four television channels. The first Intelsat VI will be launched in 1986.

The following subsections discuss (1) the general design aspects of commercial communication satellite antennas; (2) the linearly polarized Telstar/Westar, Comstar, and Satellite Business Systems (SBS) antenna designs; and (3) the circularly polarized Intelsat IVA antenna design which partially serves as the foundation for the Intelsat VI antenna design. The SBS antenna, developed by Hughes Aircraft Company, is included because it has a unique design feature, namely, the use of an offset shared aperture dual-grid reflector.

#### 4.2. General design considerations

In addition to the RF requirements of coverage gain, gain slope, polarization, and isolation, the flight design of any spacecraft antenna must also address mechanical and environmental considerations, such as launch vehicle shroud envelope, solar wind transparency, and space environment survivability. In addition, all space antenna designs must be lightweight and able to withstand vibrational loads during launch. Although there is a broad class of high gain antennas such as reflectors, phased arrays, and lens antennas, reflector antennas are mostly used for communication satellites because of their advantage in weight, fabrication ease, and cost.

The communication satellite antenna design starts with the layout of the satellite body within the launch vehicle shroud. After determining the volume available for the antennas, the antenna engineer is challenged to utilize this volume efficiently. The shroud volume limitation is illustrated in Fig. 4.1. For a spin-stabilized satellite, the aperture area available for a nondeployable antenna is limited by the shroud diameter and height. For a body-stabilized satellite, the reflectors of a large antenna system must be deployed in order to stay within the shroud envelope.

Most future commercial communication satellite designs will be required to be compatible with both the Shuttle Transportation System (STS) and the Arienne or Thor-Delta launch vehicles. This places additional volumetric constraints on the antenna designer because the dynamic envelope is significantly different between the shuttle bay and a conventional booster shroud. The orientation of a satellite in the shuttle bay must be carefully worked out to have a minimum length along the shuttle's longitudinal axis since the STS launch cost is proportional to the normalized weight or to the normalized length of the payload whichever is greater.

Solar wind transparency of the antenna is more of a constraint to the spin-stabilized satellites than to the body-stabilized satellites. For a spin-stabilized satellite design, if the antenna has a large solid reflector, the solar wind will cause a transverse force greater on the antenna side,

therefore, causing instability of the satellite orientation. For this reason antennas on spin-stabilized satellites often use reflectors with porous mesh surface. A body-stabilized satellite deploys large solar panels to both sides; therefore, the solar wind torque is more balanced and has less effect.

Materials used in the fabrication of lightweight space antennas must withstand the hostile space environment. In general, materials must have low thermal expansion coefficient and must not outgas appreciably to avoid contamination of the solar panel. To minimize distortion of the antenna structure, graphite and Kevlar fibers are commonly used because of their excellent thermal expansion properties. To reduce thermal extremes, Kapton blankets are usually used to wrap the back side of the reflector, the antenna support structure, and the feeds.

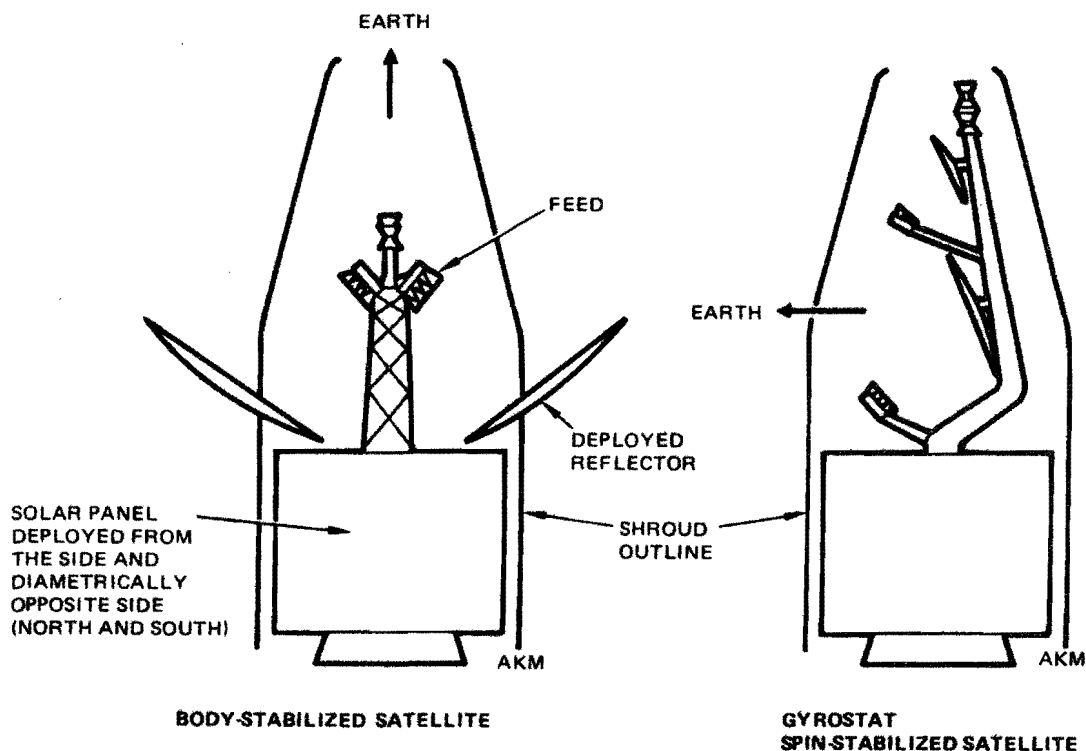


Fig. 4.1. Satellite Orientation in Booster Shroud Comparison

#### 4.3. Design factors of shaped beam reflector antennas

A general discussion of shaped beams would be concerned with the generation of beams with an arbitrarily specified dependences of gain upon angle. The present discussion is limited to a particular type of shaped beam: one that is designed to cover a specified area or solid angle and to provide the maximum gain value for the minimum constant gain contour over the area.

##### 4.3.1. Shaped-beam efficiency

As illustrated in Fig. 4.2, an ideally shaped beam is a flat-top beam with the edge of the beam conforming with the boundary of the coverage area. By the application of the law of conservation of energy, the product of the gain value,  $G$ , with the solid angle,  $\Omega$ , (in radians) covered by the beam is given by

$$G\Omega = 4\pi$$

that is, if the solid angle is expressed in square degrees,

$$G\Omega = 41,253 (\text{degrees})^2$$

In practice, a shaped beam will have a rounded top and sidelobes and will not exhibit a sharp edge at the boundary of the coverage area. Therefore, the efficiency of the beam defined as

$$\text{Shaped Beam Efficiency} = 100 \times \frac{\text{Minimum gain over area} \times \text{solid angle (degrees)}^2}{41,253}$$

will always be less than 100 percent. For best "shaped beam efficiency" the edge coverage for simple shaped beams is typically chosen to be 4 to 4.5 dB below the peak of the beam.

A shaped beam antenna requires an aperture larger than that of a pencil beam antenna, and the aperture distribution departs markedly from a gently tapered distribution. As a consequence, the beam which exhibits the higher "shaped beam efficiency" will usually be generated by an antenna

with a lower aperture efficiency than is characteristic of antennas that are used to produce simple, unshaped beams.

#### 4.3.2. Flat-topping and boundary matching

High shaped-beam efficiency is obtained in two ways. First, the flattening of the top of the beam reduces the energy radiated in the center of the beam which is in excess of the minimum value at the edge. Second, the matching of the boundary of the coverage area by the contour of the beam reduces the power radiated outside of the specified area. These two design aspects are interrelated and must be simultaneously achieved in the generation of shaped beams.

#### 4.3.3. Methods of generating shaped beams

In principle there are several types of antenna that can generate shaped beams. However, in practice the preferred choice is an offset parabolic reflector fed by an array of feed horns. In designing the feed for a shaped coverage, the field variations generated in each feed horn and in the space between feed horns should not be reproduced in the far-field of the reflector. The Fourier transforms will be used to show how the feed and reflector parameters can be selected to achieve the most shaping or squaring of the sector beam without introducing feed-horn ripples into the far-field pattern.

#### 4.3.4. Analysis by means of Fourier transforms

The analysis of reflector antennas is greatly simplified if the reflector is considered to be in the far-field region of the composite feed array. This assumption is sufficiently true so that the following analysis will give meaningful and useful results. As a consequence of the far-field approximation, the field at the reflector aperture which is the projected area of the reflector onto the plane normal to the reflector axis can be considered the Fourier transform of the fields in the feed aperture. In this analysis the fields that lie outside of the projected reflector aperture are considered negligible. The far-field radiation pattern of the reflector antenna is the Fourier transform of the field in the reflector

aperture. Since the range of angles in the aperture distribution that are passed to the far-field by the reflector is limited by the angular size of the reflector as viewed from the feed, the feed distribution is reproduced in the far-field of the reflector with a distortion determined by the angular size of the reflector.

For simplicity, in the following discussion of reflector antenna analysis by Fourier transforms, the one-dimensional case is described. However, the extension to two dimensions is generally straightforward. As an example, a multihorn feed is assumed to have a field distribution shown in Fig. 4.3. The feed aperture distribution  $f(x)$  can be considered to be the convolution of the two functions  $g(x)$  and  $h(x)$  shown in Fig. 4.4(a). The Fourier transforms of the two distributions,  $G(u)$  and  $H(u)$ , are illustrated in Fig. 4.4(b). The far-field radiation pattern of the feed aperture is the product of these two functions and is illustrated in Fig. 4.4(c). The central peak, together with its sidelobes enclosed by A-A is transformed into a sector beam in the far-field of the reflector. As the angular dimension of the reflector is increased, more sidelobes are intercepted by the reflector and the sector beam in the far-field of the reflector becomes squarer and flatter.

The first grating lobe and its sidelobes (B-B) represent the lowest order, sinusoidal component of distribution in the feed aperture. If this grating lobe is reflected to the far field, it would create a sinusoidal amplitude variation with angle in the sector beam. Since the appearance of this periodic variation, or ripple, within the sector beam is usually not desired, the angular extent of the reflector must be limited to less than the angular range bounded by the grating lobes of the feed aperture distribution. It is apparent that the angular extent of the reflector and the squareness of the sector beam can be increased if more sidelobes of the main beam can be reflected without including the grating lobe. This result can be achieved by increasing the number of horns that are contained in the feed aperture.

As a compromise between the squareness of the sector beam and the ripple within the beam, the edge of the reflector ought to be set at a point roughly midway between the primary peak and the first grating lobe of the

radiation pattern of the feed structure. For feed horn spacing such that the grating lobe is within about  $45^\circ$  from broadside and the angular extent of the reflector is modest, it can be shown that the resultant beams from each of the horns are spaced so that the peak of each beam is located at about the first null of the adjacent beam. In this case, the crossover point for  $\sin x/x$  beams is approximately 3.9 dB. The best compromise would have to be found by computation.

The grating lobes and sidelobes that are not reflected represent spillover loss. If the feed horns are arranged to be touching each other, the magnitude of the periodic components in the aperture distribution will be decreased and, hence, the spillover will be reduced. If the horns and the feed aperture are made smaller, fewer grating lobes will remain in real space further reducing the spillover. Accordingly, one may conclude that to reduce spillover, the horns should be contiguous and small enough to avoid the generation of a grating lobe in the feed radiation pattern.

The far-field pattern of the reflector is the Fourier transform of its aperture field and is given by the convolution of the aperture distribution  $f(x)$  with  $e(x)$  which is shown in Fig. 4.5. As a result one would expect to see some ripple or cyclic variation near the edges of the sector beam that is due to the abrupt cutoff of the reflections at the edge of the reflector.

#### 4.3.5. Summary

As a result of the preceding analysis, the following observations can be made in regard to the design of shaped beam antennas.

1. The feed horns should be contiguous and small enough to eliminate or significantly reduce the size of the grating lobes to reduce spillover.
2. The focal length of the reflector should be selected to obtain the desired angular extent seen by the feed horns.

3. The angular extent of the reflector should be made as large as possible without introducing an unacceptable amount of ripples into the interior of the sector beam by the reflection of a grating lobe or its sidelobes.
4. The edges of the beam can be made squarer and better defined by increasing the number of horns in the feed.

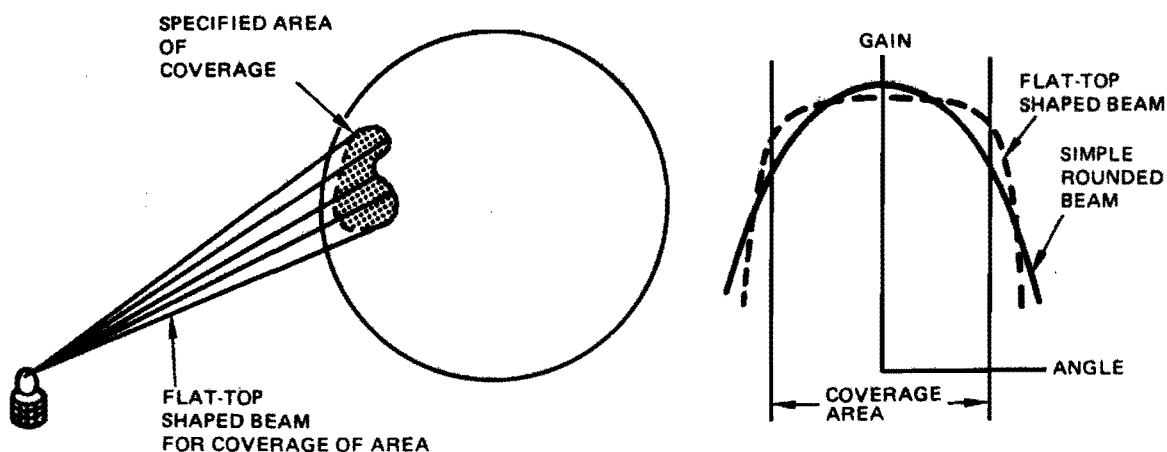
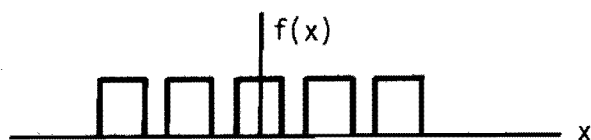


Fig. 4.2. Ideally Shaped Beam Description



$$f(x) = \text{CONVOLUTION OF } g(x) \text{ AND } h(x)$$

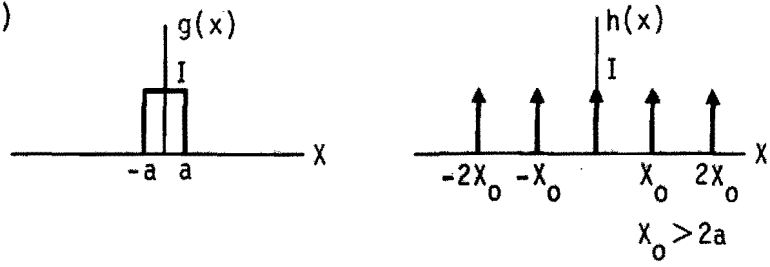
$$\text{WHERE } g(x) = 1 \text{ } -a \leq x \leq a$$

$$h(x) = \sum_{m=-2}^2 \delta(x-nx_0)$$

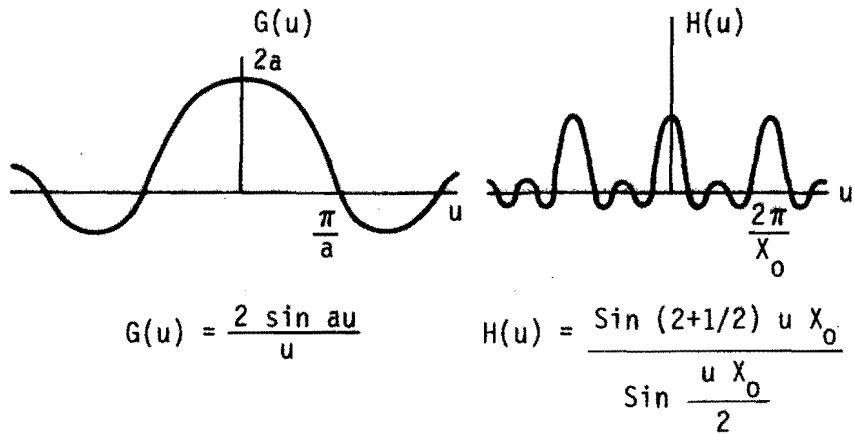
Fig. 4.3. Feed Aperture Field Distribution



a)  $f(x) = g(x) * h(x)$



b) TRANSFORMS



c) FEED RADIATION PATTERN  $F(u) = G(u) H(u)$

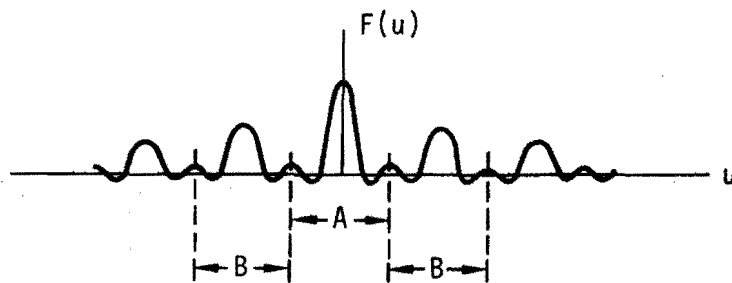
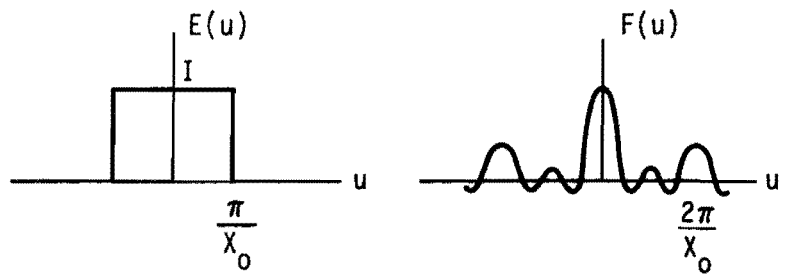
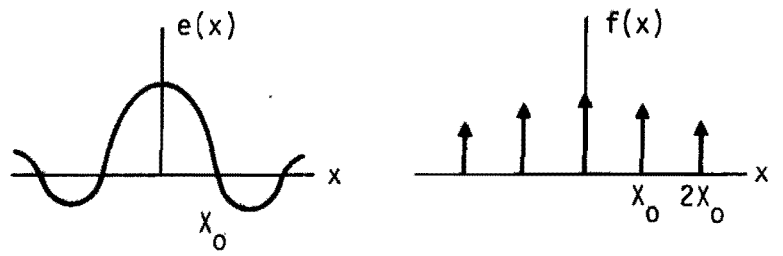


Fig. 4.4. Components of Feed Aperture Field Distribution and Their Fourier Transforms

a)  $D(u) = E(u) F(u)$



b) TRANSFORMS



c) FAR FIELD PATTERN  $d(x) = e(x) * f(x)$

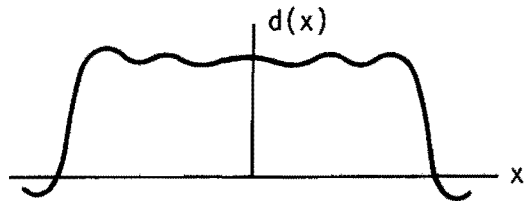


Fig. 4.5. Far-Field Radiation Pattern of Reflector

#### 4.4. Telesat (Anik A)/Westar/Palapa communications antenna

##### 4.4.1. Introduction

The Anik A mission is to place a 12-channel, 5760 telephone circuits, active repeater in synchronous orbit and to continuously operate this repeater over a 7-year life span. The principal spacecraft elements and their arrangement on the spacecraft are shown in Fig. 4.6. The spacecraft's appearance is dominated by the large parabolic reflector and the cylindrical solar panel. The opening in the reflector structure is covered with a fine metallic mesh to provide the microwave reflection. The spacecraft is spin-stabilized and the reflector and its feed are despun. A noncontacting rotary joint provides the microwave transmission path between the 12-channel repeater and the antenna feed. The reflector axis is tilted back  $7.85^{\circ}$  and a three-horn feed is designed to provide optimum coverage of Canada. Excellent coverage for any spacecraft station location from  $85$  to  $120^{\circ}$  west longitude is achieved.

##### 4.4.2. Antenna description

The antenna consists of two sections: a spinning section which is mechanically attached to the satellite thrust tube and electrically connected to the repeater and a despun section which is mechanically attached to the spinning section by a noncontacting rotary joint. Most of the antenna equipment is part of the despun section which includes the reflector, the feed and the telemetry and command (T&C) antenna. The spinning section consists of the remainder of the feed network (Fig. 4.7).

The offset parabolic reflector used for Telstar has a projected aperture 60 inches in diameter and a focal length of 30 inches. Its feed consists of three horns which provide vertically polarized receive signals at 6 GHz and horizontally polarized transmit signals at 4 GHz. The east-west pointing of the beam is controlled by the despun system. The coverage contours that are shaped to match the Canadian boundary are shown in Fig. 4.8.

The reflector consists of a skeleton structure onto which an RF reflective metallic mesh is attached. The mesh is partially transparent to the solar

wind to allow an acceptable satellite precession rate. Both the skeleton and support ribs are fabricated from an aluminum honeycomb, graphite fiber composite. Graphite was selected for its strength and low thermal expansion coefficient. The skeleton and support ribs are formed on a machined mandrel and are oven-cured.

#### 4.4.3 Transmit function

The transmit feed network, as depicted by the block diagram in Figure 4.7, has two inputs, one for the even and one for the odd numbered repeater channels, and three outputs connecting to the three feed horns. The transmit function has two modes depending upon whether the signal originates at the odd- or even-channel input. The distinction is based on the direction of azimuthal phase progression, east to west, or west to east. If a signal originates at the odd-channel input, it is trisected into equal amplitude vectors at the East, Center, and West outputs. The phase relationship among these vectors is  $-60$ ,  $0$ , and  $+60$  degrees, and the phase progression is from east to west. If a signal originates at the even-channel input, it is also trisected, but the phase relationship at the East, Center, and West outputs is  $+60$ ,  $0$ , and  $-60$  degrees; that is, the signal has the opposite sense of phase progression.

Referring to Figure 4.7, the magic tee, the waveguide squeeze section, and the orthogonal mode transducer comprise the spinning portion of the feed. A signal originating at the odd-channel input would first be power split by the magic tee and then recombined in the orthogonal mode transducer (OMT) to produce a left-hand circularly polarized wave. This wave propagates across the spinning interface through the rotary joint and is separated into orthogonal components by the despun OMT. The inputs to the phase converter have equal amplitude and are orthogonal to each other. A signal originating at the even input produces a right-hand circularly polarized wave in the rotary joint, and would also ideally produce equal amplitude orthogonal vectors at the inputs to the phase converter. However, the direction of phase progression between the inputs to the phase converter is reversed. For an ideal feed network, labeling the phase converter inputs left (L) and right (R), the phase converter relative inputs are

$$\begin{matrix} \text{Odd Input} & \text{Even Input} \\ \begin{bmatrix} L \\ R \end{bmatrix} = \begin{bmatrix} \frac{a_1}{\sqrt{2}} e^{-j\pi/4} \\ \frac{a_1}{\sqrt{2}} e^{+j\pi/4} \end{bmatrix} & \begin{bmatrix} \frac{a_2}{\sqrt{2}} e^{+j\pi/4} \\ \frac{a_2}{\sqrt{2}} e^{-j\pi/4} \end{bmatrix} \end{matrix}$$

where  $a_1$  and  $a_2$  are the amplitudes of the odd- and even-channel signal inputs and arbitrary phase constants are not included. The ideal phase converter has the following transformation matrix:

$$\begin{bmatrix} E \\ C \\ W \end{bmatrix} = \begin{bmatrix} 0.789 & -0.211 \\ 0.577 & 0.577 \\ -0.211 & 0.789 \end{bmatrix} \begin{bmatrix} L \\ R \end{bmatrix}$$

where E, C, and W refer to the East, Center, and West outputs.

Narrowband directional filters are used to couple energy at the telemetry frequency to the T&C antenna but have no effect at the transmit communication frequencies. In practice, elliptically polarized waves are generated in the rotary joint, causing the phase converter inputs to deviate from the ideal case and contain amplitude and phase variations that are functions of the spacecraft spin speed. A peak-to-peak power variation of 0.4 dB at the phase converter outputs is typical.

#### 4.4.4. Receive function

The receive feed network has three inputs connected to the East, Center, and West horns, and one output connected to the 6 GHz repeater. These three inputs then drive a 3 to 1 power combiner to form the composite receive signal. As an integral part of its design, the 3 to 1 power combiner includes a magic tee that derives a difference signal from the East and Center feed horn outputs. This difference signal is recombined with the composite receive signal at the command frequency by a directional

filter. This signal is transferred across the spinning interface by a 0.141 inch diameter coaxial cable concentric with the rotary joint. The coaxial cable is attached to the despun section of the antenna; a noncontacting choke joint is used between the coaxial outer conductor and spinning side. The coaxial center conductor forms the probe for the waveguide-to-coaxial transducers on the spinning and despun sides.

#### 4.4.5. Westar/Palapa antenna description

Both antenna designs are identical to that of Telstar except for feeds. The Westar feed is designed to provide optimum coverage of the United States including Alaska and Hawaii. The Palapa feed design is configured to provide optimum coverage of Indonesia, Thailand, Malaysia, Singapore, and the Phillipines.

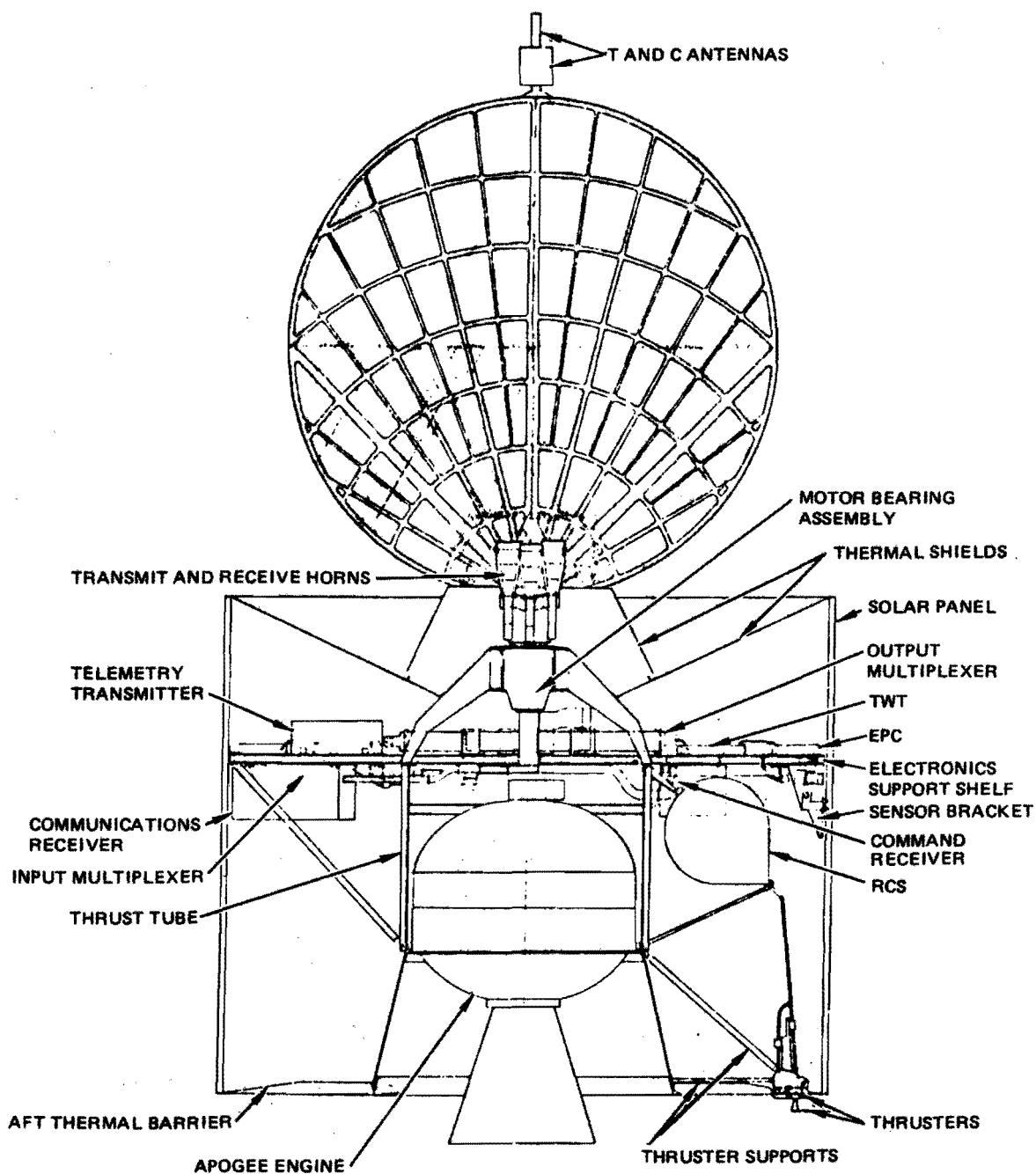


*Fig. 4.6. Telstar Spacecraft Layout*

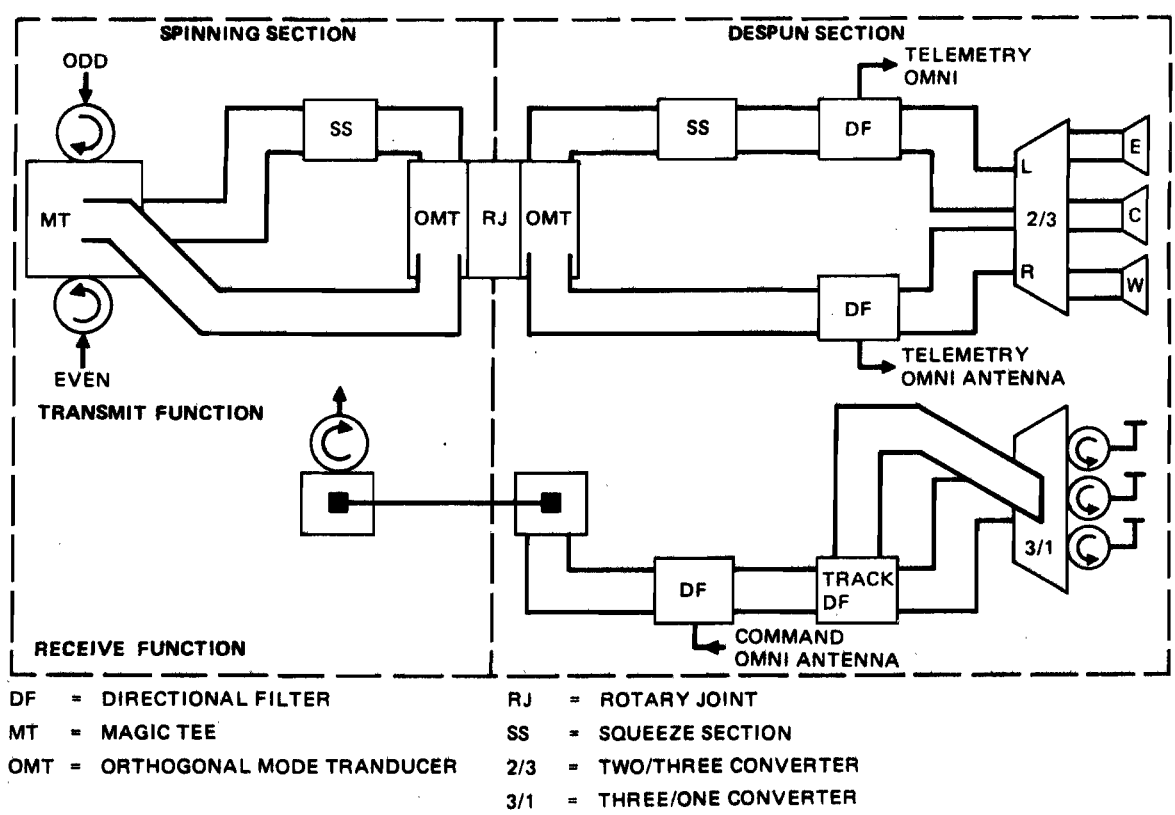


Fig. 4.7. Telstar Antenna Transmit and Receive Feed Networks

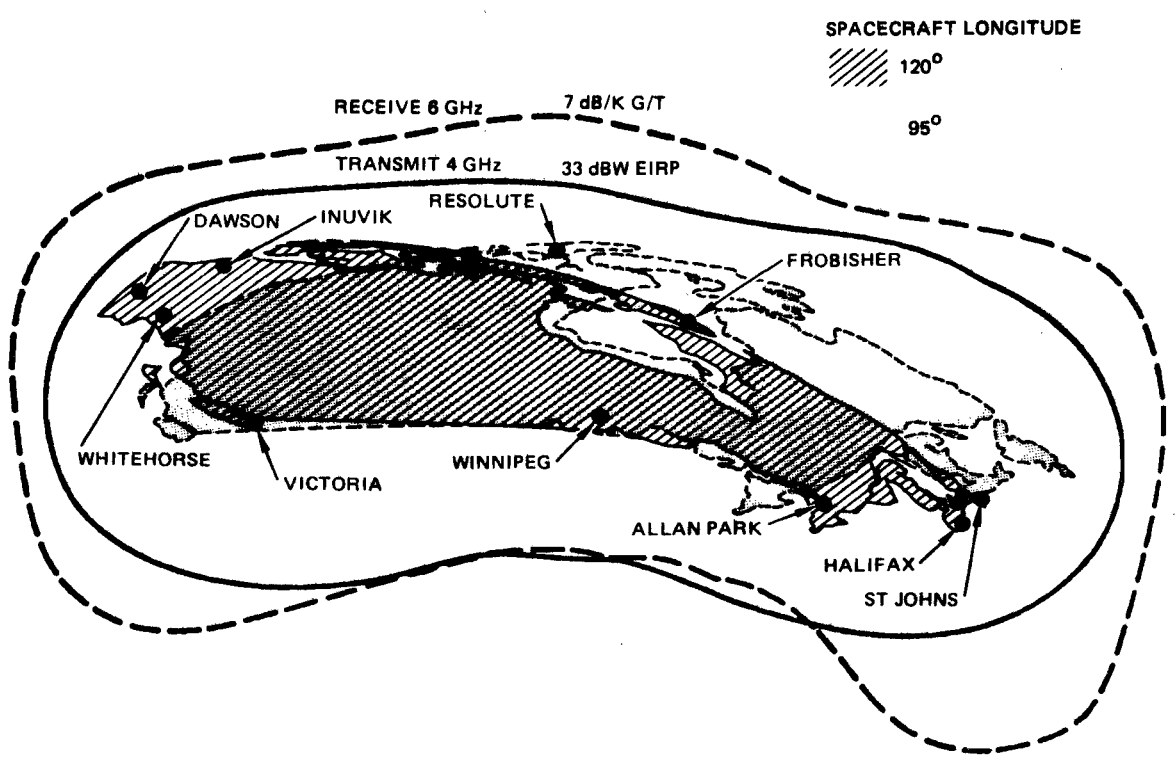


Fig. 4.8. Telstar Antenna Coverage Contours



#### 4.5. Comstar I communications antenna

##### 4.5.1. General description

###### 4.5.1.1. Introduction

The Comstar I mission objective is to place in synchronous orbit a 24-channel, 28,800 telephone circuits, active repeater, and to continuously operate this repeater over a 7-year life span. A layout of the Comstar I spacecraft is shown in Fig. 4.9. The appearance of the antenna farm is dominated by the presence of two 1.3 by 1.8 meter (50 by 70 inch) rectangular aperture, shaped beam antennas. These antennas provide communications between areas of maximum service within the continental United States, Alaska, Hawaii and Puerto Rico. The apertures of the antennas are covered with polarization screens to ensure high linear polarization purity in both transmitted and received RF signals. These screens are an essential element of the communication subsystem, which employs polarization diversity to reuse the available bandwidth for greater communications capacity.

In addition to the communications antennas, the Comstar I antenna farm includes a telemetry and command bicone antenna at the top of the antenna mast and two pairs of millimeter-wave antennas mounted below the communications antennas.

The frequency spectrum (Fig. 4.10) is divided into 24 channels, 12 vertically polarized and 12 horizontally polarized. Each channel is 34 MHz wide and spaced at 40 MHz intervals. The vertically polarized channels service CONUS and Alaska; the horizontally polarized channels service CONUS, Hawaii, and Puerto Rico. Received signals are translated in frequency by 2225 MHz to the 6 GHz band (5925 to 6425 MHz) and retransmitted with the same polarization orientation. The horizontally polarized and vertically polarized channels are shifted in frequency 20 MHz to minimize the amount of interference between the orthogonally polarized signals.

The specified coverage and polarization plan are shown in Fig. 4.11. As indicated by Fig. 4.10, the transmit signals from the odd horizontally polarized channels can be switched into either the CONUS or Hawaii spot

beams. Similarly, the even horizontally polarized channels can transmit to either CONUS or Puerto Rico. The even vertically polarized channels can be transmitted in one of three ways: all power to CONUS, all power to Alaska, or power divided between Alaska and CONUS. For receive, all the vertically polarized channels are received from the combined Alaska and CONUS area. Likewise, all horizontally polarized channels are received from the combined CONUS, Hawaii, and Puerto Rico areas.

#### 4.5.1.2. Vertically polarized antenna feed

The vertically polarized feed assembly consists of five feed horns and separate feed networks for transmit and receive as shown in Figure 4.12. A photograph of the vertically polarized feed assembly is shown in Fig. 4.13.

The arrangement of feed horns is shown in Fig. 4.14. Three horns are used to form the CONUS beam and two horns are used to form the Alaska beam. Because of the difference in horn aperture field distribution, for vertical polarization the CONUS horn array illuminates the reflector with less efficiency than if the polarization is horizontal. As a result, less gain is achieved for the vertically polarized antenna over the specified area. Larger traveling wave tubes are used to yield the same effective isotropic radiated power (EIRP) for both polarizations.

Receive and transmit signals to each feed horn are separated by a diplexer. One port of each diplexer is connected to the transmit feed network which divides the power between the feed horns and adjusts relative phase. Power from one end of the even-channel multiplexer manifold is fed to a phase network that adjusts phase between the two Alaska horns and the three CONUS horns. This phasing is required for combined service to ensure that overlapping portions of the Alaska and CONUS spot beams will combine to reinforce signal strength. Power from the other end of the even-channel multiplexer manifold (even mode) and from the odd-channel multiplexer manifold (odd mode) is routed to the dual mode power divider. The two combined signals are divided into three equal parts for each of the CONUS feed horns. These three signals are phased at 0 and  $\pm 60^\circ$  to provide the desired shaped CONUS pattern.

The receive network is simpler since it has only one output. Signals from each feed horn are phased and combined in the power dividers to provide the shaped, spot beam patterns. An additional phase network and power divider is used to form a single receive pattern which covers both Alaska and CONUS.

#### 4.5.1.3. Horizontally polarized antenna feed

The horizontally polarized assembly consists of six feed horns and separate feed networks for transmit and receive as shown in Fig. 4.15. A photograph of the horizontally polarized feed assembly is shown in Fig. 4.16.

The feed horns are arranged to form beams for CONUS, Hawaii, and Puerto Rico. The feed horn aperture configuration is shown in Fig. 4.13. Three horns are used for forming the CONUS beam, two horns for the Puerto Rico beam, and one for the Hawaii beam.

The horizontally polarized transmit network functions similar to the vertically polarized transmit network. However, the offshore spot beams are not phased to reinforce the CONUS pattern because combined coverage is not required. One end of the odd-channel multiplexer is connected directly to the Hawaii feed horn. The other end of the odd-channel multiplexer manifold and one end of the even-channel multiplexer are fed to the dual mode power divider which feeds the power independently to the three CONUS horns. The other even-channel multiplexer output port is directed to a magic tee. Here the power is divided equally between the two output ports. One magic tee output waveguide run contains a phase network to adjust the phase between the two Puerto Rico horns. This final phase adjustment is used to optimize the Puerto Rico beam coverage.

The horizontally polarized receive feed network is used to obtain essentially equal power from each of the spot beams. The signals from the feed horns are first combined in pairs. The Hawaii horn is combined with the west CONUS horn through phase networks and a magic tee which combines the signals equally. The other two CONUS horns are also combined through a magic tee. The Puerto Rico horns are combined through a coupler and phase network. The first two pairs of CONUS/Hawaii feed horns are next combined through a

magic tee to provide equal power from all four horns. The Puerto Rico horns are coupled into the CONUS/Hawaii signals through a phase network. Couplers and magic tees are used to set the relative signal level from each of the horns.

#### 4.5.1.4. Polarization screens

Waves propagated by the feed horns are linearly polarized. When these waves are reflected by the parabolic dish, cross-polarized components are produced due to reflector surface curvature. To filter out the cross-polarized field component and thereby enhance the polarization purity, polarization screens are mounted in front of the reflectors. The screens are made from parallel conductive strips which act as a waveguide beyond cutoff for the cross-polarized components and reflect these unwanted waves.

Two polarization screens are used. They are located 40.00 inches from the vertex of the reflector measured along the focal axis and centered about the reflector aperture. The reflectors are 2.25 inches apart and, thus, require that the polarization screens be 0.25 inches apart. To prevent bumping, rubber bumpers are provided along the length of the 0.25 inch gap.

#### 4.5.1.5. Reflectors

The reflector surface is formed using a fine flexible mesh cloth woven from gold plated, nickel-chromium alloy wires. This wire mesh is stretched over a frame shown in Fig. 4.17. The mesh is constrained to the desired paraboloidal surface, but it deviates from the paraboloidal surface in the openings between frame supports. These deviations reduce antenna gain very slightly. Like the Telstar antenna, the reflector frame is fabricated using aluminum honeycomb and graphite fibers.

#### 4.5.2. Design approach

The primary goal of the communications antenna design is to effectively reuse the frequency bands through polarization diversity. Hence, it requires the development of a dual, orthogonal, linearly polarized antenna

system capable of delivering sufficient uplink and downlink performance (24.5 dB edge of coverage gain and 33.0 dBw EIRP, respectively), while achieving sufficient cross-polarized isolation ( $\geq 33$  dB) between the two orthogonally polarized antennas over the coverage area.

To implement such a system, a design consisting of two offset parabolic reflectors, each fed with a multihorn array, was adopted. Each antenna will radiate 12 downlink channels over the same 3.7 to 4.2 GHz band and will use the Hughes developed dual-mode concept to feed the CONUS feed horn array. This design in conjunction with the orthogonally polarized screens provides efficient beam shaping and cross-polarization.

#### 4.5.2.1. Two-reflector/three-reflector tradeoffs

Early analysis indicated that the horizontally polarized antenna provides higher gain over a coverage area (such as CONUS) than the vertically polarized antenna because of more efficient illumination of the reflector in the azimuthal plane by the horizontally polarized feed horns. Typically, the horizontally polarized antenna CONUS coverage gain is 0.5 dB better than the vertical antenna. To improve the vertically polarized coverage, a three antenna concept (A, B, C) shown in Fig. 4.18 was considered.

Antenna A is a horizontally polarized offset reflector paraboloid.

Antenna B is a vertically polarized offset reflector antenna with only 6 downlink channels, e.g., odd channels. This removes the dual-mode constraints and enables arbitrary power division and phase distribution for the CONUS feed array. This antenna design also provides the receive functions for all uplink signals. Antenna C is another vertically polarized parabolic reflector to transmit the remaining 6 downlink channels. Again, arbitrary power division and phase distribution are allowed for optimizing the downlink coverage.

As expected, the three-reflector concept allowed more efficient shaping over the CONUS coverage area (+32.8 dBw worst case). However, due to considerations which are discussed later, the Alaska downlink and T-mode coverage gain are less than for the two-reflector case (30.0 dBw T-mode, 31.5 dBw - Alaska worst cases). The third antenna also adds to satellite

complexity, increases its weight, and increases solar torque effects. A summarized evaluation of the relative merits between the two approaches is presented in Table 4.1. Based on the tradeoff results, the two-reflector approach was adopted.

#### 4.5.2.2. Vertically polarized antenna design

Early design investigations showed that the vertically polarized antenna would yield better Alaska downlink and T-mode coverage than the horizontally polarized. To illuminate the entire Alaska coverage area with +33 dBw (EIRP), two feed horns are required. As shown in Fig. 4.19 if a small reflector (53 by 53 inch aperture) is used, beam 4 would point to far north. Lowering beam 4 would force the West CONUS horn to another position and degrade the west coast CONUS coverage. However, the problem was then solved by considering the following:

1. Increasing reflector area would minimally increase the CONUS performance.
2. By maintaining an  $F/D = 0.25$ , the far-field to near-field angle ratio ( $\beta/\alpha$ ) remains constant. The subtended angle of the reflector in the elevation angle also remains unchanged. To achieve similar reflector edge illumination, the height of the horns (E-plane dimension) remains fixed. Hence, the relative positions of horns 3 and 4 will also remain fixed.
3. Increasing the focal length while keeping  $F/D$  the same decreases the near-field angle which is inversely proportional to the focal length. Since the ratio of  $F/D$  remains fixed, the far-field angle of beam 4 must also decrease. Therefore, this drops beam 4 into a position of more efficient Alaska illumination. The result is a 50-inch wide (dictated by shroud dynamic envelope) by 70-inch high rectangular aperture reflector with a 35-inch focal length.

#### 4.5.2.3. Horizontally polarized antenna

To maintain satellite symmetry, the same reflector geometry for the horizontally polarized antenna was chosen as that of the vertically polarized antenna. The positions and sizes of the CONUS horns were optimized for the transmit band because of the tight coverage contours to the specified area. The positions and sizes of the Puerto Rico and Hawaii horns were optimized for the receive band because of the tight receive contours compared to the ample margin transmit coverage contours.

For improved CONUS coverage, a large H-plane dimension of the CONUS horns is required; however, a 5.5 inch H-plane dimension is the maximum before one of the Puerto Rico horns is moved excessively and its beam no longer covers the specified area. All three CONUS horns are identical in size to allow phase tracking over both the transmit and receive bands. Similarly the two Puerto Rico horns are identical for good phase tracking especially at the receive frequencies.

#### 4.5.3. Polarization screen design

##### 4.5.3.1. Analysis

For the optimum design of the polarizing screens, the problem of electromagnetic scattering by an infinite grating of conducting strips (shown in Fig. 4.20) was analyzed and solved numerically. To simplify the evaluation of design parameters, the two principal planes are considered for numerical calculations. Thus, the plane of incidence is either perpendicular or parallel to the strip surface. The incident plane wave is defined to be principally polarized, or cross-polarized, depending on whether its electrical field is perpendicular, or parallel, to the edges of strips respectively. For each polarization, the transmissivity of the strip grating has been evaluated for various strip widths and spacings.

The variations of transmissivities as a function of frequency are illustrated for a 1.0 inch strip width and 0.5 inch strip spacing. It is noted that the cross-polarization isolation improves at lower frequencies with insignificant changes in the transmission of the principal polarization.

For this reason the upper end of the receive frequency band was selected to illustrate the breadboard polarizer screen design.

There is no unique design unless justifications from different standpoints are made. From the electrical design standpoint, it was believed that if an infinite grating can provide theoretical cross-polarization isolation of the order of 45 and 50 dB, acceptable isolations should be obtainable from a strip grating of finite size in all planes of incidence. Based upon a value of 47.5 dB as a design criteria, the following strip grating designs were obtained.

	<u>Design 1, in.</u>	<u>Design 2, in.</u>	<u>Design 3, in.</u>
Spacing	0.4	0.5	0.5
Strip width	0.72	1.0	1.375

Design 3 required a strip width of 1.375 inches which would make the polarizer screen exceed the shroud dynamic envelope and was, therefore, eliminated. Design 2 was selected over design 1 primarily for mechanical reasons. The one-inch width would provide greater frame stiffness and strength compared to a smaller frame in cross section for a 0.72 inch width design. To obtain the same stiffness for the latter, the frame weight is expected to increase.

#### 4.5.3.2. Mechanical design

Three basic design concepts were considered for the strip polarization screen. These concepts were the stretched membrane, ice cube tray, and foam spacer. The stretched membrane approach has the advantage of least weight, solar torque, and RF insertion loss for the three concepts studied. The ice cube tray approach, although as light as the stretched membrane approach and with least solar torque, would be more difficult to fabricate. The foam spacer approach has the advantage of prior breadboard development on a Hughes-funded research project, but it would result in heavier weight (110 versus 3.5 pounds for stretched membrane approach). It has a solid profile causing solar torque and thermal shadowing, and a problem of out-gassing and decomposition of the low density (1 lb/ft<sup>3</sup>) foam required for minimal weight.



For the stretched membrane approach, both metal foil and plastic film were considered. Metal was disregarded because of its greater weight and its larger thermal and launch stresses predicted due to its high modulus and poor damping characteristics. Plastic with its low expansion coefficient and low modulus is preferable, since thermal stresses are proportional to thermal expansion coefficient and to modulus of elasticity. Furthermore, the material chosen must be space approved.

The first material studied was mylar with a modulus of 550,000 psi and an expansion coefficient of  $11.10^{-6}$  in/in/ $^{\circ}$ F. However, it degrades under ultraviolet radiation; therefore, Kapton, which is treated for ultraviolet radiation, was chosen for study. It has the same expansion coefficient as mylar except that its modulus of elasticity is lower at 430,000 psi.

To act as an RF polarizing screen, the Kapton must be metallized. There are several ways that Kapton can be aluminized. If it is aluminized on both outside surfaces, the tape temperature becomes too high. If it is aluminized on one side only, it is cooler. If it can be aluminized on the inner surface (sandwich design) where both outside surfaces are Kapton, the tape temperature is the lowest during sun illumination. The lower the strip temperatures, the least preload on the frame is required to keep the tapes in tension. Thus, the sandwich or laminate design is preferred.

Because Kapton has low tear strength, it was decided that the use of another supporting material in conjunction with Kapton might reduce the risk of tear due to handling during manufacture, assembly, and test operations. Fiberglass threads running lengthwise are sandwiched between two 0.0005 inch layers of aluminized Kapton. Each layer of Kapton has a layer of 3000 Å of vapor deposited aluminum to reduce any temperature gradient across the width due to different solar inputs across the width. The aluminum is on the inside to provide the lowest possible temperature.

Each Kapton strip is held in tension by a spring mechanism at one end of the tape while the opposite end is tied to the frame. Fiberglass string running crosswise to the tapes cross-tie the tapes and make the array of strips react to vibration and thermal loading in a predictable manner.

#### 4.5.4. Measured antenna performance

##### 4.5.4.1. Coverage contours

The CONUS downlink gain contours were measured at three frequencies for both even and odd modes. The innermost of these six contours is shown in Fig. 4.21. Puerto Rico and Hawaii downlink gain contours were each measured at two frequencies, and the innermost contours are given in Fig. 4.22 and Fig. 4.23, respectively. The innermost of the horizontally polarized uplink contours measured at three frequencies is shown in Fig. 4.24.

For the vertically polarized antenna the innermost 26.5 dB contour for CONUS transmit measured at six frequencies is shown in Fig. 4.25. The innermost of 26.5 dB contour for Alaska transmit measured at two frequencies is shown in Fig. 4.26. The innermost 24.5 dB contour for T-mode measured at two frequencies is shown in Fig. 4.27. The innermost 24.5 dB contour for receive measured at three frequencies is shown in Fig. 4.28.

##### 4.5.4.2. Carrier-to-interference

The carrier-to-interference ratio (C/I) is specified at 33 dB across the transmit and receive band anywhere within the coverage areas. For example, the transmitted cross-polarized signals of the vertically polarized antenna act as an interfering signal to the transmitting horizontally polarized antenna. The level of the cross-polarized signal of the vertically polarized antenna must be 33 dB below the principally polarized signal of the horizontally polarized antenna. The C/I ratios were measured by sweeping the frequency and measuring the principally polarized response of one antenna and the cross-polarized response of the other antenna. A sample swept frequency response is shown in Fig. 4.29. Measured in-orbit data showed that the 33 dB C/I specification is met everywhere within the CONUS.

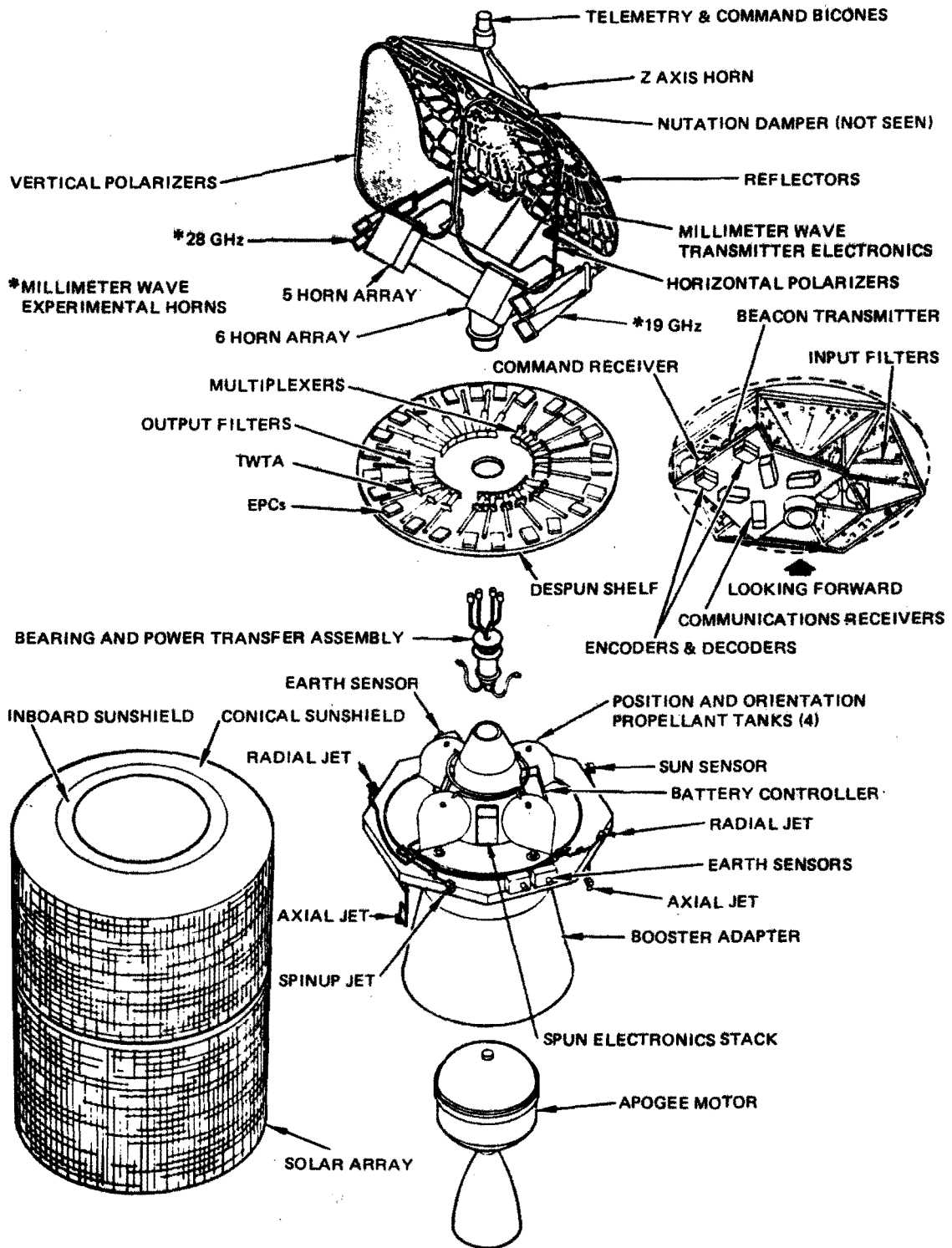
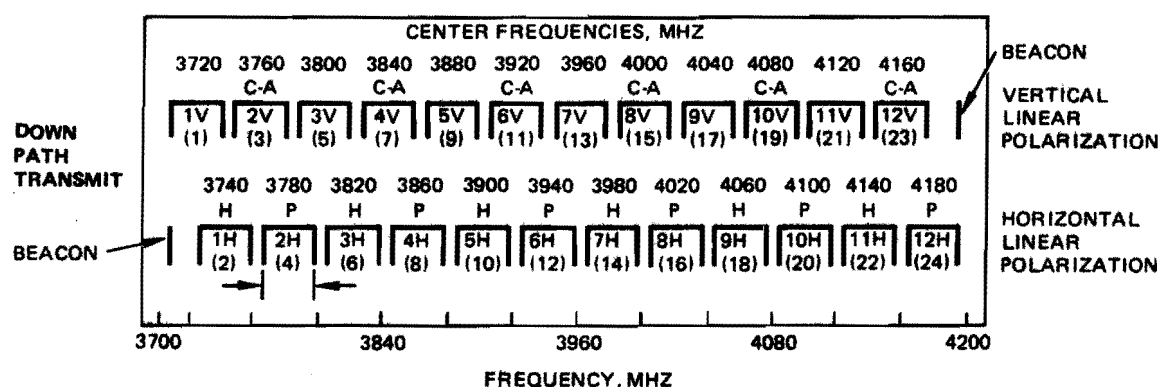
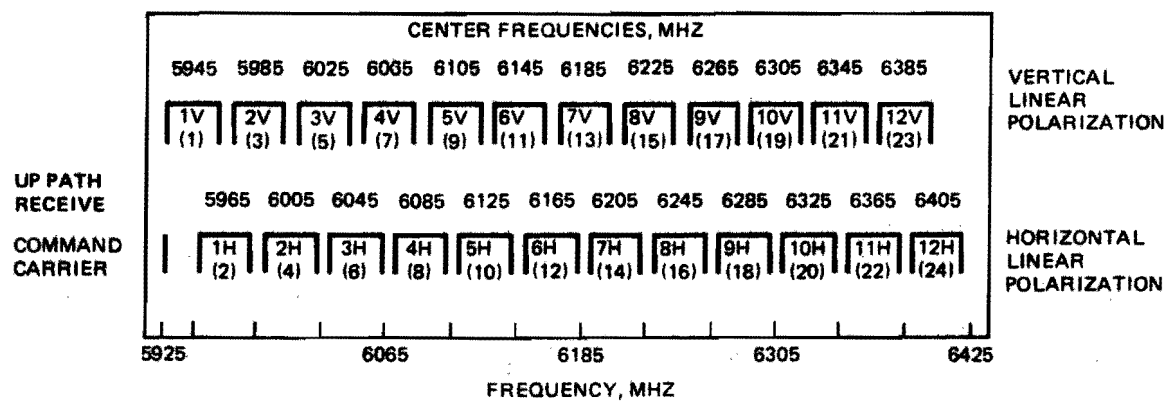


Fig. 4.9. Comstar I Spacecraft Layout



C-A TRANSPONDERS SWITCHABLE BETWEEN CONUS, ALASKA OR BOTH

H P TRANSPONDER SWITCHABLE BETWEEN CONUS AND HAWAII OR PUERTO RICO



- ALL VERTICAL UP PATH RECEIVE TRANSPONDERS AVAILABLE TO CONUS AND ALASKA
- ALL HORIZONTAL UP PATH RECEIVE TRANSPONDERS AVAILABLE TO CONUS, HAWAII, AND PUERTO RICO

NOTE: NUMBERS BELOW FREQUENCIES REFER TO TRANSPONDER IDENTIFICATION AT HUGHES. NUMBERS IN PARENTHESES ARE USED IN CONTRACTUAL DOCUMENTS AND FCC FILING

Fig. 4.10. Polarization and Frequency Plan

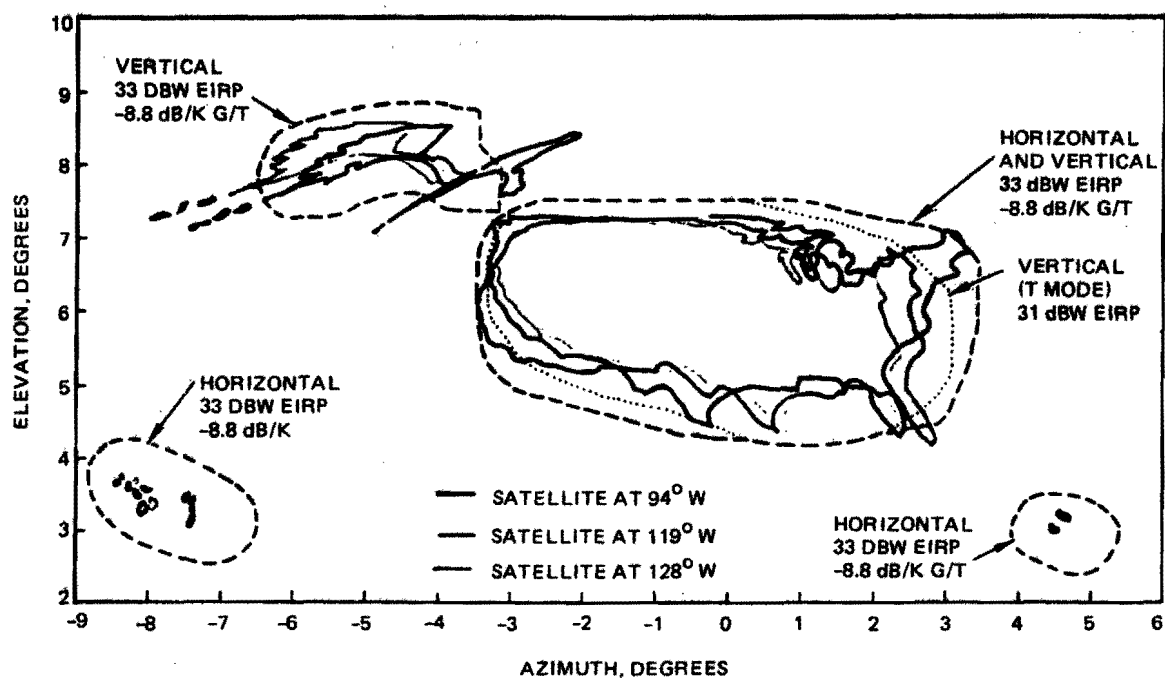
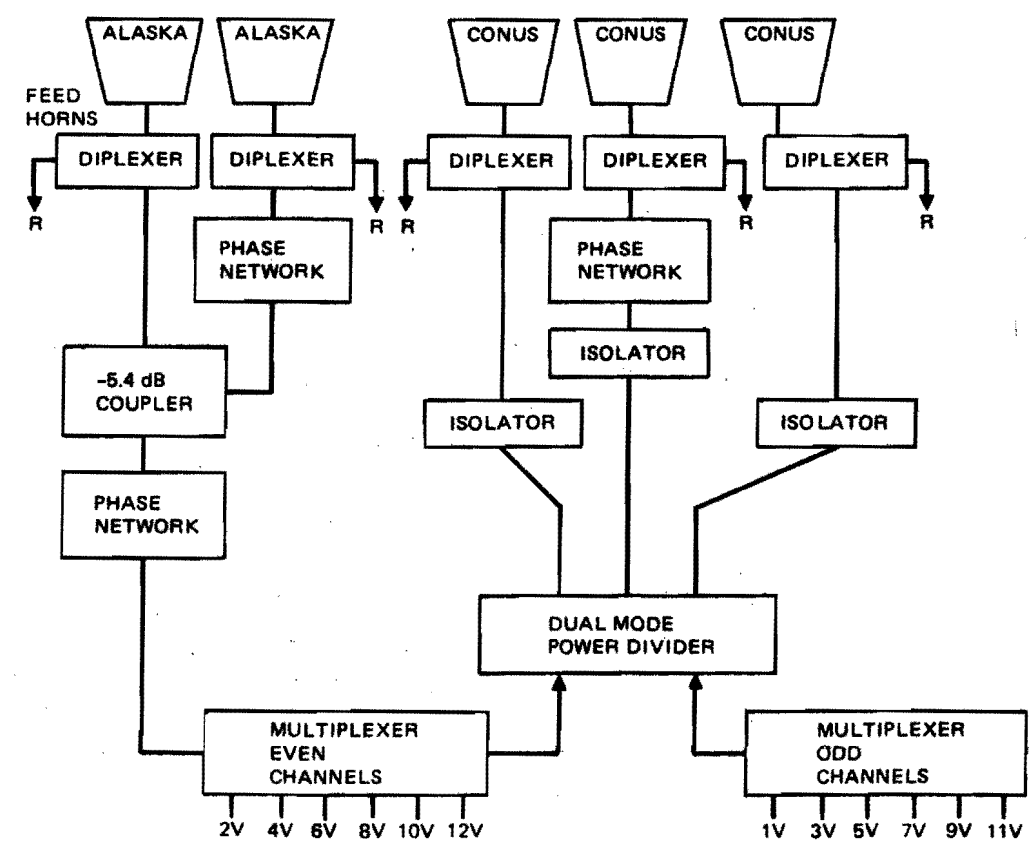
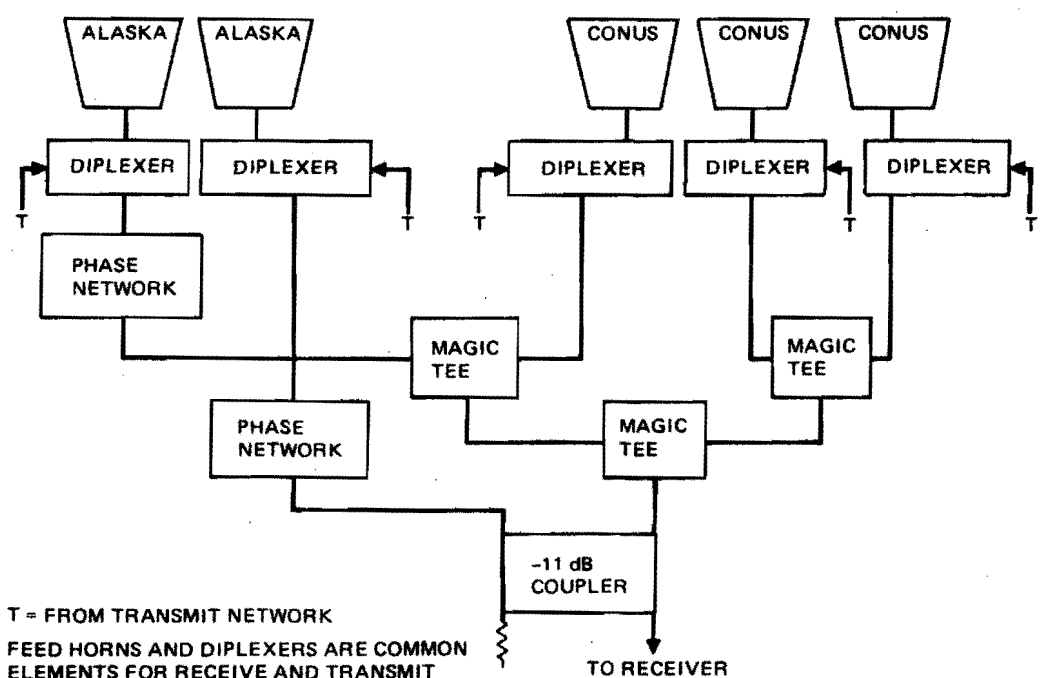


Fig. 4.11. Specified Coverage and Polarization Plan



R = TO RECEIVE NETWORK

a) TRANSMIT FEED NETWORK



T = FROM TRANSMIT NETWORK

FEED HORNS AND DIPLEXERS ARE COMMON ELEMENTS FOR RECEIVE AND TRANSMIT

b) RECEIVE FEED NETWORK

Fig. 4.12. Vertically Polarized Antenna Feed Networks



Fig. 4.13. Vertically Polarized Feed Assembly

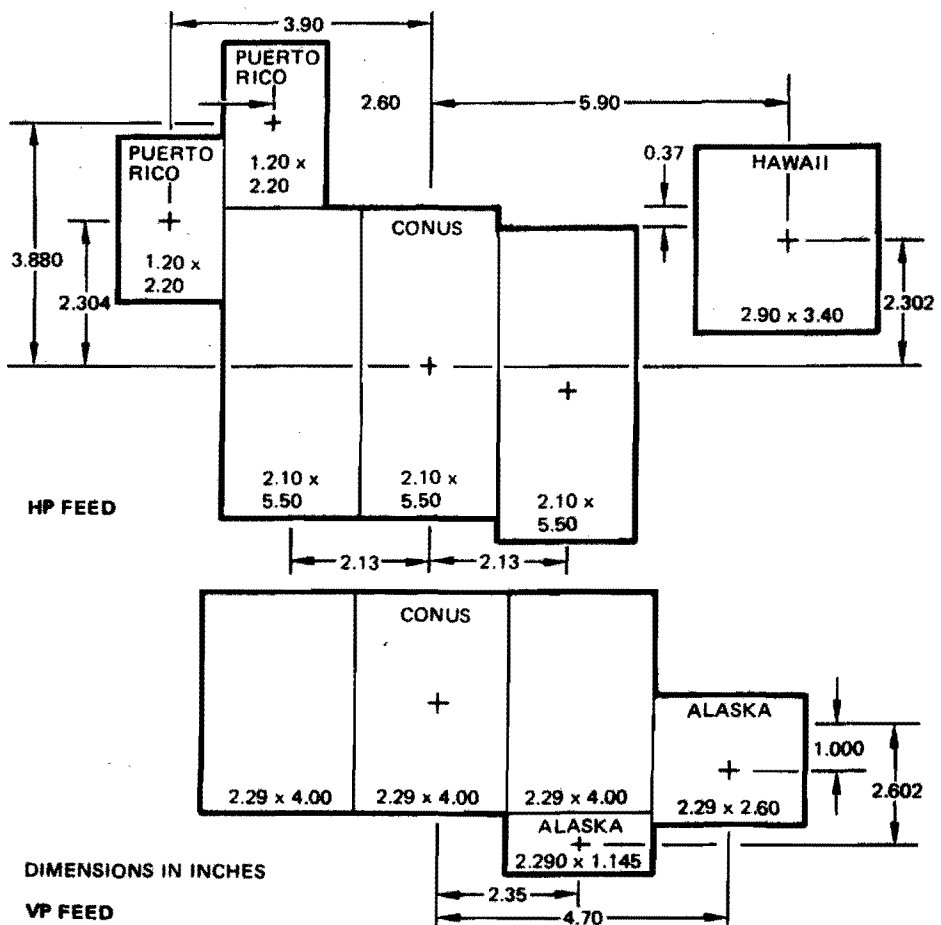
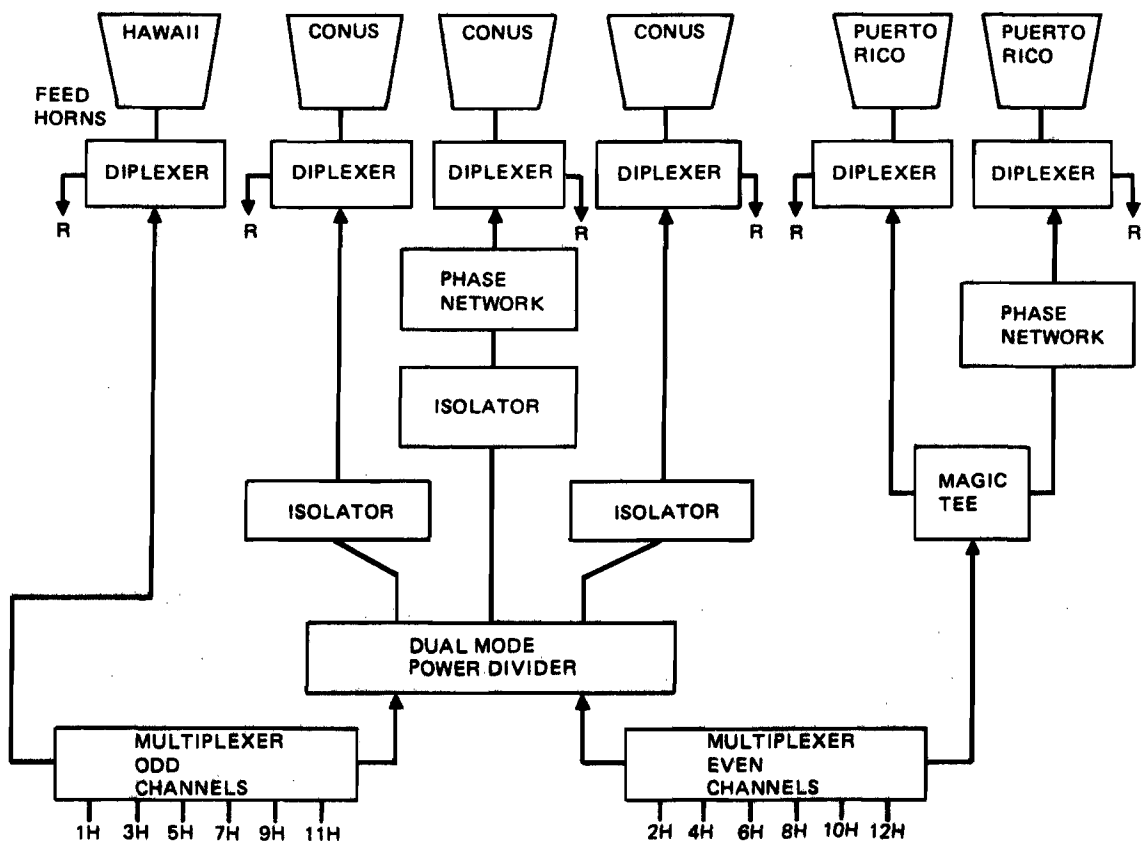
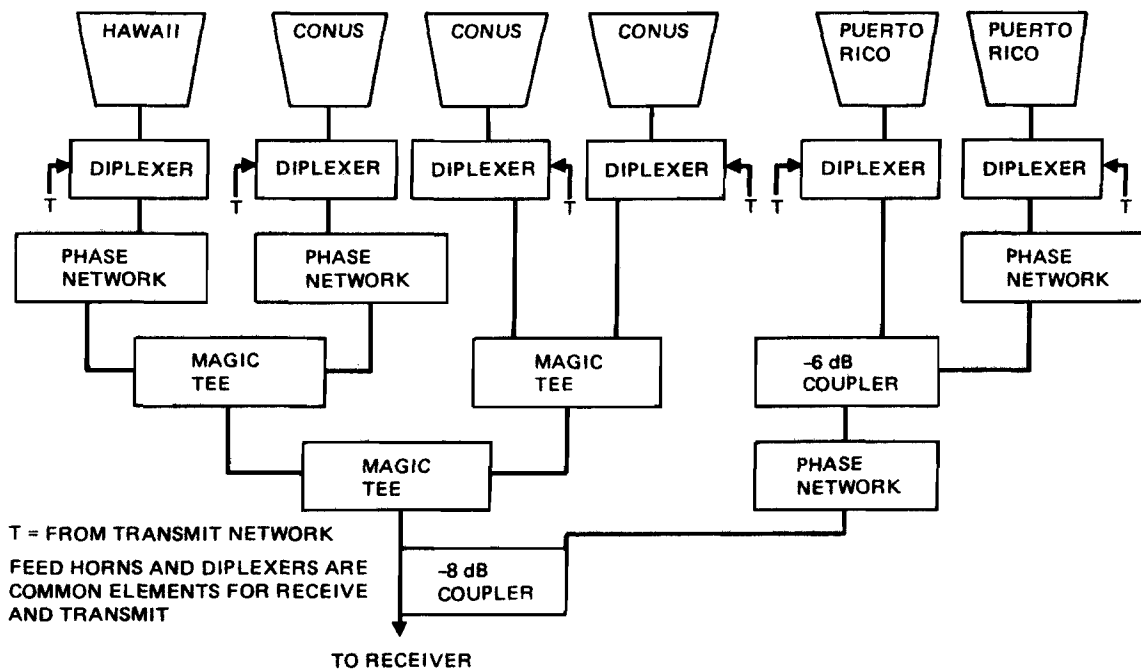


Fig. 4.14. Comstar I Feed Aperture Configuration



R = TO RECEIVE NETWORK

a) TRANSMIT FEED NETWORK



T = FROM TRANSMIT NETWORK  
FEED HORNS AND DIPLEXERS ARE  
COMMON ELEMENTS FOR RECEIVE  
AND TRANSMIT

TO RECEIVER

b) RECEIVE FEED NETWORK

Fig. 4.15. Horizontally Polarized Antenna Feed Networks





*Fig. 4.16. Horizontally Polarized Antenna Feed Assembly*



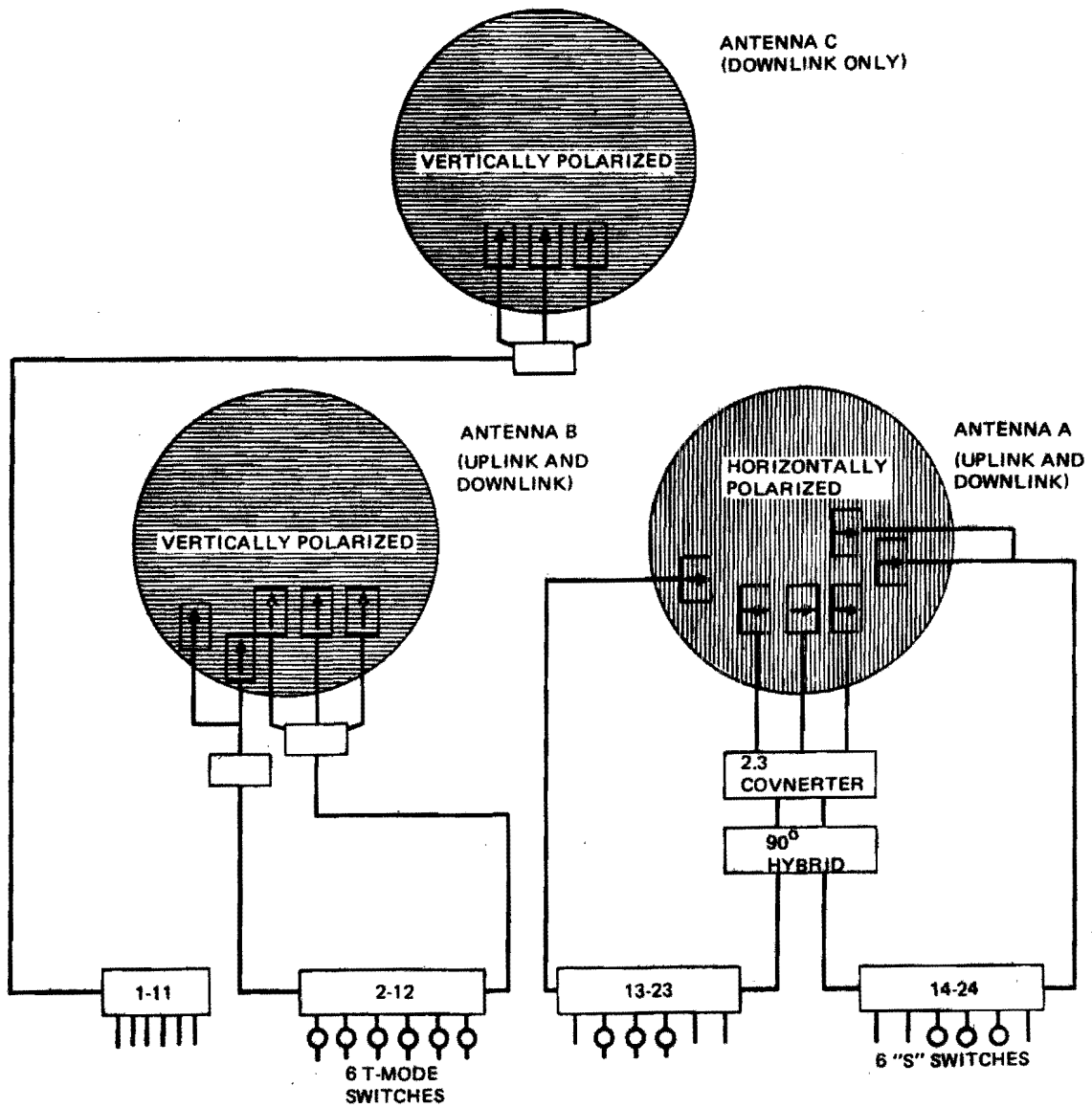


Fig. 4.18. Three-Reflector Concept

Table 4.1. Summary of Two-Reflector/Three-Reflector Tradeoff

	Two-Reflector Design*	Three-Reflector Design*
CONUS (4 GHz)	+32.4 dBw worst case	+32.8 dBw worst case
Offshore (4 GHz)	+33.0 dBw Alaska, Puerto Rico, Hawaii	+31.5 dBw Alaska, plus 33.0 dBw Puerto Rico, Hawaii, worst cases
T-Mode (4 GHz)	+31.0 dBw worst case	+30.0 dBw worst case
Uplink	+24.5 dB worst case	+24.5 dB worst case
Isolation	-33 dB attainable	Much more critical due to alignment
Complexity	Two antennas	Three antennas
Costs	—	More expensive, more weight

\* All gain values are theoretical.

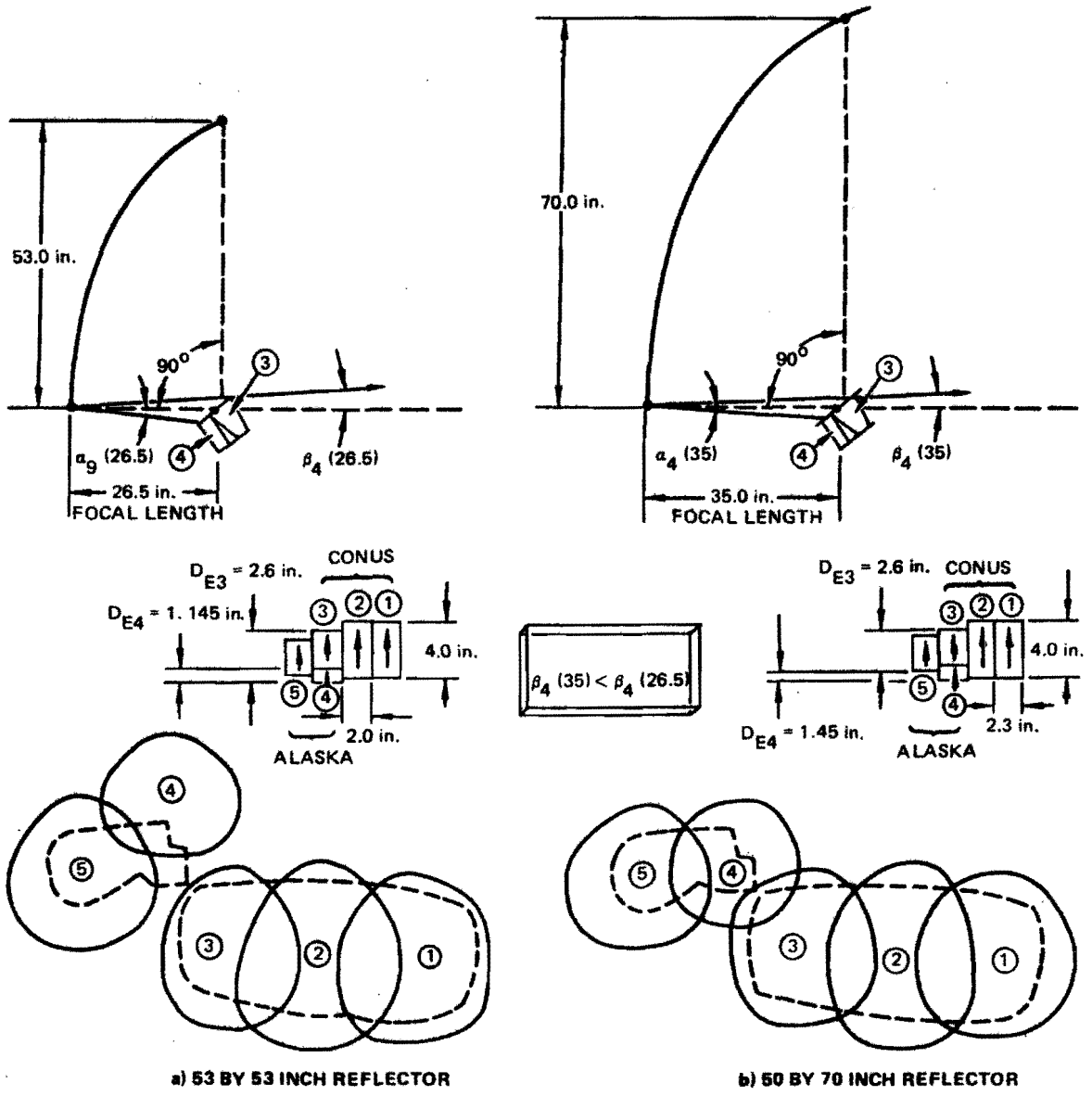


Fig. 4.19. Beam Shaping Trade

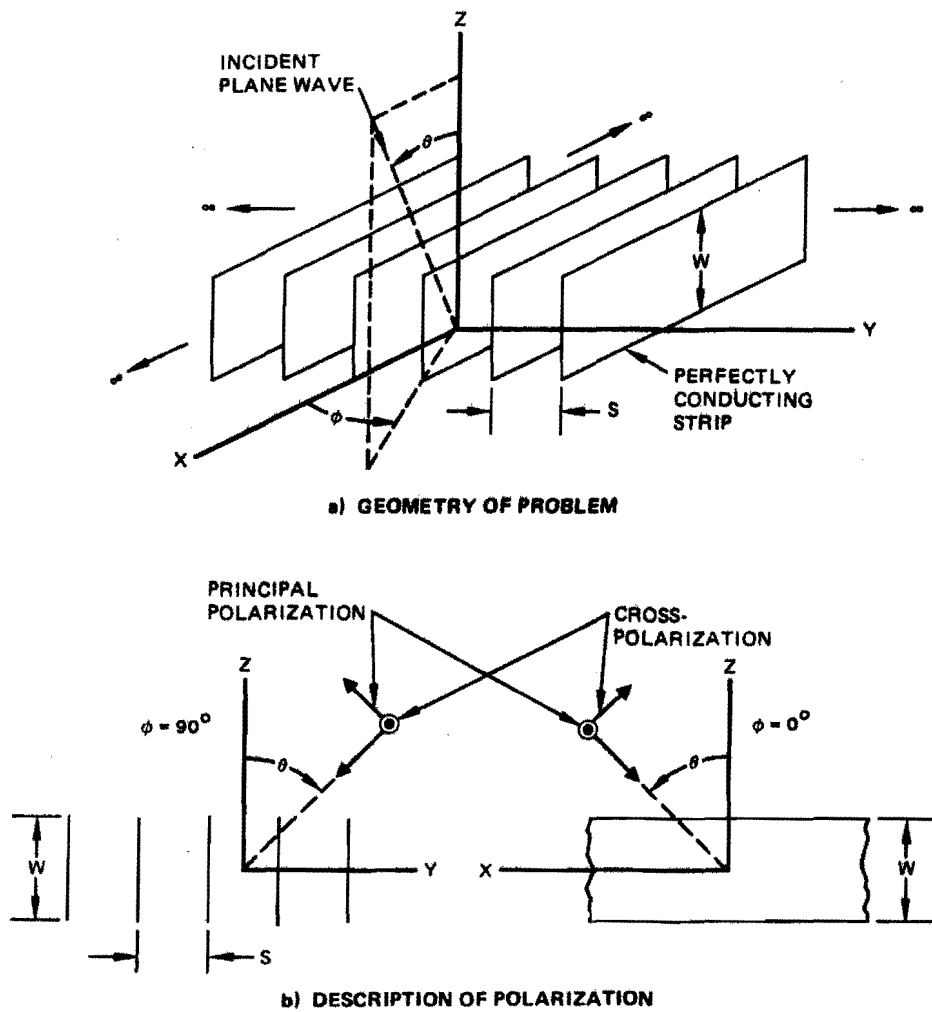


Fig. 4.20. Plane Wave Incidence on an Infinite Strip Grating

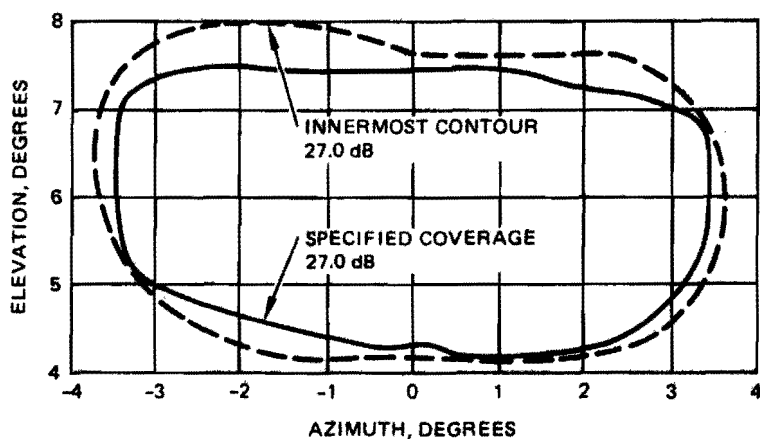


Fig. 4.21. Horizontal Polarization CONUS Downlink Innermost Contours

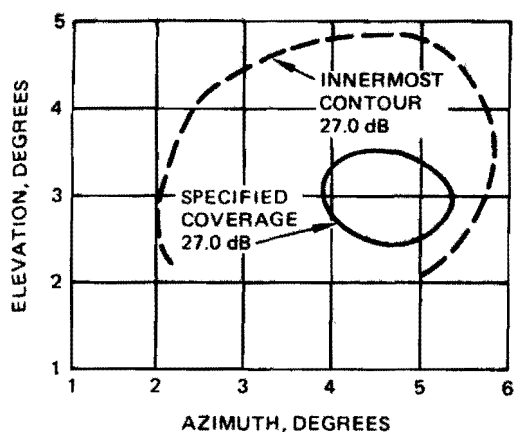


Fig. 4.22. Puerto Rico Downlink Innermost Contour

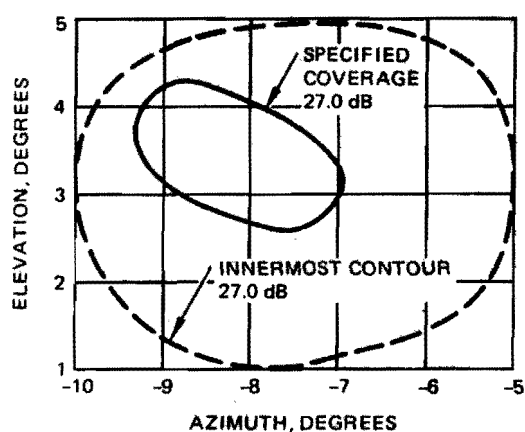


Fig. 4.23. Hawaii Downlink Innermost Contour

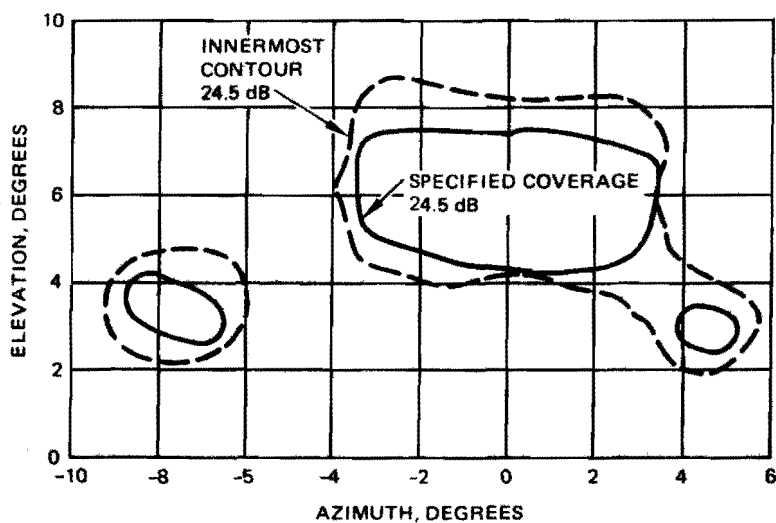


Fig. 4.24. Horizontal Polarization Uplink Innermost Contours

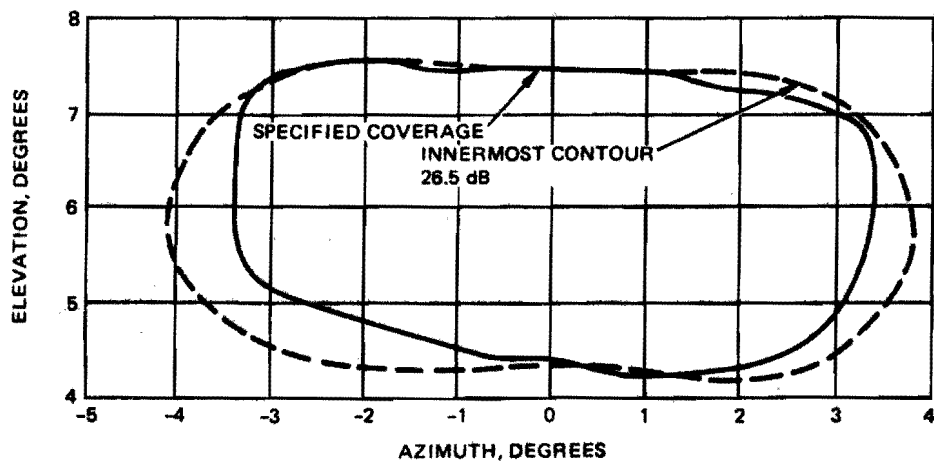


Fig. 4.25. Vertical Polarization CONUS Downlink Innermost Contours

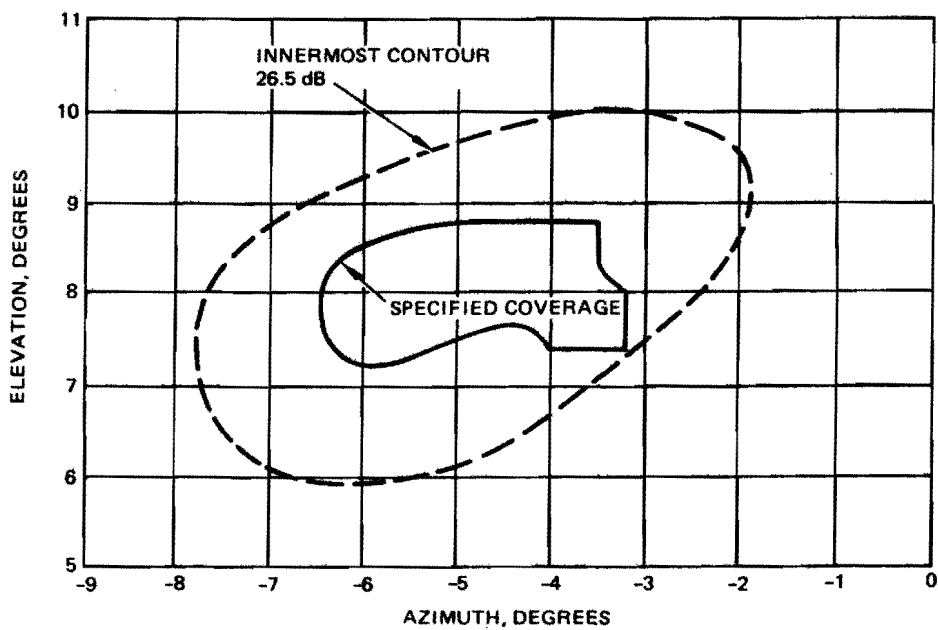
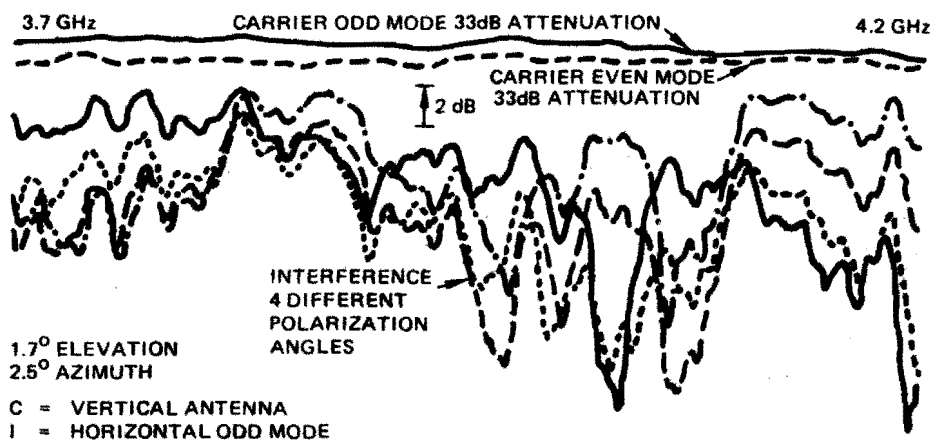
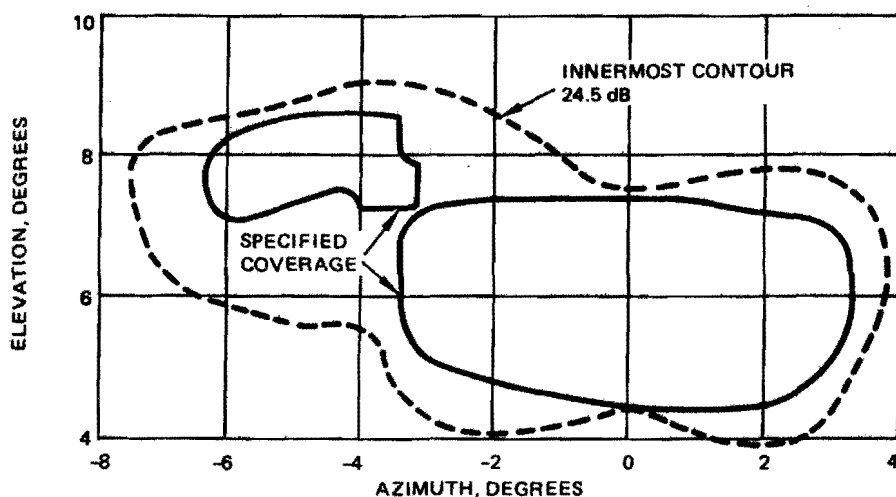
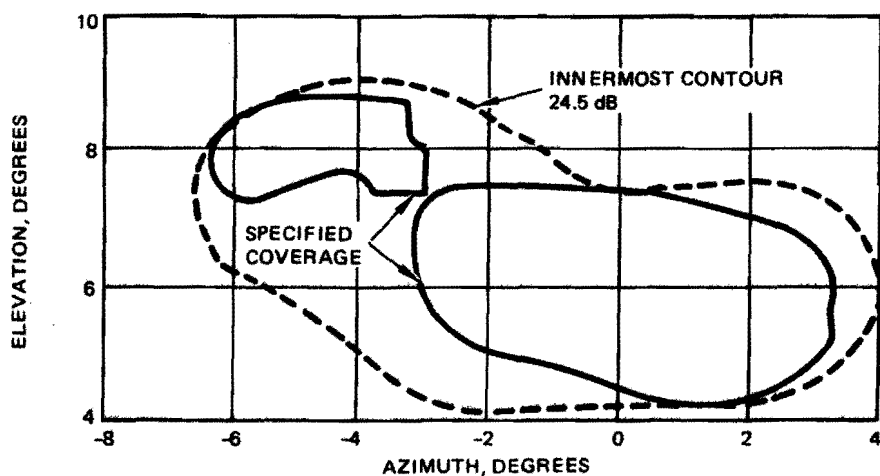


Fig. 4.26. Vertical Polarization Alaska Downlink Innermost Contours





#### 4.6. Satellite Business Systems (SBS) communications antenna

##### 4.6.1. General description

The Satellite Business Systems (SBS) communications satellite was designed to provide ten communications channels operating in the 14/12 GHz frequency band. Each channel is capable of accommodating digital data or voice in the time division multiple access (TDMA) mode, analog or digital signals in the frequency division multiple access (FDMA) mode, or frequency modulation (FM) monochrome or color television signals.

The SBS communications antenna has an unique design feature that utilizes an offset shared-aperture dual grid reflector. This linearly polarized reflector design consists of two orthogonally polarized offset grid reflectors, one behind the other, sharing the same aperture area with a projection 72 inches in diameter. The front grid reflector is horizontally polarized and is transparent to the vertically polarized signals, which are reflected by the rear grid reflector. Polarization selection for each reflector is accomplished by bonding conductive grids to a Kevlar honeycomb laminated paraboloidal shell. Thermal distortion of the reflector assembly is minimized by an aluminized Kapton sunshield covering the reflector aperture. Vacuum deposited aluminum (VDA) is applied to the rear (reflector facing) side of the sunshield and is etched to form a grid of squares which allows virtually loss-free RF transmission. The outer (feed facing) side of the sunshield is coated with a single layer of germanium to reduce optical transmittance and maintain low temperature gradients across the reflector structure.

Each grid reflector is fed by a multihorn feed. The feed for the vertically polarized rear reflector is for receive only and contains a four-horn subarray arranged in a conventional monopulse circuit to provide RF tracking. It is capable of maintaining beam pointing errors within  $\pm 0.05^\circ$ . When the spacecraft is in the transfer orbit, the reflector assembly is deployed by the antenna positioner mechanism (APM), a redundant stepper-motor-driven differential gear assembly. During this deployment, the T&C antenna orientation is maintained nearly parallel to the spacecraft spin axis by a linkage system.

#### 4.6.2. Antenna design

The antenna consists of two essentially independent offset grid reflectors, one horizontally polarized (transmit) and one vertically polarized (receive), each illuminated by a multihorn feed. Independent feed designs allow optimal performance of both the transmit beam and the receive beam.

The focal lengths (60 inches) and the projected aperture diameters (72 inches) of the two grid reflectors are identical; however, the base of the vertical grid reflector is offset 5.5 inches from the horizontal reflector to separate the focal point. This offset allows the positioning of each feed assembly at its respective focus without physical interference with the other.

##### 4.6.2.1. Reflector grid design

A grid reflector reflects waves that are polarized parallel to its conducting grid and is nearly transparent to the waves polarized orthogonal to the grids. The electrical design of the grid reflector is based on plane wave scattering properties from an infinite array of parallel conducting strips. The geometry is described by conductors of width,  $W$ , thickness,  $T$ , and spacing,  $S$ , over a thin dielectric sheet of thickness,  $t$ , and dielectric constant,  $E$ , as shown in Fig. 4.30.

The grid chosen has the following geometry:  $W = 0.015$  inch,  $T = 0.015$  inch,  $S = 0.03$  inch, and  $t = 0.0015$  inch (the Kapton thickness). The conducting grid is formed by photoetching copper-clad Kapton. Computed transmission and reflection characteristics of this grid design, where the plane of incidence is parallel and perpendicular to the strips, are shown in Table 4.2. The predicted insertion loss for the waves perpendicular to the grid is less than 0.1 dB and the reflection coefficient of waves parallel to the grid is almost unity; both were verified by measurements.

##### 4.6.2.2. Transmit feed design

The required antenna coverage is divided into six regions which are shown in Fig. 4.31. The gain specifications are given in Table 4.3 for each

region plus the cities of San Francisco and Los Angeles. Note that CONUS beam must be contoured to the CONUS shape and also weighted (shaped) to provide higher gain over the eastern third of CONUS. This higher gain is achieved with an array of eight horns (Fig. 4.32), fed by a dual-mode power distribution network which has the property of dividing the power equally or unequally to three horns from two isolated input ports. A schematic of the feed network is shown in Fig. 4.33, and a calculated gain contour plot is shown in Fig. 4.34.

#### 4.6.2.3. Receive feed design

For receive region I is required to have 4.5 dB more gain than the major CONUS coverage region (region III). Beam contouring and shaping are met with an array of thirteen horns (Fig. 4.35). Six of these horns are designed to produce a tapered aperture illumination in the E-plane and a quasi-uniform illumination in the H-plane. This design is achieved by the use of corrugated walls in the H-plane and partial dielectric loading on the walls in the E-plane. The remaining seven horns are conventional pyramidal horns. Four of the horns are connected to a conventional monopulse tracking network for beacon tracking. A schematic of this network is shown in Fig. 4.36, and a calculated gain contour plot is shown in Fig. 4.37.

Table 4.2. Computer and Measured Transmission and Reflection Characteristics of Grid Design

### Plane of Incidence Perpendicular to Strip Conductors

### Parallel Polarization: Electric Field Parallel to Strips

### Perpendicular Polarization: Electric Field Perpendicular to Strips

Frequency, GHz	Parallel Polarization Reflection Coefficient (Magnitude)				Perpendicular Polarization Transmission Loss, dB			
	Computed		Measured		Computed		Measured	
	$\theta = 0^\circ$	$\theta = 30^\circ$	$\theta = 0^\circ$	$\theta = 30^\circ$	$\theta = 0^\circ$	$\theta = 30^\circ$	$\theta = 0^\circ$	$\theta = 30^\circ$
11.7 to 12.2	0.99995	0.99996	$\approx 1.0$	—	0.04	0.02	<0.1	—
14.0 to 14.5	0.99993	0.99994	$\approx 1.0$	—	0.04	0.03	<0.1	—

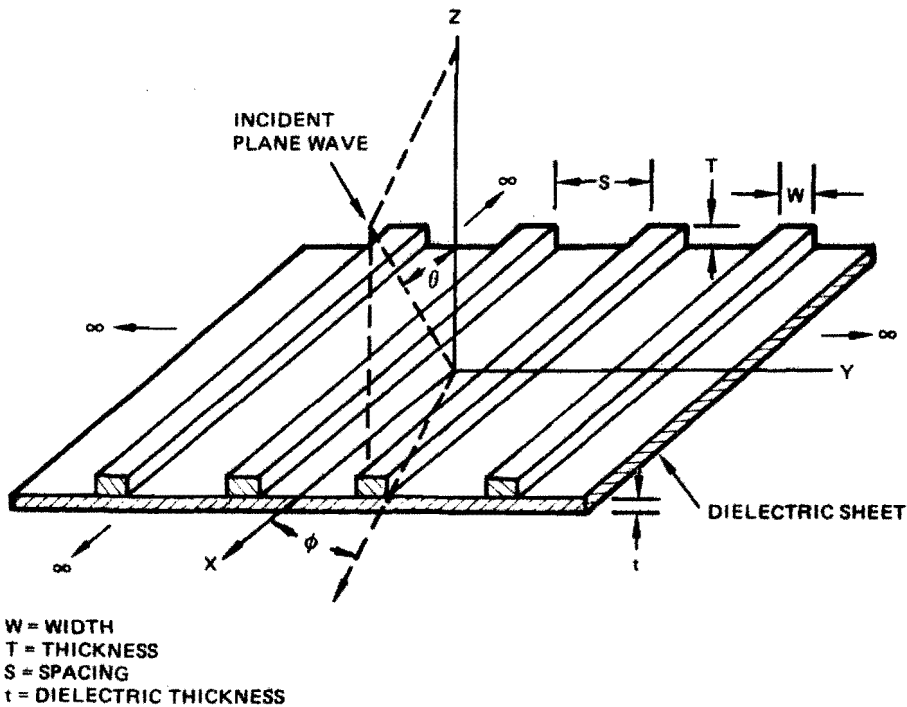
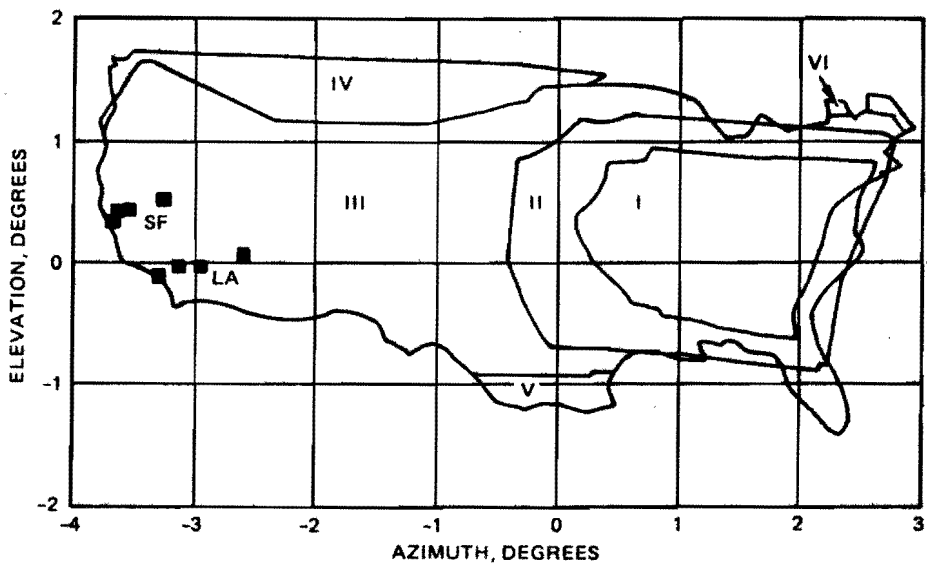


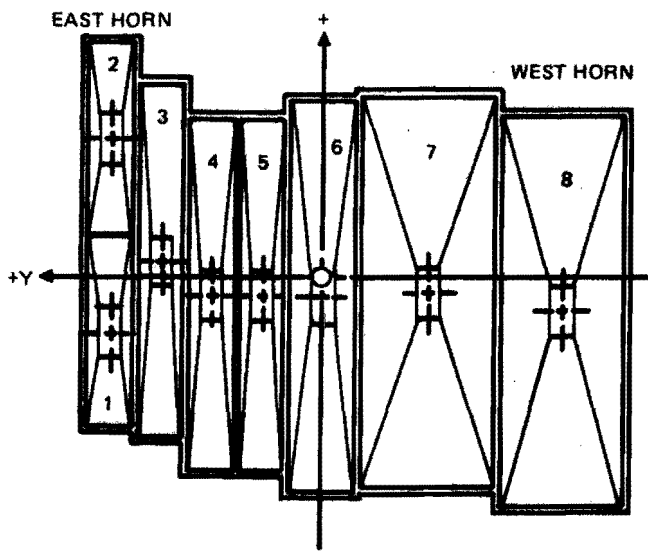
Fig. 4.30. Reflective Grids Electrical Design Model

*Table 4.3. SBS Antenna Transmit and Receive Gain Specifications*

Region	Specified Transmit Gain	Specified Receive Gain
I	33.7	33.5
II	31.7	31.5
III	30.0	29.0
IV	27.0	26.0
V	28.0	27.0
VI	29.0	26.0
San Francisco	32.0	32.0
Los Angeles	31.2	31.2



*Fig. 4.31. SBS Antenna Coverage Map - Composite of 100°, 110°, 120°, and 130° W Longitude*



HORN	E-PLANE HEIGHT, in.	H-PLANE HEIGHT, in.	HORN LOCATION	
			X	Y
1	0.78	2.83	-0.812	3.32
2	0.78	2.83	2.038	3.32
3	0.78	5.20	0.231	2.52
4	0.78	5.20	-0.280	1.72
5	0.78	5.20	-0.280	0.92
6	1.10	5.80	-0.300	-0.04
7	2.22	5.80	-0.231	-1.72
8	2.00	5.80	-0.500	-3.85

Fig. 4.32. Transmit Feed Horn Array Configuration

HORN	ODD MODE		EVEN MODE	
	POWER	PHASE	POWER	PHASE
1	0.060	-45.3°	0.069	48.6°
2	0.010	-45.3°	0.011	48.8°
3	0.132	-44.8°	0.127	43.8°
4	0.132	-44.8°	0.127	43.8°
5	0.140	-20.0°	0.139	20.0°
6	0.131	20.0°	0.134	-20.0°
7	0.195	58.5°	0.192	-63.2°
8	0.206	61.5°	0.203	-60.3°

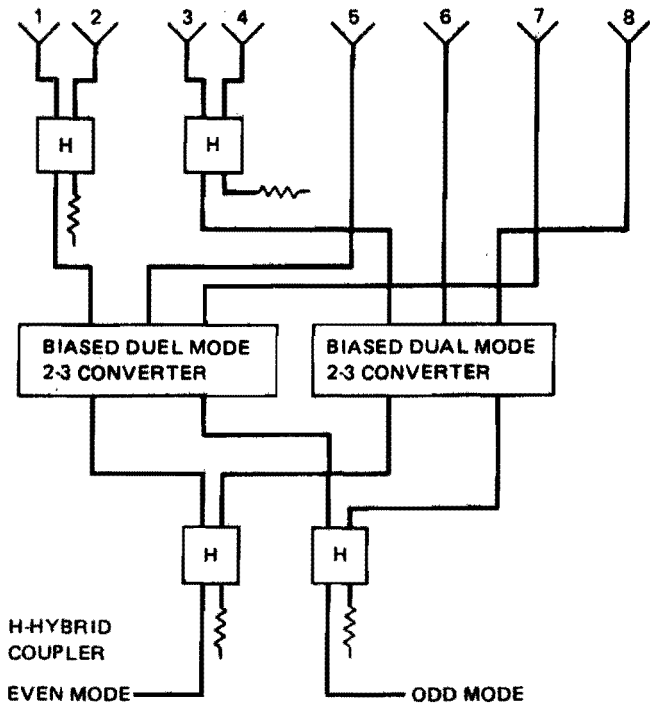


Fig. 4.33. Transmit Feed Network



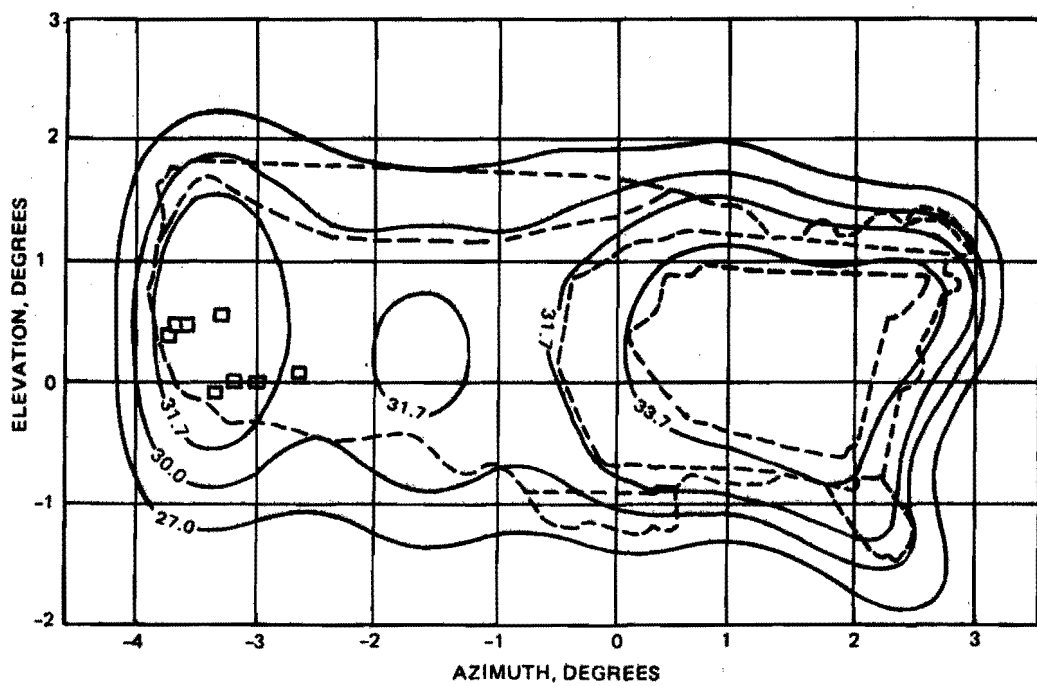
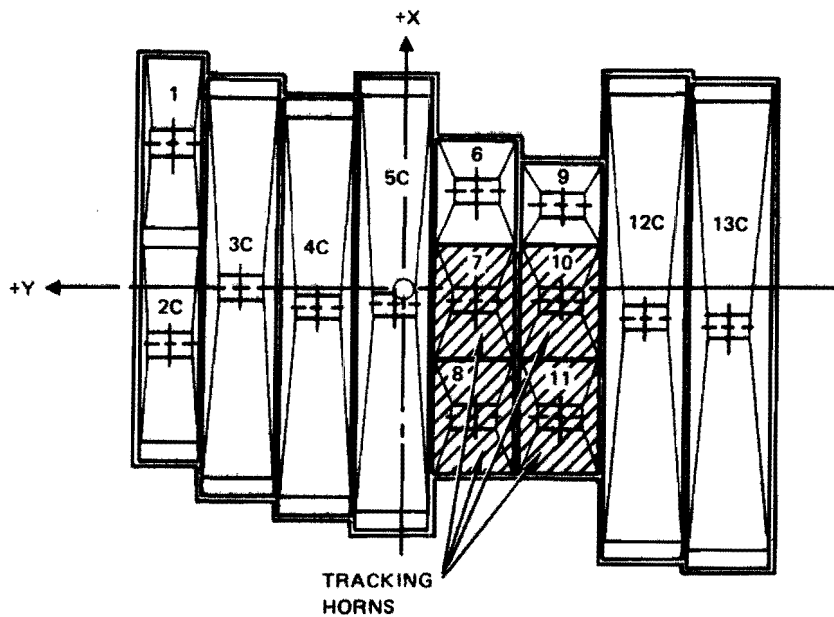


Fig. 4.34. Computed Transmit Antenna Gain Contours at 11.95 GHz



HORN	WIDTH H-PLANE*, in.	HEIGHT E-PLANE*, in.	HORN LOCATION	
			X	Y
1	0.82	2.19	1.918	3.168
2C	0.82	2.968	-0.681	3.168
3C	1.025	5.340	0.064	2.226
4C	1.025	5.340	-0.344	1.181
5C	1.025	5.810	-0.204	0.136
6	1.135	1.360	1.295	-0.965
7	1.135	1.460	-0.135	-0.965
8	1.135	1.460	-1.615	-0.965
9	1.135	1.045	1.138	-2.120
10	1.135	1.460	-0.135	-2.120
11	1.135	1.460	-1.615	-2.120
12C	1.135	6.223	-0.268	-3.275
13C	1.135	6.223	-0.548	-4.430

C - CORRUGATED FEED  
\* INCLUDES CORRUGATION WHERE APPLICABLE

Fig. 4.35. Receive Feed Horn Array Configuration

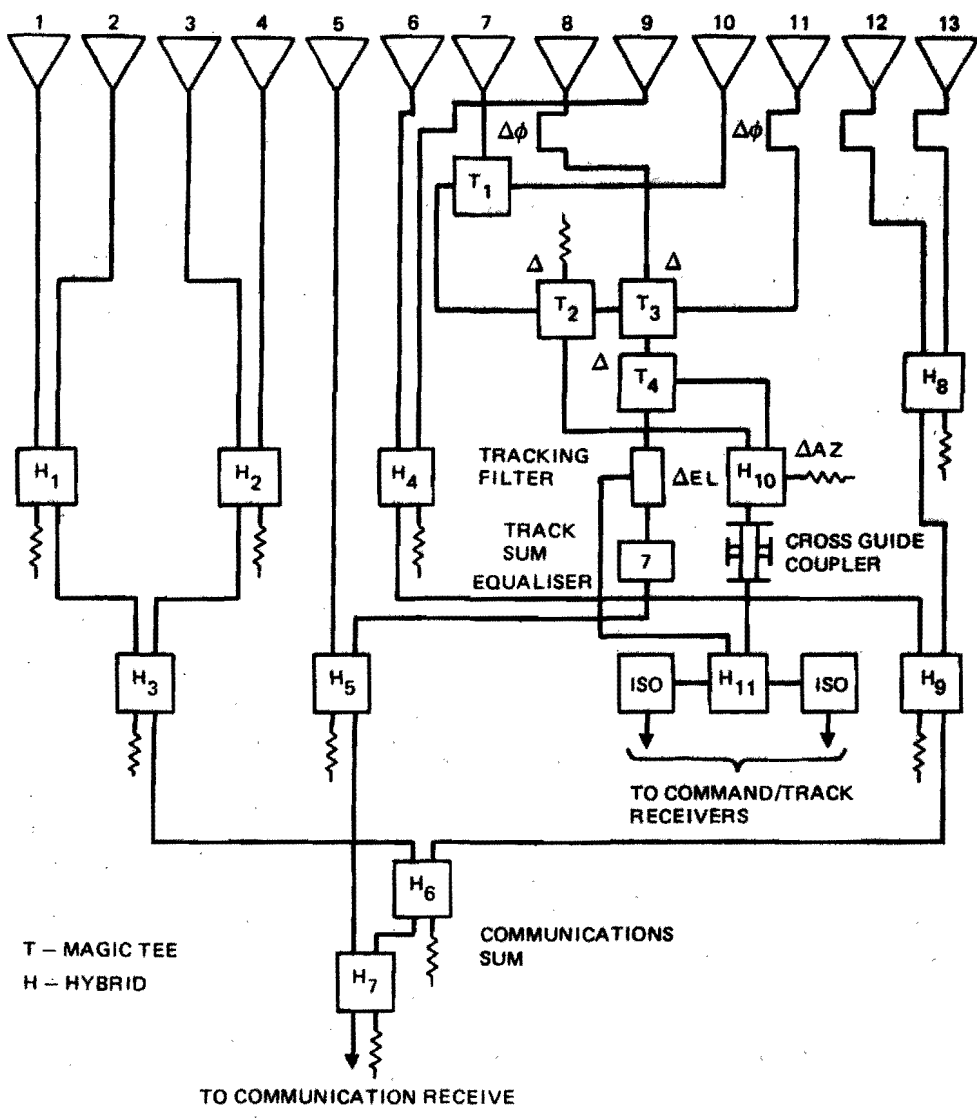


Fig. 4.36. Receive Feed Network

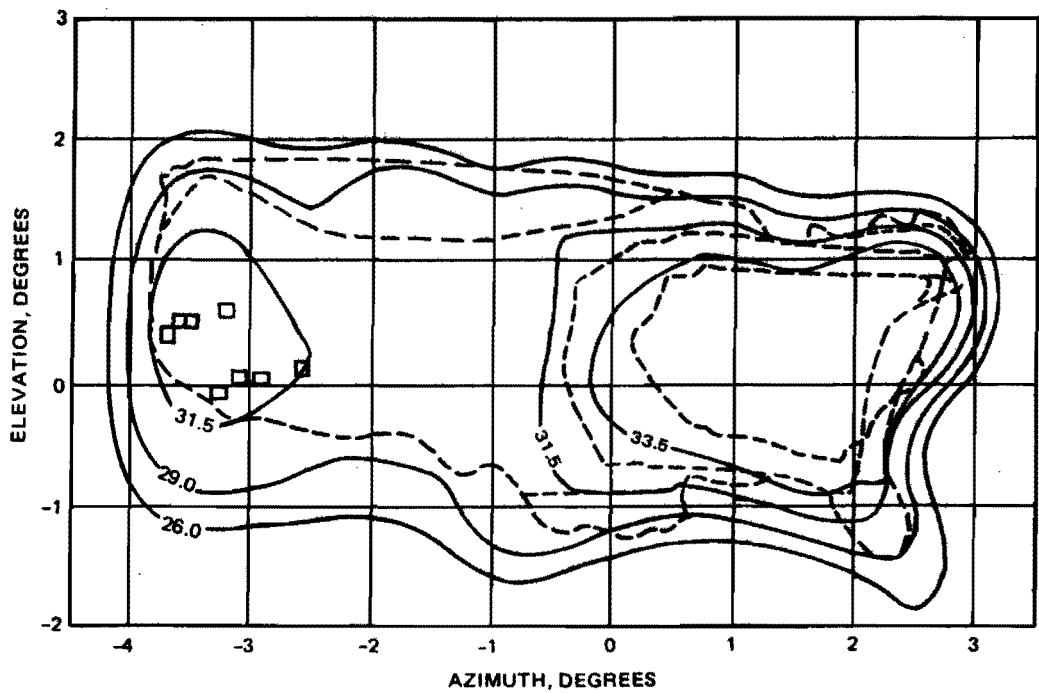


Fig. 4.37. Computed Receive Antenna Gain Contours at 14.25 GHz

#### 4.7. Intelsat IVA communications antenna

##### 4.7.1. General description

###### 4.7.1.1. Introduction

The Intelsat IVA spacecraft is the second generation of the Intelsat IV series of communication satellites. Increased channel capacity is achieved by reuse of the 500 MHz frequency spectrum by means of antenna beam shaping and spatial isolation. The communications antenna subsystem consists of two offset reflector antennas for transmit and one offset reflector antenna for receive, all supported by a tubular mast. A sketch of the antenna farm is shown in Fig. 4.38. The feed horn arrays and the earth coverage horns are cantilevered from the mast with the T&C antenna mounted at the top of the mast.

The frequency and polarization plan of Intelsat IVA is shown in Fig. 4.39. As indicated, the frequency band is divided into 12 channels, each 36 MHz wide and spaced at 40 MHz intervals. Channels 6, 8, 10, and 12 are used for earth coverage, while the other eight channels are available for frequency reuse resulting in an effective 20-channel capability. The shaped-beam coverage requirements are shown in Fig. 4.40, indicating coverage of the Intelsat stations for both the Atlantic and Pacific basins. The receive antenna provides coverage over each hemispheric area with a single beam, while the two transmit antennas provide coverage over each hemispheric area with two beams, one for the northern and one for the southern coverage.

###### 4.7.1.2. Transmit antenna

The transmit antenna consists of two identical offset parabolic reflectors, each fed by an array of circularly polarized feed horns. One antenna servicing all the odd-channel transponders provides full coverage in the eastern and western regions with both quadrant and hemispheric (T-mode) modes of operation. The second antenna servicing the four even-channel transponders provides only quadrant coverage for the northern portion of the eastern and western areas.

The feed array for the odd-channel antenna consists of 37 square horns with built-in septum polarizers, fed by a transverse electromagnetic (TEM) transverse squarax transmission line power division network. The physical arrangement of the feed horns in the aperture plane and the associated TEM networks are shown in Fig. 4.41. Two of the West horns are on or off switchable to accommodate differences between Pacific and Atlantic coverage requirements. The North and South feed clusters have separate input terminals for quadrant and hemispheric coverages. Since the even-channel antenna is not required to provide hemispheric coverages, it has only 19 feed horns, nine for the Northeast beam and ten for providing the Northwest beam.

The feed network is constructed using the squarax transmission line technology because of its packing efficiency. The TEM squarax transmission line consists of a 0.50 square inch outer conductor with a 0.20-square inch center conductor. At the input port of the feed network, a waveguide-to-squarax adapter is used for transition from the one-half height WR-229 waveguide to the square coaxial line. At the output port of each horn, signal transmission from the TEM squarax mode to the  $TE_{10}$  mode in the WR-229 waveguide is accomplished with a transition.

#### 4.7.1.3. Receive antenna

The shaped beam receive antenna consists of an offset parabolic reflector fed by a 17-horn array. This antenna forms two beams covering the eastern and western areas with an east-to-west beam isolation of 27 dB. The arrangement of the receive feed array horns, along with the power summing network, is shown in Fig. 4.42.

The design of the receive power summing network is similar to the transmit antenna: directional couplers provide the correct amplitude distribution and the transmission line length provides the correct phase distribution. Switches designed in squarax line are used to accommodate differences between Atlantic and Pacific basin coverage requirements. For the Atlantic region, the complete eastern beam is activated, while the western beam has two horns deactivated. For the Pacific region, the southern portion of the eastern beam is deactivated, while two additional horns are activated in the western beam to provide New Zealand and Fiji coverage.

#### 4.7.1.4. Reflectors

All three offset parabolic reflectors are constructed using a woven metal mesh attached to an open web frame. The transmit reflector is offset 12 inches from the focal axis and has a 50-inch focal length and a 53 by 53 inch square projected area. The reflector is further trimmed with 17-inch radial rounded corners and the sides are sloped in by 3.7 inches at the base for the payload shroud clearance. The receive reflector is offset 8 inches from the focal axis and has a 33.33-inch focal length and a 35 by 35 inch square projected aperture with 9.5-inch radial rounded corners.

#### 4.7.2. Antenna design trades

##### 4.7.2.1. Low-sidelobe pattern synthesis

Low sidelobe shaped-beam patterns can be synthesized by cancellation of sidelobes of individual feed horns. To illustrate this, consider three feed horns that are horizontally arrayed about the focal point. As shown in Fig. 4.43(a) if the relative beam displacement is equal to the nominal sidelobe width, the sidelobes of the two outer beams are in phase with each other, but are  $180^\circ$  out of phase with sidelobes of the center beam. This yields a low sidelobe beam, shown in Fig. 4.43(b), if the outer beams are properly weighed in amplitude relative to the center beam.

The success of this sidelobe suppression technique depends on three factors. First, the cancellation concept is based on the assumption that the component pattern sidelobes are uniformly spaced and are approximately equal in width. This is true for a wide variety of aperture distributions, and no severe restrictions are imposed on the design concept. Second, effective sidelobe cancellation depends upon achieving the appropriate component beam shifts. A relatively straightforward analysis indicates that the proper pattern shifts can be obtained when the outer horns of the three feed array are displaced from the focal point by the amount given by

$$X = \pm \frac{\lambda}{4} \frac{2 + (D/2f)^2}{(d/2f)}$$

Alternatively, the beam deviation factor can be measured experimentally, and the results can be used to specify the feed displacement. From this relationship, the horn size is determined.

The third factor affecting sidelobe cancellation is the selection of relative power for each of the three feedhorns. To get feed sidelobe cancellation, nominally, the relative power of the center horn should be about 6 dB greater than that of the two outer horns. In practice, the relative power usually differs from this value, and further improvement in sidelobe suppression is achieved by adjusting the relative phase of each feed horn. For the design of Intelsat IVA antennas, an optimization algorithm based on the steepest descent search technique was developed. This algorithm optimizes the amplitude and phase excitations of the feed horns to simultaneously achieve the desired beam shape and gain over a specified coverage area and sidelobe level over another specified coverage area.

#### 4.7.2.2. Effects of aperture blockage

Aperture blockage by the feed assembly can be avoided by further offsetting of the reflector with the bottom edge of the reflector raised above the focal axis. The reflectors used for the Intelsat IVA transmit and receive antenna have their bottom edge 12 and 8 inches above the focal axis, respectively.

#### 4.7.2.3. Reflector geometry/dual-mode tradeoff

Early in the design phase, the reflector geometry under consideration was a 53 inch diameter, 37.5-inch focal length, offset paraboloid projecting a circular aperture having a 7-inch offset from the focal axis. For dual-mode operation (even and off channels on same reflector), this reflector gave excessive mode shift so that the desired coverages (Fig. 4.40) could not be achieved with the innermost contours of both modes. The focal length was then increased to 50 inches, the maximum allowable. The resultant mode shift decreased slightly. If the reflector boresight is moved to the center of the North beam, the modal shift for that beam becomes less; however, the shift for the South beam increases. Consequently, the dual-mode consideration was dropped.



In the dual-reflector antenna approach, the even and odd channels are handled by separate reflectors. This approach allows greater flexibility for adjusting horn amplitude and phase for beam shaping and sidelobe control. As a result both the beam shapes and coverage gain specifications were met. However, sidelobes in the diagonal planes were too high, in particular, the sidelobes of the Southwest beam for Atlantic coverage over the Northeast region. For this reason, the reflector shape was changed, allowing the offset paraboloid to project a rounded square aperture, since the sidelobes from a square aperture in the diagonal planes are lower than that of a circular aperture.

#### 4.7.3. Antenna performance

##### 4.7.3.1. Transmit antenna performance

The feed system for the antenna servicing the odd-channel repeaters consists of 19 horns for the east coverage and 18 horns for the west coverage. Two of the west horns are switchable to discriminate between Pacific and Atlantic coverage requirements.

##### East coverage

The Northeast (NE) spot beam, plus Canary Islands and Senegal coverage, is obtained with a feed consisting of nine 2.80-inch square aperture horns (Fig. 4.41). The predicted coverage gain and sidelobe contours are shown in Fig. 4.44(a).

The Southeast (SE) spot beam, plus Ascension Island coverage (-7 dB below primary), is formed with ten 3.20-inch square aperture horns. The predicted coverage and sidelobe contours are shown in Fig. 4.44(b).

The hemispheric, or T-mode coverage, gain requirement is 3 dB less than that of spot beam coverage; the C/I specifications are identical. The optimum eastern T-mode coverage is obtained by having the T-switch network in the repeater system divide the power equally between the Northeast and the Southeast feed clusters.

#### West coverage

The western coverage has two modes of operation, namely, the Atlantic (basin) mode and the Pacific (basin) mode. To distinguish the two, the nomenclature Region/Pac and Region/Atl are used. The western primary coverage, plus the offshore coverage regions of New Zealand, Fiji and Indonesia, is achieved with a feed cluster of 18 horns. Two of these horns, switch activated to achieve coverage for New Zealand and Fiji, are used solely for Pacific operation.

The Northwest spot beam is formed with ten 3.20-inch square aperture horns. The predicted coverage gain and sidelobe contours are shown in Fig. 4.45(a). The Southwest spot beam is formed with six horns for the Atlantic mode and with eight horns for Pacific operation. All horns have 3.2-inch square apertures. Excitation of the two horns for New Zealand and Fiji (NZ/F) for SW/Pac is provided by a switchable TEM squarax hybrid coupler. The switch/coupler passes all the power in the Southwest transmission line to the six horn cluster when the switch is off and diverts 16.8 percent of the input power to the NZ/F horns when activated. The predicted spot beam gain and sidelobe contours are shown in Fig. 4.45(b) for SW/Atl and Fig. 4.45(c) for SW/Pac.

#### 4.7.3.2. Receive antenna performance

The receive antenna feed consists of 17 horns for the east coverage and 17 horns for the west coverage. Two of the west horns are switchable to discriminate between Pacific and Atlantic coverage requirements. A switched coupler is located in the West TEM feed network to provide this capability. An option is available for a switch/coupler in the East network to suppress the signal from the southern portion of the East beam for Pacific operation if sidelobes into the New Zealand region from the East beam become excessive.

#### 4.7.3.3. Measured results

Measured antenna pattern results for all the beams and C/I combinations are too numerous to include here; therefore, only a limited number of measured results are presented.

Measured transmit antenna gain contours of the principal downlink beams are shown in Fig. 4.46. Measured receive antenna contours are very close to the predicted values shown earlier and are not included. Typical C/I contours are shown in Fig. 4.47. The specified contours shown are for the cases where the carrier is the beam over the coverage area and the interference is caused by beams covering the opposite hemisphere. For example, the interference to the Northwest beam comes from the Northeast beam shown in Fig. 4.47(a) and from the Southeast beam shown in Fig. 4.47(b).

#### Reference

1. Han, C.C., et all., "Satellite communications: advanced technologies," 6th AIAA Communications Satellite Systems Conference, Montreal, 1976.

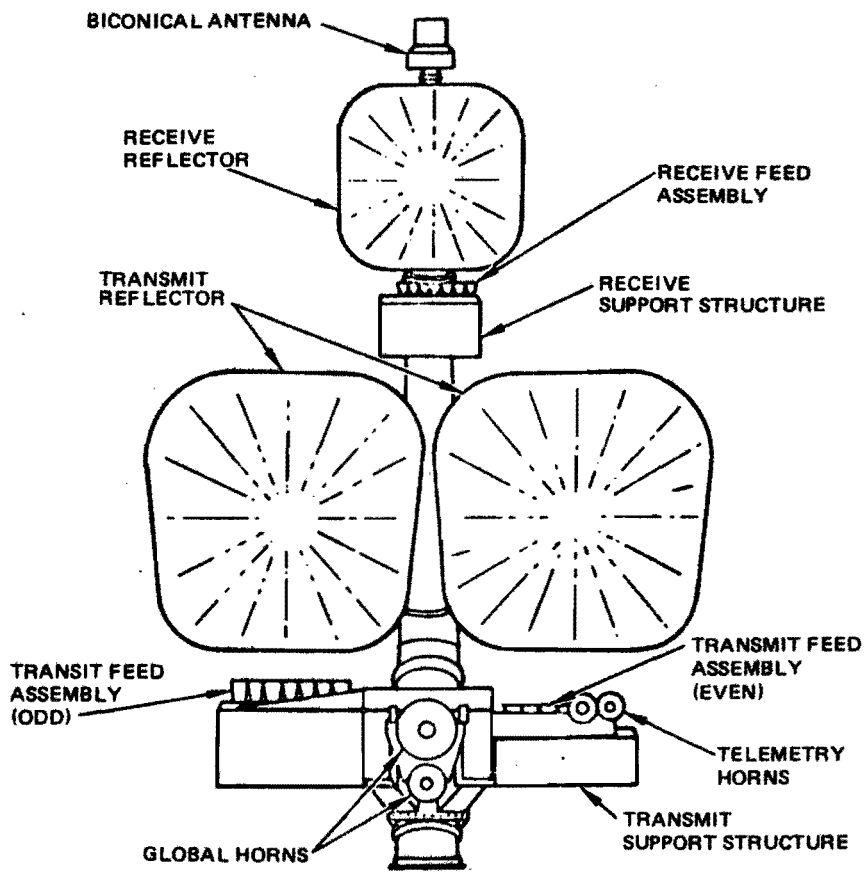


Fig. 4.38. Intelsat IVA Antenna Farm

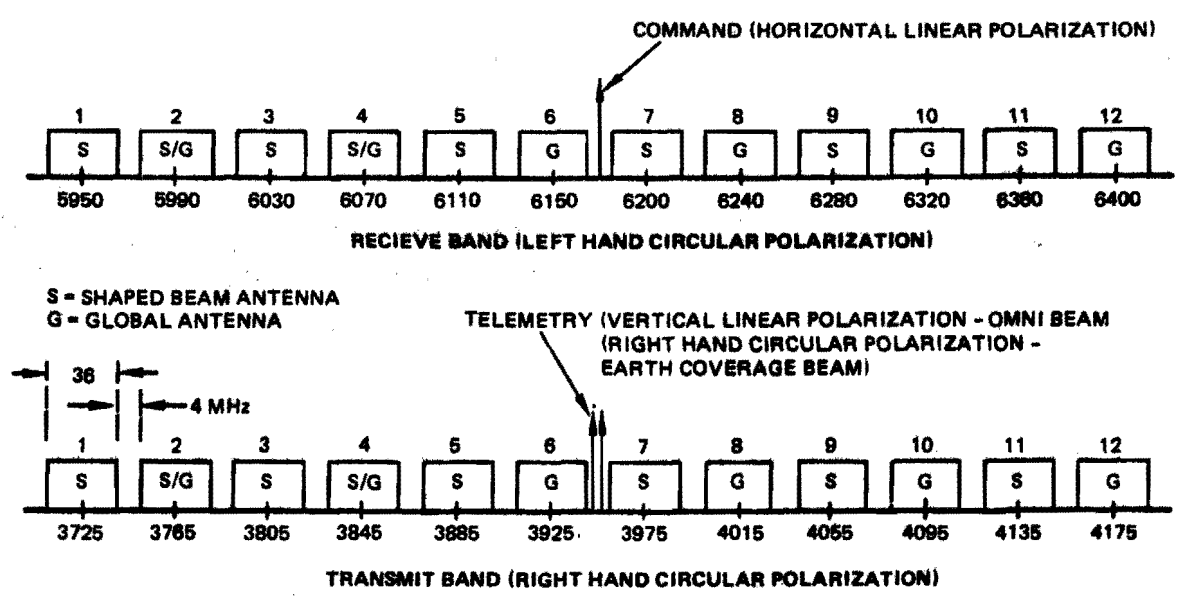


Fig. 4.39. Intelsat IVA Frequency and Polarization Plan

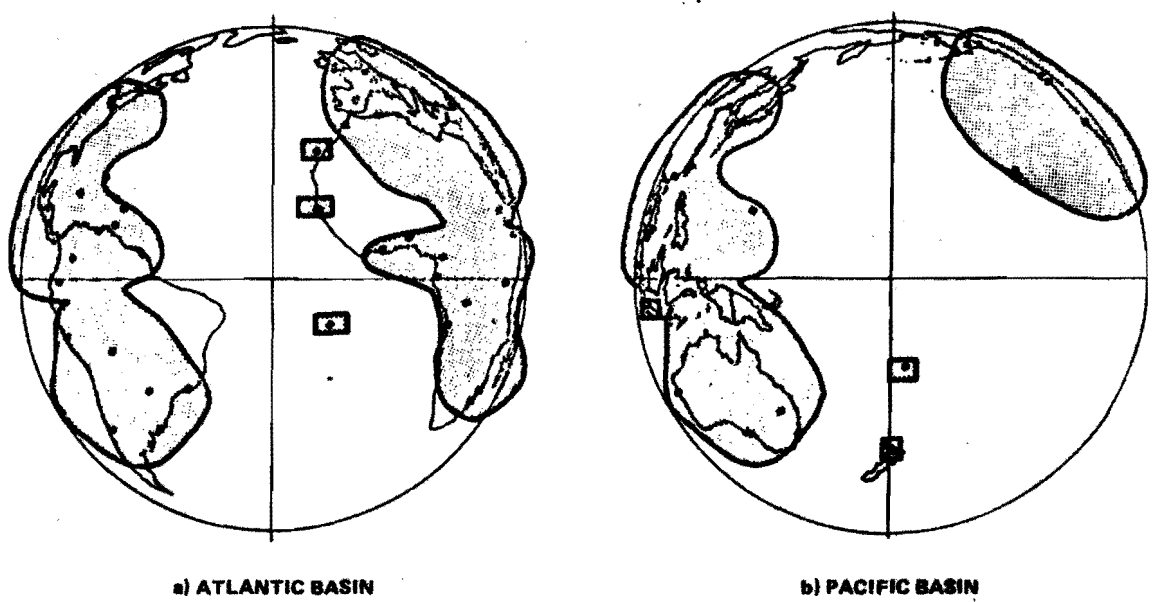
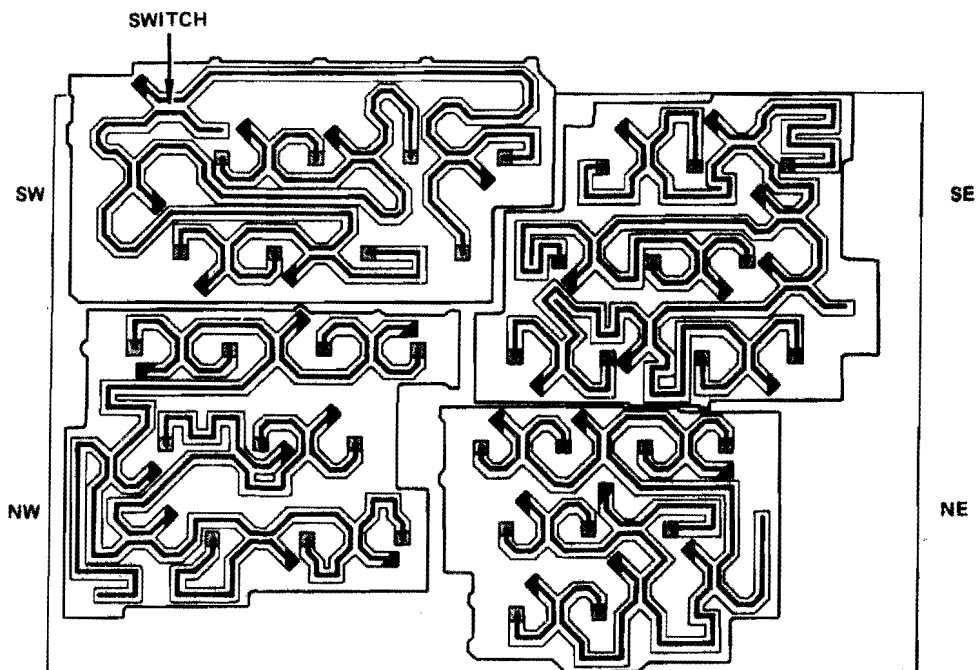
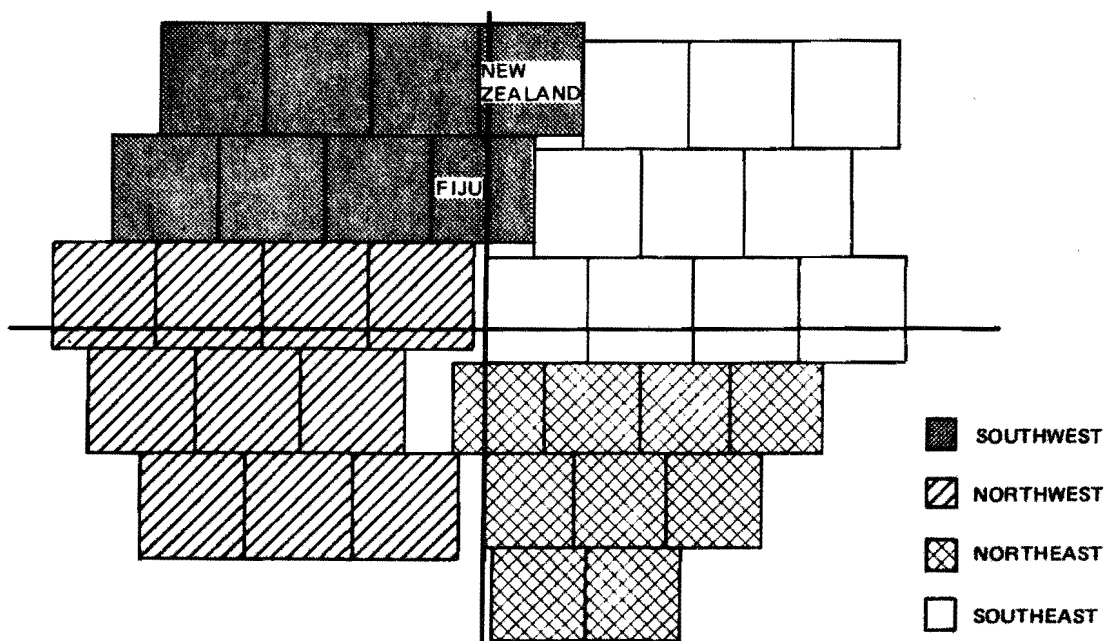


Fig. 4.40. Intelsat IVA Coverage Requirements



a) ASSOCIATED TEM SQUARAX NETWORKS



b) PHYSICAL ARRANGEMENT OF FEED HORNS IN APERTURE PLANE

Fig. 4.41. Odd-Channel Transmit Antenna Feed System

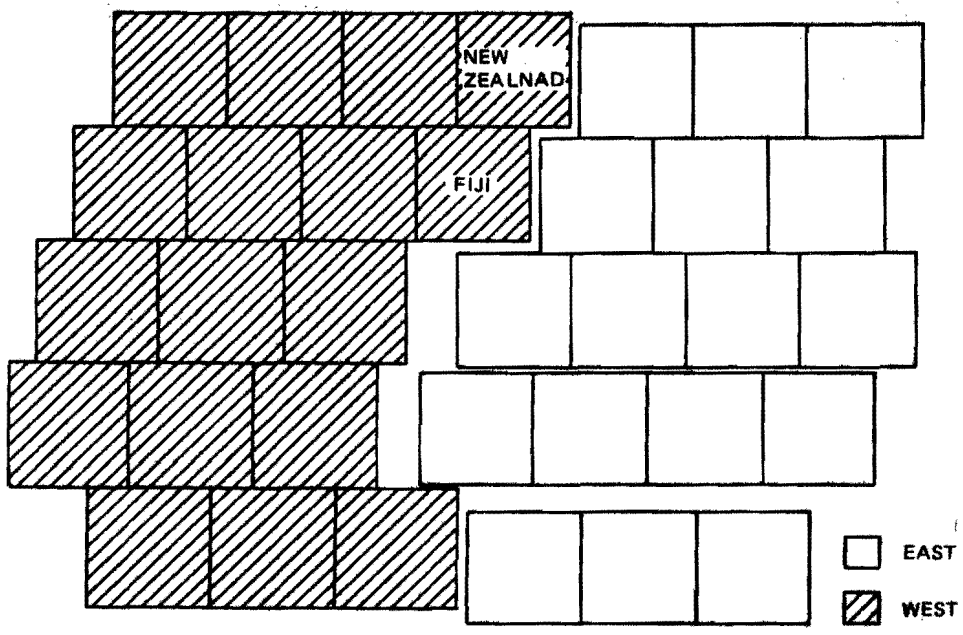
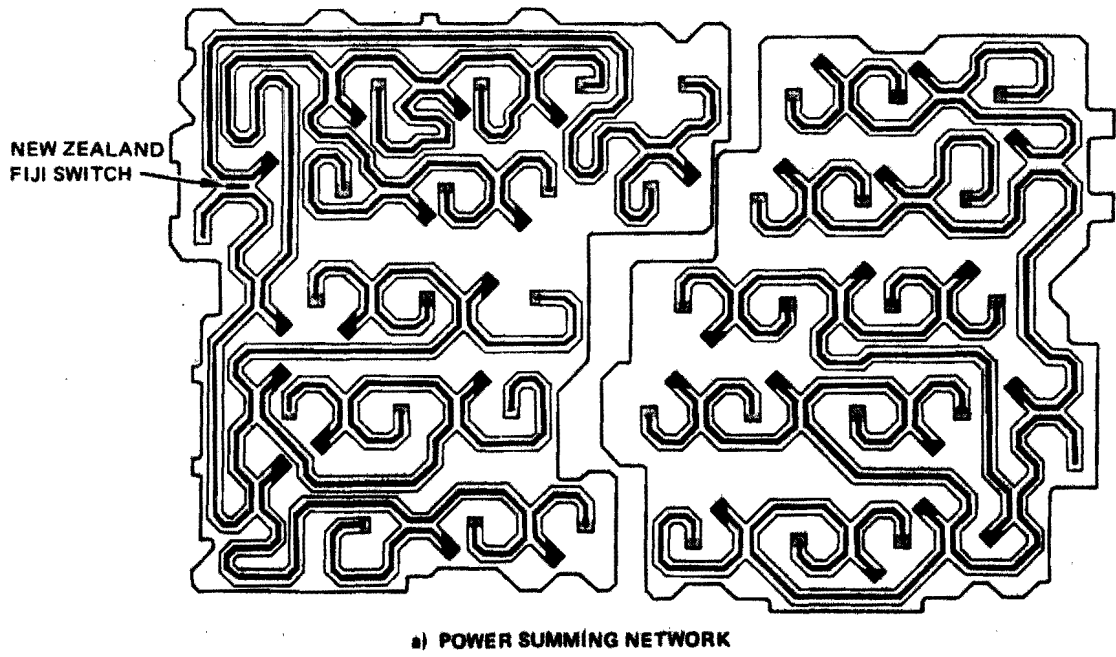
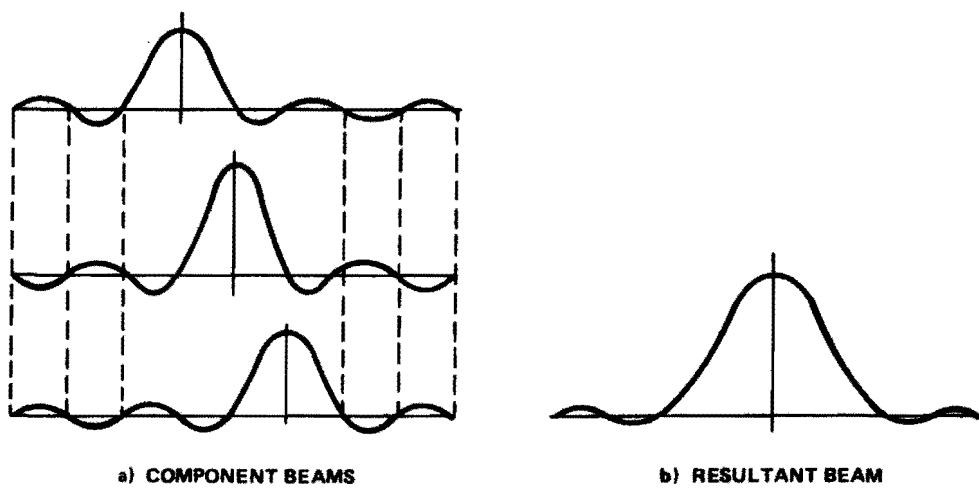
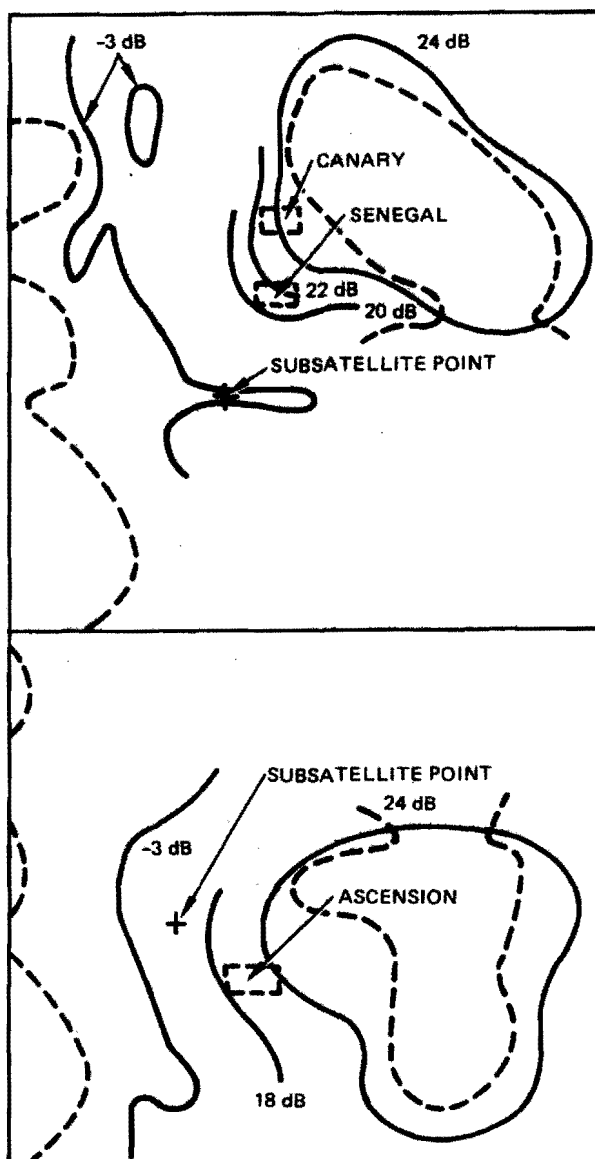


Fig. 4.42. Receive Antenna Feed System



*Fig. 4.43 Cancellation of Sidelobes of Three Beams*





a) NORTHEAST TRANSMIT CONTOURS  
ANTENNA BORESIGHT 1°N

b) SOUTHEAST TRANSMIT CONTOURS  
ANTENNA BORESIGHT 1°N

Fig. 4.44. Predicted East Coverage Gain  
and Sidelobe Contours

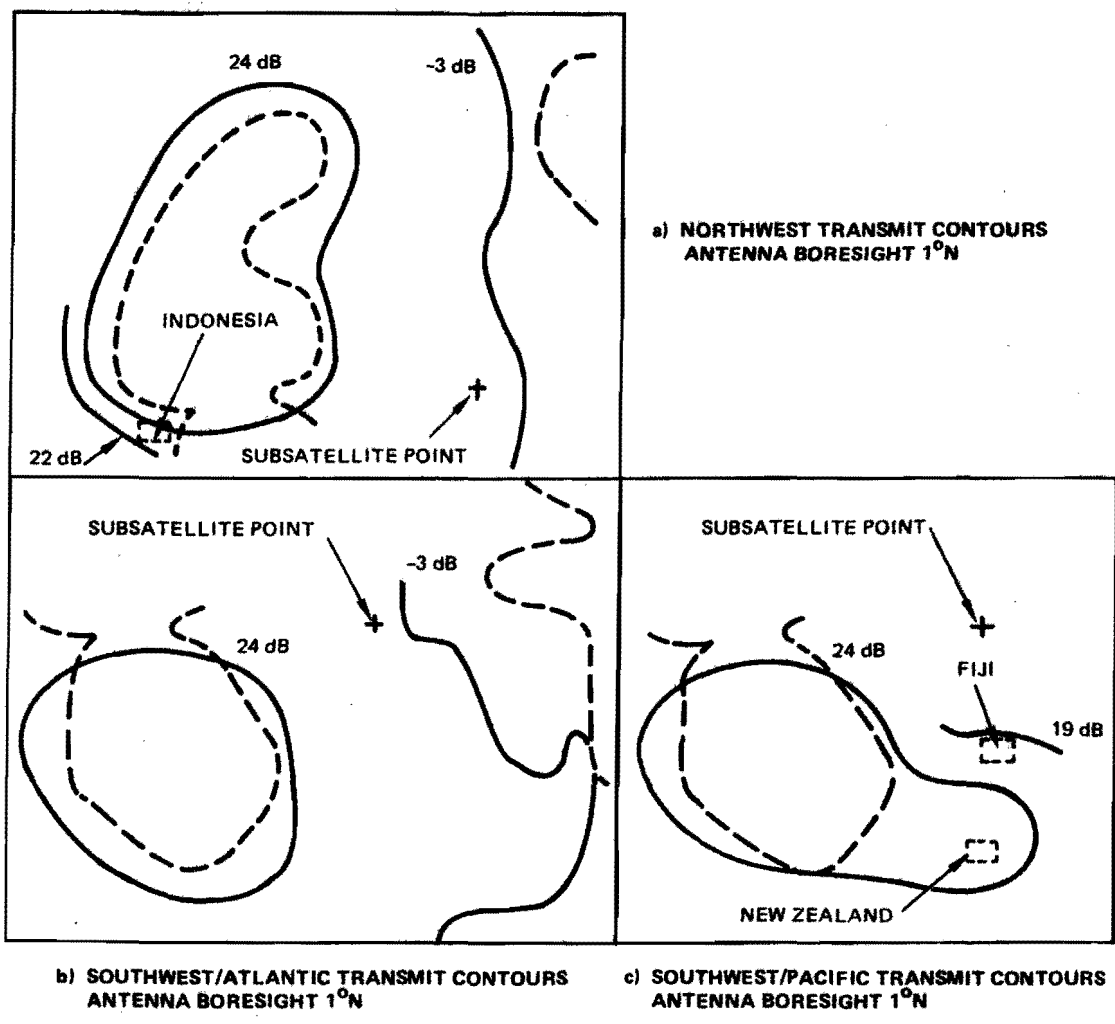


Fig. 4.45. Predicted West Coverage Gain and Sidelobe Contours

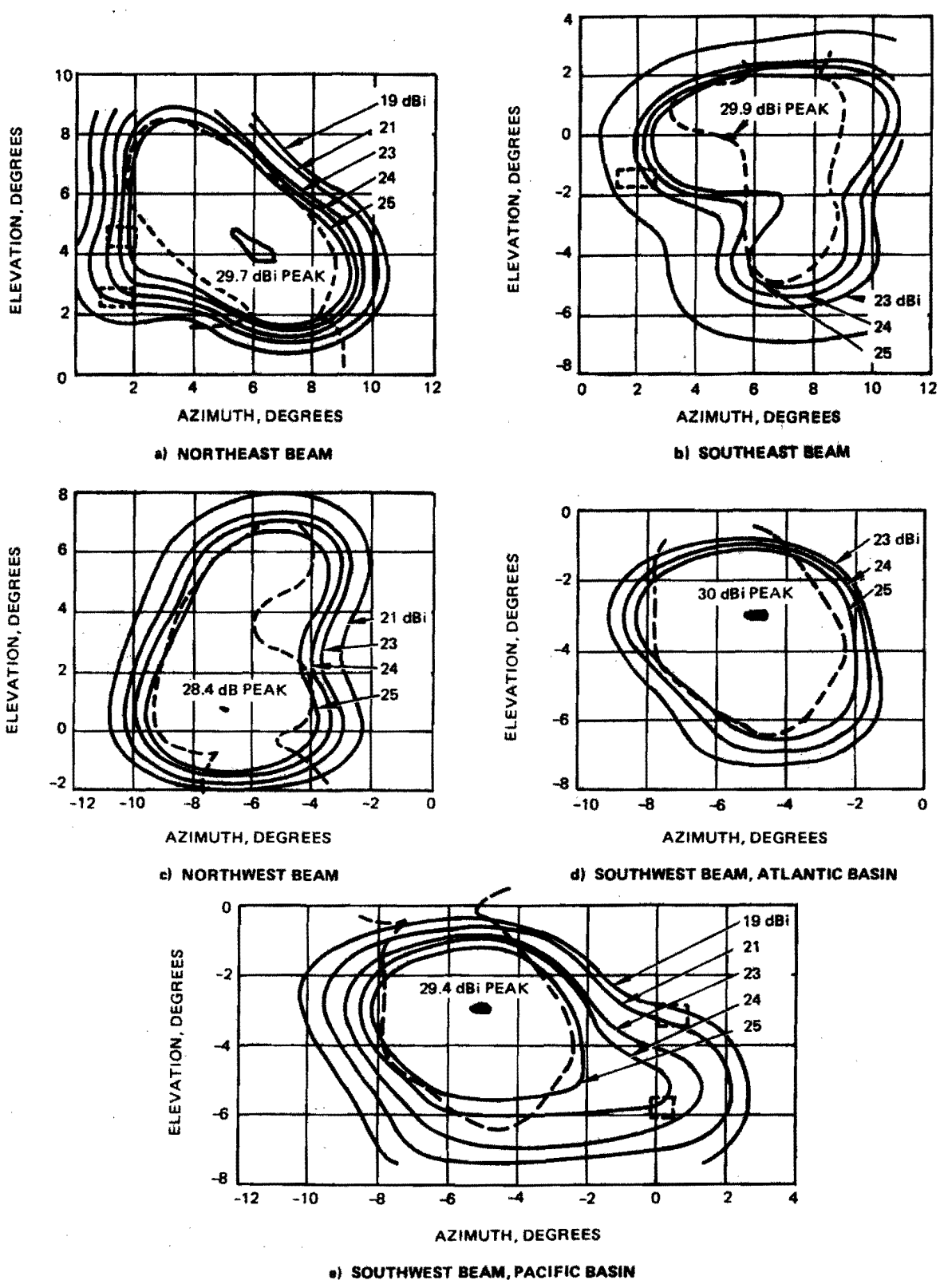
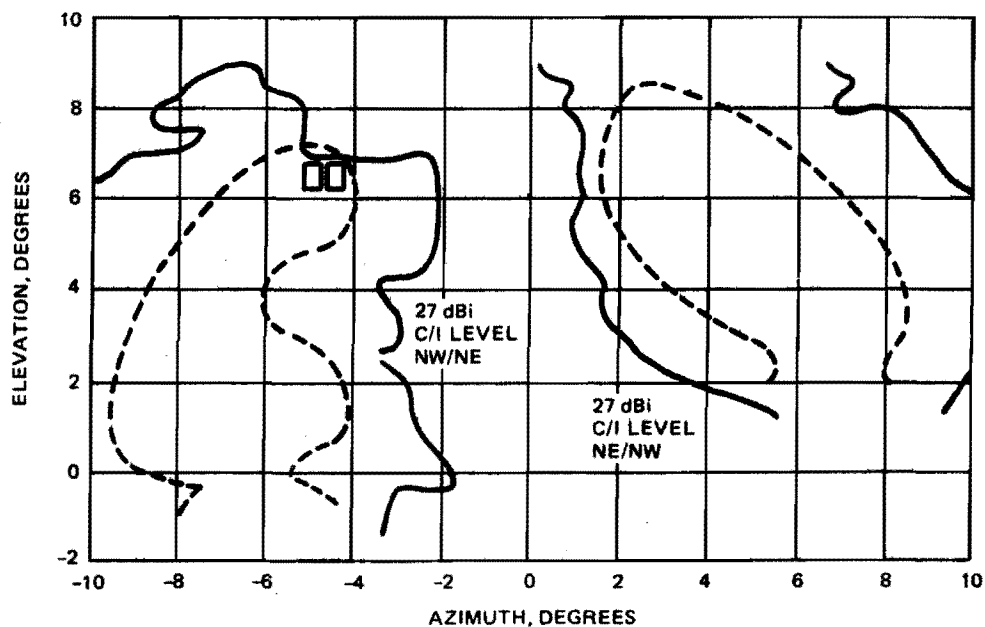
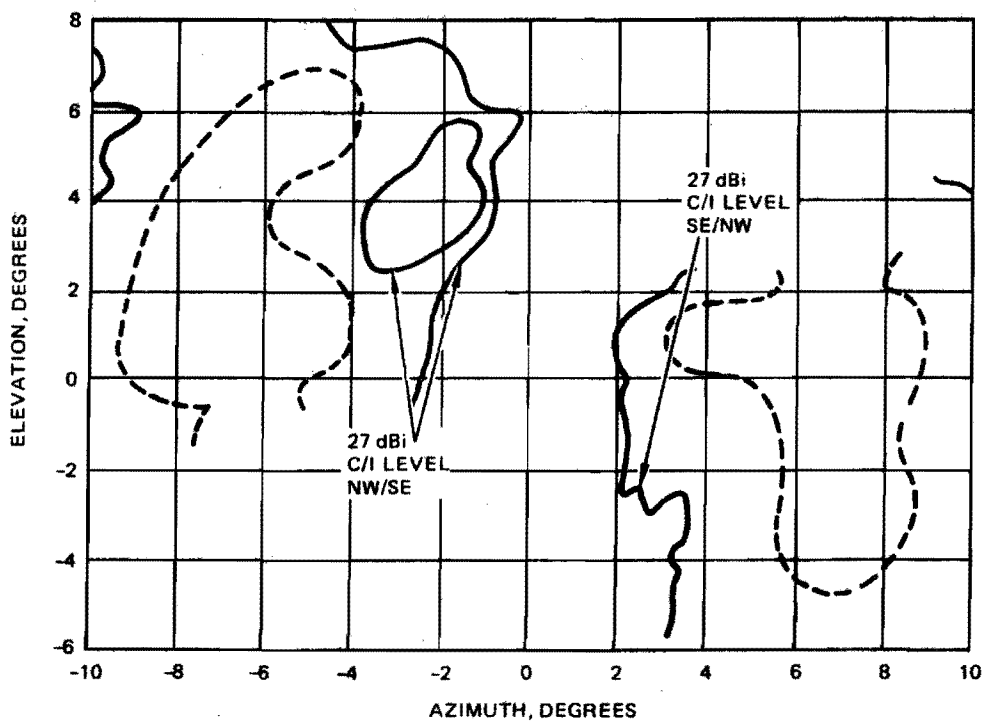


Fig. 4.46. Measured Intelsat IVA Transmit Antenna Gain Contours



a) NORTHWEST BEAM VS NORTHEAST BEAM



b) NORTHWEST BEAM VS SOUTHEAST BEAM

Fig. 4.47. Measured C/I Contours

## Chapter 5.

- I. Fourier Bessel and Launching methods for pattern computation of Cassegrainian Antenna Systems.  
pp. 5.1 - 5.23.
- II. Dual Reflector Synthesis.  
Appendix 5.1.  
Appendix 5.2.

by

R. Mittra

Electromagnetics Laboratory  
Department of Electrical Engineering  
University of Illinois  
Urbana, Illinois

## Errata Chapter 5

Page 5.14    Add to caption Fig. 1: Main and subreflector grids.

Page 5.15    See Fig. 1 should read Fig. 5

Page 5.18    See Fig. 2 should read Fig. 6

Page 5.22    Fig. 2.1 should be Fig. 5

              Fig. 2.2 should be Fig. 6

Page 5.23    Fig. 2 = Launching grid in main reflector and subreflector.

              Fig. 1    should be Fig. 4: Geometry for calculation for  
                          edge-diffracted feed.

Introduce new figure: Fig. 3: Geometry for edge of subreflector.

## 1. Computation of Induced Surface Current on Main Reflector

The computation of the radiation pattern of a dual offset shaped reflector antenna often requires the evaluation of the induced surface current on the main reflector. This induced current can be obtained readily by physical optics approximation if the magnetic field reflected from the subreflector is evaluated on the main reflector. The conventional ray-tracing approach to this problem is to search on the subreflector for the reflection point corresponding to a given field point on the main reflector and then evaluate the reflected field from this reflection point. Such a random search can be time-consuming. Since the induced current over the entire main reflector is to be computed, the searching scheme can be carried out in a more systematic manner by incorporating a scanning procedure which gives a very accurate initial guess to start the searching for the true location of a reflection point. To improve the accuracy of the radiation pattern computation the contributions of the diffracted rays from the rim of the subreflector are superimposed on the reflected rays from the surface of the subreflector. In the following sections, the computations of the reflected field and the diffracted field are discussed separately in detail.

### 1.1. Computation of Reflected Field

In this method, the subreflector is defined by specifying the surface coordinates and the surface normal at the nodes of a rectangular grid shown in Figure 1. The grid can be viewed as being composed of small rectangular patches each of which has four corners marked by numerals 1, 2, 3, and 4 in Figure 1. If the grid is defined in the x-y plane as in Figure 1, then the z-coordinate at each of the four corners of the patch defines a point on the subreflector. A total of four points is defined in such a

manner in Figure 2, where four rays are launched from the feed toward these four points, i.e., Q1, Q2, Q3, and Q4 on the subreflector. As mentioned earlier, the surface normal at each of these four points is also given, therefore, these four rays are reflected toward the main reflector in the usual manner and they intersect the main reflector at four points as shown in Figure 2. However, the point  $\bar{F}$  where the reflected field is to be evaluated is not necessarily one of these four intersections. The problem is then to find a reflection point  $\bar{R}$  as shown in Figure 2 to be associated with  $\bar{F}$ , which is shown being captured by the reflected four-ray bundle. The technique for determining whether a field point is captured by a ray-bundle or not is discussed in the following section. Meanwhile, if we have the situation in Figure 2 where the ray-bundle has captured a field point  $\bar{F}$ , we can set the initial value for  $\bar{R}$  equal to  $(\bar{Q1} + \bar{Q2} + \bar{Q3} + \bar{Q4})/4$  and solve the following system of nonlinear equations for  $\bar{R} = (x^r, y^r, z^r)$ , given  $(x_1, y_1, z_1)$ , the feed location and  $(x_2, y_2, z_2)$ , the field point:

$$\begin{cases} \{(x^r - x_1) + [f(x^r, y^r) - z_1] \partial_x f\} / d_1 + \{(x^r - x_2) + [f(x^r, y^r) - z_2] \partial_x f\} / d_2 = 0 & (1a) \\ \{(y^r - y_1) + [f(x^r, y^r) - z_1] \partial_y f\} / d_1 + \{(y^r - y_2) + [f(x^r, y^r) - z_2] \partial_y f\} / d_2 = 0 & (1b) \end{cases}$$

where  $d_n^2 = (x^r - x_n)^2 + (y^r - y_n)^2 + [f(x^r, y^r) - z_n]^2$ ,  $n = 1, 2$ . In writing (1a) and (1b), we have made use of the principle of shortest optical path length which in the present case spells

$$\begin{cases} \partial_x (d_1 + d_2) = 0 & (2a) \\ \partial_y (d_1 + d_2) = 0 & (2b) \end{cases}$$



where  $d_1$  and  $d_2$  are the distance from the feed location to the reflection point  $\bar{R}$  and the distance from the reflection point  $\bar{R}$  to the field point  $\bar{F}$ , respectively, as indicated in Figure 2.

Now a technique for determining whether a field point is captured by a ray-bundle or not is discussed. As illustrated in Figure 2, a four-sided patch is formed in the x-y plane by projecting the points of intersection on the main reflector onto the aperture in the x-y plane. The field points, one of which is shown in Figure 2 as  $\bar{F}$ , are also projected onto the aperture plane. Associated with this four-sided patch is a square window which moves along with this patch when it is scanned over the aperture plane. This window allows the computer program to test only those field points that can be viewed through the window to determine whether one of these field points is being captured by the four-ray bundle or not. In other words, only a pertinent small subset of the collection of all of the field points is tested at a time. If a field point is captured, i.e., if the projection of the field point is within the four-sided patch in the aperture, the reflected field is computed for this field point, which is then tagged and subsequently excluded in future testing. If not, the four-ray bundle is scanned to the next position and the testing is again performed on the field points seen through the new window. The scanning procedure assures that the reflection point found is associated with the field point captured. Therefore, the formulas developed for classical ray-tracing can be easily applied when the point of reflection associated with a field point has been located. The coordinates, the first and the second partial derivatives of the subreflector in the vicinity of the reflection point  $\bar{R}$ , can be obtained by Lagrangian interpolation. The coordinates and the first partial derivatives are given at the points Q1, Q2, Q3, and Q4 in Figure 2; therefore, the

coordinates and the first partial derivatives of the surface can be obtained by doing a Lagrangian interpolation for each of these quantities. When the subreflector is described by an algebraic expression such as a polynomial, the second derivatives at Q1, Q2, Q3, and Q4 are derived, and their counterparts in the neighborhood of  $\bar{R}$  are obtained by the corresponding Lagrangian interpolations. If such is not the case, numerical schemes, e.g., finite differencing, may be used to obtain these second derivatives. Once these derivatives are obtained, the reflected field at  $\bar{F}$  is computed in a straightforward manner. By the time the four-ray bundle scans through the subreflector, all of the field points have been captured, and the reflected magnetic field computed. The physical optics approximation is then used to compute the induced surface current, which is, in turn, used to compute the far-field pattern of the antenna. To improve the accuracy of the pattern computation, the diffracted field due to the rim of the subreflector must also be computed and superimposed on the reflected field due to the surface of the subreflector. The computation of the diffracted field is discussed in the next section in detail.

Now we discuss the method used in the computation of the reflected field. The problem at hand can be stated as follows: Given the surface information at the reflection point  $(x^r, y^r, z^r) = \bar{R}$ , i.e., the coordinates  $x, y, z = f(x, y)$ , the first partial derivatives  $\partial_x f$ ,  $\partial_y f$ , and the second partial derivatives  $\partial_{xx} f$ ,  $\partial_{xy} f$ , and  $\partial_{yy} f$ , all of which evaluated at  $\bar{R}$ , the feed position  $(x_1, y_1, z_1)$  the field point  $\bar{F} = (x_2, y_2, z_2)$ , and the incident field at  $\bar{R}$ , i.e.,  $\bar{H}^i(\bar{R}) = (H_x^i(\bar{R}), H_y^i(\bar{R}), H_z^i(\bar{R}))$ , compute the H-field at the field point  $\bar{F}$ . The solution can be written as

$$\bar{H}^r(\bar{F}) = D e^{-jkd_2} \{ \bar{H}^i(\bar{R}) - 2 [\bar{H}^i(\bar{R}) \cdot \hat{N}] \hat{N} \} \quad (3)$$

where  $\bar{F} = (x_2, y_2, z_2)$

$\bar{R} = (x^r, y^r, z^r)$

$$d_2 = [(x_2 - x^r)^2 + (y_2 - y^r)^2 + (z_2 - z^r)^2]^{1/2}$$

$$k = 2\pi/\lambda$$

$\lambda$  = wavelength

$\hat{N}$  is the unit surface normal at  $\bar{R}$

$D$  is the divergence factor

The above equation can be written in terms of the rectangular components as follows:

$$\begin{bmatrix} H_x^r(\bar{F}) \\ H_y^r(\bar{F}) \\ H_z^r(\bar{F}) \end{bmatrix} = De^{-jkd_2} \begin{bmatrix} H_x^i(\bar{R}) \\ H_y^i(\bar{R}) \\ H_z^i(\bar{R}) \end{bmatrix} + 2\Delta^2 [-H_x^i(\bar{R}) \partial_x f - H_y^i(\bar{R}) \partial_y f + H_z^i(\bar{R})] \begin{bmatrix} \partial_x f \\ \partial_y f \\ -1 \end{bmatrix}$$

$$\text{where } \Delta = -[1 + (\partial_x f)^2 + (\partial_y f)^2]^{-1/2}$$

(4)

$$D = (1 + K_1 d_2)^{-1/2} (1 + K_2 d_2)^{-1/2}$$

and the square roots are either positive real or negative imaginary.

The curvatures  $K_1$  and  $K_2$  in the divergence factor can be written as

$$K_1 = 1/2 \{ (Q_{11} + Q_{22}) + [(Q_{11} + Q_{22})^2 - 4(Q_{11}Q_{22} - Q_{12}Q_{21})]^{1/2} \} \quad (5a)$$

$$K_2 = 1/2 \{ (Q_{11} + Q_{22}) - [(Q_{11} + Q_{22})^2 - 4(Q_{11}Q_{22} - Q_{12}Q_{21})]^{1/2} \} \quad (5b)$$

where  $Q_{11}$ ,  $Q_{12}$ ,  $Q_{21}$ , and  $Q_{22}$  are the elements of the matrix computed in the following manner:

$$\begin{pmatrix} Q_{11} & Q_{12} \\ Q_{21} & Q_{22} \end{pmatrix} \begin{pmatrix} Q_{11}^i & Q_{12}^i \\ Q_{21}^i & Q_{22}^i \end{pmatrix} + \frac{2 P_{33}}{(P_{11}P_{22}-R_{12}P_{21})^2} \begin{pmatrix} P_{22} & -P_{21} \\ -P_{12} & P_{11} \end{pmatrix} \begin{pmatrix} Q_{11}^\Sigma & Q_{12}^\Sigma \\ Q_{21}^\Sigma & Q_{22}^\Sigma \end{pmatrix} \begin{pmatrix} P_{22} & -P_{12} \\ -P_{21} & P_{11} \end{pmatrix} \quad (6)$$

where  $Q_{11}^i = Q_{22}^i = d_1^{-1} = [(x_1 - x^r)^2 + (y_1 - y^r)^2 + (z_1 - z^r)^2]^{-1/2}$

$$Q_{12}^i = Q_{21}^i = 0$$

$$P_{11} = \frac{(z^r - z_1) - (\partial_x f)(x^r - x_1)}{\sqrt{E} [(x^r - x_1)^2 + (z^r - z_1)^2]^{1/2}}$$

$$P_{12} = \frac{-(\partial_y f)(x^r - x_1)}{\sqrt{G} [(x^r - x_1)^2 + (z^r - z_1)^2]^{1/2}}$$

$$P_{21} = \frac{-(x^r - x_1)(y^r - y_1) - (\partial_x f)(y^r - y_1)(z^r - z_1)}{\sqrt{E} [(x^r - x_1)^2 (y^r - y_1)^2 + [(z^r - z_1)^2 + (x^r - x_1)^2]^2 + (y^r - y_1)^2 (z^r - z_1)^2]^{1/2}}$$

$$P_{22} = \frac{(z^r - z_1)^2 + (x^r - x_1)^2 - (\partial_y f)(y^r - y_1)(z^r - z_1)}{\sqrt{G} [(x^r - x_1)^2 (y^r - y_1)^2 + [(z^r - z_1)^2 + (x^r - x_1)^2]^2 + (y^r - y_1)^2 (z^r - z_1)^2]^{1/2}}$$

$$P_{33} = \frac{-\Delta [(\partial_x f)(x^r - x_1) + (\partial_y f)(y^r - y_1) - (z^r - z_1)]}{[(x_1 - x^r)^2 + (y_1 - y^r)^2 + (z_1 - z^r)^2]^{1/2}}$$

$$Q_{11}^\Sigma = \Delta^2 (eG - fF)$$

$$Q_{12}^\Sigma = \Delta^2 (fE - eF)$$

$$Q_{21}^\Sigma = \Delta^2 (fG - gF)$$

$$Q_{22}^\Sigma = \Delta^2 (gE - fF)$$

In writing the above equations, we have made use of the following shorthand notations:

$$\Delta = - [1 + (\partial_x f)^2 + (\partial_y f)^2]^{-1/2}$$

$$E = 1 + (\partial_x f)^2$$

$$F = (\partial_x f)(\partial_y f)$$

$$G = 1 + (\partial_y f)^2$$

$$e = \Delta \partial_{xx} f$$

$$f = \Delta \partial_{xy} f$$

$$g = \Delta \partial_{yy} f$$

### 1.2. Computation of Diffracted Field

The diffracted field due to the rim of the subreflector can be computed most readily by the GTD technique. This edge diffraction problem has been solved satisfactorily when the surface as well as the rim are described analytically. In this section, we present a numerical method to solve the same problem when the surface and the rim are described numerically only.

Suppose that the rim of the subreflector is divided into 360 segments whose end points are specified in rectangular coordinates as shown in Figure 3. Slightly inside the rim and on the surface, a ring is similarly defined.

In Figure 3, the subreflector is being looked at from the side of the feed, i.e.,  $\hat{z}$  is pointing into the page. The rim points and the ring points are assigned numerical indices as indicated in Figure 3. The edge segment defining vector  $\bar{e}$  points in the decreasing index direction. The vector  $\bar{h}$  points from the mid-point of the neighboring ring segment to the head of  $\bar{e}$ , i.e., to the one with the smaller index of the two points defining the edge segment  $\bar{e}$ . The purpose of defining the ring and the rim in such a manner is to devise a means to compute the surface unit normal at the rim. If the ring is close enough to the rim, the unit normal to the surface in the vicinity of the rim point can be approximated by taking the vector cross product of  $\bar{h}$  and  $\bar{e}$  and properly normalizing the cross product, i.e.,

$$\hat{N} = \frac{\bar{h} \times \bar{e}}{|\bar{h} \times \bar{e}|} \quad (7)$$

The problem at hand can then be rephrased as follows: Given the rim data (x-, y-, and z- coordinates of the end points of the 360 segments) and the ring data (which provide the surface data to compute the unit normal  $\hat{N}$  to the surface near the rim), compute the diffracted  $\bar{H}$ -field at the captured field point due to the rays emitted from the feed and diffracted by the rim to the field point. Therefore, we must first find these rays. A straightforward solution to this problem is to locate the mid-point of a rim segment whose sum of the distances from the feed and from the field point is an extremum. More specifically, for each captured field point, the 360 rim segments are examined one at a time to see if the extremum condition is satisfied. The algorithm used in the present case is to compute the aforementioned distances at three consecutive segments and then compare the results.

If the middle one is the smallest (minimum criterion) or if the middle one is the largest (maximum criterion), then the midpoint of the rim segment under examination is declared a point of diffraction. Note the fact that two points should be located, one corresponds to the maximum pathlength of a ray traveling from the feed to the field point via a point on the rim and the other the minimum in this setup. For each of the point of diffraction found, the diffracted field is computed at the field point. The contributions from each of the diffraction point on the rim are superimposed and the total diffracted field is combined with the reflected field from a reflection point on the surface. The total field is then used to compute the surface current.

Now the computation of the diffracted field given the locations of the field point, the source point, and the diffraction point is discussed in detail. The first step is to set up proper coordinate systems at the point of diffraction. The plane of incidence, the plane of diffraction, and the surface patch of reflection are defined if the surface normal to each of these three planes is. These three planes can be visualized as triangles containing the rim segment and the source point (feed location), the field point and the ring point, respectively. Now imagine that a half plane whose edge paralleled to the rim segment and whose surface coincided with the triangular surface patch is introduced at the point of diffraction. The diffracted field due to the rim is taken to be the diffracted field due to this half plane. The simplest coordinate systems to be used in this canonical problem are the incident ray-fixed coordinate system and the diffracted ray-fixed coordinate system. In the former, the incident field  $\vec{E}^i$  or in the latter, the diffracted field  $\vec{E}^d$  can be decomposed into two orthogonal components, both of which are perpendicular to the incident ray in the former

or the diffracted ray in the latter, and one of which is parallel to and the other is perpendicular to the plane of incidence in the former or the plane of diffraction in the latter. Referring to Figure 4, one can easily verify that the unit vectors in these ray-fixed coordinates are given by the following expressions:

$$\hat{\phi}' = \frac{\overline{SD} \times \overline{e}}{|\overline{SD} \times \overline{e}|} \quad (8)$$

where  $\overline{SD}$  is from the source S to the rim point D; and  $\overline{e}$  is defined by two adjacent rim points.

$$\hat{S}' = \frac{\overline{SD}}{|\overline{SD}|} \quad (9)$$

$$\hat{\beta}' = \hat{\phi}' \times \hat{S}' \quad (10)$$

$$\hat{S} = \frac{\overline{DF}}{|\overline{DF}|} \quad (11)$$

where  $\overline{DF}$  is from the rim point D to the field point F.

$$\hat{\phi} = \frac{\overline{e} \times \overline{DF}}{|\overline{e} \times \overline{DF}|} \quad (12)$$

$$\hat{\beta} = \hat{\phi} \times \hat{S} \quad (13)$$

The above unit vectors define the ray-fixed coordinates used in the canonical problem. In the present problem, however, both of the incident and the diffracted fields are required to be expressed in terms of the reflector antenna coordinates.



Therefore, a coordinate transformation from the antenna system to the half plane system must be performed before the canonical solution can be found. Another coordinate transformation from the half plane system back to the antenna system must also be performed after the canonical solution has been found. Therefore,

$$\vec{E}^1 \text{ (at rim point)} = E_{\beta'}^1 \hat{\beta}' + E_{\phi'}^1 \hat{\phi}' \quad (14)$$

$$\begin{aligned} \text{where } E_{\beta'}^1 &= \vec{E}^1 \cdot \hat{\beta}' \\ &= (E_x^1 \hat{x} + E_y^1 \hat{y} + E_z^1 \hat{z}) \cdot (\beta'_x \hat{x} + \beta'_y \hat{y} + \beta'_z \hat{z}) \\ &= E_x^1 \beta'_x + E_y^1 \beta'_y + E_z^1 \beta'_z \end{aligned} \quad (15)$$

and similarly

$$E_{\phi'}^1 = E_x^1 \phi'_x + E_y^1 \phi'_y + E_z^1 \phi'_z \quad (16)$$

Now the incident field is expressed in the incident ray-fixed system, the canonical solution can be written down in a straightforward manner. First the divergence factor  $A_d(S)$  is computed as follows:

$$A_d(S) = \sqrt{\frac{|\overline{SD}|}{|\overline{FD}| (|\overline{SD}| + |\overline{FD}|)}} \quad (17)$$

Then the diffraction coefficients  $D_{s,h}$  are computed as follows:

$$\begin{aligned} D_{s,h}(\phi, \phi'; \beta', n=2) \\ = \frac{-e^{-j\pi/4}}{\sin \beta' \sqrt{8\pi k}} \left( \frac{1}{\cos \frac{\phi - \phi'}{2}} + \frac{1}{\cos \frac{\phi + \phi'}{2}} \right) \end{aligned} \quad (18)$$

where  $k = 2\pi/\text{wavelength}$

$$\phi = \cos^{-1} \left( \frac{\hat{N} \cdot \hat{\phi}}{|\hat{N}| |\hat{\phi}|} \right) \quad (19)$$

$$\phi' = \cos^{-1} \left( \frac{\hat{N} \cdot \hat{\phi}'}{|\hat{N}| |\hat{\phi}'|} \right) \quad (20)$$

$$\beta' = \cos^{-1} \left( \frac{\bar{e} \cdot \hat{S}}{|\bar{e}| |\hat{S}|} \right) \quad (21)$$

The diffracted field can be written as

$$\bar{E}^d = E_{\beta}^d \hat{\beta} + E_{\phi}^d \hat{\phi} \quad (22)$$

where

$$E_{\beta}^d = -D_s E_{\beta}^i, A_d(S) e^{-jks} \quad (23)$$

$$E_{\phi}^d = -D_h E_{\phi}^i, A_d(S) e^{-jks} \quad (24)$$

where  $s = |\overline{FD}|$ .

Now we write  $\bar{E}^d$  in terms of the antenna system coordinates.

$$\begin{aligned} \bar{E}^d &= E_{\beta}^d (\beta_x \hat{x} + \beta_y \hat{y} + \beta_z \hat{z}) + E_{\phi}^d (\phi_x \hat{x} + \phi_y \hat{y} + \phi_z \hat{z}) \\ &= E_x^d \hat{x} + E_y^d \hat{y} + E_z^d \hat{z} \end{aligned} \quad (25)$$

where

$$E_x^d = E_{\beta}^d \beta_x + E_{\phi}^d \phi_x \quad (26)$$

$$E_y^d = E_{\beta}^d \beta_y + E_{\phi}^d \phi_y \quad (27)$$

$$E_z^d = E_{\beta}^d \beta_z + E_{\phi}^d \phi_z \quad (28)$$

Since the surface current is to be computed from the  $\vec{H}$ -field rather than the  $\vec{E}$ -field, we write

$$\vec{H}^d = (\hat{s} \times \vec{E}^d) / (120\pi) \quad (29)$$

Now the total diffracted fields from all of the points of diffraction are superimposed on the reflected field computer before to give the total  $\vec{H}$ -field at the captured field point.

$$\vec{H}^{\text{total}} = \vec{H}^{\text{reflection}} + \vec{H}^{\text{diffraction}} \quad (30)$$

Then the surface current is given by

$$\vec{J}^{\text{total}} = 2\hat{n} \times \vec{H}^{\text{total}} \quad (31)$$

where  $\hat{n}$  is the unit normal to the main reflector surface. The surface current  $\vec{J}^{\text{total}}$  is then used to compute the far-field pattern.

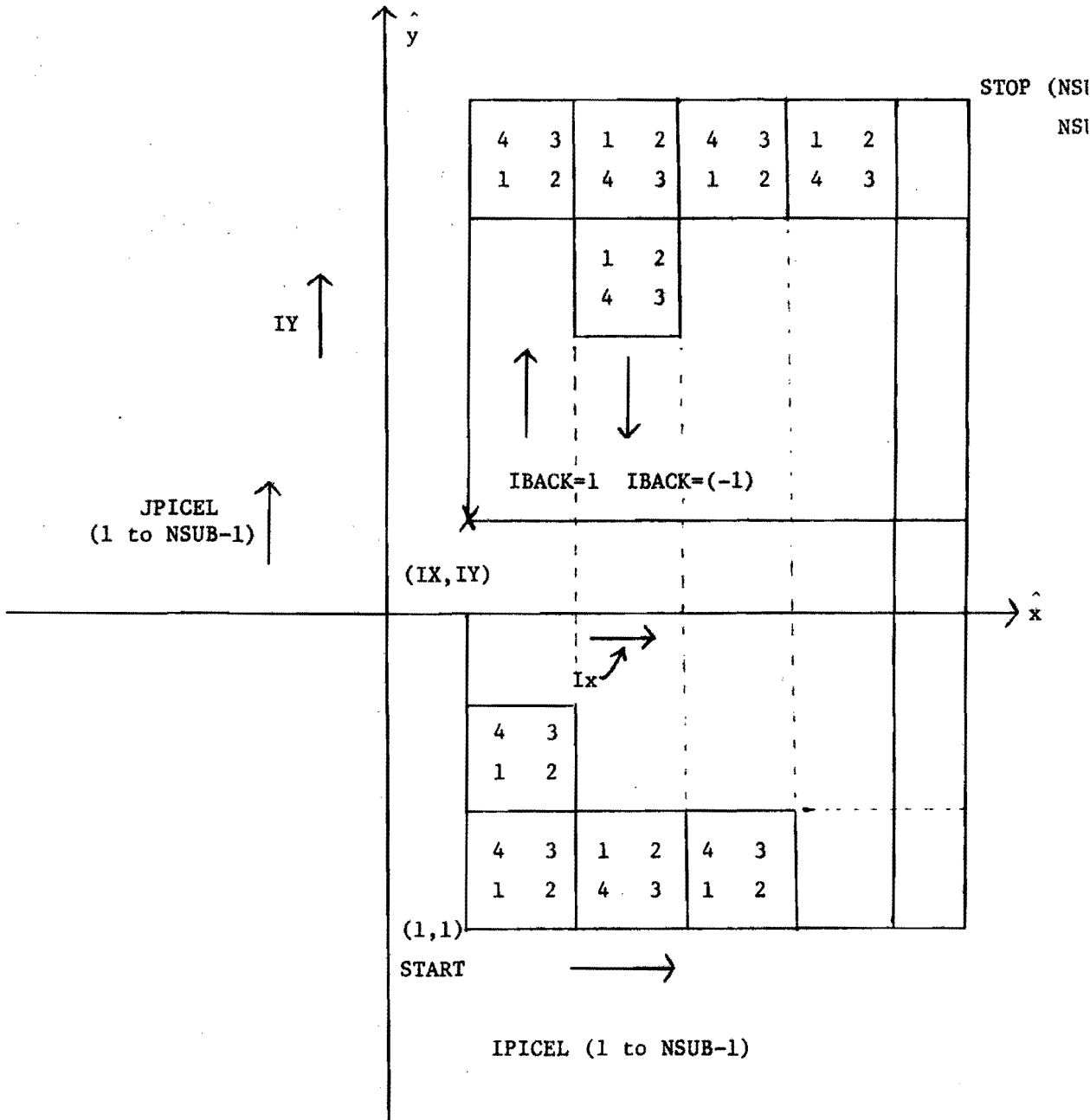


Figure 1: Scanning an (NSUB X NSUB) Point Grid

## 2. Computation of Radiation Patterns

The current distribution on the main reflector (see Fig. 1) has been computed using the method described in the previous section. We can now derive the fields generated from this current using the formulas

$$\bar{\mathbf{A}} = \int_{\Sigma} \bar{\mathbf{J}} \frac{e^{-jk|\bar{\mathbf{r}}-\bar{\mathbf{r}}'|}}{4\pi|\bar{\mathbf{r}}-\bar{\mathbf{r}}'|} ds' \quad (1)$$

$$\bar{\mathbf{H}} = \nabla \times \bar{\mathbf{A}}, \quad \bar{\mathbf{E}} = \frac{1}{j\omega\epsilon} \nabla \times \bar{\mathbf{H}}. \quad (2)$$

Introducing the usual far-field approximation  $|\bar{\mathbf{r}} - \bar{\mathbf{r}}'| \sim r - \bar{\mathbf{r}}' \cdot \hat{\mathbf{r}}$  into (1), one arrives at the far-field approximation for the fields, viz.,

$$\bar{\mathbf{H}} = jk \frac{e^{-jkr}}{4\pi r} (T_{\phi} \hat{\theta} - T_{\theta} \hat{\phi}) + O(r^{-2}) \quad (3)$$

$$\bar{\mathbf{E}} = -jk\eta \frac{e^{-jkr}}{4\pi r} (T_{\theta} \hat{\theta} + T_{\phi} \hat{\phi}) + O(r^{-2}) \quad (4)$$

where

$$\bar{\mathbf{T}}(\theta, \phi) = \int_{\Sigma} \bar{\mathbf{J}}(\bar{\mathbf{r}}') e^{jk\bar{\mathbf{r}}' \cdot \hat{\mathbf{r}}} ds'. \quad (5)$$

$$\begin{Bmatrix} T_{\theta} \\ T_{\phi} \end{Bmatrix} = \begin{pmatrix} \cos\theta \cos\phi & \cos\theta \sin\phi & -\sin\phi \\ -\sin\phi & \cos\phi & 0 \end{pmatrix} \begin{Bmatrix} T_x \\ T_y \\ T_z \end{Bmatrix} \quad (6)$$

$$\eta = \sqrt{\mu/\epsilon}$$

Note that the integration in (5) is performed directly on the surface. However, it is possible to transform it to an integration over the projected circular aperture, without loss of rigor, via the use of the Jacobian transformation. Let the surface be described by the equation

$$z' = f(x', y') = \tilde{f}(\rho', \phi'), \quad \bar{\rho}' \in \sigma \quad (7)$$

and its unit normal  $\hat{n}$  be given by

$$\hat{n} = \bar{N}/N \quad (8)$$

where

$$\bar{N} = \left[ -\frac{\partial f}{\partial x'}, \hat{x} - \frac{\partial f}{\partial y'}, \hat{y} + \hat{z} \right] \quad (9)$$

and

$$N = \sqrt{(\partial f / \partial x')^2 + (\partial f / \partial y')^2 + 1}.$$

which can be shown to be identical to  $J_\Sigma$ , i.e.,  $J_\Sigma = N$ . When the magnetic field  $\bar{H}_s$  scattered by the subreflector is known on the main reflector, the induced current on the main reflector can be derived from the physical optics approximation

$$\bar{J} = 2\hat{n} \times \bar{H}_s(\bar{r}') \quad (10)$$

Rewriting (5) in terms of an integral over the projected aperture and using  $J_\Sigma = N$  we can rewrite (5) as

$$\bar{T}(\theta, \phi) = \int_0^a \int_0^{2\pi} \bar{J}_e(\rho', \phi') e^{jk\bar{r}' \cdot \hat{r}_{\rho'}} d\rho' d\phi'. \quad (11)$$

where

$$\bar{J}_e(\rho', \phi') = \bar{J}(\bar{r}') J_\Sigma = 2\bar{N} \times \bar{H}_s(\bar{r}') \quad (12)$$

Equation (12) can be further rearranged to read

$$\begin{aligned} \bar{T}(\theta, \phi) = & \int_0^a \int_0^{2\pi} \bar{J}_e(\rho', \phi') [e^{jk\rho' \cos\theta' \cos\theta} \\ & \cdot \left\{ e^{jk\rho' \sin\theta \cos(\phi' - \phi)} \right\} \rho' d\rho' d\phi'. \end{aligned} \quad (13)$$

Note that if the factor in the square bracket in (13) were deleted we would have a representation for  $\bar{T}(\theta, \phi)$  which is just the Fourier transform of the equivalent current distribution  $\bar{J}_e$ . The presence of this factor precludes the evaluation of the radiation integral using a single Fourier transform. Nonetheless, it is possible to transform (13) into a rapidly converging series of Fourier transforms. To this end we manipulate (13) and rearrange the integrand as

$$\bar{T}(\theta, \phi) = e^{jk(L_w - L_{w0})} \int_0^a \int_0^{2\pi} \bar{J}_{es}^{jkl_0} [e^{jk\Delta}] \cdot e^{jk\rho' B \cos(\phi' - \phi)} \rho' d\rho' d\phi'. \quad (14)$$

where

$$\bar{J}_{es}(\rho', \phi') = \bar{J}_e(\rho', \phi') e^{-jk\rho'(C_u \cos\phi' + C_v \sin\phi')} \quad (15)$$

$$C_u = -\sin\theta_B \cos\phi_B - \frac{h}{2F} \cos\theta_B \quad (16)$$

$$C_v = -\sin\theta_B \sin\phi_B \quad (17)$$

$$B = \sqrt{(\sin\theta \sin\phi + C_v)^2 + (\sin\theta \cos\phi + C_u + \frac{h}{2F} \cos\theta)^2} \quad (18)$$

$$\phi = \tan^{-1} \frac{\sin\theta \sin\phi + C_v}{\sin\theta \cos\phi + C_u + (h/2F) \cos\theta} \quad (19)$$

$$\Delta = \left[ \frac{1}{4F} (\rho'^2 - a^2) + \tilde{f}_{pr}(\rho', \phi') \right] (\cos\theta - \cos\theta_0). \quad (20)$$

$$L = \left[ F \left( -1 + \frac{\rho'^2}{4F^2} \right) + \tilde{f}_{pr}(\rho', \phi') \right] \cos\theta \quad (21)$$

$$L_0 = \left[ F \left( -1 + \frac{\rho'^2}{4F^2} \right) + \tilde{f}_{pr}(\rho', \phi') \right] \cos \theta_0 \quad (22)$$

$$L_w = F \left( -1 + \frac{a^2}{4F^2} \right) \cos \theta \quad (23)$$

$$L_{w0} = F \left( -1 + \frac{a^2}{4F^2} \right) \cos \theta_0 \quad (24)$$

where

$$F = \frac{a^2}{4[f(0, a) - f(0, 0)]}$$

$$h = \frac{a^2}{2[f(0, a) - f(0, 0)]} f_{x'}(0, 0)$$

$$z_{ref} = f(0, 0) + [1 - f_{x'}^2(0, 0)] \frac{a^2}{4[f(0, a) - f(0, 0)]} \quad (25)$$

and where,  $a$  is the radius of the projected aperture (see Fig. <sup>6</sup> 2) and

$$f_{x'}(0, 0) = \partial f / \partial x' |_{0, 0}.$$

Futhermore,

$$\begin{aligned} \tilde{f}(\rho', \phi') = \tilde{f}_{pr}(\rho', \phi') + \left[ F \left( -1 + \frac{\rho'^2}{4F^2} \right) \right. \\ \left. + \frac{h}{2F} \rho' \cos \phi' + \frac{h^2}{4F} + z_{ref} \right]. \end{aligned} \quad (26)$$

We now expand  $e^{jk\Delta}$  in a power series of  $\Delta$  and obtain

$$\bar{T}(\theta, \phi) = \sum_{p=0}^{\infty} \bar{T}_p(\theta, \phi) \quad (27)$$

where

$$\begin{aligned} \bar{T}_p(\theta, \phi) = \frac{1}{p!} (jk)^p e^{jk(L_w - L_{w0} + \left[ \frac{h^2}{4F} + z_{ref} \right] \cos \theta)} (\cos \theta - \cos \theta_0)^p \\ \cdot \int_0^{2\pi} \int_0^a \bar{J}_{es} e^{jkL_0 \left[ \frac{(\rho'^2 - a^2)}{4F} + \tilde{f}_{pr}(\rho', \phi') \right]} p \\ e^{jk\rho' B \cos(\phi' - \phi)} \rho' d\rho' d\phi'. \end{aligned} \quad (28)$$



Typically the above series in  $p$  converges very rapidly, and often only two terms are sufficient for accurate results.

Now we describe a novel approach for evaluating the integrals

$$\bar{I}_p(\theta, \phi) = \int_0^{2\pi} \int_0^a \bar{Q}_p(\rho', \phi') e^{jk\rho' B \cos(\phi' - \phi)} \rho' d\rho' d\phi' \quad (29)$$

where

$$\bar{Q}_p(\rho', \phi') = \bar{J}_{es}(\rho', \phi') e^{jkl} \left[ \frac{(\rho'^2 - a^2)}{4F} + \bar{f}_{pr}(\rho', \phi') \right] p \quad (30)$$

It can be shown [1] that given a function  $f$ , which has support within a circular area of radius  $a$ , the Fourier transform  $f$ , viz.  $\bar{f}$ , may be expressed as

$$\begin{aligned} \bar{f} &= \iint f \exp j[ux + vy] dx dy \\ &= \sum_{n=-\infty}^{\infty} \sum_{m=-\infty}^{\infty} g_{mn} \bar{R} \left( u - \frac{m\pi}{a}, v - \frac{n\pi}{a} \right) \end{aligned} \quad (31)$$

where  $g$  is defined via,

$$f = Rg. \quad (32)$$

The truncation function is  $R = 1$  inside the circle  $\rho = a$ , and is identically zero outside, and  $g_{mn}$  are the Fourier series coefficients of  $g$ .

The Fourier transform of  $R$ , viz  $\bar{R}$  is given by

$$\bar{R} = 2\pi J_1(\sqrt{u^2 + v^2}) / \sqrt{u^2 + v^2} \quad (33)$$

We can insert (33) in (31) and use the latter to evaluate the integrals  $\bar{I}_p$  each of which is the Fourier transform of known functions  $\bar{Q}_p$ .

The radiation pattern of shaped reflector is calculated using the formula

$$\vec{E} = -jk\eta \frac{e^{-jkr}}{4\pi r} \left[ T_{\theta} \hat{\theta} + T_{\phi} \hat{\phi} \right] \quad (34)$$

where

$$\begin{aligned} \vec{T}(\theta, \phi) = & a^2 e^{jk\{(\frac{h^2}{4F} + z_{ref}) \cos\theta + L_W - L_{W0}\}} \\ & \times \left[ \int_0^{2\pi} \int_0^1 \left\{ \vec{J}(s, \phi) J_{\Sigma} e^{-jkas(c_u \cos\phi' + c_v \sin\phi')} + jkL_0 \right\} \right. \\ & \times e^{jkasB \cos(\phi' - \phi)} s ds d\phi' \\ & + jk(\cos\theta - \cos\theta_0) \int_0^{2\pi} \int_0^1 \left\{ \left[ \frac{a^2(s^2-1)}{4F} + \vec{f}_{pr}(s, \phi') \right] \vec{J}(s, \phi) J_{\Sigma} \right. \\ & \left. \left. \times e^{-jkas(c_u \cos\phi' + c_v \sin\phi')} + jkL_0 \right\} e^{jkasB \cos(\phi' - \phi)} s ds d\phi' \right] \quad (35) \end{aligned}$$

The various symbols used in (35) have been in the previous section. In programming (35) the factors inside { } of the first term are represented by the Fourier series

$$\sum_{I=-N/2}^{N/2-1} \sum_{J=-N/2}^{N/2-1} \left[ GR(I, J) + jGM(I, J) \right] e^{jI\pi x} e^{jJ\pi y} \quad (36)$$

and the factors inside { } of the second term by

$$\sum_{I=-N/2}^{N/2-1} \sum_{J=-N/2}^{N/2-1} \left[ \text{GR1}(I,J) + j\text{GM1}(I,J) \right] e^{j(I\pi x + J\pi y)} \quad (37)$$

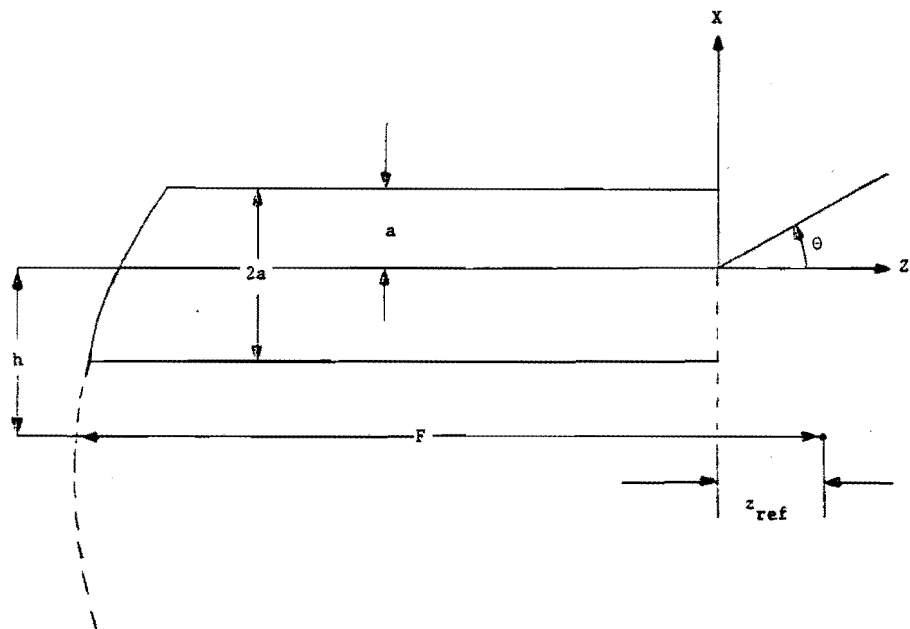
where  $x = s \cos\phi'$ ;  $y = s \sin\phi'$

Eqs. (36) and (37) may be used in (35), and using the shift theorem for Fourier transform,  $\tilde{T}(\theta, \phi)$  may be written as

$$\begin{aligned} \tilde{T}(\theta, \phi) = & a^2 e^{jk} \left\{ \left( \frac{h^2}{4F} + z_{\text{ref}} \right) \cos\theta + L_W - L_{W0} \right\} \\ & \times \left[ \sum_{I=-N/2}^{N/2-1} \sum_{J=-N/2}^{N/2-1} \left[ \text{GR}(J,J) + j\text{GM}(I,J) \right] \frac{2\pi J_1 \left( \sqrt{uu^2 + vv^2} \right)}{\sqrt{uu^2 + vv^2}} \right. \\ & \left. + jk(\cos\theta - \cos\theta_0) \sum_{I,J=-N/2}^{N/2-1} \left[ \text{GR1}(I,J) + j\text{GM1}(I,J) \right] \frac{2\pi J_1 \left( \sqrt{uu^2 + vv^2} \right)}{\sqrt{uu^2 + vv^2}} \right] \end{aligned} \quad (38)$$

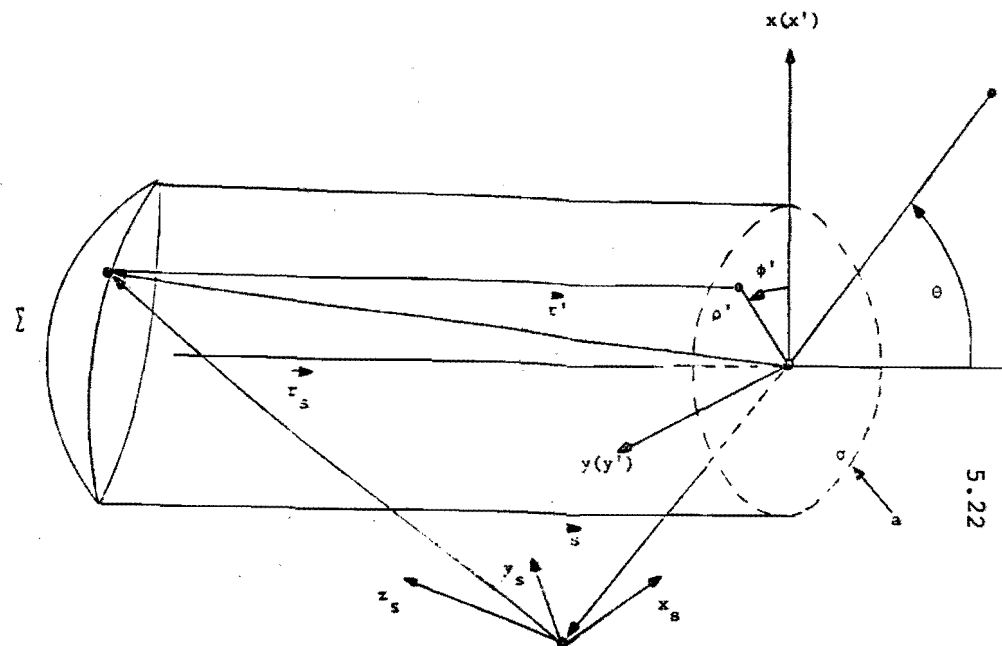
where  $J_1$  is Bessel function of first kind and order 1 and

$$uu = (kaB\cos\phi + I\pi); \quad vv = (kaB\sin\phi + J\pi)$$



6.

Figure 2.2: Definition of  $z_{\text{ref}}$  and other parameters for reflector surface.



5.22

5.

Figure 2.1: Coordinate system and geometry of reflector.

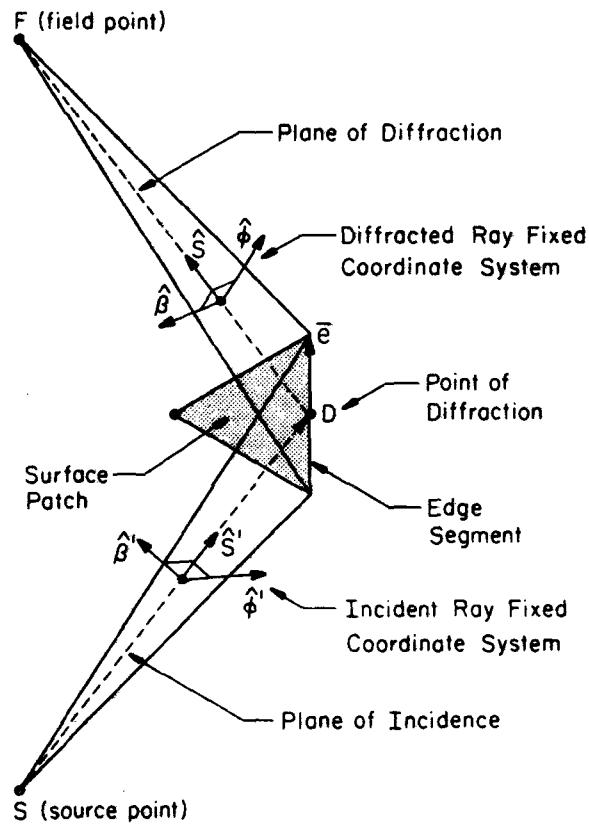


Figure 1. 4.

Geometry for calculation  
for edge-diffracted feed.

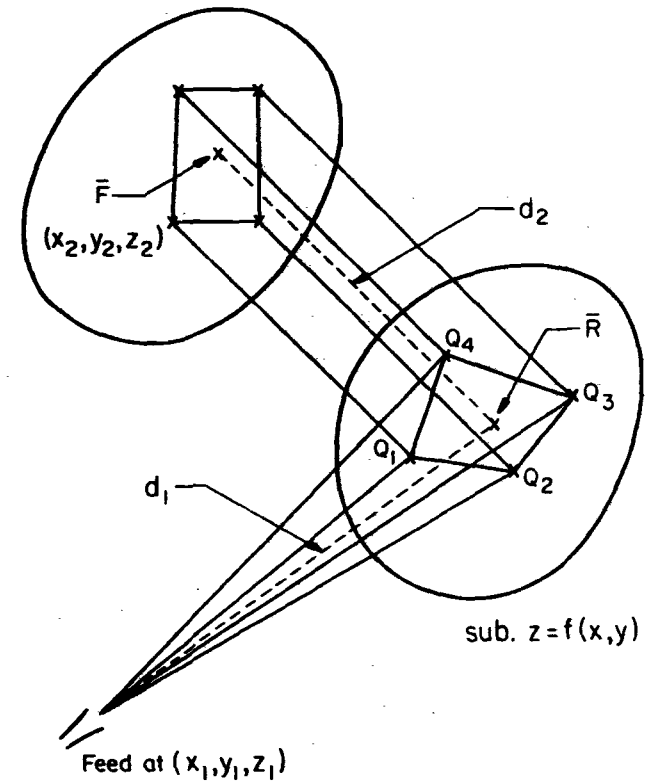


Figure 2.

Launching grid in main  
reflector and subreflector.

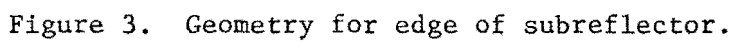


Figure 3. Geometry for edge of subreflector.

# Aperture Amplitude and Phase Control of Offset Dual Reflectors

VICTOR GALINDO-ISRAEL, FELLOW, IEEE, RAJ MITTRA, FELLOW, IEEE, AND ALAN G. CHA, MEMBER, IEEE

**Abstract**—The dual-shaped reflector synthesis problem was first solved by Galindo and Kinber in the early 1950's for the circularly symmetric-shaped reflectors. Given an arbitrary feed pattern, it was shown that the surfaces required to transform this feed pattern by geometrical optics into any specified phase and amplitude pattern in the specified output aperture are found by the integration of two simultaneous nonlinear ordinary differential equations. For the offset noncoaxial geometry, however, it is shown that the equations found by this method are partial differential equations which, in general, do not form a total differential. Hence the exact solution to this problem is generally not possible. It is also shown, however, that for many important problems the partial differential equations form a nearly total differential. It thus becomes possible to generate a smooth subreflector by integration of the differential equations and then synthesize a main reflector which gives an exact solution for the specified aperture phase distribution. The resultant energy (or amplitude) distribution in the output aperture as well as the output aperture periphery are then approximately the specified values. A representative group of important solutions are presented which illustrate the very good quality that frequently results by this synthesis method. This includes high gain, low sidelobe, near-field Cassegrain, and different ( $f/D$ ) ratio reflector systems.

## INTRODUCTION

THE UTILITY of using geometrical optics for shaping a dual-reflector system for aperture amplitude and phase control has been demonstrated in many applications such as large satellite communication ground stations throughout the world and, recently, the high-gain antennas of Voyagers I and II. Although many designs are for uniform amplitude and phase (maximum gain), the synthesis method permits accurately generated amplitude tapers for better sidelobe control with reflector antennas. These antennas have, in the past, been of circular symmetric (coaxial) design. The geometrical optics synthesis was exact for these antennas. For a given feed pattern, any aperture phase and amplitude were specified together with the input and output aperture peripheries (circular). The reflector profiles were then found by an exact solution to a pair of simultaneous first-order ordinary nonlinear differential equations. The synthesis method was first described by Galindo [1] and Kinber [2].

The offset or noncoaxial geometry for dual-reflector antennas is significant because the blockage (in the symmetrical coaxial geometry) of the feed, subreflector, and struts of the

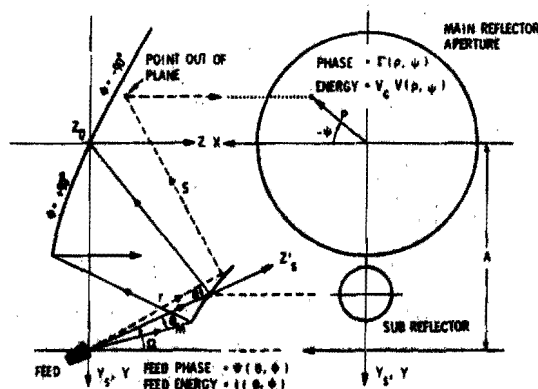


Fig. 1. Geometry of dual reflectors.

main reflector aperture reduces the gain and increases the sidelobe levels and cross polarization. The effects are important in large- as well as small-diameter reflectors.

A mathematically similar synthesis approach for the offset geometry, Fig. 1, as for the circularly symmetric geometry, leads to a pair of simultaneous first-order partial nonlinear differential equations. The existence of a solution to these equations requires that they form a total differential. This was pointed out by Kinber [2] and recently Galindo-Israel and Mittra [3]. As Kinber [2] implied and Mittra and Galindo-Israel [4] showed, in general, the exact solution to these partial differential equations does not exist for an arbitrarily specified aperture and feed distribution. However, Galindo-Israel and Mittra [3] did show that in many significant cases the partial differential equations were very nearly total. Thus solutions derived from these equations very nearly satisfied all the required conditions.

Basically, the method utilizes a concept employed by Green [5] in getting an approximately shaped solution for the circularly symmetric case. For dual-reflector systems in which the ratio of the diameters of the main reflector to the subreflector is large, it is found that most of the energy redistribution is accomplished by the subreflector. Hence, phase corrections designed into only the main reflector do not greatly alter the energy distribution.

We therefore solve the partial differential equations for a pair of reflectors which have both phase and energy errors. We retain the subreflector as solved for. We then synthesize a new main reflector which gives the exact required phase distribution. Since the original equations were nearly total, the required perturbations are very small. As a matter of fact, the original equations are so nearly total that the method works well even when the ratio of the main reflector diameter to subreflector diameter is one.

At the time this method for obtaining an approximate solution was first proposed [3], Mizusawa, Urasaki, and Tanaka

Manuscript received June 22, 1978; revised October 14, 1978. This paper presents the results of one phase of research carried out at the Jet Propulsion Laboratory, California Institute of Technology, under Contract NAS 7-100, sponsored by the National Aeronautics and Space Administration.

V. Galindo-Israel and A. G. Cha are with the Jet Propulsion Laboratory, California Institute of Technology, Pasadena, CA 91103.

R. Mittra is with the Department of Electrical Engineering, University of Illinois, Urbana, IL 61801, and Consultant to the Jet Propulsion Laboratory.

[6] also proposed a somewhat similar approach. They, as Green also does [5], synthesize a phase-correcting main reflector after determining an *initial* subreflector. Their method for determining an appropriate subreflector is, however, entirely different, and it is also apparently not nearly as flexible as the method proposed herein.

In the approximate solutions developed herein, we obtain an exact aperture phase distribution with an approximate amplitude distribution in the main reflector aperture. In addition, although an excellent approximation has always been obtained [7], either the input or the output aperture perimeter must be approximated to that specified. Mittra, Galindo, and Hyjazie have recently shown [8] how a solution with left-right symmetry can be generated from a specified dual center section ( $\phi = \psi = \pm 90^\circ$  in Fig. 1) with the same limitations on aperture perimeter specifications but with greater control over the amplitude specification. In fact, the most recent work [9] appears to indicate that when only a *single* aperture perimeter is specified—either the main or subreflector aperture perimeter—then a general solution that is correct in phase and optimum in amplitude can be generated from a single initial ray specified from the feed to the main reflector aperture. This method is very similar, mathematically, to the method employed approximately in this paper. The essential differences will be discussed in the development of the partial differential equations which follow.

#### DIFFERENTIAL EQUATION DEVELOPMENT

The fundamental problem of synthesis, as defined by Kimber [2], is illustrated in Fig. 2. We have an input "bundle" of rays; the direction and density (phase and amplitude) given by a feed pattern function (Fig. 1):

$$\Gamma(\theta, \phi) = \text{phase function} \quad (1a)$$

$$I(\theta, \phi) = \text{energy (power) function.} \quad (1b)$$

Also specified is the feed aperture perimeter or boundary of the input bundle of rays

$$\theta_M(\phi) = \text{input aperture perimeter.} \quad (1c)$$

The desired output aperture distribution is specified as (Fig. 1)

$$\Psi(\rho, \psi) = \text{output phase function} \quad (2a)$$

$$V_c V(\rho, \psi) = \text{output energy function,} \quad (2b)$$

where  $V_c$  is a normalization constant. The boundary of the output aperture perimeter is also specified as

$$\rho_M(\psi) = \text{output aperture perimeter.} \quad (2c)$$

The choice of spherical coordinates for the feed pattern and subreflector, and cylindrical coordinates for the output aperture distribution and main reflector is useful since the feed pattern phase is usually spherical so that

$$\Gamma(\theta, \phi) = \text{constant,} \quad (3a)$$

and the output aperture phase is usually chosen as planar

$$\Psi(\rho, \psi) = \text{constant.} \quad (3b)$$

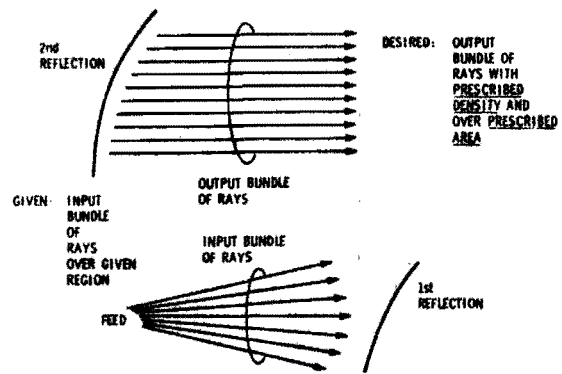


Fig. 2. Geometrical optics problem.

As discussed earlier, it is not generally possible to satisfy the output amplitude and phase conditions together with pre-specified perimeter boundaries. Nevertheless, these are the conditions which the antenna engineer would generally prefer to specify, and hence these conditions comprise and define "the synthesis problem." With this definition of the problem, it has been shown that the solution, in general, does *not* exist [3], [4], [7]–[9].

Some relaxation of these conditions is therefore required. It has been found that a minimum relaxation of the problem would be the elimination of *either* aperture perimeter specification, (1c) or (2c). It is sufficient for two or more specified conditions to be partially relaxed. It is not yet clear whether this approach does or does not lead to a better all-around approximation to the total synthesis problem. It is, in principle, the approach taken herein, where the main reflector aperture amplitude and the periphery of *either* reflector (we choose the main reflector herein) are perturbed from the specifications.

As a first step in developing the partial differential equations which must be integrated, we will write the Snell's law equations at each reflector for an arbitrary ray traced from the feed to the aperture (Fig. 1). There are four Snell's law equations—two for each reflector—because of the double curvature of each reflector. We determine these equations by writing, first, the *path length* along the trajectory to a plane located at  $z = D$ . We will assume a spherical feed phase and planar output phase (3), so the path length is

$$r + S + D - z = \text{constant} = K'. \quad (4a)$$

We can refer back to the plane  $z = 0$ ; so

$$r + S = z + K \quad (K = K' - D). \quad (4b)$$

The path length between reflectors,  $S$ , is found from

$$\begin{aligned} S^2 = & (-\rho \sin \psi + r \sin \theta \sin \phi \cos \Omega \\ & - r \cos \theta \sin \Omega + a)^2 + (\rho \cos \psi \\ & - r \sin \theta \cos \phi)^2 + (z - r \sin \theta \sin \phi \sin \Omega \\ & - r \cos \theta \cos \Omega)^2 \end{aligned} \quad (5a)$$

or

$$S \equiv (S^2)^{1/2} \equiv (\Delta x^2 + \Delta y^2 + \Delta z^2)^{1/2}. \quad (5b)$$



Fermat's principle of *minimum* length for the optical path can be applied to (4) by first holding a point on the subreflector stationary  $[(\theta, \phi) \text{ fixed}]$  and setting<sup>1</sup>

$$z_\rho - S_\rho = 0 \quad \text{and} \quad z_\psi - S_\psi = 0. \quad (6a)$$

Without any loss of generality we have tacitly made the choice of  $(z)$  and  $(r)$  as the dependent variables and  $(\rho, \psi)$  and  $(\theta, \phi)$  as the *independent* variables in any functional representation for the reflector shapes—i.e.,  $z(\rho, \psi)$  and  $r(\theta, \phi)$  define the reflectors and are the solutions for which we search.

Fermat's principle, applied to the subreflector, leads to

$$r_\theta + S_\theta = 0 \quad \text{and} \quad r_\phi + S_\phi = 0. \quad (6b)$$

After some algebra we find

$$r_\theta = \frac{rR_t}{S-R} \quad r_\phi = \frac{rR_p}{S-R} \quad (7a)$$

and

$$z_\rho = \frac{-\Delta y \sin \psi + \Delta x \cos \psi}{S - \Delta z}$$

$$z_\psi = \frac{-\Delta y \rho \cos \psi - \Delta x \rho \sin \psi}{S - \Delta z}, \quad (7b)$$

where

$$R = \Delta y [-\sin \theta \sin \phi \cos \Omega + \cos \theta \sin \Omega] \\ + \Delta x [\sin \theta \cos \phi] - \Delta z [-\sin \theta \sin \phi \sin \Omega \\ + \cos \theta \cos \Omega] \quad (8a)$$

$$R_t = \Delta y [-\cos \theta \sin \phi \cos \Omega - \sin \theta \sin \Omega] \\ + \Delta x [\cos \theta \cos \phi] - \Delta z [-\cos \theta \sin \phi \sin \Omega \\ + \sin \theta \cos \Omega] \quad (8b)$$

and

$$R_p = -\Delta y [\sin \theta \cos \phi \cos \Omega] + \Delta x [-\sin \theta \sin \phi] \\ + \Delta z [\sin \theta \cos \phi \sin \Omega]. \quad (8c)$$

In general, the *nonlinear* functional relationships shown below exist for (7):

$$z_\rho = z_\rho(z, r/\rho, \psi; \theta, \phi) \quad z_\psi = z_\psi(z, r/\rho, \psi; \theta, \phi) \quad (9a)$$

and

$$r_\theta = r_\theta(z, r/\rho, \psi; \theta, \phi) \quad r_\phi = r_\phi(z, r/\rho, \psi; \theta, \phi), \quad (9b)$$

where we have emphasized the *choice* of  $(z, r)$  as dependent variables.

Equations (9), which express Snell's law at each reflector, are used to form the "total" differentials

$$dz = z_\rho d\rho + z_\psi d\psi \quad \text{and} \quad dr = r_\theta d\theta + r_\phi d\phi. \quad (10)$$

<sup>1</sup> We adopt the notation that  $\partial Q/\partial \theta = Q_\theta$  where  $\partial Q/\partial \theta$  is the partial derivative of  $Q(\theta, \phi, \dots)$  with  $\theta$ .

In order to integrate (10) we require the transformation relationships which we shall descriptively call the "mapping" equations

$$\rho = \rho(\theta, \phi) \quad \text{and} \quad \psi = \psi(\theta, \phi). \quad (11)$$

For an arbitrary input ray from the feed, i.e., choose  $(\theta, \phi)$ , (11) selects a "mapped" point on the main reflector at  $(\rho, \psi)$ . Clearly, specification of the input perimeter  $\theta_M(\phi)$  will fix the output perimeter  $\rho_M(\psi)$  when (11) is found.

If the mapping equations (11) are known, then we could write (10) as

$$dz = (z_\rho \rho_\theta + z_\psi \psi_\theta) d\theta + (z_\rho \rho_\phi + z_\psi \psi_\phi) d\phi \quad (12a)$$

and

$$dr = r_\theta d\theta + r_\phi d\phi. \quad (12b)$$

Then, given any path  $\theta = \theta(\phi)$  in the  $(\theta, \phi)$  space, we may integrate (12) along the path for a solution.

The determination of the mapping equations is, at this point, *underconstrained*. It is well known that for a given input phase function  $\Gamma(\theta, \phi)$  only a *single* reflector is necessary to obtain a specified output phase  $\Psi(\rho, \psi)$ . We want to further constrain  $\rho(\theta, \phi)$  and  $\psi(\theta, \phi)$  by the energy relationship and the perimeter conditions.

Let us examine the energy relationship. Differentially, we require conservation of energy, as expressed by

$$V_c V(\rho, \psi) \rho d\rho d\psi \equiv I(\theta, \phi) \sin \theta d\theta d\phi \quad (13)$$

in addition to mapping equations which lead to perimeters  $\theta_M(\phi)$  and  $\rho_M(\psi)$ , so that

$$V_c \int_0^{2\pi} \int_0^{\rho_M(\psi)} V(\rho, \psi) \rho d\rho d\psi \\ \equiv \int_0^{2\pi} \int_0^{\theta_M(\phi)} I(\theta, \phi) \sin \theta d\theta d\phi. \quad (14)$$

We have stated earlier that although satisfying (13) may be possible with the proper mapping equations, in general, these mapping equations will *not* lead to (14) [4], [9] or *both* desired perimeters simultaneously.

If the mapping equations were known, then we could write (13) as

$$V_c V(\rho, \psi) \rho J(\rho, \psi/\theta, \phi) d\theta d\phi = I(\theta, \phi) \sin \theta d\theta d\phi, \quad (15)$$

where

$$J(\rho, \psi/\theta, \phi) = \text{Jacobian determinant} \\ = [\rho_\theta \psi_\phi - \rho_\phi \psi_\theta]. \quad (16)$$

Alternatively, we could mathematically define the synthesis problem, at this point of development, as that of determining the Jacobian determinant (16). In fact, it is thus possible to integrate (12) from an initial point  $(z_0, r_0/\rho_0, \psi_0; \theta_0, \phi_0)$  along a defined path  $\theta(\phi)$ , determining, *as we integrate along the path*, the Jacobian determinant and the solution, except for simultaneous satisfaction of the aperture perimeter re-

quirements (1c) and (2c). This approach will be discussed in a subsequent paper [9].

An alternative approach, which is the principal subject of this paper, is to *a priori* determine approximately suitable mapping functions (11) (i.e., before integration of (10)). In this approach, some relaxation of the main (or feed) aperture energy distribution as well as the perimeter specifications is necessary.

We proceed by *partially* specifying either  $\rho(\theta, \phi)$  or  $\psi(\theta, \phi)$  and forcing the perimeter boundary in (13) and (14), the energy conservation equations.

In the circularly symmetric (coaxial) case, for example, we know, by definition, that

$$\psi = \phi. \quad (17a)$$

$$V(\rho, \psi) \equiv V(\rho) \quad (17b)$$

$$I(\theta, \phi) \equiv I(\theta), \quad (17c)$$

$$\rho(\theta, \phi) = \rho(\theta) \quad (17d)$$

is found from (13) and (14). We find that the differential equations to be integrated (12) are *total*, since, of course, all paths ( $\phi = \text{constant}$ ) are identical, and the partial differential equations reduce to ordinary differential equations.

For the offset geometry we have chosen a mapping which behaves *functionally* as

$$\psi = \psi(\phi). \quad (18)$$

With this assumption alone, applied to the energy equations (13) and (14), both the actual specific function  $\psi(\phi)$  and

$$\rho = \rho(\theta, \phi) \quad (19)$$

can be found. For example, if we have a circularly symmetric feed pattern

$$I(\theta, \phi) \equiv \cos^{n-1} \theta \quad (20a)$$

and Gaussian aperture distribution

$$V_c V(\rho, \psi) = V_c \exp(-b\rho^2), \quad (20b)$$

then the functional mapping requirement in (18) leads to the mapping equations

$$\psi = \phi \quad (21a)$$

and

$$\rho^2 = \frac{1}{b} \ln \left[ \frac{nV_c}{(nV_c - 1) + \cos^n \theta} \right] \quad (21b)$$

where

$$V_c = \frac{2b}{n} \left[ \frac{1 - \cos^n \theta_M}{1 - \exp(-b\rho_M^2)} \right]. \quad (21c)$$

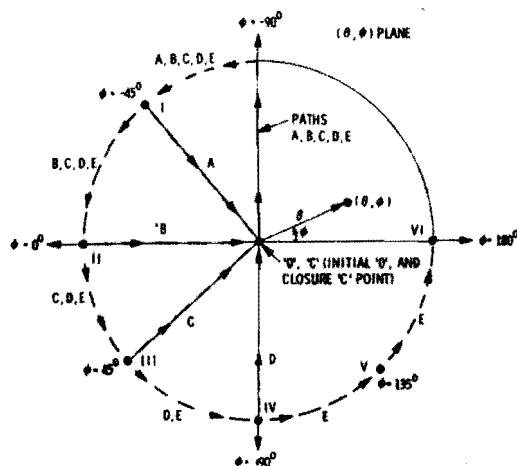


Fig. 3. Line integral paths.  $(\theta, \phi)$  plane, polar format ( $\phi = \text{angle}$ ,  $\theta = \text{radial}$ ). Paths A, B, C, D, E, depicted. Points 'O', I, II, III, IV, V, VI, and 'C', the terminal or closure point of all paths except path E. Points 'O' and 'C' coincide.

The only requirement which we have imposed *a priori* on the mapping equations is that  $\psi$  be independent of  $\theta$ , i.e., (18).

Having now obtained the transformations, we can integrate the partial differential equations (10) or (12). The test of validity of the mapping choice (18)—other choices are possible—is whether the differential equations (12) form *total* differentials or not. If they are not total differentials, then the question remains—how close are they?

Tests for the total differentiability of (12) can be made directly, or the tests can be made by integrating (12) along *closed paths* in the  $(\theta, \phi)$  plane and observing how close are the values of  $(z, r)$  determined at the initial point of the path  $(r_0, \phi_0)$  at  $(\theta_0, \phi_0)$  to those at the closure point of the path  $(z_c, r_c)$  at  $(\theta_0, \phi_0)$ .

The line-integral paths that can be chosen for a typical result are shown in Fig. 3. The independent variable  $(\theta, \phi)$  plane is shown in polar form. A series of integration paths designated by A, B, C, D, and E are illustrated. They pass through the points designated by I through VI. The paths A, B, C, and D are closed paths, originating at the origin with values  $(z_0, r_0)$  and closing at the origin with the values  $(z_c, r_c)$ .

There are two reasons why  $(z_0, r_0)$  may not equal  $(z_c, r_c)$  at the origin. One may be due to the lack of *total* differentiability of (12) under the approximated mapping conditions (21). The longer the path of integration the greater is the disagreement between  $(z_0, r_0)$  and  $(z_c, r_c)$  that can be expected. The degree of disagreement will then be a measure of lack of total differentiability. The path D is a very long path within the field of applicable values in the  $(\theta, \phi)$  plane, and it is thus a good measure of maximum deviation from a perfect solution.

However, we should also consider the error introduced by the numerical integration of the nonlinear partial differential equations. This error also increases with path length. In order to estimate this error we examine results found along the path E shown in Fig. 3. Because we do require left-right symmetry in the solutions regardless of the total differentiability, the solutions for  $(z, r)$  should agree at points II and VI and also at points III and V. Since points II and VI are separated by the longest path length, the maximum integration error can be found by comparing  $(z, r)$  values at these points. In Table I we see the integration errors incurred along the path E for two cases. The integration error occurs in the eighth and ninth

TABLE I

Case 1: Feed Energy Pattern =  $\cos^{30} \theta$  (-20 dB at Edge)Gaussian Aperture =  $\exp(-0.08 \rho^2)$ ,  $A=6$ ,  $\theta_H=10^\circ$ ,  $\rho_H=5$ ,  $\Omega=0^\circ$ Initial Point "0" =  $(z_0, r_0) = (0., 5.)$ 

Path	Closure Value	
	$z_c$	$r_c$
A	-0.005697	4.994302
B	-0.018806	4.981195
C	-0.031872	4.968913
D	-0.035955	4.964045

Integration Error-Comparison on Path E ( $\theta = 10^\circ$ )

	$z$	$r$
$\phi = 0^\circ$ Point II	0.825956390	5.19734505
$\phi = 180^\circ$ Point VI	0.825956378	5.19734478
<hr/>		
	$z$	$r$
$\phi = 45^\circ$ Point III	-0.839963265	4.89534484
$\phi = 135^\circ$ Point V	-0.839963268	4.89534485

Case 2: Same as Case 1 except

Aperture Distribution = constant (uniform)

Initial Point "0" =  $(z_0, r_0) = (0., 5.)$ 

Path	Closure Value	
	$z_c$	$r_c$
A	-0.005311	4.994690
B	-0.017548	4.982452
C	-0.029039	4.970960
D	-0.036004	4.966398

Integration Error-Comparison on Path E ( $\theta = 10^\circ$ )

	$z$	$r$
$\phi = 0^\circ$ Point II	0.859777832	5.23336233
$\phi = 180^\circ$ Point VI	0.859777820	5.23336206
<hr/>		
	$z$	$r$
$\phi = 45^\circ$ Point III	-0.806211328	4.92928158
$\phi = 135^\circ$ Point V	-0.806211331	4.92928159

decimal digits for the longer separation between points II and VI and in the ninth digit between points III and V over the shorter path difference.

In contrast, the errors in  $(z, r)$ , that is between  $(z_0, r_0) = (0., 5.)$  and  $(z_c, r_c)$  at the path closure, are in the second and third decimal digits. These errors also increase with increase in path length as observed in Table I for cases 1 and 2. These errors are thus a clear result of the fact that (12) does not form *total* differentials under the mapping transformations (21). These cases are fairly typical of a large number of results. We find that the greater the feed taper (larger  $n$ ) and the lesser the main reflector aperture taper (smaller  $b$ ), then the greater are the discrepancies indicated between  $(z_0, r_0)$  and  $(z_c, r_c)$ . Case 2 is one with a greater than average discrepancy. It is important to note that decreasing the integration error does *not* decrease path-closure error between  $(z_0, r_0)$  and  $(z_c, r_c)$ .

For an overall reflector diameter of ten and an overall optical path length from the feed to the aperture of the main reflector of about 13, the closure value discrepancies of  $\approx 0.035$  for the longest path do not appear very large. If the reflector were  $100\lambda$  in diameter then the phase error would be of the order of  $0.35\lambda$ . This error is large. It appears, however, that only small perturbations of either reflector shape are necessary to correct the phase error and would lead to a result with only small perturbations of the desired energy distribution and

perimeter values (1c) and (2c). This approach to an approximate solution is developed in the next section.

Another more direct test of the total differentiability of (12) can be found by comparing  $r_{\theta\phi}$  with  $r_{\phi\theta}$  and comparing  $z_{\rho\psi}$  with  $z_{\psi\rho}$ . When the parameter  $A$  equals zero (Fig. 1), the circular symmetric reflectors give  $r_{\theta\phi} = r_{\phi\theta} = 0$  and  $z_{\rho\psi} = z_{\psi\rho} = 0$  since  $\partial/\partial\phi = 0$  and  $\partial/\partial\psi = 0$ . Total differentiability is a *point* characteristic required everywhere in the  $(\theta, \phi)$  plane for integration of (12) to an exact solution. In Table II we observe results for  $r_{\theta\phi}$ ,  $r_{\phi\theta}$ ,  $z_{\rho\psi}$ , and  $z_{\psi\rho}$  computed *analytically*<sup>2</sup> along the path ( $\theta = 0^\circ - 10^\circ$ ,  $\phi = 90^\circ$ ) for the same cases 1 and 2 illustrated in Table I.

At the origin ( $\theta = 0$ ), we find  $r_{\theta\phi} = r_{\phi\theta}$  and  $z_{\rho\psi} = z_{\psi\rho}$  independent of the mapping equations. This occurs since the initial (or central) specified ray determines a *unique* tangent plane at each reflector. Variation of  $\phi$  or  $\psi$  at these points leaves the point at the *same* position on the reflector but at a different inclination angle on the tangent plane depending upon the offset.

Since the subreflector is about 1/5 the diameter of the main reflector, we observe that the curvature—as proportional to the second derivatives—is about five times larger.

<sup>2</sup> The equations for the second derivatives are very cumbersome and are not included herein.

TABLE II  
COMPARISON OF SECOND PARTIAL DERIVATIVES:  $\phi = -90^\circ$

Case 1: (See Case 1, Table 1)

$\theta^\circ$	$\frac{r_{\theta\phi} \times 10^8}{r_{\phi\theta} \times 10^8}$	$\frac{z_{\rho\psi} \times 10^9}{z_{\psi\rho} \times 10^9}$
0°	-0.23234 -0.23234	-0.46467 -0.46467
2°	-0.25035 -0.25220	-0.46456 -0.46467
4°	-0.27462 -0.28216	-0.46419 -0.46476
6°	-0.30574 -0.32169	-0.46352 -0.46502
8°	-0.34267 -0.36539	-0.46248 -0.46502
10°	-0.38288 -0.40912	-0.46100 -0.46131

Case 2: (See Case 2, Table 1)

$\theta^\circ$	$\frac{r_{\theta\phi} \times 10^8}{r_{\phi\theta} \times 10^8}$	$\frac{z_{\rho\psi} \times 10^9}{z_{\psi\rho} \times 10^9}$
0°	-0.23234 -0.23234	-0.46467 -0.46467
2°	-0.25148 -0.25410	-0.46456 -0.46468
4°	-0.27816 -0.28688	-0.46418 -0.46474
6°	-0.31050 -0.32518	-0.46350 -0.46465
8°	-0.34649 -0.36576	-0.46246 -0.46271
10°	-0.38545 -0.40953	-0.46097 -0.46680

The discrepancies between  $r_{\theta\phi}$  and  $r_{\phi\theta}$  are much larger than those between  $z_{\rho\psi}$  and  $z_{\psi\rho}$ . Both of the cases illustrated in Table II yield excellent results in the final approximate solutions which we shall see later. The principal errors that will be observed later are for the prescribed uniform aperture distribution—case 2. In this case the main discrepancies in aperture amplitude uniformity occur near the edges (in the geometrical optics analysis). Note also that  $z_{\rho\psi}$  differs most from  $z_{\psi\rho}$  near the edges ( $\theta$  large) in case 2. This error can then be taken as a measure of the expected error that the approximate synthesis procedure will yield.

In practice, however, by the time these second derivatives are computed, the full approximate solution may be computed and the resultant energy distribution and main reflector periphery ( $\theta_M(\phi)$ ) may be observed directly.

The discussion on the tests of whether or not (12) form a total differential has been extensive for several important reasons.

- 1) The question of the total differentialability of these equations has been repeatedly overlooked in both the published and unpublished literature. Hence, the question of the *existence* of a solution has been often neglected.
- 2) It is not generally possible to determine the total differentialability analytically. In fact, the initial point ( $z_0, r_0$  at  $\theta = 0^\circ$ ) in Table II does satisfy the criterium.
- 3) Finally, the *nearly* total differentialability that has been shown has motivated the approximate synthesis method which will be discussed next. The approximate solutions are in fact

perturbations of “solutions” generated by the equations just discussed.

### THE APPROXIMATE SOLUTION—DEVELOPMENT OF A PHASE-CORRECTED MAIN REFLECTOR

The solutions obtained by integrating (12) do not satisfy the prescribed conditions. In fact, since (12) are not total, the solutions for  $z(\theta, \phi)$  and  $r(\theta, \phi)$  will depend upon the integration path from  $(\theta_0, \phi_0)$  to  $(\theta, \phi)$ . We have shown, however, that whenever (12) are *nearly* total, then different paths yield *nearly* the same results for  $z(\theta, \phi)$  and  $r(\theta, \phi)$ . The results, however, are sufficiently inaccurate to yield large phase errors for even moderate diameters (in wavelengths) for the main reflector.

To overcome this problem, we propose to generate a smooth subreflector by integration of (12), and then, in a manner similar to [5] and [6], we will generate a main reflector with zero phase errors. This main reflector will then approximately satisfy the energy requirement  $V_c V(\rho, \psi)$  and the periphery requirement  $\rho_M(\psi)$  (alternatively we can exactly satisfy  $\rho_M(\psi)$  and approximately satisfy the subreflector periphery requirement  $\theta_M(\phi)$ ).

In order to generate a smooth subreflector, we choose to integrate (12) along the radials ( $\theta = 0 \rightarrow \theta_M, \phi = \text{constant}$ ) for arbitrarily close  $\phi$ . The analyticity of (12) insures a smooth reflector. Since (12) are not total, there exist other choices (or paths of integration) for a smooth subreflector. However, since the assumption of our approximation method is that  $r_{\theta\phi} \cong r_{\phi\theta}$

and  $z_{\rho}\psi \cong z_{\psi\rho}$  everywhere in  $(\theta, \phi)$  for  $\theta \leq \theta_M$ , then different choices for our initial subreflector must not lead to very much better or worse final approximations in the dual reflector pair. We next determine a phase-correcting main reflector.

The subreflector found from integrating (12) along the radials  $d\phi = 0$  may be considered a member of the family of surfaces

$$G(r, \theta, \phi) \equiv r - g(\theta, \phi) = C, \quad (22)$$

where  $C = 0$  denotes the subreflector. The outward normal  $\hat{n}$  is found from

$$\hat{n} \cdot \nabla G = -\hat{r} + \frac{r_{\phi}}{r \sin \theta} \hat{\phi} + \frac{r_{\theta}}{r} \hat{\theta}, \quad (23a)$$

where

$$|\nabla G|^2 = 1 + \left( \frac{r_{\phi}}{r \sin \theta} \right)^2 + \left( \frac{r_{\theta}}{r} \right)^2. \quad (23b)$$

Note that  $r_{\theta}$  is found analytically (9b), while  $r_{\phi}$  must be found numerically by considering adjacent radials of the subreflector.

The incident ray direction is given by  $\hat{r}$ , so that from Snell's law and (23) we obtain the reflected ray direction  $\hat{s}$

$$\hat{s} = \hat{r} - 2(\hat{r} \cdot \hat{n})\hat{n}, \quad (24)$$

where we note that

$$\hat{s} = \hat{x} \cos \alpha + \hat{y} \cos \beta + \hat{z} \cos \gamma. \quad (25)$$

The values  $(\cos \alpha, \cos \beta, \cos \gamma)$  are the direction cosines of the reflected ray. A linear equation for the reflected ray is therefore

$$\frac{x - x_s}{\cos \alpha} = \frac{y - y_s - a}{\cos \beta} = \frac{z - z_s}{\cos \gamma}, \quad (26)$$

where  $(x_s, y_s, z_s)$  and  $(x, y, z)$  are, respectively, sub- and main-reflector rectangular coordinates (see Fig. 1).

We note that  $(x_s, y_s, z_s)$  are known and that  $(x, y, z)$ , the ray-connected coordinates of the main reflector, are to be determined. We translate coordinates so that the point on the subreflector becomes the origin

$$x' \equiv x - y_s, \quad y' \equiv y - y_s - a, \quad z' \equiv z - z_s. \quad (27)$$

Thus  $(x', y', z')$  are our new unknowns.

If we now impose the path length requirement  $\Psi(\rho, \psi) = \text{constant}$ , then we can solve for  $(x', y', z')$ . We note that the Levi-Civita theorem [10] ensures that Snell's law at the main reflector is satisfied. The path length equation (4b) can be written

$$S = \sqrt{x'^2 + y'^2 + z'^2} = z' + h, \quad (28a)$$

where

$$h = z_s - r + K \quad (28b)$$

is known. It is thus straightforward to use (26) and (28) to

find the main reflector

$$\left\{ \begin{array}{l} x' = (\cos \alpha / \cos \gamma) z' = m z' \\ y' = (\cos \beta / \cos \gamma) z' = l z' \\ z' = \frac{h}{\sqrt{l^2 + m^2 + 1} - 1} \end{array} \right\} \quad (29)$$

Having thus constructed the main reflector to insure the exact satisfaction of the phase requirement, we have also implicitly found the mapping equations (11)

$$\rho = \rho(\theta, \phi) \quad \psi = \psi(\theta, \phi) \quad (11)$$

numerically. We note, in general, that for  $\phi = \text{constant}$  on the subreflector that  $\psi$  is *not* a constant, although we have found that when the results (satisfaction of the energy requirement) are good, then  $\psi$  varies by no more than several degrees (i.e.,  $\psi \cong \psi(\phi)$ ). Because of the left-right symmetry condition of the offset geometry considered (Fig. 1), we note that  $\psi = \phi$  when  $\phi = \pm 90^\circ$ . Furthermore, at  $\phi = \pm 90$ , the main reflector remains unaltered from the values found by integrating (12).

Since  $\psi$  is a function of  $\theta$  and  $\phi$ , if we impose the perimeter boundary on the subreflector,  $\theta_M(\phi) = \theta_M(\text{constant})$ , then the main reflector projected perimeter will not, in general, be perfectly circular. We could, of course, impose a circular projected perimeter on the main reflector and allow  $\theta_M(\phi)$  to vary, however, the solutions have generally resulted in insignificant deviations from the specified periphery boundaries.

The resultant approximate energy density in the main reflector aperture is found by the numerical construction of the Jacobian determinant (16) from the numerically determined mapping equations (11). The Jacobian determinant is then used with (15)

$$V_c V(\rho, \psi) \rho J(\rho, \psi/\theta, \phi) = I(\theta, \phi) \sin \theta$$

to find  $V(\rho, \psi)$  when given  $I(\theta, \phi)$  (or, if desired, to find  $I(\theta, \phi)$  when given  $V(\rho, \psi)$ ). It should be noted that it is very difficult to use a numerical integration of (12) to find, numerically, the mapping transformations (11), and then to numerically find the derivatives

$$(\rho_{\theta}, \rho_{\phi}, \psi_{\theta}, \psi_{\phi})$$

in the Jacobian determinant (16). The results for the energy density in the main reflector aperture that are presented next in this paper are accurate to no more than two significant figures.

## NUMERICAL RESULTS

The approximate method of solution for the offset dual-shaped reflectors that was discussed in the last section has yielded excellent results for a wide variety of important dual-reflector applications. These include high gain, low sidelobe, and near-field Cassegrain (plane wave feed illumination) systems of various  $(f/D)$  ratios and different feed tilt angles  $\Omega$ . Also various feed-subreflector spillover levels are considered.

The feed-illumination functions considered are of the form (20a). The subreflector edge angle was chosen for all cases as  $\theta_M = 10^\circ$ , with either  $-20$ -dB edge illuminations ( $n = 301$ ) or  $-10$ -dB edge illuminations ( $n = 151$ ) being used throughout the results. The only exceptions are the near-field Cassegrain results.

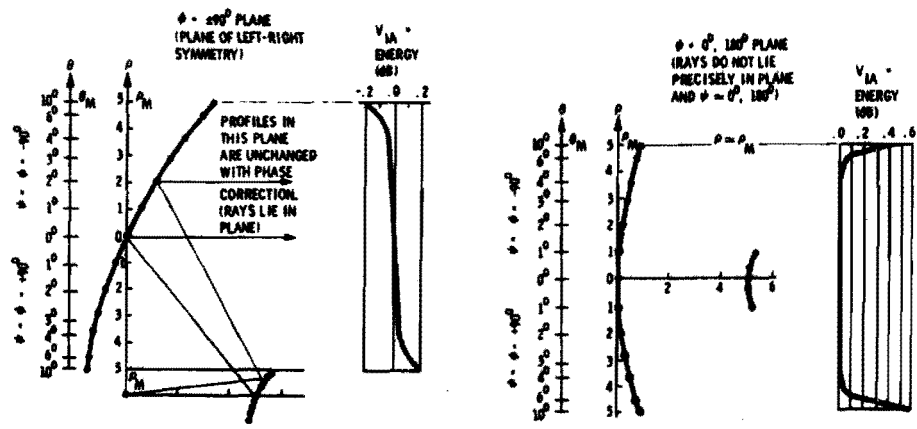


Fig. 4. Profiles and energy distribution. Feed energy pattern =  $\cos^{301} \theta$  (−20 dB at edge). Specified: uniform aperture. Computed average = 2.63.  $r_0 = 5, Z_0 = 0, A = 6, \Omega = 0^\circ$ . Ratio main/subreflector = 5:1.

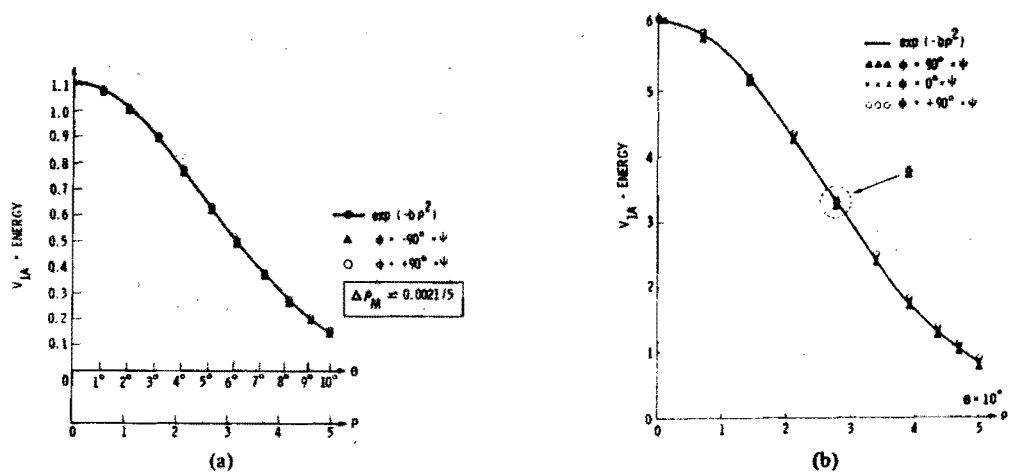


Fig. 5. Results for specified Gaussian distributions of energy in aperture. (a) Feed energy pattern =  $\cos^{151} \theta$  (−10 dB at edge). Specified: Gaussian distribution  $\exp(-0.08 \rho^2)$ .  $r_0 = 5, Z_0 = 0, A = 6, \rho_M = 5, \Omega = 10^\circ$ . (b) Feed energy pattern =  $\cos^{301} \theta$  (−20 dB at edge). Specified: Gaussian distribution  $\exp(-0.08 \rho^2)$ .  $r_0 = 5, Z_0 = 0, A = 6, \rho_M = 5, \Omega = 0^\circ$ .

In Fig. 4 we have illustrated the profiles of the subreflector and main reflector in the plane of symmetry and orthogonal to the plane of symmetry. Also shown are the final, approximate, values of energy or power obtained in the main reflector aperture. In this example we attempted to convert a feed distribution  $\cos^{301} \theta$  (−20 dB at the subreflector edge) into a uniform aperture distribution. If the final main reflector were perfectly circular, we could compute the average energy in the aperture as 2.63. Actually, the main reflector perimeters differ from perfectly circular in all cases by at most a few parts per thousand. The subreflector and the main-reflector profiles are smoother than even the plots may indicate (the small second derivative values in Table II confirm this).

Note that the rays in the symmetry plane ( $\phi = \psi = \pm 90^\circ$ ) lie in that plane. The rays connecting the  $\phi = 0^\circ, 180^\circ$  profiles do not lie in a plane. In fact, on the main reflector  $\psi$  is only approximately  $0^\circ$  and  $180^\circ$ , respectively, differing from  $\phi$  by as much as several degrees at the outer edges ( $\theta_M \cong 10^\circ$ ), so that at  $\theta = \theta_M = 10^\circ$ ,  $\rho$  is very slightly less than  $\rho_M = 5$ . For the symmetry plane the profiles remain unperturbed when constructing the phase corrected main reflector by the method of the last section.

It is very significant to note the  $\theta$  and  $\rho$  scales wherein  $\rho(\theta, \phi)$  is tabulated in effect. Since the feed-illumination

function  $I(\theta, \phi) = \cos^{301} \theta$  is highly tapered and we are attempting to distribute this energy uniformly over the aperture, we find that  $\rho$  varies very slowly for large  $\theta$ . Note that at  $\theta = 6^\circ$  ( $\theta_M = 10^\circ$ ),  $\rho$  is already equal to  $\cong 4.5$  ( $\rho_M = 5$ ). Hence, we find the maximum deviation from uniform energy near the main reflector edges or for larger  $\theta$ .

In contrast, in Fig. 5 we attempt to synthesize Gaussian main reflector aperture distributions as per (20b) with

$$V_c V(\rho) = V_c \exp(-0.08 \rho^2), \quad (\rho_M = 5).$$

The results are excellent for all aperture cuts—better than the plots indicate—and for both feed illuminations  $\cos^{151} \theta$  and  $\cos^{301} \theta$ . The variation  $\rho(\theta)$ , as shown in the abscissa scales, is relatively linear since both the feed and the aperture distributions are tapered. Of course, the parameter  $b$  in the exponential can be adjusted in order to obtain a prescribed taper giving a desired low sidelobe reflector system. Note that the maximum variation of  $\rho_M$  as a function of  $\phi$ ,  $\Delta \rho_M$  in the figure, is only two parts in 5000. Hence, the main aperture is essentially circular as prescribed (although not perfectly so).

In Fig. 6 we observe the effect of feed tilt angle  $\Omega$  on the synthesized results. The profiles for all the results look relatively similar, so the results for the main reflector aperture

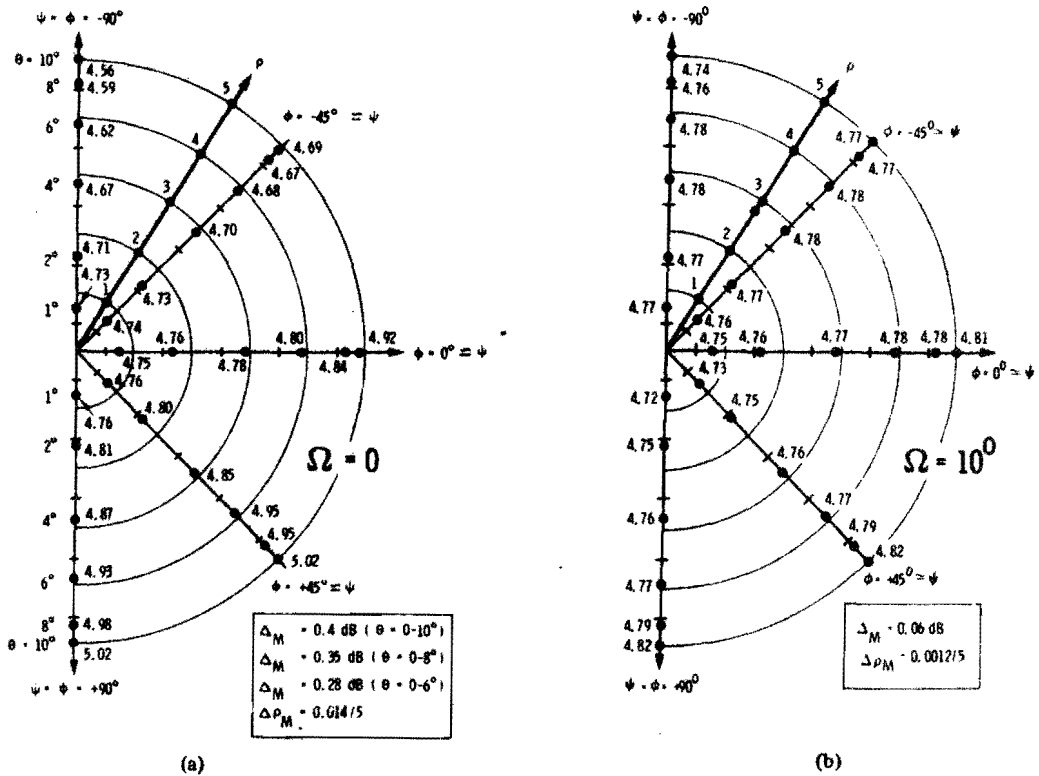


Fig. 6. Aperture energy distributions for different tilt angles ( $\Omega$ ) of feed. (a)  $\Omega = 0^\circ$ . (b)  $\Omega = 10^\circ$ . Computed average:  $4.773$ ,  $\cos^n \theta$  feed,  $n = 151$ ,  $r_0 = 5$ ,  $Z_0 = 0$ ,  $\rho_M = 5$ ,  $A = 6$ ,  $(f/D_P)_a = 7/22$ ,  $\theta_M = 10^\circ$ .

energy distribution are depicted in a polar diagram of the aperture. The resulting phase is perfect. Although  $\rho(\theta)$  still varies very slowly for large  $\theta \approx \theta_M$ , the variation is not as extremely slow as for the  $\cos^{301} \theta$  case of Fig. 4. The parameter  $\Delta_M$  denotes the maximum deviation from uniformity of the aperture energy distribution within the indicated range of  $\theta$  (otherwise for all  $0^\circ \leq \theta \leq \theta_M = 10^\circ$ ). Note again that the greatest deviation from the desired uniformity is near the reflector edges. A very marked improvement is noted for the case with  $\Omega = 10^\circ$  (this value of  $\Omega$  also gives less feed spillover in the main beam direction), from  $\Delta_M \approx 0.4$  dB to  $\Delta_M \approx 0.06$  dB, although both results are considered very good. There is also a parallel improvement in the circularity of the projected apertures as measured by  $\Delta\rho_M$ , although both apertures are essentially circular.

Advanced antenna designs require many well-shaped beams from reflector antennas. The achievability of good-quality beams scanned many beamwidths from the "focal beam" generally requires larger  $(f/D)$  ratios as well as offset geometries [11], [12]. The scannability of a beam is found to depend more strongly on the  $f/D_P$  ( $D_P$  = parent symmetric paraboloid diameter from which the offset paraboloid is derived) than the  $f/D$  [11]. For the shaped offset reflector system we have designated an

$$(\text{approximate } f/D_P) \equiv (f/D_P)_a$$

for the system. It gives a "measure" of the curvature of the system. In Fig. 7 we illustrate the numerical results obtained for a desired uniform aperture distribution as  $(f/D_P)_a$  is varied. We observe marked improvements in uniformity ( $\Delta_M$ ) and also circularity ( $\Delta\rho_M$ ) with increasing  $(f/D_P)_a$ . Hence the synthesis

method can be expected to work well for the required multi-beam reflector antennas needed for new space (and ground) applications.

The motivation for the synthesis method used herein was based partly on the earlier work of Green [5], who constructed a phase-correcting main reflector after synthesizing a "desired" energy distribution from a subreflector. Ostensibly, this method required that the main reflector diameter be much larger than the subreflector so that, essentially, the subreflector redistributed the energy and the main reflector merely corrected the phase. In Fig. 8 we show the results for a case wherein the main reflector to subreflector ratio is 1:1. The results, requiring uniform energy in the aperture, are particularly good. This can be explained by noting that the derivative equations (12) are so nearly total that only very small perturbations are required in our approximate synthesis.

Near-field Cassegrain systems wherein a planar phase front illuminates the subreflector may have application in multi-beam reflector systems since the phased array feed permits the electrical scanning of individual beams (at considerable cost in power distribution circuitry). It is likely that successful systems of this type will require an offset geometry. In Fig. 9 results are displayed for two offset near-field Cassegrain systems. In Fig. 9(a) the plane wave is inhomogeneous—tapering to  $-10$  dB at the subreflector edge, where as in Fig. 9(b) the incident field is homogeneous. Numerically, the center of the spherical wave phase pattern is placed far from the subreflector so that, effectively, a planar phase front is incident over  $0^\circ \leq \theta \leq \theta_M = 0.1^\circ$ . In both cases, excellent results are shown in achieving both the aperture energy uniformity and the circular periphery.

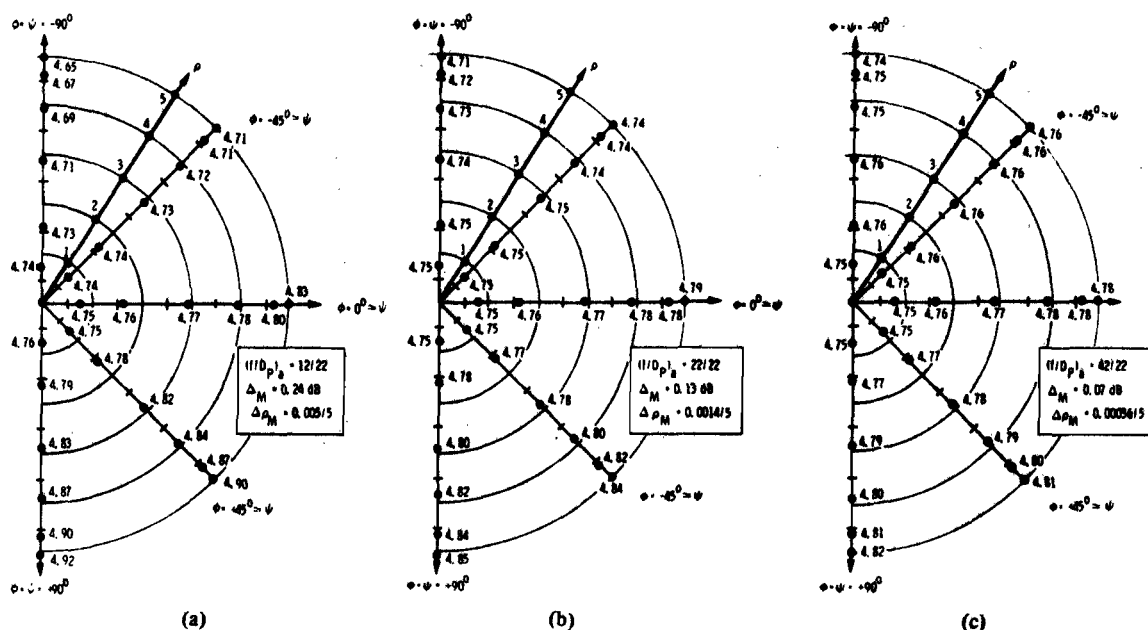


Fig. 7. Aperture energy distribution for increasing apparent  $(f/D)$  ratio. Computed average energy =  $4.773 \cos^3 \phi$  feed,  $n = 151$ ,  $r_0 = 5$ ,  $\rho_M = 5$ ,  $A = 6$ ,  $\Omega = 0^\circ$ ,  $\theta_M = 10^\circ$ , (a)  $Z_0 = 5$ . (b)  $Z_0 = -15$ . (c)  $Z_0 = -35$ .

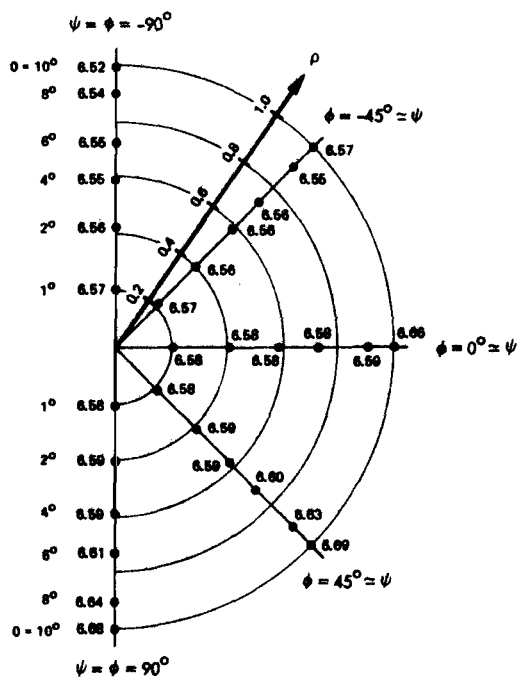


Fig. 8. Aperture energy distribution for ratio of main to subreflectors = 1:1. Feed energy pattern =  $\cos^{301} \theta$  (-20 dB at edge).  $r_0 = 5$ ,  $\theta_M = 10^\circ$ ,  $Z_0 = 0$ ,  $\rho_M = 1.0$ ,  $A = 1.25$ . Computed average aperture energy = 6.58.



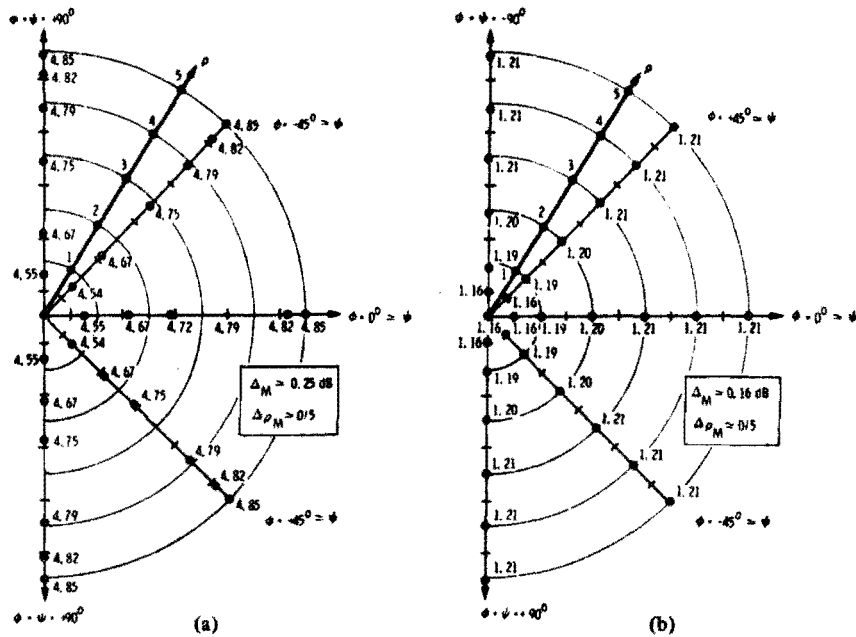


Fig. 9. Aperture energy distributions for near-field Cassegrain system with homogenous and inhomogenous incident plane wave feeds. (a)  $n = 1.511790 \times 10^6$ ,  $\cos^2 \theta$  feed (-10-dB taper). (b)  $n = 0.1$ ,  $\cos^2 \theta$  feed (uniform).  $r_0 = 500$ ,  $Z_0 = 495$ ,  $\rho_M = 5$ ,  $A = 6$ ,  $\Omega = 0$ ,  $\theta_M = 0.1^\circ$ .

### CONCLUSION

In the synthesis of dual-shaped reflectors it has been shown earlier [1], [2], for circular symmetric reflectors, that an exact geometrical optics solution could be found to the problem of transforming, by two reflections, any feed pattern into any aperture distribution. This problem involved solving two simultaneous nonlinear ordinary differential equations. The same approach for the offset geometry leads to two simultaneous nonlinear partial differential equations. It is shown herein that these equations could also be integrated numerically, except that, in general, these equations are not total and, therefore, in general, they do not have a "smooth" solution.

It is further shown herein that although the offset partial differentials do not form a total differential, they very often nearly do so in many cases of practical importance. It thus becomes possible to devise an approximate synthesis method wherein a "smooth" subreflector is generated from the partial differential equations, and a perturbed main reflector is subsequently found which corrects exactly for any phase errors in the desired aperture phase distribution. The approximation is then to the desired aperture energy distribution and to the aperture periphery. In all cases considered, the desired periphery is circular and the approximations are found to also be circular to within very few parts in a thousand (relative to apertures of diameter = 10). Excellent energy distribution approximations are also found for high-gain antennas (uniform energy desired) and for low-sidelobe antennas (Gaussian distributions are synthesized). The results also prove to be very good for near-field Cassegrain antennas (plane-wave feed illuminations) and for small to large equivalent ( $f/D$ ) main reflector curvatures. Finally, although the approximate synthesis method was motivated in part by the work of Green [5], wherein for large ratios of main reflector to subreflector diameters it is found that the energy output is formed at the subreflector and the phase controlled at the main reflector, it is

shown that the method works very well in many important designs even when the ratio of reflector diameters is 1:1.

### REFERENCES

- [1] V. Galindo, "Design of dual reflector antennas with arbitrary phase and amplitude distribution," in *IEEE Proc. Int. Symp. Antennas and Propagation*, Boulder, CO, July 1963; also in *IEEE Trans. Antennas Propagat.*, vol. AP-12, pp. 403-408, July 1964.
- [2] B. Y. Kimber, "On two reflector antennas," *Radio Eng. Electron. Phys.*, vol. 6, June 1962.
- [3] V. Galindo-Israel and R. Mittra, "Synthesis of offset dual shaped reflectors with arbitrary control of phase and amplitude," presented at USNC/URSI E.M. Symp. IEEE Symp. Antennas and Propagation, Stanford, CA, June 1977.
- [4] R. Mittra and V. Galindo-Israel, "Some fundamental questions related to the problem of dual reflector synthesis," in *Proc. Nat. Radio Sci. Meet.*, Boulder, CO, Jan. 1978.
- [5] K. A. Green, "Modified Cassegrain antenna for arbitrary aperture illumination," *IEEE Trans. Antennas Propagat.*, vol. AP-11, pp. 589-590, Sept. 1963.
- [6] M. Mizusawa, S. Urasaki, and H. Tanaka, "An offset shaped-reflector Cassegrain antenna," in *Proc. IEEE Symp. Antennas and Propagation*, Stanford, CA, June 1977.
- [7] V. Galindo-Israel, R. Mittra, and A. Cha, "Aperture amplitude and phase control of offset dual reflectors," presented at USNC/URSI and IEEE Symp. Antennas and Propagation, College Park, MD, May 1978.
- [8] R. Mittra, V. Galindo-Israel, and F. Hyjazie, "A method for synthesizing offset dual reflector antennas," presented at USNC/URSI and IEEE Symp. Antennas and Propagation, College Park, MD, May 1978.
- [9] V. Galindo-Israel and R. Mittra, "Synthesis of asymmetric dual shaped reflectors," to appear.
- [10] T. Levi-Civita, *Rend. R. Acc. Naz. Linc.*, vol. 9, p. 237, 1900.
- [11] R. Mittra and V. Galindo-Israel, "On the analysis of offset reflector antennas," presented at IEEE Symp. Antennas and Propagation, Stanford, CA, June 1977.
- [12] R. Mittra, V. Galindo-Israel, Y. Rahmat-Samii, and R. Norman, "Offset paraboloidal field computations using an efficient series expansion," presented at IEEE Symp. Antennas and Propagation, College Park, MD, May 1978, to appear as a full paper.

# Synthesis of Offset Dual Reflector Antennas Transforming a Given Feed Illumination Pattern into a Specified Aperture Distribution

RAJ MITTRA, FELLOW, IEEE, FAYEZ HYJAZIE, AND VICTOR GALINDO-ISRAEL, FELLOW, IEEE

**Abstract**—The problem of transforming a given primary feed pattern into a desired aperture field distribution through two reflections by an offset dual reflector system is investigated using the concepts of geometrical optics. A numerically rigorous solution for the reflector surfaces is developed which realizes an exact aperture phase distribution and an aperture amplitude distribution that is accurate to within an arbitrarily small numerical tolerance. However, this procedure does not always yield a smooth solution, i.e., the reflector surfaces thus realized may not be continuous or their slopes may vary too rapidly. In the event of nonexistence of a numerically rigorous smooth solution, an approximate solution that enforces the smoothness of the reflector surfaces can be obtained. In the approximate solution, only the requirement for the aperture amplitude distribution is relaxed, and the condition on the aperture phase distribution is continued to be satisfied exactly.

## I. INTRODUCTION

THE OFFSET geometry for dual reflector antennas is attractive for satellite communications where low sidelobes are necessary to achieve good isolation between adjacent main lobes operating over the same frequency band. The symmetric subreflector configuration introduces blockage by the subreflector and the supporting struts. This, in turn, has the effect of reducing the gain, increasing the sidelobe level, and enhancing the cross-polarization level in the secondary pattern. The use of offset reflectors is becoming prevalent since the limiting effects of aperture blockage can be entirely removed, and more mechanical freedom is available in the choice of the supporting structures and types of thermal control.

The problem to be addressed in this work can be stated as follows: given a primary feed pattern, design an offset two-reflector system to obtain a desired amplitude and phase distribution in the projected aperture plane of the main reflector. The synthesis procedure is based on geometrical optical analysis and, hence, diffraction effects are to be neglected. The solution thus derived can be verified by performing an analysis of the secondary pattern.

The shaping of dual reflector antennas was first suggested in 1958 for the purpose of increasing the gain [1], [2]. The discussion was restricted to circularly symmetric dual reflector antennas. For the circularly symmetric case, a method for

synthesizing the two-reflector system was first described by Galindo [3] and Kinber [4]. An exact solution for the reflector profiles was obtained by integration of a pair of simultaneous, first-order, ordinary, nonlinear differential equations.

For the offset asymmetric geometry, Kinber [4] claimed that an exact solution does not necessarily exist. In 1971, Yeh [5] developed a geometrical optical analysis for an arbitrary dual reflector antenna. Through this analysis, he utilized the trial and error techniques to construct the reflector surfaces which produce the desired aperture field distribution. In 1975, Mitzugutchi and Yokoi [6] derived a general set of equations relating the two surfaces which satisfy Snell's law and the phase constraint in the aperture. However, they concluded that simultaneous control of the aperture amplitude was not generally possible. Consequently, they restricted themselves to solutions satisfying the phase constraint in the aperture with limited amplitude control.

Galindo-Israel, Mittra, and Cha [7] previously addressed the synthesis problem for the case of an offset geometry. They developed an approximate solution which was constructed via a two-step process. In the first step, a solution was generated for a pair of reflectors which have errors in both the amplitude and the phase distributions in the aperture. This was achieved by requiring certain transformation relationships between the reflector surfaces and by enforcing a prespecified aperture perimeter for the subreflector. In the second step, the solution thus obtained was corrected, following Green's approach [8], by keeping only the subreflector and synthesizing a new main reflector which exactly satisfies the requirement for the aperture phase distribution. Mizusawa, Urasaki, and Tanaka [9] also presented an approximate solution by synthesizing a phase-correcting main reflector after first generating a subreflector.

In our synthesis method, we present a numerically rigorous procedure for generating the two-reflector surfaces in a one-step process. This solution gives an exact aperture phase distribution and enforces the condition on the aperture amplitude distribution to within an arbitrarily specified numerical tolerance. However, this procedure does not always yield a smooth solution. In the event of nonexistence of a smooth solution, we look for an approximate solution that enforces the smoothness of the reflector surfaces while relaxing the energy condition, i.e., the satisfaction of the requirement on the amplitude distribution in the aperture; however, the condition on the aperture phase distribution is continued to be satisfied exactly.

Finally, we point out that the procedure described in this paper is different from the one in an earlier paper [10] on the same subject where the synthesis problem was viewed in a different light. The primary difference is that in the earlier paper we had enforced a constraint called the consistency condition, whereas in the present work we impose the total derivative condition. The latter condition can be expressed,

Manuscript received February 4, 1981; revised April 15, 1981. This work was supported in part by the Air Force Office of Scientific Research under Grant AFOSR 80-0179, and in part by Contract NAS 7-100, from NASA at the Jet Propulsion Laboratory, California Institute of Technology, Pasadena, CA 91103.

R. Mittra is with the Electromagnetics Laboratory, Department of Electrical Engineering, University of Illinois, Urbana, IL 61801. He is also a consultant for the Jet Propulsion Laboratory, California Institute of Technology, Pasadena, CA 91103.

F. Hyjazie was with the Electromagnetics Laboratory, Department of Electrical Engineering, University of Illinois, Urbana, IL.

V. Galindo-Israel is with the Jet Propulsion Laboratory, California Institute of Technology, Pasadena, CA 91103.

in the Cartesian system, as

$$z_{xy} = z_{yx}$$

for an arbitrary point,  $x, y, z$ , on the surface given by  $z(x, y)$ . The fact that the satisfaction of the total derivative condition is a prerequisite for synthesizing a physically realizable solution has been recognized [7] recently and its importance has been adequately emphasized. The simultaneous imposition of this condition together with the satisfaction of path-length (aperture phase) and energy (aperture amplitude) requirements is considered to be the most important and new contribution of this paper since this has not been accomplished in any of the earlier papers on the subject. We should point out, however, that the present method does not offer a simultaneous and direct means for controlling the shape of the peripheries of the two reflectors, and only one of these can be specified arbitrarily. Furthermore, the polarization effects are not accounted for in the synthesis procedure.

The subject of perimeter shape is further discussed in Section II-I. For the present we proceed with the description of the synthesis procedure in Section II.

## II. METHOD OF SYNTHESIS

The geometrical optics synthesis is based on the following principles.

1) Path-length condition (or phase condition)—This condition requires a constant total length for the path in which any ray, originating from the primary source phase center  $O$  and impinging on the plane  $\Sigma$  at  $z = z_0$ , travels after two reflections from the subreflector and main reflector consecutively. (See Fig. 1(b).) We can write the following equation:

$$|\vec{OA}| + |\vec{AB}| + |\vec{BB'}| = C_0 \quad (1)$$

where  $C_0$  is a given constant (Fig. 1(b)).

2) The energy condition—This condition demands that the incident energy in the incremental solid angle  $d\Omega$  bounded by the rays  $\vec{OA_1}$ ,  $\vec{OA_2}$ , and  $\vec{OA_3}$  be equal to the total energy exiting through the corresponding incremental area  $dS$  formed by the points  $B_1'$ ,  $B_2'$ , and  $B_3'$  in the plane  $\Sigma(z = z_0)$ , as shown in Fig. 1(a).

$I_2(x, y)$ , the desired energy distribution in the plane  $\Sigma$ :  $z = z_0$ , and  $I_1(\Omega)$ , the radiation intensity of the primary source, are related by

$$I_1(\Omega) d\Omega = I_2(x, y) dS. \quad (2)$$

3) Snell's law of reflection applied to the subreflector is stated via the following two equations:

$$\hat{n}_1 \cdot (\hat{s}_1 + \hat{s}_2) = 0 \quad (3a)$$

$$(\hat{n}_1 \times \hat{s}_1) \cdot \hat{s}_2 = 0 \quad (3b)$$

where  $\hat{n}_1$  is the unit normal to the subreflector at the point  $A$  where the ray  $\vec{OA}$  intersects the subreflector (Fig. 1b), and  $\hat{s}_1$  and  $\hat{s}_2$  are the unit vectors along the incident ray  $\vec{OA}$  and the reflected ray  $\vec{AB}$ , respectively.

4) The Levi-Civita theorem [11] states that for a normal congruence of rays that undergoes only one reflection, the path-length requirement implies the satisfaction of Snell's law by the incident and reflected geometrical optical fields.

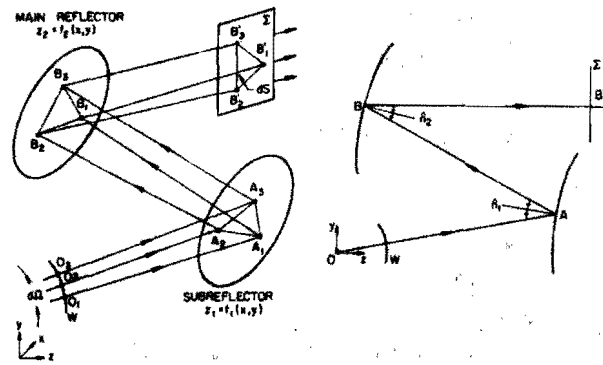


Fig. 1. Geometrical optics transformation of a given primary field into a specified aperture field through two reflections.

Hence, according to the Levi-Civita theorem, if we apply the path length condition to a ray which undergoes reflection from the two reflector surfaces, but apply Snell's law only at the subreflector, Snell's law will be automatically satisfied at the main reflector.

5) Let the subreflector surface be described by the equation

$$z_1 = f_1(x, y)$$

where  $f_1$  is defined and differentiable in a domain  $D$  of the  $xy$  plane. Assume for the moment that the first and second partial derivatives of  $f_1$  are continuous over  $D$ . According to the theorem in differential calculus [12], if the function  $f_1$ , its first partial derivatives  $f_{1x}$  and  $f_{1y}$ , and its second partial derivatives  $f_{1xy}$  and  $f_{1yx}$  are continuous in the domain  $D$ , then the mixed second partial derivatives of  $f_1$  are equal. Therefore, we can write

$$f_{1xy} = f_{1yx}$$

for the subreflector surface. Equation (5) is designated as the total differential condition which must be satisfied by physically realizable surfaces.

### A. Numerically Rigorous Solution

In this section, we present a solution for the synthesis problem which satisfies the path-length condition exactly and enforces the energy condition to within some arbitrarily small numerical tolerance imposed on the satisfaction of the amplitude distribution in the exit aperture plane. This solution is generated in a step-by-step fashion, to be outlined below, from a starting curve which is typically chosen as the line of symmetry on the subreflector surface. It is implicitly assumed throughout this work that the feed illumination as well as the specified distribution in the exit aperture plane have left-right symmetry. However, at this point no other constraints are imposed on the shape of the starting curve. Not unexpectedly one finds that the shapes of the two reflector surfaces as well as the contours of the peripheries of the reflectors are dependent on the shape of the starting line of symmetry. In fact, not all starting curves result in a solution, and as yet, we have been unsuccessful in determining *a priori* which starting curve will lead to a desirable solution. Nevertheless, the starting curve can be chosen from one of the several approximate solutions to the two reflector surfaces that can be generated using, for example, the method in [7].

Next, we introduce the following notations: 1)  $(C_{10}, C_{11}, \dots, C_{1N})$  and  $(C_{20}, C_{21}, \dots, C_{2N})$  for the two sets of curves lying on the subreflector and the main reflector surfaces, respectively, as shown in Fig. 2. These curves are all generated by the synthesis procedure described below, except  $C_{10}$  which is the starting curve. The first and second subscripts of  $C$  from the right refer to the reflector surface and the number of the curve, respectively. 2)  $(A_{1n}, A_{2n}, \dots, A_{M_n n})$  and  $(B_{1n}, B_{2n}, \dots, B_{M_n n})$  are the points of the curves  $C_{1n}$  and  $C_{2n}$ , respectively, where  $M_n$  is the total number of points of either  $C_{1n}$  or  $C_{2n}$ . The letters  $A$  and  $B$  denote the points of the subreflector and the main reflector, respectively. The first subscript of  $A$  or  $B$  from the right refers to the number of the point on the curve  $C_{1n}$  or the curve  $C_{2n}$  while the second subscript refers to the number of the curve. 3)  $(x_{1n}^m, y_{1n}^m, z_{1n}^m)$  and  $(x_{2n}^m, y_{2n}^m, z_{2n}^m)$  are the coordinates of the points  $A_{mn}$  and  $B_{mn}$ , respectively.

The starting curve  $C_{10}$  can be presented as a mathematical function or it can be described by a discrete set of points and its derivatives at those points. The curve  $C_{10}$  may be considered as the foundation on which the subreflector surface is to be constructed. The first step in our method of synthesis of the reflector surfaces is to determine the curve  $C_{20}$  from which the main reflector surface is to be generated.

The curve  $C_{20}$  intercepts all the rays reflected from points along the curve  $C_{10}$  such that the path-length condition (1) is satisfied between the input and output geometrical fields of the system as shown in Fig. 3. We determine  $C_{20}$  point-by-point starting from  $B_{10}$  and ending at  $B_{L0}$ . We now present the procedure for determining the point  $B_{K0}$  given the point  $A_{K0}$  and the derivatives at  $A_{K0}$ .

#### B. Determination of $B_{K0}$ Given $A_{K0}$ and the Derivatives at $A_{K0}$

Given  $A_{K0}$  and the derivatives at  $A_{K0}$ , we construct a tangent plane  $P_1$  at  $A_{K0}$  as shown in Fig. 4. The plane  $P_1$  represents to the first degree of approximation the subreflector surface locally at  $A_{K0}$ . A ray  $\vec{S}_i$  incident on  $P_1$  at  $A_{K0}$  from the primary source at  $O$  gets reflected from  $P_1$  as the ray  $\vec{S}_r$  in the direction given by Snell's law of reflection, i.e.,

$$\hat{s}_r = \hat{s}_i - 2(\hat{s}_i \cdot \eta_1)\eta_1 \quad (6)$$

where  $\hat{s}_i$  and  $\hat{s}_r$  are unit vectors in the direction of the incident and reflected rays, respectively. A linear equation of  $\vec{S}_r$  is given by

$$\frac{x - x_a}{\cos \alpha_x} = \frac{y - y_a}{\cos \alpha_y} = \frac{z - z_a}{\cos \alpha_z} \quad (7)$$

where  $(\cos \alpha_x, \cos \alpha_y, \cos \alpha_z)$  are the direction cosines of the reflected ray  $\vec{S}_r$  and  $(x_a, y_a, z_a)$  are the rectangular coordinates of  $A_{K0}$ .

We now introduce a tangent plane  $P_2$  in the path of the ray  $\vec{S}_r$  as shown in Fig. 4. We require that the ray  $\vec{S}_r$  be reflected in the  $z$ -direction as the ray  $\vec{S}_r'$ , which meets the exit plane  $\Sigma (z = z_0)$  at the point  $B_{K0}$ . The point  $B_{K0}$  is determined from the intersection of the plane  $P_2$  with the ray  $\vec{S}_r$  such that the total path length traveled by the rays  $\vec{S}_i$ ,  $\vec{S}_r$ , and  $\vec{S}_r'$  is constant (see principle 4). This is accomplished by solving the equations of the path-length condition 1) and the reflected ray  $\vec{S}_r$ . Similarly, given any point belonging to the subreflector surface and the derivatives at that point, we determine the corresponding

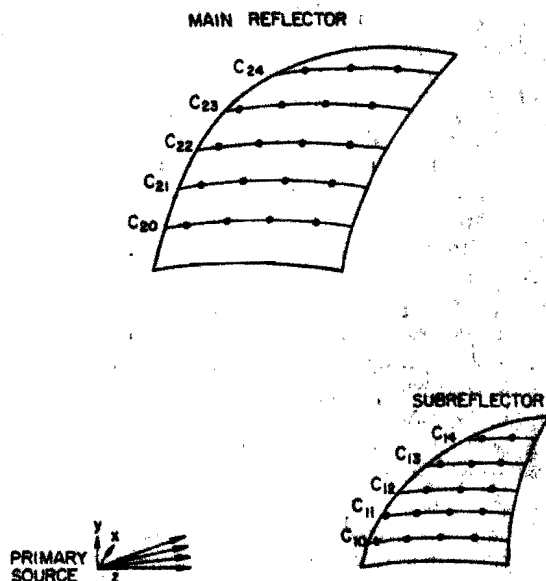


Fig. 2. Synthesized curves  $C_{1n}$  on the subreflector and  $C_{2n}$  on the main reflector surface.

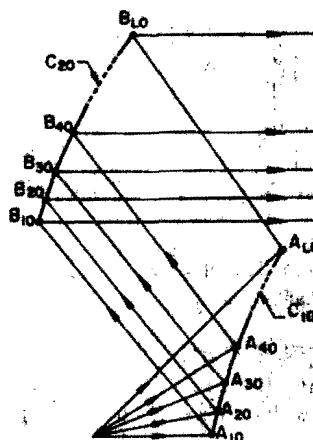


Fig. 3. Description of the initial curve  $C_{10}$  of the subreflector and the first generated curve  $C_{20}$  of the main reflector.

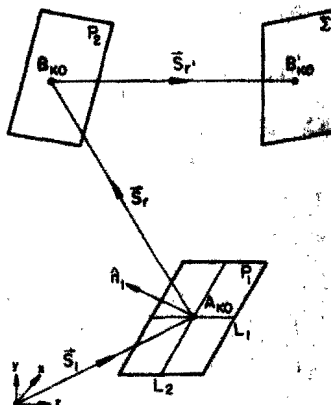


Fig. 4. Illustrating the determination of a point on the main reflector given a point on the subreflector and the derivatives  $\partial z_1/\partial x$  and  $\partial z_1/\partial y$  at this point.

point on the main reflector surface by applying the path-length condition.

### C. An Overview of the Method of Construction of the Reflector Surfaces

In a step-by-step procedure, we construct the reflector surfaces from single curves in space separated by small finite distances as shown in Fig. 2. These curves are individually generated as follows. For the subreflector surface, we first generate point-by-point the curves  $C_{11}$  and  $C_{21}$  from the initial curves  $C_{10}$  and  $C_{20}$ . Each time the location of a new point of  $C_{11}$  and the derivatives at this point are found, we determine the corresponding point of the curve  $C_{21}$  of the main reflector surface as explained in Section II-A. From the curves  $C_{11}$  and  $C_{21}$ , we next generate the curve  $C_{12}$  of the subreflector surface with its corresponding curve  $C_{22}$  of the main reflector surface following the same procedure, and so on. We continue building up the reflector surfaces by generating other curves until the incident energy (ray cone) from the primary source is captured by the generated subreflector surface.

### D. Determination of the Point $A_{mn}$

The coordinates of the point  $A_{mn}$ , the  $m$ th point of the  $n$ th curve of the subreflector surface, are given by the following equations:

$$x_{1n}^m = x_{1(n-1)}^m + \Delta x \quad (8a)$$

$$y_{1n}^m = y_{1(n-1)}^m \quad (8b)$$

$$z_{1n}^m = z_{1(n-1)}^m + \left[ \frac{\partial z_1}{\partial x} \right]_{(n-1)}^m \cdot \Delta x. \quad (8c)$$

Equation (8c) is the Taylor's series expansion about  $A_{m(n-1)}$  with only the linear terms.

### E. Determination of $\partial z_1 / \partial y$ at the Point $A_{mn}$

The partial derivative  $\partial z_1 / \partial y$  of the generated subreflector surface at  $A_{mn}$  is determined from its Taylor's series expansion about  $A_{m(n-1)}$  and the total differential condition (5). If terms of order  $\geq 2$  are neglected,  $\partial z_1 / \partial y$  is given by the equation

$$\left. \frac{\partial z_1}{\partial y} \right|_{\text{at } A_{mn}} = \left. \frac{\partial z_1}{\partial y} \right|_{\text{at } A_{m(n-1)}} + \frac{\partial}{\partial x} \left[ \left. \frac{\partial z_1}{\partial y} \right|_{\text{at } A_{m(n-1)}} \right] \cdot \Delta x. \quad (9)$$

Substituting (5) in (9), we obtain

$$\begin{aligned} \left[ \frac{\partial z_1}{\partial y} \right]_n^m &= \left[ \frac{\partial z_1}{\partial y} \right]_{(n-1)}^m \\ &+ \frac{\left[ \frac{\partial z_1}{\partial x} \right]_{(n-1)}^{(m+1)} - \left[ \frac{\partial z_1}{\partial x} \right]_{(n-1)}^m}{[y_1]_{(n-1)}^{(m+1)} - [y_1]_{(n-1)}^m} \end{aligned} \quad (10)$$

where the second term of (10) is written in a finite difference form and where the symbol  $[\cdot]_q^p$  means that the function inside the brackets is to be evaluated at the point  $A_{pq}$ .

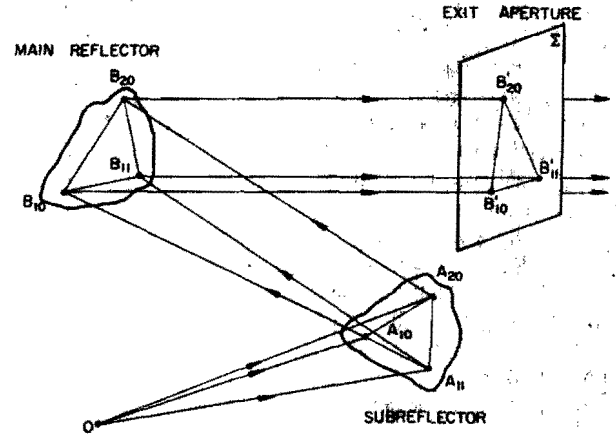


Fig. 5. The beam of rays incident on the constructed portion of the subreflector surface at the points  $A_{m(n-1)}$ ,  $A_{(m+1)(n-1)}$  and  $A_{mn}$  and the reflected from the constructed portion of the main reflector at the points  $B_{m(n-1)}$ ,  $B_{(m+1)(n-1)}$  and  $B_{mn}$ .

### F. Determination of $\partial z_1 / \partial x$ at $A_{mn}$ and the Point $B_{mn}$

The clue to finding  $z_{1x}$  rests on the energy condition (2). The location of  $A_{mn}$  and the partial derivative  $z_{1y}$  at  $A_{mn}$  are not sufficient to determine the point  $B_{mn}$  of the curve  $C_{2n}$  of the main reflector surface.  $z_{1x}$  at  $A_{mn}$  is also needed for that purpose. We begin by assigning to  $z_{1x}$  at  $A_{mn}$  an appropriate value which is a slight perturbation of  $z_{1x}$  at  $A_{m(n-1)}$ . Next, we determine  $B_{mn}$  as discussed in Section II-A. We continue to change monotonically  $z_{1x}$  at  $A_{mn}$  until the energy condition is satisfied. This is tested for the triad of rays incident on the constructed portion of the subreflector surface at the points  $A_{m(n-1)}$ ,  $A_{(m+1)(n-1)}$  and  $A_{mn}$  and reflected from the main reflector surface at the points  $B_{m(n-1)}$ ,  $B_{(m+1)(n-1)}$  and  $B_{mn}$ , respectively (Fig. 5). For each choice of  $z_{1x}$ , we calculate the energy in the incremental solid angle formed by the rays  $OA_{m(n-1)}$ ,  $OA_{(m+1)(n-1)}$  and  $OA_{mn}$  incident on the generated portion of the subreflector surface (Fig. 5). Next, from (2), we calculate the energy distribution  $I_2'$  in the incremental area  $dS$  defined by the points  $B_{m(n-1)}$ ,  $B_{(m+1)(n-1)}$ , and  $B_{mn}$  where the rays reflected from the generated portion of the main reflector surface at  $B_{m(n-1)}$ ,  $B_{(m+1)(n-1)}$ , and  $B_{mn}$ , respectively, intersect the exit aperture  $\Sigma$  (Fig. 5). Then, we compare the energy distribution  $I_2'$  obtained for the value assigned to  $z_{1x}$  at  $A_{mn}$  with the energy distribution  $I_2$  desired in  $dS$ . Furthermore, we define a comparison factor  $R$  given in decibels by the equation

$$R = 10 \log \frac{I_2'}{I_2} \quad (11)$$

and require that  $R$  be within a specified numerical tolerance. We terminate this procedure when this condition  $R$  is reached.

### G. Determination of the Derivatives at the Point $B_{mn}$

The distance traveled by the ray from the point  $A_{mn} = (x_a, y_a, z_a)$  to the point  $B_{mn}' = (x, y, z_0)$  via the point  $B_{mn} = (x, y, z_2)$  is given by

$$d = \sqrt{(x - x_a)^2 + (y - y_a)^2 + (z - z_a)^2} + z_0 - z_2. \quad (12)$$

According to Fermat's principle, the distance  $d$  is stationary

Thus,

$$\frac{\partial d}{\partial x} = \frac{\partial d}{\partial y} = 0. \quad (13)$$

Solving (13), we obtain the derivatives  $z_{2x}$  and  $z_{2y}$  at  $B_{mn}$  by the following equations:

$$z_{2x} = \frac{x - x_a}{d_1 - z_2 + z_a} \quad (14a)$$

$$z_{2y} = \frac{y - y_a}{d_1 - z_2 + z_a} \quad (14b)$$

where

$$d_1 = \sqrt{(x - x_a)^2 + (y - y_a)^2 + (z - z_a)^2}.$$

#### H. Approximate Solution

The procedure described in the last section, though numerically rigorous, does not always yield a physically acceptable solution, particularly for small  $R$ , defined in (14). The curves generated by this procedure sometimes have slopes that vary much too rapidly. Occasionally, the solution becomes unstable or even runs away and ceases to exist for  $n$  greater than a certain value.

In order to ensure that the reflector surfaces are smooth when the above situation occurs, it becomes necessary to relax the energy condition and settle for only an approximate satisfaction of this condition where  $R$  is a finite nonzero number, say  $\pm 0.2$  dB, and not arbitrary close to zero ( $\approx \pm 0.00001$  dB) as in the numerically rigorous solution.

Let us say that after the construction of a certain curve  $C_{1n}$  of the subreflector and its corresponding curve  $C_{2n}$  of the main reflector is completed, we notice that the curve  $z_{1x}(y)$  or the derivative  $z_{1x}$  at the points of  $C_{1n}$  plotted versus  $y$  is discontinuous (or vary very rapidly) which, in turn, causes the curve  $C_{2n}$  to be discontinuous. When this occurs, we first smooth the curve of  $z_{1x}(y)$  by the least square polynomial approximation. Using the location of the points of  $C_{1n}$ , and the new smoothed derivative  $z_{1x}$  and the derivative  $z_{1y}$  at these points, we determine the new curve  $C_{2n}$  of the main reflector surface by applying Snell's law at the subreflector in conjunction with the path length condition. Obviously, the smoothing of the curve  $z_{1x}(y)$  slightly changes  $z_{1x}$  at the points of  $C_{1n}$ . Thus, the new curve  $C_{2n}$  also changes; hence,  $R$  of (11) is altered. We now check if  $R$  is within the specified numerical tolerance, and if not, we conclude that there does not exist a solution for that choice of  $R$ .

#### I. The Perimeter of the Reflector Surfaces

As mentioned earlier, we do not specify the perimeters of the reflector surfaces in our synthesis problem. Instead, we build up the reflector surfaces from the initial curves  $C_{10}$  and  $C_{20}$  until all of the energy from the primary source is intercepted by the generated subreflector surface. After the construction of the reflector surfaces is finished, the perimeters of one of these surfaces can be arbitrarily specified as long as the perimeter is within the boundaries of illumination from the source. Usually, the projected aperture of the main reflector surface is desired to be circular because of symmetry advantages. In this case, we may carve out a portion from the

generated main reflector surface whose projected perimeter is a circle within the maximum available radius. This carved-out portion can then be used as the main reflector and its corresponding portion of the generated subreflector surface can be used as the subreflector. If, however, we wish to impose the condition that there be no spillover from the subreflector surface, we may carve out a portion of the subreflector which is within a conical region whose apex is at the origin. The corresponding portion of the main reflector will not, in general, have a circular projection, and the user has to judge whether the resulting solution is acceptable.

### III. RADIATION PATTERN ANALYSIS

Given the reflector surfaces, the radiation intensity, and the polarization of the primary source, we calculate the electric field in the exit aperture. Having the aperture field distribution, we determine the far-zone electric field. For this purpose, we use the series representation method of the radiation integral developed by Galindo and Mittra [13] and Rahmat-Samii *et al.* [14].

We apply this method to evaluate the radiation pattern of the electric field aperture distribution over the circular aperture of the main reflector with radius  $a$ . The electric field aperture distribution is derived using geometrical optics and is expanded into trigonometric functions and a modified form of the Jacobi polynomials which are particularly suitable for circular apertures. The radiation integral is, then, analytically represented by a rapidly convergent series whose coefficients are independent of the observation angles. Thus, the series can be computed rapidly for a large number of observation angles.

In determining the aperture field and the radiation pattern, we consider the following coordinate systems which are shown in Fig. 6: 1) a feed-centered system  $(x', y', z')$  in which the radiation intensity and the polarization of the primary source are given; 2) an  $(x, y, z)$  coordinate system in which the reflector surfaces are described and the electric field on the aperture in the  $(x, y, z_0)$  plane is calculated; and 3) an  $(x_1, y_1, z_1)$  coordinate system which we define by the transformation:  $x_1 = x$ ,  $y_1 = y - b$ ,  $z_1 = z$  where  $(0, b, z_0)$  is the center of the circular aperture of the main reflector.

#### A. The Electric Field in the Main Reflector Aperture

To determine the electric field distribution in the aperture, we form an irregular grid of triangles in the aperture by constructing each triangle from every set of three neighboring points as shown in Fig. 7. Next, we calculate the electric field inside each triangle as follows.

Consider a triangle  $T$  formed by the points  $B_{mn}$ ,  $B_{m(n-1)}$ , and  $B_{(m+1)(n-1)}$ . Let  $G$  be a pencil of three rays exiting the aperture through the vertices of triangle  $T$ . We now trace back the pencil  $G$ . The pencil of rays  $G$  originates from the primary source at  $O$  and intersects the subreflector at the points  $A_{mn}$ ,  $A_{m(n-1)}$ , and  $A_{(m+1)(n-1)}$ . After reflection from the subreflector,  $G$  intersects the main reflector at the points  $B_{mn}$ ,  $B_{m(n-1)}$ , and  $B_{(m+1)(n-1)}$ . Then  $G$  is reflected from the main reflector and intersects the exit aperture at the points  $B_{mn}$ ,  $B_{m(n-1)}$ , and  $B_{(m+1)(n-1)}$  (Fig. 7). Let  $P$  be the energy in the pencil of rays exiting the aperture through the vertices of triangle  $T$ . From the law of conservation of energy,  $P$  must be equal to the energy in the pencil of rays incident on the subreflector at the points  $A_{mn}$ ,  $A_{m(n-1)}$ , and

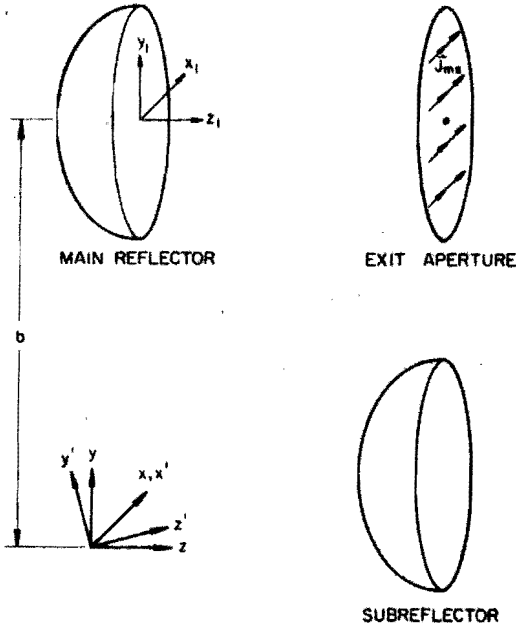


Fig. 6. Description of the coordinate systems.

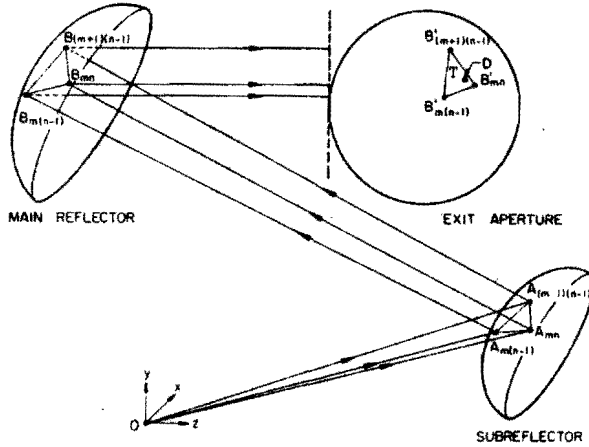


Fig. 7. Pencil of rays originating from the primary source.

$A_{(m+1)(n-1)}$ . Thus, we can write from (2)

$$P = I_2 dS = I_1 d\Omega. \quad (15)$$

The magnitude of the electric field  $E_a$  at any point inside the triangle  $T$  is approximately given by

$$E_a = (\zeta_0 P)^{1/2} \quad (16)$$

where  $\zeta_0$  is the intrinsic impedance of free space.

Let  $D$  be a point inside triangle  $T$ , and let  $\hat{e}_1, \hat{e}_2, \hat{e}_3$  be the directions of the electric field at  $B_{mn}$ ,  $B_{m(n-1)}$ , and  $B_{(m+1)(n-1)}$ , respectively. We approximately represent the electric field direction  $\hat{e}_a$  at the point  $D$  by using a weighted average of the electric field directions  $\hat{e}_1, \hat{e}_2$ , and  $\hat{e}_3$  defined by the following equation:

$$\hat{e}_a = \frac{d_2 d_3 \hat{e}_1 + d_3 d_1 \hat{e}_2 + d_1 d_2 \hat{e}_3}{|d_2 d_3 \hat{e}_1 + d_3 d_1 \hat{e}_2 + d_1 d_2 \hat{e}_3|} \quad (17)$$

where  $d_1, d_2$ , and  $d_3$  are the distances from  $D$  to  $B_{mn}$ ,  $B_{m(n-1)}$ , and  $B_{(m+1)(n-1)}$ , respectively.

Each of the electric field directions  $\hat{e}_1, \hat{e}_2$ , and  $\hat{e}_3$  at the vertices of  $T$  is calculated as follows. Assuming that the primary source is polarized in the  $\hat{y}'$ -direction, the direction of the electric field  $\hat{e}_i$  incident on the subreflector is given by

$$\hat{e}_i = \frac{\hat{r}' \times (\hat{y}' \times \hat{r}')}{|\hat{r}' \times (\hat{y}' \times \hat{r}')|} \quad (18)$$

in the  $(x', y', z')$  coordinate system. We transform (18) into the  $(x, y, z)$  coordinate system of the reflector surfaces. Then from the boundary conditions for the tangential electric field on a conducting surface, we determine the direction  $\hat{e}_r$  of the electric field reflected from the subreflector with the following equation:

$$\hat{e}_r = 2(\hat{n}_1 \cdot \hat{e}_i)\hat{n}_1 - \hat{e}_i. \quad (19)$$

$\hat{n}_1$  is a unit vector along the normal to the subreflector surface and is given by

$$\hat{n}_1 = \frac{\hat{x} z_{1x} + \hat{y} z_{1y} - \hat{z}}{\sqrt{1 + z_{1x}^2 + z_{1y}^2}} \quad (20)$$

where  $z_{1x}$  and  $z_{1y}$  are the partial derivatives of the subreflector surface. Also, from the boundary conditions applied to the main reflector, the direction of the electric field reflected from the main reflector is

$$\hat{e} = 2(\hat{n}_2 \cdot \hat{e}_r)\hat{n}_2 - \hat{e}_r. \quad (21)$$

$\hat{e}_r$  in (21) is the direction of the electric field incident on the main reflector after reflection from the subreflector, and  $\hat{n}_2$  is a unit vector along the normal to the main reflector surface and is given by

$$\hat{n}_2 = \frac{-\hat{x} z_{2x} - \hat{y} z_{2y} + \hat{z}}{\sqrt{1 + z_{2x}^2 + z_{2y}^2}} \quad (22)$$

where  $z_{2x}$  and  $z_{2y}$  are the partial derivatives of the main reflector surface. Hence, the electric field directions  $\hat{e}_1, \hat{e}_2$  and  $\hat{e}_3$  can be determined from (18)–(22).

In summary, the electric field at any point inside each triangle in the exit aperture has a magnitude given by (16) and a direction given by (17). Furthermore, the phase of the electric field in the exit aperture is equal to a constant given by (1) because the primary source is on focus.

#### IV. NUMERICAL RESULTS

For the sake of illustrating the synthesis procedure, we consider the case where the feed illumination function  $I_1$  is given by  $I_1 = \cos^n \theta'$ . The subreflector edge angle is given by  $\theta_{\max} = 10^\circ$  with a 10 dB edge illumination which correspond to  $n = 151$ . We let the desired energy distribution in the projected aperture of the main reflector be a Gaussian, and assume it to be of the form

$$I_2 = I_m \exp[-\alpha\{x^2 + (y-b)^2\}]$$

where  $b = 6$  and  $I_m = 1.15 \times 10^{-3} \text{ W/m}^2$ . The main reflector



projected aperture is desired to be circular and of radius equal to 5 with  $-8.7$  dB edge taper which corresponds to  $\alpha = 0.08$ .

In our method, we assume that the starting curve  $C_{10}$  is given as the center line of a subreflector surface, and we obtained the starting curve from a solution presented by Galindo *et al.* [7] for the synthesis problem of the offset dual reflector antennas. It is worth mentioning that we only retain the center line of the subreflector surface from the solution of the reflector derived by Galindo *et al.*

Since the feed pattern function and the desired aperture field distribution are symmetric, the solution that we generate has left-right symmetry. Hence, the derivatives  $\partial z_1/\partial x$  and  $\partial z_2/\partial x$  at all the points along the starting curves  $C_{10}$  and  $C_{20}$ , respectively, are equal to zero.

The comparison factor  $R$  is nominally chosen to be within  $\pm 0.2$  dB, i.e., the resultant amplitude distribution in the exit aperture is required to approximate the specified value to within  $\pm 0.2$  dB.<sup>1</sup> The subreflector surface is also required to be convex in shape. Hence, when determining  $z_{1x}$  at the point  $A_{mn}$ , we increase  $z_{1x}$  at the point  $A_{m(n-1)}$  by a small positive increment. The process is repeated  $K$  times until the requirement on the amplitude distribution in the exit aperture is satisfied to within  $\pm 0.2$  dB. Once all the points of a certain curve  $C_{1n}$  of the subreflector surface and its corresponding curve  $C_{2n}$  of the main reflector surface are determined together with the derivatives at these points, we observe that the resultant curve of the derivative  $z_{1x}$  at the points of  $C_{1n}$  plotted against the  $y$ -coordinates of these points is discontinuous, as illustrated in Fig. 8(c) for the curve  $C_{11}$ . The discontinuities in the curve  $z_{1x}(y)$  cause the curve  $C_{2n}$  of the main reflector to be discontinuous also, which is undesirable. Hence, we disregard the curve  $C_{1n}$  and smooth the curve of the derivative  $z_{1x}(y)$ . Then, we determine the new curve  $C_{2n}$  by applying Snell's law of reflection to the subreflector and by satisfying the phase condition.

The effect of smoothing  $z_{1x}(y)$  on  $R$  for the curves  $C_{11}$  and  $C_{1(21)}$  is illustrated in Fig. 8(b) where  $R$  is plotted versus  $N$ , the index number of the points in each curve. As shown in Fig. 8(b),  $R$  fluctuates between 0.04 dB and 0.13 dB for all points on  $C_{11}$  and, thus, remains within the required tolerance  $\pm 0.2$  dB. However, this is not true for all the generated curves of the subreflector. Therefore, in order that we obtain a smooth solution such as the one shown in Fig. 8(a), we may have to relax  $R$  even further for  $C_{11}$ . Fortunately,  $|R|$  does not exceed 0.5 dB for the entire set of curves, and it exceeds 1.2 dB only over a small portion of the reflected surfaces.

As for the main reflector, the generated curves are typically smooth. This may be seen with reference to Fig. 9 which shows a typical curve on the main reflector is  $C_{2(21)}$  whose projections in the  $xz$  plane and  $yz$  plane are displayed in Figs. 9(a), 9(b), and 9(c).

For the example considered, the subreflector edge angle is initially desired to be  $10^\circ$  in the feed-centered coordinate system, and the main reflector projected perimeter is desired to be circular and of radius 5. Although in our solution for the synthesis problem we are able to get a  $10^\circ$  illumination cone angle for the subreflector, the projected perimeter of the main reflector is not circular. This is illustrated in Fig. 10(a) where the projected perimeters of the subreflector (left) and the main reflector (right) are shown. Therefore, in our solution for

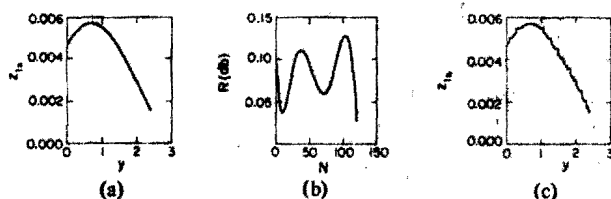


Fig. 8. (a) The derivative with respect to  $x$  at the points of the subreflector curve  $C_{11}$  plotted against the  $y$  coordinates of these points after being smoothed. (b) Plot of  $R_{m+B}$ , the departure from the specified energy condition plotted against  $N$ , the index for the points on the subreflector curve  $C_{11}$ . (c) The derivative with respect to  $x$  at the points of the subreflector curve  $C_{11}$  plotted against the  $y$  coordinate of these points before being smoothed.

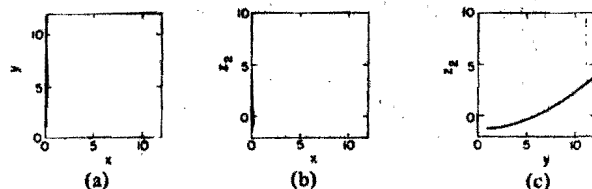


Fig. 9. (a) The projection of the second generated main reflector curve  $C_{21}$  on the  $xy$  plane. (b) The projection of the second generated main reflector curve  $C_{21}$  on the  $xz$  plane. (c) The projection of the second generated main reflector curve  $C_{21}$  on the  $yz$  plane.

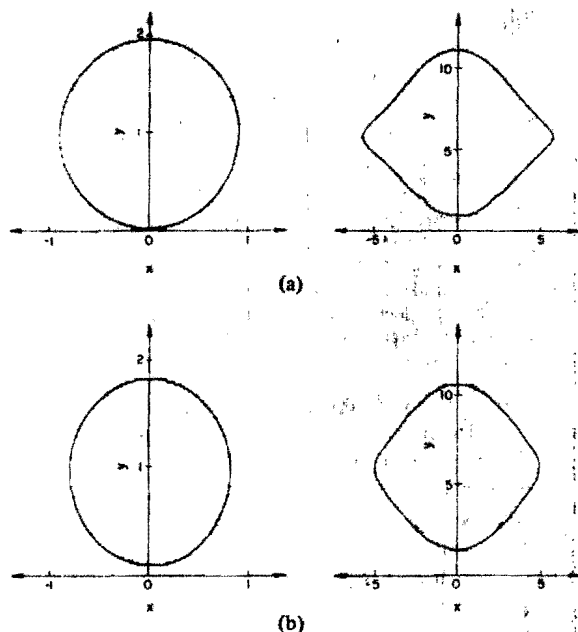


Fig. 10. (a) The projections on the  $xy$  plane of the boundaries of the subreflector (left) and the main reflector (right) corresponding to a subreflector illuminating edge angle of  $10^\circ$ . (b) The projections on the  $xy$  plane of the boundaries of the subreflector (left) and the main reflector (right) corresponding to a subreflector edge angle of  $9^\circ$ .

the synthesis problem, we are unable to meet simultaneously the desired constraints on both of the perimeters of the reflectors, namely, that the projected edge contour be circular for the main reflector for  $10^\circ$  cone angle illumination of the subreflector. When the subreflector edge angle is reduced to  $9^\circ$  or  $8^\circ$ , the projected perimeters of the main reflector tend to be closer to a circle, as illustrated in Figs. 10(a) and 10(b), respectively. However, the radius of the main reflector projected perimeter reduces from the specified value of 5. On the other

<sup>1</sup> It was found that for  $|\max |R| < 0.2$  dB no smooth solution existed for the reflectors.



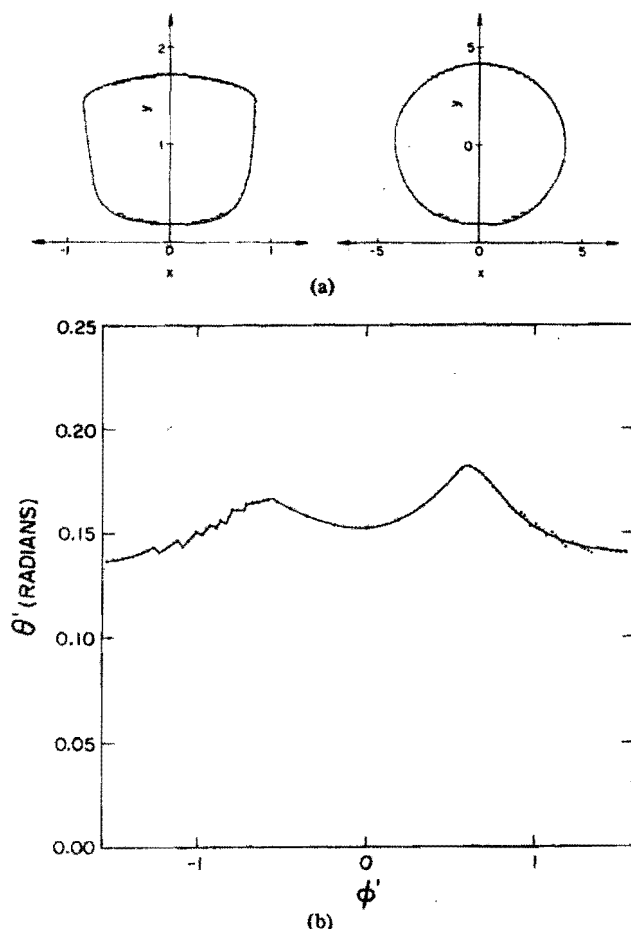


Fig. 11. (a) The projections on the  $xy$  plane of the boundaries of the subreflector (left) and the main reflector (right) corresponding to a circular main reflector projected perimeter of radius 4.2. (b) The resultant subreflector edge angle  $\theta'$  versus  $\phi'$  for all points along the edge of the subreflector corresponding to a circular reflector projected perimeter of radius 4.2.

hand, if we desire that the projected perimeter of the main reflector be circular, we can carve out a circle with the maximum available radius from the projected perimeter of the main reflector as shown in Fig. 10(a), which corresponds to a circle of, for this case, the projected perimeter of the subreflector shown in the left of Fig. 11(a).

Clearly, for the change of projected circular aperture for the main reflector, the edge angle of the subreflector is no longer a constant. Instead, it varies between  $\theta' = 7.7^\circ$  and  $10.3^\circ$  as shown in Fig. 11(b) where we plot  $\theta'$  versus  $\phi'$  for all points along the edge of the subreflector. Next we plot in Fig. 12 the curves for the calculated energy distribution together with the desired one, designated by the plus signs and the solid line, respectively. The projected aperture of the main reflector is chosen to be a circle of radius 4. The curves of the calculated energy distribution for the three radial cuts in Fig. 12 match quite well with the curves of the desired ones. The magnitude and phase of the electric field radiation patterns in the planes  $\phi_1 = 0$  and  $\phi_1 = \pi/2$  are shown in Figs. 13 and 14, respectively. The solid line in Figs. 13 and 14 corresponds to the desired electric field patterns whereas the plus signs represent the calculated electric field patterns of the calculated aperture field. The electric field radiation patterns of Figs. 13 and 14 are calculated for a frequency of 0.3 GHz.

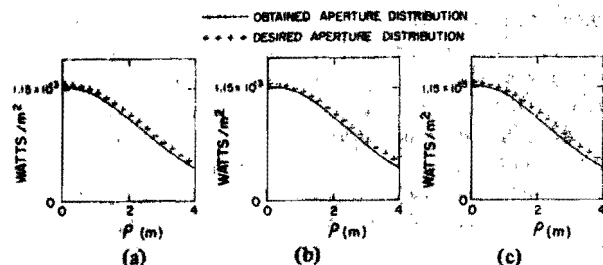


Fig. 12. The energy distribution in the aperture for three radial cuts (a)  $\phi_1 = 0$ , (b)  $\phi_1 = 45^\circ$ , and (c)  $\phi_1 = 90^\circ$ .

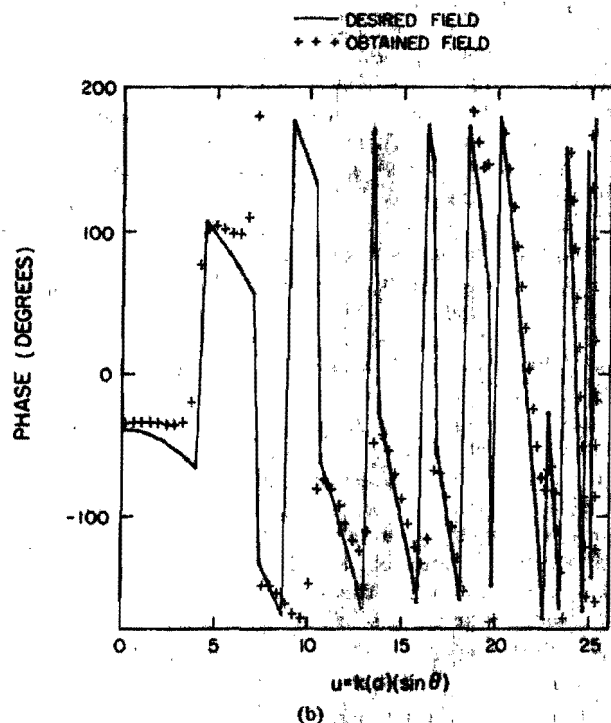
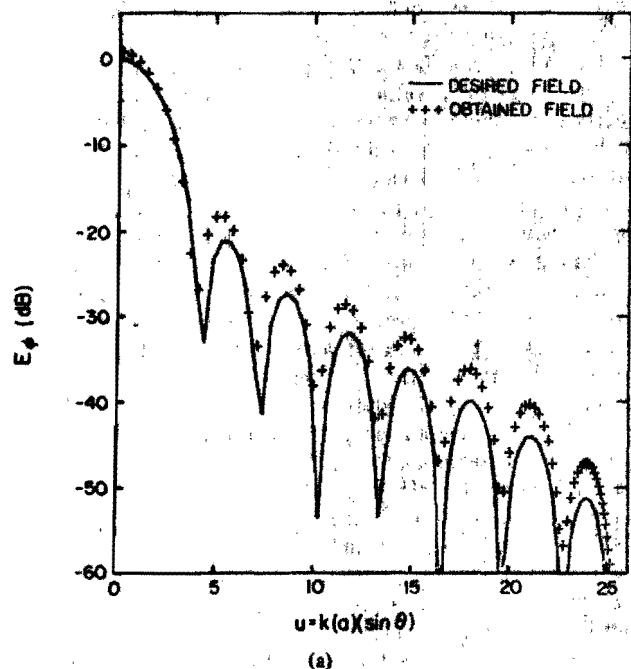


Fig. 13. (a) Electric field pattern in  $\phi_1 = 0$  plane. (b) Electric field phase pattern in  $\phi_1 = 0$  plane.

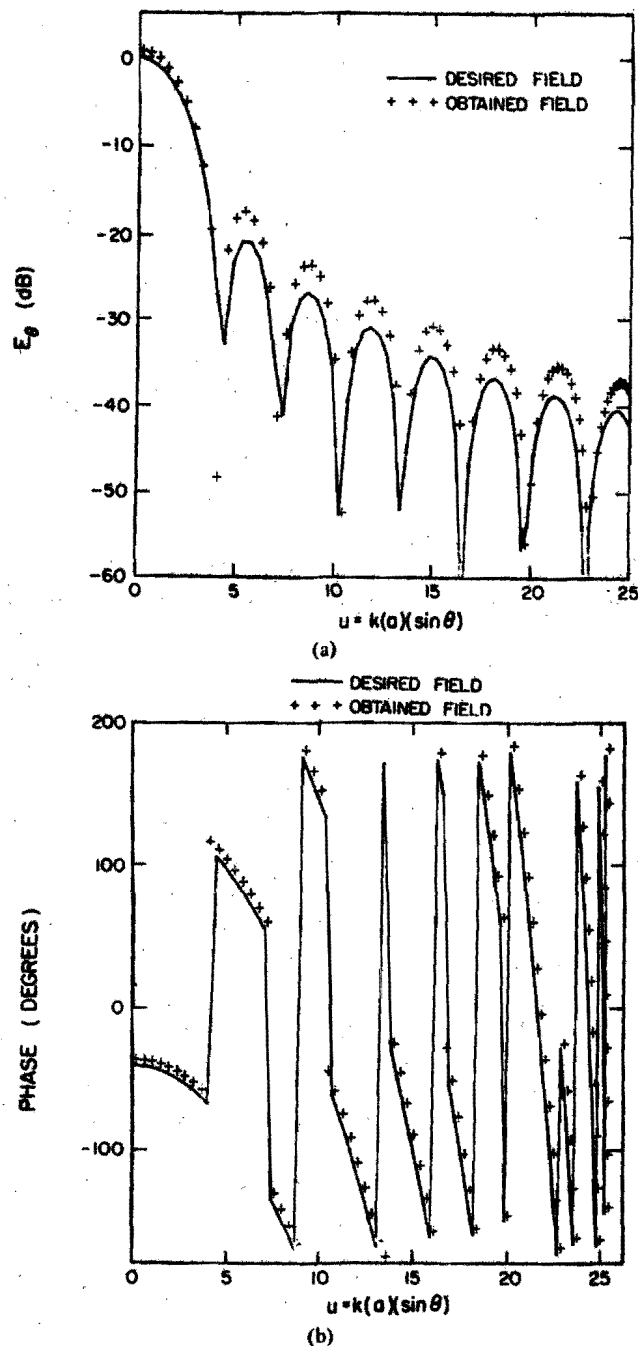


Fig. 14. (a) Electric field pattern in  $\phi_1 = \pi/2$  plane. (b) Electric field phase pattern in  $\phi_1 = \pi/2$  plane.

We observe that the calculated energy distributions in Figs. 12(a), 12(b), and 12(c) are slightly greater than the desired ones, especially at the edges. This, in effect, increases the gain and raises the sidelobe level as illustrated in Figs. 13(a) and 14(a). However, the two curves are much closer together when the computed patterns are normalized at  $\theta = 0$ .

V. CONCLUSION

In this work, we have studied the problem of transforming, through two reflections by an offset dual reflector system, a given primary feed pattern into a desired aperture field distribution. We have developed a numerically rigorous solution for the surfaces of the offset two-reflector system in a one-step process. This solution, which is based on geometrical optics

analysis, gives an exact aperture phase distribution and enforces the condition on the aperture amplitude distribution to within a small numerical tolerance. However, we find that for a given set of specifications a smooth solution may not always exist, i.e., the reflector surfaces may not be continuous or their slopes may vary much too rapidly. In the event of non-existence of a numerically rigorous smooth solution, an approximate solution that enforces the smoothness of the reflector surfaces can be obtained. In the approximate solution, we relax the requirement for the aperture amplitude distribution but we continue to satisfy exactly the condition on the aperture phase distribution. However, we are unable to meet simultaneously the desired requirements for both of the reflector perimeters. It is pertinent to remark here that, according to Kinber [4], there does not, in general, exist a solution which simultaneously satisfies the aperture amplitude and phase as well as the conditions on the perimeters of the reflectors.

*Addendum:* Since writing this paper the authors have developed an alternative synthesis scheme that does not depend on an initial starting curve as in the present method, but carries out the synthesis procedure with only a single starting point. This method will be described in a future communication.

REFERENCES

[1] L. D. Bakharakh and V. M. Grishina, "On the construction of antennas with optimum patterns," *A. S. Popov Soc. Radio Eng. Commun.*, 1958.  
[2] B. Ye Kinber, T. Ye Sharuyera, and A. I. Medvedev, "Investigation of two reflector antennas with enhanced gain," *A. S. Popov Soc. Radio Eng. Commun.*, 1958.  
[3] V. Galindo, "Design of dual reflector antennas with arbitrary phase and amplitude distributions," *IEEE Trans. Antennas Propagat.*, vol. AP-12, pp. 403-408, July 1964.  
[4] B. Ye Kinber, "On two reflector antennas," *Radio Eng. Electron. Phys.*, vol. 6, pp. 914-921, June 1962.  
[5] C. Yeh, "Arbitrarily shaped dual reflector antennas," *JPL Tech. Rep. 32-1503*, p. 1, May 1971.  
[6] Y. Mitzuguchi and H. Yokoi, "On surface of offset type dual reflector antenna," *IECE*, vol. 58-B, no. 2, 1975.  
[7] V. Galindo-Israel, R. Mittra, and A. Cha, "Aperture amplitude and phase control of offset dual reflectors," *IEEE Trans. Antennas Propagat.*, vol. AP-27, no. 2, pp. 154-164, Mar. 1979.  
[8] K. A. Green, "Modified Cassegrainian antennas for arbitrary aperture illumination," *IEEE Trans. Antennas Propagat.*, vol. AP-11, pp. 589-590, Sept. 1963.  
[9] M. Mizusawa, S. Urasaki, and H. Tanaka, "An offset shaped-reflector Cassegrainian antenna," in *Proc. IEEE Symp. Antennas Propagat.*, June 1977, Stanford, CA, pp. 444-447.  
[10] R. Mittra, V. Galindo-Israel, and F. Hyjazie, "A method for synthesizing offset dual reflector antennas," *USNC/URSI and IEEE Symp. Antennas Propagat.*, May 1978, College Park, Md., pp. 239-242.  
[11] T. Levi-Civita, *Rend. R. Acc. Naz. Line.*, vol. 9(1900), p. 237.  
[12] W. Kaplan and D. J. Lewis, *Calculus and Linear Algebra*. New York: Wiley, 1971, p. 957.  
[13] V. Galindo-Israel and R. Mittra, "A new series representation for the radiation integral with application to reflector antennas," *IEEE Trans. Antennas Propagat.*, vol. AP-25, pp. 631-641, Sept. 1977.  
[14] R. Mittra, Y. Rahmat-Samii, and V. Galindo-Israel, "A plane-polar approach for far-field construction from near-field measurements," *IEEE Trans. Antennas and Propagation*, vol. AP-28, no. 2, pp. 216-230, Mar. 1980.

Raj Mittra (S'54-M'57-SM'69-F'71), for a photograph and biography please see page 833 of the November 1981 issue of this TRANSACTIONS.

Fayez Hyjazie, photograph and biography not available at time of publication.

Victor Galindo-Israel (S'52-M'57-SM'75-F'77), for a photograph and biography please see page 230 of the March 1980 issue of this TRANSACTIONS.

29 April 1982

CHAPTER 6

ADAPTIVE AND MULTIBEAM ANTENNA SYSTEMS<sup>\*†</sup>

by Leon J. Ricardi  
Massachusetts Institute of Technology, Lincoln Laboratory  
Lexington, Massachusetts 02173

COURSE NOTES FOR PRESENTATION AT  
TECHNISCHE HOGESCHOOL EINDHOVEN  
23-27 AUGUST 1982

<sup>\*</sup>This work has been sponsored by the Dept. of the Air Force .

<sup>†</sup>"The U.S. Government assumes no responsibility for the material presented."

## 6. Adaptive and Multibeam Antenna Systems

by L. J. Ricardi

### 6.1. Adaptive Antennas

Adaptive antennas were first used in an intrinsic form as radar antennas with sidelobe canceling characteristics. The sidelobe-canceler antenna consists of a conventional radar antenna with the outputs of much lower gain auxiliary antennas coupled to the receiver input. The gain of the auxiliary antennas is slightly greater than the gain of the maximum sidelobe of the radar antenna. Adding the weighted signals received by the auxiliary antenna to those received by the radar antenna permitted suppression of interfering sources located in the directions other than the main beam of the radar antenna. This early use of adaptive antennas evolved to adapted array and multiple-beam antennas.

This chapter presents a description of the major components of an adaptive antenna and develops general relationships and rules governing the performance of an adaptive antenna. A fundamental definition of resolution is developed enabling one to determine the minimum tolerable angular separation between desired and interfering signals. This resolution leads naturally to the definition of degrees of freedom and to a conceptual method of determining the potential and actual degrees of freedom available to a given adaptive antenna. It is shown that often an adaptive antenna with  $N$ -degrees-of-freedom can suppress more than  $N-1$  interfering sources.

The algorithm governing the adaption process can be based on one of three classical methods. Two methods named for the inventors, use a feedback weight control system. The first method requires prior knowledge of the actual, or potential location of the desired sources and is commonly referred to as the power-inversion or Applebaum-Howells algorithm. The second weight determining method using feedback control is called the

Widrow algorithm and requires a known characteristic of the desired signal in order to maximize the signal-to-noise ratio of signals received from a single desired source. The third or sample matrix inversion (SMI) algorithm is a completely computational process that uses the signals received at the N-ports of an adaptive antenna and the desired source angular locations to suppress interfering signals in the computed output. This SMI algorithm does not use feedback to correct for implementation inaccuracies.

Finally, some general remarks about transient effects and the comparative performance of planar array and multiple-beam antennas are presented.

#### 6.1.1. Fundamental Characteristics

Adaptive antennas are primarily used for receiving signals from desired sources and suppressing incident signals from undesired or interference sources. The basic configuration shown in Figure 6-1 consists of an antenna with N ( $N > 1$ ) ports, N complex weights, a signal summing network, and a weight-determining algorithm. The N ports of the antenna can be the output terminals (ports) of the elements of an array antenna or the ports of a multiple-beam antenna (MBA) or a mixture of these. A complex weight, in general, attenuates the amplitude and changes the phase of the signals passing through it and is usually assumed to have a frequency independent transfer function. The summing network is often a corporate-tree arrangement of four-port "tees". Each tee sums the in-phase components of the signals at the two input ports in one output port and has a matched load at the other output port to dissipate those components of the input signal that are 180° out-of-phase. The weight-determining algorithm (or simply the algorithm) makes use of a priori or measured information, or both, and specifies the complex weight,  $W_n$ , applied to the signal received at the  $n^{\text{th}}$  port as

$$W_N = g e_{cn} \quad . \quad (6.1)$$

As shown in Figure 6.1, the algorithm uses information derived solely from the output signal  $e_o$  (as in a weight-dither algorithm), or solely from the input signals  $e_n$  (as in the matrix-inversion algorithm) or from both  $e_o$  and  $e_n$  as in the Applebaum-Howells and Widrow algorithms. An intrinsic algorithm need not use either  $e_o$  or the  $e_n$ ; hence, these inputs to the weight determining algorithms are indicated by dashed lines in Figure 6.1. Note that these inputs are indicated as "loosely" coupled, as opposed to direct connection, to the  $e_n$  and  $e_o$  signal ports.

Clearly the antenna (array, MBA, or hybrid) is that essential component of an adaptive antenna system which is uniquely related to the disciplines of antenna design. The weight and summing circuits can operate at the antenna operating frequency,  $f_o$ , an intermediate frequency, IF, or be part of a digital signal processor. Although the design and development of the antenna, the weights, and the summing network are important, the weight determining algorithm almost always determines the uniqueness of an adaptive antenna. Consequently, this chapter will only briefly describe the antenna, the weights, and the summing network. Considerably more attention will be given to the fundamental limitations (i.e., degrees of freedom and resolution) of all classes of adaptive antennas and to a conceptual description of the classical weight-determining algorithms.

#### 6.1.2. Antenna

Although adaptive antenna systems use antennas of various types and configurations, it is possible to separate these into three basic classes - phased arrays<sup>1</sup>, multiple-beam antennas<sup>2</sup>, and a mixture of these two. Each configuration has several ports where received signals,  $e_n$ , appear in response to sources located in the antenna's field of view (FOV). Phased arrays characteristically have many identical elements, each of which has a port where the output signal can be represented by

$$e_n = \sum_{m=1}^M I_m F_n(\theta_m, \phi_m) e^{jH_n(\theta_m, \phi_m)} \quad (6.2)$$

where

$$I_m = \frac{\lambda^2 P_m G_m}{(4 \pi R_m)^2}$$

$P_m$  = Power radiated by the  $m^{\text{th}}$  source

$G_m$  = Gain of the antenna used by  $m^{\text{th}}$  source

$R_m$  = Distance between  $m^{\text{th}}$  source and the adaptive antenna

$\lambda$  = Operating wavelength.

The amplitude and phase that relates  $I_m$  to a signal at the antenna port is given by  $F_n$  and  $H_n$ , respectively. The angular location of the  $m^{\text{th}}$  source is given by the coordinate pair  $\theta_m, \phi_m$  measured in a suitable spherical coordinate system.

It is important to note that in most, if not all, phased array adaptive antennas, the  $F_n$  are identical; whereas  $H_n$  is generally different for all elements of the array. For signals at the output ports of an MBA, the  $H_n$  are nearly equal and the  $F_n$  differ. It will be shown later that this fundamental difference between a phased array and an MBA results in the inherently larger bandwidth of the latter.

Phased arrays are either filled or thinned. Filled arrays do not have significant grating lobes, or high sidelobes within the FOV of an array element of the array; whereas thinned arrays characteristically have either grating lobes or high sidelobes ( $\sim 10$  dB) in the FOV of the array element. Grating lobe characteristics are extremely important because even when interference and desired sources are separated by a large angle (i.e., compared to the array HPBW), the desired source is suppressed by approximately the same amount as the interference source when an interference source is located on a grating lobe.

Although there is not a suitable, formal definition of thinned or filled arrays, it is convenient to consider the thinned array as having an inter-element spacing,  $S$ , greater than  $S_T$ ; where

$$S_T = \frac{\lambda}{\sin(\theta_e/2)} \quad (6.3)$$

and  $\theta_e$  is the HPBW of an element of the array. Unfortunately, (6.3) cannot be used in all cases, but it does serve as a conceptual definition.

Hybrid antenna systems usually consist of an array antenna with each element of the array configured as a multiple-beam antenna. The directive gain of the MBA permits thinning of the array without forming harmful grating lobes, while retaining the capability of scanning the instantaneous FOV over a larger field of view. Chapters 3, 16, 17, 20, 21, and 35 discuss some applicable antennas in greater detail.

#### 6.1.3. Weights

Just as the excitation of phased arrays (see Chapter 3) determines the antenna radiation pattern, weighting of signals received at the ports of an adaptive antenna determines the antenna's directional response to incident signals. Since the discussion of adaptive antennas presented here assumes a receiving as opposed to a transmitting antenna system, it is necessary to introduce and use the concept of weighting and combining receiving signals instead of "exciting" the array or MBA to produce a radiation pattern. However, it is often much clearer to represent the antenna's angular discrimination of received signals in the form of "radiation" patterns. The reader is cautioned to ignore the literal meaning of radiation patterns and think of the  $F_n$  and related functions as receiving antenna patterns.

Weights attenuate and alter the phase of received signals. They are designed to be either frequency independent or adaptively varied as a



function of frequency. Some adaptive antennas operate entirely at the received frequency and use RF weights as indicated in Figure 6.1. Still others have a mixer-amplifier at each antenna port, and the weights operate at a lower intermediate frequency, IF, as indicated in Figure 6.2. The latter customarily uses lossy weights consisting of attenuators and hybrid power dividers as indicated in Figure 6.3. The use of lossy weights in this way does not degrade system performance since the mixer-IF amplifier establishes the local signal-to-noise (S/N) ratio such that subsequent losses in the weights and combining, or summing, network attenuate both signal and noise without altering the S/N. For RF weighting, the weight circuit is usually a corporate configuration of "lossless" variable power dividers and a single phase shifter at each antenna port, such as shown in Figure 6.4. Four-port variable power-dividing junctions (Figure 6.4) are customarily used in weight and summing networks to prevent the resonant effect encountered with the use of three-port junctions. This effect is produced by small but significant reflected waves between input and output ports. Dissipative loads at the fourth port of a four port junction (Figure 6.4b) absorb reflected waves that do not couple to the input port; reflected waves at the input do, however, degrade the input match of the circuit. Although this effect is not uniquely associated with adaptive antennas, it is an important and significant consideration in the design of all adaptive-antenna systems.

All antenna systems have a frequency dependent response to incident signals. Whenever frequency independent weights are used, suppression of undesired signals will vary with frequency. This inherent performance characteristic cannot be succinctly and accurately described because it is scenario-dependent. However, it can be shown<sup>3</sup> that, for frequency independent weights, the cancellation,  $C$ , (i.e., suppression of an interfering signal) of an adaptive array antenna is limited as

$$C \leq 20 \log \left[ K \left( \frac{2\pi}{c} \right) D W \sin \theta_m \right] \text{ dB} ; \quad (6.4)$$

where  $2\theta_m$  = the maximum angle subtended by the FOV,  $D$  = maximum dimension of the antenna aperture,  $W$  = nulling bandwidth, and  $c$  = velocity of light in free space. The constant,  $K$ , is a function of the array configuration and the particular scenario of interfering and desired sources; it ranges between  $\sim 5$  and  $\sim 15$ . It is important to note that  $C$  varies as the square of  $W$  and the square of the maximum scan angle  $\theta_m$  and that (22-4) takes only antenna related dispersive effects into account; it assumes frequency independent weights and identical antenna array elements. When the antenna array uses time delay circuits, which in effect reduces  $\theta_m$ ,  $C$  increases accordingly.

One form of frequency-dependent weight consists of a delay line with two or more taps. The received  $e_n$  is delivered to the output of each tap, weighted, and summed with the output of all  $N$  taps (Figure 6.5). The weights are frequency independent, and the delay between successive taps<sup>3</sup> depends on  $W$ ,  $D$ ,  $\theta_m$ ,  $\lambda$ , and the distribution of interfering sources. Observing that the maximum delay,  $\tau_{max}$ , occurring between elements located at opposite edges of an array aperture is given by

$$\tau_{max} = (D/c) \sin \theta_m ; \quad (6.5)$$

the number of taps  $N_\tau$  should exceed

$$N_\tau > \tau_{max} W = (WD/c) \sin \theta_m . \quad (6.6)$$

Although the use of frequency-dependent weights will increase with the development of the associated technology, adaptive antennas using frequency-independent weights are currently most popular. Hence, the discussions in this chapter are limited accordingly; the weight shown in Figure 6.5 is introduced primarily because of its potential importance to broadband operation of large phased arrays.

#### 6.1.4. Resolution

Since the primary purpose of an adaptive antenna is to suppress interfering sources while maintaining adequate response to desired sources, the system designer needs to know the minimum tolerable angular separation between desired and interfering sources. In other words, the inherent ability of the antenna to resolve desired and undesired sources is fundamental to the system design. Clearly, the antenna's "resolving power" increases with its aperture size,  $D$ . Quantitative resolving characteristics of adaptive antennas will be discussed in this section.

The signals,  $e_n$ , received at the ports of the antenna (Figure 6.1) are "multiplied" by a weight,  $W$ , and summed to produce the output signal,  $e_o$ . That is

$$e_o = \sum_{n=1}^N W_n e_n \quad (6.7)$$

Adaptive antennas select the  $W_n$  so as to place "nulls" in the radiation pattern in the direction of interfering sources. Using matrix notation and representing the weights as the vector

$$\underline{W} = [W_1, W_2, \dots, W_N] \quad (6.8)$$

it can be shown<sup>4</sup> that the optimum set of weights,  $\underline{W}_o$ , is given by

$$\underline{W}_o = M^{-1} \underline{V} \quad (6.9)$$

where  $\underline{V}$  is called the steering vector and represents the quiescent weights which establish the antenna receiving pattern in the absence of interfering sources.

In Equation (6.9),  $M$  is the covariance matrix of the  $e_n$  received signals. That is,

$$M = \begin{bmatrix} \overline{e_1 e_1}^* & . & . & . & \overline{e_1 e_N}^* \\ \vdots & & & & \\ \overline{e_N e_1}^* & . & . & . & \overline{e_N e_N}^* \end{bmatrix} \quad (6.10)$$

where the overbar indicates averaging over the correlation interval, and the asterisk indicates the complex conjugate. Clearly all adaptive antennas strive to determine or estimate  $M$  or  $M^{-1}$  which enables  $\underline{W}_0$  to be determined from (6.9) or an equivalent algorithm. This optimum produces that spatial discrimination, available with the associated antennas, which maximizes the ratio of the desired signal power to the interfering plus internally generated noise power. Now the covariance matrix  $M$  and its inverse  $M^{-1}$  are key to the determination of the fundamental properties of an adaptive antenna. For example,  $M^{-1}$  can be written in the form

$$M^{-1} = \sum_{n=1}^N \frac{\underline{u}_n \underline{u}_n^\dagger}{\lambda_n} \quad (6.11)$$

where " $\dagger$ " indicates the complex-conjugate transpose,  $\underline{u}_n$  is the  $n^{\text{th}}$  eigenvector of  $M$  with eigenvalue  $\lambda_n$ , and the  $N$  eigenvalues of  $M$  represent the antenna output power  $e_0 e_0^*$  obtained when  $\underline{W} = \underline{u}_n$ . Hence, if a single source is in the antenna's field of view, one eigenvalue (i.e.,  $\lambda_1$ ) will be much larger than all other eigenvalues. If two sources are in the FOV, at least one and maybe two eigenvalues will be larger than the others. Since the  $\underline{u}_n$  ( $n = 1, 2, \dots, N$ ) are an orthogonal set forming the basis of  $M^{-1}$ , two equal eigenvalues will result when two sources of equal intensity are located at spatially orthogonal positions in the FOV. In other words, if source  $S_1$  is located in a null of the "radiation" pattern resulting when  $\underline{W} = \underline{u}_2$ , two equal-value eigenvalues will result.

The resolution of an adaptive antenna can be determined by first placing two sources,  $S_1$  and  $S_2$ , with intensity,  $P$ , at the same point in the antenna's FOV. The resulting covariance matrix will have only one large eigenvalue,  $\lambda_1$ , indicating that a single degree-of-freedom of the array is used, and setting  $\underline{W} = \underline{u}_1$  will maximize the power delivered to the output

port of the adaptive antenna. Conversely, setting  $\underline{W}$  such that  $\underline{W} \cdot \underline{u}_1 = 0$  will reduce the output power to zero.

Now as the angular separation between two sources increases from zero,  $\lambda_1$  decreases, and a second significant eigenvalue,  $\lambda_2$ , increases. When  $S_1$  and  $S_2$  are separated by an angle,  $\alpha_0$ ,  $\lambda_1 = \lambda_2$  and two of the  $N$  degrees of freedom are required to establish a radiation pattern which maximizes the output power. A detailed analysis<sup>5</sup> of this process indicates that when the  $S_1$  and  $S_2$  are at the same location  $\lambda_1 = 2P$  and when they are separated at an angle  $\alpha_0$ ,  $\lambda_1 = \lambda_2 = P$ . The angular resolution,  $\alpha_0$ , is approximately equal to the half-power beamwidth (HPBW) measured in the plane  $R$  containing the two sources and the adaptive antenna. The HPBW is calculated from the known antenna aperture dimension in the plane  $R$  and an assumed uniform excitation of all elements of a phased array or excitation of a single port of an MBA.

The results presented in the previous paragraph can also be derived mathematically by substituting (6.11) into (6.9) to obtain

$$\underline{W}_0 = \sum_{n=1}^N \frac{\underline{u}_n \underline{u}_n^{\dagger}}{\lambda_n} \cdot \underline{v} \quad (6.12)$$

where the  $\underline{u}_n$  span the weight space. The radiation pattern produced by the  $N$  eigenvectors form a complete orthogonal set whose approximately weighted combination will form any radiation pattern the adaptive antenna is capable of forming. (The concept of a radiation pattern is introduced to clarify the pattern synthesis implied. When receiving signals, the "receiving" pattern is identical to the radiation pattern for  $\underline{W}_n = \underline{I}_n^*$  where  $\underline{I}_n$  is the excitation coefficient of the  $n^{\text{th}}$  port of the adaptive antenna.) Note that when  $\lambda_1$  is the only large eigenvalue (i.e.,  $S_1$  and  $S_2$  are at the same location),  $\underline{W}_0$  does not include  $\underline{u}_1$  and the output of the adaptive antenna will not contain energy received from  $S_1$  and  $S_2$ ; only weak signals or noise determine the value of the other eigenvalues,  $\underline{W}_0$  and the antenna "receiving" pattern. It follows that, since  $\underline{W}_1 = \underline{u}_1$  maximizes

the signal from  $S_1$  and  $S_2$ , the resulting receiving pattern, obtained using  $\underline{W}_1$  for the weights, must be identical to that radiation pattern that maximizes the adaptive antenna's directivity in the direction of the location of  $S_1$  and  $S_2$ .

As described in the foregoing, separating the sources gives rise to two large eigenvalues equal to  $P$  when the angular separation equals  $\alpha_0$ . From (6.12), when  $\lambda_1 = \lambda_2 = P$  and all other  $\lambda_n \ll P$

$$\underline{W}_0 \cdot \underline{u}_1 = \underline{W}_0 \cdot \underline{u}_2 = 0 \quad (6.13)$$

minimizes the output power and suppresses the interference from  $S_1$  and  $S_2$ . However, if  $S_2$  is a source of desired signals and its radiated power  $\ll P$ , the angular separation between  $S_1$  and  $S_2$  must be equal to or greater than  $\alpha_0$ , if the receiving pattern is to have a null in the direction of the interfering source and maximize the signal received from the desired source.

Since any adaptive antenna must have internal noise sources, all  $\lambda_n$  of  $M$ , must be greater than zero; consequently,  $\underline{W}_0$  given by (6.12) is always finite. It is, however, customary to normalize  $\underline{W}_0$  such that their magnitude varies between 0 and 1, and their phase varies between  $0^\circ$  and  $360^\circ$ .

In summary, the resolution,  $\alpha_0$ , of any adaptive antenna in a given direction  $\theta_0, \phi_0$ , is approximately equal to the minimum half-power beamwidth of the radiation pattern which can be generated by the antenna and has maximum directivity in the direction  $\theta_0, \phi_0$ . The half-power beamwidth is determined in the plane containing the resolution angle  $\alpha_0$ . It follows that larger aperture antennas have higher resolution. Further, when an interfering source and desired source have angular separation  $\alpha_0$  or larger, an adaptive antenna with resolution  $\alpha_0$  can suppress the interfering source without altering its receiving pattern or directivity

(i.e., with respect to the interference free values) in the direction of the desired source.

#### 6.1.5 Degrees of Freedom

Clearly any adaptive antenna with  $N$  ports and  $N$  weights has  $N$  degrees of freedom (DOF). However, the number of DOF required to satisfy a given scenario is not easily determined. Often it is misunderstood that an  $N$ -port antenna can only suppress  $N-1$  interfering sources. Nothing could be further from the truth. It is in fact difficult, and sometimes impossible to find that set of  $N$  interference sources that can disable an adaptive antenna with  $N$  DOF.

In particular, consider an adaptive antenna with but two degrees of freedom and the ability to suppress an interfering source,  $P_J$ , 30 dB with respect to the desired signal. Assume that the interference-free signal-to-noise power ratio ( $S/N$ ), at the output of the adaptive antenna, is 13 dB in the absence of adaptive nulling, and it decreases to -10 dB in the presence of signals from the interference source. Spatial discrimination of the adaptive antenna pattern will increase the  $S/N$  to slightly less than 13 dB. The addition of four more interfering sources, each with effective radiated power,  $ERP = P_J$ , at the same location will reduce  $S/N$  to 10 dB! The set of  $N$  eigenvectors into which the covariance matrix can be decomposed is unique only for a given set of signals,  $e_n$ . Determining the strength and location of  $N$  sources which will capture the  $N$  eigenvalues of the covariance matrix,  $M$  (or the  $N$  DOF of an  $N$ -port adaptive antenna), is in general difficult and often impossible. However, an intelligent method for locating the interfering sources may result in disabling an  $N$ -port adaptive antenna with only slightly more than  $N$  interference sources. Consequently, it is helpful to derive some rule of thumb which enables the antenna designer to determine how many DOF are potentially available for suppressing sources in a specified FOV. The following guidelines are based on the foregoing and a conceptual, as opposed to rigorous, mathematical derivation.

Although an N-port adaptive antenna has N DOF, the antenna aperture may not be large enough to use all N degrees of freedom in the specified FOV. Using the foregoing definition of  $\alpha_0$ , it is conceptually acceptable to assume that an N-port adaptive antenna with a circular aperture has N circular resolution cells each of which subtends an angle  $\alpha_0$  measured at the antenna aperture. The composite of all N ( $N = 12$ ) resolution cells "covers" the antenna FOV as indicated in Figure 6.6a, where  $\alpha_0$  is the angular diameter of each cell. As for the small but finite area at the intersection of three adjacent cells, one might consider hexagonal cells with diagonals equal to  $\alpha_0$ ; however, this carries the concept far beyond its intended accuracy.

If the FOV is larger than that indicated in Figure 6.6, increasing N accordingly would still guarantee one DOF for each resolution cell within the FOV. Conversely, if the FOV is smaller than the composite area formed by the N resolution cells either the antenna aperture size must be increased or some of the antenna ports can be eliminated without affecting the adaptive antenna performance over the field of view.

For those adaptive antennas designed to serve a circular FOV with a circular aperture, the foregoing concept can be placed in mathematical form. That is, the number  $N_c$  of equal diameter, non-overlapping circles, that can be inscribed in a larger circle is maximum when the centers of the "smaller" circles are on a hexagonal grid and is given by

$$N_c = 1 + \sum_{m=1}^{M-1} 6m \quad . \quad (6.14)$$

Setting the diameter of the smaller circles equal to  $\alpha_0$  gives

$$M = \text{Odd integer of } \lceil \gamma_0 / \alpha_0 \rceil \quad (6.15)$$

where  $\gamma_0$  is the angular diameter of the larger circle defining the FOV. Recalling that  $\alpha_0$  is the HPBW when the antenna weights are chosen to produce maximum directivity,  $\alpha_0$  can be approximated as



$$\alpha_o \approx \frac{60\lambda}{D} \text{ degrees} \quad , \quad (6.16)$$

where  $D$  is the antenna aperture diameter. Substituting (6.16) into (6.15) gives

$$M = \text{Odd integers of } [(D/\lambda)(\gamma_o/60)] \quad ; \quad (6.17)$$

then  $D/\lambda = \frac{60M}{\gamma_o}$ . For example, if  $M = 5$ ,  $N_c = 19$ , the antenna  $D/\lambda$  must be greater than  $300/\gamma_o$  if 19 degrees of freedom are required. If the antenna has more than 19 ports, only 19 will be useful in forming nulls within the FOV. If there are less than 19 ports, say 10, and the antenna aperture is not thinned, the adaptive antenna still has 19 degrees of freedom, nine of which are not available to the adaptive algorithm; however, they can be used to shape the quiescent (interference-free) receiving pattern. In particular an adaptive antenna with a 19-beam MBA, nine of whose ports are short-circuited, will have nineteen DOF within the FOV defined by  $\gamma_o$  if its aperture diameter  $D = 300(\lambda/\gamma_o)$ . Notice, however, that signals originating from nine "short circuited" resolution cells couple to the adaptive antenna only through the sidelobes of the receiving pattern associated with the 10 ports that are not short-circuited.

#### 6.1.7. Weight Determining Algorithms

In order to achieve the desired antenna performance, an algorithm for choosing  $\underline{W}_o$  must be formulated. The algorithms must take the form of hardware or software, and they range from the very simple and straightforward to the complicated and sophisticated. The algorithms all have the same common goal; they must derive the desired  $\underline{W}_o$ . It is helpful to separate these algorithms into two general classes -- those with and those without feedback. Specifically the latter, or feed-forward systems, determine the desired  $\underline{W}_o$  from a given set of input data and install the weights with some small, but finite, error. They are not further

corrected by examining the output signals, as is done in an algorithm which uses feedback. Truly adaptive algorithms adjust the weights by observing the output or some other metric related to system performance.

The algorithm for deriving weights is undoubtedly the central issue in determining the value and performance of any adaptive antenna system. Consider first the simplest algorithm and then the more sophisticated methods for deriving  $\underline{W}_0$ . Most adaptive algorithms operate when the interfering signal power is much larger than the desired signal power, when both are measured in the nulling band  $W$ . This assumes that the interfering signal occupies a bandwidth,  $W$ , which is much larger than the instantaneous bandwidth of the desired signal.

All algorithms depend on two basic and distinct components; namely, the inverse of the covariance matrix of the received signals,  $e_n$ , and the steering vector,  $V$ . First, recall that the voltages,  $e_n$ , at each antenna terminal are produced by thermal noise, interfering sources, and desired sources in the FOV; that is,  $e_n = e_{\text{noise}} + e_{\text{in}} + e_{\text{dn}}$ . The goal of any algorithm is to choose the weights such that the total power received from the interference sources is minimized and the output voltage,  $e_o$ , is dominated by the desired signals. Since  $e_{\text{noise}}$ ,  $e_{\text{in}}$ , and  $e_{\text{dn}}$  are not correlated with one another, the covariance matrix  $M$ , formed by determining the time average value of  $e_n e_q^*$ , equals the sum of the covariance matrices of the thermal noise, interfering signal sources, and desired sources; that is  $M = M_N + M_I + M_d$ . In most adaptive antenna applications, the interfering signals dominate  $M$ , (i.e.,  $M_I \gg (M_N + M_d)$ ), and a good estimate of  $M_I$  can be obtained from the voltages  $e_n$ . In the absence of interfering signals (i.e.,  $M_I = 0$ ), the weights are chosen to maximize the signals received from the desired sources. Choosing the desired weights,  $\underline{W}_0$ , in accordance with (22-9) will maximize the desired signal to total-noise-power ratio (i.e.,  $P_d/(P_I + P_N)$ ) at the output of the adaptive antenna. This maximization will occur for all user signals if  $\underline{W}_0$  is chosen appropriately.

Consider a common scenario to illustrate this basic algorithm. Assume that all signal-source locations and the relative intensity of each desired signal source effective radiated power (ERP) are known. Let us further assume that the antenna response to a signal source located anywhere in the FOV can be calculated. Following the flow chart given in Figure 6.7, the desired signal and interference signal components of  $e_n$  can be calculated from the foregoing information. The interference covariance matrix,  $M_I$ , and its inverse can be calculated from  $e_{In}$ . The covariance matrix,  $M_d$ , can be used to calculate  $\underline{V}$  which will maximize the power received from each desired signal source. Choosing the weights  $\underline{W}_0$  equal to the product  $M^{-1} \underline{V}$  will minimize the difference between the actual and the desired antenna directive gain in the direction of the desired signal sources while suppressing the interfering signals. It is conceptually helpful<sup>6</sup> to assume that, in the absence of interfering signals, the desired signals are maximized when  $\underline{W}_0 = \underline{V}$ . Introduction of interfering signals causes the adaptive antenna to form a radiation pattern that is a least-mean-square fit to the quiescent receiving pattern, with nulls in the direction of the interfering sources.

All adaptive nulling algorithms, in their steady state, attempt to choose  $\underline{W}_0 = M^{-1} \underline{V}$ . Consequently, specific performance differences among various algorithms are manifested in their transient behavior, their choice of  $\underline{V}$ , their hardware and/or software implementation and the degree to which they are sensitive to errors.

#### 6.1.6.1. Power Inversion Algorithm

Assume that the locations of the interference signals are unknown and their ERP is much greater than the ERP of the desired signals; that is,  $M_I \gg (M_d + M_N)$ . Further, assume that  $\underline{V}$  is selected to provide the desired antenna directive gain in the known direction of each desired signal source. Since  $e_{In}$  is unknown,  $M_I$  cannot be calculated. However,

direct measurement of the  $e_n$ , or  $\overline{e_n e_p^*}$  would enable  $M$  or  $M^{-1}$  to be estimated; this estimate becomes more accurate as the interfering signals become much stronger than the desired signals. By choosing the nulling bandwidth appropriately, one can usually guarantee that troublesome interference will result in  $M_I \gg M_d$  and that the algorithm will be very effective in choosing  $W_d$ . Conversely, an inappropriate choice of nulling bandwidth, effective noise level, etc., will result in an undesirable reduction in the desired signals if it (they) and the interference signal(s) have approximately the same amplitude (i.e.,  $|e_{in}| \sim |e_{sn}|$ ).

This algorithm is often referred to as the "power inversion" or Applebaum-Howells algorithm<sup>7</sup>. It is one of the best known analog algorithms. A schematic representation of the fundamental circuit is shown in Figure 6.8. The antenna element, or beam port, output signals,  $e'_n$ , are indicated for an  $N$  element (beam) array (multiple-beam) antenna. A mixer followed by a preamplifier (and perhaps appropriate filtering) establishes  $e_n$  over the nulling band,  $W$ . For the purpose of the present discussion, assume that  $e_n$  is a frequency-translated, band-limited representation of  $e'_n$  and consider the "loop" that is connected to antenna terminal #1. The signals,  $e_n$ , are weighted by  $W_n$  and summed to give an output signal,  $e_o$ , that is

$$e_o = \sum_{n=1}^N W_n e_n \quad (6.18)$$

Thus far everything is exactly as described in the foregoing. However, in this circuit, the complex weights,  $W_n$  are proportional to the complex control voltages,  $e_{cn}$ . As in any analog adaptive algorithm, the derivation of  $e_{cn}$  is of interest. Note that the signal,  $e_1$ , is mixed with  $e_o$ . The output of the mixer is filtered and amplified giving a complex voltage proportional to correlation of  $e_1$  with  $e_o$ . The correlator's output is subtracted from a beam steering voltage  $V_1$  to give  $e_{c1}$ . For the moment, assume  $W_1 = V_1$ . If  $e_o$  is correlated with  $e_1$ , the low-pass filter integrates the output of the correlator to produce  $e_{c1} \neq 0$  which changes

the weight  $W_1$  so as to reduce the correlation between  $e_0$  and  $e_1$ , reducing the output of the correlator. Similar responses in the other loops reduce  $e_0$  to a minimum. Combined noise in the circuit and in  $e_1$  prevents  $e_0$  from vanishing. Hence we see that any signal (in  $e_1$ ) above the effective noise level will be sensed by the loop and weighted to reduce  $e_0$ ; the combined effect of all  $N$  loops is to reduce  $e_0$  below the effective noise level of the correlators. Furthermore, in the absence of signals (interfering or desired) greater than the front-end noise level, the weights will be determined by the noise. However, if the  $V_n$  are not zero, they will determine the weights, and the antenna receiving pattern will assume its quiescent shape.

The quiescent weights are determined a priori from known or expected desired source locations, etc. It can be shown that when  $M_I \gg M_N > M_D$ ,  $M \sim M_I$ , and the steady-state weights assume the optimum values given by (6.9). The transient performance and convergence to stable steady-state weights that equal  $\underline{W}_0$  are of paramount concern and will be discussed later.

In summary, the Applebaum-Howells<sup>7</sup> circuit establishes  $\underline{W}_0$  when the desired signal locations and antenna receiving pattern are known and used to determine  $\underline{V}$ . It is also necessary to choose the nulling bandwidth,  $W$ , such that the level of the desired signal received power,  $S$ , is approximately equal to or less than the front-end noise power in the band  $W$  (i.e.,  $M_S \leq M_N$ ). This circuit senses the locations of all interfering sources and reduces their received signals below the front-end noise level. If the interfering and desired sources are located near one another, the desired signal may also be reduced, but the ratio  $e_{in}/e_{dn}$  will not be increased; it will probably be decreased.

#### 6.1.6.2. Maximization of Signal-To-Noise Ratio

When there is a single desired signal source present in an environment of one or many interfering sources, the definition of S/N is clear. This is not true when more than one desired source is present; however, the Applebaum-Howells circuit, discussed in the previous sections, allows for optimum adaption when several desired sources and several interfering sources exist simultaneously. When there is only a single user and its location is known, the Applebaum-Howells circuit will maximize S/N if the quiescent weights,  $\underline{V}$ , are chosen to form a single receiving pattern with maximum directivity in the direction of this desired source. By comparison, the circuit shown in Figure 6.9 will form and steer a high-directivity beam in an unknown desired signal-source direction while simultaneously placing a null on all interfering sources. This is accomplished without knowledge of the location of either the desired or the interfering sources. However, it is necessary to derive a reference signal that is a suitable replica of the expected desired signal. This can lead to the dilemma that if the desired signal must be known prior to adaption, there is no need to send it to the receiver. However, the desired signal might have a deterministic component (i.e., a pseudonoise sequence or frequency hopped "carrier") and a random component (i.e., that modulation on the carrier that contains unknown information). The former would be used to permit the adaption circuit to recognize a desired signal and maximize the associated S/N.

The circuit shown in Figure 6.9 is identical to the Applebaum-Howells circuit (Figure 6.8) discussed in the previous section except for the output portion and the absence of steering weights. A reference signal  $e_{REF}$  is subtracted from  $e_0'$  to generate an error signal with which the  $e_n$  are correlated and the  $W_n$  determined. Some sort of spread-spectrum modulation is assumed so that a reference signal can be obtained by despreading  $e_0'$  and bandpass filtering it in order to increase the S/I of  $e_{REF}$  compared to the S/I of  $e_0'$ . Amplifying the demodulated  $e_0'$  (i.e., to

obtain  $e_0$ ) and modulating it with the known pseudonoise sequence results in a reference signal,  $e_{REF}$ .

To understand the operation of this circuit, assume that the interfering component of  $e_0$  is much larger than the desired signal component. Consequently, the error signal is dominated by the interference signal and the correlators drive the weights to reduce  $e_0$  by placing nulls in the direction of the interfering sources. Reduction of the interfering source will not, in general, reduce the desired signal. Because the reference signal is principally an amplified replica of the desired signal, the correlators drive the weights to increase the desired signal in order to reduce the error signal,  $e_{ERR}$ . This adjustment of the weights is identical to "steering" a receiving pattern with maximum directivity toward the desired source while simultaneously placing nulls in the direction of the interfering source.

This circuit (Figure 6.9) is commonly referred to as the "Widrow" circuit after its inventor<sup>8</sup>. It is often recommended for use in time-division-multiple-access (TDMA) communication systems employing pseudonoise modulation as spread spectrum protection against interfering sources. The Widrow circuit is limited to multiple-interference source scenarios with a single desired source because the beam will be acquired by only a desired signal that is in synchronism with the spread spectrum modulation.

It is interesting to note that, if there is one desired source in the FOV, the Applebaum-Howells and Widrow circuits produce the same steady weights if the  $\underline{V}$  are chosen to steer the beam in the direction of the desired source. That is, the Widrow circuit contains a closed loop determination of the  $\underline{V}$ ; whereas the Applebaum-Howells circuit requires that  $\underline{V}$  be an externally generated open-loop constraint. Consequently, the former is applicable for scenarios with a single desired source; whereas, the latter is applicable for any scenario for which a prescribed quiescent receiving pattern is essential, such as satellite communication system spacecraft

antennas that must have an earth-coverage or multiple-area-coverage receiving pattern to serve multiple users simultaneously.

#### 6.1.6.3. Transient Characteristics

All analog and essentially all computational nulling algorithms require a finite time to respond to the onset of an interfering signal. These transient effects and a computational algorithm which eliminates them will be discussed in this section.

It can be shown<sup>4</sup> that for a single interfering source the time constant of the  $n^{\text{th}}$  cancellation loop (Figures 6.8 or 6.9) is inversely proportional to the product of the loop gain and the power,  $P_n$ , received at the  $n^{\text{th}}$  port. Hence, increasing the loop gain decreases the time to adapt; however, the loop gain must be low enough to prevent unstable operation. Therefore, setting the loop gain in accordance with the strongest expected interference signal source prevents loop instability and determines the shortest possible time required for the antenna system to complete its adaption function. If two interfering sources are present, one strong and one weak, the strongest source is at first reduced rapidly to a level somewhat higher than its steady-state level. Then at a much slower rate its signal strength is reduced until both interfering signals are reduced to their steady-state level at the same time. Consequently, it is important to set the loop gain so that the weakest expected interfering signal strength will result in a tolerable loop time constant. If the spread in strength of all troublesome interference sources is sufficiently large, it may not be possible to choose a suitable loop gain. This situation is often referred to as an excessive spread in the eigenvalues of the covariance matrix,  $M$ .



#### 6.1.7.4. Sample Matrix Inversion

Although the circuits shown in Figures 6.8 and 6.9 indicate the use of analog devices, it is not uncommon to use digital devices between the output of the correlator and the control terminal of the weights. Within the scope of this report, these changes do not modify the preceding discussions. However, consider a processor which converts the antenna terminal voltages,  $e_n$ , to a digital representation and completes the adaption process entirely within a computational processor. For example, the processor indicated in Figure 6.10 (LPF=lowpass filter) first demodulates the spread-spectrum modulation of the received signals and establishes an intermediate frequency bandwidth that retains the necessary power differences between interfering and desired signals. The signals are amplified, to establish the system thermal noise level, and divided into two identical channels, except for a relative phase of  $90^\circ$ . The signals are then converted to baseband and divided into a narrow "signal" band and a wider "nulling" band. All signals are then converted to a digital representation; the wideband signals are used to compute the covariance matrix,  $M$ , its inverse  $M^{-1}$ , and the optimum weights. The narrowband signals are stored in a buffer while the weights are being computed. As the narrowband signals leave the buffer, they are then weighted, summed, and filtered to yield a digital representation of the desired signals. Notice that this processor eliminates the transient performance of the weights and has the linearity characteristics of a digital computer. However, the signals must undergo a delay while the weights are computed, and there is not a feedback loop as with the Applebaum-Howells and Widrow algorithms. As with all feed-forward systems, the implementation must have accuracy commensurate with the desired signal suppression. In other words, the covariance matrix,  $M$ , must be estimated from the measured "samples" of the received signals. The performance of this algorithm is determined by the accuracy with which  $M$  is estimated, the rate at which the computations can be made, and the speed and accuracy of the analog-to-digital converters.

#### 6.1.8. MBA vs Phased Array

Historically, adaptive antennas have either used an array antenna or a multiple-beam antenna, MBA. It is often important to be aware of the fundamental differences of these devices and how they affect the adaptive antenna system performance. In this section, the inherent bandwidth is discussed as an aid in choosing one antenna instead of the other.

##### 6.1.8.1. Bandwidth

Classically and historically, phased array antennas are focused to receive signals from a given direction by adjusting an array of phase shifters. Specifically, the differential time delay,  $\tau_n$ , associated with signals arriving at the ports of the array elements is corrected by inserting a variable delay,  $\tau_n$ , in the range  $0 < \tau_n < \tau - p\lambda/c$ , where  $p$  is an integer. Consequently, the array is perfectly "focussed" at the design frequency,  $f_0$ , and becomes defocussed as the operating frequency,  $f$ , varies from  $f_0$ .

For a signal source located near the boresight direction of the array,  $p$  is small, and the array antenna does not become appreciably defocussed even for a large bandwidth  $\Delta f = |f_0 - f|$ . A rule of thumb relating  $\Delta f$  to antenna aperture,  $D$ , and  $\theta$ , the angle between the signal source direction and a normal to the plane of a planar antenna array, can be derived as follows. The maximum differential path delay,  $S_{\max}$ , is given by

$$S_{\max} = (D/\lambda) \sin \theta \quad . \quad (6.19)$$

The phase shifter inserts a "delay",  $S_1$ , less than  $\lambda$  and the "error",  $\epsilon$ , in differential path delay is given by

$$\epsilon = \text{Integer}[(D/\lambda)\sin \theta] \cdot \frac{\Delta f}{2f_0} \quad . \quad (6.20)$$

For  $(D/\lambda) \sin \theta \gg 1$ , the integer-value operation can be removed without seriously affecting the results. Solving (6.20) for the fractional bandwidth yields

$$\frac{\Delta f}{f_0} = \frac{2 \epsilon \lambda}{D \sin \theta} \quad (6.21)$$

Assuming  $\epsilon$  must be less than 0.1 (i.e., a path length error =  $\lambda/10$ ),  $\theta = 10^\circ$  and  $D = 120\lambda$ , (6.21) indicates a 1% frequency bandwidth. Calculated results<sup>3</sup> indicate that for  $\epsilon = 0.1$  the interference signal will be suppressed  $\sim 20$  dB; doubling, or halving  $\Delta f$ , changes the signal suppression to 14 dB or 26 dB, respectively. That is, signal suppression varies approximately as  $\Delta f^2$ .

Most multiple-beam antennas use a lens, or a paraboloid, which focuses received signals by introducing differential path delays (as opposed to phase shifting) and translating a feed located in the focal region of the lens or paraboloid. Consequently, the system remains focussed over a very wide frequency band. However, the sidelobes and receiving pattern shape change with frequency and tend to alter the amplitude instead of the phase of the received signals. Studies have indicated that this effect of varying frequency does not degrade the associated adaptive antenna performance as much as that of an "equivalent" planar array because each beam of the MBA performs like a phased array with its receiving beam in the boresight direction. Since the sidelobes of an MBA do not dominate the determination of the weight applied to a beam port, an MBA with an aperture  $D = 120\lambda$  can suppress interfering signals more than 20 dB for  $\Delta f/f \sim 5\%$ .

In some applications, the use of an array antenna is preferred to an MBA. Using the foregoing, the operating bandwidth can be estimated. If the expected  $\Delta f/f_0$  meets, or exceeds, the system requirements, the phased array may be the best choice. If the estimated  $\Delta f/f_0$  is less than required, an MBA may be the best choice.

#### 6.1.8.2. Channel Matching

Adaptive antennas suppress interfering signals in accordance with the qualitative relationship<sup>3</sup> given in Section 6.1.2 and the similarity among the transfer functions,  $L_n$ , of each of the  $N$  channels. In large aperture,  $D$ , antennas operating over a large bandwidth,  $W$  such that  $DW/C > 1$ , the natural dispersion of array antennas may limit the cancellation ratio,  $C$  (see Section 6.1.2).  $C$  can also be limited by channel mismatch  $\Delta L_{mn} = L_n - L_m \neq 0$  when frequency independent weights are used. The use of frequency dependent weights (Figure 6.5) improves  $C$  in the presence of both antenna dispersion and channel mismatch. Rigorous simulation is usually required to determine the expected value of  $C$ . However, as a guide to the tolerable rms variation of  $\Delta L_{mn}$ , it is useful to refer to Figure 6.11 where the required rms amplitude and phase variation of  $L_n$  of a two channel system is given as a function of the cancellation ratio,  $C$ . The reader is cautioned to apply these results only to obtain a qualitative estimate of the expected performance of adaptive antennas with more than a few elements or beam ports.

### 6.2 Multibeam Antennas

The following is addressed to those who have an interest in but who are not necessarily well informed in the field of multiple-beam antennas (MBAs). Special attention and general consideration is given to their application to the spacecraft of a satellite communication system. The scope of these notes does not contain comprehensive detail design techniques; rather, only the general concept is presented. Consequently, the antenna specialist is advised to use these notes as a guide to the detail design techniques described in the references.

First, the general description of an MBA, and why and how it is, or might, be used are presented. This is followed by a discussion of some of its performance characteristics and experimental results. Included in this

discussion are analytic techniques, the beam- (or pattern) forming network (BFN), beam scanning characteristics and the generation of earth-coverage (EC) patterns with prescribed minima. The inherent frequency bandwidth of a constrained lens, constructed of waveguide, is discussed and a new design<sup>9</sup> having very wide band properties is presented.

#### 6.2.1. General Description of an MBA

Any antenna which has more than one input (or output) port is technically an MBA if different radiation patterns are obtained when signals are injected at these different ports. However, it is generally accepted that the shape of these patterns is that of a pencil beam and that, say, more than five ports are used. The restriction of more than five ports is needed to eliminate five horn monopulse systems or four horn sequential lobing antennas. The similar beam shape restriction eliminates monopulse, etc., tracking antennas even though they are technically multiple-beam antennas. Still further, a multiple-horn fed reflector, or lens, etc., using an organ pipe scanner, etc., is not considered in the class of MBA discussed here. In fact, the general MBA considered here consists of a collimating aperture illuminated by a multiple feed (port) array, or a planar array excited by a Butler Beam Forming Matrix (BBFM). Signals injected into each port generate beams of nearly the same shape but with each beam axis in a different direction.

Generally, the concepts involved are easier to understand if the antenna is considered to be radiating, as opposed to, receiving signals. Consequently, the discussions will consider the antenna to be radiating unless otherwise stated. However, the same performance prevails when the antenna is receiving signals since it is a reciprocal device. The ferrite phase shifters in the BFN are the one exception to this rule, and this will be pointed out when they are discussed.

#### 6.2.1.2. Lens

Let us consider the stepped waveguide lens schematically indicated in Figure 6.12. (The lens could have been made of solid dielectric, a "bootlace" or other; its precise character is not essential to this discussion.) Signals into feed horn #1 produce a beam (i.e., #1) coincident with the focal axis of the lens. The beam direction is along the focal axis because the feed horn is located on or near the focal point and focal axis. Signals into feed horn #2 produce a beam squinted off the focal axis of the lens as indicated by beam #2. The angular displacement of beam #2 is approximately equal to the angular displacement of feed horn #2. Both angular displacements have their vertex coincident with the vertex (center) of the lens. Similarly, signals into feed horn #3 produce beam #3. Clearly, a beam with essentially the same shape but pointing in a different direction is produced by signals into any feed horn located in or near the focal plane. The spacing, location, and size of these feed horns is critical to the MBA performance and will be discussed in detail later. The principal point to be derived here is that each port (feed horn input) provides a place to inject signals and produce a beam pointing in a different direction; hence, it is an MBA.

Similarly, the lens in Figure 6.12 could have been a "paraboloid" reflector. Although the radiation patterns will be changed substantially by the introduction of aperture blockage, the feed horn array will produce a corresponding "pin cushion" of beam patterns, and hence the antenna is an MBA.

About 20 years ago, J. Butler invented a configuration of 3-dB couplers and fixed phase shifters that has  $N$  input ports and  $N$  output ports. The network, called a Butler Beam Forming Matrix (BBFM), has the property, when connected to a linear array of  $\lambda/2$  spaced radiators, that a signal into any one of the input ports produces a beam pointing within  $90^\circ$  of a perpendicular bisector of the array's axis.

Moreover, the composite pattern generated by exciting all ports with equal amplitude, in phase, signals results in essentially uniform coverage of the half space into which the elements radiate. In other words, it is an MBA. A two-dimensional arrangement of these BBFM fed linear arrays will result in a planar array of radiating elements (i.e., horns, dipoles, etc.) which has  $N^2$  ports and a corresponding number of beams covering the field of view (FOV). The FOV is loosely defined as the space subtended by the half-power beamwidth of the radiating elements. (Necessary to the foregoing is that the beam of each radiating element be identical and point in the same direction.) There exists many other multiple-beam antenna configurations that are variations of the foregoing three; these were described to give examples and provide a departure point for the following sections.

Just as the MBA is important; the BFN used to combine the ports is essential and critical to the performance of the MBA system. In fact, in many communication applications, the BFN is the "heart" of the system in that it provides the desired flexibility and/or control of the antenna radiation pattern shape and/or direction.

#### 6.2.2. Degrees of Freedom and Aperture Size

Continuing with a general discussion of MBAs, let us consider the all important aperture size and the number of beams. From a straightforward fundamental consideration, it is clear that the larger the aperture the greater the resolving power that can be obtained. This leads to the concomitant conclusions that the radiation pattern can be made to change more rapidly, as a function of direction angle, as the aperture size is increased. Still in other words, the radiation field can be specified at closer spaced observation points as the aperture is increased. The number of points at which the radiation pattern shape can be specified is limited to the number of beams and may be less.

#### 6.2.2.1. Pattern Shape

Let us consider two specific MBA configurations to illustrate the point intended in the previous paragraph. Case A is an MBA aperture just large enough such that with seven ports it will generate a set of seven beams each with a half-power beamwidth (HPBW) of approximately  $6^\circ$  and arranged as indicated in Figure 6.13. Case B is a larger aperture MBA with 19 ports so that each beam has a HPBW  $\sim 3.5^\circ$ . They are also arranged in a hexagonal grid as shown in Figure 6.13.

Clearly, each MBA can determine the radiation field in one point of each of its beam pattern "footprints" on the earth; this is true even with the probable mutual coupling between beams. Although it is not clear from the foregoing, it would be substantially more difficult to produce a given field at more than one observation point within a given beam footprint. Certainly it is not impossible, but the task becomes increasingly difficult as these observation points move closer together. Nevertheless, it is important to note that the MBA of Case B can produce a given field at more points, in the FOV, than can the smaller MBA. It follows that the specified points can be closer together for the former than for the latter. Although this may be considered an obvious conclusion in the cases considered, the general ideas have been supported<sup>10,11</sup> with considerable rigor and hence can be used in predicting the performance of a general radiation pattern shape; that is, larger apertures and more beam ports lead to a better realization of the desired pattern.

#### 6.2.2.2. Patterns with Prescribed Nulls

In many cases the exact pattern shape is not essential to the desired system performance; rather the pattern can vary within some specified limits. In these instances, the radiation pattern can be "specified" at a number of points  $P$ ; where  $P$  is greater than  $N$ , the number of ports in the MBA. However, a popular pattern requirement specifies the position of the



nulls in the radiation pattern so as to reduce the noise received from an interfering source. Because a null, or a very low minimum, imposes a severe constraint on the radiation pattern (as compared with specifying say the value of a maximum within a few tenths of a dB) generally the number of nulls,  $M$ , that can be generated must be one less than  $N$ . However, given a sufficient tolerance on the depth of the null, it is possible that  $M$  can be greater than  $N-1$ . The degree to which  $M$  can exceed  $N-1$  depends strongly on the scenario(s) considered and the reduction in signal desired.

At this point, it is important to point out that, with respect to degrees of freedom and resolution, phased array antennas (PAA) have the same general performance limitations as an MBA. The particular  $M$  cannot exceed the number of elements  $N_a$  in the array minus one. The principal difference between the two manifests itself in the general character of the signals received at the ports. The signals received at the ports of a PAA have essentially the same amplitude, but the phase of the signals at any one port differs widely from that of any other port. In contrast, the signals received at the ports of an MBA have essentially the same relative phase but are quite different in amplitude. There are other advantages and disadvantages of these two cannonic antenna forms but a rigorous comparison is beyond the scope of these notes.

In general the algorithms, for determining the beam weights of an MBA or the element weights of a PAA, deal principally with the radiation patterns and ignore the details of the manner in which they are produced. Hence the frequency variation of the antenna, its BFN, and other network components determine the overall performance degradation. As these degrading effects may be peculiar to any specific design, we will consider here only the most general approach to synthesizing radiation patterns of a particular antenna. In particular, the beam scanning and nulling algorithms are extremely simple and serve only to demonstrate a means of achieving design parameters; it is readily admitted that a more

sophisticated and rigorous approach would improve the performance shown. It is conjectured that the latter would not change the design parameters (i.e., number of beams, aperture size, feed horn spacing and size, etc.); it would, however, improve the performance.

### 6.2.3 Performance Characteristics

Principally because of this designer's preference, the constrained waveguide lens illuminated by an array of conical feed horns is chosen as the MBA under consideration. It is also chosen here because a great deal of analytic and experimental data are available. It is also true that the antenna can be modeled analytically both accurately and rather simply. This mathematical model is quite suitable to high-speed digital computer analysis; consequently, much of the data shown in the following pages has analytic as opposed to experimental derivation. In order to satisfy those not so willing to accept calculated performance, experimental data will also be shown so that a comparison can be made to satisfy one's personal standards.

#### 6.2.3.1. Waveguide Lens

The reader is referred to the literature<sup>12,13</sup> for a more detailed description of the antenna under consideration; however, for completeness, it is shown in Figure 6.14. It consists of a waveguide lens ~ 30 inches in diameter with focal length = 30 inches and contains approximately 700 titanium waveguides with 1.0" x 1.0" square cross section and a .005-inch wall thickness. This assembly of waveguides (not including the outer support ring or the booms) weighs only 7 lbs. It is illuminated by an array of 19-conical horns arranged in an equilateral triangular grid. The circular apertures of these horns lie in a plane perpendicular to the focal axis of the lens and ~ 30 inches from the vertex of the lens. The inner surface of the lens is spherical with a radius of 30 inches. The length of the individual waveguides in the lens is adjusted to produce the

phase advance necessary to convert the incident "spherical" wave (i.e., considering the antenna as transmitting signals) into a "plane" wave. The length of those waveguides which introduce a phase advance greater than  $360^\circ$  is reduced so as to decrease the phase advance by  $n \times 360^\circ$  where  $n = 1$  or  $2$ . This results in a "stepped" or "zoned" lens as characterized by the outer surface of the lens.

The conical horns have circular apertures with diameter,  $d$ , equal to the spacing,  $s$ , between adjacent horns. Since  $s$  is an important parameter in obtaining a desired performance, specific values will be given later. The horns are excited so that each feed radiates a linearly polarized signal. The measured data reported here was obtained by exciting the feed horns through the BFN shown in Figure 6.15.

#### 6.2.3.2. Beam Forming Network

The beam forming network is indicated schematically in Figure 6.16. There are many networks by which the multiple feeds can be connected to a transmitter to obtain variable radiation patterns. This network, which is appropriately called a beam-forming network (BFN), largely determines the versatility of the antenna system. The BFN described in this note is a corporate feed network made of continuously variable, as opposed to fixed, power dividing junctions. (Switches are not considered variable power dividers since they provide a finite fixed set of power distributions.) With this network, any desired power distribution may be obtained at the output ports. With such a network, one is not limited to only 19-pencil beams, as would be the case if energy were merely switched from one of the 19 horns to another, but, by properly dividing the power among the several adjacent horns, pencil beams may be formed in any desired direction within the field of view.

The variable power dividing junctions (VPDs) consist of a 3-dB hybrid coupler, two nonreciprocal latching ferrite phase shifters, and a modified

magic "tee" with a matched waveguide load on its "difference" port. Let us first discuss these components separately and then as a complete assembly.

The 3-dB hybrid coupler is shown in Figure 6.17. Understanding its properties is the key to understanding the VPD. Basically, it is made of two standard rectangular waveguides which have a common "narrow", or side, wall. The energy traveling in one guide is coupled to the other by removing the common wall between guides for an appropriate length along the guide axis. Small sections of the common wall are shown (Figure 6.17) at the input and output ends of the device.

Consider first a wave incident on port 1. The energy contained in this wave is divided equally between ports A and B; none of this energy appears at port 2. The signals at port A and B are in phase quadrature, with the signal at port A lagging that at port B as indicated. Due to the symmetry of the junction, the energy in a wave incident on port 2 will also divide equally between ports A and B; however, the signal at port B will lag that at port A by  $90^\circ$ . It is important to note that ports A and B are isolated, hence the load on port A does not affect the power delivered to port B and vice versa. Now let us assume that simultaneously signals at the same frequency and of  $\sqrt{2}E_1$  and  $\sqrt{2}E_2$  amplitude are incident on ports 1 and 2. If the signals are in-phase and have equal amplitude, the signals at port A and B will also be in-phase and have an amplitude of  $\sqrt{2}E_1$ . If the signal at port 1 leads that at port 2 by  $90^\circ$ , the two signals arriving at port B are  $180^\circ$  out-of-phase and hence vanish; at port A, they add in-phase to produce an amplitude  $2E_1$ . Similarly, if the signal at port 2 leads that at port 1 by  $90^\circ$ , there is no output at port A, and all the energy exits from port B. Suffice it to say that appropriate choice of the phase difference, in the range  $\pm 90^\circ$ , between signals at ports 1 and 2 will deliver any fraction of the total input power to port A or port B, and the sum of the output power will be equal to the total input power minus any power dissipated in the coupler or reflected from ports A and

B. Typically, the power dissipated in the coupler (i.e., its insertion loss)  $\sim 0.05$  dB at 7.5 GHz.

A modified "magic tee" is also a four-port device. It is customary to refer to it as having input "sum" and "difference" ports and two "output" ports. Signals incident on the sum port divide equally between the output ports, and these output signals are in-phase. Signals incident on the difference port also divide equally between output ports, but the output signals are  $180^\circ$  out-of-phase. The device is reciprocal, linear, and bilateral; consequently, equal-amplitude signals incident on the output ports appear only at the sum port if they are in-phase and at the difference port if they are  $180^\circ$  out-of-phase. If this device is connected to the 3-dB coupler through identical phase shifters as indicated schematically in Figure 6.18, signals ( $E_0$ ) incident on the sum port of the magic tee will divide between the output ports (i.e., ports A and B) in the ratio indicated below.

$$E_A = E_0 \cos\left(\frac{\pi}{4} + \frac{(\theta - \phi)}{2} + \frac{\pi}{4}\right) \exp\left[j\left(\frac{\phi + \theta}{2} - \frac{\pi}{4}\right)\right] \quad (22.1a)$$

$$E_B = E_0 \sin\left(\frac{\pi}{4} + \frac{(\theta - \phi)}{2} + \frac{\pi}{4}\right) \exp\left[j\left(\frac{\phi + \theta}{2} - \frac{\pi}{4}\right)\right] \quad (22.1b)$$

Note that the insertion phase of  $E_A$  and  $E_B$  depends on the sum of  $\theta + \phi$ . Keeping the  $\theta + \phi$  constant, while varying  $\theta - \phi$ , a beam-forming network using this power dividing junction can produce an arbitrary distribution of the input power among output ports, with no phase variation of the output signals.

The variable insertion phase shifts,  $\theta$  and  $\phi$ , can be obtained by the use of latching ferrite phase shifters. These consist of a ferrite torroid mounted in the center of a rectangular waveguide as indicated in Figure 8. The state of magnetization of the ferrite controls the phase shift of the signal passing through it. A single-turn control wire determines the magnetic flux density in the ferrite. The wire enters the

waveguide parallel to the broad wall and hence has negligible interaction with the waveguide fields. To insure that essentially all of the r.f. energy passes through the ferrite torroid, matching end sections are used to reduce the insertion loss of the device and provide essentially reflection-free performance.

The desired insertion phase is obtained by first driving the ferrite into saturation. This establishes a "calibration" condition enabling a second drive pulse of controlled width (and amplitude) to change the flux, an amount  $\Delta\psi$ , to establish the desired remanent flux in the ferrite. The change in insertion phase is proportional to  $\Delta\psi$ . In Figs. 6.20 and 6.21, measured change in insertion phase of a single phase shifter and power division of a VPD are shown as a function of drive pulse width. In Figure 6.2.1, the data was obtained by applying a pulse width,  $\tau$ , to one phase shifter and  $5.05 \mu\text{s} - \tau$  to the other phase shifter. This insures  $\theta + \phi \sim \text{constant}$ . However, it is important to point out that since this data was taken, the manufacturer (i.e., Electromagnetic Sciences, Inc.) has made significant advances in linearizing the phase versus pulse width curve shown in Figure 6.20. He has also reduced the insertion loss to  $\sim 0.2$  dB. A detail accounting of this and other performance improvements are beyond the scope of these notes.

#### 6.2.3.3. General Description of Analytic Techniques

The performance of a lens antenna with a multiple-feed horn array can be calculated using physical optics and an extrapolation of measured feed horn radiation patterns. The waveguide lens, feed horn array, and associated geometry under consideration are shown in Figure 6.22. The inner surface of the lens has a radius equal to the focal length  $F$  and a minimum thickness  $0_2 - 0_1$  at its center. The waveguides have a square cross section  $a$  on a side and are positioned by the subscripts indicating the  $m^{\text{th}}$  row and  $n^{\text{th}}$  column. The center line of each waveguide is located by the radius vector  $\rho_{mn}$ . The feed horn array is located in the plane

$z = -F$ , and the feed horn apertures are located by the subscripts indicating the  $i^{\text{th}}$  row and the  $j^{\text{th}}$  element in that row.

The radiation pattern of each feed horn is represented by an analytic expression derived from measured data and known frequency behavior. The beam-forming network is shown only to indicate its location and function. The excitation of each feed horn is specified; it is assumed that the beam-forming network will produce it.

The far-zone radiation patterns are determined by calculating the physical optics field incident on the lens inner surface, the reflection, and transmission at the inner and outer surface of the lens, the path length through the lens, and hence the excitation of each of the individual radiating waveguide apertures. The far-zone radiation pattern is calculated by summing the contribution of each of these apertures. Although this analysis assumes the antenna is transmitting signals, identical radiation properties exist when it is receiving signals because it is a reciprocal device. However, the ferrite phase shifters used in the beam-forming network are not reciprocal, and hence they cannot be used for simultaneous transmission and reception of signals. In this case, a separate beam-forming network would be required, one for transmitting signals and one for receiving signals. The far-zone field is given by

$$G(\theta, \phi) = \frac{G_o a^4}{P_t \lambda^2 F^2} |E(\theta, \phi)|^2 \quad (6.2.2)$$

with

$$E(\theta, \phi) = \sum_i \sum_j \sum_m \sum_n a_{ijn} \frac{f(\theta, \phi) \cos^{1/2} \gamma_{mnij} h(\theta, \phi) e^{-jk(r_{mnij} + n d_{mn} - \vec{P}_{mn} \cdot \vec{u})}}{\frac{r_{mnij}}{F} \cos^{1/2} \alpha_{mn}}$$

where

- $G_o$  = gain of a feed horn
- $f(\theta, \phi)$  = radiation pattern of a feed horn
- $n$  =  $[1 - (\lambda/2a)^2]^{1/2}$  is the index of refraction of the lens

$\vec{u}$	= unit vector in the direction $\theta, \phi$
$h(\theta, \phi)$	= function which accounts for steps in waveguide lens
$a_{ij}$	= complex excitation of feed horn $ij$
$k$	= $2\pi/\lambda$
$P_t$	= $\sum_i \sum_j  a_{ij} ^2$
$F$	= focal length
$\lambda_{mnij}$	= angle between focus and center of horn $ij$ measured at the inner surface of the lens at cell $mn$
$\alpha_{mn}$	= angle subtended by vertex and cell $mn$ measured at focus

and the other parameters are defined in Figure 6.22.

The step introduced in the lens surface reduces the weight of the lens and increases its operating frequency band. Phenomenologically this is due to the compensating variation in insertion phase as a function of frequency introduced by the dispersion characteristic of the waveguide and the fixed "free space" length of the removed section of waveguide. However, it has the disadvantage of changing the radiation pattern of each waveguide element adjacent to the step. As indicated in Figure 6.23, the pattern is different for the electric field ( $E$ ) perpendicular, and parallel, to the plate formed by the step. Both patterns differ from that of a waveguide element not adjacent to the step. The latter is preferred since it is the only one that illuminates the entire FOV; when the element pattern does not illuminate the FOV, that element does not contribute as well to the far zone field. Consequently, there is a loss in gain and perhaps an increase in sidelobe radiation levels. In designs evaluated by the researcher, this loss is  $\sim 0.3$  dB per step in the lens surface.

#### 6.2.4. Scanning Beam Characteristics

Scanning a beam with a MBA is often misunderstood to consist of a series of steps from one beam position (i.e., from one feed horn) to the next. Actually the composite beam can be scanned smoothly over the entire FOV. Let us consider a simple scan of the "antenna" beam from one fixed beam



case when all the power is fed into it, the beam direction varies smoothly and almost linearly from  $0^\circ$  to  $\sim 3.8^\circ$ . Note that both experimental and analytic data are shown indicating the excellent agreement between measured and calculated data. Also note that the antenna gain varied  $\sim 1.0$  dB, pointing out one of the salient disadvantages of a MBA; it has a significant loss associated with scanning a beam over its FOV. In order to determine this scan loss more accurately, let us consider the loss encountered when attempting to scan a maximum gain beam over the entire FOV.

#### 6.2.4.1. Minimum Directive Gain over the Field of View (FOV)

A communication system designer requires a knowledge of the directive gain of the antenna in order to establish an accurate estimate of the link margin. Directive gain is the product of the antenna directivity and its normalized radiation pattern. The designer must size the communication system for the minimum expected value of directive gain over the entire FOV. With a mechanically scanned paraboloid antenna, all that is needed is knowledge of its radiation pattern and directivity. For a multiple-beam antenna, the situation is somewhat more complicated. First, one must devise a means of "scanning" a beam over those angular positions between the beam directions obtained by exciting any single feed horn, because the decrease in directive gain at a direction between these beam peaks is usually unacceptable (that is, if the beam is not scanned). Due to the flexibility of the variable power divider, this "scanning" can be accomplished in either a continuous or a stepwise fashion. Secondly, the change in beam shape during "scanning" must be ascertained -- in general, the pattern formed by exciting two or more feeds simultaneously will be different from that obtained by exciting a single feed -- so that the actual coverage provided may be determined. We first analyze a stepwise method of scanning, in which either one, two, or three adjacent feeds are excited, and then consider the case of continuous scanning.

#### 6.2.4.2. Stepwise Scanning

It appears that a useful mode of operation of a multiple-beam antenna generating a single beam is to restrict it to a relatively simple set of controls such as excitation of one feed, or two adjacent feeds, or three adjacent feeds arranged in the form of a triangle. Restricting our consideration to this set of controls also simplifies the optimization problem. Assuming a FOV =  $18^\circ$ , which is  $0.6^\circ$  larger than the solid angle subtended by the earth at synchronous altitude (also allowing for some satellite attitude variation), the minimum directive gain was calculated for operation of the multiple-beam antenna with either one, two, or three feeds excited in-phase and with equal amplitude. The diameter of the lens and the feed horn spacing were varied (keeping focal length = diameter), and the directive gain at 7.5 GHz was calculated. Since interest is in determining the minimum value of directive gain anywhere in the FOV, it is necessary to examine two situations. These are, the minimum directive gain obtained within, and at the edge of, the field of view.

With a fixed lens diameter in the range 20 to 34 inches, the analysis begins with a spacing so small (i.e.,  $S < \lambda$ ) that the FOV is less than  $18^\circ$ . Increasing the spacing decreases the minimum directive gain,  $G_e$ , at the edge of the FOV to a maximum,  $G_{\max}$ , at a spacing  $S = S_{\max}$ .  $G_e$  will vary between  $G_{\max}$  and  $\sim 1/2 G_{\max}$  for  $S > S_{\max}$  and increasing.

Considering the same initial conditions ( $S < \lambda$ ), the minimum directive gain  $G_i$ , within the FOV, is larger than the gain at the edge of the FOV and decreases as  $S$  is increased. Hence, there exists a unique spacing,  $S_0$ , for a given lens diameter and frequency of operation, for which the minimum directive gain,  $G_{\min}$ , over entire FOV, is maximum. At this spacing  $G_e = G_i$ . In order to determine  $S_0$ ,  $G_e$  and  $G_i$  were calculated and are plotted in Figure 6.25 for various lens diameters between 20 and 34 inches. Since  $S_0$  must be less than  $S_{\max}$ ,  $S$  is varied over that range which demonstrates the equality of  $G_e$  and  $G_i$ .

It is reasonable to pass a curve through all points for which  $G_e = G_i$  to obtain the solid curve of minimum directive gain versus spacing. However, it is necessary to recognize that for each feed spacing, there exists only one lens diameter that will give the indicated  $G_{\min}$ . The plot of  $G_{\min}$  versus lens diameter shown in Figure 6.26 can be derived from the data shown in Fig. 6.25.

The data, described in the previous paragraphs of this section, were calculated for a planar array of conical feed horns. With this feed configuration, the exterior beams have a slightly different phase with respect to the center beam. Adjusting the relative phase of the signals exciting the feed horns increases the directive gain when more than one feed horn is excited simultaneously. The long dashed curve shown in Figs. 6.25 and 6.26 show this increase in  $G_{\min}$  and the corresponding value  $S_0$ .

In summary, Figs. 6.25 and 6.26 show that a waveguide lens antenna illuminated by a planar array of 19 conical feed horns excited in the  $TE_{11}$  mode will have a minimum directive gain of 27.9 dB over an  $18^\circ$  FOV if operation is limited to the excitation of a single feed or equal distribution of input power between two adjacent feed horns or three feed horns arranged in the form of a triangle. The device is reciprocal hence the same is true when the antenna is receiving signals.

Finally, it is well recognized that the conical feed is not the most efficient feed to use in the assumed configuration. In particular, the aperture does not fill the hexagonal space available, and its aperture field must vanish at the aperture edge in the H-plane. Hence increasing the feed horn directivity by adding an end-fire device such as a polyrod, or a traveling-wave antenna such as a yagi, or helix, etc., will result in an increase in the directive gain over the FOV. In order to investigate the effect of a more efficient feed, a hypothetical uniformly excited hexagonal aperture was assumed as the element in a 19-element feed array

for the lens. It was felt that the gain of  $4\pi/\lambda^2$  times the feed area which is obtained with this model is the maximum physically realizable gain, without incurring undesirable interaction between the feeds. The resulting minimum directive gain over an  $18^\circ$  FOV was calculated and is given by the lower curve plotted in Figure 6.27. Notice that the maximum value of  $G_{\min}$  has increased to 28.9 dB -- approximately a 1-dB increase over the previous case. The corresponding maximum directivity is 32 dB. It is interesting to note that a 50% efficient 28-inch diameter paraboloid operating at the same frequency also has a directivity = 32 dB. It follows that the added flexibility of the multiple-beam antenna does not compromise its directivity, it is the losses in the beam-forming network and those due to scanning which compromise its gain. For the design considered here, the scanning loss is  $\sim 3$  dB. This can be reduced to  $\sim 2.4$  dB by using continuous scanning and appropriate excitation of all feeds.

The nature of the coverage obtained by exciting either one feed horn, or two, or three simultaneously so as to maximize  $G_{\min}$  is demonstrated in Figure 6.28. The solid curves shown represent the directive gain contours corresponding to the excitation of a single uniformly illuminated hexagonal cell located at feed horn positions 31, 32, or 21. The dotted contour corresponds to the simultaneous and equal excitation of two adjacent cells located at 31 and 32, 31 and 21, 32 and 21. The dashed contour is obtained when all three cells are excited simultaneously and with equal-amplitude signals. All contours represent a directive gain of 28.9 dB; the directive gain within any closed contour is  $> 28.9$  dB. The directive gain over most of the triangle (shown by the dash-dot lines) is  $> 30$  dB. The edge of the  $18^\circ$  FOV is indicated by a dashed line.

Before leaving this subject, it may be of interest to note the results obtained when the 19-hexagonal feed element array is enlarged to a 37-hexagonal feed array. The minimum directive gain obtained by exciting one, two, or three feeds varies with lens diameter as indicated by the

upper curve in Figure 6.27. The maximum value of  $G_{\min}$  increases  $\sim 3$  dB, and the corresponding lens diameter is 40 inches (an increase of 43%), as would be expected.

Because the desired FOV is circular, one might suggest removing the six feed elements located at the ends of the three seven-element rows of a hexagonal 37-element feed, because their beams lie partly outside the circle. Alternatively, one might consider arranging 32 feed elements on a square grid of six rows and six columns with the corner feed elements removed. Limiting operation, in the latter case, to excitation of one, two, or four feed elements, and to one, two, or three feeds in the former case,  $G_{\min}$  was calculated. The variation of  $G_{\min}$  with lens diameter is plotted in Figure 6.27 for further comparison. Of particular interest is the superior performance obtained when the feed elements are hexagonal and arranged on a triangular instead of a square lattice.

In conclusion, continuous beam scanning is possible, and may increase the minimum value of directive gain over that achievable as calculated in the foregoing by exciting one, two adjacent, or three adjacent feeds. A detailed presentation of the actual increase in directive gain is beyond the scope of this note. Some limited calculations indicate that more than 0.5 dB increase is possible, and the beam cross section can be made circular even when the beam direction is midway between two "feed horn directions". This improvement must be weighed against the added control commands that would be required.

#### 6.2.4.3. Earth-Coverage Pattern with Prescribed Minima

The use of multiple-beam antenna systems in the receiving mode on communication satellites is often justified by the need to suppress interfering signals by radiation pattern shaping. A particularly useful radiation pattern shape is one which provides uniform coverage of that portion of the earth's surface which is visible to the satellite with

exception of the points where interfering signals originate. Since, in a practical sense, only a finite reduction in the antenna's directive gain in the direction of the interfering source can be realized, the title of this section is a logical description of that radiation pattern which will produce the intended discrimination. The following is a description of methods, to realize such patterns, which are well within the state-of-the-art.

#### 6.2.4.4. Obtaining Minima by Turning Off Selected Feed Horns

This analysis assumes circular polarization, hexagonal feed horn apertures spaced 2.1 inches, lens diameter = 26 inches, and frequency = 8.15 GHz. The horns are arranged in a triangular lattice and the earth-coverage radiation contour plot obtained with all feeds excited with equal amplitude and in-phase is shown in Figure 6.29a. This lens and feed were designed to produce an  $18^\circ$  FOV which is indicated by the dashed line. Increasing the amplitude of excitation of six feeds, in the outer ring, 2.8 dB more than all other feeds improves the earth-coverage pattern by making it conform more closely to the desired circular FOV. In particular, increasing the excitation of feeds numbered 12, 21, 24, 51, 44, and 52 produces the radiation contour plot shown in Figure 6.29b. The -2 dB contour conforms very closely to the edge of the FOV. The minimum directive gain is increased  $\sim 0.7$  dB, and the lower directive gain is mostly over the center of the FOV where the path loss to the earth is minimum.

Let us consider a simple algorithm for obtaining the earth-coverage radiation pattern with prescribed minima (ECPMIN). Specifically, the ECPMIN is obtained by exciting all feed horns except those which produce beams pointing in the direction of the interfering source or sources. When the source falls between two or three adjacent beams, it is necessary to "turn off" those two or three beams to produce the desired spatial discrimination. In order to determine the effectiveness of this method of

forming an ECPMIN, contour plots of radiation patterns obtained by the excitation of all but one or two or three adjacent feeds were calculated. For example, excitation of all but feed horn No. 23 produces the contour plot shown in Figure 6.30. The contours are shown for directive gain of 0, 1, 2, 3, 4, 5, 10, 15, 20, 25, and 30 dB below the antenna directivity indicated in the figure. This feed excitation produced a minimum directive gain  $\sim 22$  dB below the antenna directivity (i.e., peak value of directive gain). An area corresponding to a  $\geq 15$ -dB reduction in directive gain has been cross-hatched to emphasize its existence.

Similar plots with each of the other six feed horns located in the upper left-hand quadrant turned off, one at a time, were calculated, and a composite representation of these minima is shown by the solid areas in Figure 6.31 which indicates that this technique alone is not capable of producing a  $\geq 15$ -dB reduction in directive gain at every point in the FOV.

If all but two adjacent feed horns are excited, the angular area of the minimum is approximately doubled, and it includes essentially the composite angular area of the minima created by turning off either of the feeds separated and that angular area joining them. For example, when all except feed horns numbered 22 and 23 are excited, the radiation contour is as indicated in Figure 6.32. Similarly radiation contours were calculated by successively turning off the remaining pairs of feed horns located in the upper left quadrant of the array. A composite presentation of the areas with  $\geq 15$  dB reduction in directivity similar to that shown in Figure 6.31 is best represented by showing only those areas where a  $\geq 15$ -dB reduction in directive gain was not obtained. That is, the small dotted angular area about the satellite's nadir position and the six cross-hatched areas indicated in Figure 6.31. Reduction in the directive gain over the six cross-hatched areas can be produced by turning off corresponding triangular clusters of feeds. A contour plot of the radiation pattern when the triangular feed horn cluster 21, 31, 32 is turned off is shown in Figure 6.33.

Unfortunately, it is not possible to produce a  $\geq 15$  dB minimum over the small dotted area centered on the satellite's nadir by merely turning off any combination of one, two, or three feed horns. However, if the center horn (No. 33) is excited  $180^\circ$  out-of-phase with the remaining 18 and with a relative amplitude  $\sim 0.25$ , a  $\geq 15$ -dB reduction in directive gain (indicated by the solid circle shown in Figure 6.31) can be produced in the center of the field of view.

In summary, the foregoing set of calculated data demonstrates that an earth-coverage pattern with prescribed minima can be realized by merely turning off one, two adjacent, or three adjacent feed horns. Referring to Figure 6.31, a signal originating from the direction corresponding to the solid darkened angular areas can be reduced by at least 15 dB if the single feed horn most tightly coupled to this signal is turned off. If the signal originates from an angular direction corresponding to the blank (white) angular area within the FOV, it can be reduced by  $\geq 15$  dB by turning off the two appropriate feed horns. Signals originating in the cross-hatched areas can be reduced  $\geq 15$  dB by turning off the three appropriate feed horns. If the undesirable signal originates from a direction within  $0.2^\circ$  of the satellite's nadir position, the signal can be reduced  $\geq 15$  dB by exciting the center feed  $180^\circ$  out-of-phase with the remaining feeds and with a relative amplitude  $\sim 0.25$ .

This method of producing minima in an earth-coverage radiation pattern is straightforward, within the state-of-the-art and can be accomplished with very little complexity of control. Even the  $180^\circ$  is readily obtained from the VPD described earlier. It has the disadvantage of reducing the directive gain over an area that is sometimes larger than necessary in order to reduce the directive gain in the desired directions (i.e., when three feeds must be turned off to reduce the signal). This can be avoided at the expense of some additional complexity, by "steering" the "null" in a manner analogous to steering beams as described in an earlier section of this note. This method will be described and discussed in the next section.



#### 6.2.4.5. Null Steering

An earth-coverage pattern with prescribed minima can be obtained if the multiple-beam antenna is excited such that all except two adjacent feed horns are excited with in-phase and equal-amplitude signals, say  $0^\circ$  and 1 volt, respectively. The remaining two adjacent feed horns, say 31 and 32, are excited with  $-90^\circ$  and  $+90^\circ$  relative phase, respectively. By varying their relative excitation between 0 and 1 volt, a minimum in the radiation pattern can be made to move from the direction obtained with feed horn No. 31 turned off to that obtained with feed horn No. 32 turned off.

In order to demonstrate this method, the radiation contours of a 26.0-inch diameter lens ( $f/D = 1$ ) operating at 7.5 GHz and illuminated by a 19-element hexagonal feed horn array were calculated. The antenna was designed to have an  $18^\circ$  FOV, and the initial earth-coverage pattern without prescribed minima was obtained by increasing the relative excitation amplitude of feed horns numbered 12, 21, 24, 41, 44, and 52 as before to improve the shape of the earth-coverage pattern.

Feed horns 21 and 22 were excited with  $+90^\circ$  and  $-90^\circ$  phase relative to the re earth-coverage pattern with prescribed minima can be obtained if the multiple-beam antenna is excited such that all except two adjacent feed horns are excited with in-phase and equal-amplitude signals, say  $0^\circ$  and 1 volt, respectively. The remaining two adjacent feed horns, say 31 and 32, are excited with  $-90^\circ$  and  $+90^\circ$  relative phase, respectively. By varying their relative excitation between 0 and 1 volt, a minimum in the radiation pattern can be made to move from the direction obtained with feed horn No. 31 turned off to that obtained with feed horn No. 32 turned off.

In order to demonstrate this method, the radiation contours of a 26.0-inch diameter lens ( $f/D = 1$ ) operating at 7.5 GHz and illuminated by a

19-element, hexagonal feed horn array were calculated. The antenna was designed to have an  $18^\circ$  FOV, and the initial earth-coverage pattern without prescribed minima was obtained by increasing the relative excitation amplitude of feed horns numbered 12, 21, 24, 41, 44, and 52 as before to improve the shape of the earth-coverage pattern.

Feed horns 21 and 22 were excited with  $+90^\circ$  and  $-90^\circ$  phase relative to the remaining feeds\*. With the ratio of power into feed horn No. 21 to that into feed horn No. 22,  $P_{21}/P_{22}$ , set successively to 0, 0.1, 1, 10,  $\infty$ , the radiation contours over the FOV were calculated. The composite angular area over which the directive gain is reduced by at least 15 dB is indicated by the dashed curves in Figure 6.34. A similar set of data with feed horns No. 32 and No. 21 instead of feed horns No. 21 and No. 22 is represented by the dotted curves in Figure 6.34. The solid curves in Figure 6.34 define the areas that result with feed horns No. 22 and No. 31 instead of No. 21 and No. 22. From this composite representation, we see that a greater than 15 dB reduction in directive gain can be realized over the triangular area defined by the beam axes of the single excitation of feed horns No. 31, 32, and 21. Consequently, this "null" steering method can be used to produce a greater than 15 dB reduction in directive gain anywhere in the FOV.

---

\*It was necessary to incorporate the phase correction, described earlier, which "converts" the planar array of feeds to feeds located on the surface of a sphere centered on the vertex of the lens.

A contour plot of the radiation pattern obtained when  $P_{31}/P_{32} = 1$  is shown in Figure 6.35. Note that the angular area, where the directive gain is reduced by at least 15 dB, is approximately equal to that when a single feed is turned off as indicated by Figure 6.30. Null steering thus sacrifices less coverage than does turning off two or three beams to achieve a minimum.

In conclusion, it is important to point that the addition of  $360^\circ$  phase shifters at each port would enable any feed excitation including those which would produce an arbitrarily deep (i.e.,  $> 40$  dB) minimum (or minima) anywhere in the FOV. Further still, several algorithms exist for not only determining those weight which will produce appropriately located minima but will simultaneously provide the best least-mean-square fit to a desired pattern (i.e., earth-coverage, area-coverage, pencil-beam, etc.). Finally, adaptive loops could be used<sup>14</sup> to drive these weights just as with adaptive array antennas and as discussed in Section 6.1 of these notes.

#### 6.2.5 Wideband Waveguide Lens

The narrow band properties of a stepped waveguide lens can be demonstrated by the set of curves shown in Fig. 6.36. The curves represent the radiation pattern obtained when a null is produced in an earth-coverage pattern. (In this case the excitation is chosen without limitation to phase and amplitude distribution.) The solid curve is obtained at the design frequency; the dashed curves are for a 2% increase and decrease in the operating frequency, with respect to the design frequency. Dion<sup>9</sup> recognized this limitation of the waveguide lens and developed a wideband waveguide lens capable of producing performance indicated in Fig. 6.37. To explain this performance degradation and Dion's improvement, first consider the step waveguide lens discussed in the foregoing part of these notes, then consider a variation created by Colbourn<sup>16</sup>, and then the scheme introduced by Dion.

The waveguide lens discussed in the previous sections of this report were of the constant thickness type; where a step is introduced whenever the differential phase shift introduced by a waveguide exceeds  $360^\circ$ . At the design frequency,  $f_0$ , there is perfect (in theory) phase correction introduced to convert an incident spherical wave (i.e., from the focal point of the lens) into a plane wave exiting from the lens external (stepped) surface. However, varying the frequency of operation from  $f_0$  introduces a phase error across the lens aperture as indicated in Fig. 6.38. Note that it has a "saw tooth" variation superimposed on a linear increase with the dimension  $S$  shown in Fig. 6.38. (Although a compound lens is shown, the inner surface is the same shape for all lens under consideration here.) The linear slope can be changed by introducing more steps or removing some.

Colbourn found that by increasing the number of steps (and the lens thickness), an appropriate balance between the waveguide dispersive characteristic and the nondispersive characteristic of free space, which replaces the removed length of waveguide, could result in significant reduction in the phase error introduced by operating at a frequency different from  $f_0$ . The phase error of a corresponding "minimum phase error zoned lens" is also shown in Fig. 6.38.

Dion considered the compound lens indicated in Fig. 6.39. The lens is made of a stepped (or zoned) part and a smoothly varying compensating part. The zoned part consists of half-wave plates located in each waveguide cell and hence has the constant thickness,  $T$ . He assumes square or circular waveguide cells and circularly polarized incident spherical waves. The half-wave plate changes the sense of polarization and introduces a relative insertion phase equal to twice the relative angular rotation of the polarizing "plate" in the waveguide structure<sup>17</sup>. Hence by setting the angular position of the plates, this part of the compound lens can be designed to give perfect "stepped" phase correction at  $f_0$ .

The second part of the lens consists of a section of unloaded waveguide with the easily calculated concomittant dispersive characteristic. Choosing the length of the latter permits one to achieve perfect phase correction at two frequencies. Choosing these frequencies at 8.0 and 8.3 GHz one obtains the phase error indicated in Fig. 6.38.

Needless to say this analysis points out the advantages of the compound lens and explains the calculated performance shown in Figs. 6.36 and 6.37.

#### Acknowledgments

The work reported here was carried out by many of my colleagues at Lincoln Laboratory. The principal professionals include Drs. A. R. Dion, A. J. Simmons, B. M. Potts, and L. K. DeSize. Most of the work was supported by the Military Satellite Office of the Defense Communication Agency under the direction of Dr. F. Bond. In addition, Dr. C. W. Niessen, Program Manager, and P. Rosen, Division Head, at Lincoln Laboratory were strongly influential in encouraging, guiding, and supporting the associated efforts. Finally, the SAMSO program office and its Aerospace counterparts helped tremendously in helping the development and ultimate use of an MBA similar to that described in the foregoing pages. The interaction with members of Ford Aerospace (Palo Alto, CA), General Electric Co. (Valley Forge, PA), Hughes Aircraft Co. (El Segundo, CA), and Lockheed Missiles and Space Division (Palo Alto, CA) also contributed to the results reported here. The author also wishes to point out that much of the text presented here is derived from Lincoln Laboratory Technical Note 1975-3<sup>13</sup>. Special thanks to Mrs. K. Martell for her patience in preparing this manuscript.

#### REFERENCES

1. IEEE Trans. on Ant. and Prop., Special Issue on Active and Adaptive Antennas, AP-12, (March 1964).
2. J. T. Mayhan, "Adaptive Nulling with Multiple-Beam Antennas," IEEE Trans. on Ant. and Prop., AP-26, No. 2 (March 1978) p. 267.
3. J. T. Mayhan, A. J. Simmons, and W. C. Cummings, "Wideband Adaptive Antenna Nulling Using Tapped Delay Lines," Lincoln Laboratory, M.I.T. Technical Note 1979-45 (26 June 1979) AD-A0828541.
4. W. F. Gabriel, "Adaptive Arrays - An Introduction," Proc. IEEE, 64, p. 239 (February 1976).
5. A. J. Fenn, "Interference Sources and DOF in Adaptive Nulling Antennas," 1981 Symposium on Antennas, Allerton Park, IL (23-25 September 1981).
6. J. T. Mayhan and L. J. Ricardi, "Physical Limitations on Interference Reduction by Antenna Pattern Shaping," IEEE Trans. on Ant. and Prop., AP-23, p. 639 (1975) AD-A017357/5.
7. S. P. Applebaum, "Adaptive Arrays," Report SPL TR 66-1, Syracuse University Research Corporation, Syracuse, New York (August 1966).
8. B. Widrow, et. al., "Adaptive Antenna Systems," Proc. IEEE 55, pp. 2143-2159 (1967).
9. A. R. Dion, "A Wideband Waveguide Lens," Technical Note 1977-8, Lincoln Laboratory, M.I.T. (2 February 1977).

10. J. T. Mayhan and L. J. Ricardi, "Physical Limitations on Interference Reduction by Antenna Pattern Shaping," IEEE Trans. Antennas Propag., AP-23 (September 1976).
11. J. T. Mayhan, "Nulling Limitation for a Multiple-Beam Antenna," IEEE Antennas Propag., AP-24 (September 1976).
12. A. R. Dion and L. J. Ricardi, "A Variable Coverage Satellite Antenna System," Proc. IEEE 59, 252 (1971).
13. L. J. Ricardi, et. al., "Some Characteristics of a Communication Satellite Multiple-Beam Antenna," Technical Note 1975-3, Lincoln Laboratory, M.I.T. (28 January 1975).
14. J. T. Mayhan, "Adaptive Nulling with Multiple-Beam Antennas," Technical Note 1976-18, Lincoln Laboratory, M.I.T. (30 September 1976).
15. B. M. Potts, "Radiation Pattern Calculations for a Waveguide Lens Multiple-Beam Antenna Operating in the AJ Mode," Technical Note 1975-25, Lincoln Laboratory, M.I.T. (14 October 1976).
16. C. A. Colbourn, "Increased Bandwidth Waveguide Lens Antenna," The Aerospace Corporation, Report No. TR-0076(6403-01)-3, Los Angeles, CA (8 December 1975).
17. A. G. Fox, "An Adjustable Waveguide Phase Changer," Proc. IRE, 35, pp. 1489-1498 (1947).

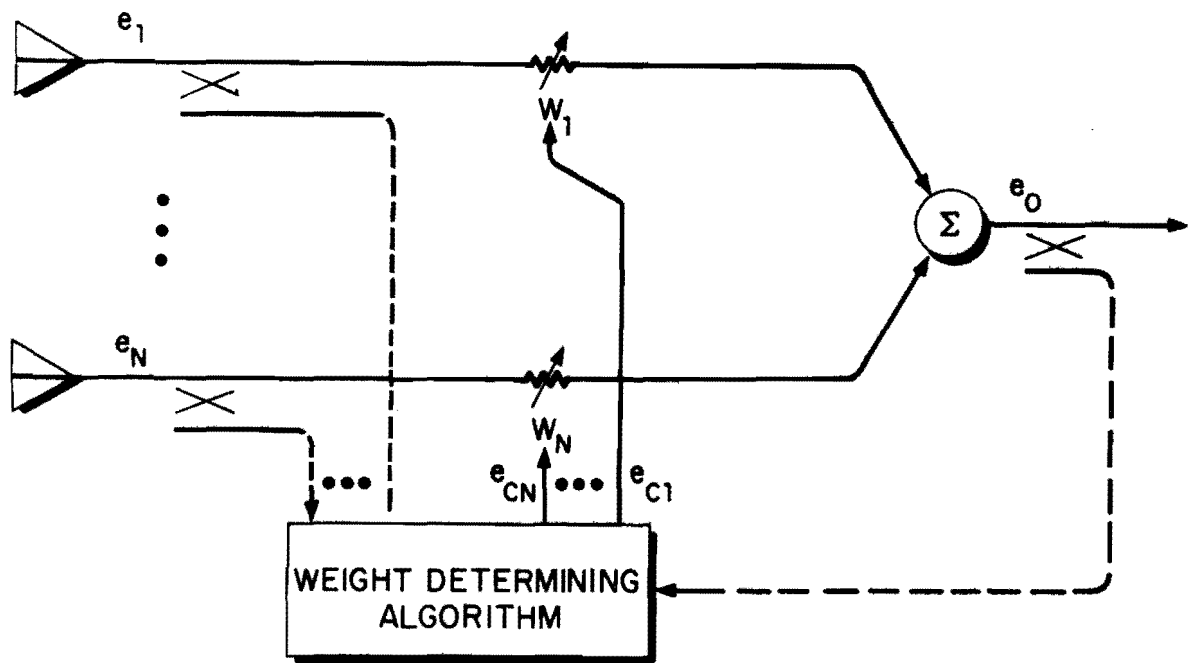


Figure 6.1 Fundamental adaptive nulling circuit.

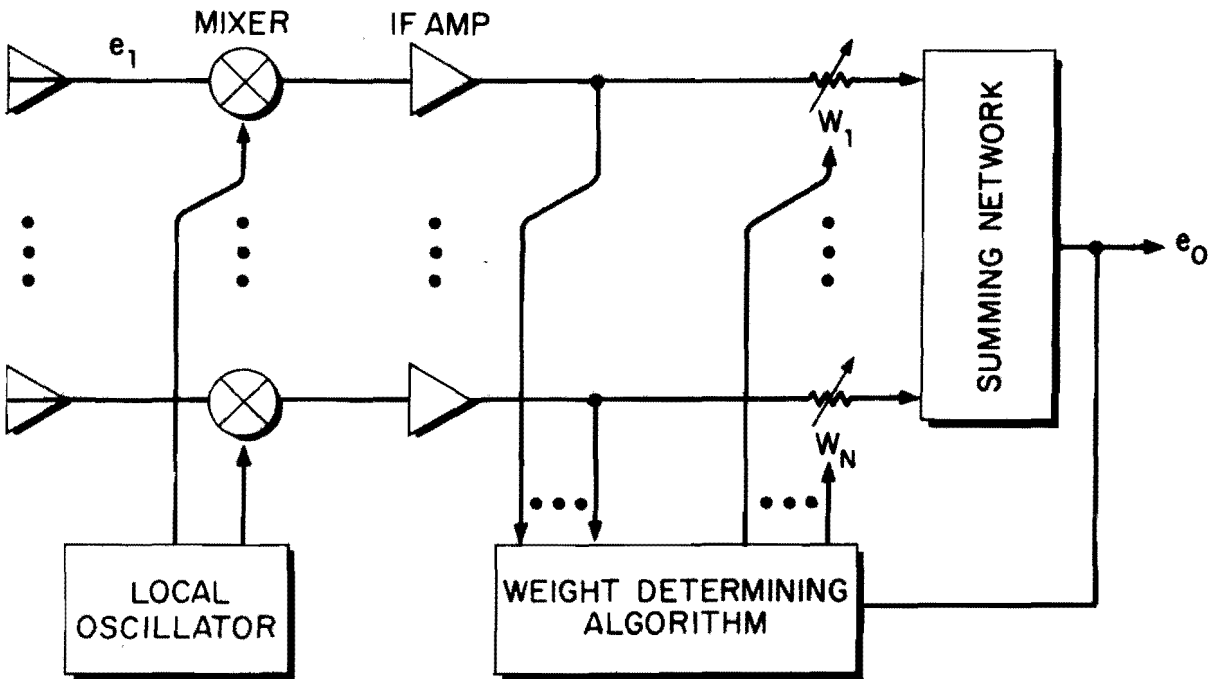


Figure 6.2 IF adaptive nulling circuit.



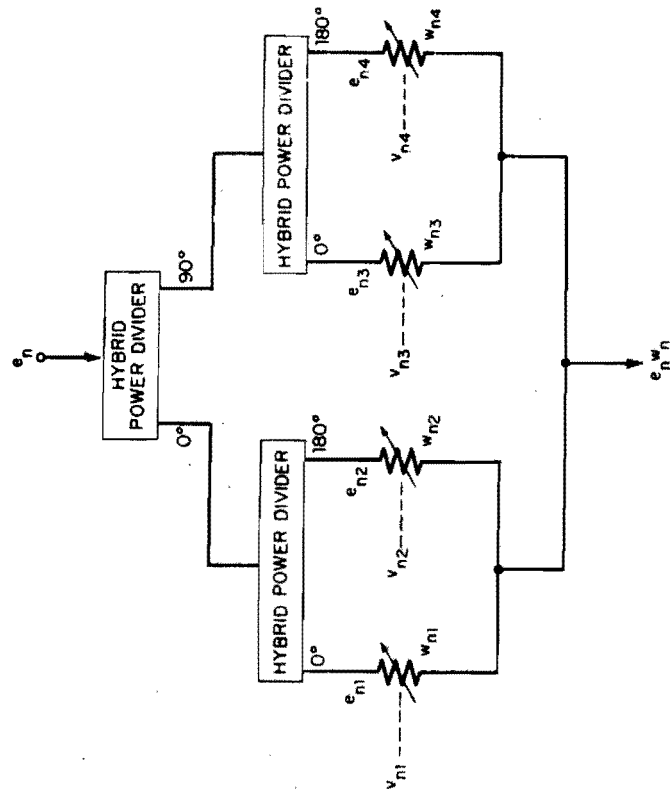


Figure 6.3 Typical IF weight circuit.

114372-N

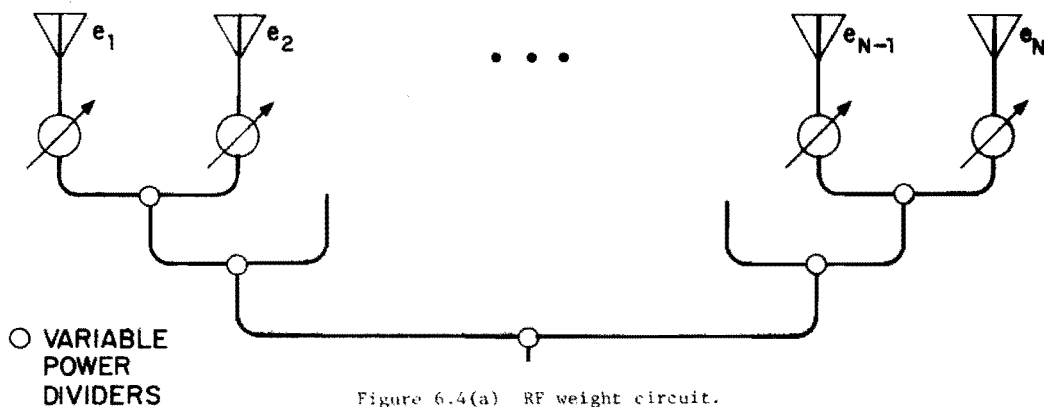


Figure 6.4(a) RF weight circuit.

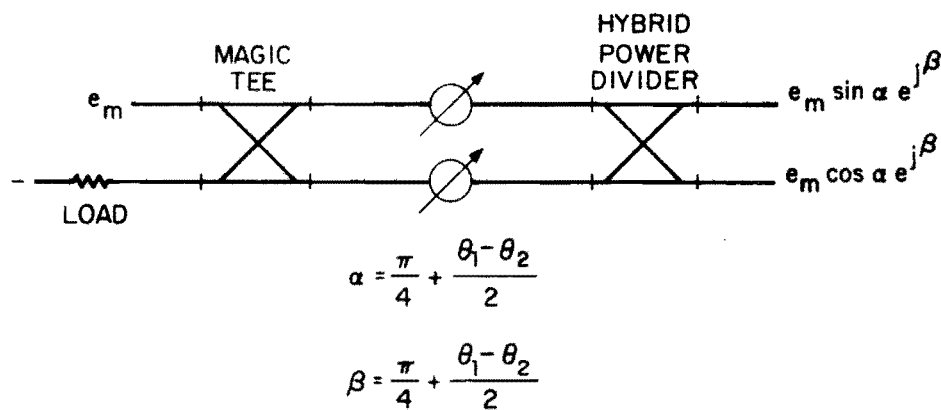


Figure 6.4(b) Variable power divider circuit.

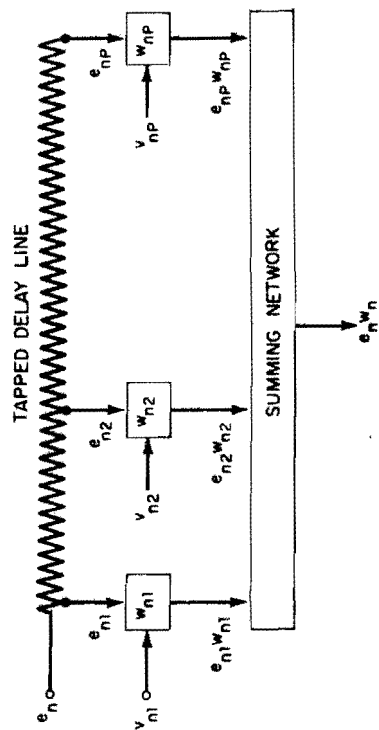


Figure 6.5 Frequency dependent adaptive weights.

114373-N

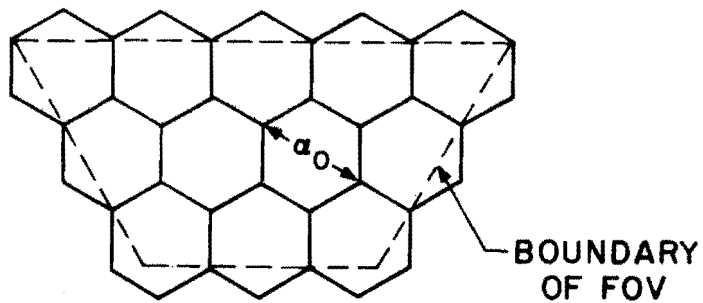
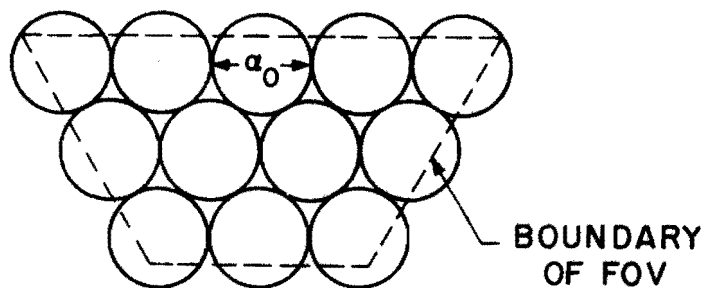
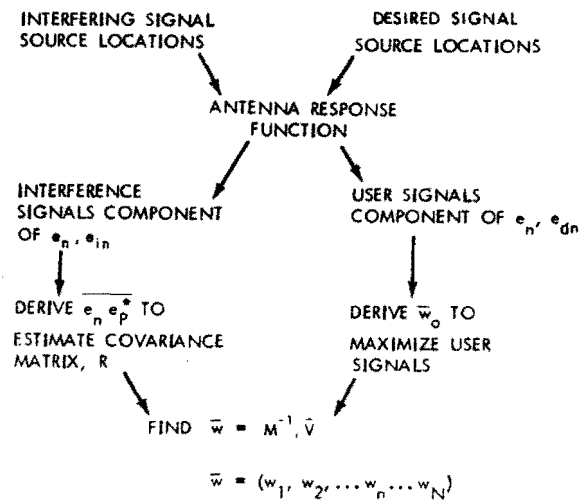


Figure 6.6 Resolution calls and DOF.



NOTE  $e_{in} + e_{dn} = e_n$

Figure 6.7 Basic algorithm.

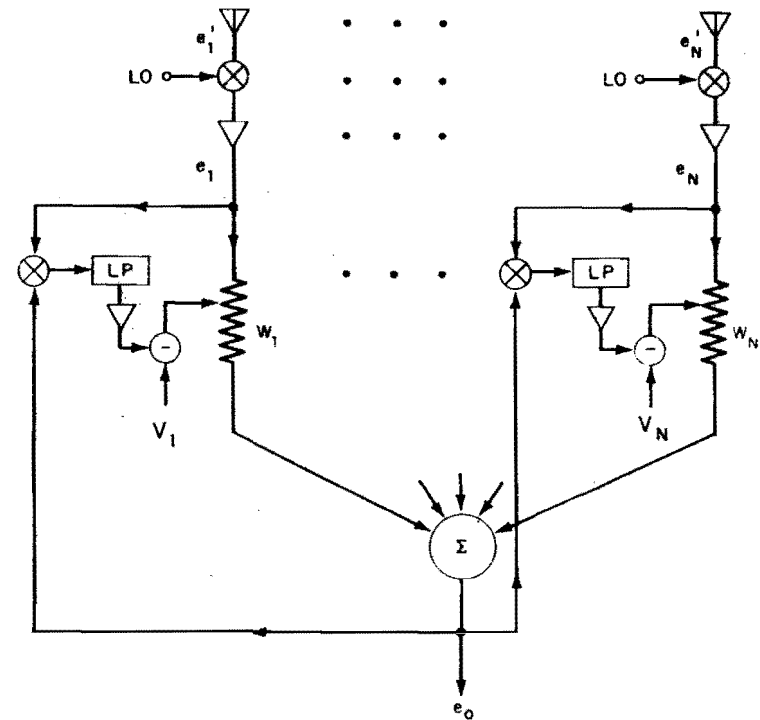


Figure 6.8 Applebaum-Howell Circuit.

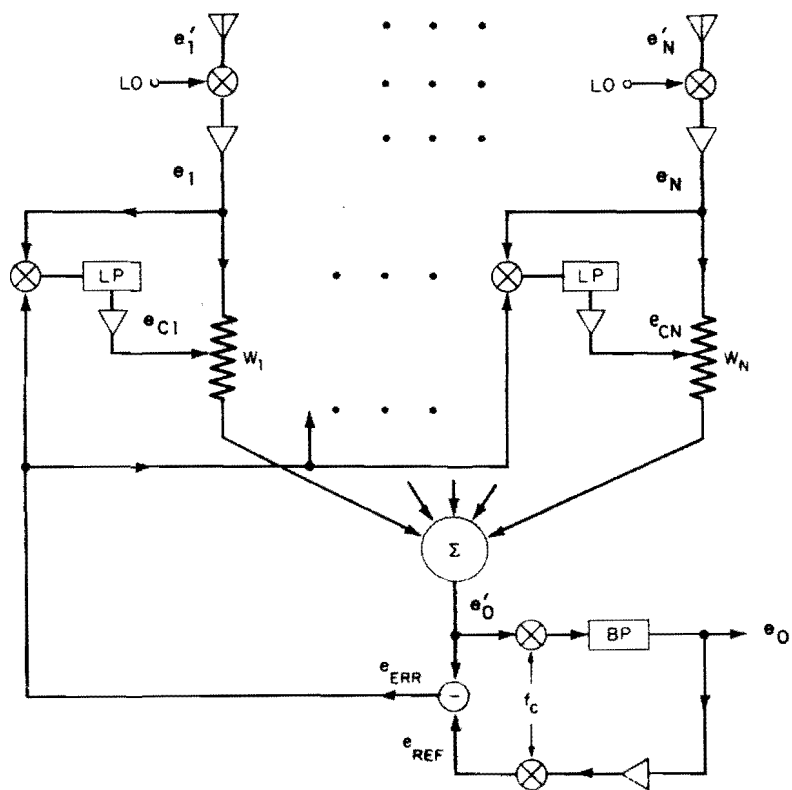


Figure 6.9 Widrow algorithm.

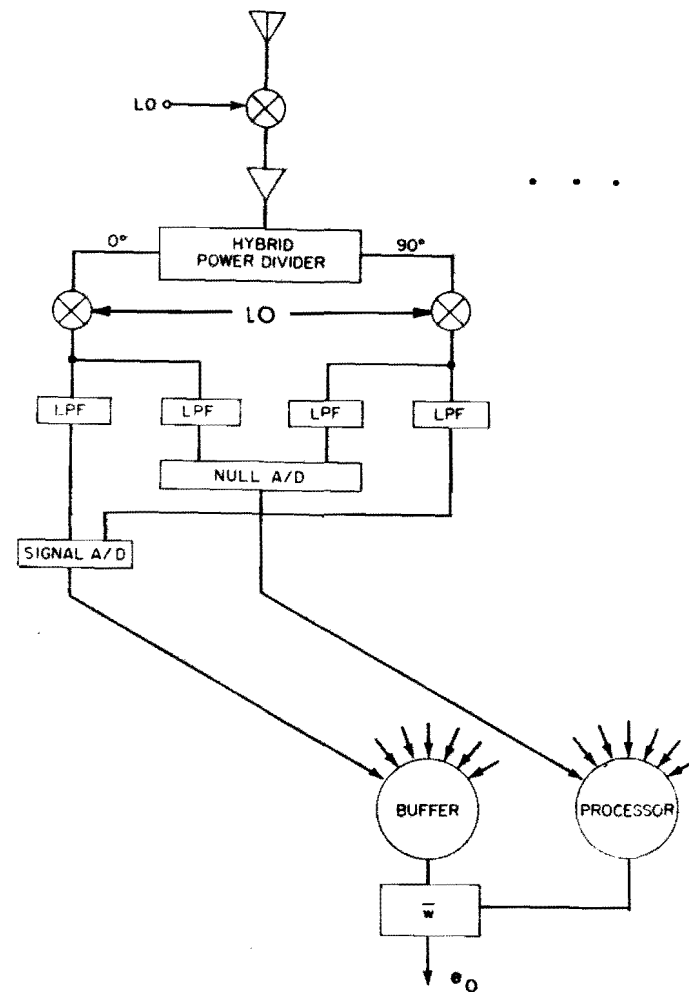


Figure 6.10 Sample matrix inversion.

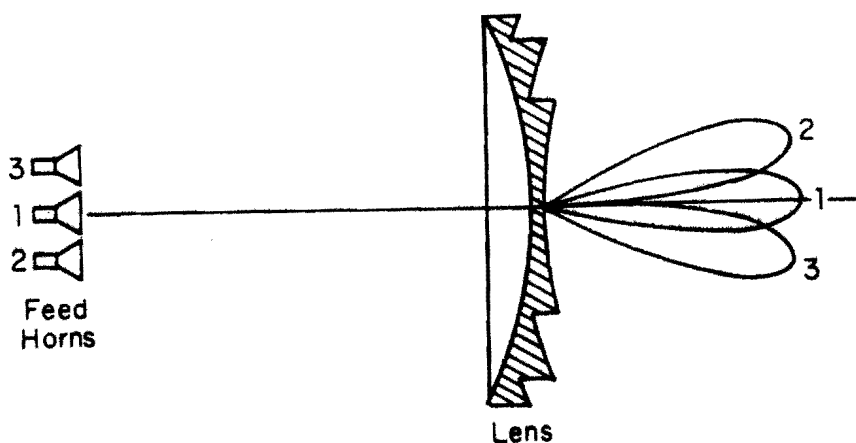


Figure 6.12 Horn-lens configuration.

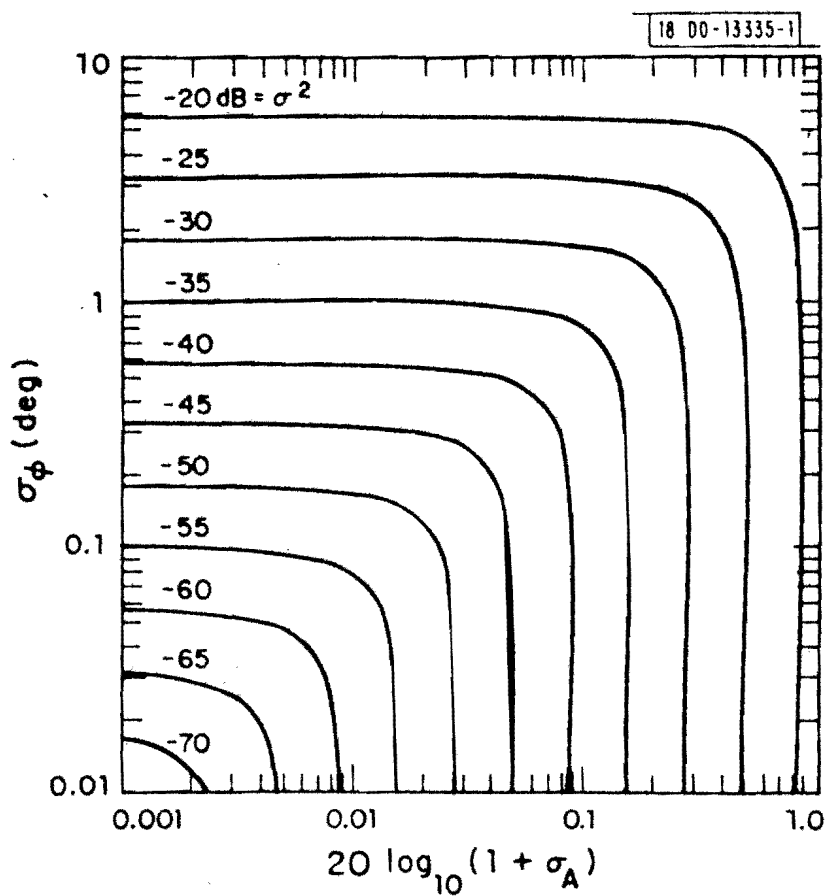


Figure 6.11 Estimated cancellation.

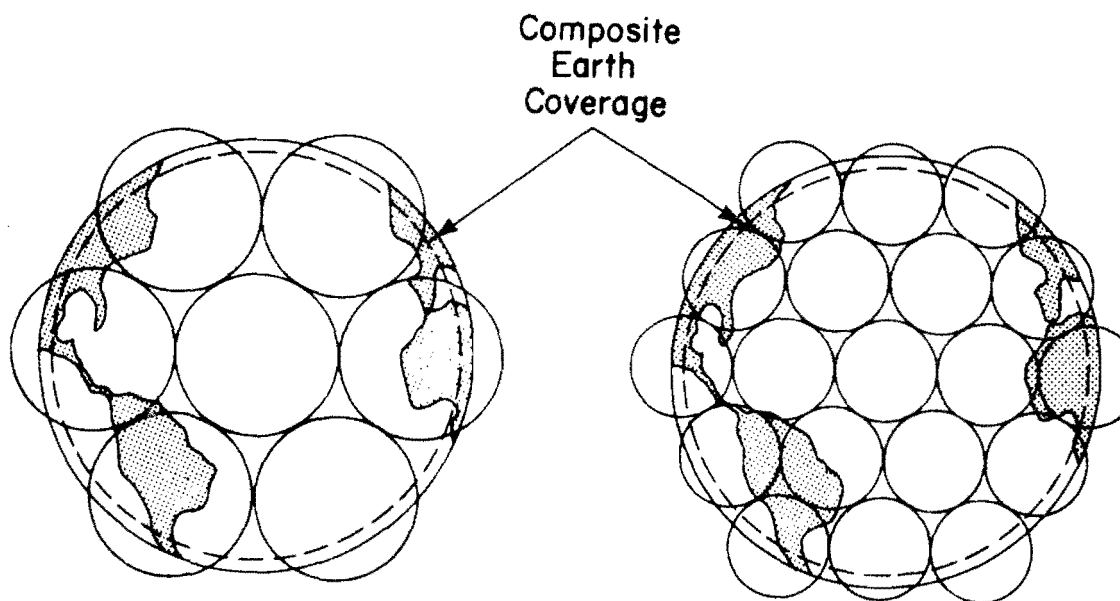


Figure 6.13 Beam arrangements.

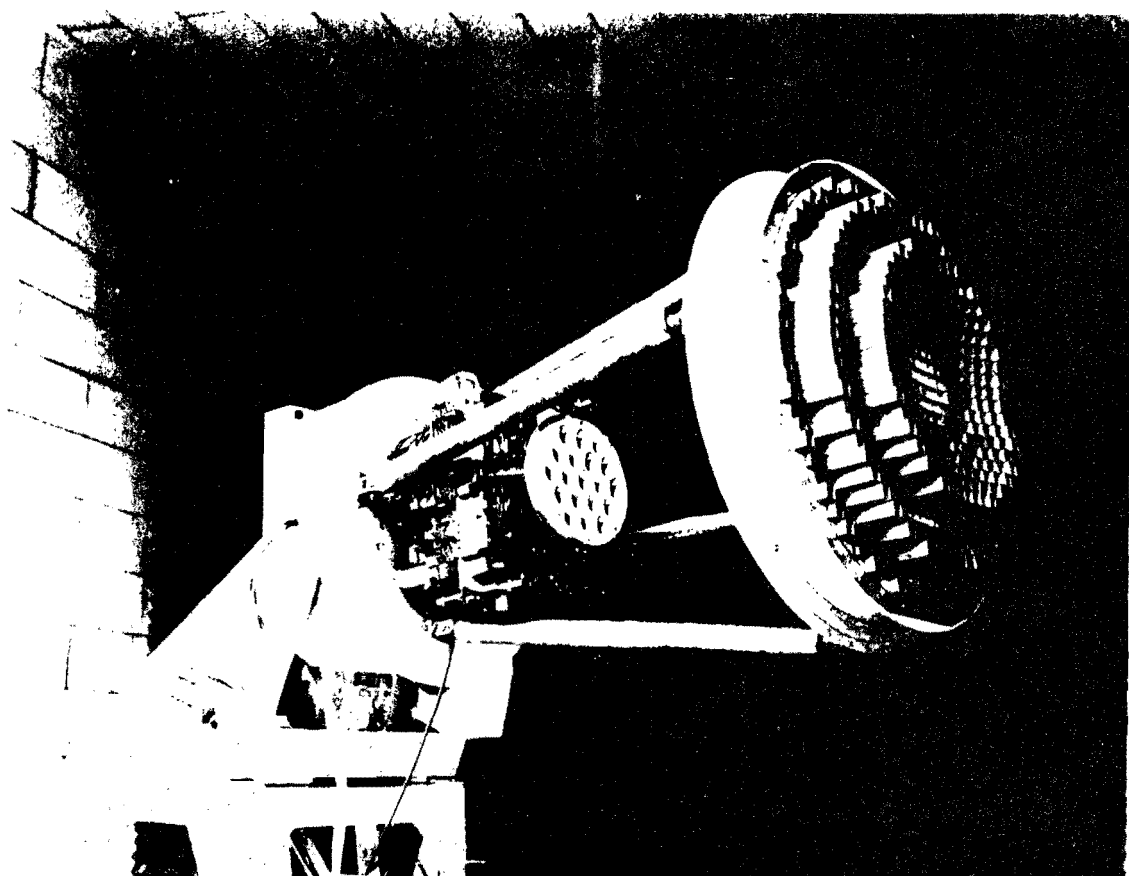


Figure 6.14 The MFA System.

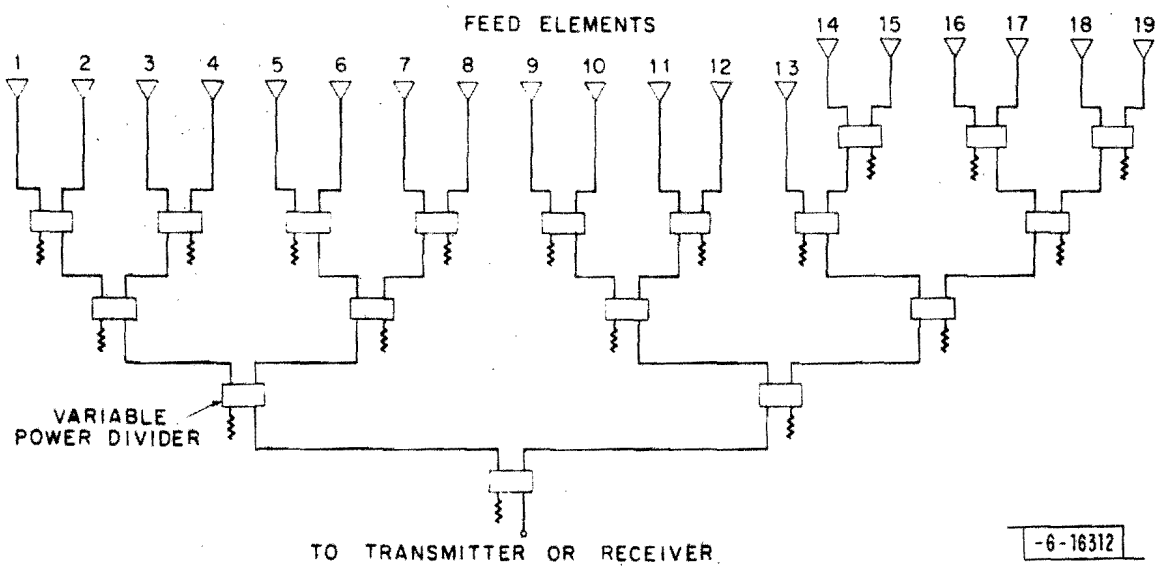


Figure 6.10 BFN schematic representation.

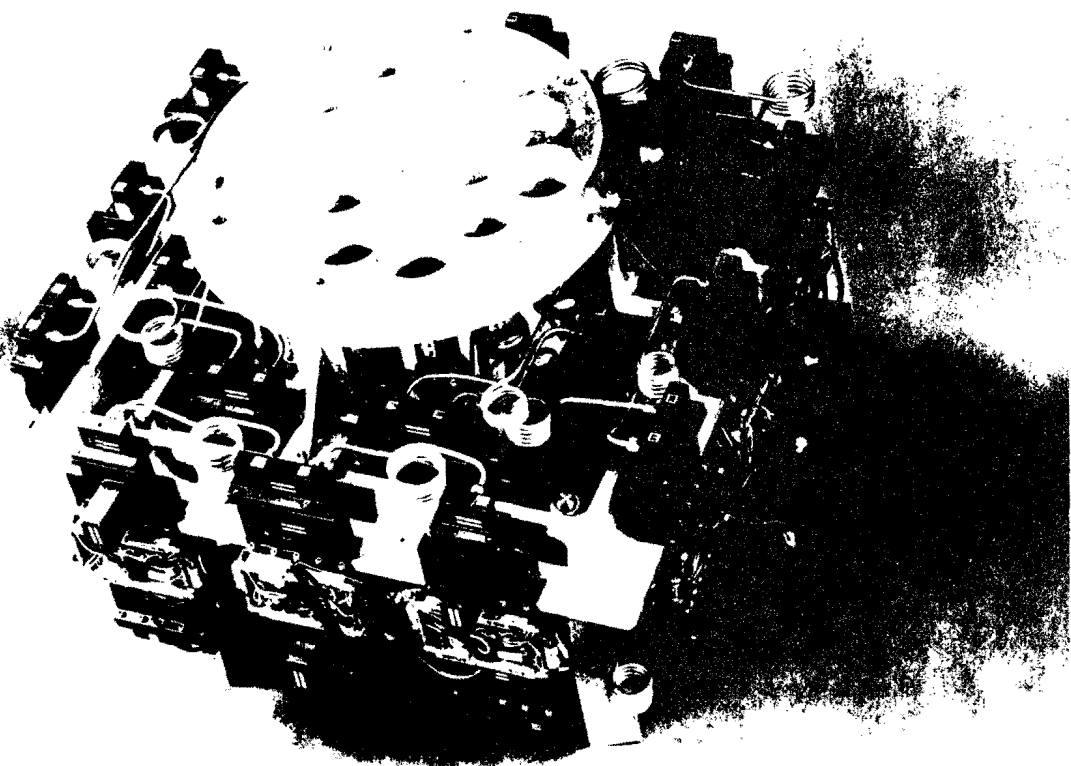


Figure 6.11 BFN and feed array.

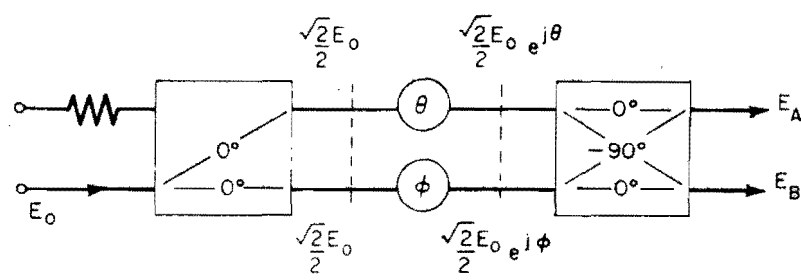


Figure 6.18 Schematic representation of a variable power divider.

18-6-16313

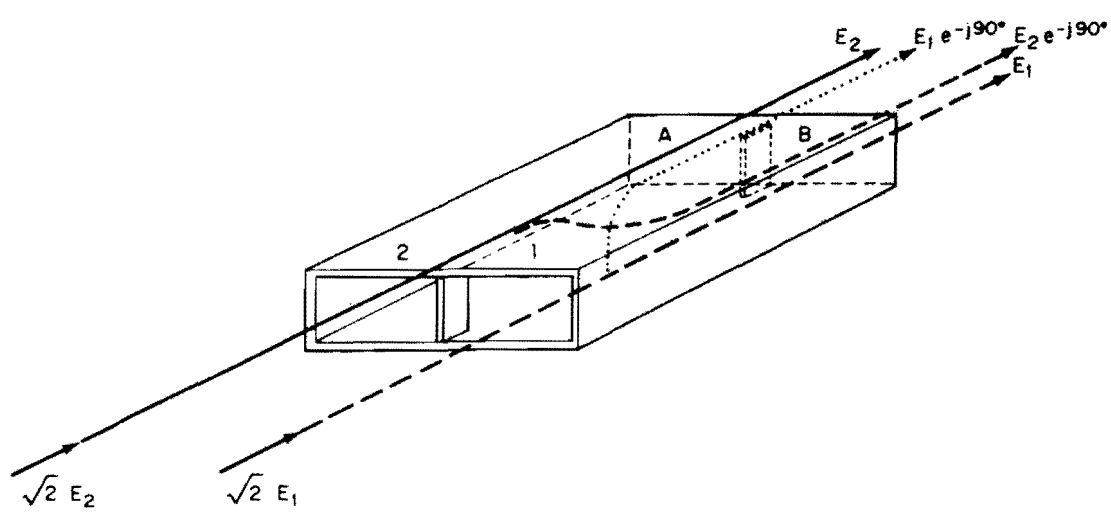


Figure 6.17 3-dB hybrid coupler.



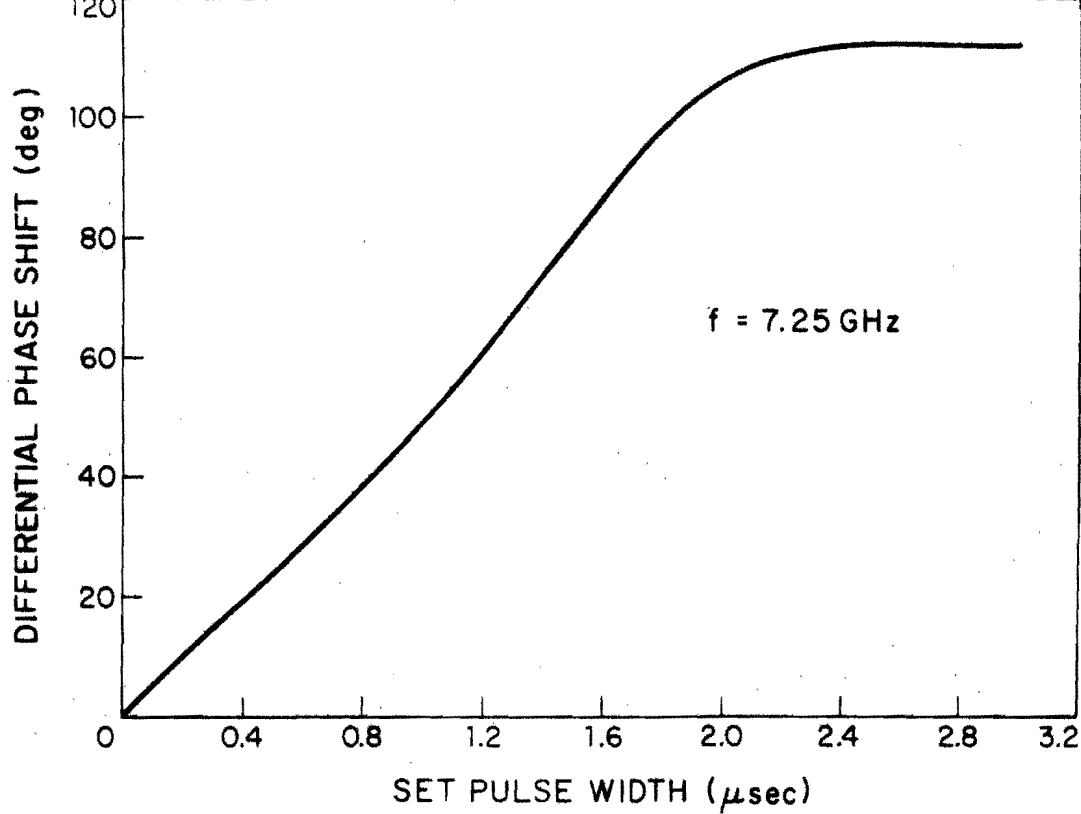


Figure 6.20 Performance of a ferrite phase shifter.

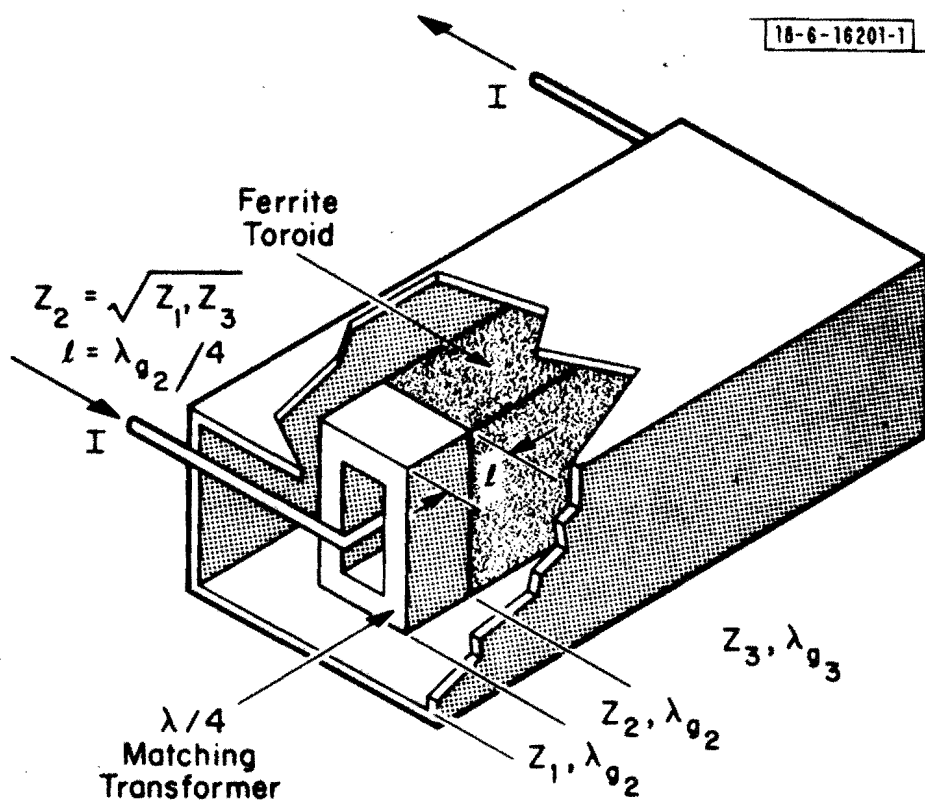


Figure 6.19 Latching ferrite phase shifter.

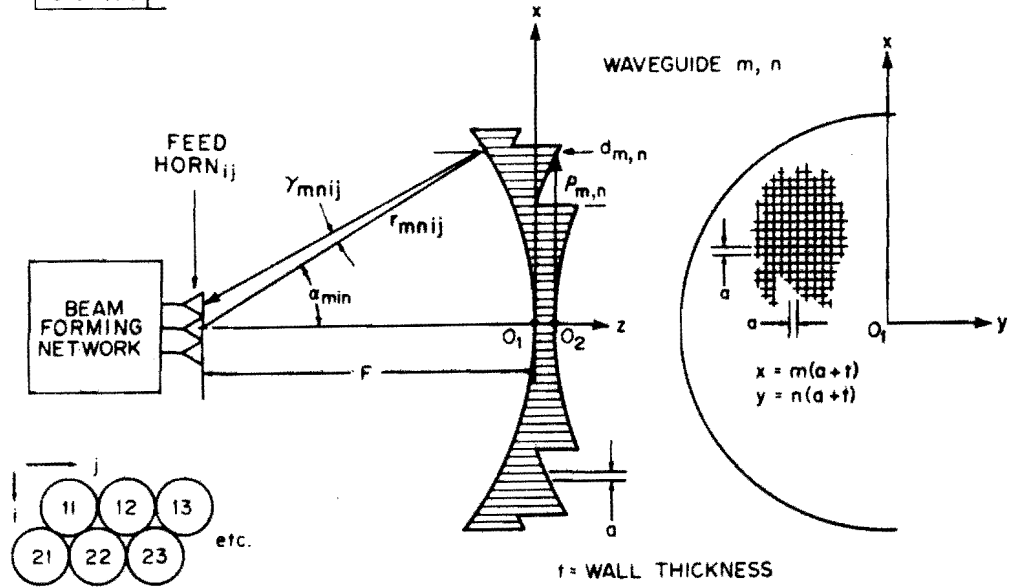


Figure 6.22 Lens and feed geometry.

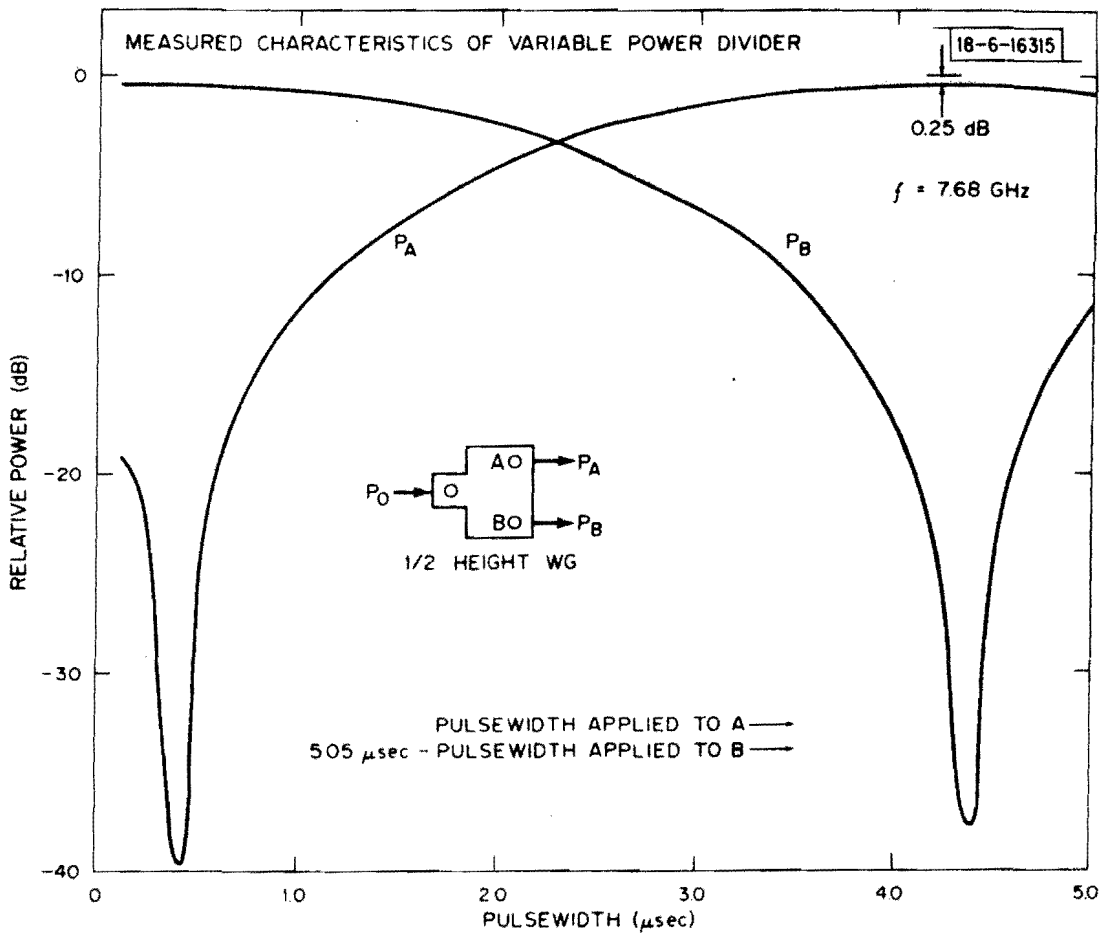


Figure 6.21 Performance of a VPD using ferrite phase shifters.

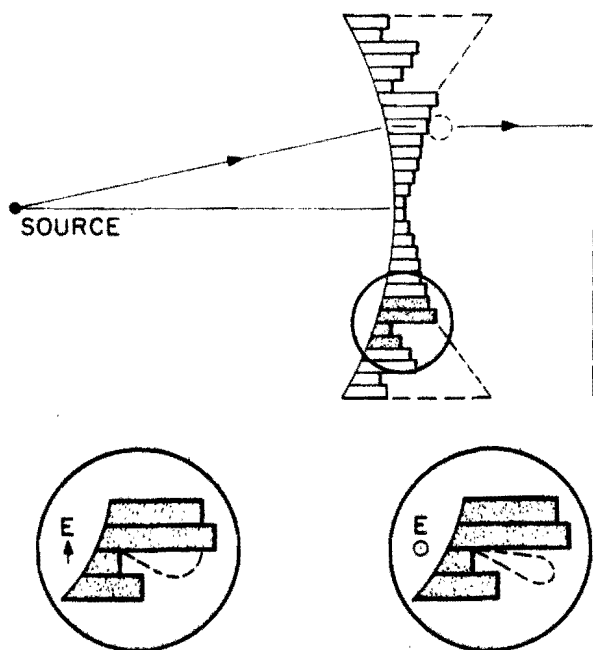


Figure 6.23 Effect of steps in the lens.

18-6-16592

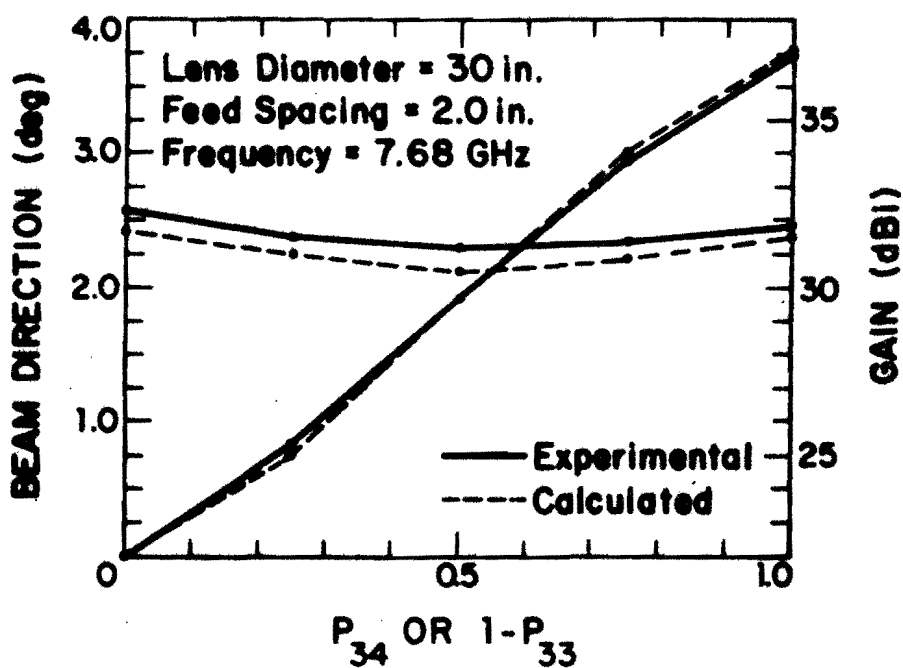


Figure 6.24 Scan characteristics using the waveguide lens, feed cluster and VPD feed network.

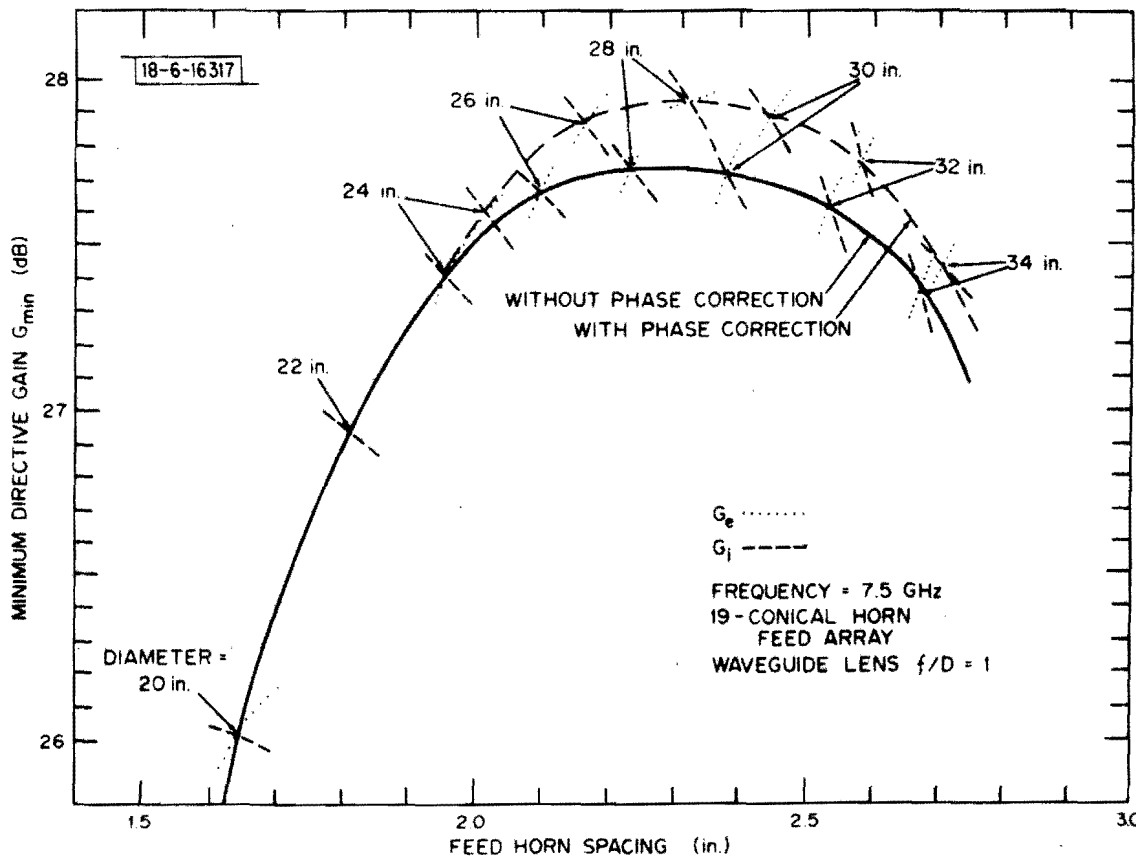


Figure 6.25 Minimum directive gain over field-of-view vs feed horn spacing.

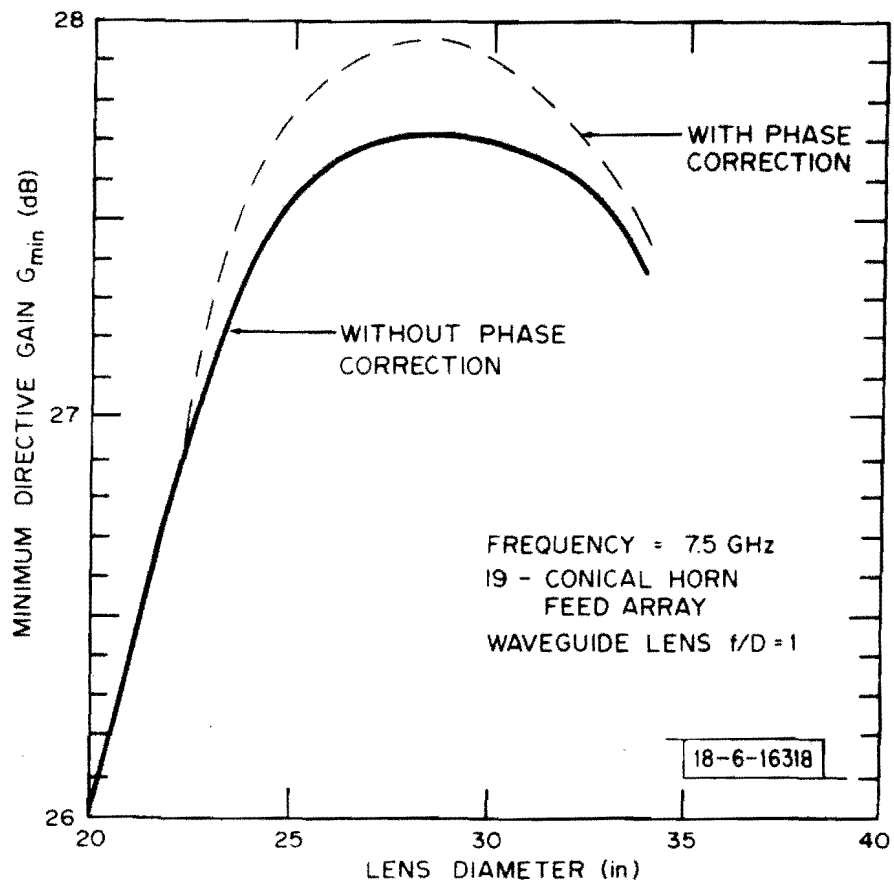


Figure 6.26 Minimum directive gain over field-of-view vs lens diameter.

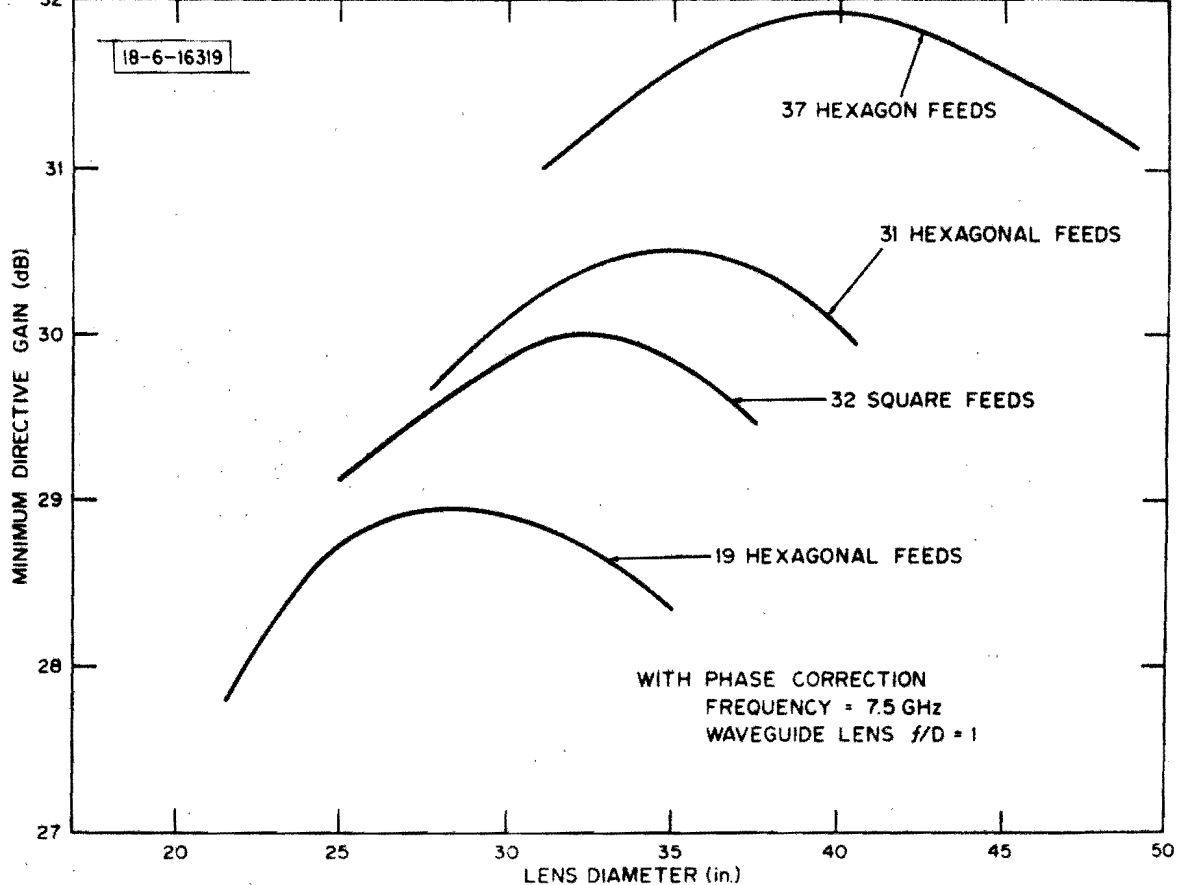


Figure 6.27 Minimum directive gain vs lens diameter for various feed clusters.

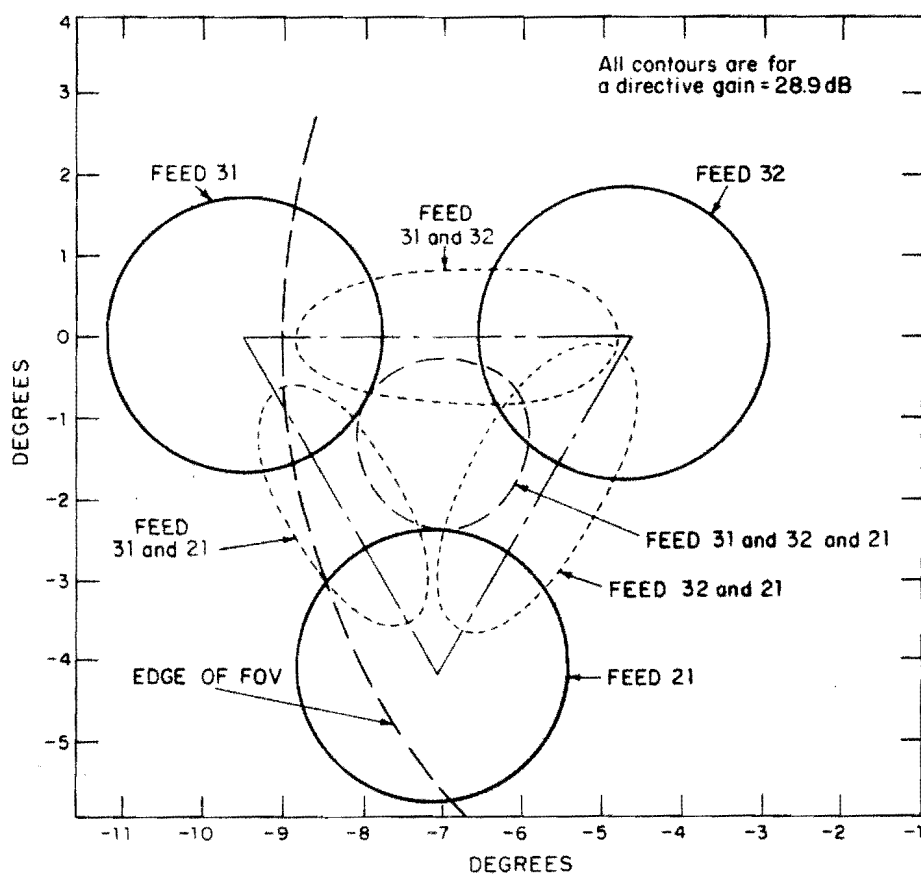


Figure 6.28 29.8-dB radiation contours for indicated feeds excited.

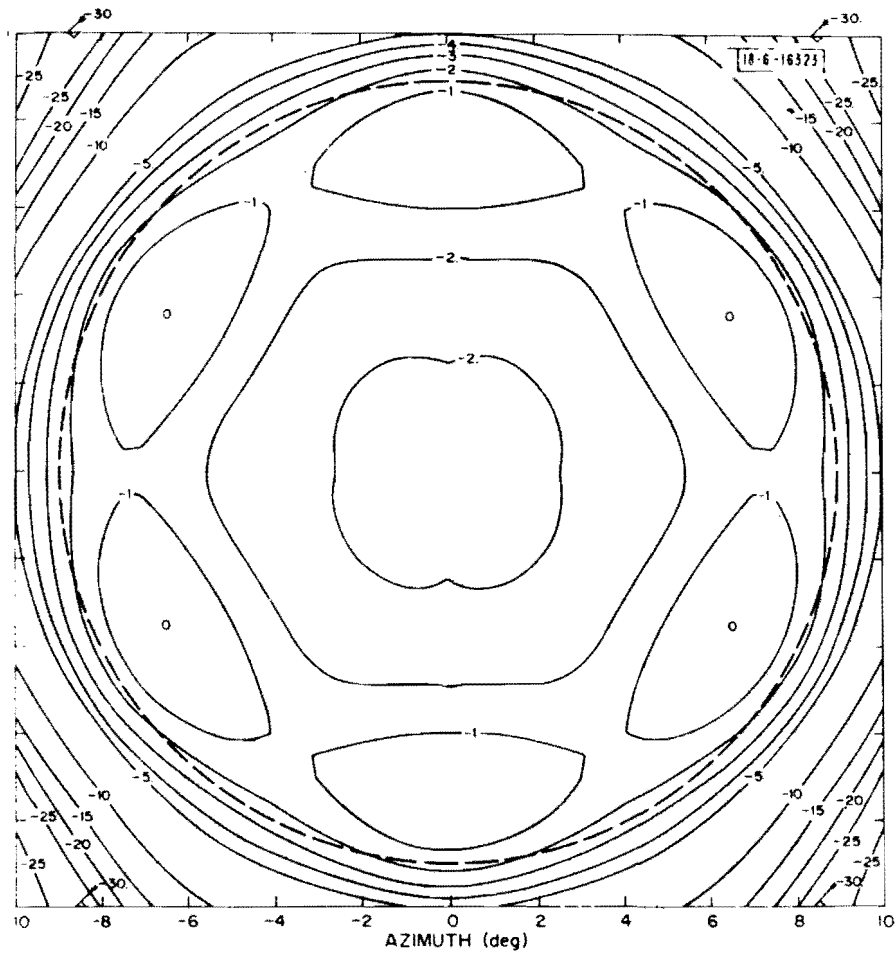


Figure 6.29b Earth-coverage pattern contours, selected feeds excited more strongly (Directivity = 21.6 dB).

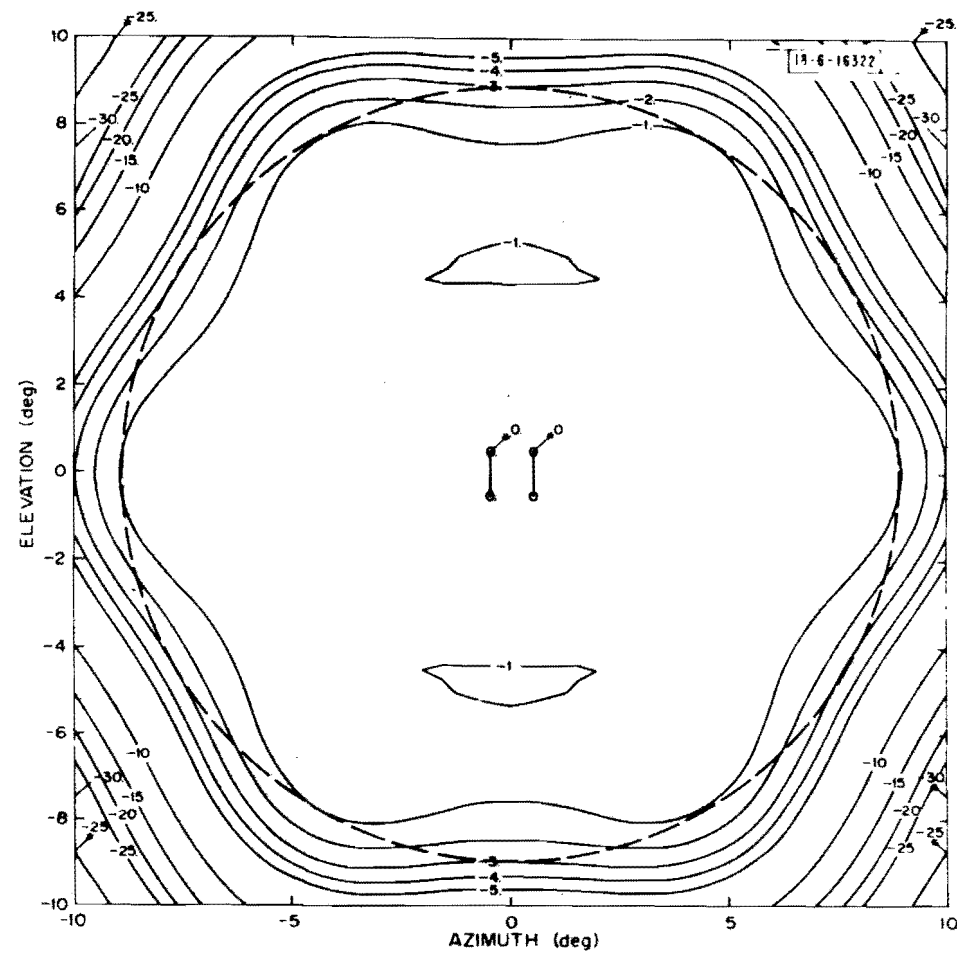


Figure 6.29a Earth-coverage pattern contours, all feeds excited equally (Directivity = 21.2 dB).

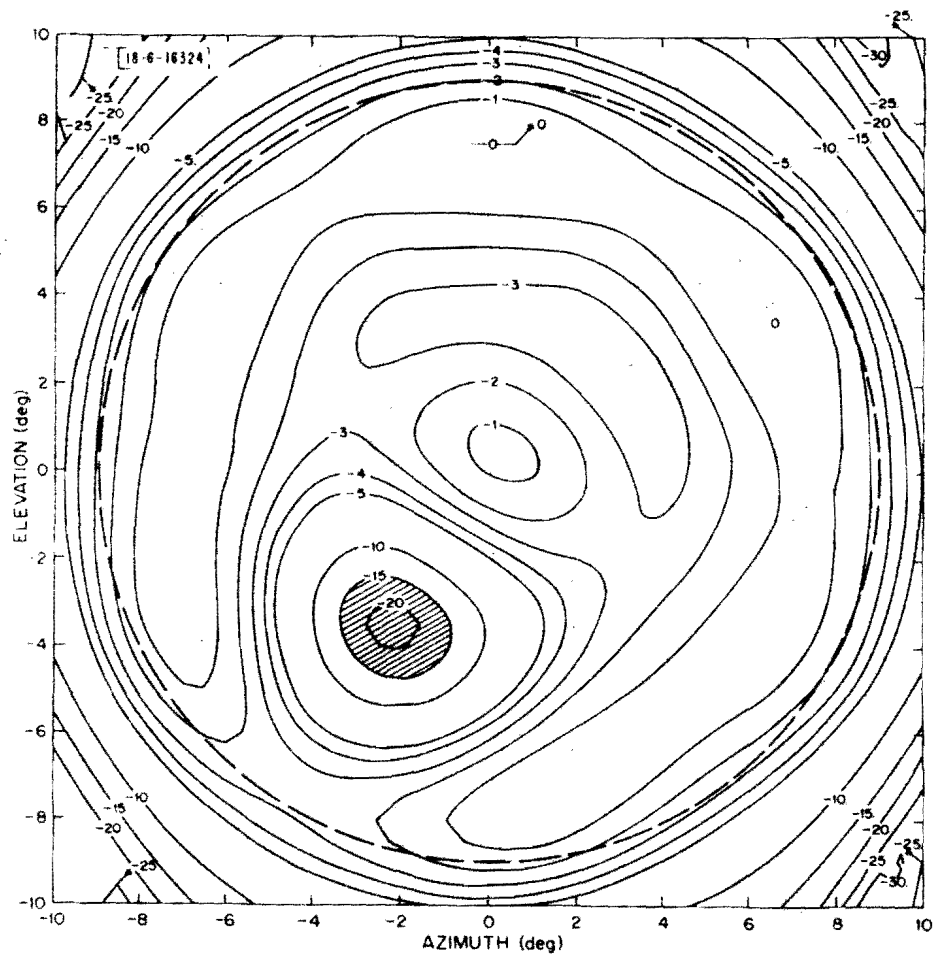
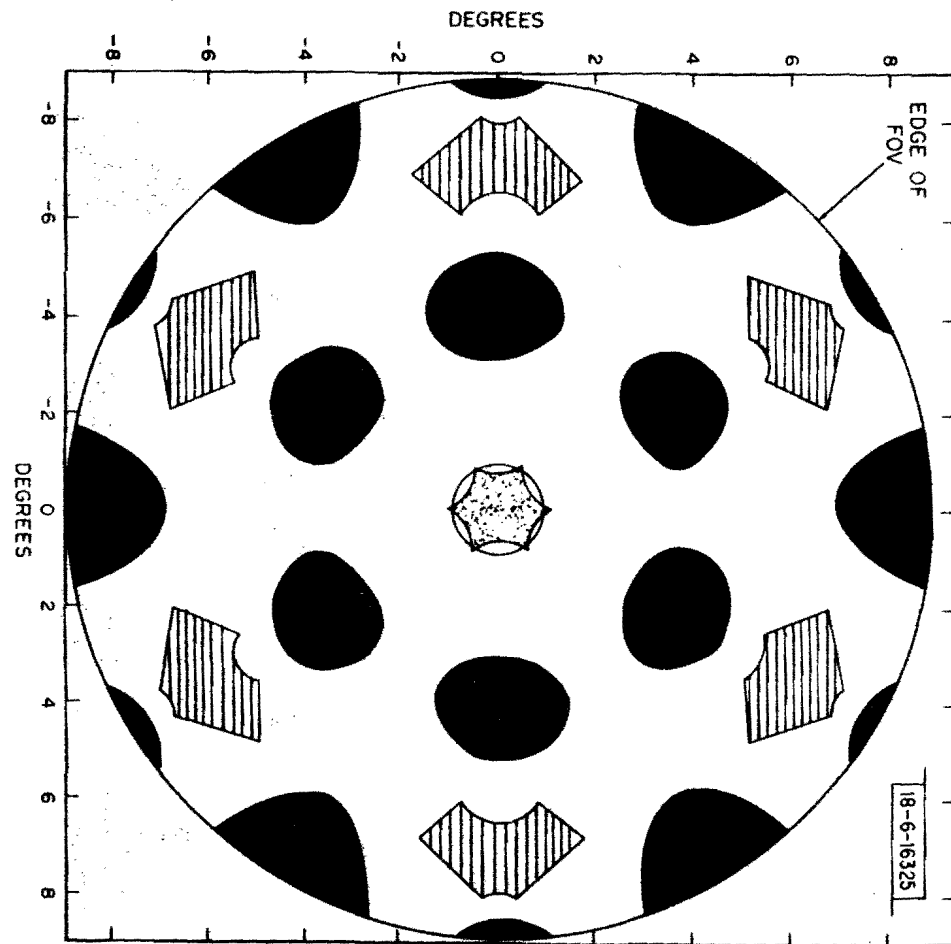


Figure 6.30 Earth-coverage pattern with one beam turned off (Directivity = 21.9 dB).

Figure 6.31 Composite earth-coverage pattern with Nulls.



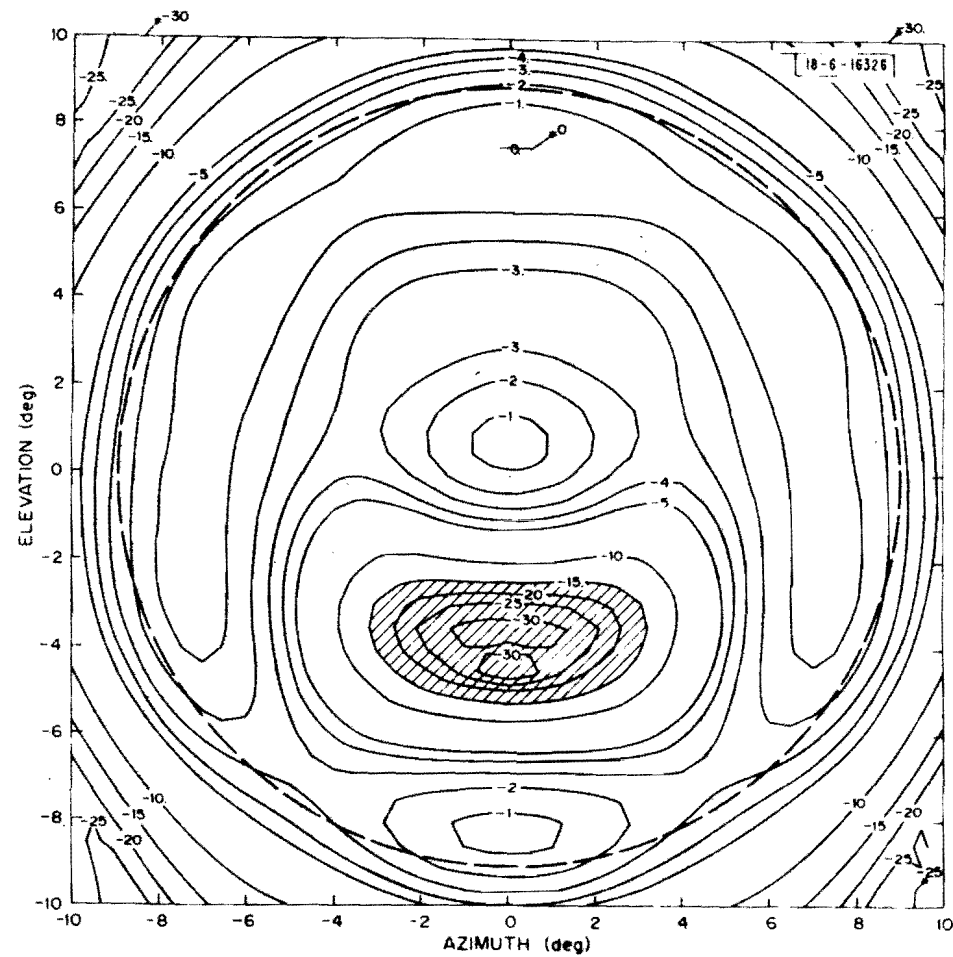
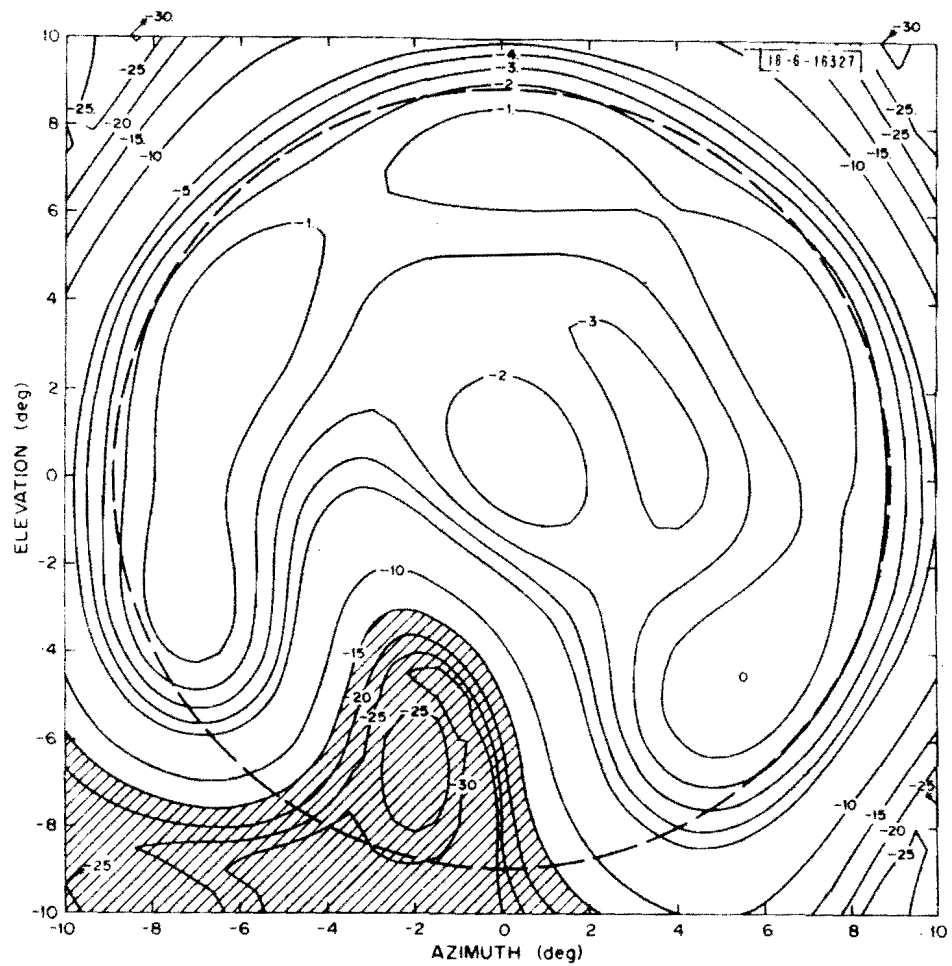


Figure 6.32 Earth-coverage pattern with two beams turned off (Directivity = 22.2 dB)

Figure 6.33 Earth-coverage pattern with three beams turned off (Directivity = 22.5 dB).



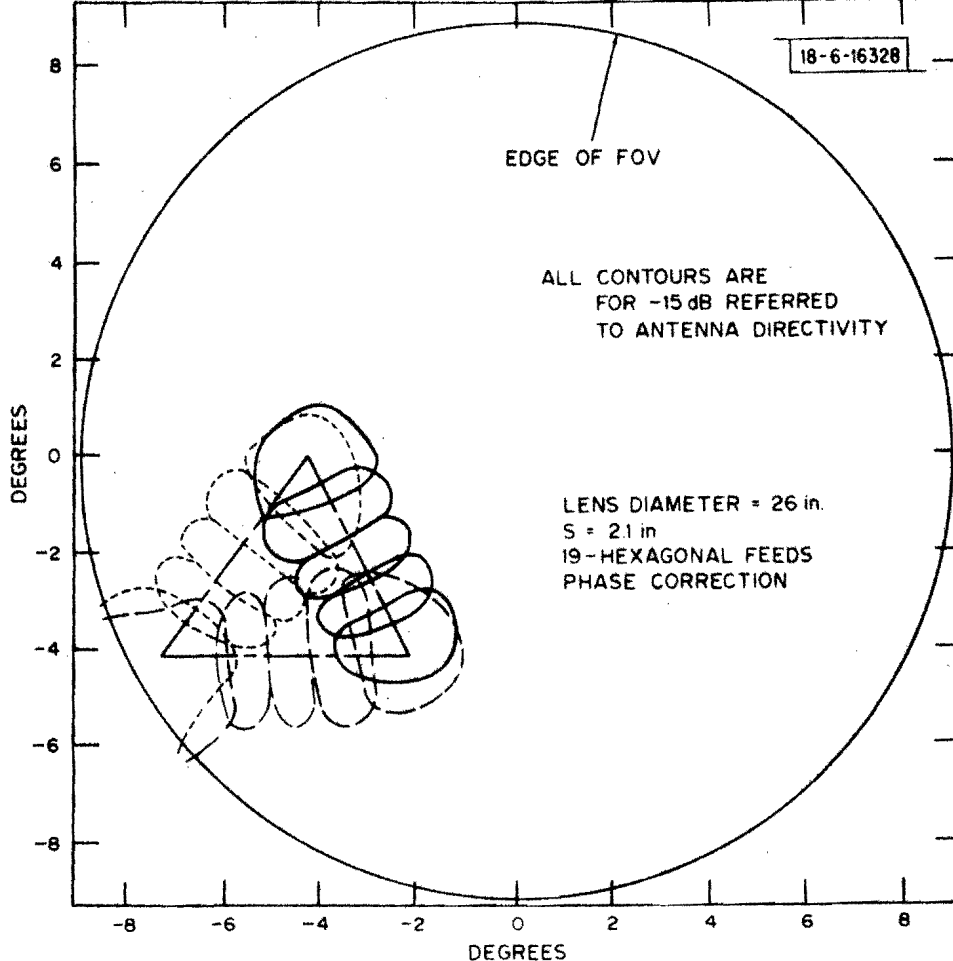


Figure 6.34 Composite radiation patterns for null steering.

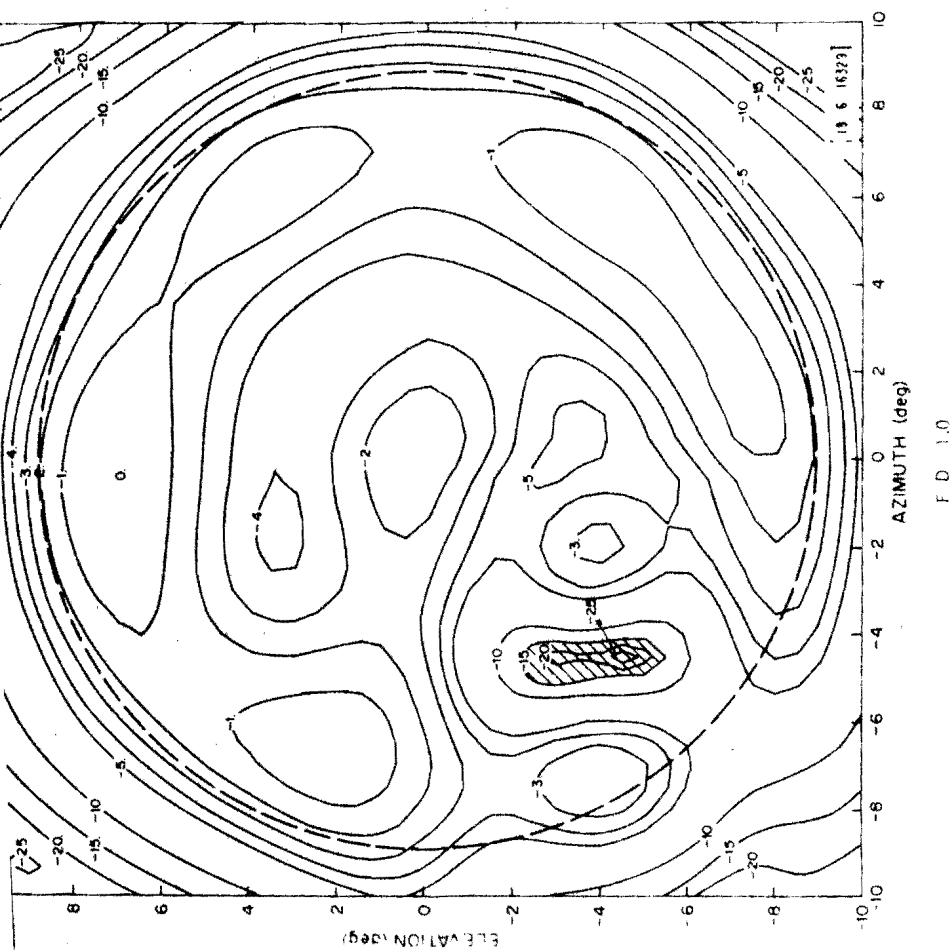


Figure 6.35 Earth-coverage pattern with two feeds at  $90^\circ$  and  $-90^\circ$  relative phase (Directivity = 22.0 dB).

# 19-BEAM MBA (Broadband Lens)

DIAM. = 28 in.      FREQUENCY = 8.15 GHz  
 SPACING = 2.35 in.      PEAK GAIN = 20.89 dB  
 F/D = 1.0      LENS DESIGN FREQ. = 8.15 GHz

PLANE OF PATTERN CUT = 90 deg  
 CIRCULAR POLARIZATION

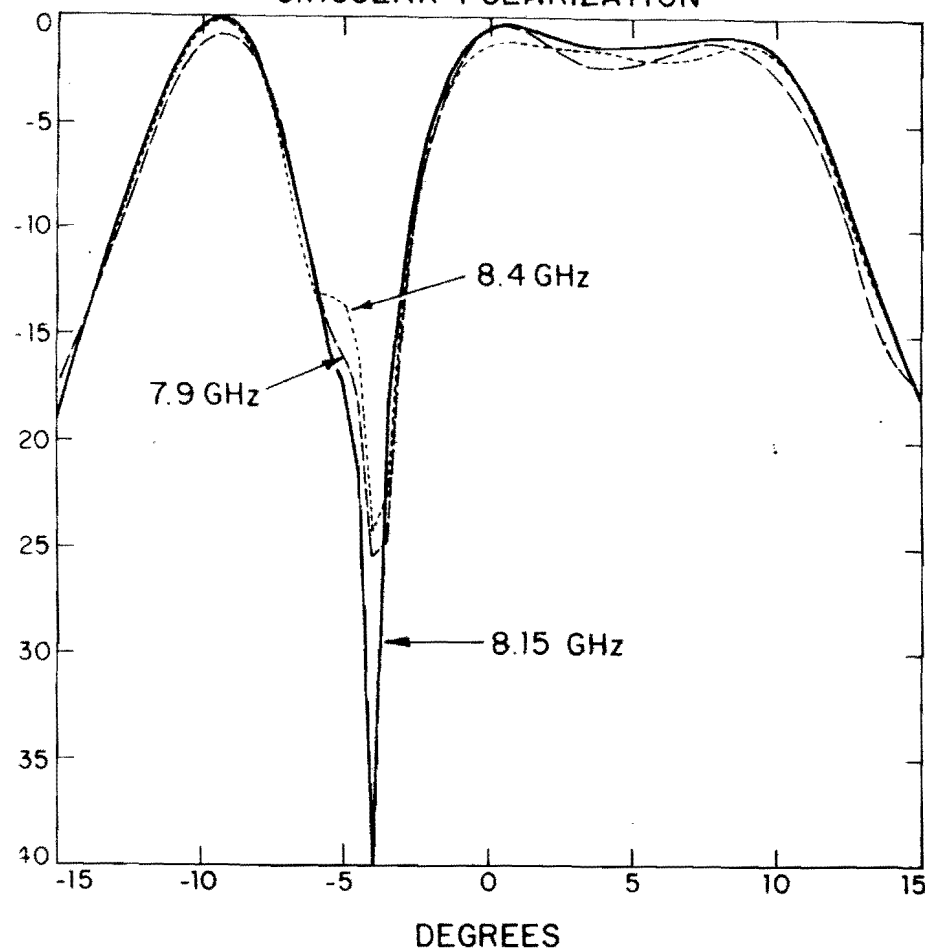


Figure 6.37 Broadband waveguide lens performance.

# 19-BEAM MBA

DIAM. = 28 in.      FREQUENCY = 8.15 GHz  
 SPACING = 2.35 in.      PEAK GAIN = 20.55 dB  
 F/D = 1.0      LENS DESIGN FREQ. = 8.15 GHz

PLANE OF PATTERN CUT = 90 deg  
 CIRCULAR POLARIZATION

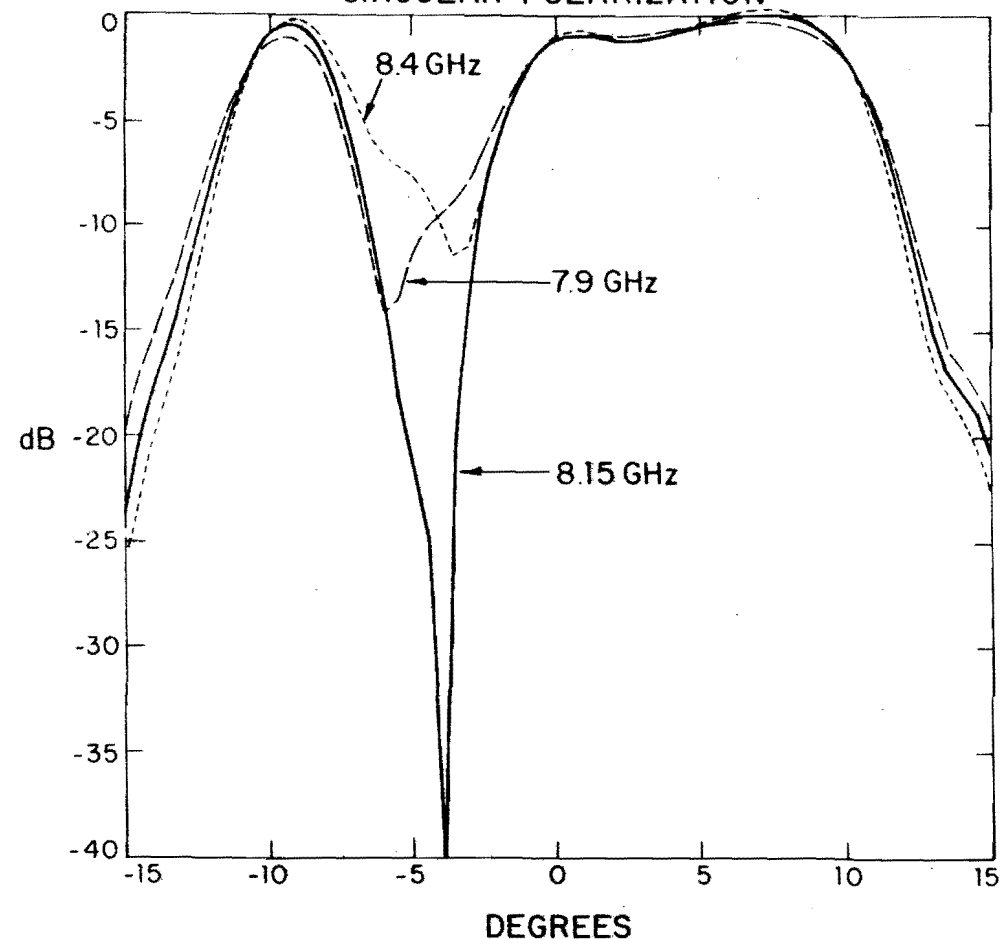


Figure 6.36 Frequency variation of null depth.

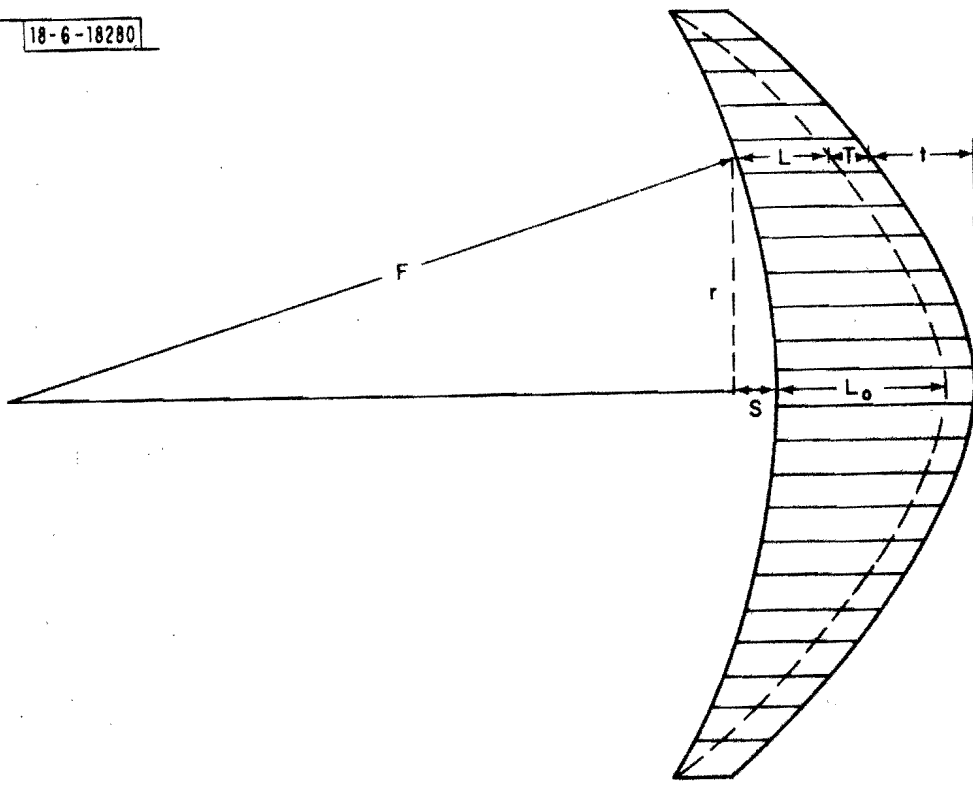


Figure 6.39 Compound Lens.

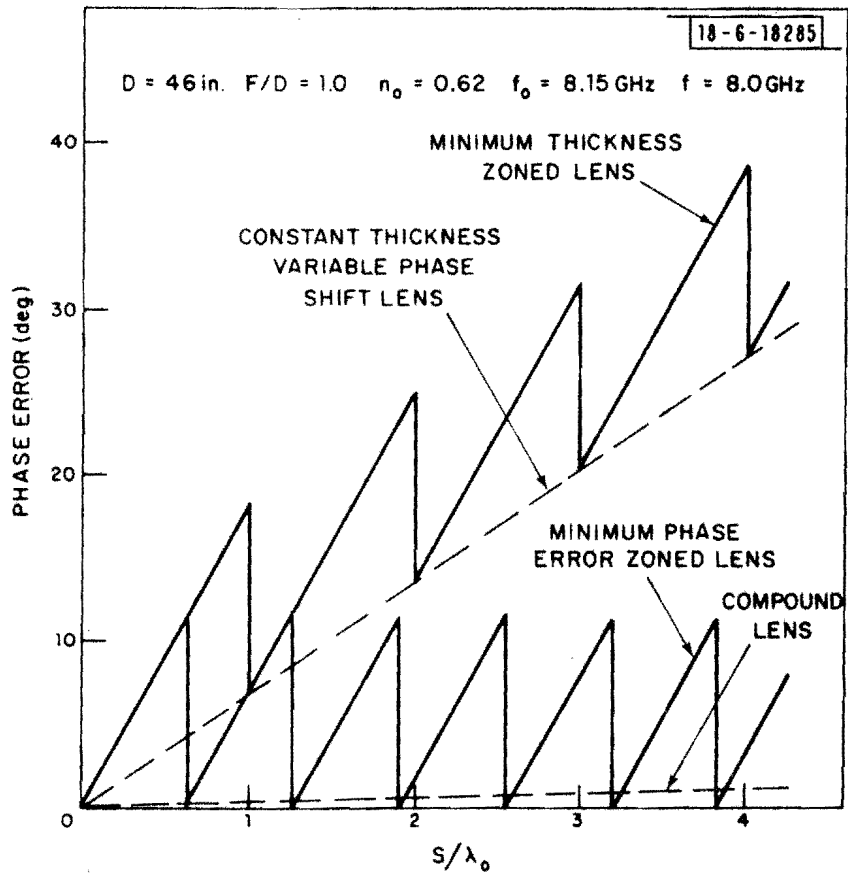


Figure 6.38 Phase error of various waveguide lens.

PHASED ARRAYS  
FOR  
SATELLITES  
AND  
THE TDRSS ANTENNAS

Dr. William A. Imbriale  
Jet Propulsion Laboratory  
California Institute of Technology  
Pasadena, California

SUMMER SCHOOL ON COMMUNICATION SATELLITE ANTENNA TECHNOLOGY  
23-27 August 1982  
Eindhoven University of Technology  
Eindhoven, Netherlands

# PHASED ARRAYS FOR SATELLITES AND THE TDRSS ANTENNAS

Dr. W. A. Imbriale  
Jet Propulsion Laboratory  
California Institute of Technology  
Pasadena, California

## ABSTRACT

The following material is intended to be instructive on the subject of phased array systems for satellites. Section 1 introduces the subject and describes the terminology commonly used for phased array systems. Section 2 discusses elementary adaptive array theory and is based on the work by Dr. Jim DuFree of reference (5). Section 3 describes the JARED antenna, and adaptive phased array which can be used null jammer signals while providing coverage to specified user areas. Section 4 describes the algorithm used in the JARED antenna and section 5 describes a technique which can be used to detect and locate jammers. The appendix describes the Multiple Access phased array used on the Tracking and Data Relay Satellite System (TDRSS). Portions of this work was performed while the author was with the TRW Defense and Space Systems Group in Redondo Beach, California.

## 1.0 Introduction - Phased Arrays for Satellites

Many future satellite programs will require the use of antennas that will radiate high effective power levels at UHF, L, S, X, K or higher frequency bands. In addition these antennas will be required to provide these power levels over a large portion of the satellite field of view.

The possible solutions for the antennas of such satellites can be divided into two general classes. The first class (herein termed reflector type antennas) consists of antennas with a feed of N elements plus a refractor (lens) or reflector which focusses the feed patterns into a number of narrow beams. The second class (herein termed phased arrays or simply arrays) consists of an array of antenna elements each of which has a wide (earth coverage) beam pattern. The N elements are distributed over an aperture having approximately the same diameter as in the case of the narrow beam elements and the pattern is controlled by the amplitude and phase excitation of each element.

Arrays have a number of advantages over the reflector type antennas such as:

- Distribution of power amplification at the elementary radiator level
- Increased flexibility - electronic scanning allows for changes in radiation patterns to adjust for traffic fluctuations
- Increased reliability - failure of a few elements might be tolerable
- Increased aperture efficiency - no losses due to spillover, coma lobe or aperture blockage
- Possible electronic compensation for attitude errors

However, at the present state of the art arrays also have some major drawbacks such as:

- Complexity
- Weight
- Relatively high losses in the power distribution system
- Lack of operational components (efficient linear RF solid state amplifiers, variable phase shifters for beam scanning at higher frequencies)

Phased arrays for satellites are generally classified into three groups:

- Fixed beam - either single or multiple fixed beams which can provide high gain and/or flexibility in power allocation to different areas.
- Electronically steerable or beam scanning arrays - which have the capability to track a moveable user or compensates for satellite attitude errors - in addition these arrays may provide pattern shape control.
- Adaptive arrays - which can automatically point a beam towards a user or null a jammer.

A typical array system is composed of a radiating aperture, an RF amplifier or transmitter which generally includes a filter or diplexer, the beam forming network, and the control circuitry.

Design considerations for each of the various subsystems are as follows:

- The radiating aperture
  - Determination of optimum element number and arrangement
  - Determination of optimum element pattern shape
  - Determining the characteristics of high gain element radiators in an array environment
  - Determination of the optimum amplitude and phase distribution
- The RF amplifier
  - Specifying gain and 1 dB compression points
  - Designing for low noise figure
  - Determining allowable amplitude and phase tracking errors
  - Determining effects of interfering signals and intermodulation products
  - Achieving low loss light weight filtering and diplexers
- Beam forming network
  - Determining allowable phase and amplitude quantization errors
  - Evaluating analog verses digital control
  - Achieving low loss lightweight design

- Control circuitry

- Determining type of control circuitry ~ i.e., special purpose hardware or interface with general purpose computer
- Developing algorithms and software
- Determining required speed for processing control and configuration changes



## 2.0 Adaptive Arrays - Fundamental Background

Adaptive arrays provide the capability to shape the antenna beam to provide antenna gain for desired users while simultaneously placing jammers in antenna nulls. The degree of anti-jam protection that can be achieved by this method is a function of

- Size of antenna aperture
- Antenna degrees of freedom (elements in a phased array)
- Number of jammers
- Angular separation between jammers and desired signal

Adaptive phased arrays are frequently used in a complementary fashion with spread spectrum signals to provide increased levels of anti-jam protection.

Adaptive algorithms can be used to provide real time processing in antenna arrays or can be used as a synthesis tool for determining the weight coefficients to form a desired antenna beam pattern. It is the latter use that is of concern in the following.

Many phased array algorithms have appeared in recent years. Many are variations of the Widrow LMS algorithm [1]. It is based on a least mean square error criterion. Though less well known than the popular LMS theory, a signal to noise S/N maximization criterion has been applied to the spatical filtering problem. The most well known is the Applebaum algorithm [2]. Riegler and Compton [3] have also applied the Applebaum sidelobe cancellation technique but chose an implementation based on the LMS algorithm. Previous work done by AIL in developing their AGIPA system used the method of conjugate gradients [4]. In what follows a S/N maximization criterion is used to develop a computational algorithm. It is also shown that the results achieved via the maximum S/N approach are equivalent to the LMS approach.

### 2.1 Theoretical Basis for the Adaptive Algorithm

The theoretical basis for adaptive algorithms rests on the fundamental concepts of linear vector spaces. In what follows a general knowledge of linear vector spaces is assumed with an outline of the theory given and the proofs of well known results omitted. The material as presented was derived from a report by Jim Dupree [5].

Let  $n$  be a positive integer. As ordered set  $(w_1, w_2, \dots, w_n)$  of complex numbers is called a vector with  $n$  complex elements, or a point on  $n$ -dimensional Euclidean space,  $e^n$ . For example, the set of array signals induced by a point source is a vector,  $(t)$ . In this space, the inner product of two vectors is expressed by the notations

$$(\underline{x}, \underline{y}) = \underline{x}^{*T} \underline{y} = x_1^* y_1 + x_2^* y_2 + \dots + x_n^* y_n = \sum_{i=1}^n x_i^* y_i \quad (2.1)$$

where  $*$  means conjugate and  $T$  means transpose of a matrix. A column vector is treated as an  $n \times 1$  matrix. Its transpose is a  $1 \times n$  row matrix, or row vector. The inner product is the basic operation done by the beamformer. The array signal vector,  $\xi(t)$ , and the complex weight vector,  $\underline{w}$ , form the scalar output of the array through the inner product

$$(\underline{\xi}(t), \underline{w}) = \underline{\xi}^{*T}(t) \underline{w} = \sum_{i=1}^n \xi_i^*(t) w_i \quad (2.2)$$

The metric, or measure of length, is the norm-squared, or inner product of a vector with itself, defined by

$$(\underline{x}, \underline{x}) = \underline{x}^{*T} \underline{x} = \|\underline{x}\|^2 = \sum_{i=1}^n |x_i|^2 \quad (2.3)$$

For example, the instantaneous power of  $\xi$  is  $(\underline{\xi}, \underline{\xi})$ .

The correlation matrix describes the relationship between elements of two vectors. For example:

$$\underline{x} \underline{y}^{*T} = \begin{bmatrix} x_1 y_1^* & x_1 y_2^* & \dots & x_1 y_n^* \\ x_2 y_1^* & x_2 y_2^* & & x_2 y_n^* \\ \cdot & \cdot & & \cdot \\ \cdot & \cdot & & \cdot \\ \cdot & \cdot & & \cdot \\ x_n y_1^* & x_n y_2^* & & x_n y_n^* \end{bmatrix} \quad (2.4)$$

If the elements of  $\underline{x}$  and  $\underline{y}$  are time or statistical variables, the elements of the matrix may be time or statistical average products, usually denoted by an overbar. If the elements of  $\underline{x}$  and  $\underline{y}$  each have zero mean values, the correlation matrix is called a covariance matrix.

The basic spatial filter system for maximum s/n ratio is shown in Figure 3.1. A scalar signal  $S(t)$  is transformed by a modulation vector  $\underline{C}$  into a vector  $\underline{X} = S(t)\underline{C}$ . A channel noise vector  $\underline{N}$ , including coherent (point source) jamming and thermal noise (receiver and external heat sources) is added to produce the received vector

$$\underline{Z} = S(t) \underline{C} + \underline{N} \quad (2.5)$$

The spatial filter forms the scalar output  $\underline{Z}^{*T} \underline{W} = (Z, W)$ , where  $(*T)$  means conjugate transpose. The total output power is

$$S_o + N_o = \overline{|\underline{Z}^{*T} \underline{W}|^2} = \underline{W}^{*T} \overline{\underline{Z} \underline{Z}^{*T}} \underline{W} = (\underline{W}, \phi_{\underline{Z}} \underline{W}) \quad (2.6)$$

where the overbar implies averaging (time or statistical) and,  $\phi_{\underline{Z}}$  is the covariance matrix of the received vector  $\underline{Z}$ . The output noise power is

$$N_o = \overline{|\underline{N}^{*T} \underline{W}|^2} = \underline{W}^{*T} \overline{\underline{N} \underline{N}^{*T}} \underline{W} = (\underline{W}, \phi_{\underline{N}} \underline{W}) \quad (2.7)$$

where  $\phi_{\underline{N}}$  is the covariance matrix of the noise vector.

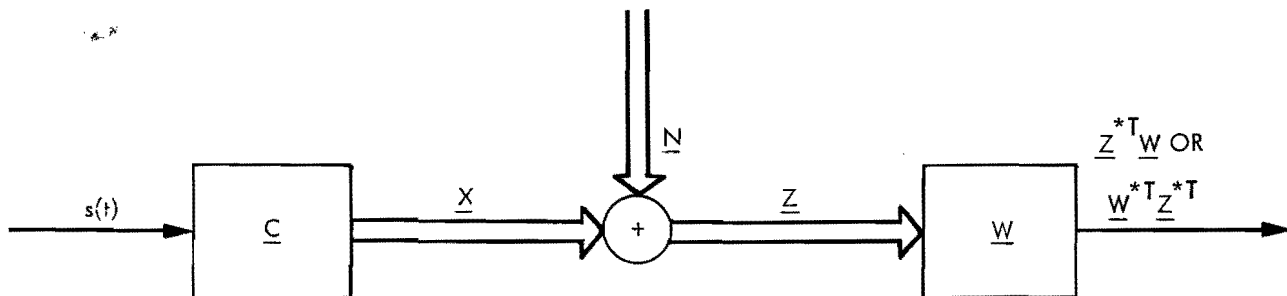


Figure 2.1. Spatial Filter System for Maximum S/N

The maximum s/n criterion requires maximizing the ratio

$$1 + R = (\underline{W}, \phi_Z \underline{W}) / (\underline{W}, \phi_N \underline{W}) \quad (2.8)$$

$$= 1 + \frac{(\underline{W}, \phi_S \underline{W})}{(\underline{W}, \phi_N \underline{W})}$$

By the Rayleigh-Ritz inequality, if  $\phi_S$  and  $\phi_N$  are Hermitian and  $\phi_N$  is positive definite, then  $R \leq \lambda_1$  where  $\lambda_1$  is the largest eigenvalue satisfying

$$\phi_S \underline{W} = \lambda_1 \phi_N \underline{W} \quad (2.9)$$

Furthermore,  $R = \lambda_1$  if and only if  $\underline{W}$  is proportional to the eigenvector satisfying (2.9) for  $\lambda = \lambda_1$ .

For an example, consider a single signal and a single jammer in thermal noise. The covariance matrix of the signal is

$$S\phi_S = S \xi_1 \xi_1^{*T} \quad (2.10)$$

where

$$\xi_1 = \begin{pmatrix} e^{j\omega t_1} \\ e^{j\omega t_2} \\ \vdots \\ e^{j\omega t_n} \end{pmatrix}$$

is an  $n \times 1$  "beam-space" vector, describing the direction of arrival of the desired signal and  $S$  is the signal power. The noise is described by

$$\sigma^2 \phi_N = \sigma^2 \left( I + \frac{J}{\sigma^2} \xi_2 \xi_2^{*T} \right) \quad (2.11)$$

where  $\sigma^2$  is the thermal noise power assumed to be the same on each element, and  $J$  is the jammer power at each element output.  $\xi_2$  describes the direction of arrival of the jamming signal (assumed to be a point source)

By the Rayleigh-Ritz inequality,  $\underline{W}$  must satisfy

$$S \xi_1 \xi_1^{*T} \underline{W} = \lambda_1 \sigma^2 \phi_N \underline{W} \quad (2.12)$$

or

$$\frac{S}{\sigma^2} (\xi_1, \underline{W}) \xi_1 = \lambda_1 \phi_N \underline{W} \quad (2.13)$$

This can be put in the form

$$\lambda_1 \underline{W} = \frac{S}{\sigma^2} (\xi_1, \underline{W}) \phi_N^{-1} \xi_1 \quad (2.14)$$

If we equate

$$\underline{W} = \phi_N^{-1} \xi_1 \quad (2.15)$$

then

$$\lambda_1 = (\xi_1, \phi_N^{-1} \xi_1) \frac{S}{\sigma^2}$$

We assert that this is the maximum signal-to-noise ratio available from the array processor.

A direct solution is given below. Since  $\xi_1$  is not, in general, orthogonal to  $\underline{\xi}_1$ , it can be represented as

$$\xi_2 = \underline{\xi}_3 + \frac{(\underline{\xi}_2, \underline{\xi}_1)}{(\underline{\xi}_1, \underline{\xi}_1)} \underline{\xi}_1 \quad (2.17)$$

where

$$(\underline{\xi}_3, \underline{\xi}_1) = 0 \quad (2.18)$$

and

$$(\underline{\xi}_2, \underline{\xi}_1) = \underline{\xi}_2^{*T} \underline{\xi}_1 \quad (2.19)$$

Assume

$$\underline{W} = \underline{\xi}_1 + \alpha \underline{\xi}_3 \quad (2.20)$$

and substitute into (2.8). The result of a little manipulation is

$$\frac{nS}{\sigma^2} \underline{\xi}_1 = \lambda_1 \left[ \underline{\xi}_1 + \alpha \underline{\xi}_3 + \frac{J}{\sigma^2} \left( \underline{\xi}_3 + \frac{(\underline{\xi}_2, \underline{\xi}_1)}{n} \underline{\xi}_1 \right) \left( \alpha (\underline{\xi}_3, \underline{\xi}_3) + (\underline{\xi}_2, \underline{\xi}_1)^* \right) \right] \quad (2.21)$$

where we have used the metric

$$(\underline{\xi}_1, \underline{\xi}_1) = n \quad (2.22)$$

Two simultaneous equations are found for  $\lambda$  and  $\alpha$  by projecting (2.21) onto  $\underline{\xi}_1$  and  $\underline{\xi}_3$ . Thus,

$$\frac{n^2 S}{\sigma^2} = \lambda_1 \left[ n + \frac{J}{\sigma^2} (\underline{\xi}_2, \underline{\xi}_1) \left[ \alpha (\underline{\xi}_3, \underline{\xi}_3) + (\underline{\xi}_2, \underline{\xi}_1)^* \right] \right] \quad (2.23)$$

and

$$0 = \left[ \alpha (\underline{\xi}_3, \underline{\xi}_3) + \frac{J}{\sigma^2} (\underline{\xi}_3, \underline{\xi}_3) \left[ \alpha (\underline{\xi}_3, \underline{\xi}_3) + (\underline{\xi}_2, \underline{\xi}_1)^* \right] \right] \quad (2.24)$$

Solve for  $\alpha$

$$\alpha = - \frac{\frac{J}{\sigma^2} (\underline{\xi}_2, \underline{\xi}_1)^*}{1 + \frac{J}{\sigma^2} (\underline{\xi}_3, \underline{\xi}_3)} \quad (2.25)$$

where

$$(\underline{\xi}_3, \underline{\xi}_3) = n \left[ 1 - \frac{|(\underline{\xi}_2, \underline{\xi}_1)|^2}{\eta^2} \right] \quad (2.26)$$

Also,

$$\lambda_1 = \frac{\eta S}{\sigma^2} \left[ \frac{1 + \frac{\eta J}{\sigma^2} \quad 1 - \frac{|(\underline{\xi}_2, \underline{\xi}_1)|^2}{\eta^2}}{1 + \frac{\eta J}{\sigma^2}} \right] \quad (2.27)$$

This is the maximum signal/noise ratio obtainable. Later, suboptimal schemes are compared with the above result.

It is shown that  $\frac{|(\underline{\xi}_2, \underline{\xi}_1)|^2}{\eta^2}$  is the ratio of sidelobe power to mainlobe power (antenna power) of the simple beamformer.

## 2.2 S/N Performance of Simple Beamformer

To form a beam in the direction of the user, let

$$\underline{W} = \underline{\xi}_1 \quad (2.28)$$

Then, the output signal power is

$$S(\underline{W}, \phi_s \underline{W}) = n^2 S \quad (2.29)$$

and the output noise power is

$$\sigma^2 (\underline{W}, \phi_n \underline{W}) = n\sigma^2 \left( 1 + \frac{nJ}{\sigma^2} \frac{|(\underline{\xi}_2, \underline{\xi}_1)|^2}{n^2} \right) \quad (2.30)$$

The output signal/noise ratio is

$$\frac{S_o}{N_o} = \frac{\frac{nS}{\sigma^2}}{1 + \frac{nJ}{\sigma^2} \frac{|(\underline{\xi}_2, \underline{\xi}_1)|^2}{n^2}} \quad (2.31)$$

In the absence of thermal noise, the ratio of signal power/jammer power is

$$\frac{S_o}{N_o} = \frac{S}{J} \frac{n^2}{|(\underline{\xi}_2, \underline{\xi}_1)|^2} \quad (2.32)$$

Physically, the ratio

$$\frac{S_o/N_o}{S/J} = \frac{n^2}{|(\underline{\xi}_2, \underline{\xi}_1)|^2} \quad (2.33)$$

is the peak to sidelobe ratio for a signal on the peak of the beam and the jammer at an angle on the sidelobes of the antenna. Thus, when

$$\frac{|(\underline{\xi}_2, \underline{\xi}_1)|^2}{n^2} = 0 \quad (2.34)$$



the signal and jammer are said to be orthogonal in beam space. The degree of nonorthogonality defines the degradation in signal/jammer performance in this method.

For example, the array factor for a uniformly spaced and weighted linear array is

$$\frac{|(\underline{\xi}_2, \underline{\xi}_1)|^2}{n^2} = \frac{\sin^2 \left[ \frac{n\pi d}{\lambda} (\sin \theta_s - \sin \theta_j) \right]}{n^2 \sin \left[ \frac{\pi d}{\lambda} (\sin \theta_s - \sin \theta_j) \right]} \quad (2.35)$$

which contains factors relating the influence of

$n$  = number of elements

$d$  = spacing

$\lambda$  = wavelength

$\theta_s$  = signal direction of arrival

$\theta_j$  = jammer direction of arrival

The effect of a single jammer on the signal/noise ratio degradation is given in Figures 2.2 and 2.3 for the cases of optimum filtering and for the simple beamformer, for various ratios  $\frac{nJ}{\sigma^2}$  and values  $|(\underline{\xi}_2, \underline{\xi}_1)|^2/n^2$ .

### 2.3 S/N Performance for Jammer Nulling

The maximum signal/noise ratio for a single user and single jammer is asymptotic to

$$\frac{S_o}{N_o} = \frac{nS}{\sigma^2} \left[ 1 - \frac{|(\underline{\xi}_2, \underline{\xi}_1)|^2}{n^2} \right] \quad (2.36)$$

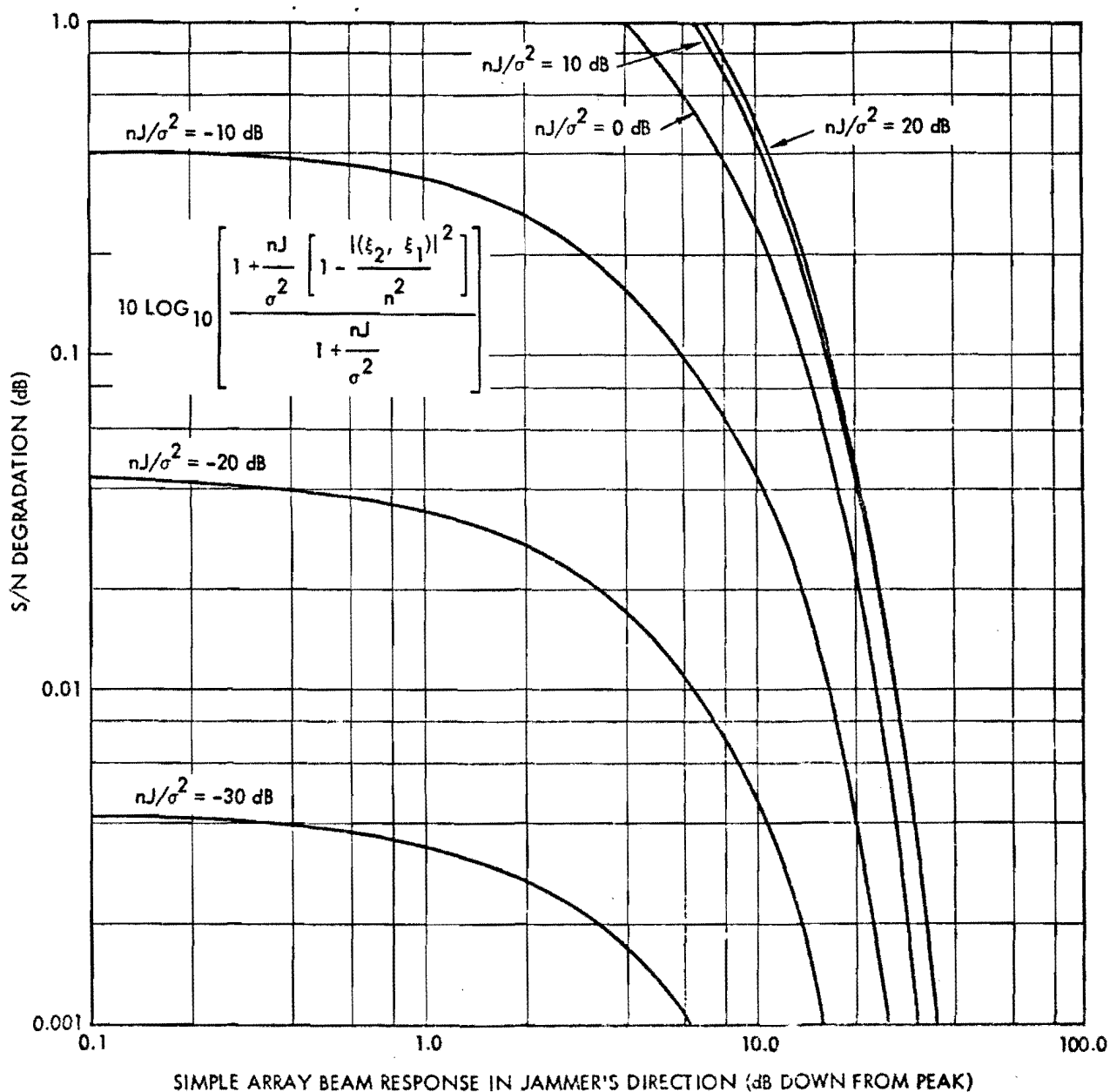


Figure 2.2. Single-Jammer Optimum Spatial Filter S/N Degradation as a Function of Simple Array Beam Sidelobe Response and Jammer to Thermal Noise Ratio

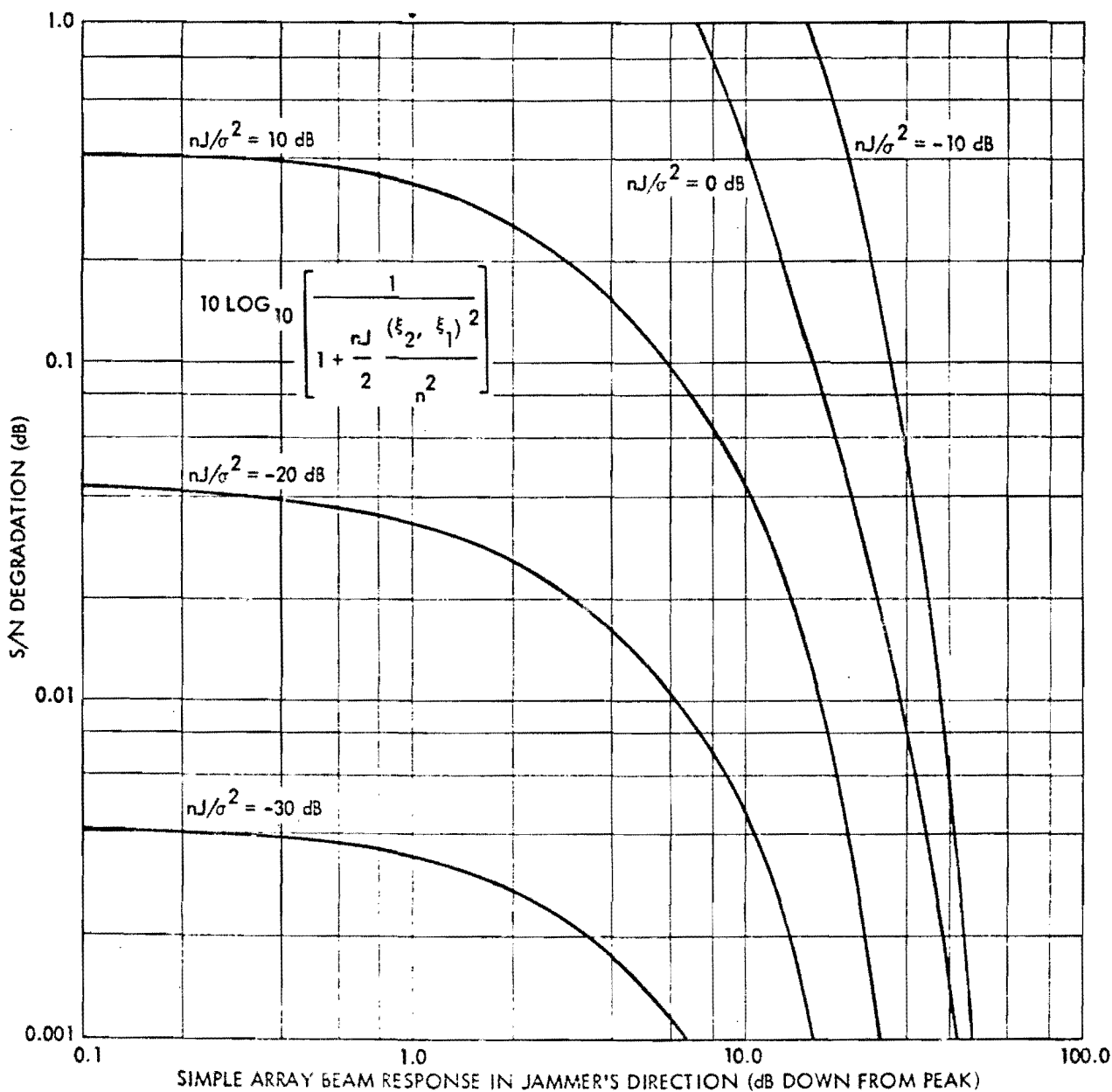


Figure 2.3. Single-Jammer Simple Beamformer S/N Degradation as a Function of Simple Array Beam Sidelobe Response and Jammer to Thermal-Noise Ratio

in the limit as  $\frac{nJ}{\sigma^2} \rightarrow \infty$ . This is the result obtained in the suboptimum case when

$$\underline{W} = \underline{\xi}_3 = -1 - \frac{(\underline{\xi}_2, \underline{\xi}_1)}{(\underline{\xi}_2, \underline{\xi}_2)} \underline{\xi}_2 \quad (2.37)$$

This choice of weights nulls the jammer and forms a beam in the direction of a user. There is some degradation of the signal to thermal/noise ratio as presented in Figure 2.4.

#### 2.4 S/N Performance for Full Field of View with Nulling

To obtain a pattern with broad coverage and a beam in the direction  $\underline{\xi}_2$ , use a weighting function

$$\underline{W} = \underline{1} - \frac{\underline{\xi}_2}{n} \quad (2.38)$$

where  $\underline{1}$  is a column vector with unity corresponding to the element at the phase-center and zero everywhere else,  $\underline{\xi}_2$  is the direction of arrival vector of the jammer and  $n$  is the number of elements. For a symmetrical array,

$$\frac{(\underline{\xi}_2, \underline{\xi}_1)}{n} \quad (2.39)$$

is real. The output signal power for a signal arriving from  $\underline{\xi}_1$  is

$$S(\underline{W}, \underline{\xi}_1 \underline{\xi}_1^{*T} \underline{W}) = S \left[ 1 - \frac{(\underline{\xi}_2, \underline{\xi}_1)}{n} \right] \quad (2.40)$$

and the noise is

$$\sigma^2 \underline{W}^{*T} \left[ \underline{I} + \frac{J}{\sigma^2} \underline{\xi}_2 \underline{\xi}_2^{*T} \right] \underline{W} = \sigma^2 \left( 1 - \frac{1}{n} \right) \quad (2.41)$$

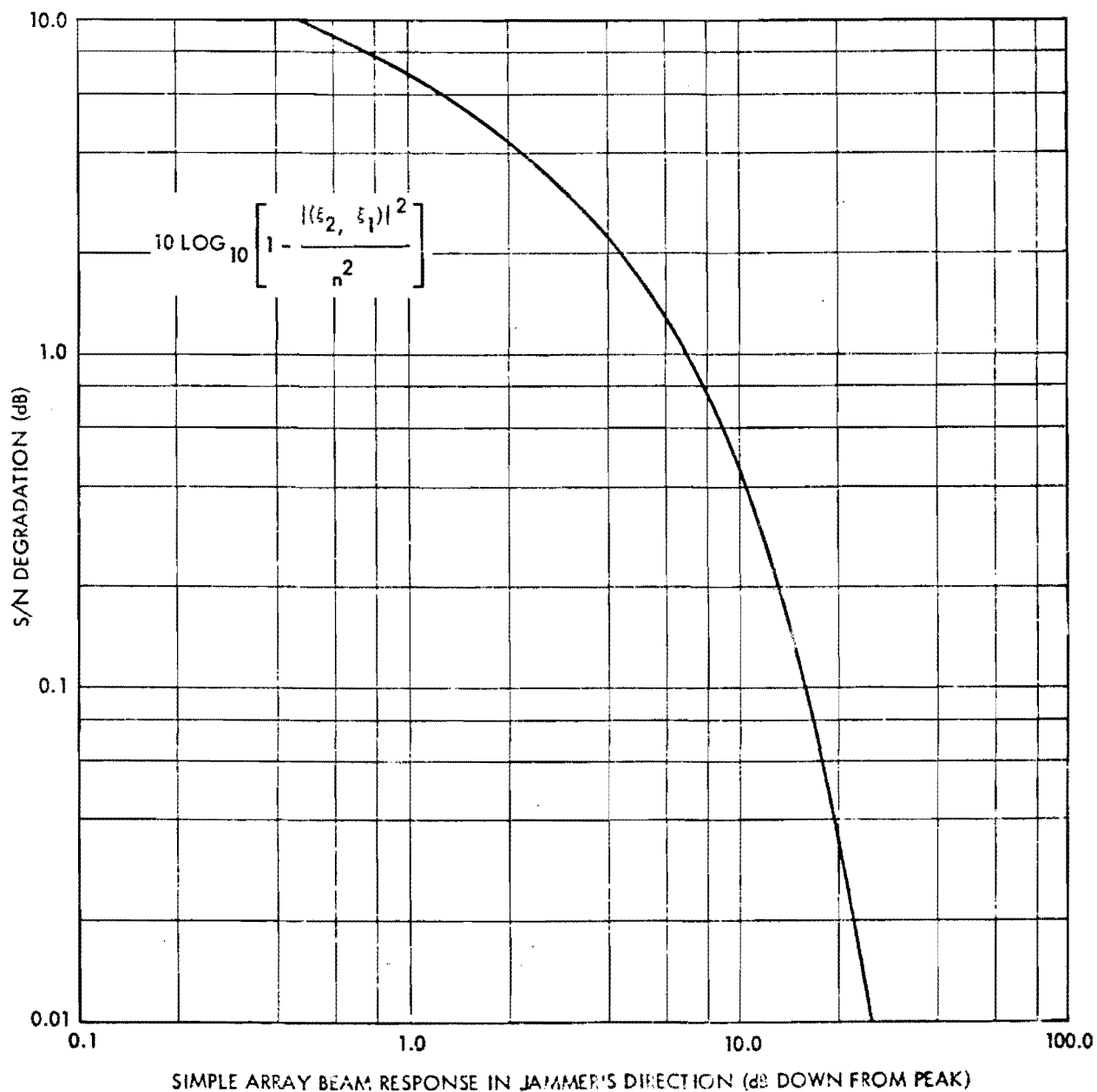


Figure 2.4. Single Jammer (Ideal Nulling) S/N Degradation as a Function of Simple Array Beam Sidelobe Response

The output signal/noise ratio is

$$\frac{S_o}{N_o} = \frac{n}{n-1} \frac{S}{\sigma^2} \left[ 1 - \frac{(\xi_2, \xi_1)}{n} \right] \quad (2.42)$$

A table of degradation factors is given in Figure 2.5.

## 2.5 S/N Performance for MMSE Criterion

During the above discussion, we have analyzed the performance of spatial filters based on the maximum S/N criterion. We now show that equivalent S/N performance is obtained if the minimum mean square error (MMSE) criterion is used to design the filter.

Referring to Figure 2.6 let  $d(t)$  be the desired output signal. Minimize the minimum mean-square error:

$$\begin{aligned} e^2 &= E \left\{ \left[ d(t) - \underline{Z}^{*T} \underline{W} \right]^2 \right\} \\ &= E \left\{ \left[ d - \underline{W}^{*T} \underline{Z} \right] \left[ d^* - \underline{Z}^{*T} \underline{W} \right] \right\} \end{aligned}$$

To minimize  $e^2$ ,  $\underline{W}$  must satisfy the orthogonality principle of linear estimation theory:

$$E \left\{ \underline{Z} \left[ d^* - \underline{Z}^{*T} \underline{W} \right] \right\} = 0$$

or

$$\underline{Z} \underline{Z}^{*T} \underline{W} = \underline{Z} \underline{Z}^{*T} \underline{d}^* \rightarrow \underline{W} = (\underline{Z} \underline{Z}^{*T})^{-1} \underline{Z} \underline{d}^*$$

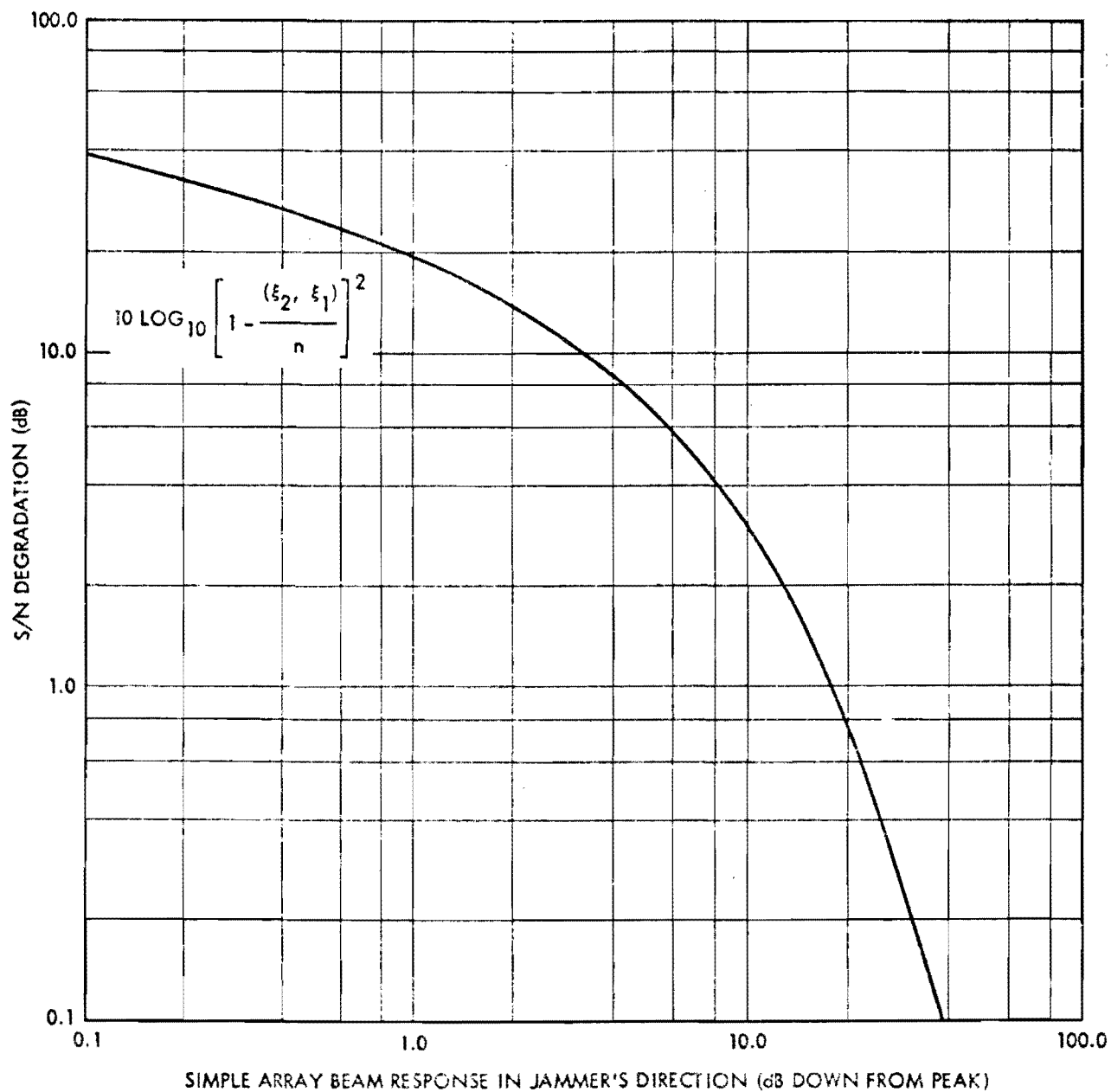


Figure 2.5. Single Jammer (Full Field with Null) S/N Degradation as a Function of Simple Array Beam Sidelobe Response

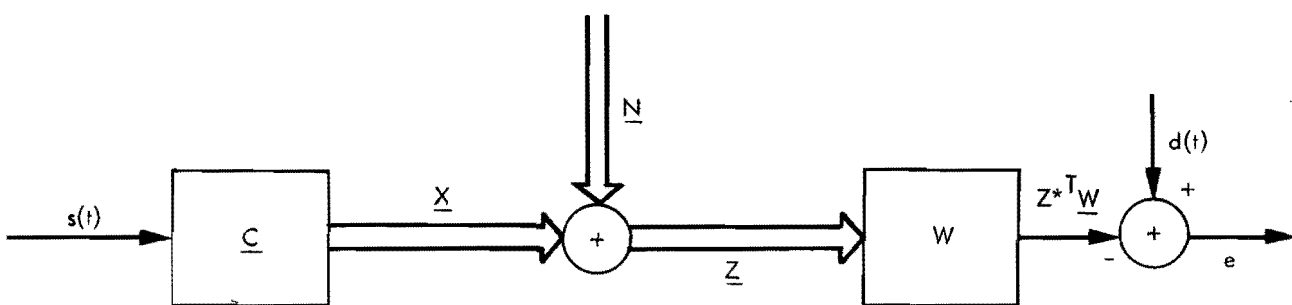


Figure 2.6. Spatial Filter System for Minimum Mean-Square Error

The minimum error is

$$e_{\min}^2 = E \left\{ d \left[ d^{*T} - Z^{*T} W \right] \right\} = |d|^2 - d Z^{*T} W$$

As an example, consider the single user, single jammer case. The solution is sought for

$$\left( I + \frac{S}{\sigma^2} \underline{\xi}_1 \underline{\xi}_1^{*T} + \frac{J}{\sigma^2} \underline{\xi}_2 \underline{\xi}_2^{*T} \right) \underline{W} = \frac{nS}{\sigma^2} \underline{\xi}_1$$

As a trial solution, take

$$\underline{W} = \lambda_1 \underline{\xi}_1 + \lambda_2 \underline{\xi}_3 = \left( \lambda_1 + \frac{(\underline{\xi}_2, \underline{\xi}_1)}{n} \right) \lambda_2 \underline{\xi}_1 + \lambda_2 \underline{\xi}_3$$

where  $\underline{\xi}_3$  is a vector constructed orthogonal to  $\underline{\xi}_1$

$$\underline{\xi}_3 = \underline{\xi}_2 - \frac{(\underline{\xi}_2, \underline{\xi}_1)}{n} \underline{\xi}_1$$



Substitute and solve for  $\lambda_1$  and  $\lambda_2$  with the results

$$\lambda_2 = - \frac{\frac{nJ}{\sigma^2} (\underline{\xi}_2, \underline{\xi}_1)^* \lambda_1}{1 + \frac{nJ}{\sigma^2}}$$

and

$$\lambda_1 = \frac{\frac{nS}{\sigma^2} \left(1 + \frac{nJ}{\sigma^2}\right)}{1 + \frac{nJ}{\sigma^2} + \frac{nS}{\sigma^2} \left(1 + \frac{nJ}{\sigma^2}\right) \left(1 - \frac{|(\underline{\xi}_2, \underline{\xi}_1)|^2}{n^2}\right)}$$

With these values for the coefficients, the output S/N is

$$\frac{S_o}{N_o} = \frac{n^2 S}{e_{\min}^2} - 1 = \frac{nS}{\sigma^2} \left[ \frac{1 + \frac{nJ}{\sigma^2} \left(1 - \frac{|(\underline{\xi}_2, \underline{\xi}_1)|^2}{n^2}\right)}{1 + \frac{nJ}{\sigma^2}} \right]$$

which is the same result as for the maximum S/N criterion.

## 2.6 Advantage of Optimum Filtering

The relative advantage of optimum filtering is the ratio of the degradation factors for the optimum spatial filter and for the simple beamformer, using a given array. A plot of the relative advantage is shown in Figure 2.7, as a function of the array beam response and the maximum jammer-to-thermal noise ratio. The maximum advantage occurs at the -3 dB point of the array response. This plot shows most clearly when optimum spatial filtering is advantageous. The improvement in S/N is less than 0.5 dB when  $\frac{nJ}{\sigma^2} < 1$ . When  $\frac{nJ}{\sigma^2} \geq 10$ , very significant improvements, amounting to more than 5 dB, are possible.

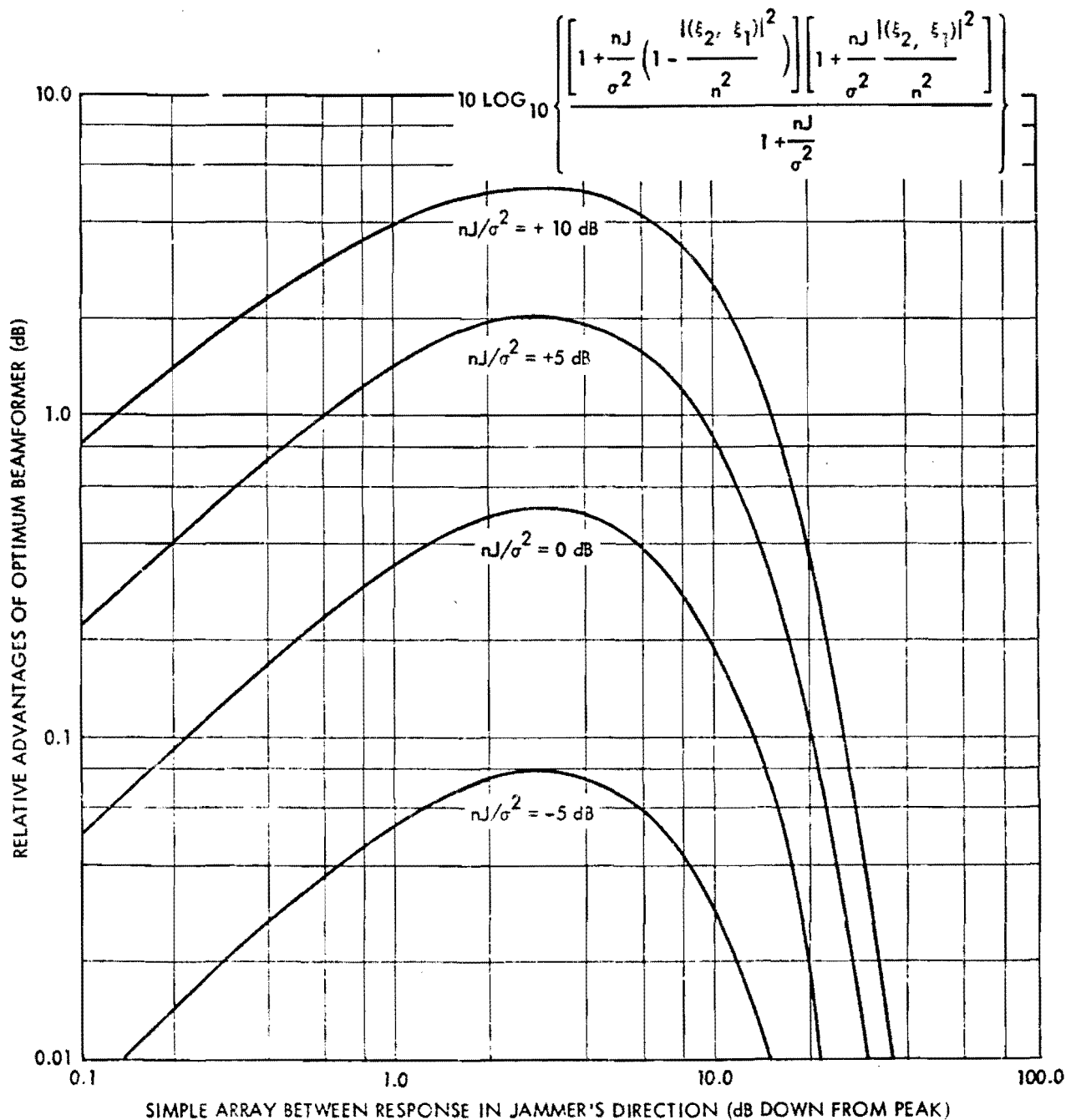


Figure 2.7. Relative Advantage of Optimum Spatial Filter Over a Simple Array as a Function of the Simple Array Sidelobe Gain in Jammer's Direction and the Maximum Jammer-to-Thermal Noise Ratio

### 3.0 The JARED Antenna

A JAMmer REDuction Antenna System (JARED) was designed, fabricated and tested to show the feasibility of nulling jammers with a phased array antenna compatible with existing satellite configurations. The basic objectives were to provide jammer nulling at any point on the earth while providing coverage over several specified user areas. RF tests with simulated users and jammers were performed. Various algorithms for nulling jammers and simultaneously providing broad high gain user areas were studied. Consideration was given to the ability to resolve closely spaced users and jammers, sensitivity to impact on ground control complexity and computer computation time. Initially it was assumed that the location of the jammers was known and that control was provided from the ground. In a later section a technique for detection and location of the jammers is provided.

This section describes the results of the JARED antenna testing. Two antenna systems were tested. 1) Radiating Aperture tests - The first array was constructed of linearly polarized horns, ferrite phase shifters and attenuators. The basic purpose of the tests was to demonstrate the correlating between the analysis and experiment and to examine the effects of component errors on array performance. By showing that the theoretical designs and analyses could be implemented in actual hardware, the component errors allowable were within reasonable design limits, and the frequency sensitivity of the array was minimal, these tests serve to demonstrate the feasibility of a JARED type antenna. 2) JARED System tests - The second array tested used a FET amplifier, digital phase shifters and attenuators, and a circularly polarized corrugated horn. These components are similar to those proposed for a spacecraft type antenna and the tests serve to demonstrate the feasibility of a JARED antenna utilizing digital components.

#### 3.1 Radiating Aperture Tests

The block diagram of the first JARED antenna components is shown in Figure 3.1. Ferrite phase shifters, ferrite variable power dividers and an equal 8 way power with two ports terminated are used to provide amplitude and phase control for the six Scientific-Atlanta Standard gain horns positioned as shown in Figure 3.2. The frequency range of the components is 7.25-7.75 GHz. The phase shifters and attenuators are controlled by variable with pulses which

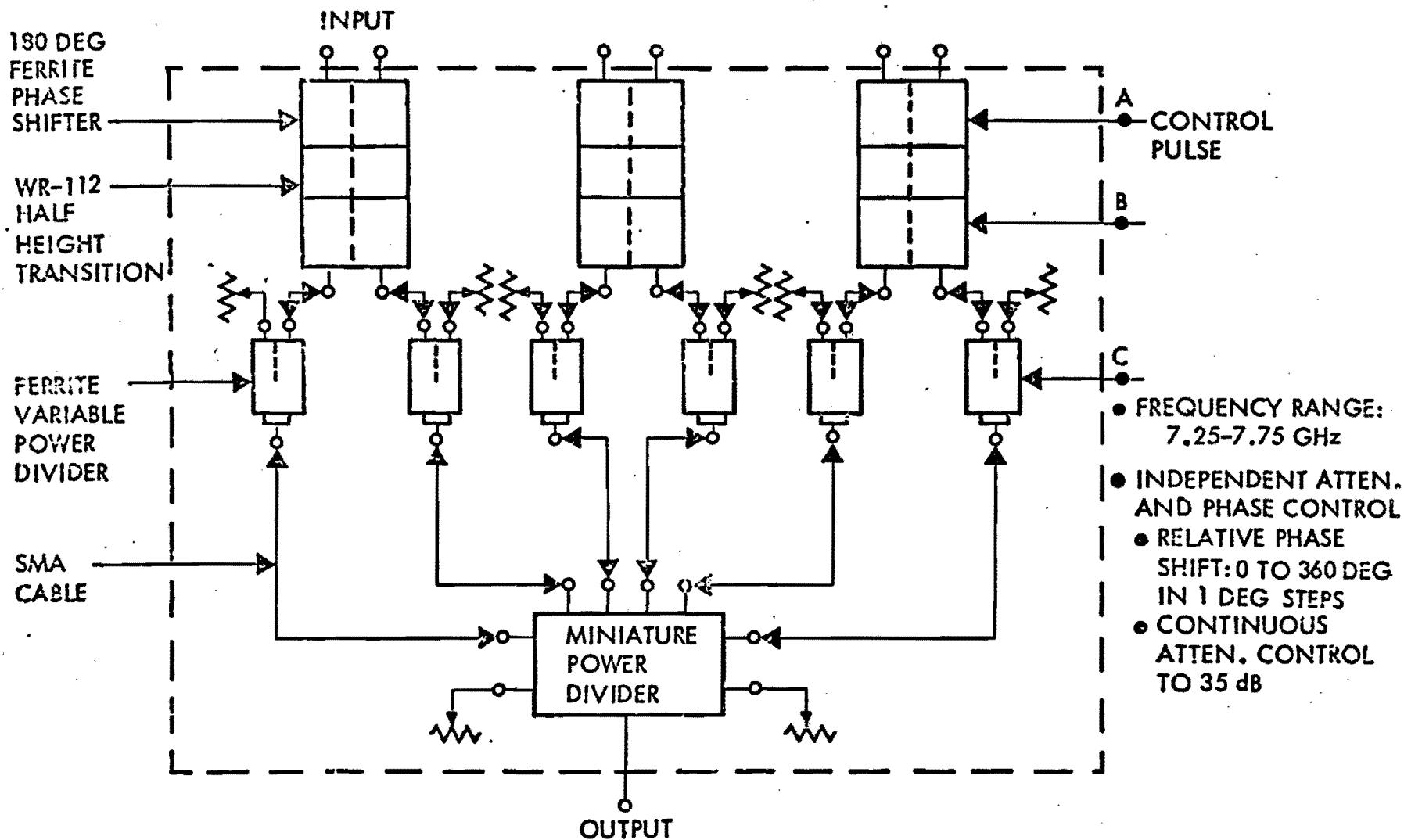


Figure 3.1 Block Diagram of JARED Array Using Ferrite Devices

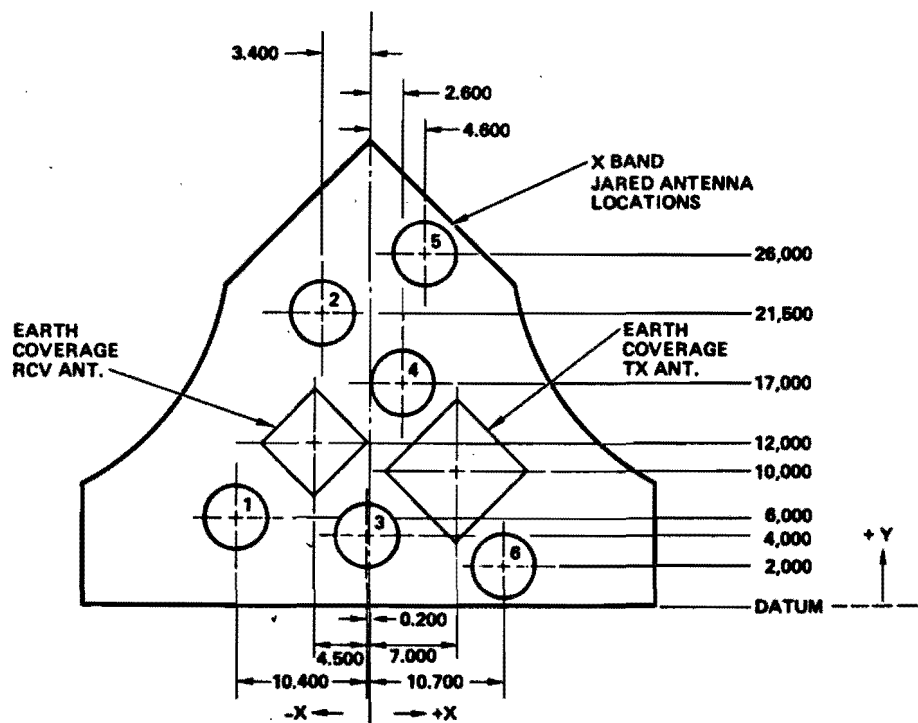


Figure 3.2 JARED Antenna Engineering Breadboard Demonstration Model

provides 0 to 360 degree phase shift control in 1 degree steps and continuous attenuation control to 35 dB.

Three types of tests were performed on the array:

- 1) Linear array tests
- 2) Two dimensional array tests and
- 3) Tests with a user and jammer transmitting.

For the linear array and two dimensional array tests patterns were recorded in the form of linear array cuts and contour radiation patterns.

### 3.1.1 Linear Array Tests

The radiating elements were arranged in a linear pattern in order to provide an easy test setup to examine the data taking accuracy, determine a suitable calibration technique, and debug the JARED algorithm. The calibration of the array was performed in the following manner:

- 1) Since varying the phase shifter had a negligible change in attenuation and varying the attenuator introduced only a small phase shift at higher attenuation states each component was calibrated independently. A table lookup of phase shift or attenuation verses pulse width was generated for each component and utilized in determining the desired weight setting.
- 2) To align the array in amplitude and phase from channel to channel, the channels were energized two at a time. With the array installed in the test chamber and a transmit source radiating amplitude and phase settings were determined experimentally that would generate a null when only two of the horns were connected to the weighting network and the other ports terminated in a matched load. A null on axis with two horns excited would be produced when the amplitudes were equal and the phases 180 degrees out of phase. A phase shift of 180 degrees was then added to one of the horns and the weight settings to put the two horns in phase and of equal amplitude were thus determined. Using one horn as a reference and doing the above with each of the other horns determined the weight settings to provide

equal phase and amplitude across the array. Other weight settings of the array were then referenced to this initial set.

Extensive tests were performed on the linear array and demonstrated excellent agreement between the theoretical and measured antenna patterns. Tests were made for single spot beams and for various user and jammer combinations up to 2 users and 2 jammers. Several examples of the measured and theoretical patterns are shown in Figures 3.3, 3.4 and 3.5. Figure 3.3 gives the theoretical and measured patterns of a uniform illuminated array (equal amplitudes and zero phase differences) and shows agreement to better than 0.5 dB down to below the 30 dB level. Figure 3.4 is a single user, single jammer case with the user at 5 degrees and the jammer at -5 degrees. Also shown is a theoretical plot with a random  $\pm 2$  degree error in each channel. Again the agreement is good to below the 30 dB level. Figure 3.5 is a 2 user 2 jammer case with the same degree of agreement.

### 3.1.2 Two Dimensional Array Tests

The horns were arranged in the pattern of Figure 3.2 and tests of the array were made for various user-jammer combinations. The data was recorded in the form of contour plots and in each case was compared to the theoretical result. In general the agreement was better than 1 dB for the higher DB levels ( $>-10$  dB) and within 2-3 dB for lower gain contours. A sample case is shown in Figures 3.6 and 3.7. The data is for a 2 user 2 jammer case using 0.2 degree null broadening at 7.55 GHz. Null broadening was a technique used to obtain wide nulls with the existing algorithm. To broaden the null each jammer was considered to be made up of five jammers, one at the center of the null area and four around the center jammer a specified distance apart. Figure 3.6 is the theoretical contour and Figure 3.7 the measured contour. The measured data was recorded over a 200 MHz frequency band for this case and the data at 7.45 and 7.65 GHz is shown in Figures 3.8 and 3.9. As can be seen by the plots there was very little pattern change with frequency. The higher db levels  $>-10$  dB are almost unchanged ( $<1$  dB change) and there is no appreciable null shift and a modest amount (2-3 dB) of null filling.

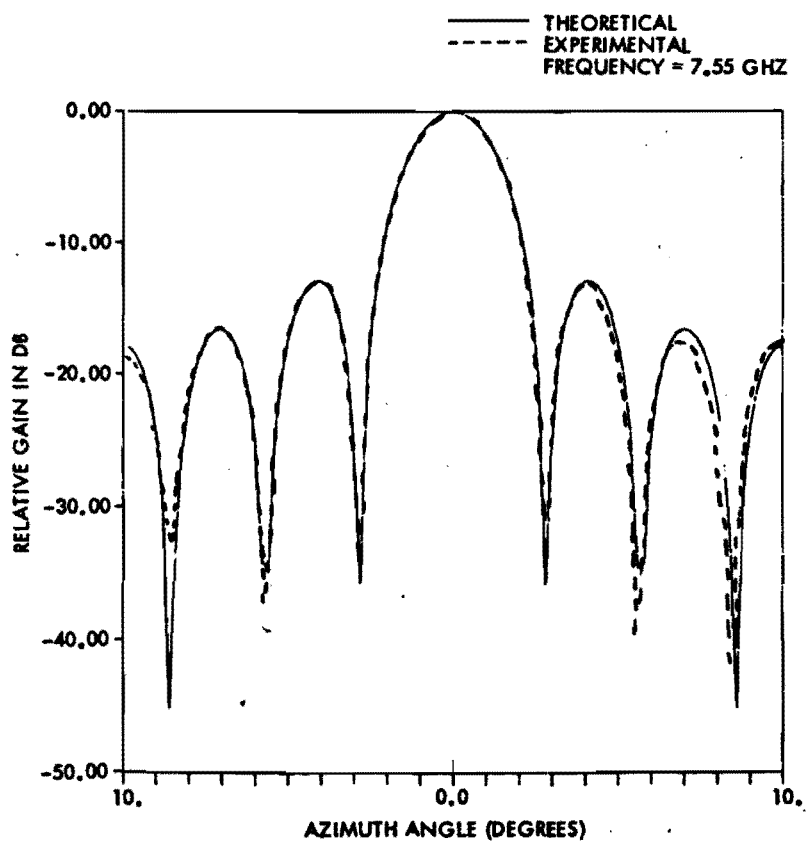


Figure 3.3 Six Element Uniform Array



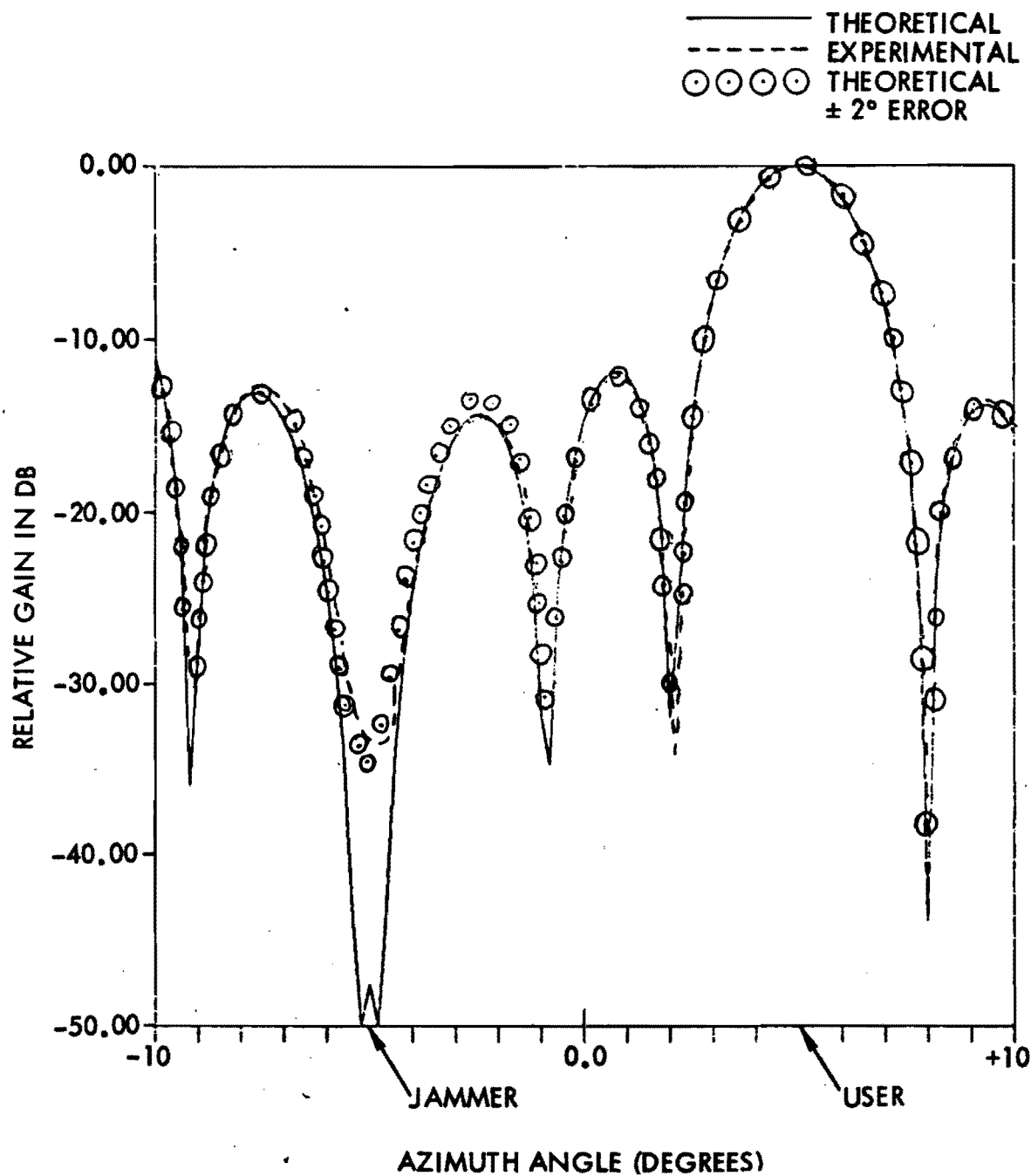


Figure 3.4 One User, One Jammer Case

— THEORETICAL  
- - - EXPERIMENTAL

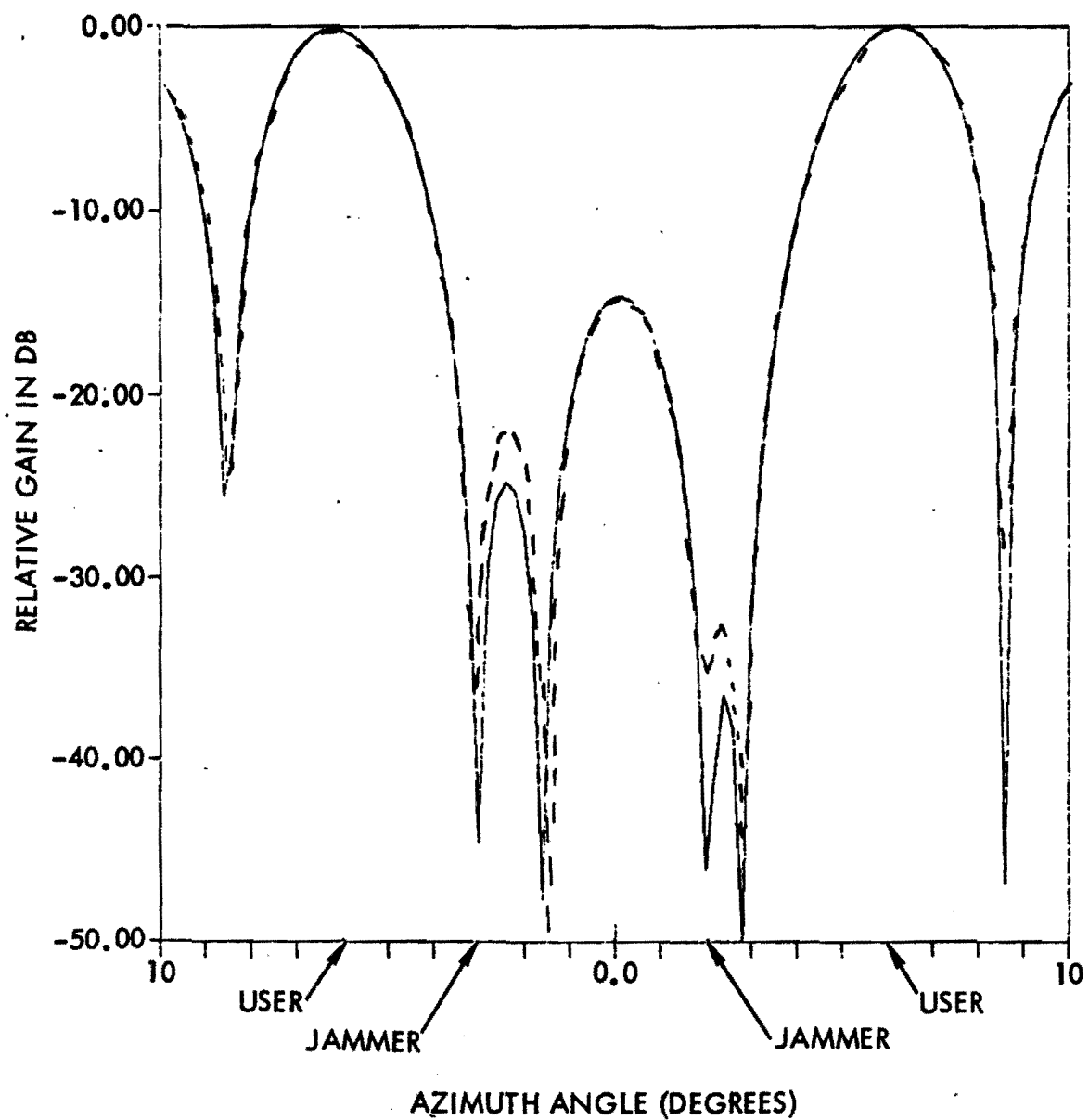


Figure 3.5 Two User, Two Jammer Case

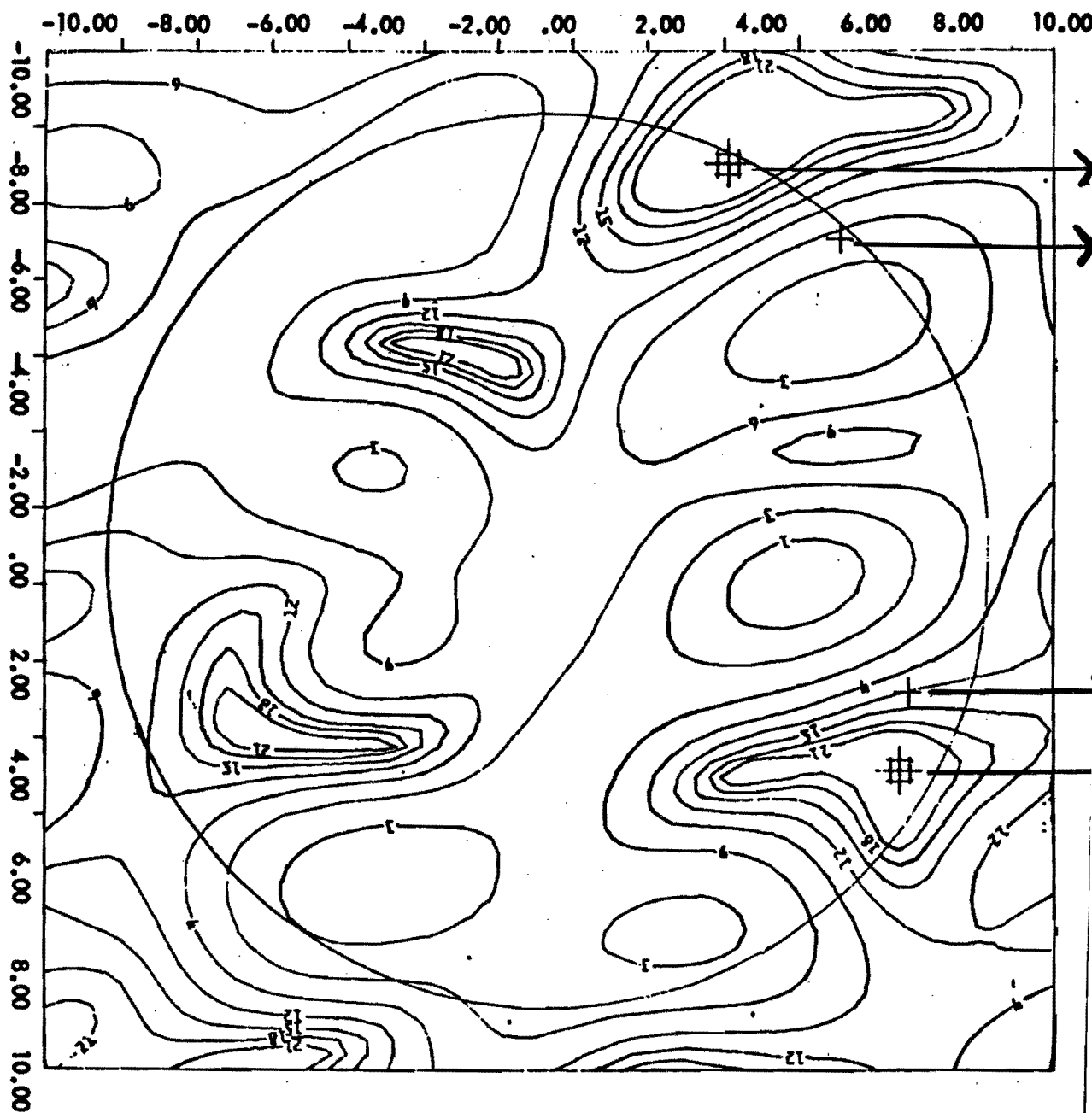


Figure 3.6

Two User, Two Jammer Case  
Using J2ALG and 0.2-Degree  
Null Broadening - Theoretical  
Data at 7.55 GHz

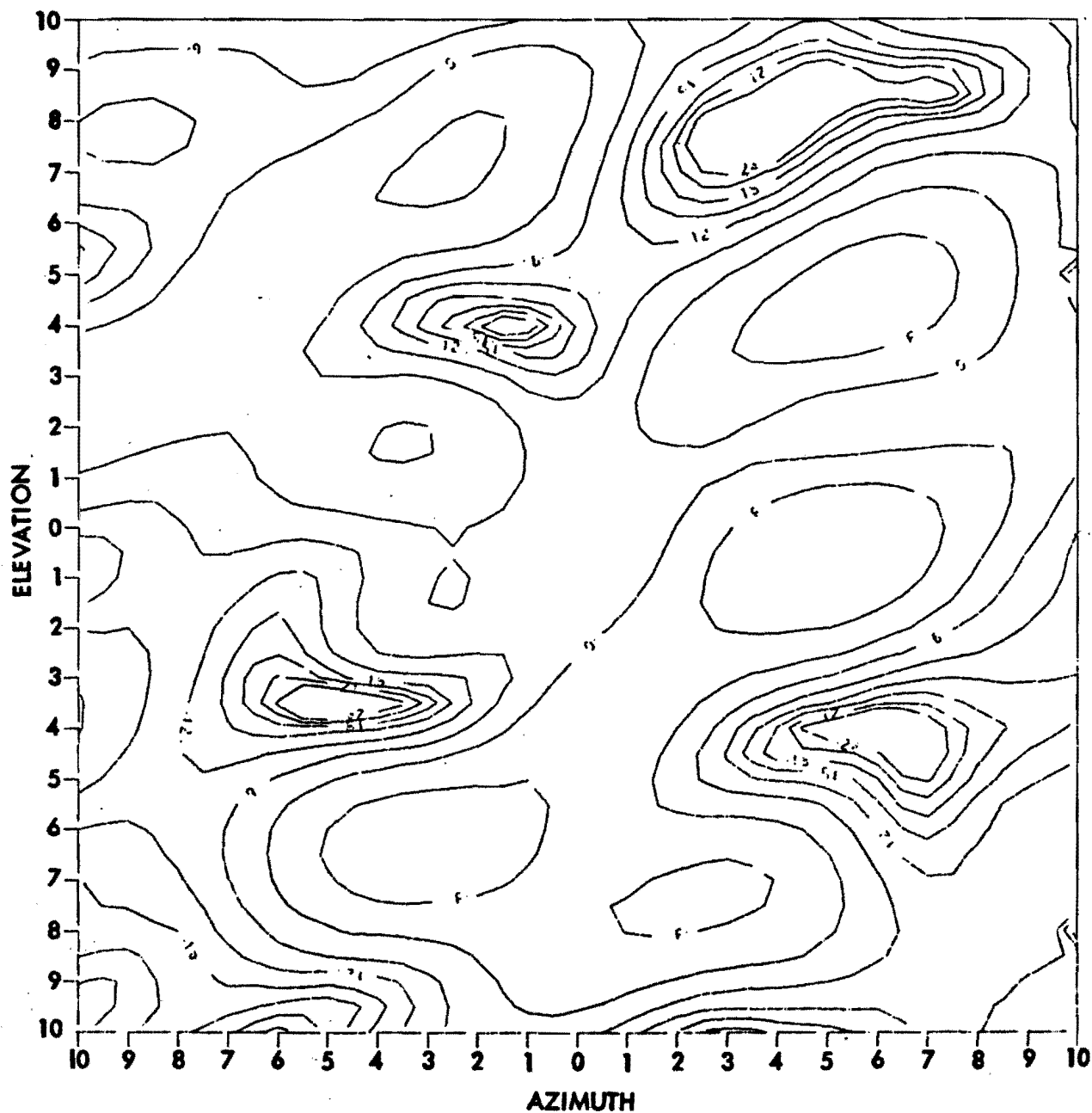


Figure 3.7 Two User, Two Jammer Case Using  
J2ALG and 0.2-Degree Null  
Broadening - Measured Data at  
7.55 GHz

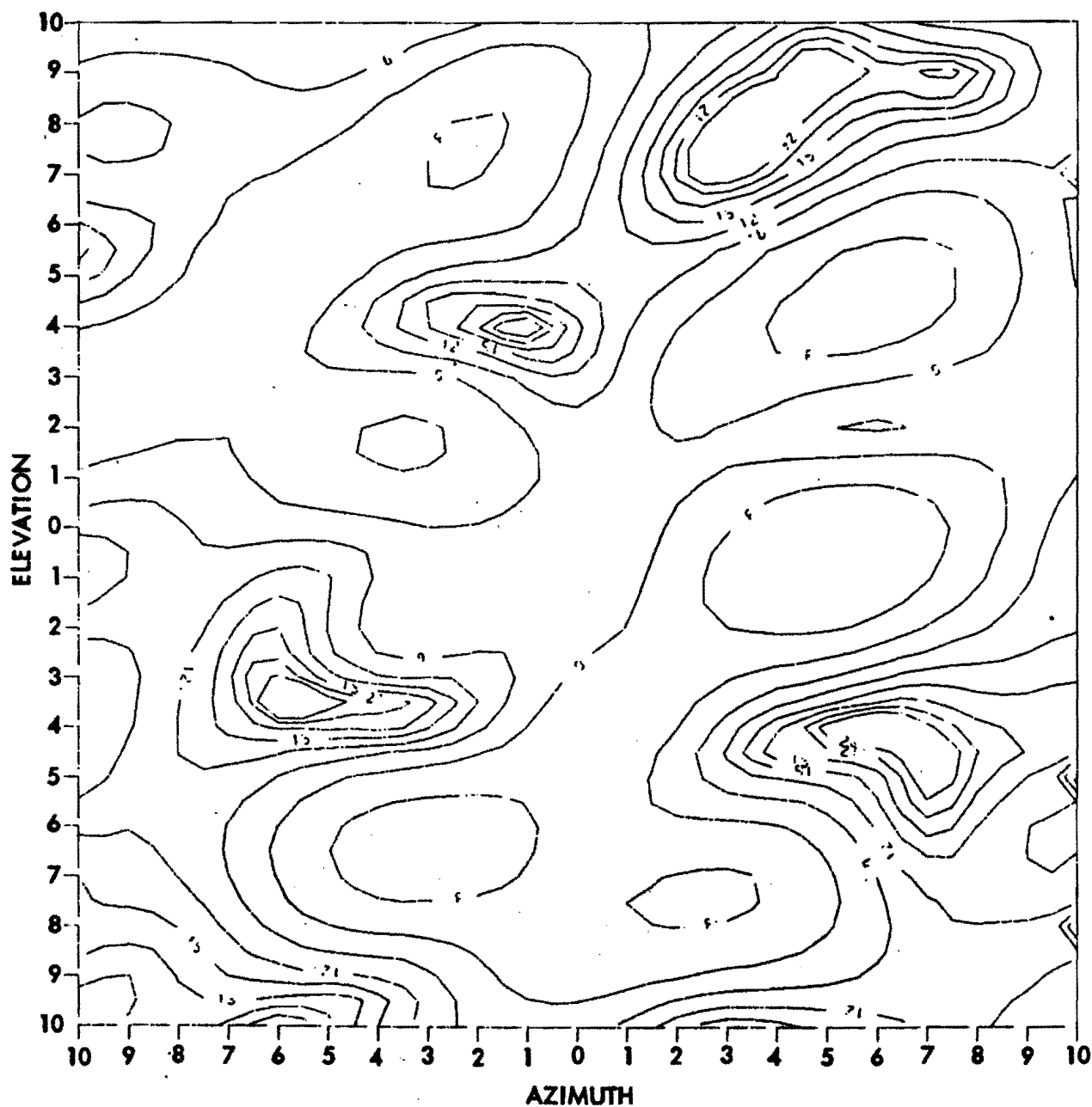


Figure 3.8

Two User, Two Jammer Case Using  
JZALG and 0.2-Degree Null  
Broadening - Measured Data at  
7.45 GHz

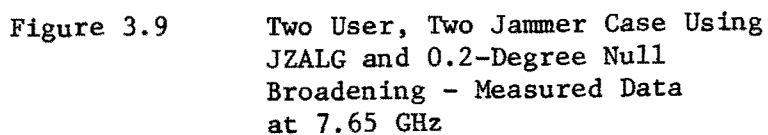


Figure 3.9 Two User, Two Jammer Case Using  
JZALG and 0.2-Degree Null  
Broadening - Measured Data  
at 7.65 GHz

### 3.1.3 User-Jammer Tests

Tests were made with two transmit horns spaced a specified angular distance apart which simulated both a user and jammer transmitting. The tests were performed in the following manner:

- 1) With both transmitters on at  $f_1$  and  $f_2$  respectively the signal was displayed on a spectrum analyzer
- 2) With the user at  $f_1$  and the jammer varying over a designated frequency range the ratio of user to jammer signal was recorded as a function of jammer frequency
- 3) The tests were repeated for several different angular separations.

An example of the data taken is shown in Figure 3.10 for a 350 MHz frequency range with user-jammer separations from 0.8 degrees to 2.6 degrees. The performance verses frequency indicates that even for the jammer as close as 0.8 degrees the user/jammer ratio can be maintained below 15 dB for a substantial frequency range. For 2.6 degrees the user to jammer ratio was maintained below 20 dB.

### 3.2 JARED System Tests

While the above array was being tested, breadboard models of flight type components were being developed to verify the acceptability of array performance utilizing the digital components and FET amplifiers. The block diagram for the array is shown in Figure 3.11. It consists of a FET amplifier, digital phase shifters and attenuators and an eight way power divider with two ports terminated. Pictures of the components are given in Figure 3.12 and the array setup in Figure 3.13. The array is controlled by a HP 2100 Mx mini-computer which also controls the data acquisition equipment.

Once again data was taken on a linear array setup and a two-dimensional array with data recorded in the form of contour plots. Again there was good agreement between the theoretical and measured antenna patterns which served to demonstrate the feasibility of a JARED array. The details of the results are given below.

JAMMER AT 0.8° USER AT 0°

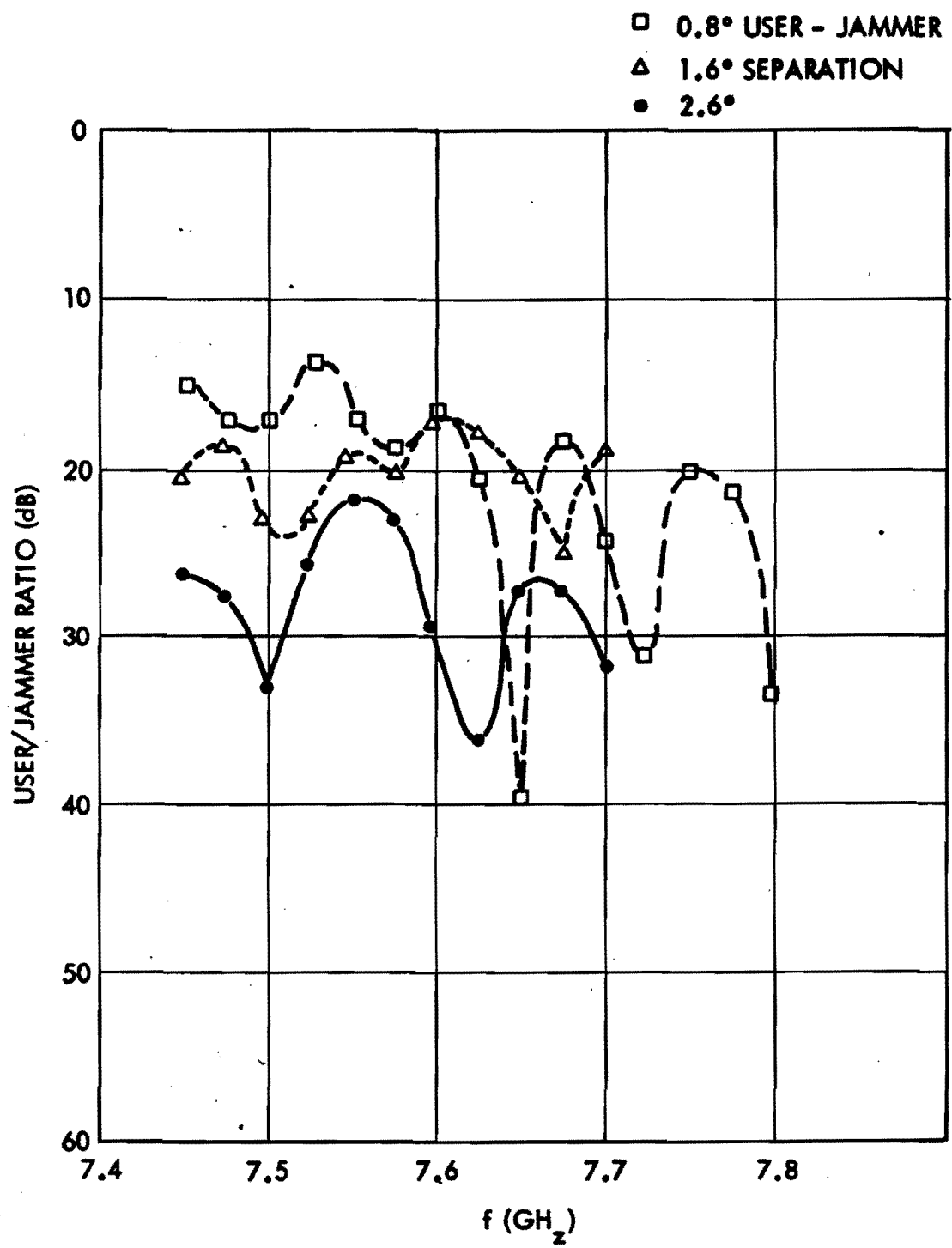


Figure 3.10 Measures Data of User-Jammer  
Suppression Versus Frequency



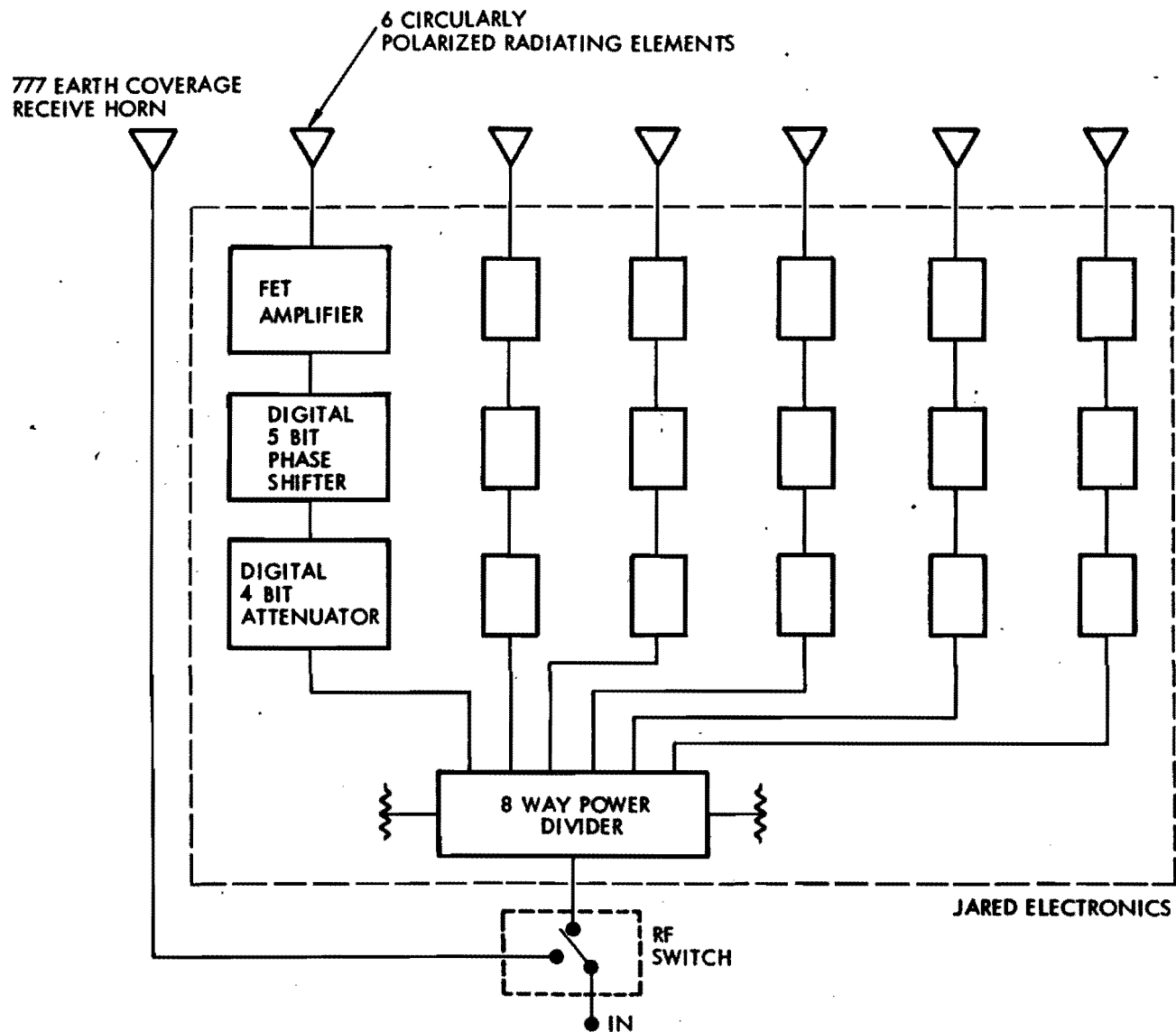


Figure 3.11

Block Diagram of JARED Array Using  
FET Amplifiers and Digital Components

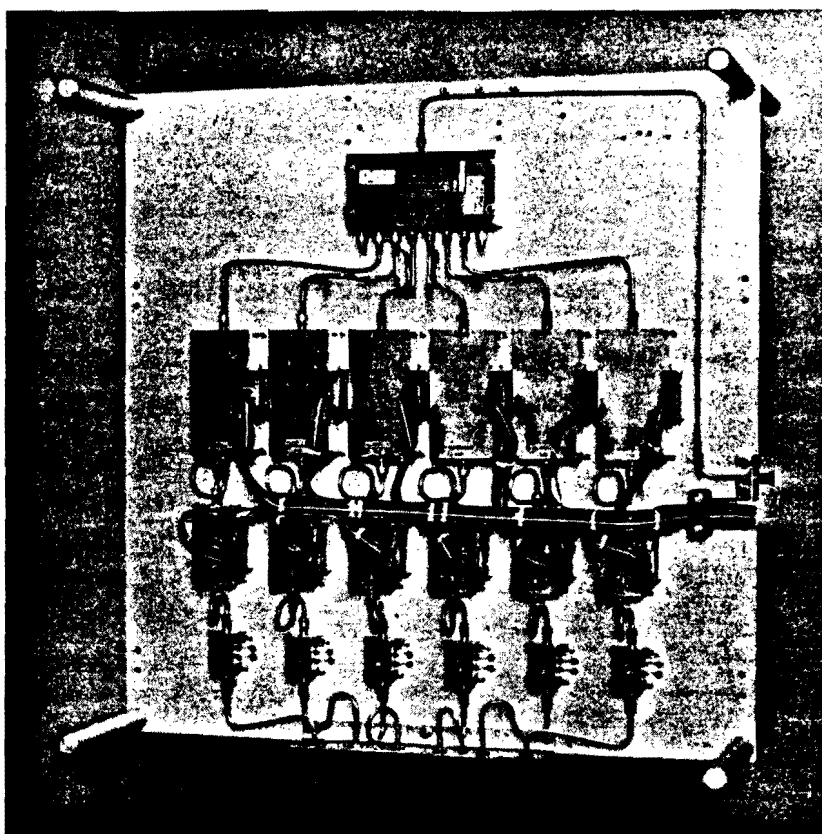


Figure 3.12      JARED Electronics

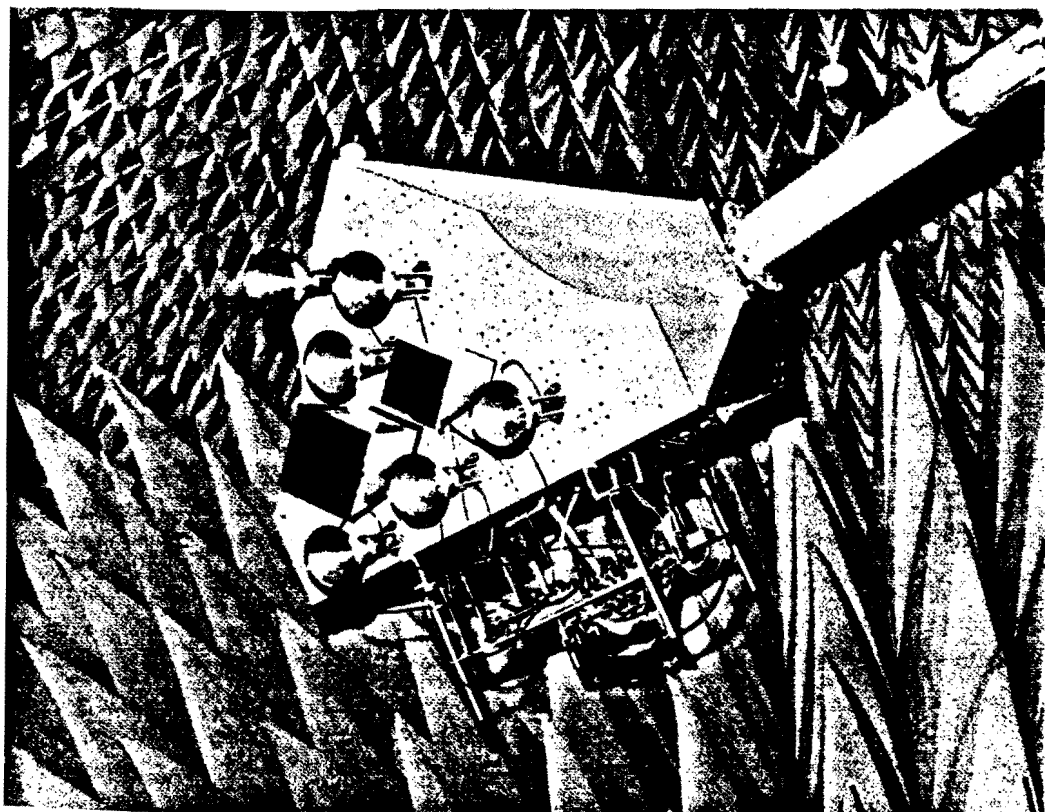


Figure 3.13      JARED Array - Engineering  
Model Under Test

### 3.2.1 Linear Array Tests

Again, to check out the system and provide an easily obtainable set of measured data to compare with the theoretical computations, data was taken on a linear arrangement of linear horns using the digital electronics. The results were essentially the same as for the first array and will not be repeated here for brevity.

### 3.2.2 Contour Data

Extensive contour data was taken for cases of varying users and jammers up to 4 users and 3 jammers. At the calibrated frequency (0.15 GHz) the measured data and the calculated data utilizing the quantized weights were in excellent agreement. Examples are shown in Figures 3.14-3.17. These results verify the utilization of the theoretical data to compute expected antenna performance. Because the breadboard components were manufactured with many substrates to facilitate ease of repair if it were necessary, the VSWR of the breadboard components would be higher than would be anticipated with the flight type components. The effect of the higher VSWR was to degrade the performance verses frequency. The first array adequately demonstrated that when the VSWR interactions are at a minimum that excellent performance verses frequency can be maintained. Figure 3.14 is the theoretical contour with no quantization and figure 3.15, the measured data for a one user case. At the user position the received power was 4.1 dB higher than a typical spacecraft earth coverage horn (transmitter at 5 degrees azimuth, 5 degrees elevation) to the power received when the array was pointed to simulate a user transmitting at 5 degrees azimuth and 5 degrees elevation.

Figures 3.16 and 3.17 are the theoretical with quantized weights and measured data for a two user, two jammer case. Again the agreement between measured and calculated is evident.

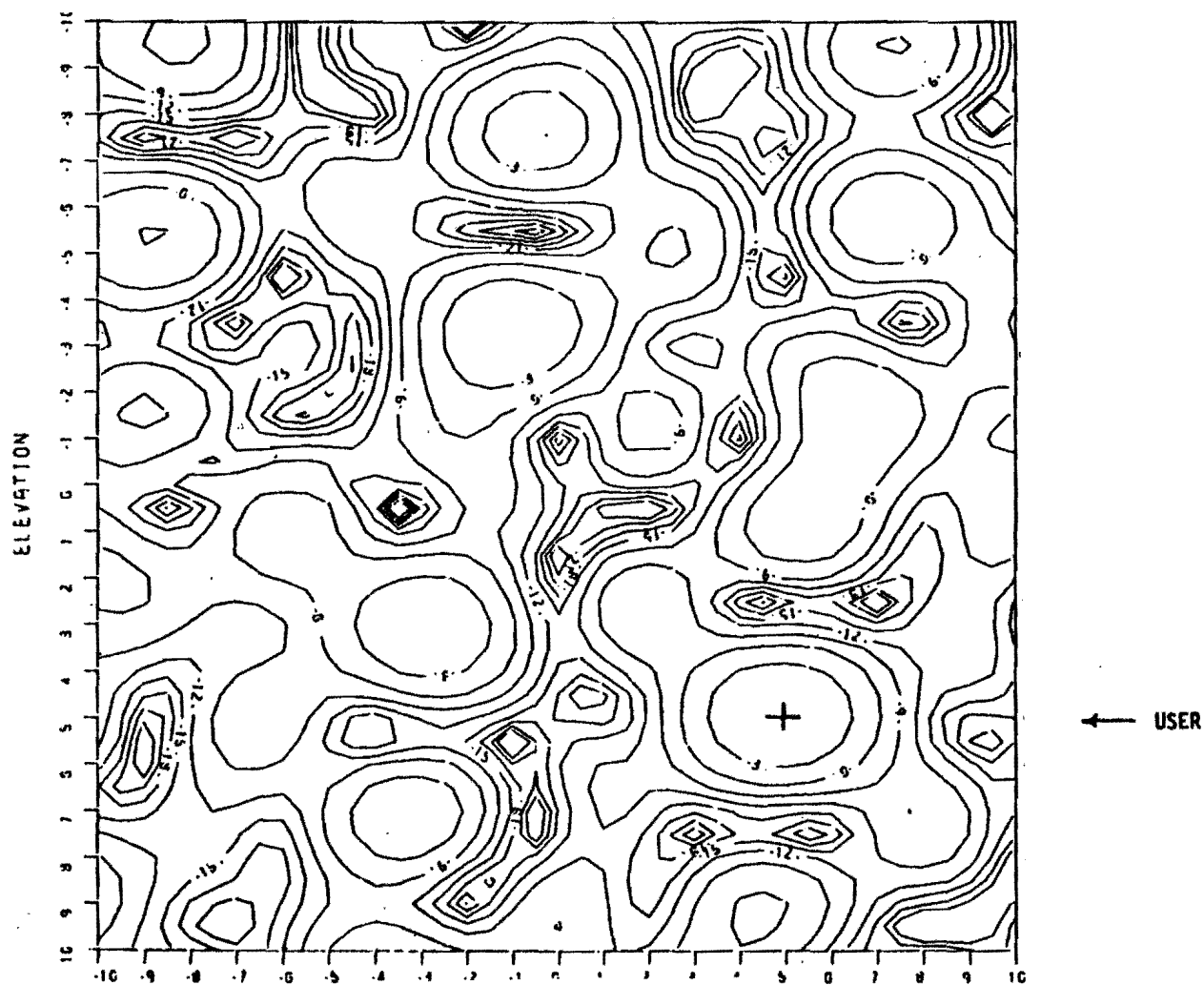
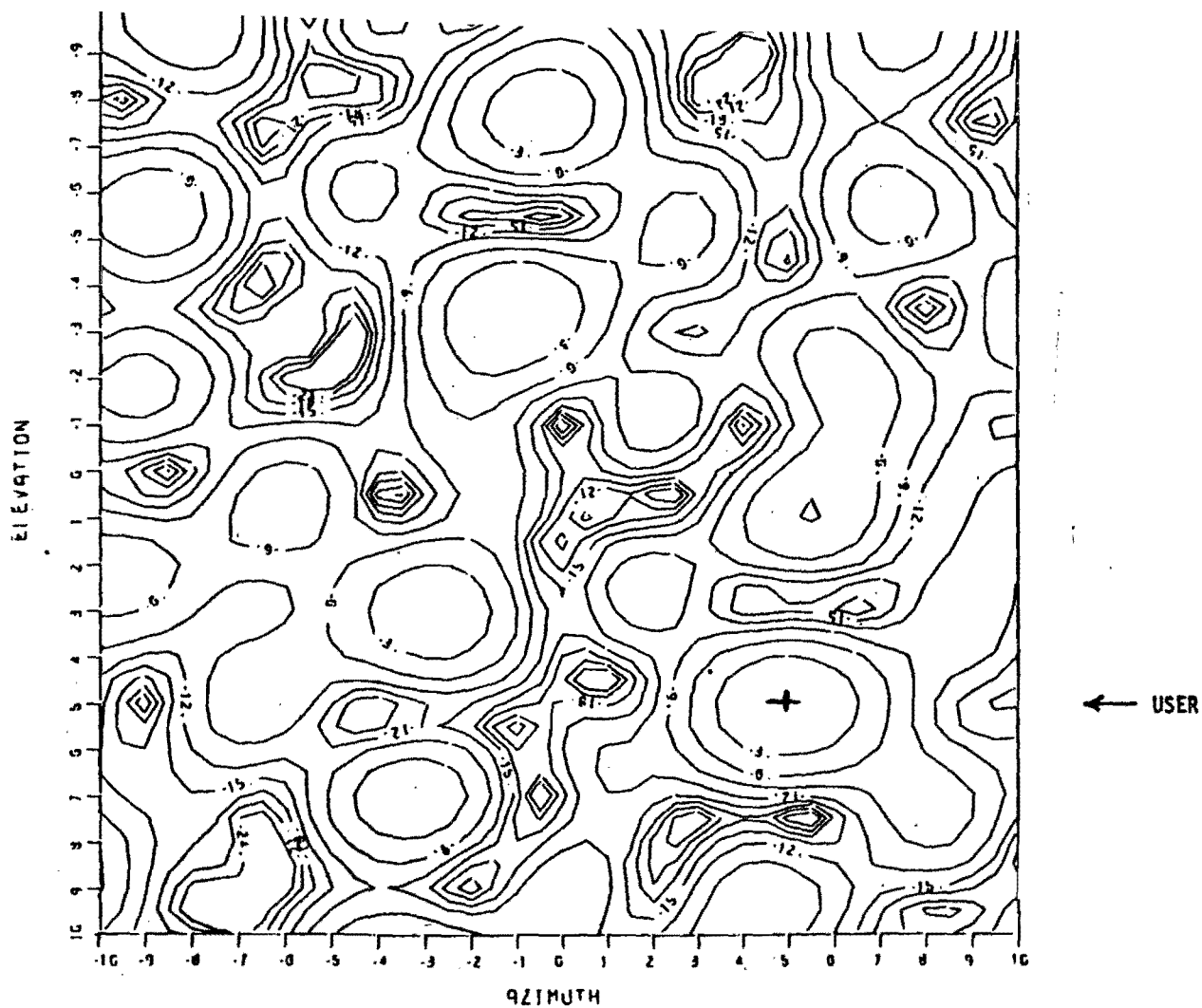


Figure 3.14 Thoretical Data, No Quantization,  
One User



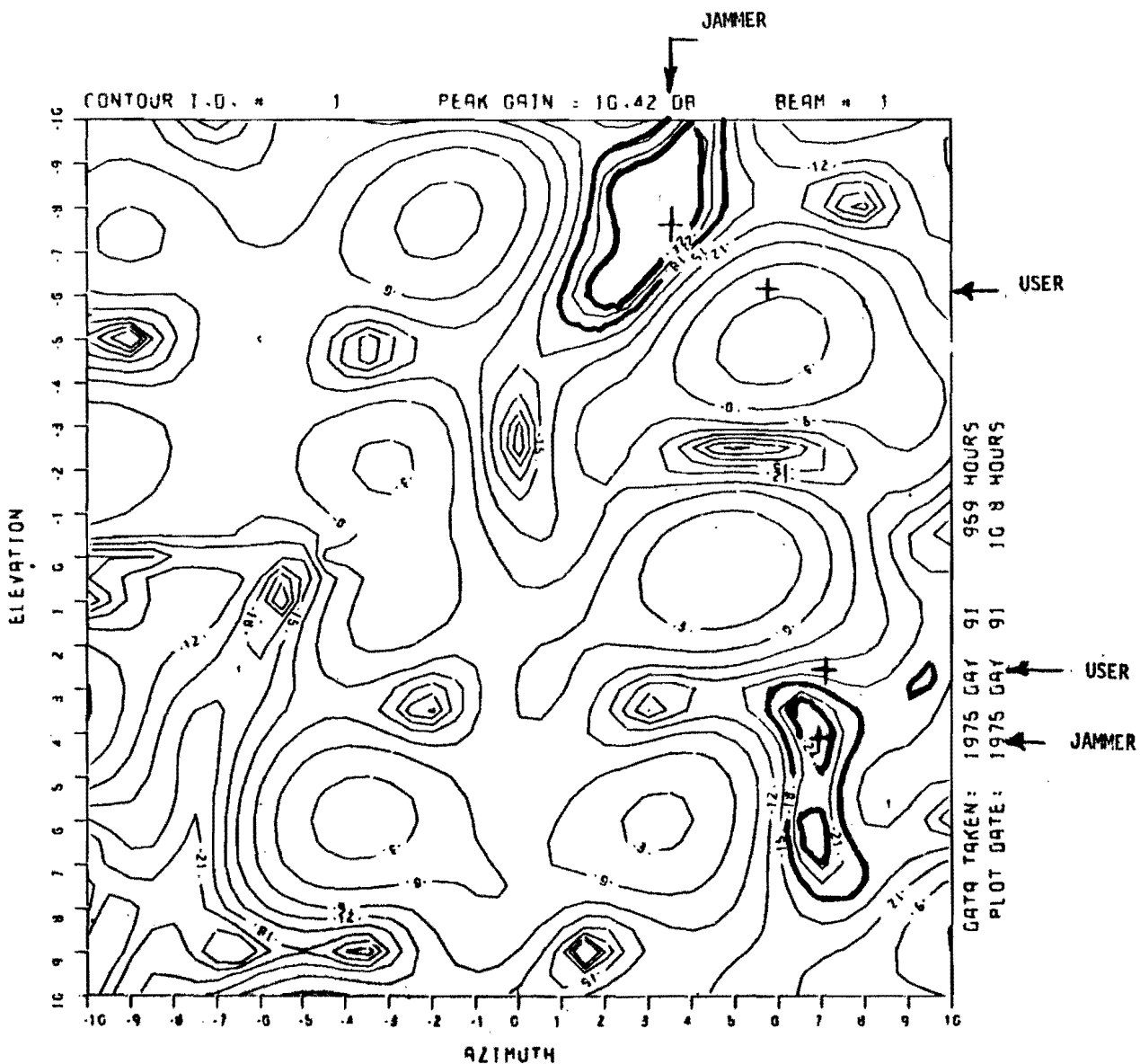


Figure 3.16      Theoretical Plot with Quantized Weights  
Two Users and Two Jammers

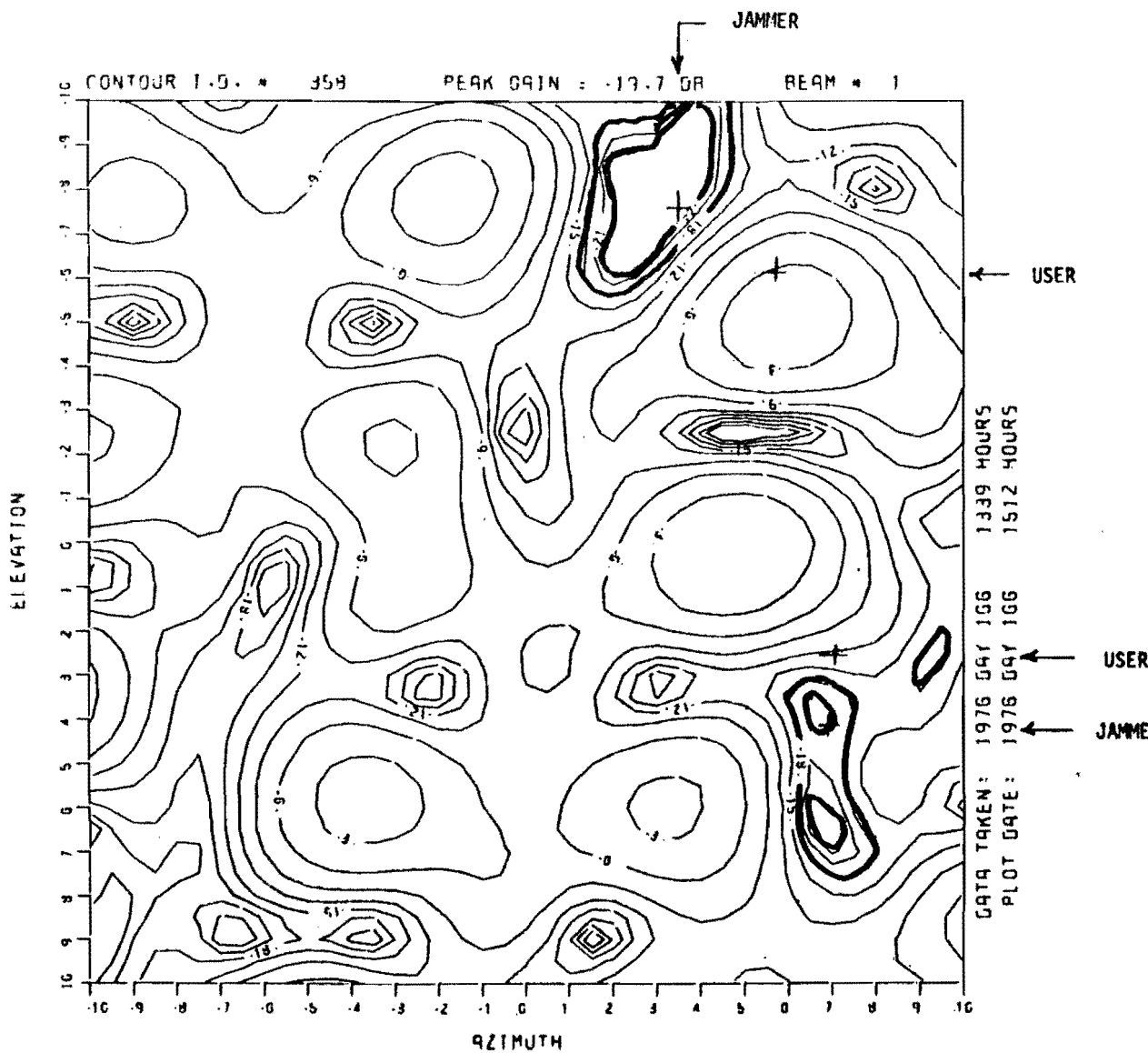


Figure 3.17 Measured Data, Two Users and Two Jammers



#### 4.0 Algorithm Program Description

The antenna array weight optimization program is designed to minimize the array output noise power subject to constant total output signal power. A necessary condition for the optimum is that the weight vector,  $\underline{W}_{\text{opt}}$ , should be the dominant eigenvector solution of the general eigenvalue problem

$$\lambda \Phi_N \underline{W}_{\text{opt}} = \Phi_S \underline{W}_{\text{opt}}$$

where

$$\Phi_S = \sum_{i=1}^n S_i \underline{\xi}_i \underline{\xi}_i^{*T}$$

is the signal covariance matrix and  $\underline{\xi}_i$  is a vector whose elements are  $g(\theta_i) \exp [j\beta \vec{r}_k \cdot \vec{u}_i]$  where  $\beta$  is the propagation constant,  $\vec{r}_k$  is a vector from the origin of the antenna coordinate system to the  $k$ th element and  $\vec{u}_i$  is a unit vector in the  $i$ th user direction, and  $g(\theta_i)$  is the element pattern factor. The factor  $S_i$  is the received element signal power in the  $i$ th user direction and  $\lambda$  is a Lagrange multiplier. Intuitively,  $\lambda$  represents the signal to noise power ratio at the array output.

An iterative method for solving the eigenvalue problem is used, based on the method of successive approximations:

$$\underline{W}_{k+1} = G_o(k) \Phi_N^{-1} \Phi_S \underline{W}_k$$

where

$$G_o(k) = \frac{1}{\sqrt{(\underline{W}_k, \Phi_S \underline{W}_k)}} .$$

The initial guess,  $\underline{W}_0$ , is  $(1, 0, 0, \dots, 0)^T$ . This weight vector is transformed by the matrix  $\Phi_N^{-1} \Phi_S$ . The scalar factor,  $G_o(k)$  is, intuitively, the gain of an AGC amplifier that maintains constant output signal power. The sequence of gains  $G_o(0), G_o(1), \dots, G_o(k), \dots$  converges to the reciprocal of the dominant eigenvalue, and the weight vector converges to the corresponding dominant eigenvector, corresponding to the maximum signal/noise power ratio. A conceptual block diagram of this process is pictured in Figure 4.1.

RECURSION  $\underline{W}(k+1) = G_o(k) \Phi_N^{-1} \Phi_S \underline{W}(k)$   
RULE:  $G_o^2(k) (\underline{W}(k), \Phi_S \underline{W}(k)) = 1$

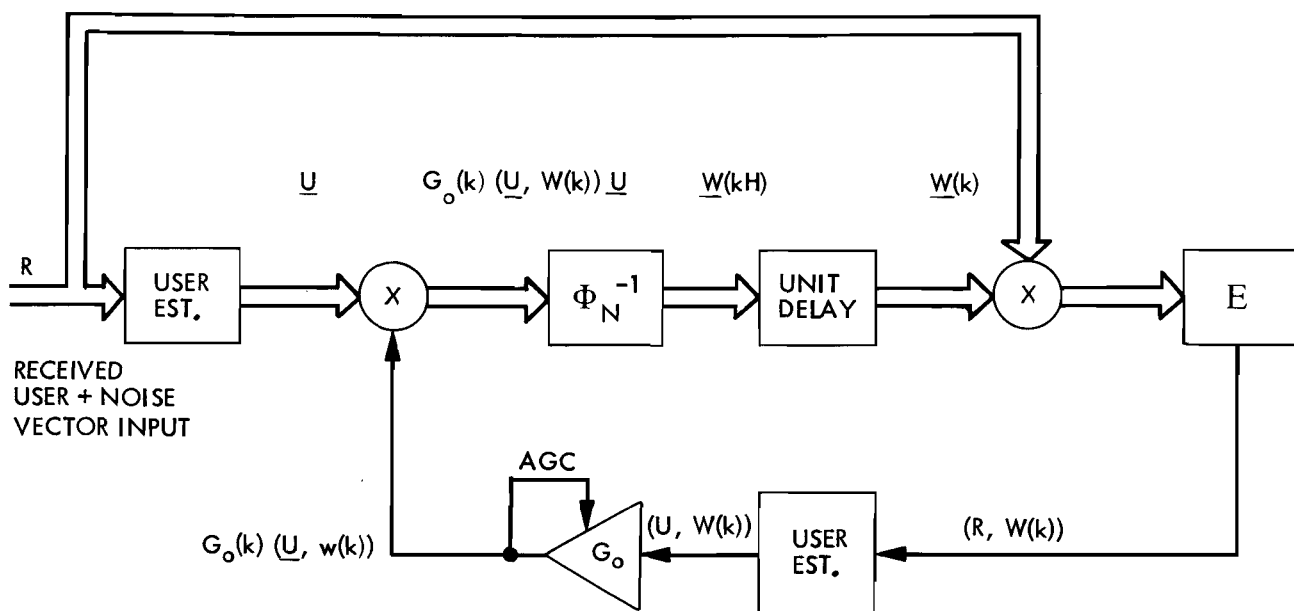


Figure 4.1. Conceptual Block Diagram for Maximum S/N Iterative Algorithm

## 5.0 Jammer Detection and Location

The conventional approach to jammer detection is energy detection, based on power measurements at the output of the antenna. However, readily available aperture sizes, while adequate for nulling, limit the resolution of location systems using this approach to angles larger than the expected nulling coverage area, and provides no sidelobe discrimination, making unambiguous jammer location difficult with the conventional method.

High resolution signal location with arrays and other multi-element sensor systems, based on improved signal processing methods, has been successfully applied with seismic arrays for detection of nuclear underground tests and earthquakes and reported in the literature. The signal processing problems are similar to the present application.

A preliminary design of a high resolution antenna array jammer detection and location system, requiring only power measurements, based on statistical hypothesis testing of the estimated signal to noise ratio in a jammer search beam formed by the array. The high resolution is obtained by performing additional power measurements in the elements of the array at the same time the output power measurement is made. Classical statistical theory is applied to the estimated signal to noise ratio based on these measurements.

The basic system block diagram is shown in figure 5.1. Tests were made with a six element placed array on the antenna range using a simulated jammer source transmitting and making use of the computerized range equipment to implement the power measurement comparisons and threshold testing required for the detector system. Figures 5.2 and 5.4 showed the conventional radiation pattern of the six element array and Figures 5.3 and 5.5 respectively the high resolution beams made using the additional power measurements described in Figure 5.1. As can be seen from the high resolution beam plots substantial improvements in jammer location results from using the additional power measurements.

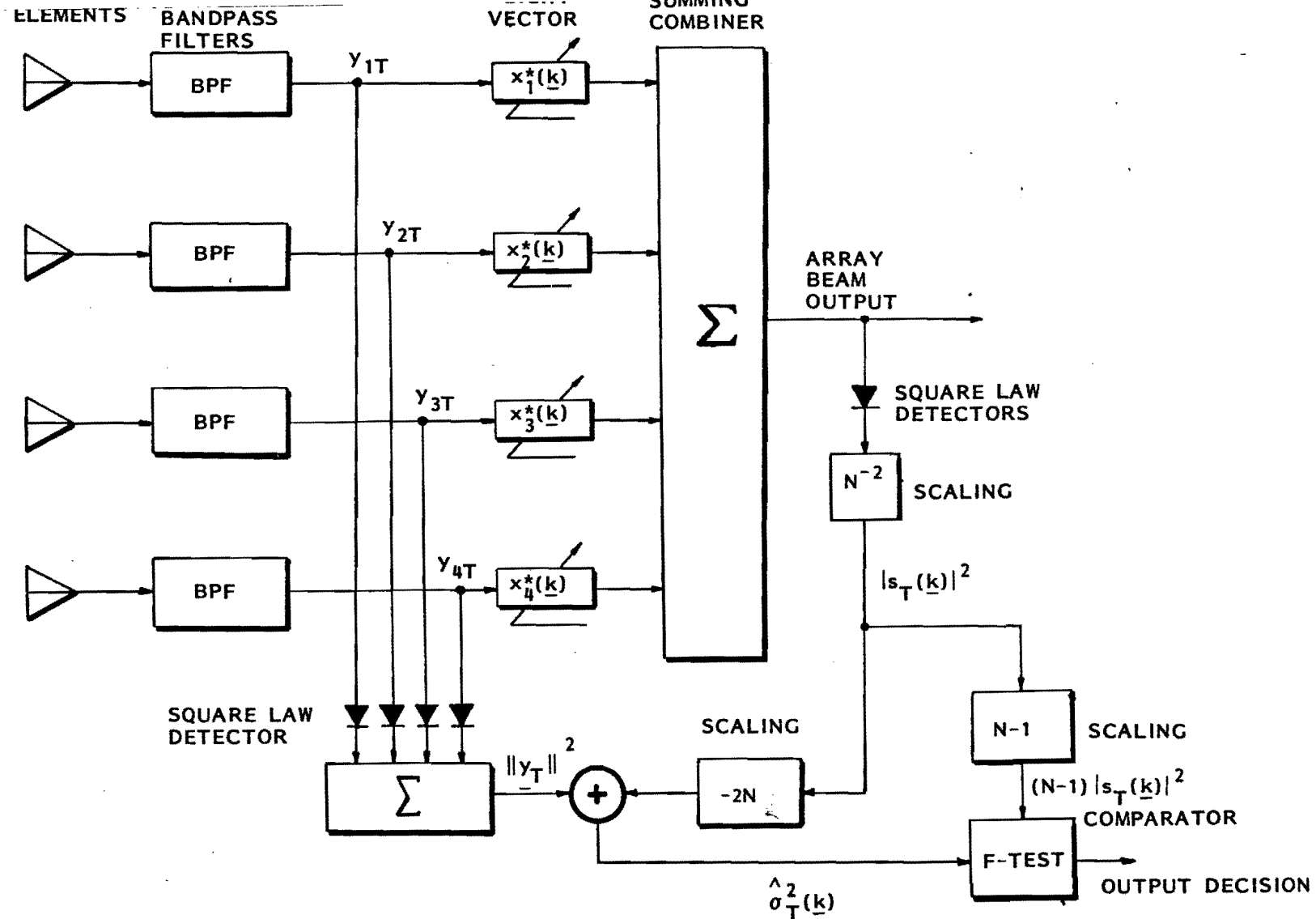


Figure 5.1

Jammer Detector and Location System

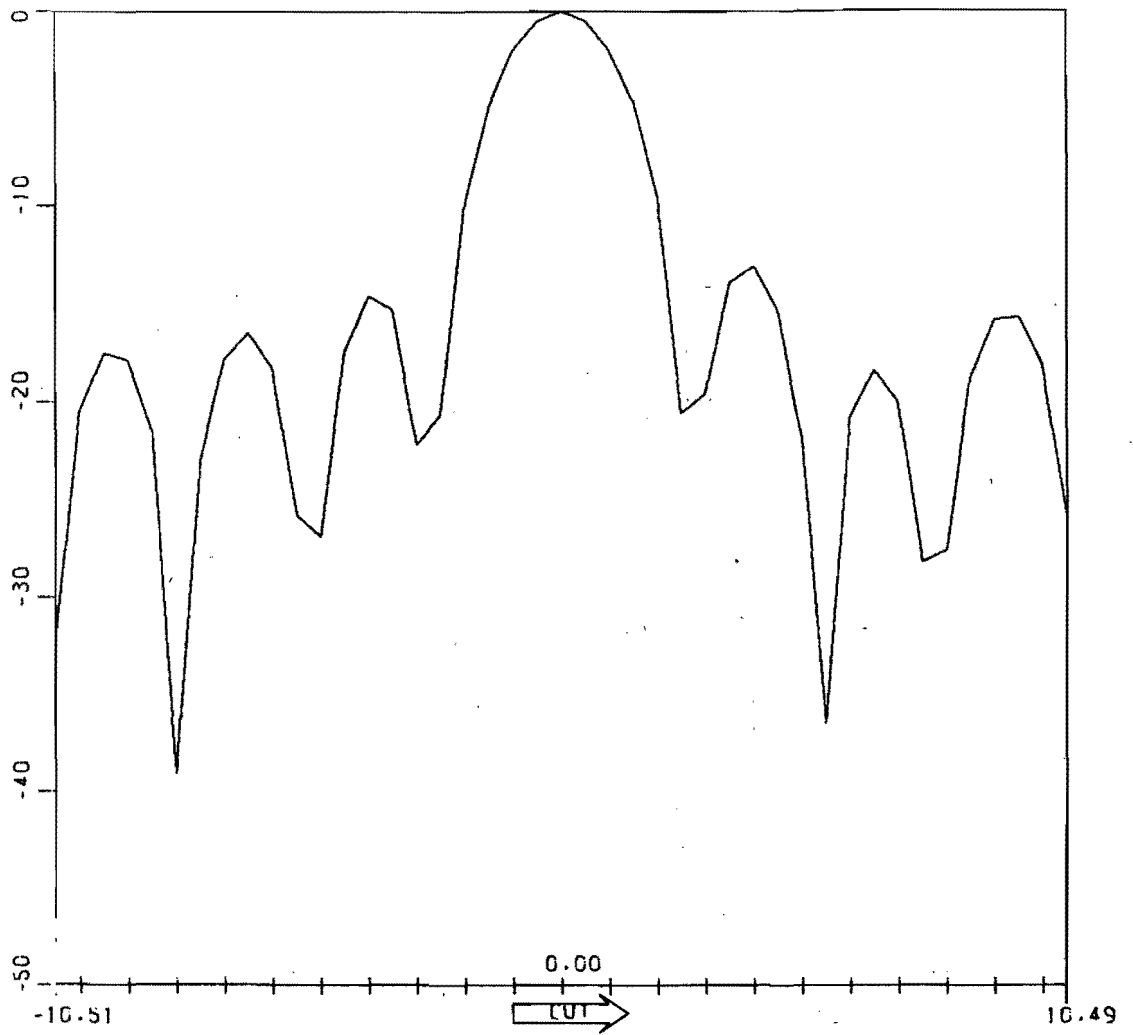


Figure 5.2 Measured Pattern On-Axis

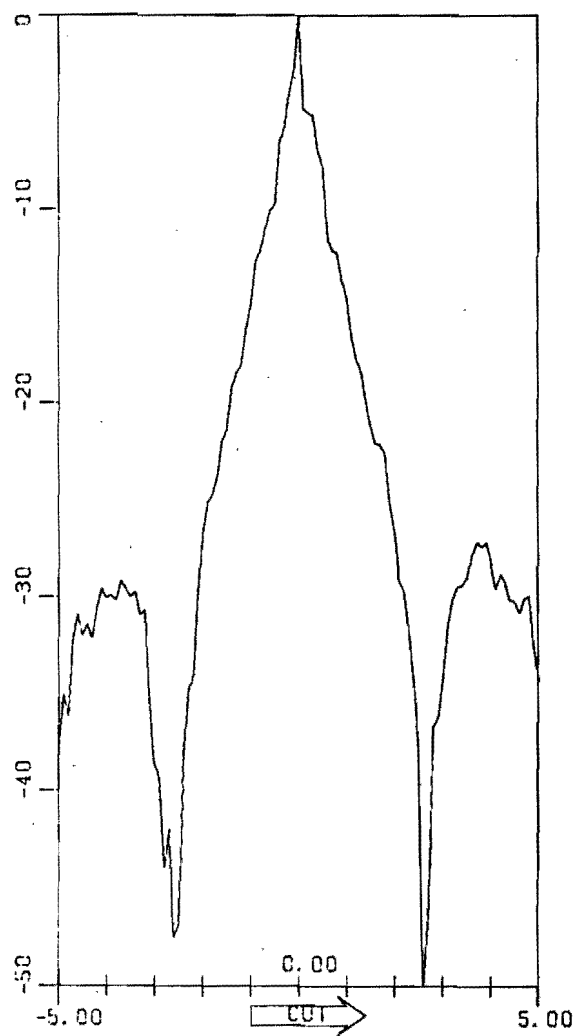


Figure 5.3 High Resolution Beam-Jammer On-Axis

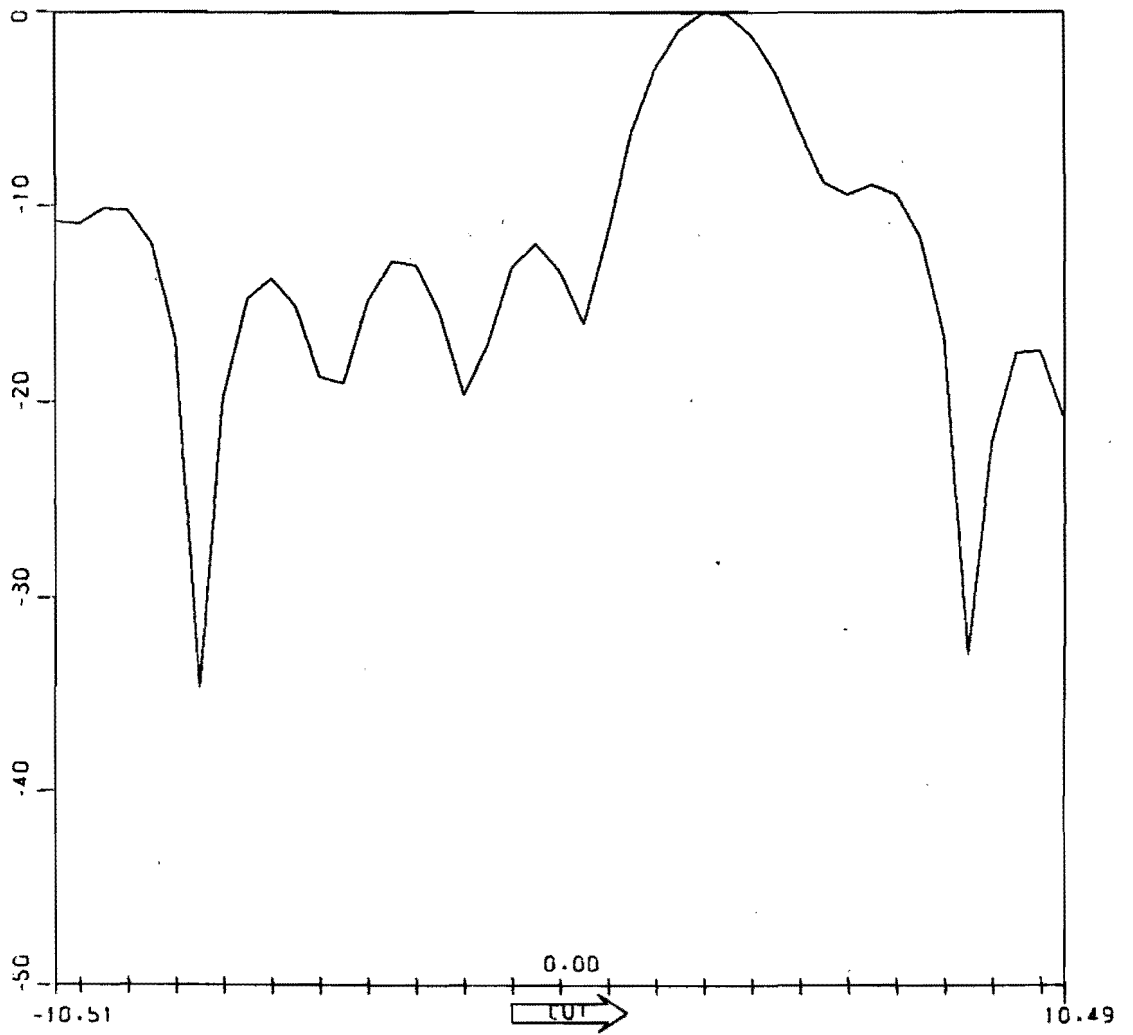


Figure 5.4 Antenna Beam Scanned to 3°

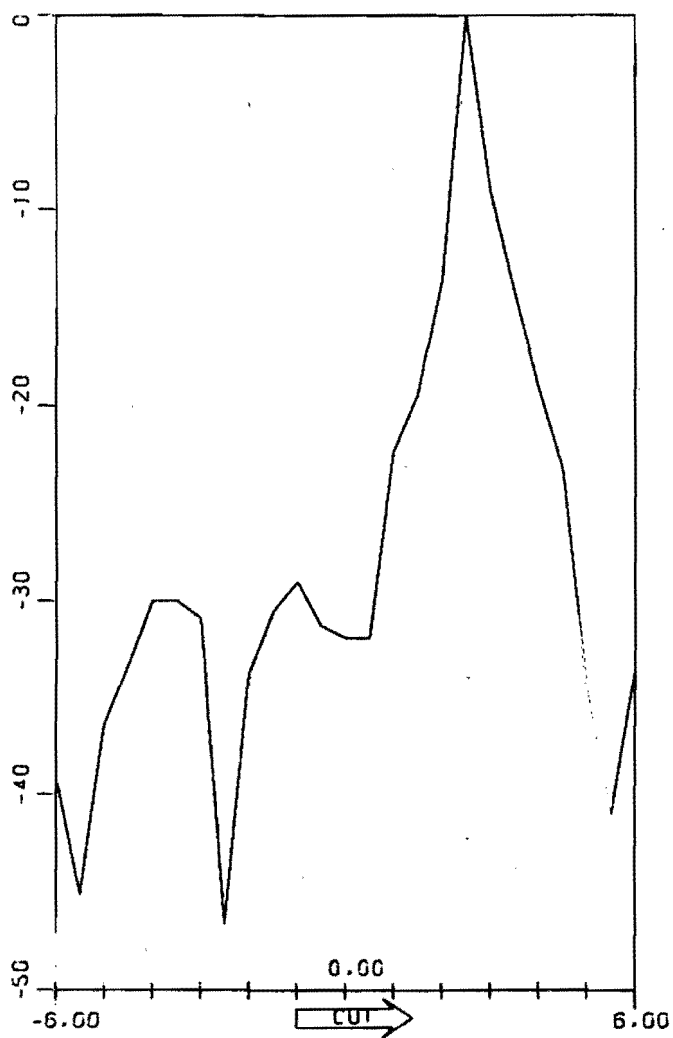


Figure 5.5 High Resolution Beam-Jammer at 3°



## REFERENCES

- [1] B. Widrow, P.E. Mantey, L.J. Griffiths and B.B. Goode, "Adaptive Antenna Systems", Proceedings of the IEEE Dec. 1967 pp. 2143-2159.
- [2] Sidney P. Applebaum, Adaptive Arrays SPL TR66-1, Syracuse, New York, SURC August 1966.
- [3] Robert L. Riegler and Ralph T. Compton Jr., "An Adaptive Array for Interference Rejection", Proceedings of the IEEE, June 1973 pp. 748-758.
- [4] J.W. McIntyre, Special Report, Tracking and Data Relay Satellite Telecommunication Link Simulation, Initial Report, Laurel Maryland, Applied Physics Lab., Johns Hopkins University, CSC-1-465 Aug. 1975.
- [5] James E. DuPree, "An Algorithm for S/N Maximization in Adaptive Arrays", Appendix O of TRW proposal "Telecommunications Services via a Tracking and Data Relay Satellite System", prepared for NASA, Goddard Space Flight Center in response to RFP No. 5-34500/476.

# AN S-BAND PHASED ARRAY FOR MULTIPLE ACCESS COMMUNICATION

## APPENDIX

W. A. Imbriale and Gary G. Wong  
TRW Defense and Space Systems Group  
Redondo Beach, California

### Abstract

The S-Band multiple access phased array antenna will be used on the Tracking and Data Relay Satellite System (TDRSS) is described. The antenna consists of a 30 element array with 10 elements multiplexed between transmit and receive and 20 elements dedicated to receive. For transmit a single antenna beam is formed. For receive, a ground implemented beam-former is used to provide 20 simultaneous beams. This paper describes the system and provides substantial detail on the antenna element design.

### Introduction

A phased array for a synchronous orbit satellite differ in many aspects from a "conventional" design. The use of the limited field-of-view (FOV) and the desire to limit the number of elements due to weight and complexity considerations. In a "conventional" phased array design the suppression of grating lobes is of major importance and a closely spaced radiating element with a relatively small aperture size (low  $f/D$ ) is generally chosen. However, for a limited FOV or coverage it may only be necessary to keep the grating lobe out of the FOV permitting use of fewer elements with larger spacings which will simplify the electronics design.

Published studies on arrays for space application, involving hardware, are limited. Reference [1] by J. Brumbaugh et al describes an array of helices for space application, [2] by J. H. Nitardy et al introduces an adaptive array principle for satellite attitude control, [3] by S. H. Durrani describes an array of helices for maritime communications, and [4] by C. Chen describes a short backfire antenna for space application. Texas Instruments [5] has done studies of a helical array as well as some work on a multipurpose S-band spiral array using phase shifters. In addition, the European Space Agency (ESA) has been sponsoring array feasibility studies [6, 7] for aeronautical satellites and work on performance prediction with experimental verifications [8]. Some work is also reported by Anderson et al [9] on short backfire arrays for space communication. A good review of the subject is given by W. H. Kummer and A. Kanpensky in reference [10].

This paper describes an S-band multiple access phased array antenna for use on the Tracking and Data Relay Satellite System (TDRSS). The Multiple Access antenna consists of a 30 element array with 10 elements multiplexed between transmit and receive and the remaining 20 elements dedicated to receive. For transmit, a single antenna beam is formed. The beam is steered by ground command of phase shifters in each of the ten transmit elements. For receive, a ground implemented beam-former is used to provide communication with 20 simultaneous users. The beams may either be adaptively controlled [11, 12] or open loop pointed to the user. Both techniques are currently under consideration for TDRSS but this paper only discuss the adaptive system and concentrate only on the antenna design and describe only briefly the electronics and adaptive processing.

### Multiple Access Antenna

The baseline MA antenna is a 30 element array. The elements are diplexed between transmit and receive

and the remaining 20 elements are dedicated to receive. The array is mounted on the body of the spacecraft and points to spacecraft nadir. All elements have been carefully arranged to minimize coupling and to obtain space clearance for mounting an additional reflector antenna onto a common fixed surface so that deployment of these antennas would not be necessary. The radiating elements are helices nominally triangularly spaced 13.5 inches apart as shown in Figure 1. On transmit, a single command steered antenna beam is formed. The

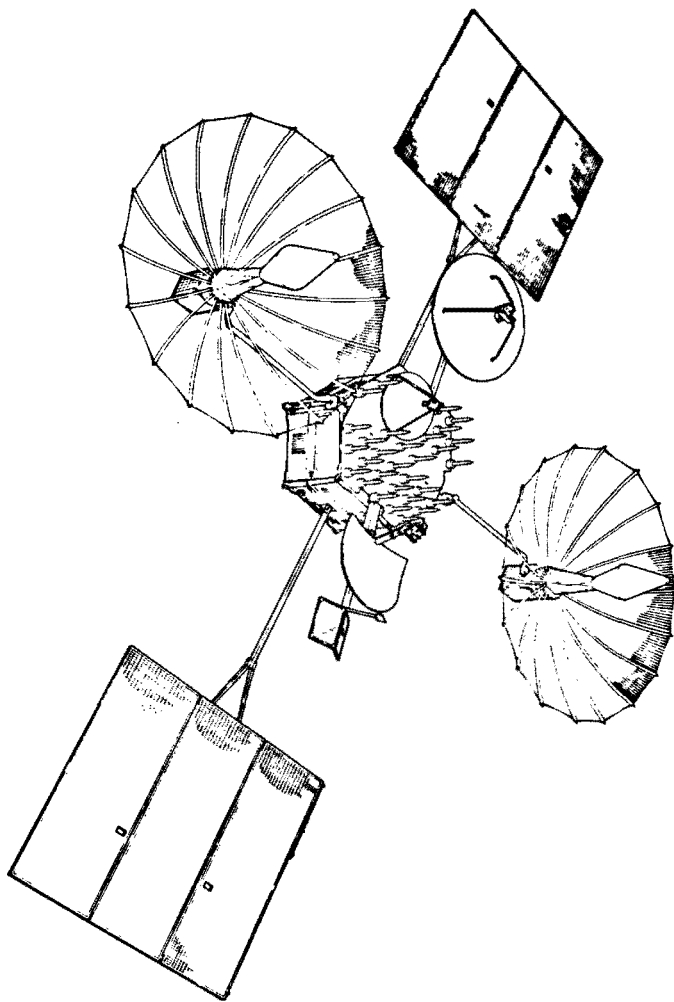


Figure 1. Layout of MA elements on TDRSS spacecraft.

beam is steered by ground command of phase shifters in each of the ten transmit elements. For the return link, signals from each of the MA users are received and preamplified at each of the 30 receiver elements, down-converted, and bandpass filtered to a common IF frequency. They are then frequency-division-multiplexed into 7.5 MHz center-to-center spacing, combined with other return signals and transmitted to the ground. Here they are demultiplexed and routed to beam-forming equipment, which synthesizes an adaptive beam pointing at each MA user.

All user satellite signals are pseudo-noise (PN) coded. The MA user PN code performs several functions. PN modulation spreads the user transmitter power to help keep the flux-density at the surface of the earth

below specified limits. Assigning a different quasiorthogonal code to each user greatly reduces mutual interference. Many MA users can share the same frequency band using PN code division multiple access (CDMA). Narrowband interference sources are also rejected by the PN code tracking receiver to the same extent as are other MA users. The return and forward link PN codes are made synchronous. Accurate range measurements of the communication path are available by comparing the relative phases of the transmit and receive PN code generators in the ground terminal.

The PN code tracking receiver modulates the input signal, noise, and interference with a synchronized version of the MA user code. The code is removed from the user signal, and any narrow band interference is modulated and spectrum spread. Interference from receiver or thermal noise is already broadband. The resulting narrowband MA user signal is then demodulated by a Costas-loop phase tracking receiver.

The NASA required field-of-view is  $\pm 13$  degrees referred to the earth center. Because of attitude control system errors, an additional  $\pm .5$  degrees coverage is needed for individual array element to meet NASA's specified FOV.

The transmit and receive bands are, respectively 2.1039 to 2.1089 GHz and 2.285 to 2.290 GHz. The transmit array is required to provide 23 dB gain over the FOV. Gain in dB for an array can be estimated from the equation  $G_a = 10 \log N_e + G_e$  where  $N_e$  is the number of array elements and  $G_e$  is the element gain in dB. Since 10 elements are used for the transmit array the element for this array must have a minimum gain of 13 dB over the  $27^\circ$  FOV. Similarly, the element required for the receive mode is also a minimum edge coverage of 13 dB. In addition, the following characteristics were specified: 1) Circular Polarization, 2) Low Axial Ratio ( $<1.5$  dB over the FOV), 3) 5 MHz Bandwidth and 4) Mechanical Simplicity. For the available space in the array, it was concluded that a traveling wave end fire antenna was best for these requirements, and an axial mode helical antenna was chosen.

### Element Design

In the TDRSS MA array, each array element must provide 13 dB of gain over the required  $\pm 13.5$  degrees field-of-view (FOV). It is desirable that the element design have its gain at the edge of the FOV or scan limit about 3 to 4 dB below the peak gain on boresight (along spacecraft nadir). Thus, the element should have a half-power beam width slightly less than the  $27$  degrees FOV. Thus, for this application, the peak element gain is approximately 16 dB.

Array element types evaluated fall into three categories: single-element, large subarray of low gain elements, and a small subarray of relatively high gain elements. This single-element does not have distribution network losses associated with the power divider and transmission lines and was therefore considered to be the prime candidate.

A number of designs were considered for the array element. Weight and size considerations preclude the conventional reflector and horn designs. For maximum gain within the available space, the axial mode helix and the short backfire antenna designs are the most qualified candidates. Candidate antennas were designed and fabricated for electrical performance evaluation. The test results showed that the long helical antenna provided acceptable gain with the smallest aperture and lightest weight. Short-backfire antennas were

eliminated because of their narrow bandwidth. The helix had the advantage of good bandwidth, inherent circular polarization, acceptable axial ratio and gain with mechanical simplicity.

However, in the presence of the conducting ground plane and surrounding elements, the helix behaves quite differently compared to its free-space performance. The conventional helix performance was substantially affected by the element spacing resulting in gain loss and axial ratio degradation. Since the TDRSS spacecraft has a very complex geometry (Figure 1) it is necessary to have an element whose pattern performance remains practically unchanged in the presence of other elements and surrounding structures. A technique whereby the end of the helix terminates in a cone spiral was used to attain low axial ratio performance over the required field-of-view and over both the transmit and receive frequencies. With the aid of spiral termination, the axial ratio was within 1 dB as opposed to 2.5 dB without a spiral termination. A large cup was used to help suppress the strong normal mode radiation near the base of the helix, leaving the axial mode traveling waves propagating efficiently along the helix. This resulted in lower sidelobe and reduced coupling performance. The selected helix geometry is shown in Figure 2. The critical dimensions are helix and cup diameters, and cup height. For good

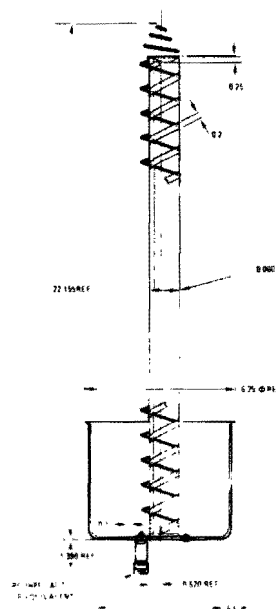


Figure 2. Helix Geometry

gain performance, the cavity diameter was chosen to be 6.0 inches and the cup height to be 5 inches. Larger diameter cups when tested, showed evidence of circular guide  $TE_{01}$  mode being radiated from the cavity and resulted in a pattern dip on axis. Small diameters or taller cups tested showed poorer gain performance accompanied by beam broadening. The helix has 19 active turns and 3 taper turns. The wire is supported by a triangular 2 ply Kevlar tube (.008 inches wall). The Kevlar is a light weight and thermally stable material which prevents excessive pointing variation due to varying orbital thermal exposure.

During the mechanical design study several configurations of helix wire support were considered. Holding the wire by a straight tube, or tubes with shallow or deep grooves were evaluated. In each case, the thermal protective paint degrades the coverage ga

formance. For straight tube, the gain degradation most pronounced; as much as .8 dB. The thermal t had no effect on a triangular support tube. this reason, the triangular support configuration selected.

The helical radiating element is fabricated from a 1-inch diameter beryllium copper wire wound into a 4-inch diameter helical pattern. The pitch angle 2 degrees; spacing per turn is 1.06 inches. The re structure is thermally protected by a thin coat (1) of SI3GL0 zinc oxide silicone base paint. The nna element is matched to a 50 ohms line via a le quarter wavelength coaxial transformer which has designed with a TNC connector input. Over the ating frequencies, the measured input VSWR is less 1.2:1. A picture of the helix element is shown in re 3.

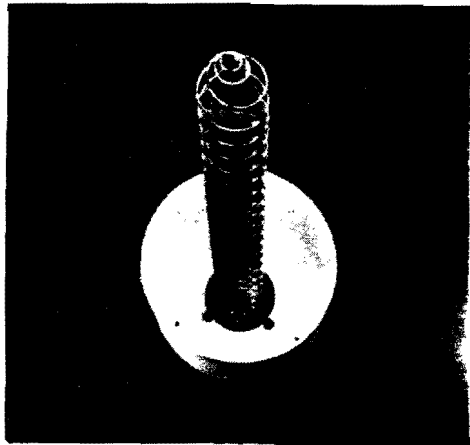


Figure 3. Helix element

Critical evaluation of the element performance in space included the detailed measurement of input , gain, and axial ratio characteristics over the ating frequencies. The element was also evaluated 7-element cluster (see Figure 4) to insure the

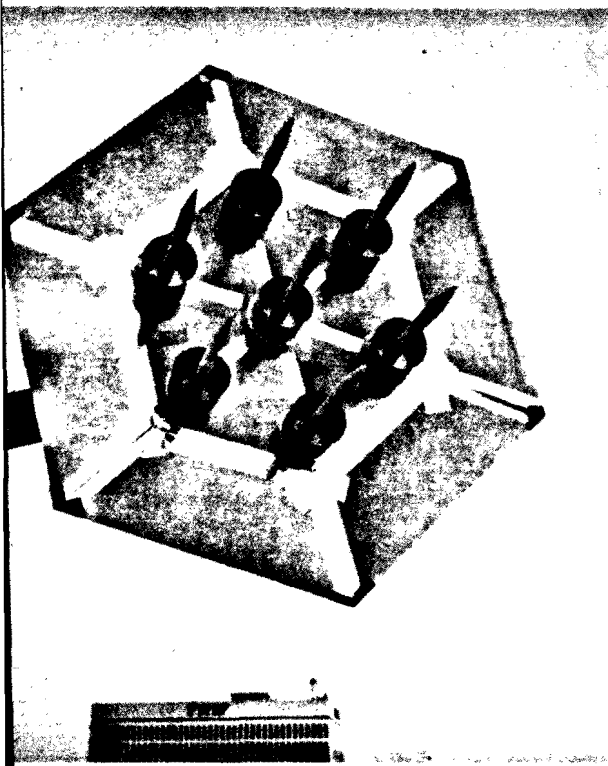


Figure 4. Seven-element cluster

effect of conducting ground plane and the effect of mutual coupling from the neighboring elements were included. Pattern and gain measurements were made for a number of array element spacings from 7.5 inches to 13.5 inches. The result of the tests established the optimum minimum spacing of 11.5 inches. For conserva- tive-reasons the element spacing of 13.5 inches was selected. Shown in Figure 5 is the measured gain in the array environment vs spacing. The FOV (13.5°) gain is greater than 13 dBi for all spacing and the axial ratio is less than 1.0 dB over the field-of-view as shown in Figure 6. Figure 7 and 8 show the measured element patterns in the seven-element cluster in comparison with the single element pattern.

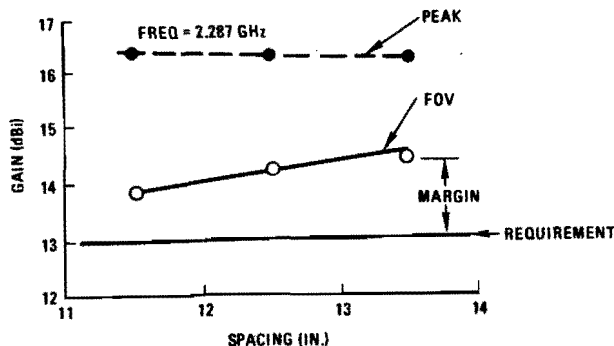
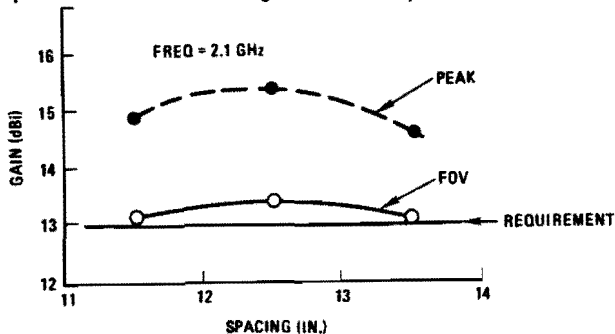


Figure 5. Measured gain of helix in 7-element cluster

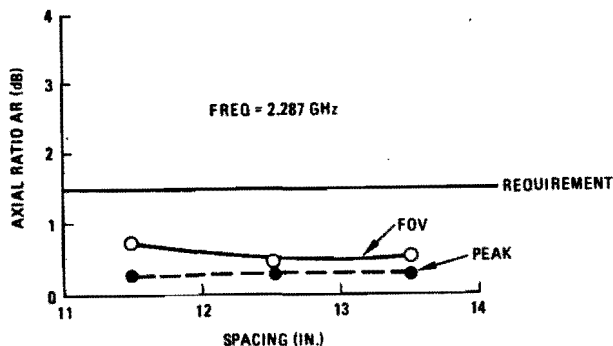
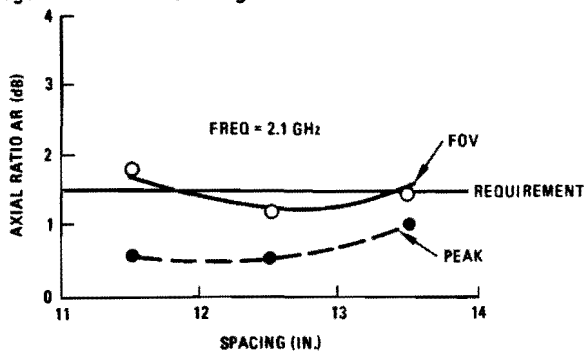


Figure 6. Measured axial ratio of helix in 7-element cluster

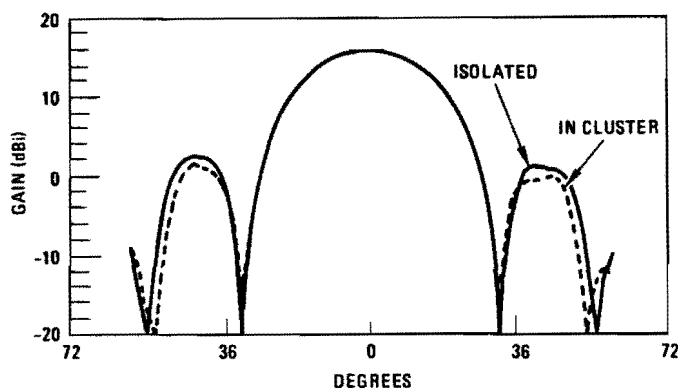


Figure 7(A) Comparison of MA helix element patterns measured isolated and in 7-element cluster, spacing = 13.5 inches.

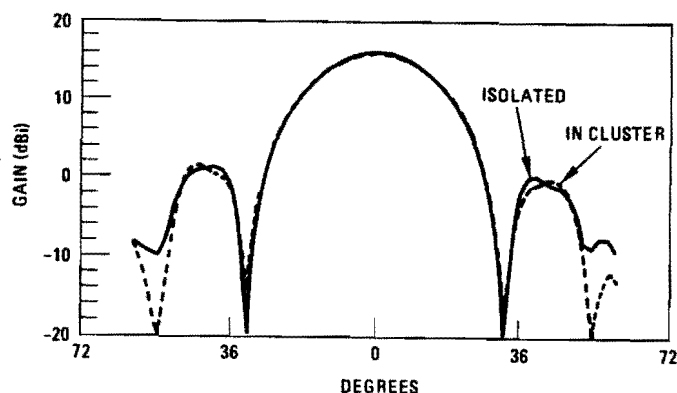


Figure 7(B) Comparison of MA helix element patterns measured isolated and in 7-element cluster, spacing = 11.5 inches.

#### Transmit Array

Ten elements are used for the transmit array. To prove out the design a ten element breadboard array as shown in Figure 9 was fabricated and tested.

Elements were mounted on a 48" x 48" ground plane in an equal triangular grid with 14 inch separations. A schematic block diagram of the array is shown in Figure 10. Each channel was a TTL controlled 4-bit phase shifter and a transfer switch. A 10 way power divider is used to sum the 10 channel signals. All these electronic devices are mounted behind the array ground plane. The array element used in this test was

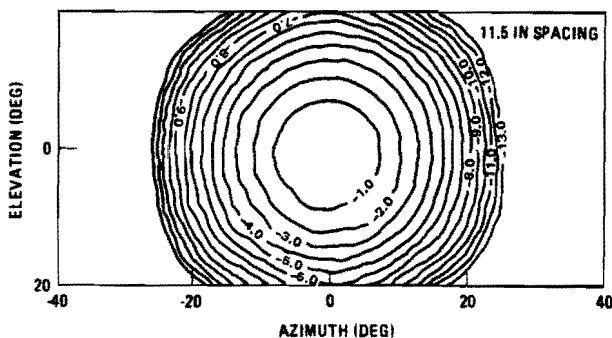
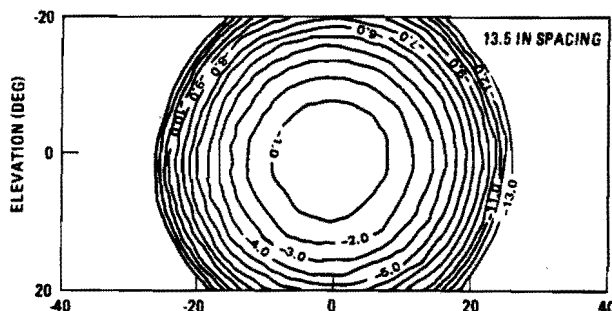
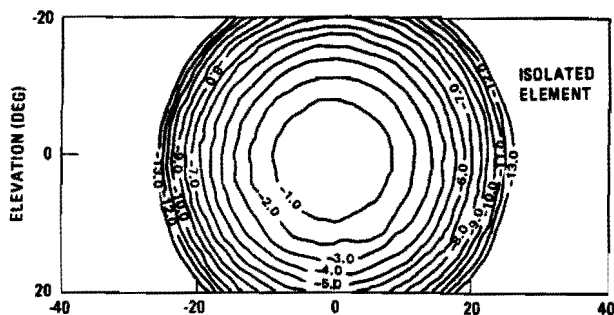


Figure 8. Measured contours of MA helix element isolated and in 7-element cluster (contour levels are in relative dB)

an earlier design having a long tapered tip and a shallow feed cup and the 14 inch separation was based upon the analytical and test results of an active element in a 7-element cluster environment. Subsequently in the element design with the short tapered tip and an enlarged cup it was shown that a spacing of 13.5 inches could still achieve the required 13 dB element gain. This spacing was, therefore, chosen for the final array design depicted in Figure 1.

The array measurements were taken in an anechoic chamber with a HP9601 computer controlled automatic test facility. The phase shifters and switches were also computer controlled. Contour measurements were made of each individual element and the array pattern for several beam positions. A typical active element pattern is shown in Figure 11. Figure 12 shows the boresight beam and Figure 13 the beam scanned to  $\theta=15^\circ$ ,  $\phi=45^\circ$ . Observe that the grating lobes can be equal to or even greater than the desired beam. However, the gain in the desired direction meets the specified requirements. This is a significant result since one might be concerned that the array gain would be very sensitive to scan angle in the presence



Figure 9. Photo of the 10-element array.

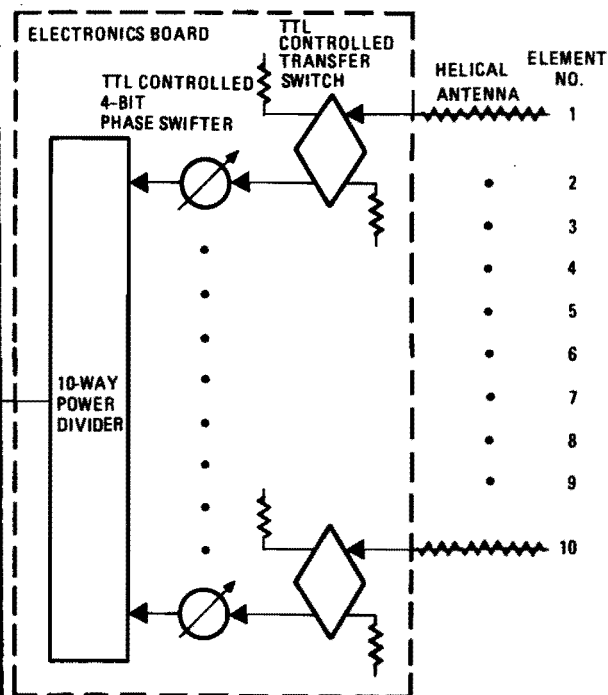


Figure 10. Schematic diagram of 10-element array  
1 coupling effects. The gain does not appear to  
versely affected by mutual coupling effects beyond  
expected by the approximate formula,

$$G_a = G_e + 10 \log N_e$$

It is also observed that the axial ratio of the  
ed array beam is much better than that of the  
idual elements. This is presumably due to the  
ging effects of the various polarization ellipses  
e individual elements.

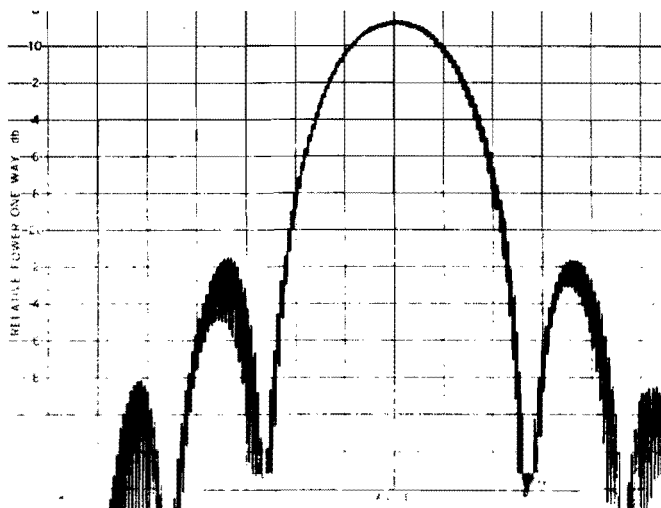


Figure 11. Typical active element pattern.

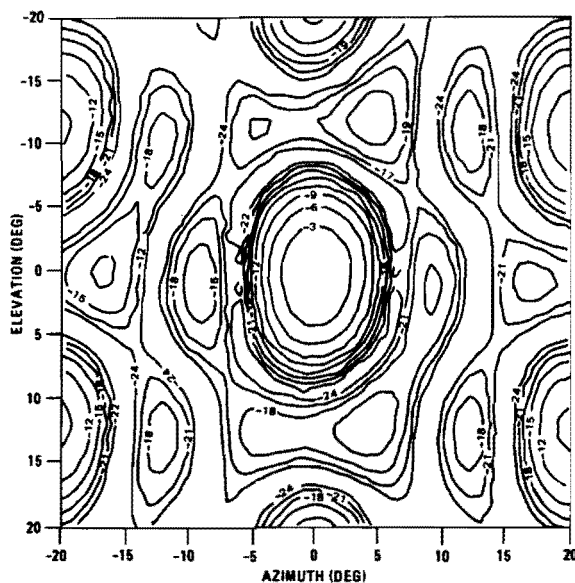


Figure 12. Performance of a boresight beam.

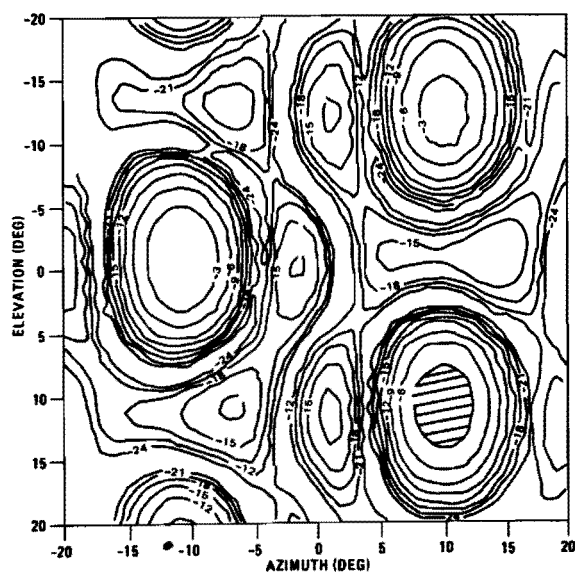


Figure 13. Performance of a scanned beam at (15°, 15°)

## Receive Array

The receive antenna must service 20 users simultaneously over a 13.5 degrees FOV with each user having a 5 MHz bandwidth at a nominal center frequency of 2287.5 MHz. The antenna is left hand circularly polarized; axial ratio is 1 dB or less over the FOV. These requirements are met with an antenna having a nominal gain of 27 dB at edge of coverage.

The basic design shown in Figure 14, consists of 30 helical elements, preamplifiers, a frequency division multiplexer, a space-to-ground link, demultiplexer, and an adaptive beam forming network to generate the users output.

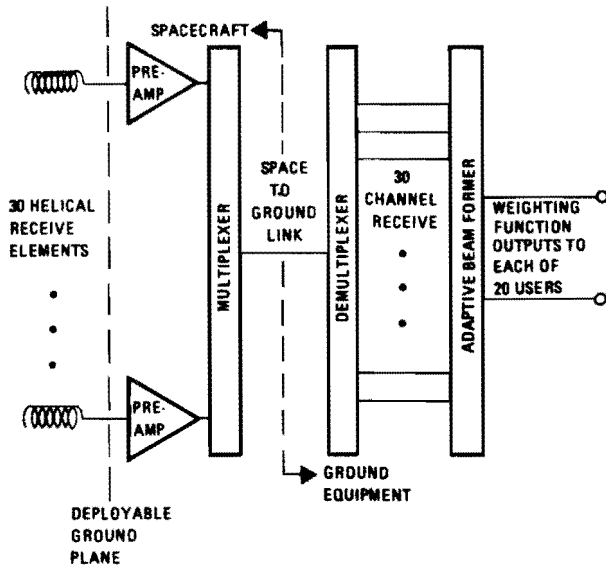


Figure 14. MA receive block diagram

The adaptive algorithm, theory of operation and system performance is documented in Reference [13] and the electronic hardware in Reference [14]. Only a very brief description of the adaptive beamformer and a few examples of pattern performance is presented.

A block diagram of the multiple access beamformer is viewed by a given user is shown in Figure 15. The major functional blocks are the remote beamformer, gradient measurement equipment, time shared micro-processor and PN receiver. The method of optimization is a gradient technique, starting from an initial weight estimate, measuring the gradient vector of the signal/noise ratio and advancing in the direction of the gradient until an optimum is reached. The interactive equation which describes the operation of the beamformer is,

$$\underline{\omega}(k+1) = \left( \underline{I} - \epsilon \underline{\phi}_{nn} \right) \underline{\omega}(k) + \epsilon G_0(k) \underline{\phi}_{yy} \underline{\omega}(k) \quad (\text{Eq. 1})$$

Where,  $\underline{\omega}(k)$ ,  $\underline{\omega}(k+1)$  are column matrices containing the weight functions (one per element) which form the beam of the phase and amplitude modulated array;  $\underline{I}$  is the identity matrix,  $\epsilon$  is the step size;  $G_0$  is the gain of the AGC amplifier; and  $\underline{\phi}_{yy} = \underline{\phi}_{ss} + \underline{\phi}_{nn}$  where  $\underline{\phi}_{ss}$  is the signal correlation matrix and  $\underline{\phi}_{nn}$  is the noise correlation matrix. For purposes of computer simulations the signal correlations are assumed to be related only to the relative path lengths to the elements and thus reduce simply to the phase differences between the elements. Thus, if  $\underline{V}$  is a column matrix of the phases

incident on the elements, then  $\underline{\phi}_{ss}$  is given by  $\underline{\phi}_{ss} = \underline{V}^T \underline{V}^*$  where  $\underline{V}^*$  is the conjugate of  $\underline{V}$  and  $\underline{V}^T$  is the transpose of  $\underline{V}$ .

Similarly  $\underline{\phi}_{nn} = \underline{I} N_0 + \sum_{i=1}^{NI} \underline{V}_i^* \underline{V}_i$  where  $N_0$  is the

noise at each element. NI is the number of interferers and  $\underline{V}_i$  is the matrix of incident phases due to the  $i^{\text{th}}$  interferer. Note that this simulation assumes isotropic array elements. This iterative equation may be viewed as implementing two loops - an inner loop which effectively forms the inverse of the  $\underline{\phi}_{nn}$  matrix

$\left( \underline{I} - \epsilon \underline{\phi}_{nn} \right) \underline{\omega}(k)$  and an outer loop which satisfies a constraint equation  $\left( G_0(k) \epsilon \underline{\phi}_{yy} \underline{\omega}(k) \right)$

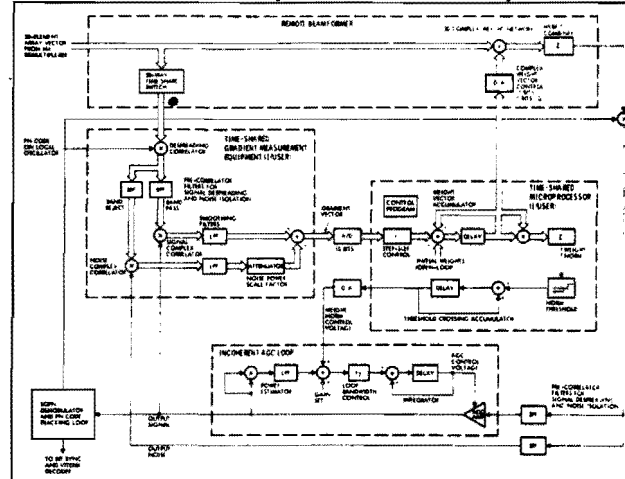


Figure 15. Multiple access remote beamformer.

As an example of the adaptive pattern performance let us consider a scenario with a 50 kbps user and five randomly placed 50 kbps interferers. This choice of scenario is extreme for TDRSS considerations since it has more 50 kbps users than specified by NASA. However, it is a simple, illustrative case. The interferers were selected to be 15 dB below the desired user and the desired user signal to thermal noise ratio selected as -7 dB before the array processing gain. Figure 16 shows the initial pattern before adaption and Figure 17 shows the adaptive patterns. A signal noise and interferer ratio improvement of .2 dB over what would be expected by open loop pointing was obtained. Because of the limited EIRP's and large PN spread spectrum processing gains, the TDRSS MA return link is dominated by noise. As a result dramatic improvements in the signal to noise ratio due to nulling of interferers by the adaptive system should not be expected.

## References

- [1] "Shaped Beam Antenna for the Global Positioning Satellite System", C. T. Brumbaugh et al, AP-S International Symposium Digest, Oct. 1976, pp 117-120
- [2] "Appa: A Phased Array System Designed for Space Application", J. H. Nitardy et al, IEEE Trans. on Aerospace and Electronics Systems, Vol AES-6 No 4 July 70 p 575.
- [3] "Maritime Communications via Satellites Employing Phased Arrays", S. H. Durrani, IEEE Trans. on Aerospace and Electronics, Vol AES-9 No 4 July 1973 p 504.
- [4] A Canonical Phasing Technique for Phase Compens-



on of Circularly Polarized Array Antennas" C. C. and Taro Yodakawa, AP-S International Symposium Oct. 1976, pp 149-152.

"Airborne Electronically Steerable Phased Array" Report (Texas Instruments) July 1972 NASA-CR-11 FICHE N73-18219.

"Planar Array for an Aeronautical Satellite" Report (Siemens AG) March 1974 ESTEC Contract 73 SK.

"Planar Array Antenna Study" Final Report (Monsen CSF) Nov. 1974 ESTEC Contract 1929/73 SK.

"Antenna Arrays Using High Gain Element Radiators" Report (LM Ericsson) April 1974 ESTEC Contract 73 HP.

"Short Backfire Antenna Arrays for Space Communications", A. Anderson et al, AP-S International Symposium Digest, June 1977 pp 194-197.

[10] "Phased Array Antennas for Applications on Spacecraft", W. H. Kummer and A. Kanpensky, Phased Array Antennas edited by A. A. Oliner and G. H. Knittel, ARTEC HOUSE, Inc.

[11] "Adaptive Ground Implemented Phased Array" (AIL) Final Report Contract No NAS 5-21653 Feb. 1973.

[13] "Tracking and Data Relay Satellite Telecommunication Link Simulation", J. W. McIntyre Initial Report Applied Physics. Laborator John Hopkins University CSC-1-465 Aug. 1975 Prepared for NASA Goddard Space Flight Center.

[13] "Telecommunications Services Via Tracking and Data Relay Satellite System", TRW Systems Group Proposal in response to RFP No 5-34500/476, Goddard Space Flight Center, Jan. 1976, Appendix O.

[14] "Telecommunications Services Via a Tracking and Data Relay Satellite Systems", TRW Systems Group Proposal in response to RFP No 5-34500/476 Goddard Space Flight Center Jan. 1976 Vol 2.

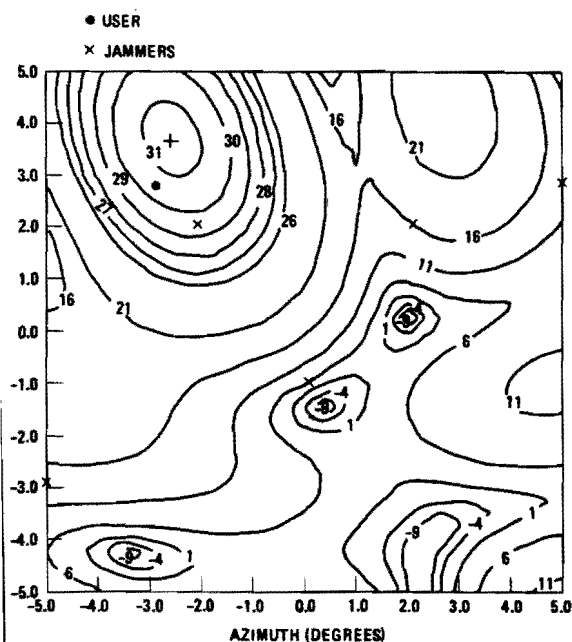


Figure 16. Multiple interference scenario: Initial patterns, one 50 KBPS user, five 50 KBPS interferers randomly placed.

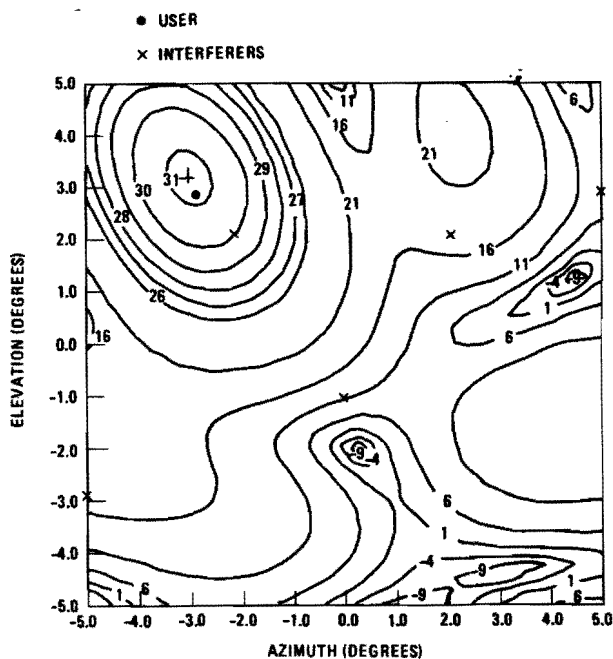
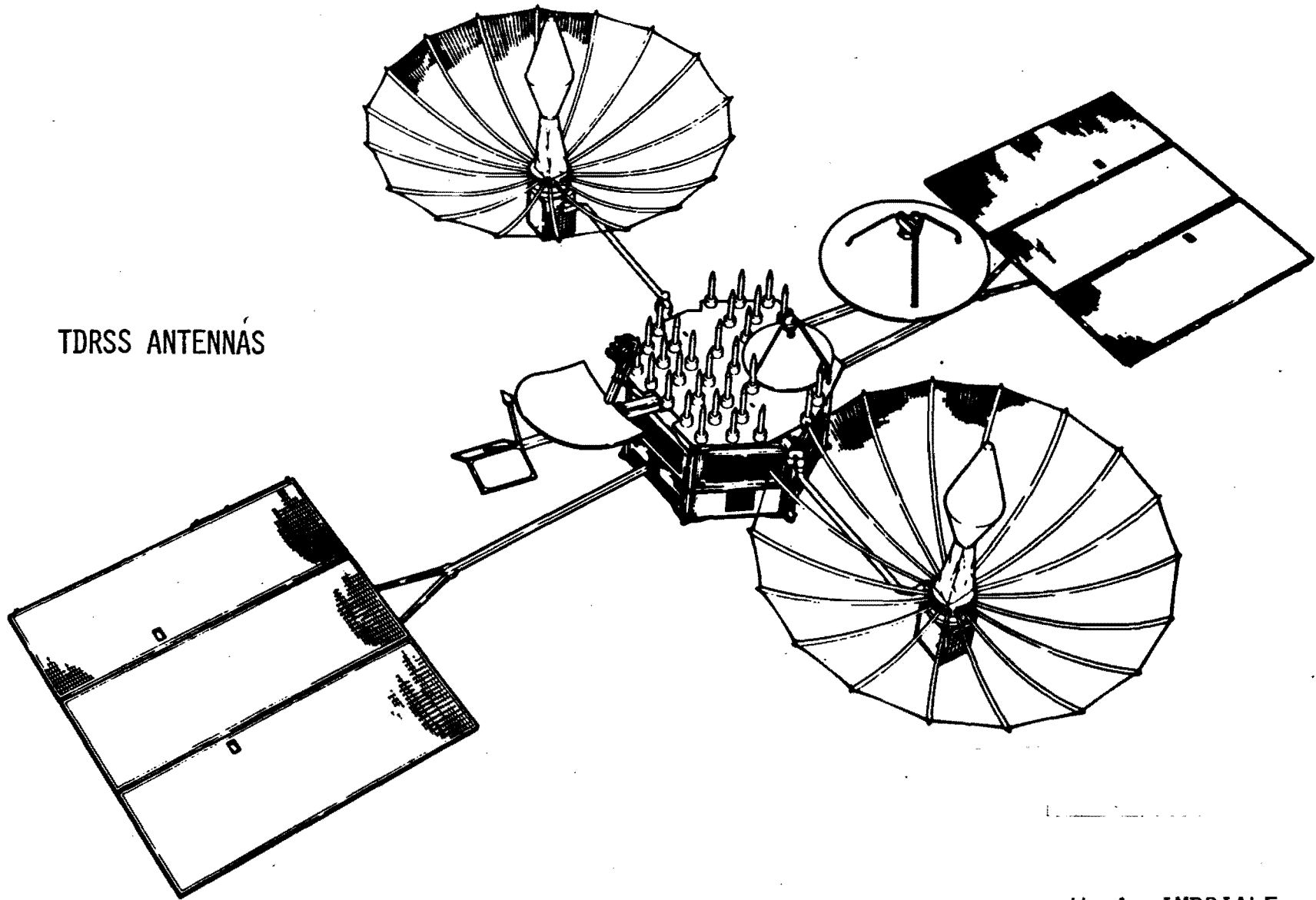
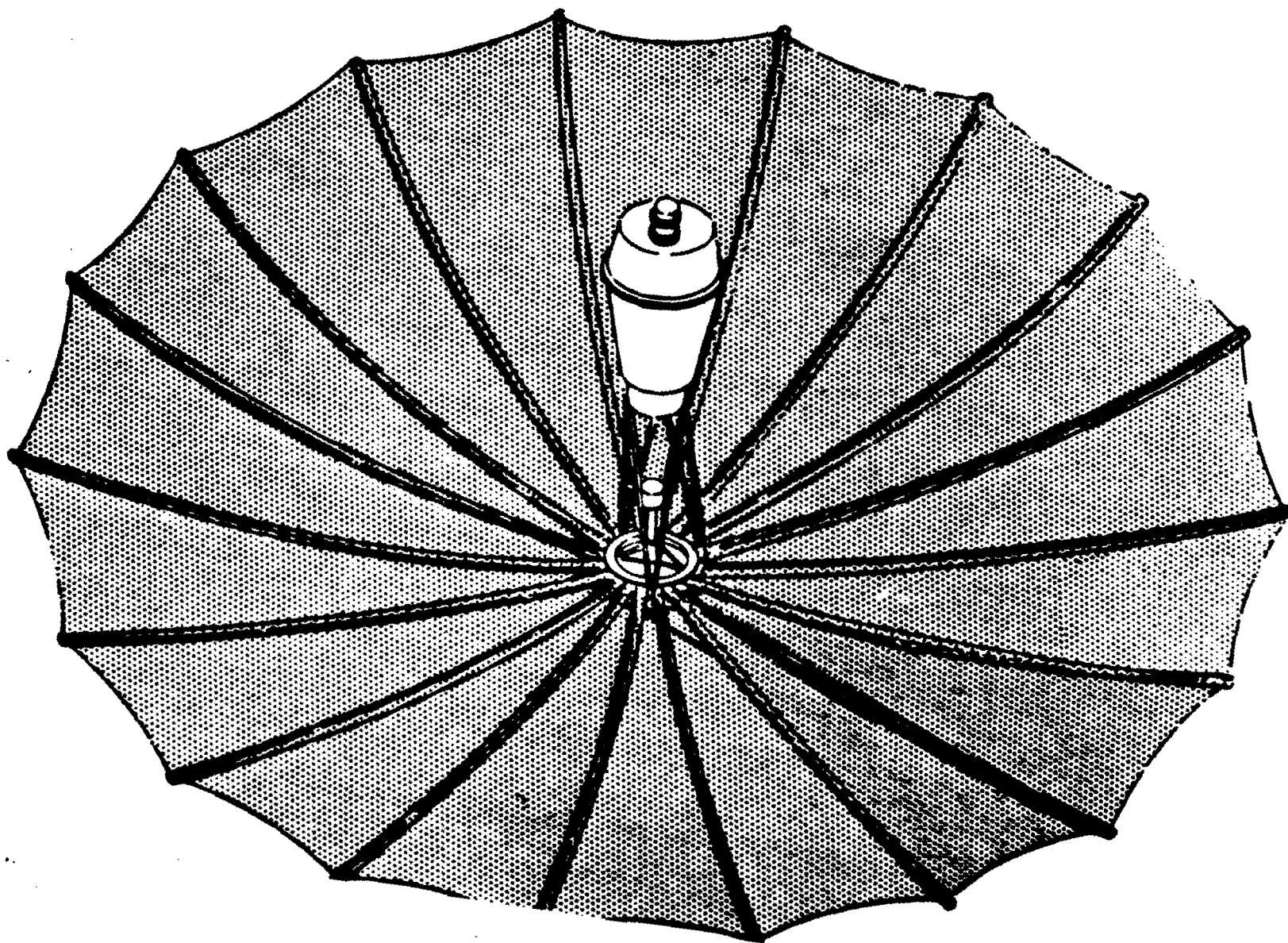


Figure 17. Multiple interference scenario: Adapted patterns, one 50 KBPS user, five 50 KBPS interferers randomly placed.

TDRSS ANTENNAS



W. A. IMBRIALE  
AUGUST 26, 1982  
VIEWGRAPHS



## DESIGN CONFIGURATION OVERVIEW

- HUB AND MECHANICAL DEPLOYMENT SYSTEM
- RIB ASSEMBLY
- REFLECTIVE SURFACE DESIGN
- SUPPORT TRUSS DESIGN
- RADOME DESIGN
- RIB RESTRAINT STRUCTURE/RELEASE SYSTEM
- FEED SYSTEM

INBOARD INTERCOSTAL  
49 STRAND INVAR

FRONT MESH  
GOLD PLATED  
MOLYBDENUM

GRAPHITE STRIP  
GOPE BORDER

FRONT QUARTZ  
CORD

CORD-TO-CORD  
TIES

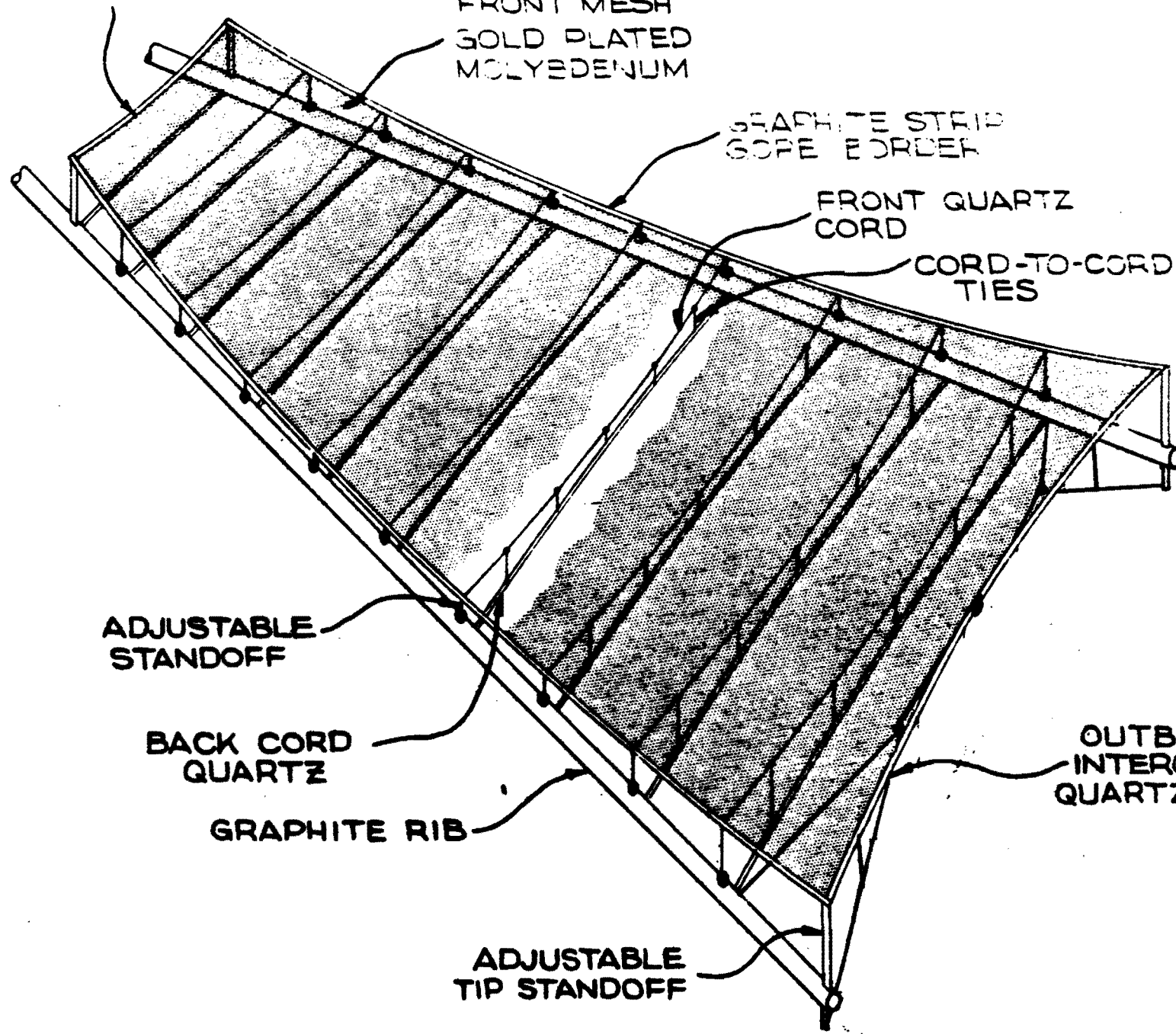
ADJUSTABLE  
STANDOFF

BACK CORD  
QUARTZ

GRAPHITE RIB

OUTBOARD  
INTERCOSTAL  
QUARTZ CORD

ADJUSTABLE  
TIP STANDOFF





## KU-BAND FEED ASSEMBLY

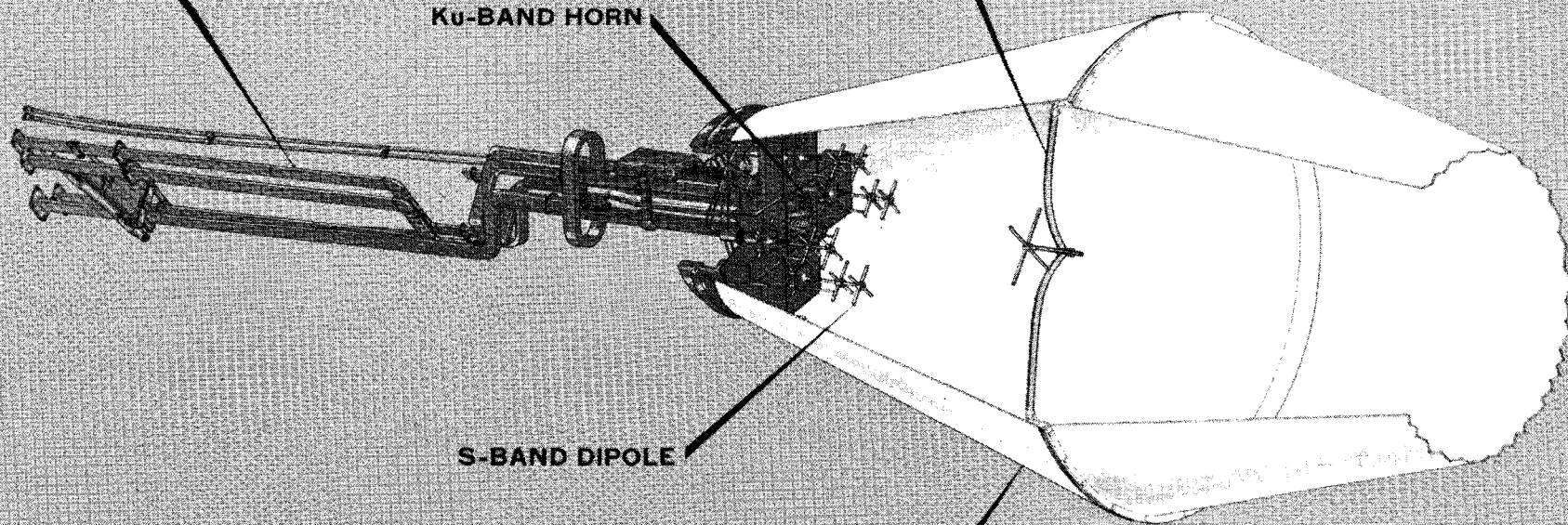
WAVEGUIDE  
FROM  
SPACECRAFT

SHAPED SUBREFLECTOR

KU-BAND HORN

S-BAND DIPOLE

RADOME



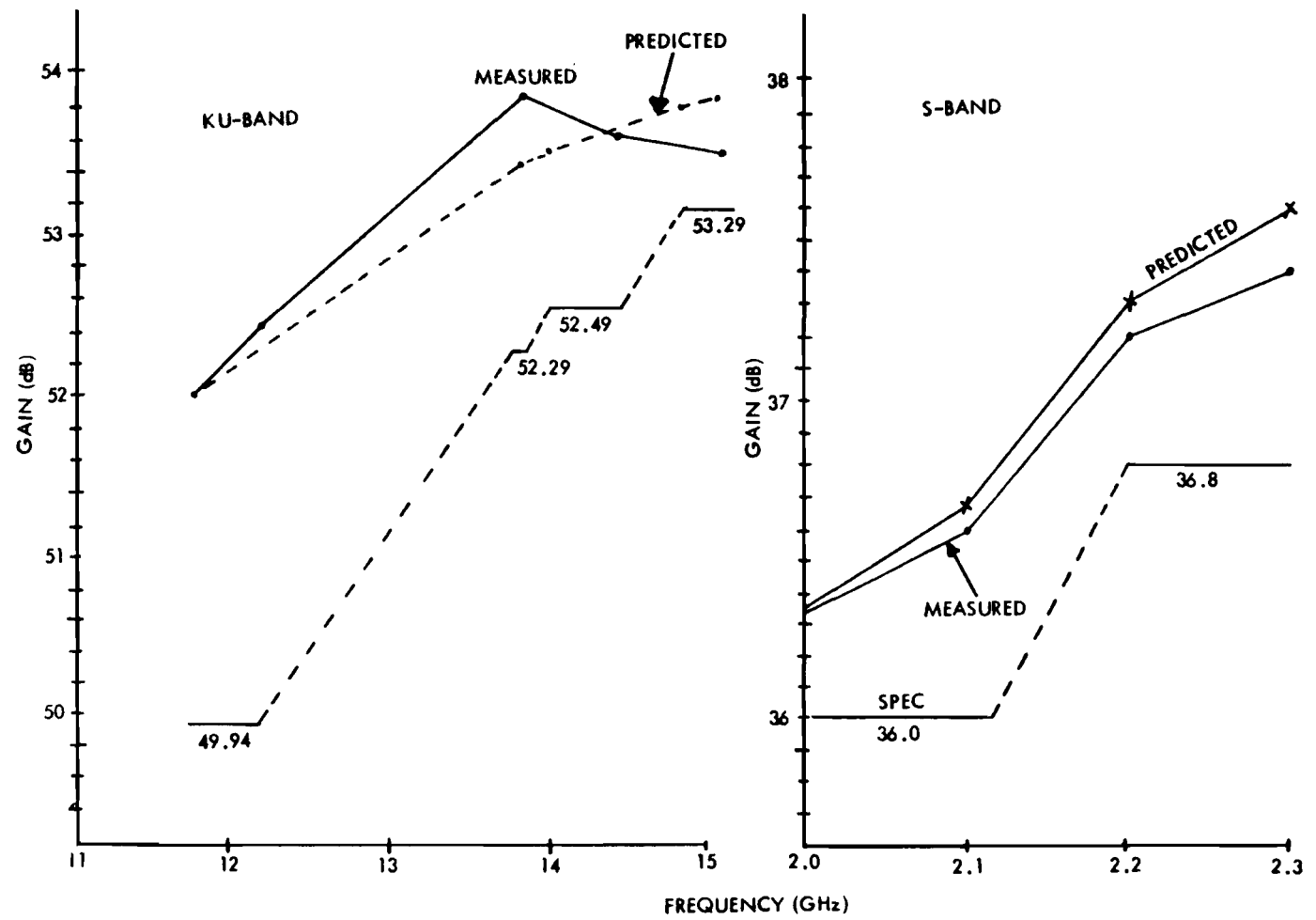


Figure 6.3.2.10. Gain Versus Frequency (Predicted and Measured Versus Specification)

## MULTIPLE ACCESS REQUIREMENTS

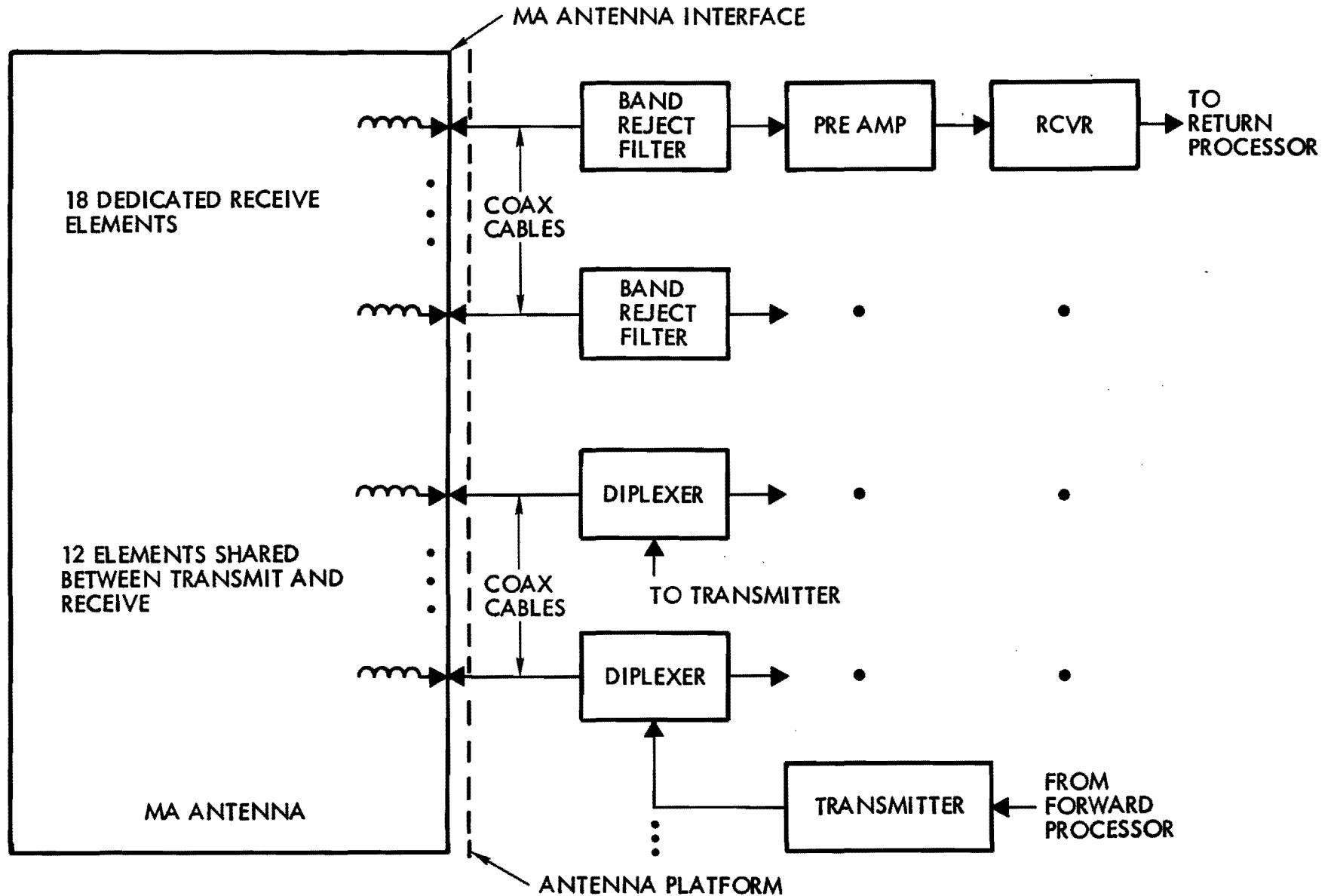
- MULTIPLE USERS IN SAME FREQUENCY BAND  
20 USERS S-BAND 2287.5 MHz
- MOBILE USER  $1^\circ$ /MINUTE ANGULAR MOTION
- CCIR FLUX DENSITY RESTRICTIONS LIMIT USER EIRP
- SPREAD SPECTRUM ENVIRONMENT
- $27^\circ$  CONICAL FIELD OF VIEW - EARTH COVERAGE PLUS LOW ORBITS
- STATIONARY ORBIT FOR TDRS
- TDMA FORWARD LINK

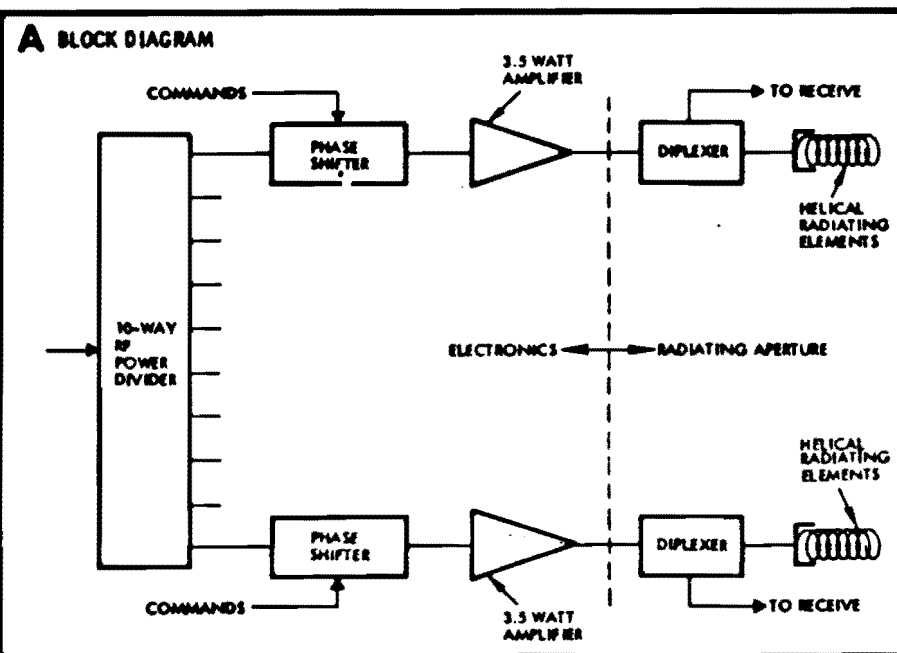


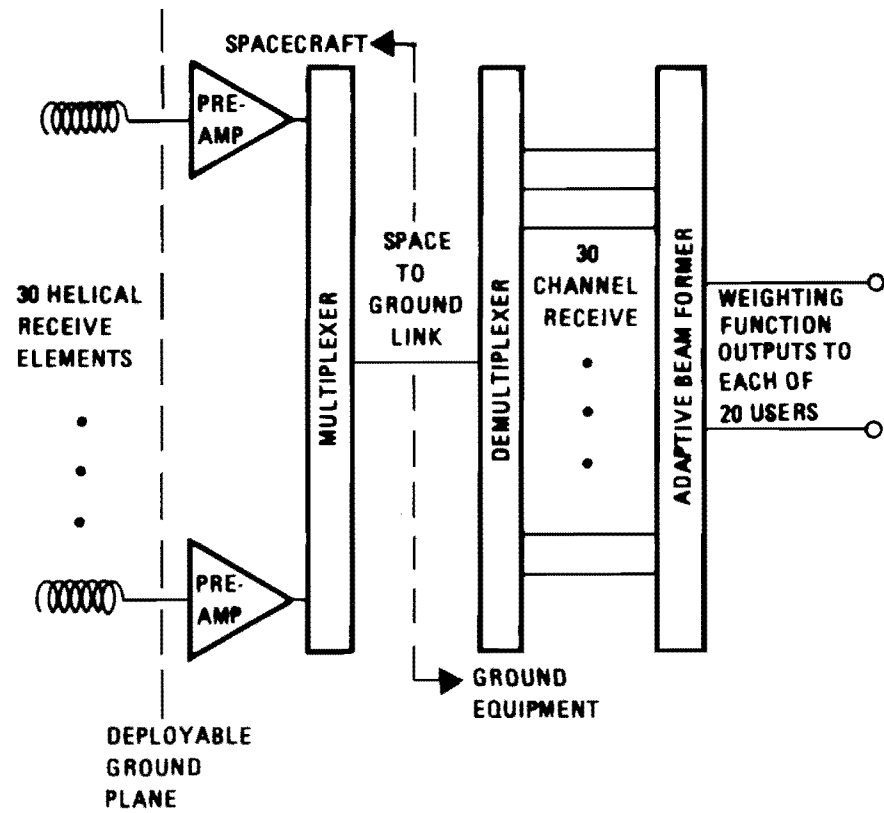
## MULTIPLE ACCESS ANTENNA IMPLEMENTATION

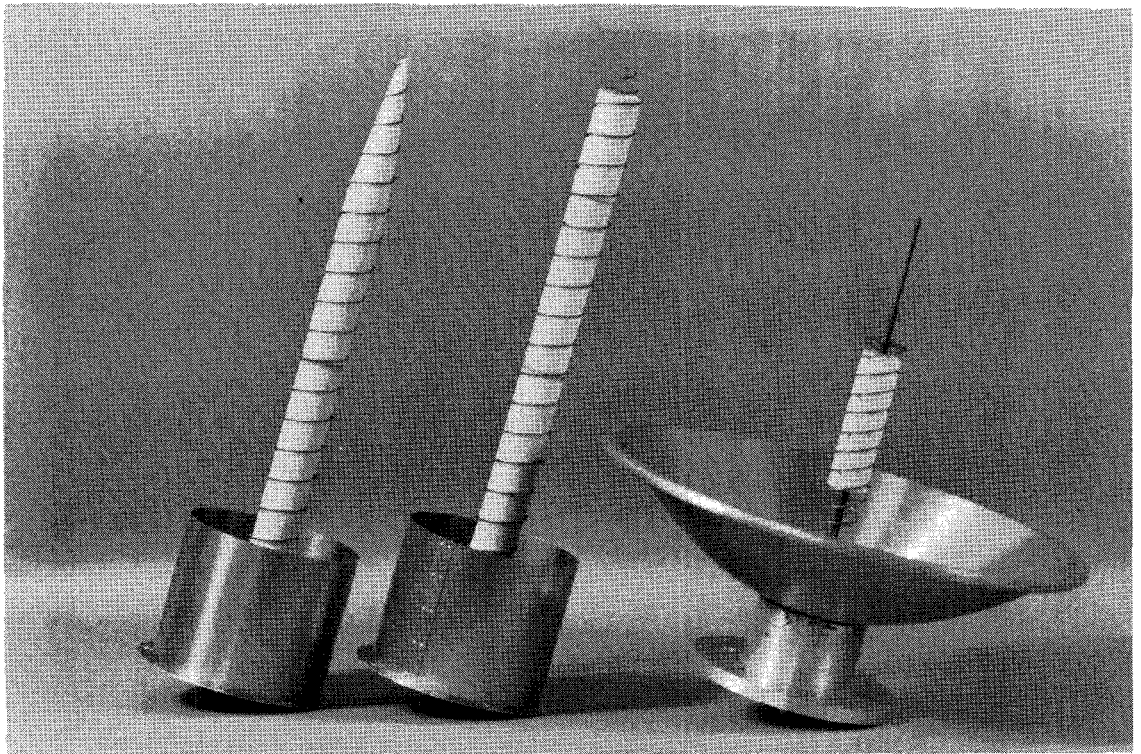
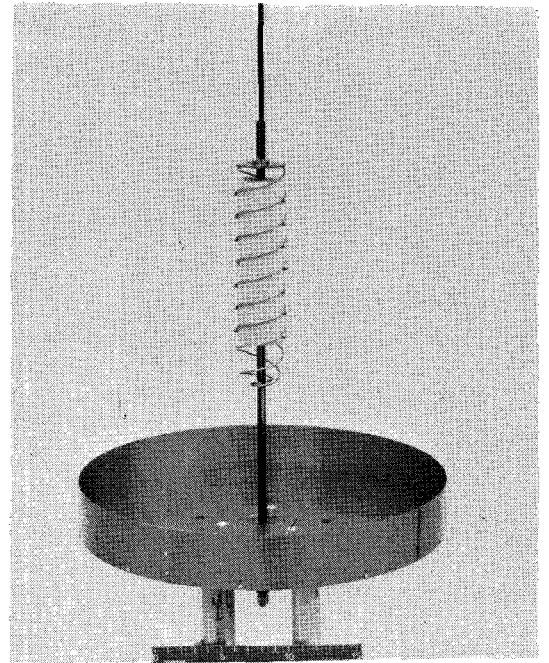
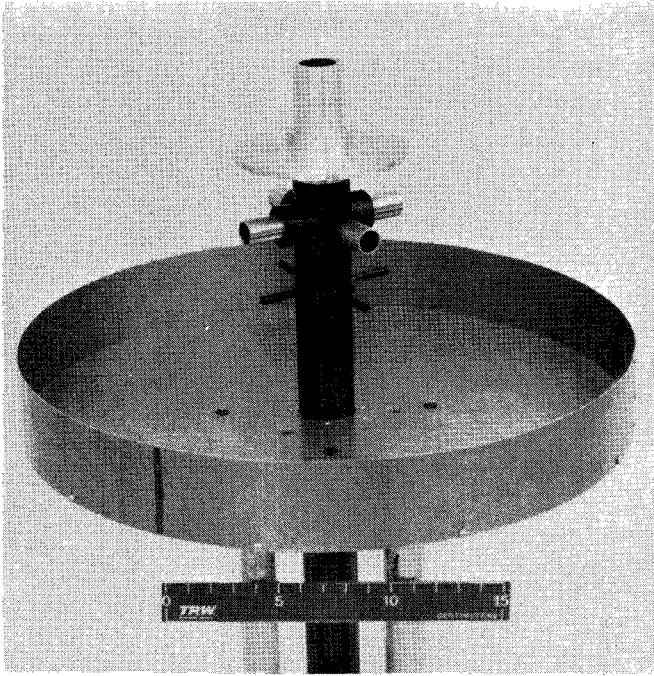
- 30 ELEMENT PHASED ARRAY
  - 30 ELEMENTS USED FOR RECEIVE
  - 12 ELEMENTS DIPLEXED FOR TRANSMIT
- 16 DB GAIN HELICAL ELEMENTS
  - 13 DB AT EDGE OF COVERAGE ( $\pm 13.5^\circ$ )
  - 1 DB AXIAL RATIO IN FORMED BEAM
- PHASE SHIFTERS GROUND CONTROLLED FOR TRANSMIT BEAM
- MULTIPLEXER - DEMULTIPLEXER LINK FOR TRANSFER OF RECEIVE ARRAY CHANNELS TO GROUND STATION
- GROUND CONTROLLED PROCESSING TO FORM INDIVIDUAL BEAMS FOR 20 USERS

# MA ANTENNA BLOCK DIAGRAM



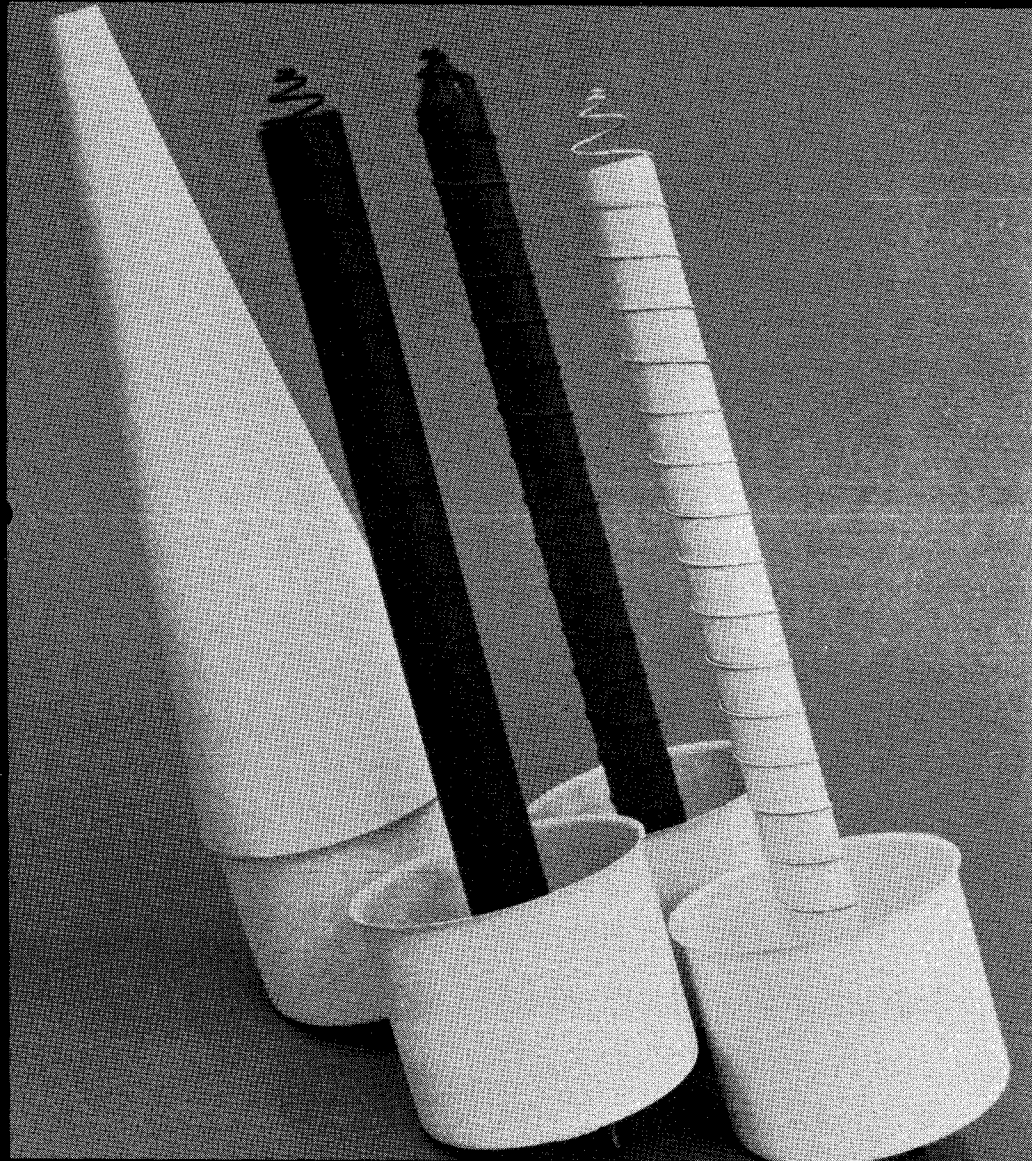


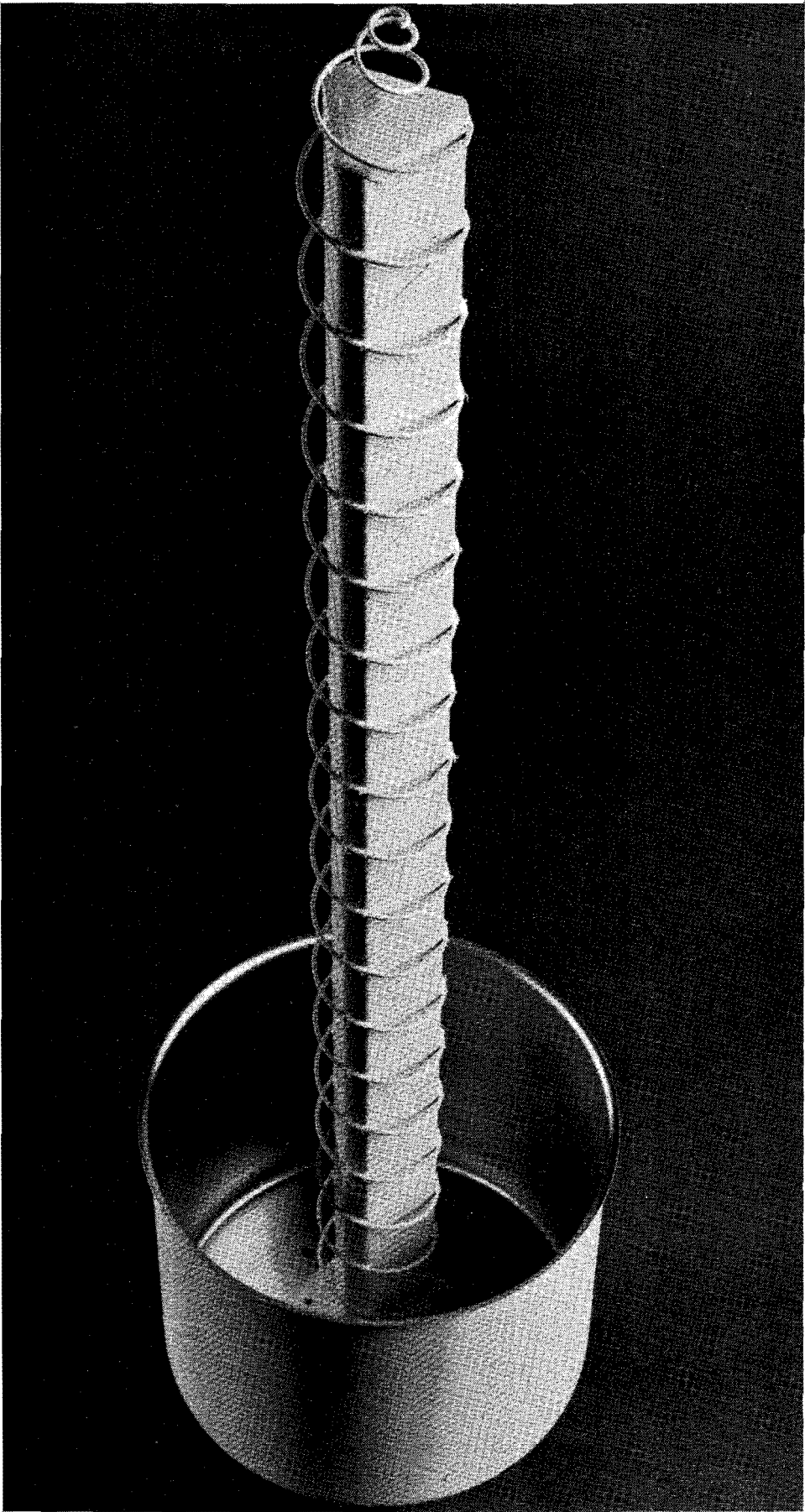


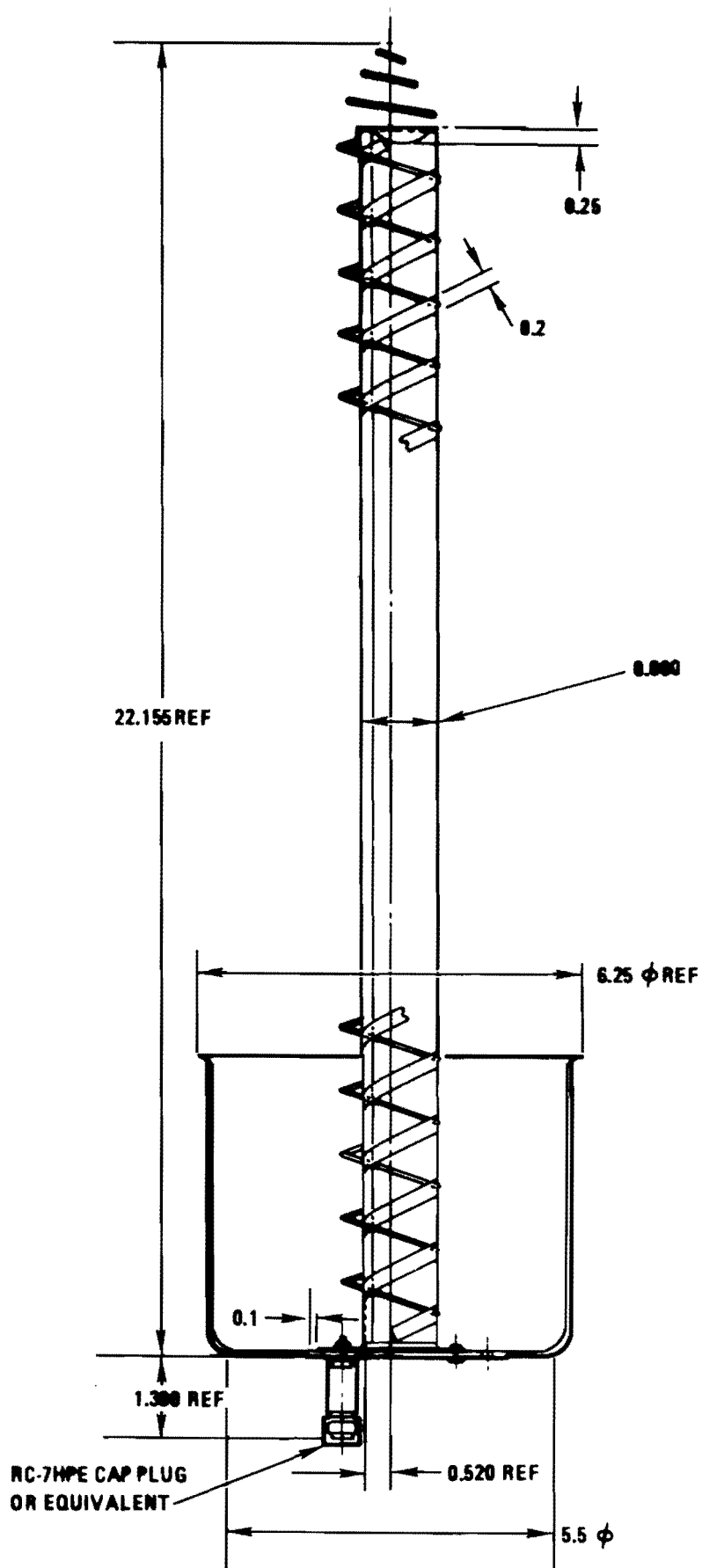


- Antennas considered as possible candidates for MA element.
- (a) Short backfire with cross dipole feed.
  - (b) Short backfire with bifilar helix feed
  - (c) Long helices and reflector with bifilar helix feed

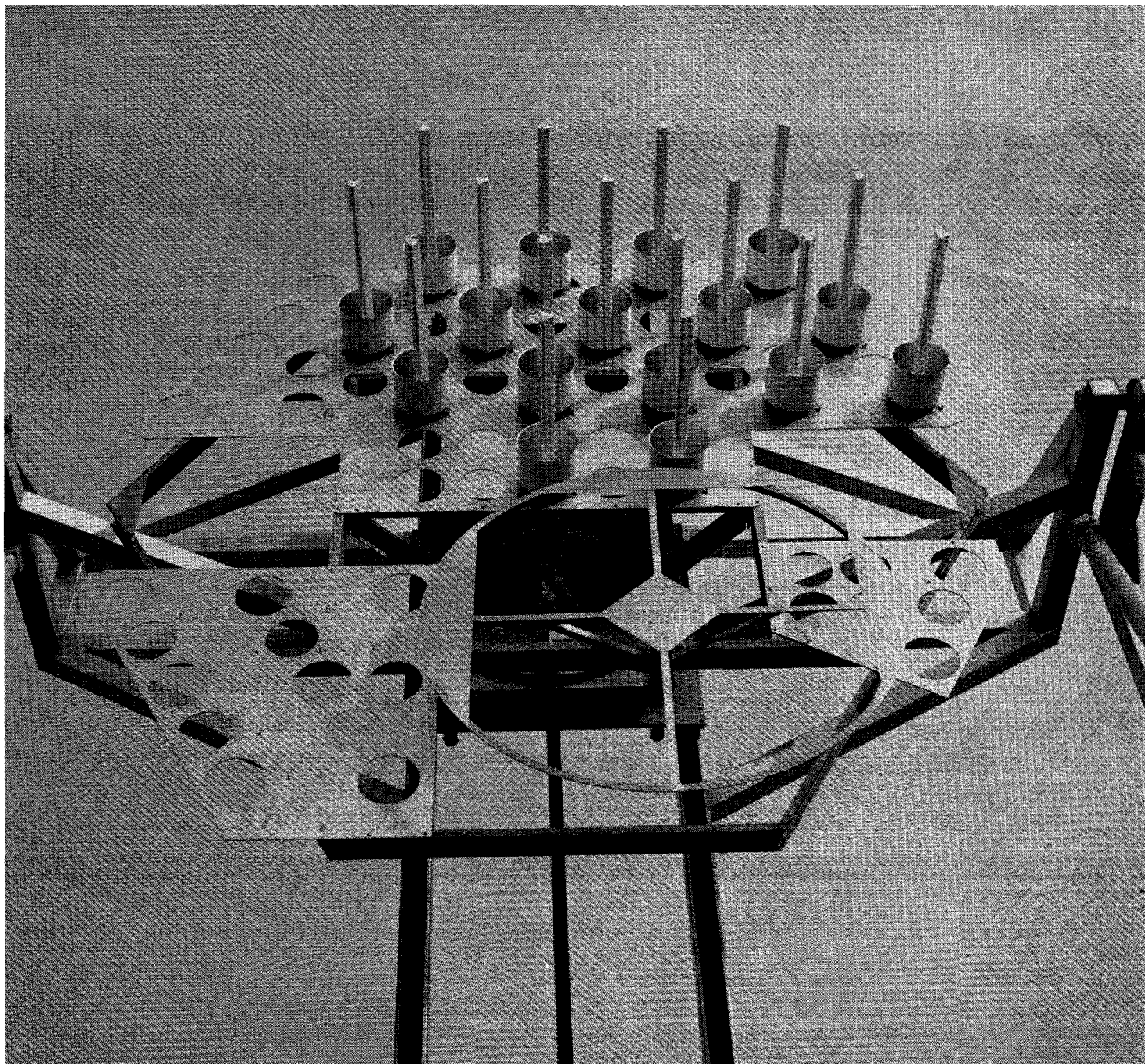
## ELEMENT CONFIGURATIONS EVALUATED









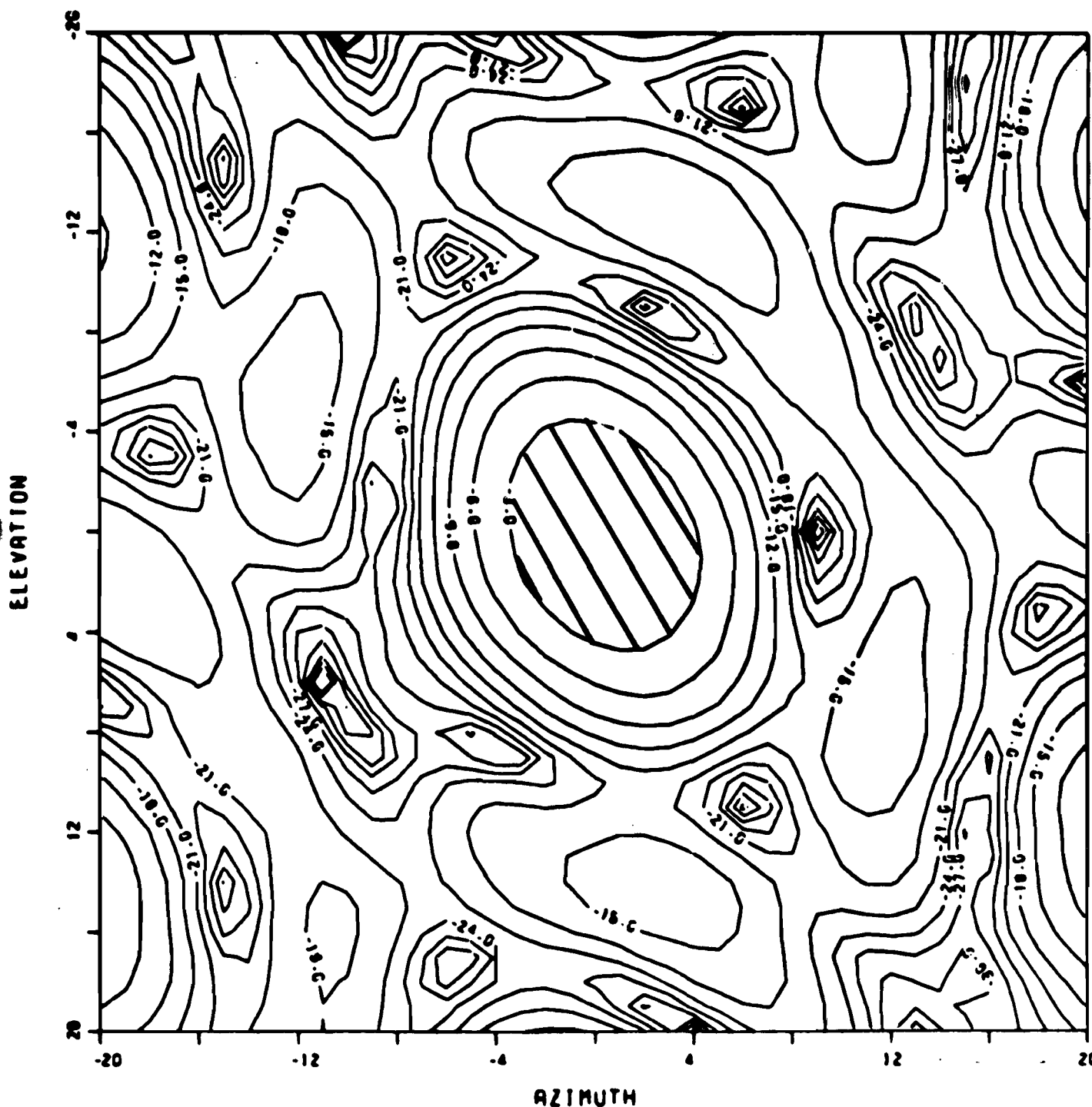


# MA TRANSMIT ARRAY RADIATION CONTOURS - MEASURED

SCAN ANGLE:  $AZ = 0^\circ$ ,  $EL = 0^\circ$

FREQUENCY: 2106.5 MHz

ACTIVE ELEMENTS: 4, 5, 9, 10, 11, 16, 17, 18

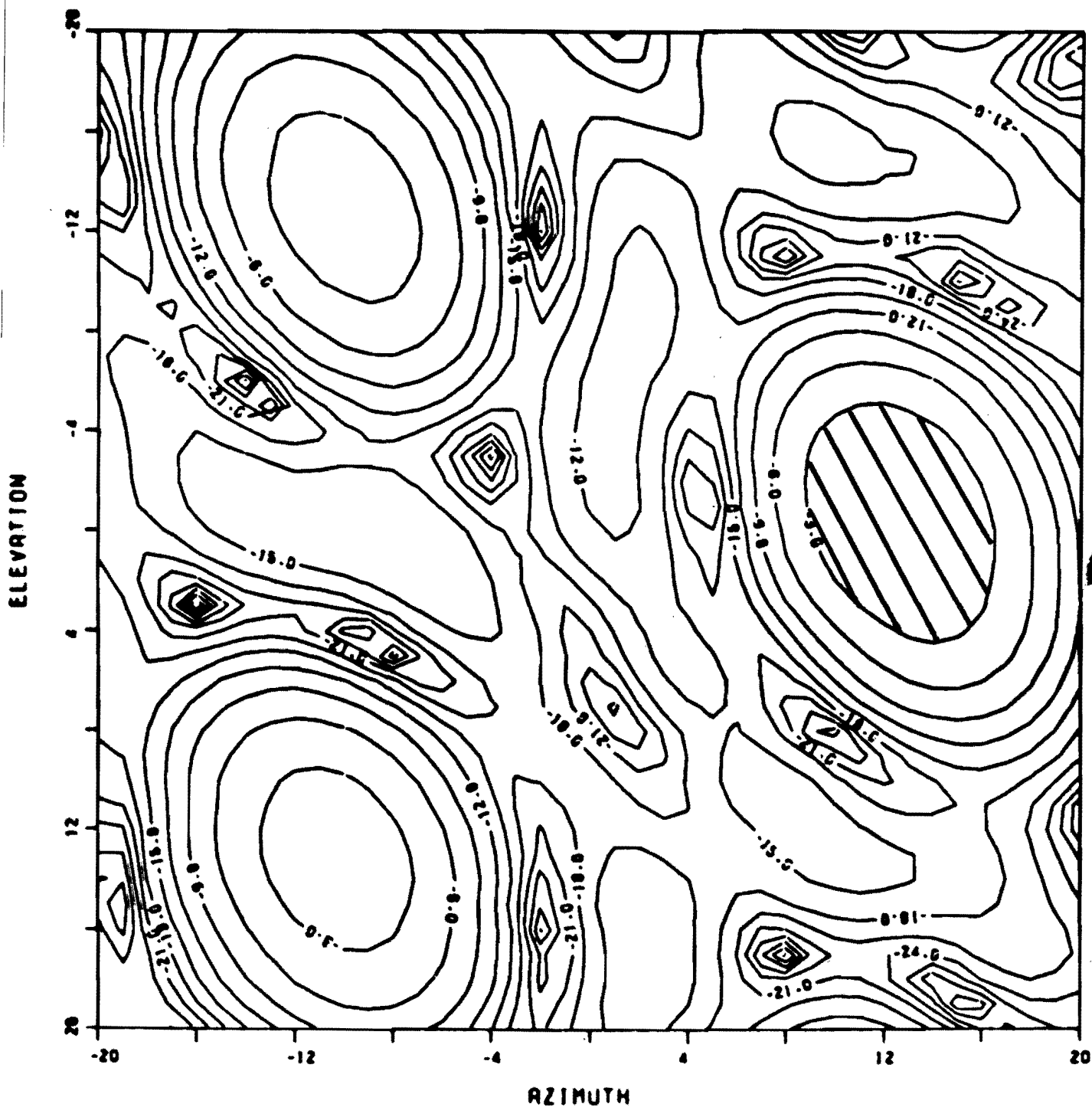


# MA TRANSMIT ARRAY RADIATION CONTOURS - MEASURED

SCAN ANGLE:  $AZ = 13.5^\circ$ ,  $EL = 0^\circ$

FREQUENCY: 2106.5 MHZ

ACTIVE ELEMENTS: 4, 5, 9, 10, 11, 16, 17, 18

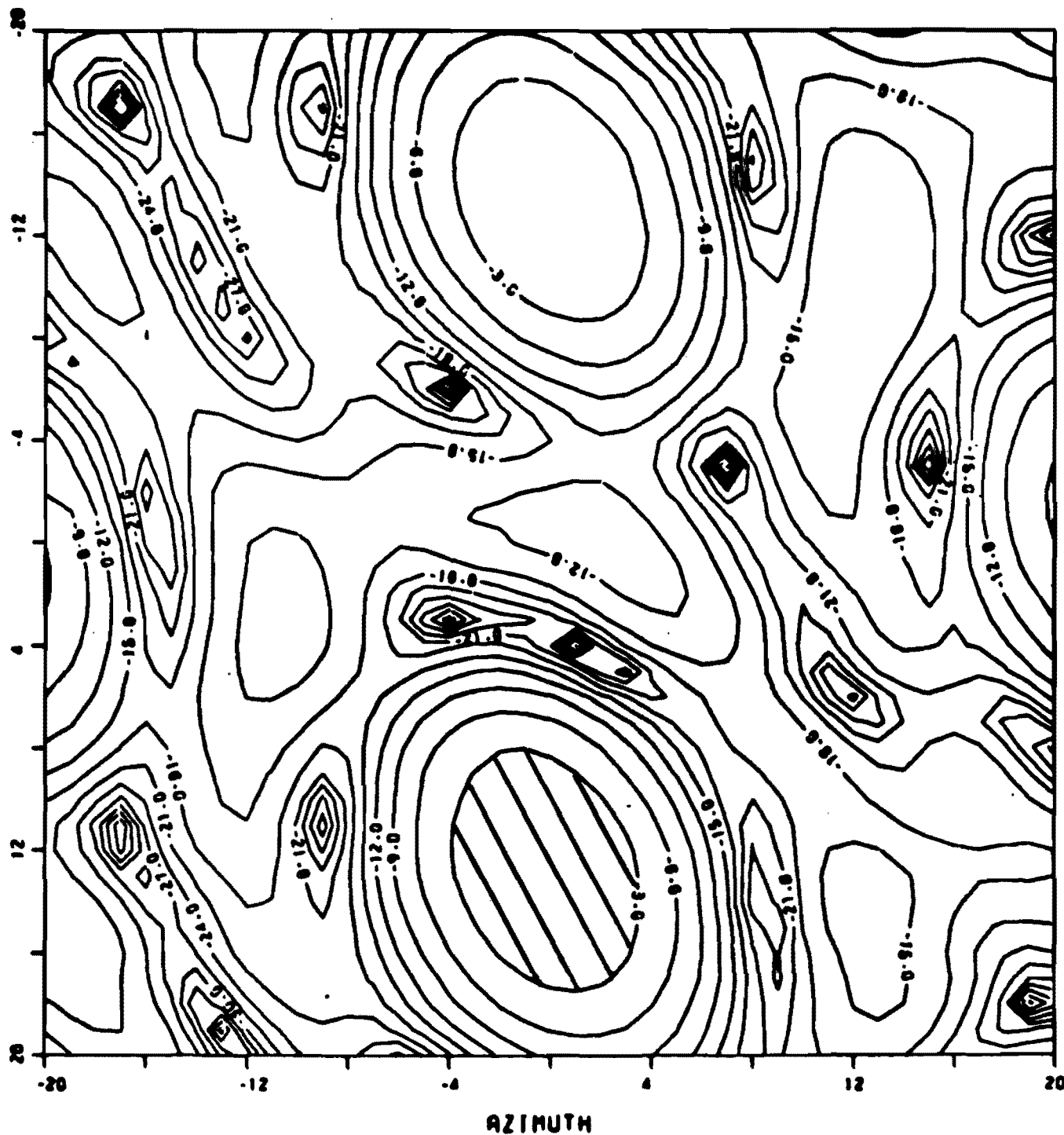


# MA TRANSMIT ARRAY RADIATION CONTOURS - MEASURED

SCAN ANGLE:  $AZ = 0^\circ$ ,  $EL = 13.5^\circ$

FREQUENCY: 2106.5 MHz

ACTIVE ELEMENTS: 4, 5, 9, 10, 11, 16, 17, 18



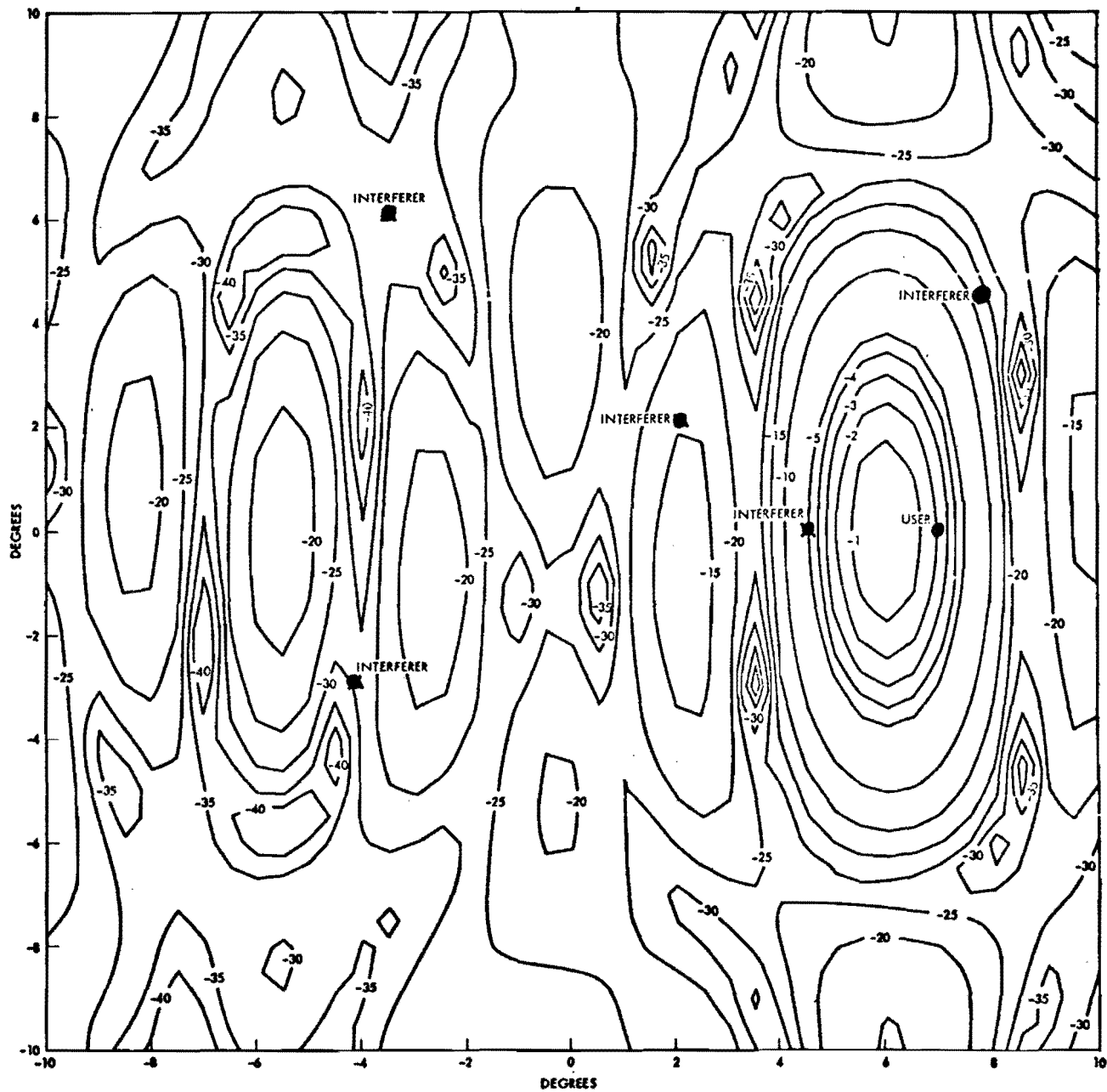


FIGURE 2. MA ARRAY POINTED NEAR USER

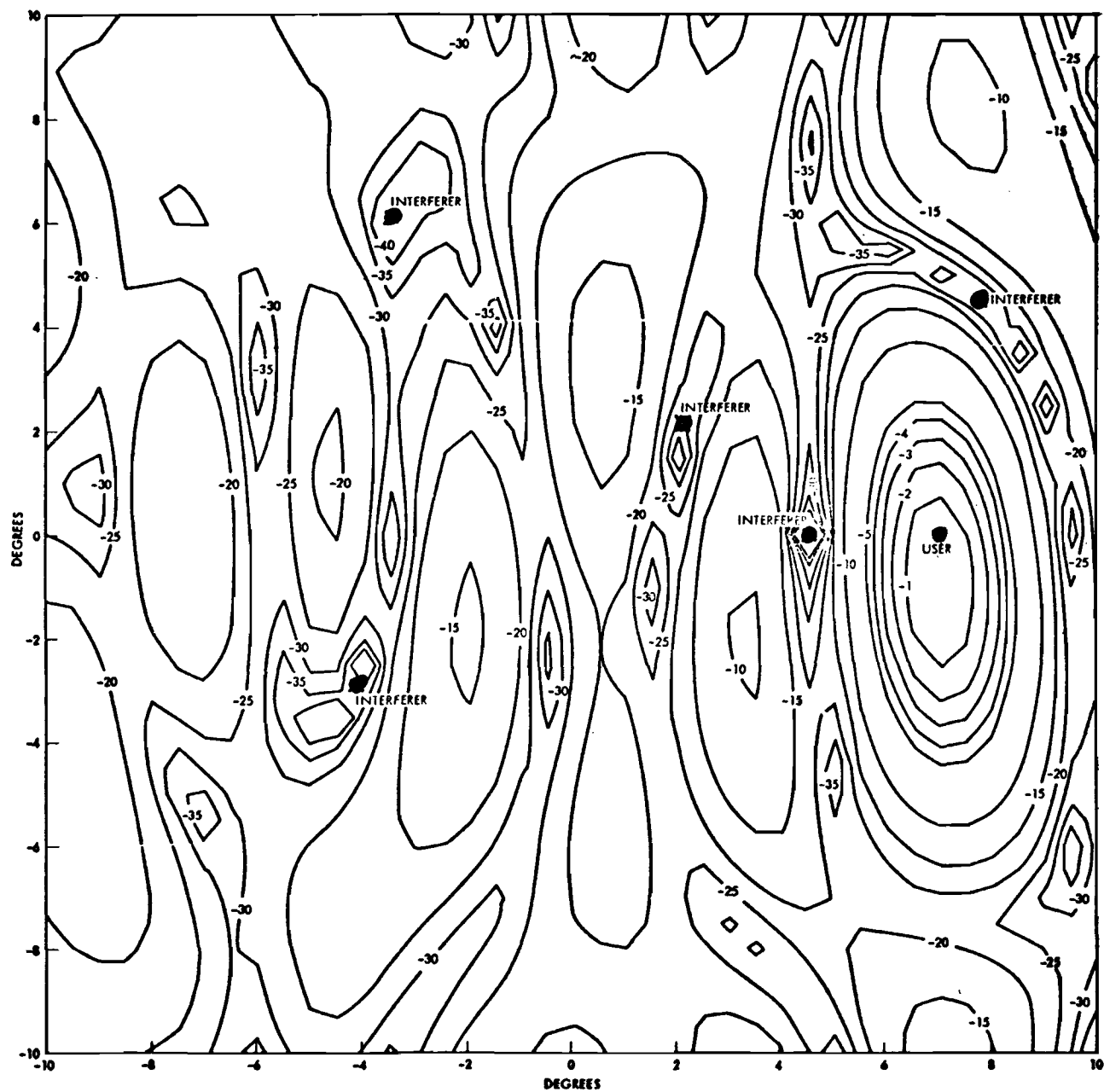
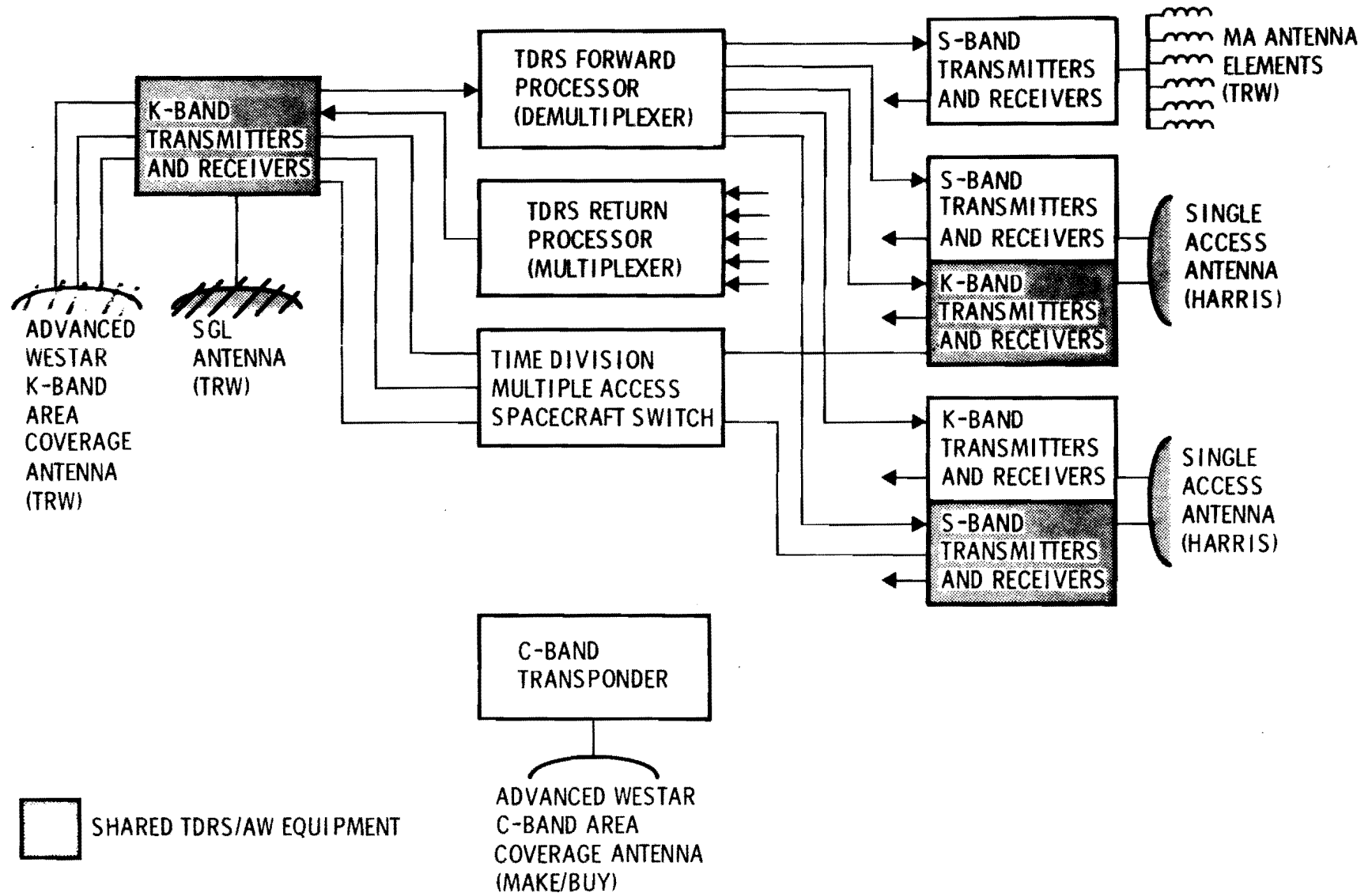


FIGURE 3. ADAPTED MA ARRAY PATTERN

## **ADVANCED WESTAR SYSTEM**

- **EAST AND WEST AREA COVERAGE BEAMS FROM ADVANCED WESTAR K-BAND AREA COVERAGE ANTENNA**
- **CENTRAL AREA AND EAST SPOTS COVERAGE FROM SGL ANTENNA**
- **ISOLATION BETWEEN ANTENNAS VIA FREQUENCY ALLOCATION**
- **ISOLATION BETWEEN BEAMS IN SAME ANTENNAS VIA A COMBINATION OF AMPLITUDE AND POLARIZATION**

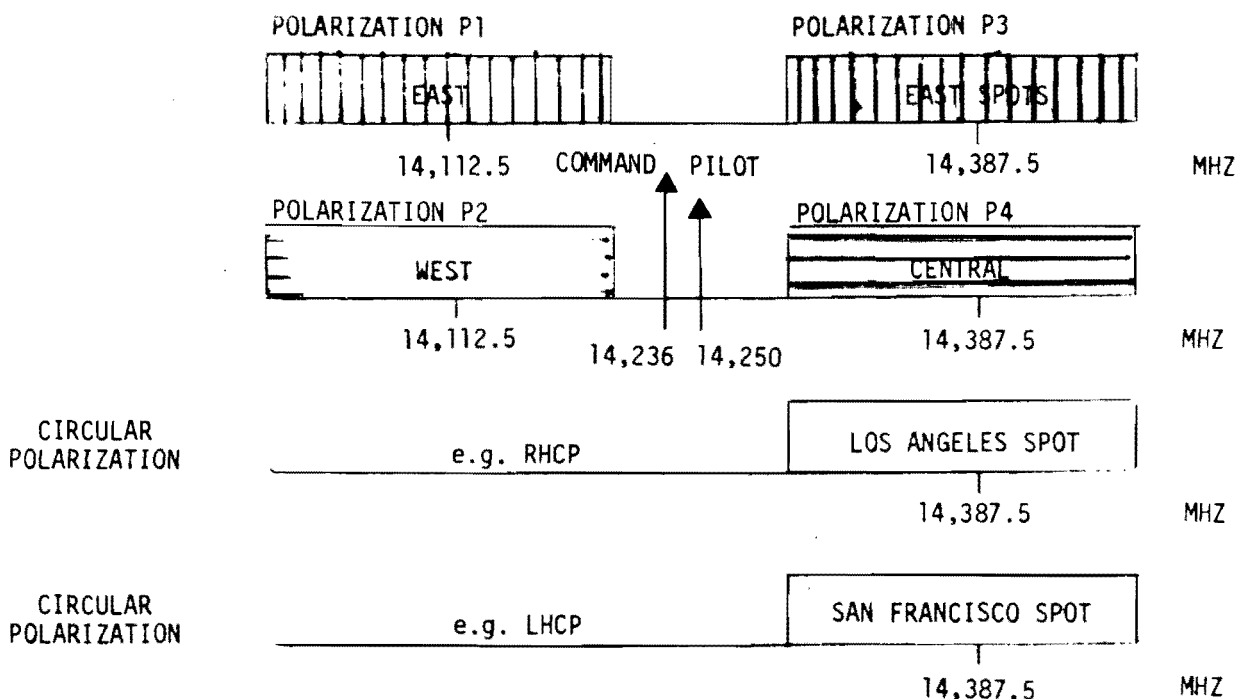
# COMBINED TDRS/AW SIMPLIFIED BLOCK DIAGRAM



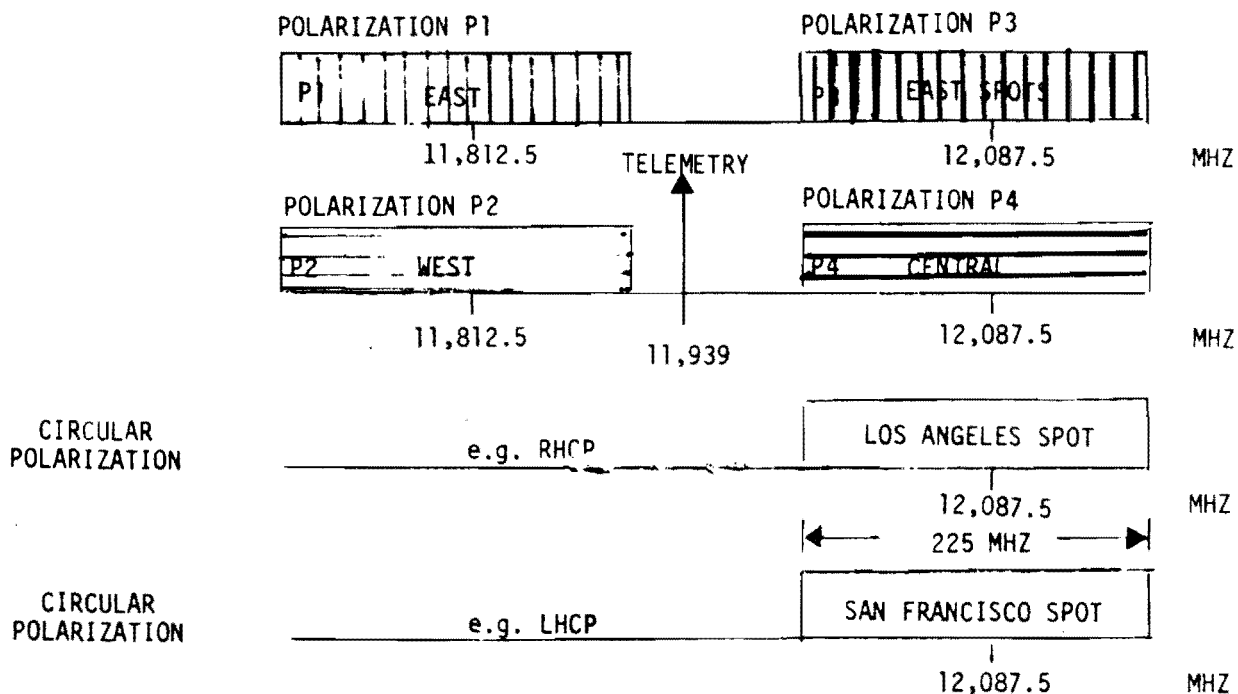


# ADVANCED WESTAR K-BAND COMMUNICATIONS SYSTEM FREQUENCY AND POLARIZATION PLAN

## RECEIVE CHANNELS

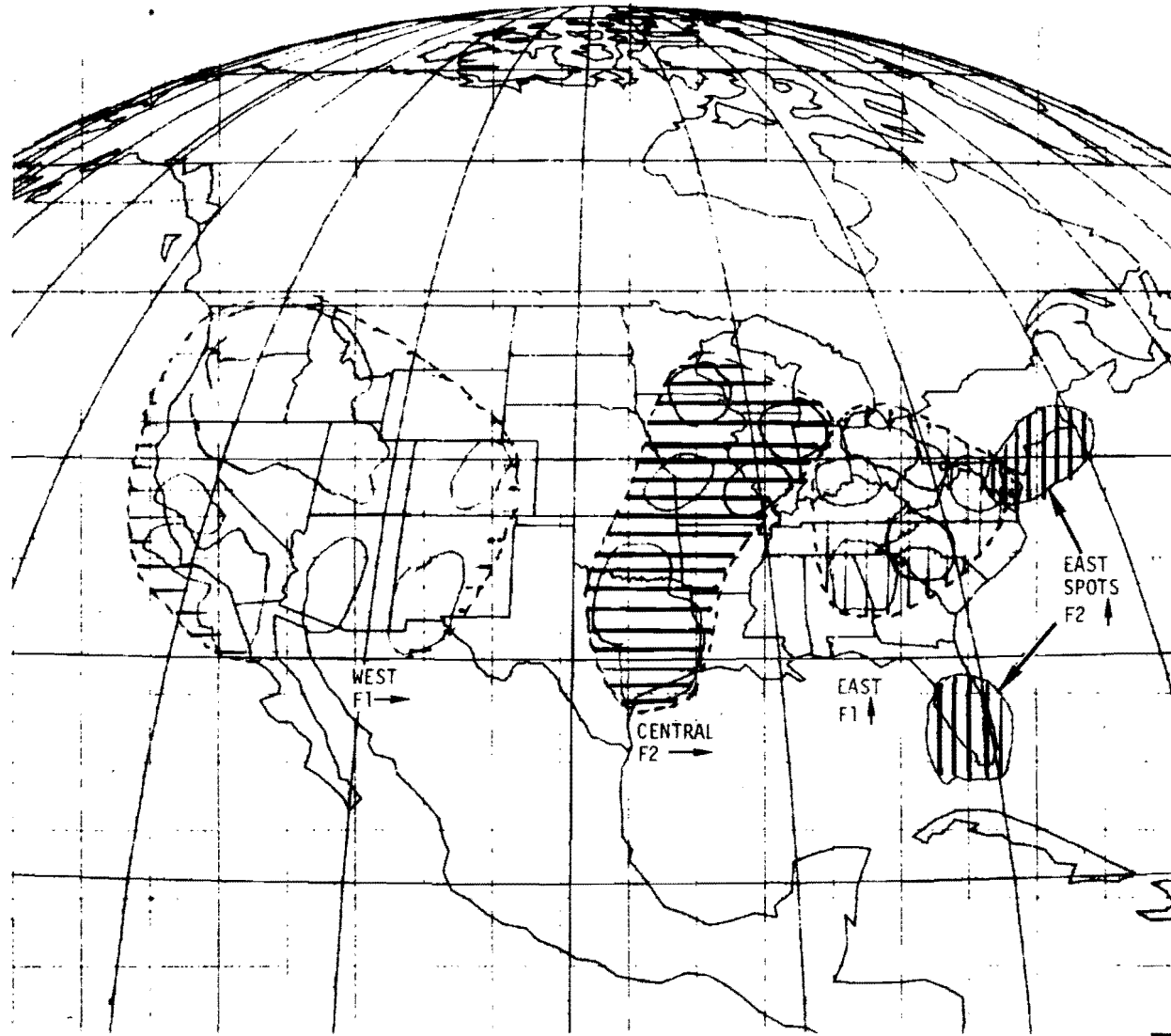


## TRANSMIT CHANNELS



P1 is perpendicular to P2  
P3 is perpendicular to P4

CONUS FROM SYNCHRONOUS SATELLITE AT -99 DEGREES  
LONGITUDE, +7 DEGREES LATITUDE



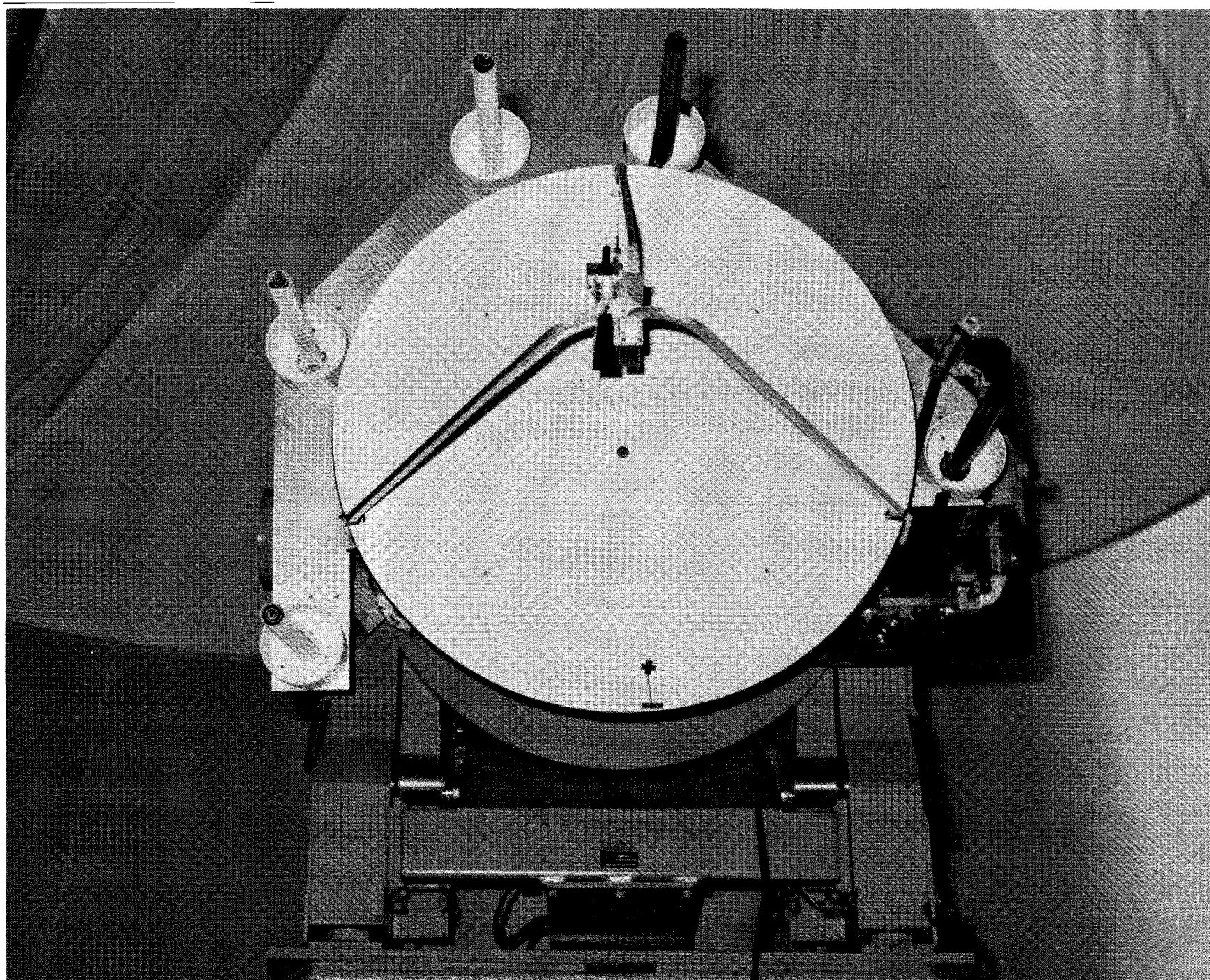
## **AW K-BAND ANTENNA**

### **3.1.1 AW K-BAND ANTENNA FUNCTIONAL CHARACTERISTICS**

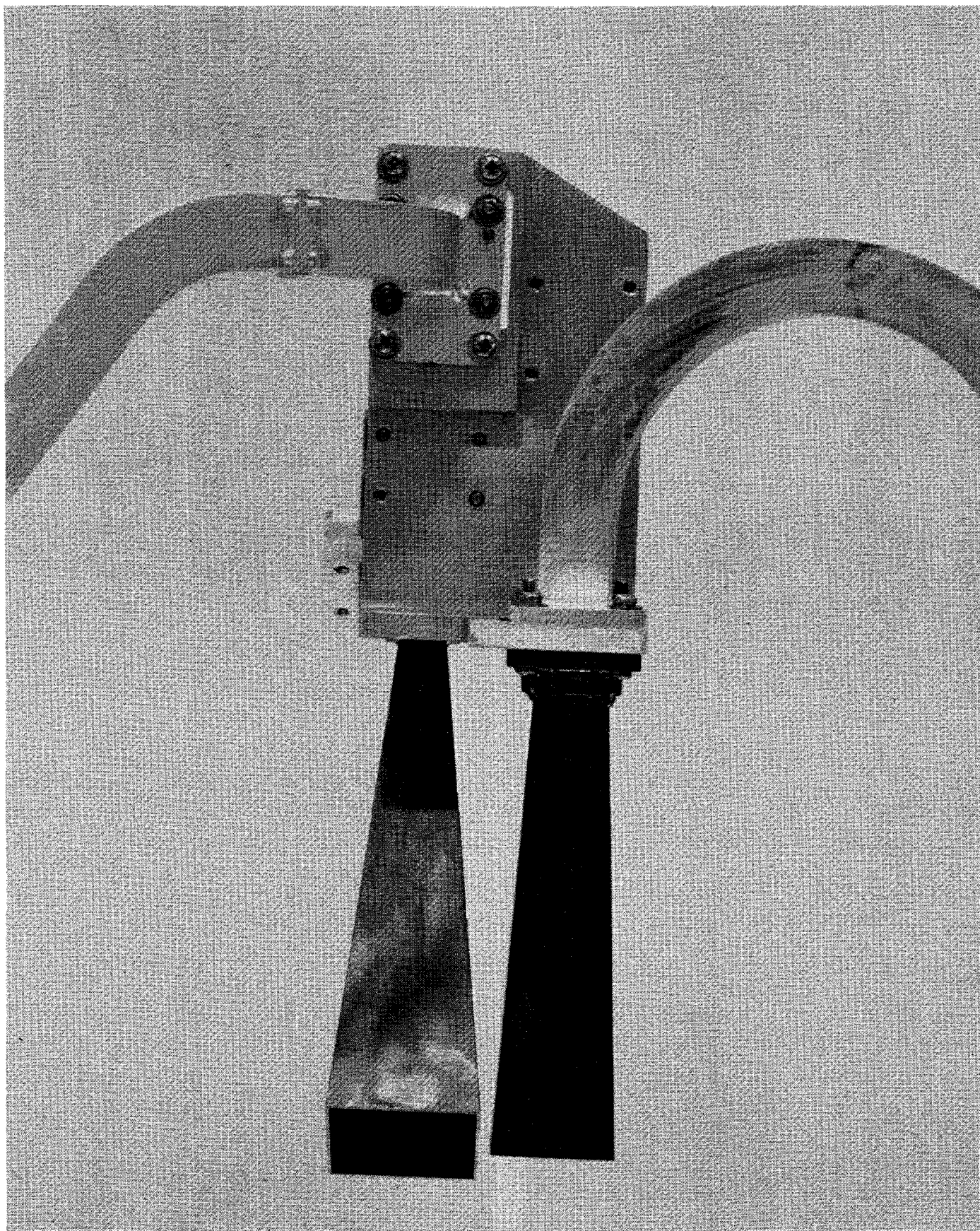
- **TRANSMISSION AND RECEPTION OF K-BAND SIGNALS BETWEEN SELECTED CONUS GROUND TERMINALS AND TDRSS**
- **FRONT-FED PARABOLIC REFLECTOR ANTENNA**
- **TWO WAVEGUIDE RECTANGULAR APERTURE FEED HORNS**
- **PART OF AW K-BAND TELECOMMUNICATIONS PAYLOAD**
- **FIXED MOUNTING ON TDRSS PLATFORM**
- **TWO LINEAR (ORTHOGONAL) POLARIZED SHAPED BEAMS (EAST AND WEST)**
- **WR-75 ALUMINUM WAVEGUIDE TRIPOD FEED SUPPORT**

## ELEMENT CONFIGURATIONS EVALUATED









# K-BAND ANTENNA (ADV. BB.)

FREQUENCY (MHZ) = 11700

CNT153

M4--F2

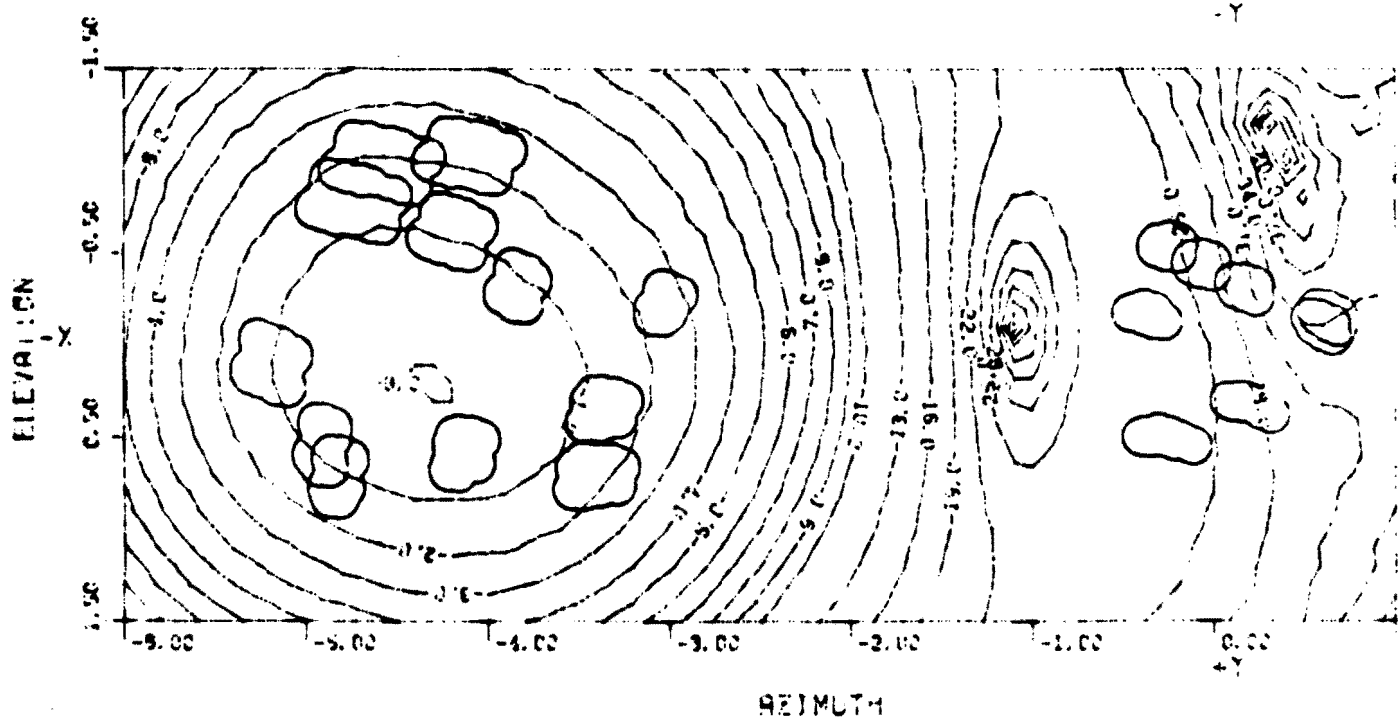
WEST HORN (PRINC. POL.) PHI: 1=90.000 R=0

MA ARRAY RES CDS 8.3" SPACERS BOTH HORNS

WEST HORN MOVED .073" TOWARD THE +Y AXIS

ACQUISITION TIME 10:37:01 AM MAY/26/78

PLAT TIME 12:32:33 PM JUN/01/78



# K-BAND ANTENNA (ADV. BB.)

FREQUENCY (MHZ) = 11700

CNT151

M4--E2

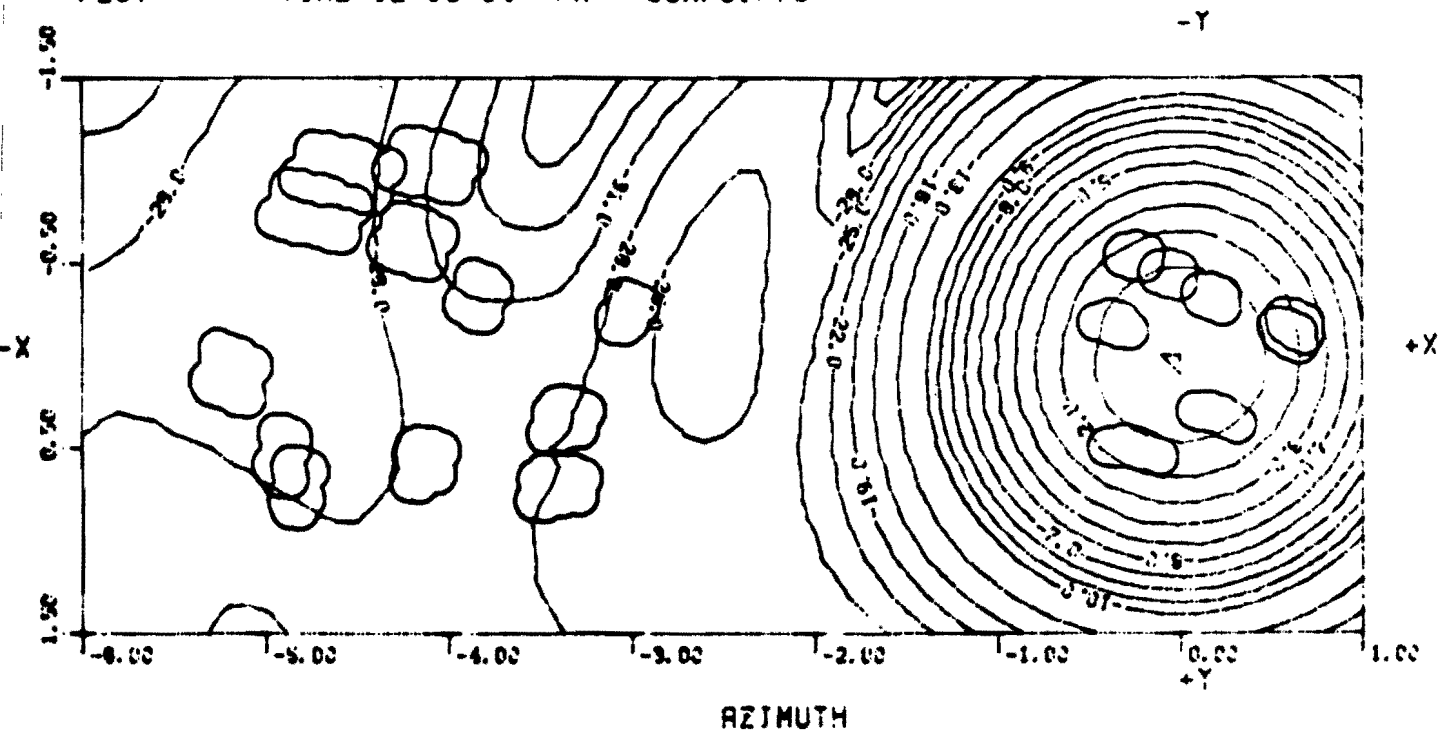
EAST HORN (PRINC. POL.) PHI: 1 = 0.000 R=0

MA ARRAY RES CDS 6.3" SPACRS BOTH HORNS

WEST HORN MOVED .073" TOWARD THE Y AXIS

ACQUISITION TIME: 09:17:01 AM MAY/26/78

PLOT TIME: 12:09:04 PM JUN/01/78





## 2-METER GRAPHITE PARABOLIC REFLECTOR

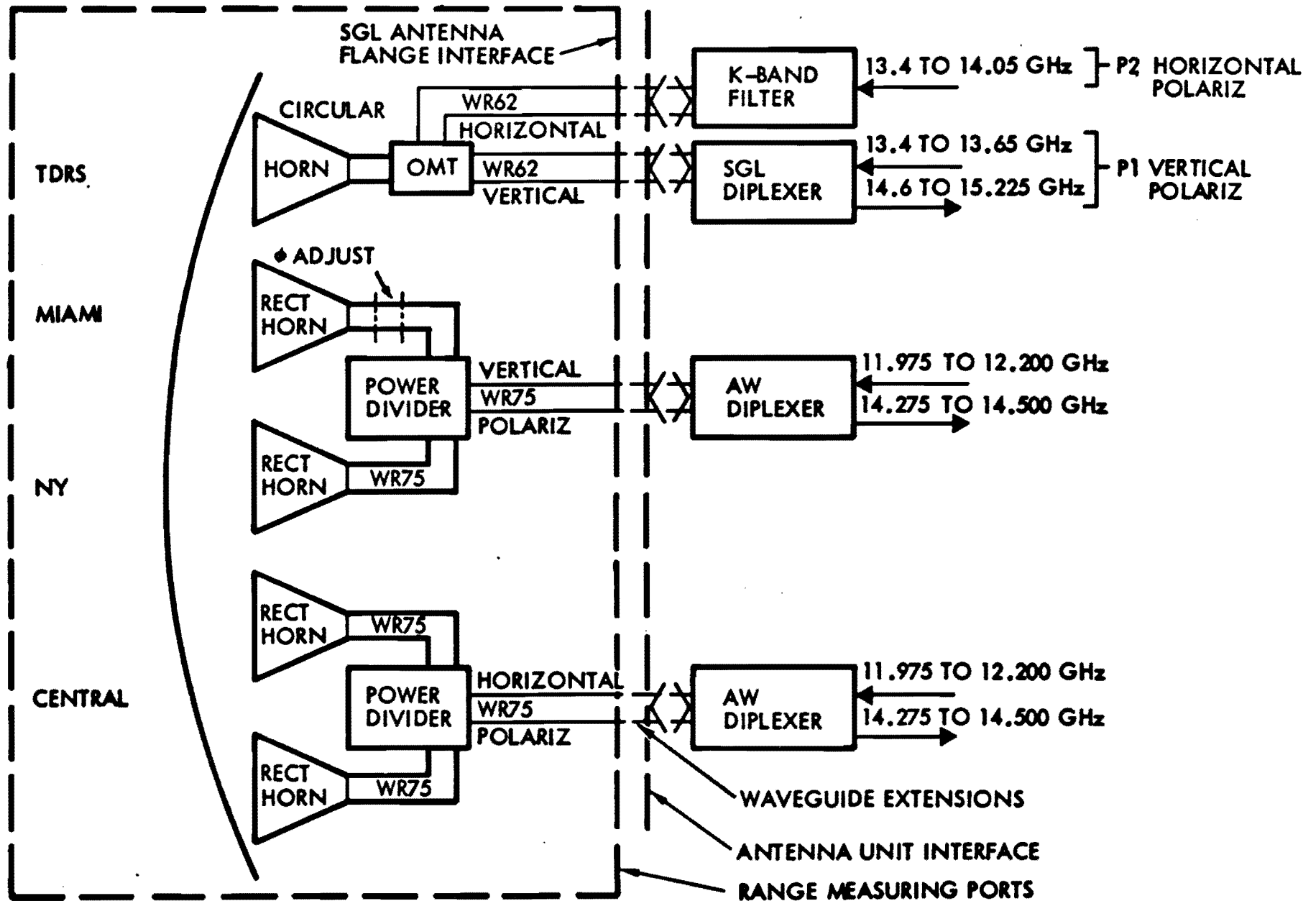
- DIAMETER 2.0 METERS (78.74 INCHES)
- FOCAL LENGTH 1.067 METERS (42 INCHES)
- F/D RATIO 0.533
- SURFACE RMS <0.25 MILLIMETER (0.010 INCH)
- CONSTRUCTION<sup>0</sup> 4000 Å VDA OVER A SANDWICH OF FOUR GRAPHITE PLIES  
EPOXY BONDED TO A CORE OF ALUMINUM HONEYCOMB.  
VDA SURFACE COATED WITH THERMAL CONTROL PAINT
- MOUNTING TO A BERYLLIUM BOOM VIA A CENTRAL HUB
- POINTING BIAXIAL DRIVE STEPPER MOTOR ALSO USED FOR  
DEPLOYMENT

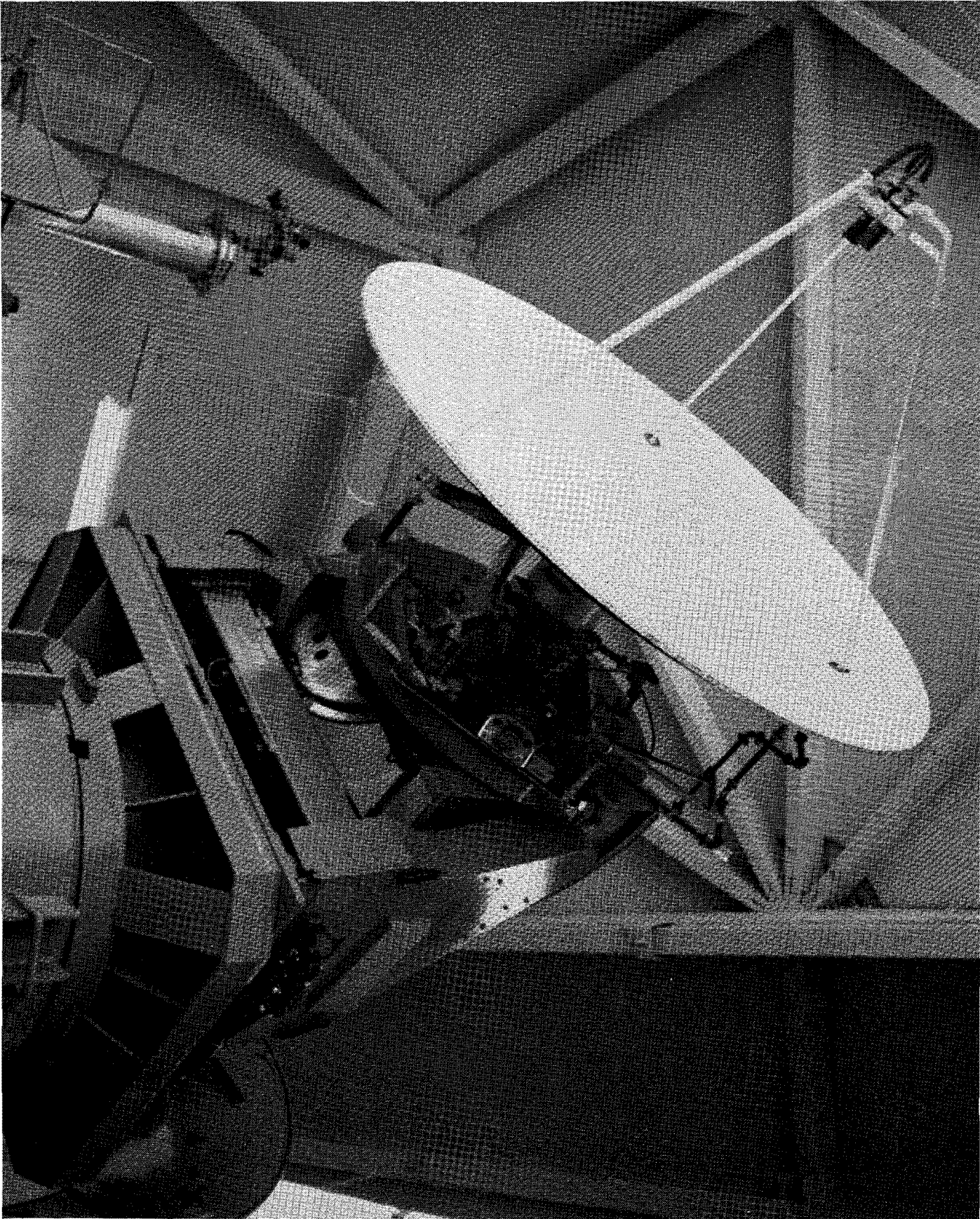
## SGL ANTENNA TDRSS KEY DESIGN FEATURES

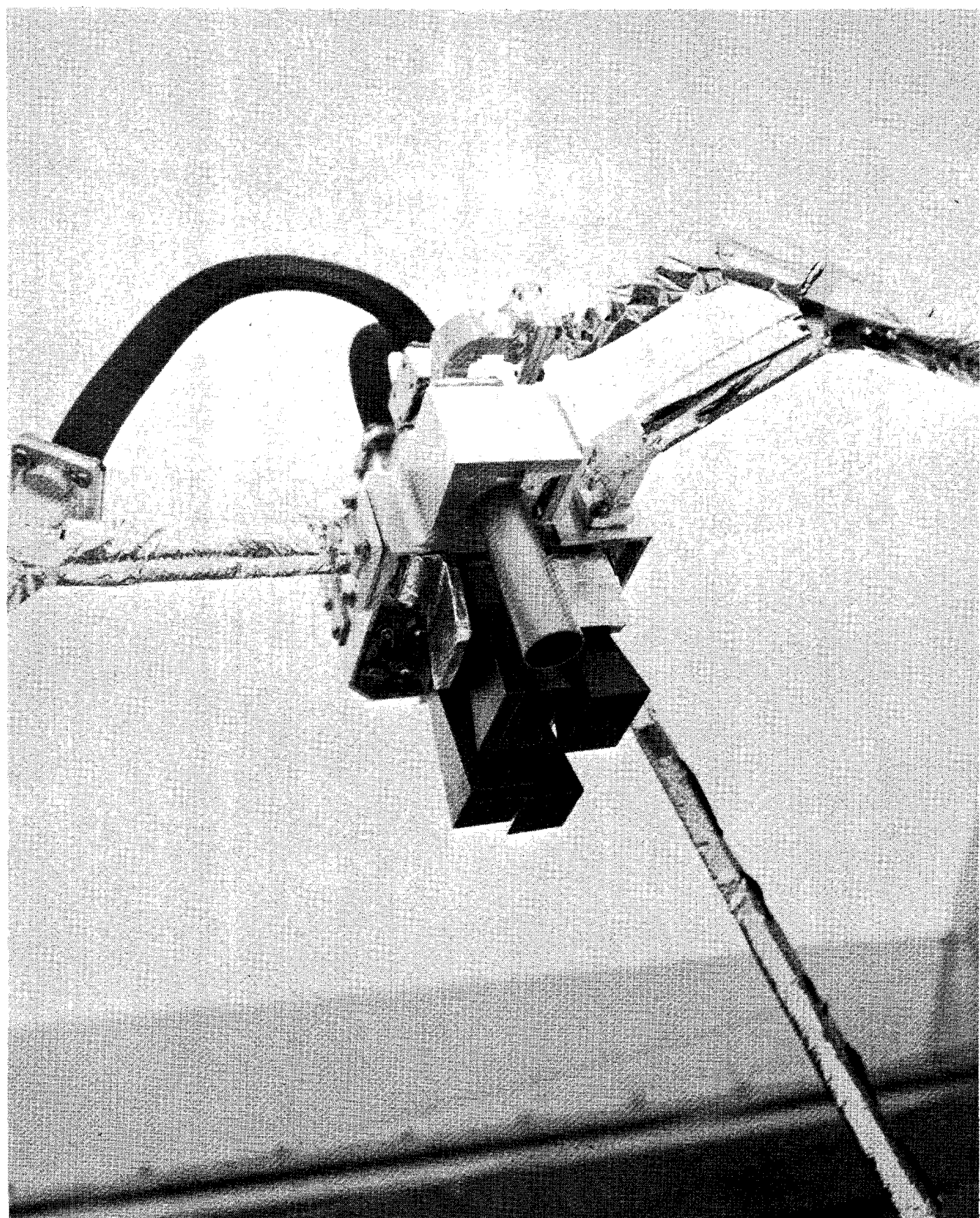
- PROVIDES A HIGH-GAIN BEAM TO TDRSS GROUND TERMINAL
- RECEIVES TDRS COMMANDS, USER FORWARD LINK COMMANDS, AND PILOT TONE WITH VERTICAL LINEAR POLARIZATION IN 14.6 TO 15.225 GHZ BAND
- TRANSMITS ONE KSA CHANNEL IN 13.4 TO 14.05 GHZ BAND WITH VERTICAL LINEAR POLARIZATION
- TRANSMITS MULTIPLEXED CHANNEL CONTAINING OTHER KSA CHANNEL, BOTH SSA CHANNELS, MA SIGNALS, AND TDRS TELEMETRY DATA WITH HORIZONTAL LINEAR POLARIZATION IN 13.4 TO 14.05 GHZ BAND

# SGL ANTENNA

## BLOCK AND INTERFACE DIAGRAM







S. G. L. ANTENNA (ADV. BB.)

15/MAY/78

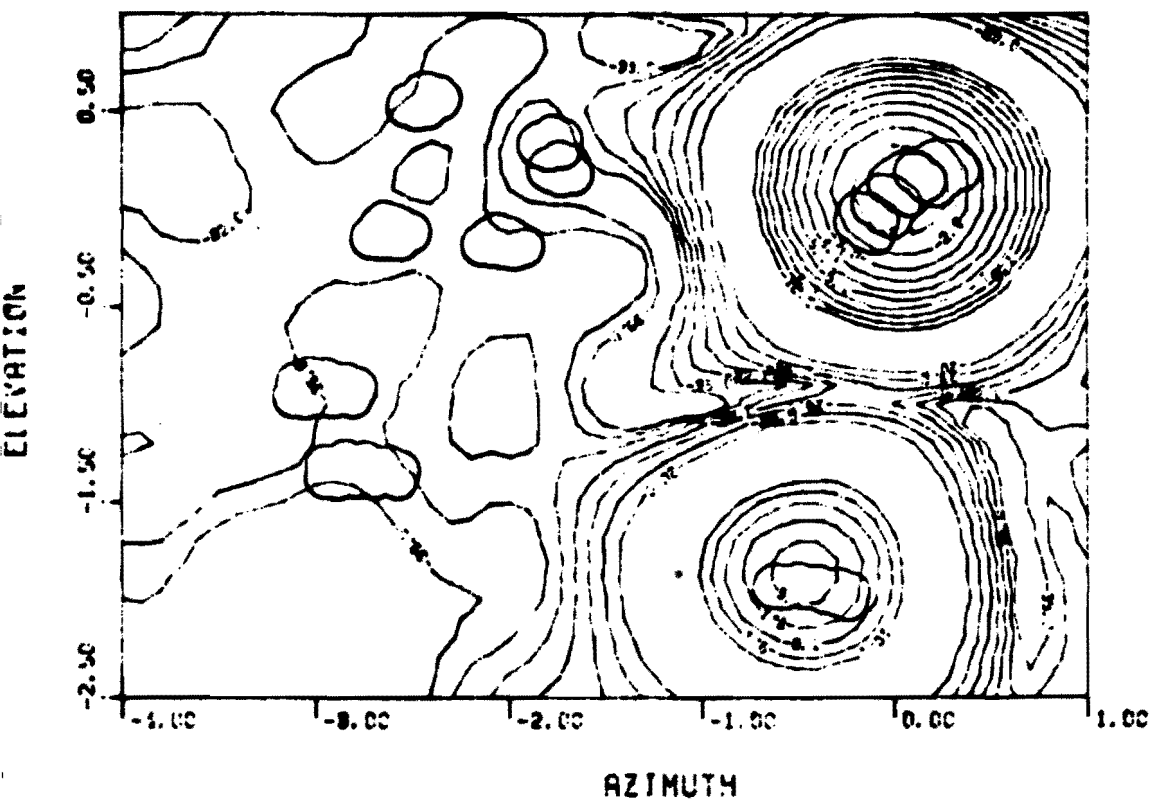
FREQUENCY (MHZ) = 14500

CT5214 CT516A

NY-MIAM! PORT (PAIN) PH! : TX=0 RX=0

CENTRAL HORNS .4" IN FRONT

RESISTANCE CARDS IN ALL 4 HORNS

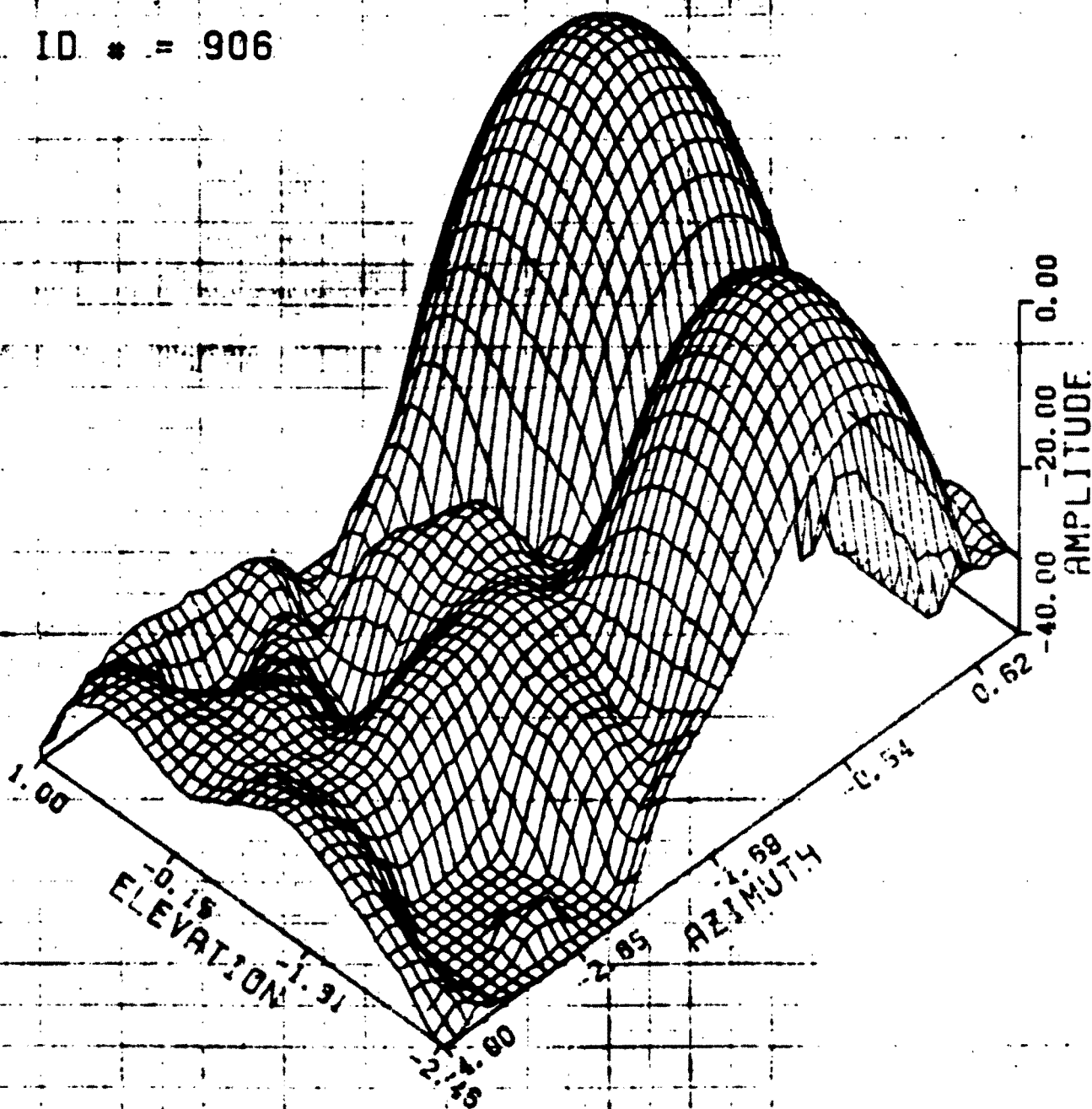




# S G L ANTENNA (ADV. BB.)

PORT # NY/MIAMI

ID # = 906



AQUIS TIME: 03:06:01 PM OCT/31/78

(ADV. BB.)

16/MAY/78

FREQUENCY (MHZ) = 14500

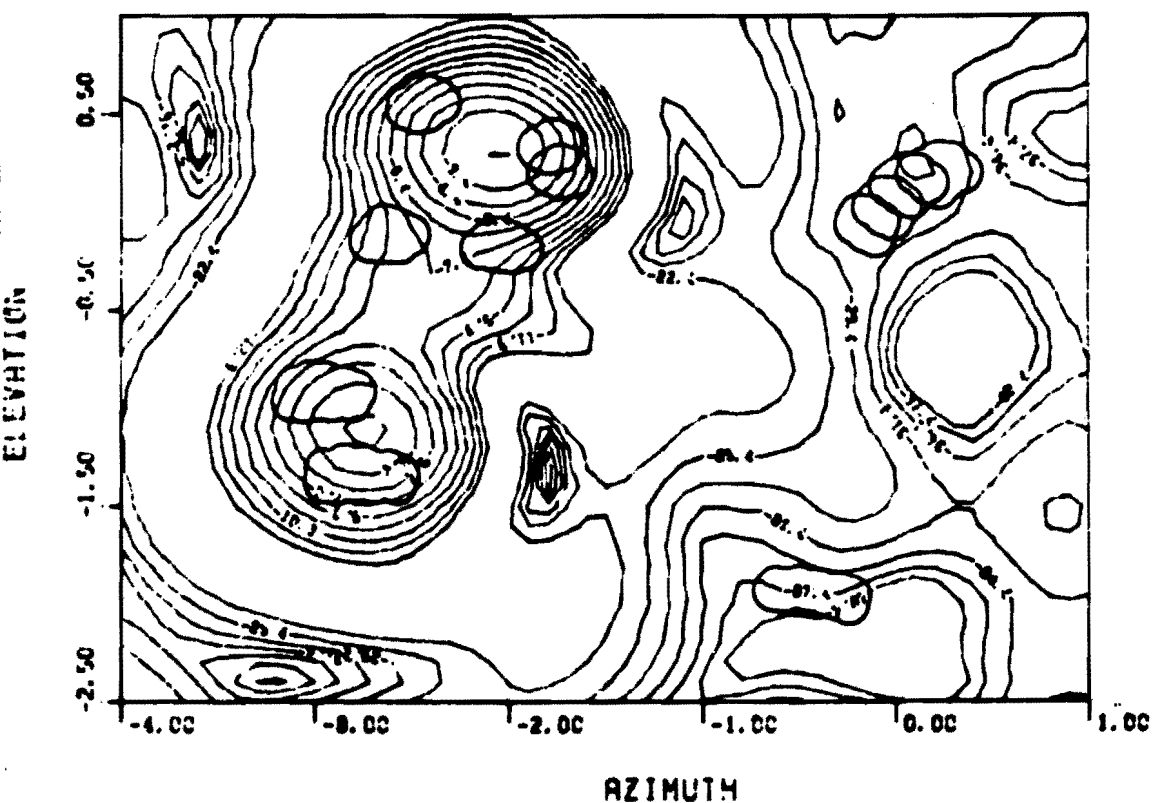
CTS216

CTS16A

CENTRAL PORT (PRIN) PHI: TX=90 RX=0=0

CENTRAL HORNS .4" IN FRONT

### RESISTANCE CARDS IN ALL 4 HORNS

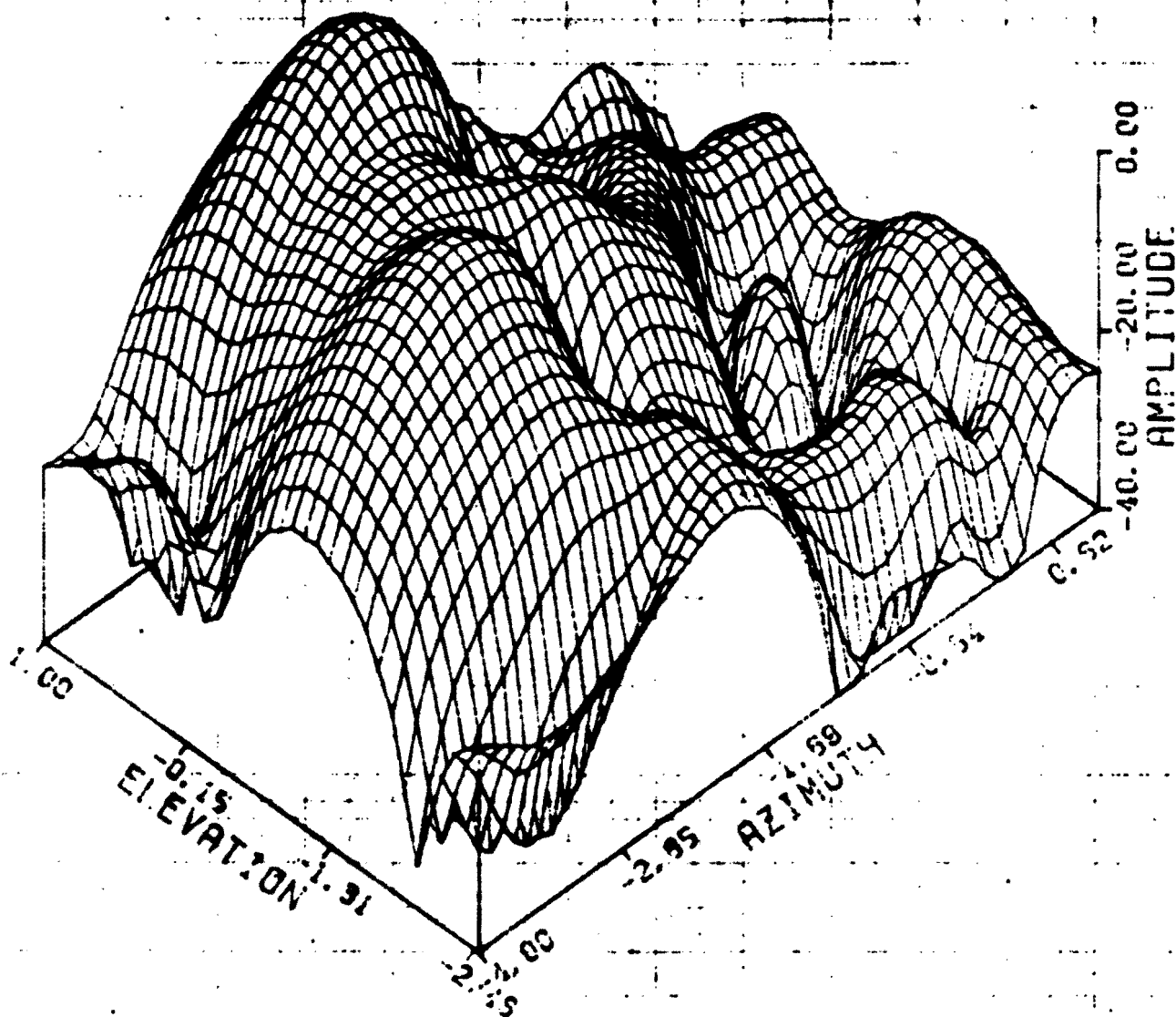




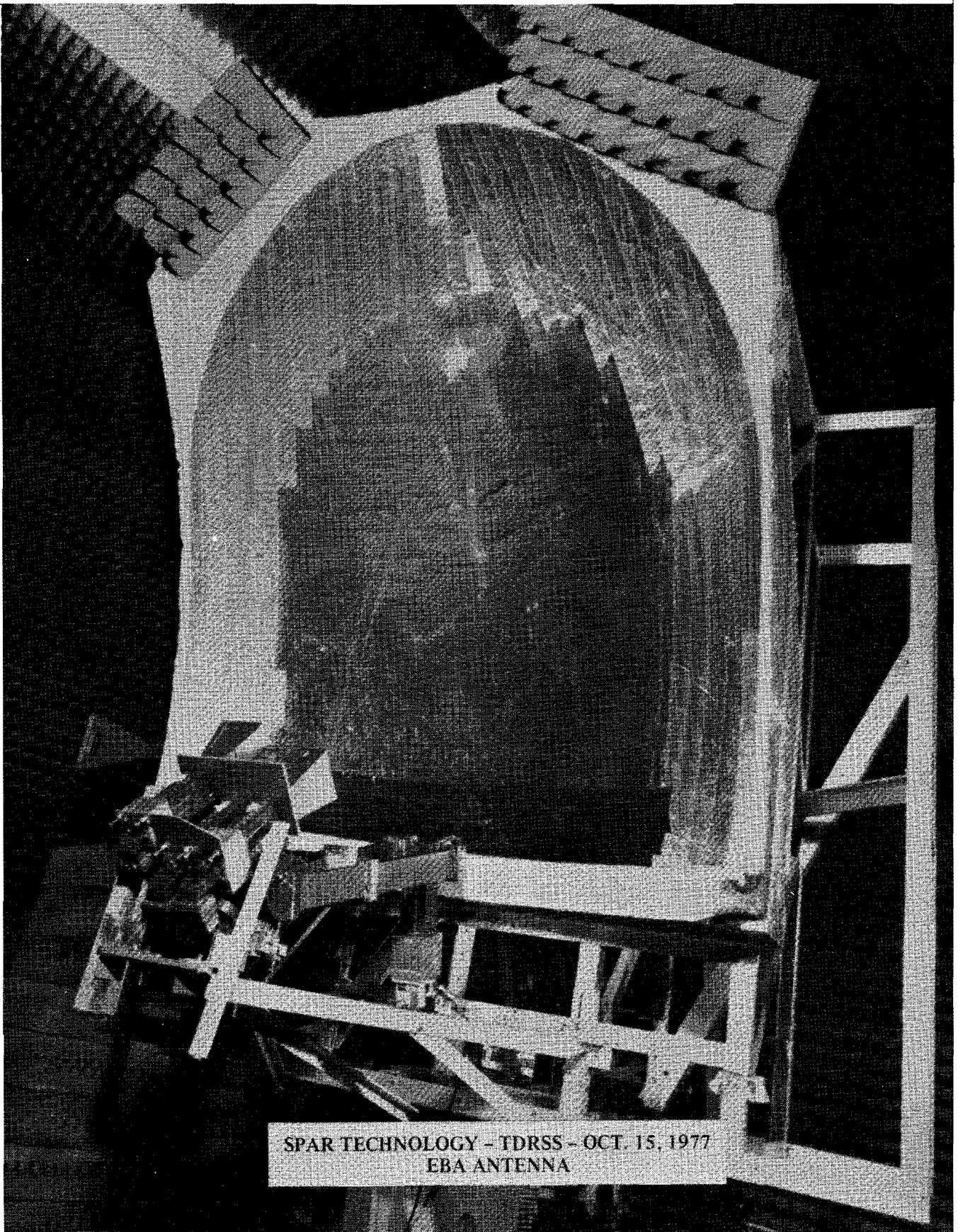
S G L ANTENNA (ADV. BB. I)

PORT = CNTRAL

ID # = 909



AQUIS TIME: 04:26:01 PM OCT/31/78

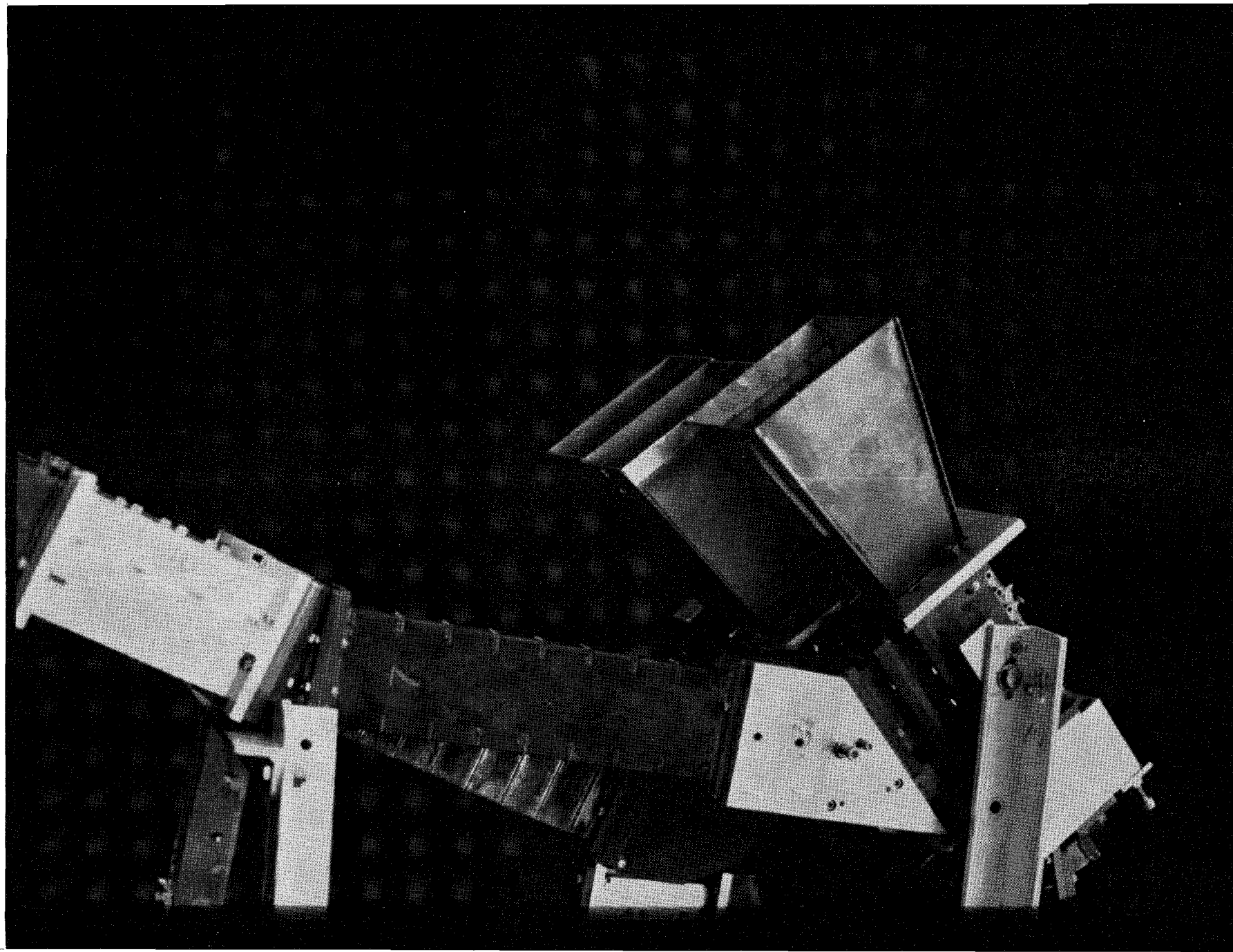


SPAR TECHNOLOGY - TDRSS - OCT. 15, 1977  
EBA ANTENNA

TDRSS  
C-BAND ANTENNA REFLECTOR  
SPAR - 1978







SPAR

PROJ TBASS

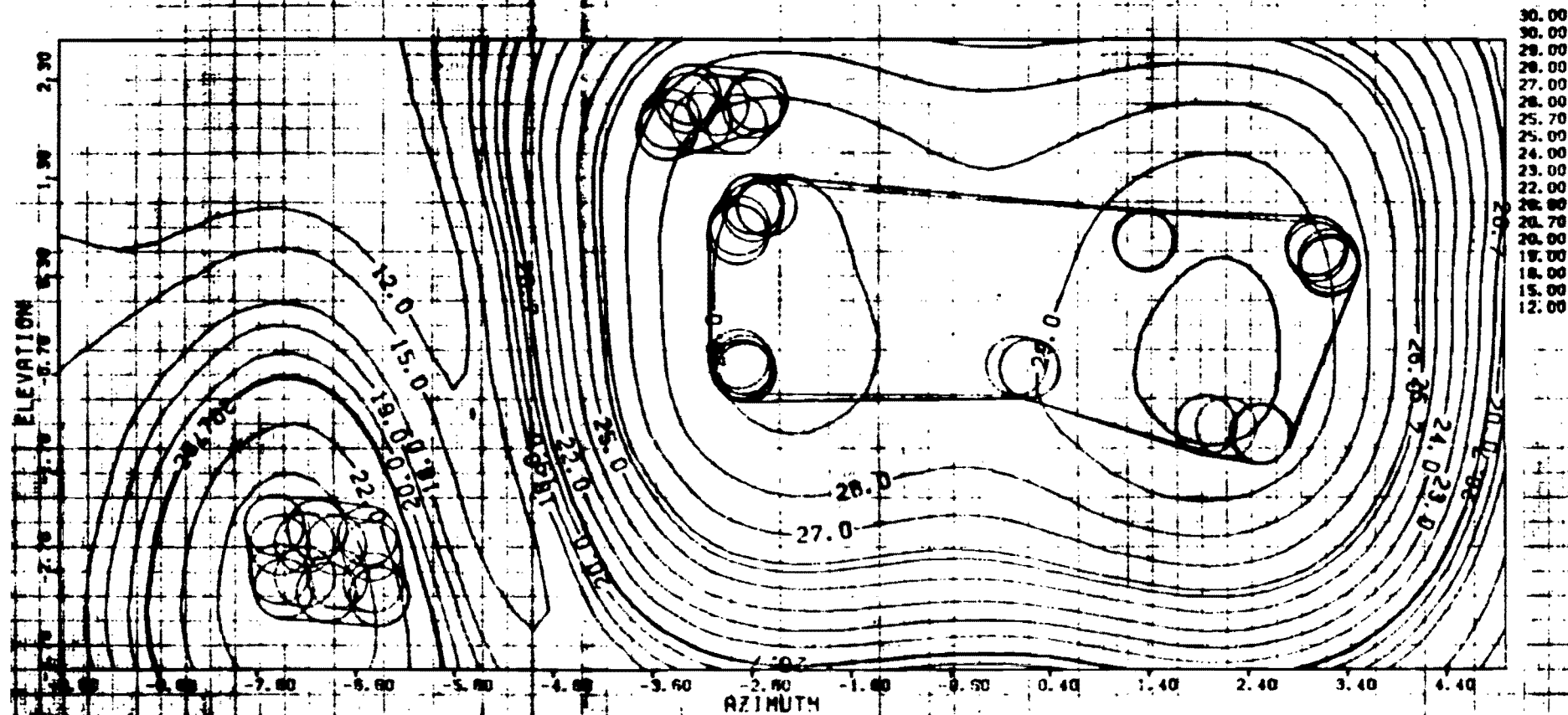
PATTERN # 1012

DATE 21/ 1/19

GAIN AT MECH B. S. = 30.00 DBI

FREQUENCY = 5945 MHZ

PLOT LEVELS (DBI)



Chapter 8.

**The Role of Antennas in Advanced Communication Systems**

---

*D. O. Reudink*

Bell Laboratories  
Crawford Hill Laboratory  
Holmdel, New Jersey 07733

## **I. Historical Sketch of Satellite Research at Bell Laboratories**

### **a. The Early Days**

Satellite systems research at Bell Laboratories began in 1955. In that year, J. R. Pierce [1]. published a paper in which he explored the possibility of using a satellite repeater for transoceanic communication. At that time, the American Telephone and Telegraph Company and the British Post Office had announced their intention to jointly construct a submarine cable across the Atlantic Ocean. This cable would have the capability of carrying 36 two-way telephone circuits and cost 35 million dollars. Pierce wondered whether a cable with 30 times that capacity, to accommodate either 1080 telephone conversations or one television channel, would be worth 30 times the cost (\$1 billion). Also, might an artificial earth satellite be capable of providing this capacity? Pierce presented a set of satellite calculations establishing basic communication parameters needed to accomplish such a task. Pierce proposed the use of pulse-code-modulation [2] to exploit the large communication bandwidth which might be provided by a satellite.

Pierce found that an antenna diameter of 250 feet (very large by today's standards) a transmit power of 100 kilowatts (also quite large) at 10 centimeter wavelength, and a receiver with 6 dB noise figure would be adequate to permit use of a string of 100 foot diameter spherical reflector satellites at an altitude of 2200 miles. Because a passive satellite intercepts and reflects only a small portion of the transmitted power, the overall path loss varies inversely with the product squared of the up-link and down-link distances.

An alternative is to use satellites in the geostationary orbit. This is a circular orbit in the equatorial plane, 22,000 miles above the surface of the earth. The period of revolution in this orbit is exactly one day, so that from any point on earth, the satellite appears stationary in the sky. Pierce found that a 100 foot plane reflecting mirror in such an orbit would permit a reduction of transmit power to about 50 kilowatts; although the path loss is much higher, the directive property of the plane reflector relative to the omnidirectional scattering from a spherical reflector more than compensates for this additional path loss. Finally, Pierce considered an active repeating satellite with a 10 foot antenna in geosynchronous orbit. Here, the round-trip path loss is greatly offset by means of amplifying the up-link signal received at the satellite prior to retransmission back to earth. For this case, 100 watts would be needed by the ground transmitter and only 30 milliwatts would be needed by the satellite transmitter. The possibility of transoceanic communication by satellite was explored further by Pierce and R. Kompfner [3]. Availability of the low noise maser reduced the power needed for a passive reflector satellite by a factor of about 100.

Early in 1956 a proposal was made by W. J. O'Sullivan of the National Advisory Committee for Aeronautics to orbit balloon satellites in order to measure air density at high altitudes. His work led to the construction of a 100-foot diameter balloon made of 0.5 thousandths inch thick aluminized plastic, light enough to be launched to 1000 mile altitude by existing rockets.

When Pierce and Kompfner learned of the balloon they conceived the idea of using it as a passive reflector for a satellite communication experiment, and in early 1959 Project ECHO was born [4].

On August 12, 1960, the 100-foot-diameter balloon was placed in orbit around the earth by the National Aeronautics and Space Administration (NASA). The objective was to demonstrate the feasibility of long distance communication by means of reflection of microwaves from a satellite. It was intended that a two-way coast-to-coast voice circuit be established between the Jet Propulsion Laboratory's (JPL) facility at Goldstone, California, and a station provided for this purpose by Bell Laboratories at Holmdel, New Jersey. Similar tests were also planned with the Naval Research Laboratory (NRL) and other stations. The satellite-tracking facility of the JPL was located at Goldstone, California, about one hundred miles northeast of Los Angeles. The Bell Telephone Laboratories (BTL) station was located at Holmdel, New Jersey, and the

NRL facility was located at Stump Neck, Maryland.

An east-west channel was provided by transmission from a 60-foot paraboloid antenna at BTL to an 85-foot paraboloid at JPL via reflection from the balloon, using a frequency of 960 MHz and transmitter power of several kilowatts. The west-east channel utilized transmission from another 85-foot dish at JPL to a specially constructed receiver and horn-reflector antenna at BTL having a 20- by 20-foot aperture [5]. The radiation in each channel was circularly polarized in order to avoid the necessity of tracking polarization during the satellite pass. Over most of the region of mutual visibility the baseband S/N ratio was expected to be at least 45 dB. After the successful launching of the ECHO I balloon on August 12, 1960, operations were carried on by the BTL station for about 120 passes up to March 1, 1961.

#### **b. Active Satellite Systems**

Following the successful completion of Project ECHO, attention turned toward the feasibility demonstration of an active satellite repeater. Such a satellite would greatly reduce the power required to transmit television bandwidth signals. The TELSTAR Experiment, undertaken exclusively by AT&T with NASA being reimbursed for satellite launch costs and certain tracking and telemetry functions, was designed to demonstrate the operational feasibility of a broadband active repeater in the space environment. Again a low earth orbit (2000 miles) was chosen, and an omidirectional antenna was provided to avoid the need for spacecraft attitude control. The experimental effort that went into TELSTAR [6] was huge compared with that of Project ECHO, with Bell Laboratories responsible for the satellite as well as the ground stations.

The first TELSTAR satellite was launched on July 10, 1962, and soon produced the world's first demonstration of transatlantic television transmission. By demonstrating the ability of spacecraft communications electronics to survive a launch and operate reliably in the space environment, and by generating valuable data pertaining to the effects of radiation in space, TELSTAR represented a major milestone toward the realization of a commercial satellite system.

In 1968 L. C. Tillotson showed that the equivalent of 100 million voice circuits could be provided by a network consisting of 50 ground stations and 50 active repeater satellites placed in geosynchronous orbit [7]. His model system used highly directive multibeam antennas, interference resistant modulation, and solid-state microwave repeater electronics, and operated in the 20 and 30 GHz frequency bands. Although, in principle, the number of beams might be increased, reuses of the frequency in the same polarization must be separated by several beam widths to keep interbeam interference sufficiently low [8].

Another approach, the scanning spot beam concept, [9,10] combines the wide-area accessibility of an area coverage system with the high antenna gain of a spot beam system. It is intimately tied in with time division multiple access (TDMA). For an area coverage system employing TDMA, the satellite interconnects a single user pair (one transmitting and one receiving) at every point in time. A satellite capable of forming a pair of rapidly movable spot beams (one receiving and one transmitting) can thereby produce the same accessibility as does the area coverage system, provided the beams are scanned synchronously with the TDMA bursts to interconnect the correct user pairs. More details on this will be given in a later section.

## **II. Propagation**

### **a. Background**

Some of the fundamental limitations on the performance of satellite communication systems at frequencies greater than 10 GHz result from strong interaction of radio waves with rain and ice [11-14] in the lower atmosphere. Therefore, the economic design of reliable satellite communication systems in the frequency bands of 12-14 GHz and 20-30 GHz depends on detailed knowledge of the effects of these interactions.



Direct measurements of the effects of the hydrometeors on radio waves transmitted from satellites are required to provide empirical design data; and as checks on the theoretical models [15-17] needed for predicting communication system performance in geographical regions where measurements are not available.

Before signal-sources (beacons) on satellites were available, radiometers tracking the sun [18,19] and radiometers measuring the thermal emission from raindrops [20,21] were used to determine signal attenuation caused by rain. However, the measuring range of thermal emission radiometers is limited to about 10 dB attenuation and the varying elevation angle of the sun complicates the interpretation of suntracker data. Also, depolarization and dispersion cannot be measured in suntracker and radiometer experiments because the signal sources are non-coherent and non-polarized.

Some propagation information was obtained at 15, 20 and 30 GHz using beacons on the NASA experimental ATS-5 and ATS-6 satellites. Comprehensive propagation measurements and continuous long-term statistics could not be collected because total power constraints on these satellites did not allow uninterrupted operation of the beacons.

Beacons were placed on the COMSTAR communication satellites to satisfy the need for continuously-transmitting sources in geostationary orbit [22-29]. These beacons were specially configured to facilitate comprehensive continuous propagation measurements at 19 and 28 GHz. The single-frequency 19 GHz beacon signal was switched between two orthogonal linear polarizations. The 28 GHz beacon signal included coherent modulation sidebands and was transmitted at a single linear polarization.

Other orbital signal sources for propagation experiments were also available concurrently: At 11 GHz over North America on the CTS satellite; at 11, 14 and 17 GHz over Europe on the OTS and SIRIO satellites; and at 1.7, 11, 20 and 30 GHz over Japan on the ETS II, CS and BS satellites. The experiments and results obtained using these other signal sources and using the COMSTAR beacons at geographical locations other than Crawford Hill were described recently by Lin, et al. [17], Ippolito [30], Brussaard [31], Cox, [32] and Chu [16].

The 19 and 28 GHz beacons on the COMSTAR satellites have been used to make unique space-earth propagation measurements at Crawford Hill, New Jersey. The purpose of these experiments was to provide detailed propagation information not previously available. The major emphasis was on depolarization measurements important to dual-polarized satellite communication systems and on phase and amplitude dispersion measurements important to wideband digital systems. The measurements made use of the polarization-switched 19 GHz beacon signals and the coherent modulation sidebands on 28 GHz beacon signals. Many of the most important results are readily extendible to the entire 10 to 30 GHz frequency range and can provide useful parameter estimates for even higher and lower frequencies.

In addition to depolarization and dispersion measurements, space-earth rain attenuation measurements were made over a greater attenuation range than ever before. Measurements over a wide range were needed for checking frequency, elevation angle and polarization scaling relationships in the 10 to 30 GHz frequency range. Measurements were also made of rain scatter coupling, [33] angle-of-arrival effects [34] and cloud-produced amplitude scintillation [35].

#### **b. COMSTAR Results [36]**

Rain attenuation is an important parameter in communication system design. It will dominate the system power margin for high-reliability systems operating above 10 GHz. The COMSTAR beacon attenuation measurements confirm the high probabilities of occurrence of severe rain attenuation obtained earlier from radiometer and suntracker measurements. These results reinforce the earlier conclusions that site diversity will be required to meet long-haul transmission objectives at 30 GHz and will also be required to meet these objectives at 19 and 12 GHz for low path elevation angles at some geographic locations (Figure 1).

Over the 10 to 30 GHz range, attenuation in dB scales approximately as the square of frequency. Although the attenuation variation is a little less than frequency squared, the error in using frequency squared scaling is considerably smaller than the year-to-year variation in measured attenuation distributions (Figures 2, 3).

For path elevation angles above 10° rain attenuation in dB scales linearly with the cosecant of the elevation angle. This scaling relationship is good for cumulative attenuation distributions spanning at least a year, but it becomes less applicable for shorter time periods and is not generally applicable for scaling attenuation from individual rain storms (Figure 4).

Attenuation probabilities are significantly greater during summer months. The probabilities of severe attenuation (greater than 10 dB) are often more than a factor of 10 larger in July and August than for the remainder of the year. These results were obtained in New Jersey, but, since they are influenced by thunderstorm activity, they are probably representative of the eastern half of the U.S. (Figures 5, 6).

Probabilities of severe attenuations are significantly greater during the business hours and are greater still during the afternoon. For example, severe attenuation is more than three times as likely between 1 p.m. and 5 p.m. than it is for the remainder of the day (Figures 7, 8). Probabilities of moderate attenuation are more uniformly distributed throughout the day.

Depolarization is a source of crosstalk (co-channel interference) in dual-polarized frequency-reuse communication systems.

Depolarization on earth-space paths is caused by non-spherical raindrops and ice particles (snowflakes and small ice crystals). The raindrops also strongly attenuate radio signals above 10 GHz but ice particles cause only minimal attenuation. Cumulative distributions of ice depolarization alone and of mixed rain and ice depolarization for Crawford Hill indicate that mixed rain and ice depolarization is about ten times more prevalent than ice depolarization alone.

Depolarization is usually strongest for fixed linear polarizations oriented 45° from vertical and horizontal and for circular polarizations. Depolarization is usually minimized for vertical and horizontal polarizations. These minima and maxima occur for linear polarizations because the axes of minimum depolarization for raindrops and ice particles are usually oriented vertically and horizontally (Figures 9, 11).

Phase and amplitude dispersion are potential sources of bit errors in high-rate digital systems. Using the COMSTAR beacons, a comprehensive investigation was made of the dispersive properties of space-earth propagation for frequency separations of 264 MHz, 528 MHz and 9.5 GHz at 28 GHz. No evidence was found of any amplitude or phase dispersion other than the frequency dependence due to the properties of raindrops. No dispersion (frequency selective fading) was found of the type caused by multipath propagation or by resonances in the propagation medium. Therefore, amplitude and phase dispersion should not pose a problem for wideband (on the order of 1 GHz) space-earth communication systems operating above 10 GHz with path elevation angles greater than about 15°.

A potential source of co-channel interference in multi-satellite communications systems is rain-scatter coupling into a satellite-earth radio path from a different adjacent communication satellite. Rain-scatter coupling was measured at Crawford Hill for two satellite paths displaced in angle by 0.85°. For rain attenuation up to 15 dB, there was no evidence of rain-scatter coupling and it should not be a significant source of co-channel interference in multi-satellite communication systems.

#### **c. Impact of Attenuation and Depolarization on System Performance**

For a single-polarization system, outage occurs whenever the CNR falls below that value yielding barely-acceptable performance. Outage time as a function of clear-air CNR is then easily obtained from the measured or predicted cumulative distribution of attenuation. For a

dual-polarization system, the above CNR-crosstalk relation defines a range of attenuation and depolarization values causing outage. Outage-time calculations for dual-polarization systems thus require knowledge of the joint attenuation-depolarization density function. Outage time is found by integrating the joint density function over the range of attenuation and depolarization values producing outage. Results here are based on direct attenuation-depolarization COMSTAR measurements.

Attenuation has been shown to scale directly with path length and approximately as the square of the frequency ratio, and is assumed here to be independent of polarization angle. (This neglects the small contribution from differential attenuation.) Combining these relations,

$$A_{f_2, \theta_2, \phi_2} = A_{f_1, \theta_1, \phi_1} \left( \frac{f_2}{f_1} \right)^2 \left( \frac{\csc \theta_2}{\csc \theta_1} \right).$$

All attenuations  $A$  and depolarizations  $D$  are given in dB. Frequencies are denoted by subscripts  $f_i$ , elevation angles above the horizon by  $\theta_i$ , and incident polarization angles (measured from vertical polarization) by  $\phi_i$ . Depolarization amplitude scales approximately linearly with the frequency ratio. The variation in depolarization with elevation angle has two components. Depolarization amplitude varies with the square of the average raindrop oblateness viewed along the path and with the path length through the storm. The variation in depolarization amplitude with frequency is assumed to be that of a differential-phase-shifting medium with vertical and horizontal symmetry axes. Combining these relations,

$$D_{f_2, \theta_2, \phi_2} = D_{f_1, \theta_1, \phi_1} + 20 \log \left[ \frac{f_2}{f_1} \cdot \frac{\cos^2 \theta_2}{\cos^2 \theta_1} \cdot \frac{\csc \theta_2}{\csc \theta_1} \cdot \frac{\sin^2 \phi_2}{\sin^2 \phi_1} \right].$$

For digital modulation with co-channel interference, the relations between allowable CNR and CIR are obtained from [37] at a bit error rate BER of  $10^{-6}$ . These assume no band-limiting in the RF channel, and are thus independent of transmission rate and channel bandwidth.

A typical satellite FDM-FM system considered transmits 1200 voice circuits in a 40 MHz RF bandwidth with a baseband noise power ratio (NPR) of 30 dB. Baseband noise contributions from thermal noise and interference are additive. For an equal comparison with the staggered-frequency FDM-FM system above, a 1200-voice-circuit 16-PSK system is postulated operating in the same 40 MHz channel with a BER of  $10^{-3}$ . A 4-pole Butterworth transmitting filter with 24 MHz bandwidth is used for interference suppression. The interference power transferred from the two frequency-staggered interferers into the desired-channel bandwidth [38] is added to the terminal-noise power to determine the bit error rate as a function of CNR and CIR [39].

Figure 12 illustrates the effects of path elevation angle and incident polarization angle on the performance of a 19 GHz 16-PSK earth-space link. Link outage time is the total time per year that the BER exceeds  $10^{-6}$ . Each curve indicates, for a specific pair of elevation and polarization angles, the relation between clear-air CNR (on the abscissa) and link outage time (on the ordinate) for attenuation and depolarization. The tic-mark scale along each curve shows the clear-air CNR needed to achieve the link outage time on the ordinate in the absence of depolarization. The tic marks thus give the clear-air CNR needed for a single-polarization link.

For any outage time, the difference between the CNR on the abscissa and the CNR given by the tic marks is the increase in CNR needed to maintain the given outage time in the presence of depolarization. Since systems are usually designed for a specific outage objective, this number gives the increase in RF power and/or antenna gain required due to depolarization.

High reliability on a 19 GHz 16-PSK link is clearly difficult. CNRs of up to 65 dB are needed for 0.01% outage. The increase in CNR needed at low elevation angles is also greater for higher reliability. For an elevation angle range of 20 to 40 degrees, the change in CNR needed is 18.9 dB at 0.01% outage and only 5.6 dB at 0.1% outage.

The additional  $\Delta$ CNR required due to crosstalk from depolarization is greater at low elevation angles. Increased reliability requires a higher  $\Delta$ CNR also. At low elevation angles the required  $\Delta$ CNR increases greatly as the incident polarization angle increases. For polarization angles of more than 10 degrees, it is nearly impossible to attain 0.01% outage for elevation angles much below 40 degrees. For 0.1% outage, however, the change in  $\Delta$ CNR with polarization angle is small for a 40-degree elevation angle. Only at 20 degrees elevation will 45 degree polarization permit 0.1% outage.

Figure 13 compares the performance of 19-GHz 8-PSK, 16-QAM, 16-PSK and FDM-FM links for elevation angles of 20° and 40°. An incident polarization angle of 20° is used. A digital BER of  $10^{-6}$  and an FM NPR of 30 dB are required.

The performance of 16-QAM under attenuation alone is nearly as good as that of 8-PSK. An additional 1.6 dB CNR is required by 16-QAM. 16-PSK requires 5.8 dB greater CNR than does 8-PSK. FDM-FM performs nearly identically to 16-PSK. In all cases, however, over 60 dB CNR is required for 0.01% outage at 20° elevation.

FDM-FM with co-channel crosstalk cannot achieve 0.1% outage for any elevation angle considered. This illustrates the poor resistance of FDM-FM to co-channel interference.

The relative performance at 12 GHz of all four modulation techniques under attenuation alone is unchanged from that at 19 GHz. More modest CNRs (41 dB or less) are needed at 12 GHz to achieve 0.01% outage, even at 20° elevation. The  $\Delta$ CNR required due to depolarization is lower at 12 GHz than at 19 GHz. For 0.1% outage, only 16-PSK at 20° elevation among the digital techniques is seriously degraded by depolarization. For 0.01% outage, all three digital techniques are usable at 40° elevation. Only 8-PSK can attain this outage rate at 20° elevation, however. FDM-FM can achieve 0.1% outage at 40° elevation. Its performance under co-channel crosstalk is still markedly inferior to that of all digital techniques considered, however (Figure 14).

Crosstalk from depolarization is more severe at low elevation angles. For an incident polarization angle 20° from vertical or horizontal, depolarization prohibits 0.01% outage on a 20° elevation path above 12 GHz for nearly all modulation considered. At 0.1% outage, 16-level digital modulation requires large increases in clear-air CNR due to depolarization. These are smaller at higher elevation angles, and are reduced as well at 12 GHz. The choice of incident polarization angles close to vertical and horizontal can also significantly reduce the effects of depolarization. 16-QAM shows a significant performance advantage over 16-PSK. In addition to a 4 dB lower CNR requirement from attenuation alone, 16-QAM requires less additional CNR increase from depolarization. FDM-FM is devastated by co-channel crosstalk from depolarization.

### III. Motivation for Spot Antenna Beams

#### a. Maximum Effective Isotropic Radiated Power (EIRP)

The effective isotropic radiated power (EIRP) transmitted by a radio system is determined by the product of the output power of the transmitter and the gain of the antenna. For a communications system which has limited mass such as communications satellite or spacecraft,

there is an optimum antenna gain and transmitter power which maximizes the EIRP.

When both the radiated power from the transmitter and the gain of the antenna are expressed as functions of mass, then the optimum is easily determined. For example, let the mass associated with the transmitter be expressed as

$$M_p = M'_p + m_p(P) \quad (1)$$

and likewise with the antenna gain as

$$M_G = M'_G + m_G(G) \quad (2)$$

The quantity  $M'_p$  is the mass which increases in direct proportion to the RF power and is given by

$$M'_p = P/\alpha \quad (3)$$

where  $P$  is the RF output power and  $\alpha$  is a conversion factor which relates mass to power and will be discussed in more detail later.  $M'_p$  is envisioned as consisting mainly of solar cells and batteries. Similarly  $M'_G$  is the mass associated with producing antenna gain and is related to it by

$$M'_G = G/\beta \quad (4)$$

where  $G$  is the actual antenna gain and  $\beta$  is a conversion factor (similar to  $\alpha$ ) which converts mass to gain and will be discussed in later paragraphs.  $M'_G$  is assumed to consist primarily of the material used in the fabrication of the antenna.

The quantities  $m_p(P)$  and  $m_G(G)$  represent quantities which are indirectly related to the generation of power and gain, respectively. It is envisioned that  $m_p$  would include the weight of the power amplifier itself, voltage regulators, heat sinks, etc.;  $m_G$  is the overhead indirectly connected with the communications antenna which would consist primarily of antenna back-up and support structures and feeds. Both  $m_p$  and  $m_G$  are weakly increasing functions of the transmitter power and antenna gain, respectively. It is beyond the scope of this note to try to quantify these parameters. Thus, two cases will be assumed, (1) either that  $m_G$  and  $m_p$  are constants which do not depend on the actual powers and gains; and (2) both  $m_G$  and  $m_p$  grow in direct proportion to  $P$  and  $G$ .

Let  $M_T$  represent the total mass available for this portion of the communications package, that is

$$M_T = M_p + M_G \quad (5)$$

Case (1)  $m_G$ ,  $m_p$  are Constant

Using Eq. (1) through (5), P and G can be expressed as

$$P = \alpha(M_p - m_p) \quad (6)$$

$$G = \beta(M_T - M_p - m_G) \quad (7)$$

The desire is to maximize the power-gain product for a given  $M_T$ ,

$$PG = \alpha\beta(M_p - m_p)(M_T - M_p - m_G). \quad (8)$$

Taking the derivative with respect to  $M_p$  and setting to zero gives

$$\frac{\partial PG}{\partial M_p} = 0 = M_T - m_G - m_p - 2M_p \quad (9)$$

Thus

$$M_p = \frac{M_T + m_p - m_G}{2} \quad (10)$$

$$M_G = \frac{M_T + m_G - m_p}{2} \quad (11)$$

Neglecting  $m_p$  and  $m_G$ , as in the case where  $M_p \gg m_p$  and  $M_G \gg m_G$  the maximum effective radiated power is obtained when the payload mass is divided *equally* between the antenna and the power system, independent of efficiencies or required EIRP. Substituting (10) and (11) into (6), (7), and (8) provides the values for maximum transmission:

$$P_{\max} = \frac{\alpha}{2}(M_T - m_G - m_p) \quad (10)$$

$$G_{\max} = \frac{\beta}{2}(M_T - m_G - m_p) \quad (11)$$

$$PG_{\max} = \frac{\alpha\beta}{4}(M_T - m_G - m_p)^2 \quad (12)$$

Case (2)  $m_p(P) \propto P$ ,  $M_G(G) \propto G$

Assume the overhead masses associated with power and gain grow linearly with proportionality constants  $f$  and  $g$ , respectively. Then (1) and (2) become

$$M_p = (1+f)M'_p \quad (13)$$

$$M_G = (1+g)M'_G \quad (14)$$

and expressions for  $P$  and  $G$  are

$$P = \alpha M_p / (1+f) \quad (15)$$

$$G = \beta M_G / (1+g) \quad (16)$$

Since  $M_T = M_p + M_G$ , substituting for  $M_p$  in (15) and taking the derivative of  $(PG)$  with respect to  $M_G$  yields a maximum when

$$M_G = M_p = \frac{1}{2} M_T \quad (17)$$

with  $P_{\max}$  and  $G_{\max}$  given by

$$P_{\max} = \alpha M_T / 2(1+f) \quad (18)$$

$$G_{\max} = \beta M_T / 2(1+g) \quad (19)$$

$$(PG)_{\max} = \alpha \beta M_T^2 / 4(1+f)(1+g) \quad (20)$$

#### b. Conversion of Mass To Power and Gain

The conversion factors  $\alpha$  and  $\beta$  require further examination. The quantity  $\alpha$  can be expressed as

$$\alpha = \eta \left( \frac{1}{s} + \frac{1}{b} \right)^{-1} \quad (21)$$

where  $s$  is the power generating efficiency of the solar cells expressed in watt/kg,  $b$  is the battery reserve employed during solar eclipse expressed in watt/kg and  $\eta$  is the efficiency of producing RF power from DC power.

By way of example\*, the INTELSAT V spacecraft, which uses modern but conservative technology, has solar panels which generate electrical power at 21.3 watts per kilogram, and each kilogram of nickel cadmium batteries aboard this spacecraft supplies 15 watts of power through solar eclipse. Newer lightweight solar cell arrays generate about 50 percent more power for the same mass. The most optimistic predictions for solar generation of DC power run around 40 watts per kilogram. The use of nickel hydrogen batteries is expected to improve the performance compared to nickel cadmium batteries by a significant margin, yielding approximately 26 watts per kilogram. Finally, the efficiency of generating RF power from DC power depends in part upon the total radiated power of the amplifier and whether the amplifier is driven into saturation. Efficiencies greater than 50 percent for saturated amplifiers are rarely achieved, while for linear amplification efficiencies less than 10 percent are not uncommon.

The gain of an antenna is given by the formula

$$G = 4\pi \eta' A / \lambda^2 \quad (22)$$

where  $\eta'$  is the efficiency of the antenna in terms of effective antenna area,  $A$  is the actual area of the antenna aperture and  $\lambda$  is the wavelength.

---

\* A good source for state-of-the-art spacecraft component parameters is NASA report NASA 5-25091, "Future Large Broadband Switched Satellite Networks," by D. H. Staelin and R. L. Harvey.



For a circular aperture of diameter  $d$ ,  $A = \pi d^2/4$ , and for large focal length antennas the reflector has very little curvature and the surface area of the antenna can be approximated as being equal to the aperture area. For material having a density of  $c$  kg/m<sup>2</sup>, antenna gain expressed as a function of mass becomes

$$G = \beta M_G' = \frac{4\pi\eta'A}{\lambda^2} \quad (23)$$

therefore,

$$\beta = \frac{4\pi\eta'}{\lambda^2 c} \quad (24)$$

Lightweight solid antennas and precision deployable antennas, suitable for operation up to millimeter-wave frequencies with apertures smaller than 5m, have densities (including struts) around 2-4 kg/m<sup>2</sup>. Mesh deployable antennas, on the other hand, are much lighter; for example, the 10m antenna used on the ATS-F satellite weighed 182 pounds (1.27 kg/m<sup>2</sup>).

#### c. Exotic Antenna Structures

In the previous calculations conventional solid material antenna structures with mass increasing in direct proportion to area, i.e.,  $d^2$ , were assumed. However, as shown in Fig. 16, antenna mass may grow more slowly. The areas enclosed in the figure represent projected mass vs antenna diameters for various technologies. The straight lines are examples where mass increases proportional to  $d^2$ ,  $d^{1.5}$ , and  $d^{1.3}$ . Conceivably, if the surface material is sufficiently lightweight so as to be insignificant and the ribs and other skeleton structure dominate, then antenna mass would be proportional to  $d$ .

The optimum division of  $M_T$  between  $M_p$  and  $M_G$  changes according to the way in which gain is expressed as a function of mass. For simplicity let  $m_p(P) = m_G(G) = 0$ . Then

$$P = \alpha M_p \quad (25)$$

and

$$G = K_1 M_G^{4/3} \text{ when } M_G \propto d^{1.5} \quad (26)$$

$$= K_2 M_G^{20/13} \text{ when } M_G \propto d^{1.3} \quad (27)$$

$$= K_3 M_G^2 \text{ when } M_G \propto d \quad (28)$$

It is a simple task to maximize  $PG$  for the three cases, yielding, for  $M_G \propto d^{1.5}$

$$M_G = \frac{4}{7} M_T \quad (29)$$

$$(PG)_{\max} \propto M_T^{2/3} \quad (30)$$

for  $M_G \propto d^{1.3}$

$$M_G = \frac{20}{33} M_T \quad (31)$$

$$(PG)_{\max} \propto M_T^{2.54} \quad (32)$$

for  $M_{G\text{ood}}$

$$M_G = \frac{2}{3} M_T \quad (33)$$

$$(PG)_{\max} \propto M_T^3 \quad (34)$$

#### d. A 900 MHz Satellite Example

Using the INTELSAT V as a baseline,  $1/s = 0.047$  kg/watt,  $1/b = 0.067$  kg/watt and  $\eta = 25\%$ ; then,  $\alpha = 2.19$  watts/kg. Rounding down to help account for the overhead,  $m_p$ , an estimate for  $\alpha$  obtained using state-of-the-art technology becomes 2 watts/kg.

At 900 MHz,  $\lambda = 0.333\text{m}$ , and an antenna efficiency of  $\eta' = 0.6$  can be expected. Taking the density of the ATS-F antenna as state-of-the-art, gain/mass ratio becomes

$$\beta = \frac{(4\pi)(0.6)}{(0.333)^2(1.27)} = 53.4 \text{ gain units/kg}.$$

Again rounding down to help account for overhead,  $m_G$ ,  $\beta = 50$  can be assumed for some example calculations.

Figure 17 shows plots of  $P_{\max}$ ,  $G_{\max}$ , and  $(PG)_{\max}$  as functions of payload mass for the above  $\alpha$  and  $\beta$  and assuming, for simplicity,  $m_g = m_p = 0$ . It is apparent that, with the assumed

parameters, power-gain products exceeding 60 dBW require payload mass of the order of 200 kg. Of course, at higher frequencies, higher EIRP is obtained through increased antenna gain (Eq. 23) as long as antenna surface accuracies are good.

Batteries for eclipse purposes consume a significant portion of the payload mass and are used infrequently. Providing battery back-up for only half of the transmitter results in a 50 percent increase in  $\alpha$  from 2 RF watts/kg to 3 RF watts/kg, while providing no battery back-up increases  $\alpha$  to 5 RF watts/kg. The results of these changes are plotted as the solid curves in Fig. 18, which show the EIRP as a function of total communications payload mass. Also, shown as dashed curves in Fig. 18 is the increased EIRP obtained assuming (1) improved solar cells with  $\alpha = 11$  RF watt/kg; (2) improved antenna materials with one fourth the density of the ATS-F antenna; and (3) the resultant of having both improved solar cells and improved antenna materials. The dotted curve shows the results when antenna gain is held constant (30 dB), corresponding to U.S. Coverage. It shows that for EIRP's greater than 50 dBW, a U.S. Coverage antenna is suboptimal. This result is increasingly more dramatic as frequency increases.

In the example of Figure 18, assume a system requirement of 55 dBW. A conventional U.S. coverage approach requires a 180 kg payload, whereas the same EIRP could be obtained with 110 kg using a multibeam antenna. Returning to Figure 17, the optimum power is about 110 watts and an antenna gain of 34.5 dB, implying that the U.S. be covered by 3-4 spotbeams rather than a single beam.

#### e. A 4 GHz Satellite Example

Assume the following:

$$\alpha = 2; c = 3 \text{ kg/m}^2;$$

$$\beta = 450 \text{ gain units/kg}; f = .4, g = .25$$

A conventional U.S. coverage satellite with 90 kg payload provides about 51 dBW EIRP (gain  $\sim 30$  dB, power  $\sim 125$  watts). According to Eq. (20), this payload could have provided an EIRP of 60 dBW using 64W RF power and spotbeams with 42 dB gain (requiring about a 4m aperture). Alternatively, again using Eq. (20), a 51 dB EIRP requirement can be met with a 32 kg payload, transmitting  $\sim 20$  watts and employing a 38 dB gain antenna ( $\sim 2.5$ m aperture). This would appear to imply a 6-beam configuration; however, since spatial frequency reuse is not a major consideration, different frequencies can be used in adjacent beams which can be arranged to overlap, thus reducing gain loss to earth stations not located on the axis of the main antenna beam.

### IV. Antenna Research at Bell Labs

#### a. Earth Station Antennas

The first satellites required the use of ground stations with antennas of large aperture. Thus, these antennas were expensive and were designed to minimize cost and maximize efficiency.

For ground stations, it would be desirable to operate an antenna with several feeds communicating simultaneously with several satellites. Furthermore, the antennas should be able to operate in a noisy environment, requiring use of interference resistant antennas, i.e., very low side-lobes. Also these antennas should be broadband, with good cross polarization discrimination.

Most reflector antennas use the same kind of reflecting surfaces that were used more than 50 years ago; namely paraboloids, hyperboloids and ellipsoids. When the aperture is large, the main reflector is usually combined with a subreflector, and the arrangement is often similar to the 17-th century optical telescope which was devised by Abbe Cassegrain. In most satellite earth stations now in commercial use, the main reflector is derived from a paraboloid and its aperture is centered around the axis of this paraboloid. The feed is usually a horn, with its metal walls corrugated so as to minimize longitudinal currents. The horn is located between the vertex and the focus of the paraboloid, and the subreflector is needed to transform the wave radiated by the horn into a spherical wave originating from the paraboloid focus.

In 1978 construction was completed at Crawford Hill, New Jersey of a Cassegrainian antenna without aperture blockage having an aperture of 7-meters. This antenna was used for the COMSTAR propagation experiments discussed previously, and is used for radio astronomy and other experiments related to satellite communications [41].

An important advantage of the above antenna [42,43] is that it can be used to communicate simultaneously with many satellites. The only modification needed to permit efficient operation with many feeds is that the subreflector size must be increased in order to reflect all the rays emanating from the various feeds. The main reflector aperture need not be increased. In fact, by properly orienting the axis of each feed it is possible to illuminate efficiently the entire antenna aperture with each feed. Hence, the entire aperture is used effectively by each feed, and the antenna cost divided by the number of feeds is low. If the number of feeds is large, the antenna is very economical. In a conventional Cassegrainian arrangement, on the other hand, use of many feeds is limited by the subreflector, whose size cannot be increased appreciably, without causing a significant increase in aperture blockage.

#### **b. Satellite Antennas**

In a satellite antenna the equivalent focal length must be reduced, since the focal length determines the size of the feeds and their separation. Furthermore, since aberrations increase as the focal length is decreased, they must be minimized by properly choosing the subreflector parameters.

When several feeds are placed in the focal plane of such a satellite antenna, and each feed is properly designed so as to illuminate efficiently the main reflector, then each beam produces on the earth an image of the corresponding feed aperture. An important feature of such an antenna is its simplicity, provided the number of beams is small and each beam is produced by a separate feed.

An imaging arrangement of two cylindrical reflectors, suitable for a satellite antenna, was designed by Dragone [44] to produce over the continental USA a magnified image of the aperture field distribution of a corrugated feed. A multibeam antenna using a periscopic arrangement of a spherical reflector and a flat plate was designed by Turrin [45]. A similar antenna was designed by Semplak [46]. Recently, [47,48] an imaging arrangement of reflectors has been combined with a relatively small array for use in a satellite to form a scanning beam to be discussed next.

### **V. Scanning Beam Concept**

Although spot beams provide high EIRP a disadvantage stems from the fact that each spot beam covers only a small area. To avoid cochannel interference, a dead space between any two adjacent beams much larger than the beam coverage area (e.g., 3 dB contour) is required. Also, there are regions needing service which do not have enough traffic to justify a dedicated spot beam.

Area coverage satellites, use broad antenna beams covering an entire region. They are capable of providing total service everywhere within the coverage area but lack channel capacity because the allotted spectrum can be reused at most once by polarization reuse. A more significant

disadvantage, however, is the power penalty associated with the gain of an area coverage antenna. For example, the 3 dB contour gain of a shaped U.S. coverage antenna is only 27 dB and there is little that can be done to improve it further. To obtain the same SNR as a spot beam antenna system, the required RF power to transmit 600 Mb/s data rate would be 3 kW. This enormous power penalty is the unfortunate price one must pay to use a wide area coverage antenna.

Now, we discuss a new concept which allows area coverage by a rapidly scanned spot beam. The beam is steered so that all parts of the country are covered, but at different times. This works perfectly with a (TDMA) configuration. Because only one ground station accesses the satellite at a time, a spot beam toward that ground station is all that is needed and there is no need to spread energy all over the entire region; to achieve total coverage however, it is necessary to move this beam across the service region at a rapid rate such that it can pick up and drop traffic at different ground stations sequentially in time. Suppose we use a spot beam with 50 dB gain covering 1 percent of U.S. The continental U.S. can be covered by sweeping the beam to 100 different points in one frame period, perhaps a few milliseconds.

Let us examine the potential advantage of such a scanning spot beam system. At 12/14 GHz, with polarization reuse, an area coverage satellite has enough bandwidth (1 GHz total) to support about a 1.2 Gb/s data rate. The required RF power would be 6 kW or 15 kW dc (allowing 40 percent overall transmission efficiency). With the satellite dc power being generated at the rate of 0.1 kg/W without battery support the required weight for 15 kW dc power is  $\sim 1500$  kg. Even using the 10 dB less margin as in the SBS proposal, the required weight still amounts to 150 kg. In a scanned beam system only 60 watts of RF power or 15 kg of solar cells are needed to supply the electrical power. It therefore appears that the scanned beam concept offers significant potential savings in satellite weight, provided the scanning system can be realized without an exorbitant cost in weight. Furthermore, with simultaneous scanning of multiple beams, frequency reuse which cannot be achieved with area-coverage systems may be possible.

#### **a. TDMA Burst Organization**

There may be hundreds of ground stations in a scanned spot beam system. Take for example, 100 ground stations in the system, the possible distinct links amount to 4950 pairs. Of course, at any particular time the total number of connected links may be far less than this and the number of channels required between any two particular earth stations would be by no means equal. We shall discuss one possible organization format that provides the connections among the ground stations in the following paragraphs.

To illustrate the complexity of such a system let us refer to Figure 19. Shown here in the time domain are time interleaved bursts from 100 ground stations which are repeated at a frame length  $T$ . Each burst occupies a time length  $\tau_k$  and consists of preambles as well as data streams for all other earth stations as illustrated by the burst  $\tau_2$  in Figure 19. The preamble enables carrier and timing recovery on the satellite. At the satellite the data bursts are detected and remodulated onto a carrier and are sent down to the ground stations via the scanned spot beams as shown in the time sequence plot of Figure 20. Consider burst  $\tau_1$ , it consists of many sub-bursts intended for different ground stations. The scanned spot beam has to be formed and moved fast enough at the sub-burst rate to illuminate all the ground stations in the duration of the burst length  $\tau_1$ . Each ground station only receives the intended message; the time domain sequence of the received sequence of sub-bursts is shown in Figure 20. Again, each sub-burst should carry a preamble to facilitate carrier and timing recovery at the ground station.

With 500 MHz bandwidth available, we assume the bit rate to be 600 Mb/s or 300 Mbauds/s using 4-phase PSK modulation. Assuming 64 kb/s per channel, the total capacity is 9400 circuits or 4700 2-way circuits. Allowing the simultaneous participation of 100 ground stations and that each station might communicate with 10 other stations, each burst would then average 47 circuits and each sub-burst carries only 4.7 circuits. In fact, it is quite possible that some

sub-bursts may carry only one circuit at a time. For a frame length of 125  $\mu$ sec, i.e., 8 kHz sampling rate, a sub-burst carrying one voice circuit consists of only 4 bauds. This is far less than the preamble requirement and results not only in inefficiency but also in an unrealistically high switching rate of the spot beam. However, if we allow buffering at ground stations, the frame length may be lengthened by a factor of 100 to say, 12.5 msec. The added round trip delay of 50 msec is still small compared to the 500 msec round trip path delay and would not cause significant echo degradation. In this way, each sub-burst contains a minimum of 400 bauds and the necessary preamble (20~40 bauds) becomes a small penalty, even in the case of single channel sub-bursts. The required switching time of the spot beams should be achieved in the order of a few bauds, e.g., 10 ns.

The number of bits in a frame is simply  $600 \frac{\text{Mb}}{\text{s}}$  times 12.5 ms =  $7.5 \times 10^6$  bits. A station using one percent of the capacity of the channel would need to buffer only 150 ks for both up and down-link transmission. Since 16k bits of memory are available on integrated circuits chips today, the buffer requirement can be readily satisfied with minimal cost and effort.

A controller must perform the following functions:

- Assign time slots to all the ground stations according to their traffic demand. For example,  $\tau_{12} = 0$  if there is no traffic from station 1 to station 2,  $\tau_{12} = 1$  if one channel is needed, and  $\tau_{12} = 100$  if 100 channels are required. In the case  $\tau_{12} = 1$ , it is understood that 400 bauds is required, and that amounts to 1.32  $\mu$ sec time slot.
- Have the satellite form an up-link spot beam toward ground stations No. 1, 2, ..., 100 according to an on-board memory of  $\tau_{11}, \tau_{12}, \tau_{100}$ . For a 12.5 ms frame time, the average up-link burst duration is 125  $\mu$ sec.
- Have the satellite form down-link spot beams toward ground stations according to an on-board memory of the  $\tau_{jk}$ 's. A simpler alternative may be that the ground stations insert 8-bit destination headers at the beginning of each sub-burst [at least 400 bauds long], which the satellite receiver decodes and directs a down-link beam accordingly.

The memory matrix may look like the following:

$\tau_{1,1}$	$\tau_{1,2}$	$\tau_{1,3}$	.....	$\tau_{1,100}$	$\tau_1$
$\tau_{2,1}$	$\tau_{2,2}$	$\tau_{2,3}$	.....	$\tau_{2,100}$	$\tau_2$
$\tau_{100,1}$	$\tau_{100,2}$	$\tau_{100,3}$	$\tau_{100,100}$	$\tau_{100}$	

The total number of  $\tau_{ij}$ 's is  $10^4$ . Allowing 8 bits per entrant, i.e., 128 to 1 variation in number of channels per sub-burst, the required storage is 80 kbits. Since updating is infrequent, low-speed random access memory, can be used. An the power consumption certainly can be confined to the range of a few watts.

#### b. Beam Forming Using Phased Arrays

Phased arrays have some characteristics different from reflector antennas that effect their performance. When a phased array is scanned off axis there is a difference in path length between the array edge and its center. This limits its useful bandwidth. Also, it is most convenient to form a beam using discrete phase steps and using steps which are too coarse will reduce the array gain. Another source of gain degradation arises when elements fail. Finally, component phase drift may make it impossible to form beams in an open loop manner. In the following paragraphs each of these sources of performance degradation is analyzed in more detail.

### 1. Array Bandwidth

The array is intended to produce about 50 dB gain at the center of the scan region and 47 dB gain at the edge of the scan region. for a uniform circular aperture with 50 dB gain, the diameter is

$$D = \sqrt{\frac{10^2}{\pi^2}} \lambda = 100\lambda . \quad (1)$$

Allowing 70 percent aperture efficiency, the diameter of the array becomes  $120\lambda$ . The maximum scan angle of U.S. coverage is  $\pm 3^\circ$ , thus the peak path length difference from array edge to the center is

$$\Delta\phi_{\max} = + - 60\lambda \cdot 0.05 = \pm 3\lambda . \quad (2)$$

For a broadband signal the peak differential phase shift from band edge to the band center at these extreme scan angles is,

$$\Delta\theta_{\max} = \pm \frac{2\pi}{\lambda} \cdot \frac{\Delta f}{f_c} \cdot 3\lambda = \pm 6\pi \frac{\Delta f}{f_c} . \quad (3)$$

For reliable detection we want to restrict  $\Delta\theta_{\max} \leq \pi/8$ , thus we obtain

$$\frac{\Delta f}{f_c} = \pm \frac{1}{48} , \quad (4)$$

or

$$\text{Array B.W.} \approx \frac{2\Delta f}{f_c} = \frac{1}{24} = 4\% . \quad (5)$$

It is therefore reasonable to expect that the proposed phased array parameters would satisfy the bandwidth requirement of 500 MHz at 12 GHz carrier frequency with little degradation.

### 2. Minimum Phase Steps of the Phase Shifter

The on-axis far field pattern of an N element array formed using digital phase shifters can be written as

$$E = \sum_{k=1}^N e^{j\phi_k} \quad (6)$$

where  $\phi_k$  is random within  $\pm \theta/2$  where  $\theta$  is the step size of the phase shifter. The distribution function of  $\phi_k$  is

$$f(\phi_k) = \begin{cases} \frac{1}{\theta} & -\theta/2 \leq \phi_k \leq \theta/2 \\ 0 & \text{otherwise} \end{cases} \quad (7)$$

This represents the far field pattern of an N-element array with phase shifter steps of  $\theta$ . The expected gain of the main beam is

$$\langle E \rangle = N \langle e^{j\phi_k} \rangle = N \frac{\sin \theta/2}{\theta/2} \quad (8)$$

The variance of the main beam gain is

$$\sigma_E^2 = \langle \left[ E - N \frac{\sin \theta/2}{\theta/2} \right]^2 \rangle = N \left[ 1 - \frac{\sin^2 \theta/2}{(\theta/2)^2} \right] \quad (9)$$

Since E is the summation of a large number of random variables, it tends to a Gaussian random variable with mean and variance given by Equations (8) and (9). The ideal gain is N, but the mean value of E is degraded due to the finite phase shifter steps.

We see that with 45° phase steps we expect an average gain degradation of only 0.2 dB, and there is only 0.14 percent chance that the gain will degrade more than 0.8 dB. To allow 90° phase steps would produce considerable gain degradation and requiring 22.5° phase steps amounts to overkill.

### 3. Array Gain Degradation Due to Failure of Elements

The gain of an N-element array is N. Let each element radiate unity power, the EIRP in the main beam direction is  $P_o = N^2$ . If M-elements fail, the array gain reduces to N-M and the EIRP becomes  $(N-M)^2$ . We are assuming, of course, that there is no mutual coupling between elements; this is reasonable considering the large aperture size of the elements. Thus, the EIRP for case of failed elements becomes



$$P = P_0 \left[ \frac{N-M}{N} \right]^2 \quad (10)$$

where

$P_0$  is the EIRP of the array if all elements are working.

$M$  is the number of failed elements

$N$  is the number of elements of the array.

It is interesting to note that Equation (10) is identical to the failure performance of cascaded hybrid power combiners. According to Equation (10), if 10 percent of the elements fail, 19 percent of the radiated power would be lost compared to a perfectly functioning phased array.

In both the case of failed elements and discrete phase shift settings the sidelobe performance may be adversely affected. This does not pose a significant problem in these considerations because only one spot beam is considered. However, for a more sophisticated system which would have two or more movable spot beams the questions of sidelobe performance and mutual interference would have to be seriously addressed.

#### 4. Beam Forming

The remaining major problem is that of producing the proper phase progressions across the array elements to form receiving and transmitting beams toward specified ground stations. Referring to Figure 2, the radiated far-field pattern of the array at a specified angle  $\Omega$  is given by

$$E(\Omega) = \sum_{k=1}^N e^{j\theta_{k\Omega} + j\beta \vec{d}_k \cdot \hat{R}_\Omega + j\alpha_k} \quad (11)$$

where

$\theta_{k\Omega}$  is the phase shifter setting

$\beta$  is  $2\pi/\lambda$

$\vec{d}_k$  is the position of the k-th element

$\hat{R}_\Omega$  is a unit vector along the direction of  $\Omega$

$\alpha_k$  is the phase shift associated with the distribution network and the power amplifier of the k-th element, and is nominally adjusted to be equal among all the elements.

In an open loop control system, the parameters  $\vec{d}_k \cdot \hat{R}_\Omega$ , and  $\alpha_k$  are assumed to be known and time invariant through the useful life of the satellite. The appropriate values of  $\theta_{k\Omega}$ 's are determined before hand and are stored on board the satellite such that

$$\theta_{k\Omega} = -\beta \vec{d}_k \cdot \hat{R}_\Omega . \quad (12)$$

However, it is extremely difficult, if not impossible, to keep the phase shifts through a distribution network (hundreds of wavelengths long) invariant under extreme temperature variations and over a long period of time. Also, the phase shifts through the microwave amplifiers may drift differently with time and temperature.

Realizing that the  $\alpha_k$ 's may vary, a close-loop system for phase control is desirable. Such a system would be basically open loop most of the time, i.e., the required  $\theta_{k\Omega}$ 's are stored in memory and retrieved to form spot beams. However, occasional updating is performed to track out the variation of  $\alpha_k$ 's. Since the  $\alpha_k$ 's would be the same for any spot beam angle  $\Omega$ , the required updating of the  $\alpha_k$ 's can be performed with the help of only one ground station.

A technique to update the  $\alpha_k$ 's is briefly described below. Referring to Equation (11), let us inject a cyclic modulation  $\gamma(t)$  through the phase shifts associated with the No. 1 element. The radiated far field is

$$E'_1(\Omega) = e^{j\theta_{1\Omega} + j\beta \vec{d}_1 \cdot \hat{R}_\Omega + j\alpha_1 + j\gamma(t)} + Ae^{j\theta} , \quad (13)$$

where

$$Ae^{j\theta} = \sum_{k=2}^N e^{j\theta_{k\Omega} + j\beta \vec{d}_k \cdot \hat{R}_\Omega + j\alpha_k} .$$

At the ground station in this spot beam let us square  $E'_1(\Omega)$  and look at the baseband output where we obtain

$$Y_1(t) = \frac{1}{2} + \frac{A^2}{2} + A \cos[\theta_{1\Omega} + \beta \vec{d}_1 \cdot \hat{R}_\Omega + \alpha_1 + \gamma(t) - \theta] . \quad (14)$$

The dc terms are of no interest but the ac term is detected yielding,

$$Z_1(t) = A \cos[\theta_{1\Omega} + \beta \vec{d}_1 \cdot \hat{R}_\Omega + \alpha_1 + \gamma(t) - \theta] . \quad (15)$$

Similarly, we can put the modulation  $\gamma(t)$  on the No. 2 element to obtain

$$Z_2(t) = A' \cos[\theta_{20} + \beta \vec{d}_2 \cdot \hat{\Omega}_k + \alpha_2 + \gamma(t) - \theta'] \quad (16)$$

Since  $\theta$  and  $\theta'$  are the same, the phase difference between Equations (4) and (5) can be detected giving

$$\Delta = \theta_{10} - \theta_{20} + \beta(\vec{d}_1 - \vec{d}_2) \cdot \hat{R} + \alpha_1 - \alpha_2 \quad (17)$$

Since  $\theta_{10} = -\beta \vec{d}_1 \cdot \hat{\Omega}$  and  $\theta_{20} = -\beta \vec{d}_2 \cdot \hat{\Omega}$  originally, Equation (6) becomes

$$\Delta = \alpha_1 - \alpha_2 \quad (18)$$

Thus, we have detected the static differential phase shift between elements 1 and 2. This information can be relayed back to the satellite to adjust the phase of element 2. The adjustment can be done simply by putting a bias in the phase memory of  $\theta_{20}$ 's. This same updating technique can be used in the receiving system for the formation of receiving beams.

### c. Scanning Fan Beam Antenna

An antenna which would produce an elliptically shaped beam that could be scanned across the continental United States (CONUS) in the east-west direction is proposed for an experimental Ku band communications package as shown in Figure 22. The frequency band is 11.7 GHz to 12.2 GHz for the down-link and 14.0 GHz to 14.5 GHz for the up-link. To cover the CONUS north-south dimension the 3 dB beamwidth should be about 3 degrees to provide the greatest absolute gain at the north-south limits of the beam. (Although a wider beam would bring the antenna gain at the north-south limits of the beam nearer that at the center, the absolute gain at the center would be reduced.) To conserve space on the satellite it is desirable to use the same antenna aperture for up-link and down-link frequency bands. The frequency ratio between these two bands ( $14.25/11.95=1.2$ ) suggested the use of different polarization in a rectangular horn to keep the north-south beamwidth approximately the same for the two frequency bands. For vertical (north-south) polarization the field is uniform over the horn aperture in the vertical direction giving a north-south 3 dB beamwidth [49] of  $50.4 \frac{\lambda}{a}$  degrees\* and for horizontal polarization the field has a cosine distribution over the horn aperture in the vertical direction producing a beamwidth of  $68.8 \frac{\lambda}{a}$  degrees,\* where  $a$  is the vertical height of the horn aperture and  $\lambda$  is the free space wavelength. Thus using a 19 inch aperture height the north-south beamwidth is 3.0 degrees at 14.25 GHz with a horizontally polarized aperture and is

\* Assuming no phase error in the aperture.

2.6 degrees at 11.95 GHz with a vertically polarized aperture. To prevent the horns from being too long, it is common practice to allow some phase error in the aperture. A  $1/8\lambda$  phase error at 14.25 GHz and correspondingly  $1/10\lambda$  phase error at 11.95 GHz would cause negligible gain and pattern degradation and widen the above beamwidths to 3.1 degrees and 2.8 degrees, respectively.

In the east-west direction the beamwidth should be narrow enough to fit about 10 beams on CONUS, i.e., about 0.6 degrees bandwidth =  $50.4 \frac{\lambda}{b}$ . At 13.05 GHz, the geometric mean of the two frequency bands, the required horizontal width,  $b$ , of the array aperture is 76 inches for 0.6 degree beamwidth. To make the beam scan in the east-west direction the 76 inch aperture could be divided into 16 elements  $4\text{-}3/4$  inches wide. such elements would have 3 dB east-west beamwidth of 14.3 degrees at 11.95 GHz (vertically polarized, cosine distribution in horizontal plane) and 8.8 degrees at 14.25 GHz (horizontally polarized, uniform distribution in horizontal plane). Such element antenna beams imply, for a 3.5 degree scan to the edge of CONUS, 0.5 dB scan loss at 11.95 GHz and 1.75 dB scan loss at 14.25 GHz. Separation between grating lobes would be 12 degrees at 11.95 GHz and 10 degrees at 14.25 GHz. Increasing the number of elements in the 76 inch wide aperture with narrower width elements would reduce the scan loss and increase the grating lobe spacing but increase the electronic complexity with more phase shifters, etc. The choice of sixteen elements results in a feasible electronics package and, being a power of two, simplifies the power division and combining networks. Although the  $76 \times 19$  aperture of such a 16-element horn array is small enough to include on an operational satellite, the horn length (436 inches for  $\frac{\lambda}{8}$  phase error at 14.25 GHz) is too large. Even with the use of horn lens elements or horn reflector elements the horns are still too bulky. However, the elements can be reduced to an acceptable size with the aid of imaging reflectors [47]. To avoid excessive aberrations when scanning, the focal length of the main reflector should be on the same order as its maximum aperture dimension (76 inches). Therefore, to make the antenna more compact it is desirable to divide the width of the main reflector into sections until the width of each section is equal to its height. This results in four subassemblies each with four horns as shown in Fig. 23.

Each subassembly in Fig. 23 contains a pair of parabolic reflectors in a Gregorian arrangement with a magnification of five. Each main reflector has a focal length of 19" and a square aperture 19" on a side. The four feed horns are each  $17\text{-}1/2$  inches long with  $3.8 \text{ inches} \times 0.95 \text{ inch}$  apertures. An inverted five times image of each four horn array is produced at the aperture of each main reflector so that side by side they form the 16 element  $19 \times 76$  array aperture discussed above, except the overall antenna is only 23 inches deep. The inputs to the horns are square waveguides so that the up-link and down-link frequency bands are readily separated by a square waveguide polarization diplexer. A side view of a subassembly is shown in Fig. 24. Three geometric optics rays (top, center and bottom) are traced through the antenna. Also shown is the null width of the Airy disc at 11.95 GHz for diffraction from the main reflector, which demonstrates that there is very little blockage from the horns. The far field of the antenna is imaged at its focal plane; e.g., the extent of the CONUS image at the focal plane is indicated in Fig. 24. An RF model of the above-described antenna was constructed as shown in the photograph, Fig. 25. The reflectors were numerically machined aluminum. Fig. 26 shows the measured scanning characteristics of the RF model at 11.95 GHz. As the array is scanned off boresight, there is an immediate drop in gain of about 0.8 dB due to the increase of phase shifter insertion loss. For a scan of 3.5 degrees the gain has dropped an additional 1 dB. Of this 1 dB,  $1/2$  dB is due to the individual horn element pattern and  $1/2$  dB is due to mutual coupling between horns as verified by measuring the horn arrays without the imaging reflectors. Measurements over the down-link frequency band show negligible variation with frequency. After subtracting out network losses due to electronic phase shifters, line stretchers, coaxial cable, and power dividers, the absolute gain of the RF model referred to the coaxial connector ports of the horn inputs was measured to be 40.7 dB at 11.95 GHz, with an azimuth beamwidth

0.7 degrees and an elevation beamwidth of 2.8 degrees. The measurements indicate that this design would perform satisfactorily as a scanning fan beam satellite antenna and is relatively insensitive to mechanical alignment errors.

**d. Limited-Scan Concept**

Suppose the total region over which service is to be provided is completely covered or spanned by a large number  $M$  of spot beam footprints. For example, if we wish to cover the  $3^\circ \times 6^\circ$  area of the continental United States as seen from geostationary orbit, we would need approximately  $M = 100$  footprints, each with 3 dB beamwidths of  $0.5^\circ$ . Let the traffic between each of these  $M$  spot beam footprints be denoted by the matrix

$$\mathbf{I} = \begin{bmatrix} t_{1,1} & t_{1,2} & \cdots & t_{1,M} \\ t_{2,1} & t_{2,2} & \cdots & t_{2,M} \\ \vdots & \vdots & \ddots & \vdots \\ t_{M,1} & t_{M,2} & \cdots & t_{M,M} \end{bmatrix} \quad (1)$$

where element  $t_{ij}$  represents the traffic originating in footprint  $\#i$ , destined for footprint  $\#j$ . There are  $N \ll M$  identical satellite transponders available, each of capacity  $C$  voice circuits. Let

$$R_i = \sum_{j=1}^M t_{ij} \quad , \quad 1 \leq i \leq M \quad (2)$$

$$S_j = \sum_{i=1}^M t_{ij} \quad , \quad 1 \leq j \leq M \quad (3)$$

We note that  $R_i$  represents the total traffic originating within footprint  $\#i$ , and  $S_j$  represents the total traffic destined for footprint  $\#j$ .

Suppose  $R_i \leq C$ ,  $S_j \leq C$ , all  $i, j$ .

If these conditions are not satisfied, then it is impossible to serve  $\mathbf{I}$  since, then, two or more transponders would be simultaneously connected to the same up-link or down-link footprint, resulting in severe cochannel interference. We require, further, that the total traffic of  $\mathbf{I}$  be less than the total satellite capacity, i.e.,

$$\sum_{i=1}^M R_i = \sum_{j=1}^M S_j = \sum_{i=1}^M \sum_{j=1}^M t_{ij} \leq NC \quad .$$

The above inequalities represent necessary conditions imposed upon the traffic  $\mathbf{I}$  in order that universal service be provided via a multiple scanning beam satellite system. The following theorem, proven in [50], establishes these as sufficient conditions as well. Thus, provided that the above inequalities on the row and column sums and on the total traffic of the matrix  $\mathbf{I}$  are satisfied, it is possible to assign the  $N$  transponders to the  $M$  up-link and  $M$  down-link spot beam footprints on a time division basis such that the footprint-to-footprint traffic can be accommodated on a nonconflicting basis, that is, at any point in time, only one transponder is connected to a given up-link or down-link footprint. Furthermore, if the total traffic of  $\mathbf{I}$  is identically equal to the total available capacity of the  $N$  transponders, then there are no unused time slots associated with the TDMA frames of any transponder, and all transponders are used with an efficiency of 100 percent. Thus, this condition may be used to establish the minimum number of transponders needed.

We define a diagonal of  $\mathbf{I}$  as a set of  $N$  nonzero entries selected such that no two entries occupy the same row or column. The following is then true: [50].

**Theorem 1:** Given  $N$  satellite transponders, each of capacity  $C$ . If the traffic matrix inequality conditions are satisfied, then at least one diagonal always exists which covers all rows and columns (if any) which sum to  $C$  exactly.

Using this theorem, we assign traffic to the satellite transponders as follows. Let us select a diagonal from  $\mathbf{I}$  covering all rows and columns summing exactly to  $C$ . We assign one unit of traffic from each element of the diagonal to the first time slot of the TDMA frame associated with each satellite transponder. By construction, during this time slot, no transponder is connected to more than one up-link or down-link footprint. We delete the  $N$  units of assigned traffic from matrix  $\mathbf{I}$  and note that, in the reduced matrix, no row or column sums to more than  $C - 1$ , and the total traffic does not exceed  $N(C-1)$ . Also each satellite transponder has  $C - 1$  remaining units of unassigned capacity. We see that the conditions of Theorem 1 are again satisfied, with  $C - 1$  replacing  $C$ . Thus, we can repeat the steps of the assignment for successive TDMA time slots, until all traffic has been assigned.

Implementation of the above approach requires that each transponder be connected to a spot beam antenna port capable of being scanned anywhere over the total service region. Additionally, the traffic-to-transponder assignment, while nonconflicting, does not ensure that cochannel interference via antenna sidelobes is always negligible. In the following, we present a satellite system concept enjoying the high antenna gain and efficient resource allocation advantages of the multiple independent scanning spot beam approach, but for which implementation is greatly facilitated. Moreover, the traffic-to-transponder assignment can be made such that cochannel interference via antenna sidelobes is negligible.

Suppose it is possible to divide the total service area into  $N$  transmit zones and  $N$  receive zones with the following characteristics:

- 1) The  $N$  transmit zones are mutually noninterfering, that is, no two or more up-link transmissions occurring from different zones can interfere with a level higher than  $-20$  dB at the satellite.
- 2) The  $N$  receive zones are mutually noninterfering, that is, no two or more down-link transmissions destined for different zones can interfere with a level higher than  $-20$  dB.
- 3) The traffic originating from and destined for each zone is equal to  $C$ .

A possible subdivision is as shown in Figure 27, drawn for linear zonal boundaries. Polarization usage is alternated among zones to satisfy the interference criteria. We denote the  $i^{\text{th}}$  transmit zone by  $R_i$ , and the  $j^{\text{th}}$  receive zone by  $S_j$ . We note that the transmit, and receive zones need not be the same, nor must all zones include an identical number of footprints.

From the original traffic matrix  $\mathbf{T}$  we can define a new  $N \times N$  traffic matrix  $\mathbf{I}$  whose elements  $\tau_{ij}$  represent the total traffic originating from transmit zone  $R_i$  destined for receive zone  $S_j$ :

$$\mathbf{I} = \begin{bmatrix} \tau_{1,1} & \tau_{1,2} & \cdots & \tau_{1,N} \\ \tau_{2,1} & \tau_{2,2} & \cdots & \tau_{2,N} \\ \vdots & \vdots & \ddots & \vdots \\ \tau_{N,1} & \tau_{N,2} & \cdots & \tau_{N,N} \end{bmatrix} \quad (4)$$

For this matrix, we can use the algorithm of Reference [50] to assign the traffic to the  $N$  transponders in a noninterfering manner. From matrix (4), one unit of traffic is extracted from each row and column such that no row or column has more than one unit of capacity removed. This is always possible. There  $N$  traffic units are assigned to the same TDMA time slot and are distributed over the  $N$  satellite transponders. Having completed this step, the remaining traffic has the property that each row and column now contains  $C - 1$  units of capacity. We repeat these steps until all traffic has been assigned and all transponders are fully loaded.

A possible transponder assignment is illustrated by the  $N$  transponder TDMA frames of Figure 28. We note that the up-link of transponder  $k$  is always connected to the  $k^{\text{th}}$  transmit zone, and that at any point in time, no two transponders are connected to the same receive zone. Similarly, the assignment could have been made such that the down-link of transponder  $k$  is always connected to the  $k^{\text{th}}$  receive zone, and no two transponders are simultaneously connected to the same transmit zone.

Consider now transponder No. 1. In Figure 28, we expand the time period for which  $R_1$  is connected to  $S_1$ . Denote the footprints which span  $R_1$  by  $f_{1,1}, f_{1,2}, \dots, f_{1,K_1}$ , and denote the footprints which span  $S_1$  by  $f_{1,1}, f_{1,2}, \dots, f_{1,K_1}$ . The capacity allocated to communication between  $R_1$  and  $S_1$  is exactly equal to the total traffic originating from the  $K_1$  footprints of  $R_1$  and destined for the  $K_1$  footprints of  $S_1$ . Thus, while  $R_1$  is connected to  $S_1$ , we first park the up-link of transponder No. 1 over  $f_{1,1}$  and sweep the down-link in time sequence over all  $K_1$  footprints of  $S_1$ . Having completed this, we move the up-link over the footprint  $f_{1,2}$  and again sweep the down-link over  $S_1$ . We continue in this manner, as shown, until each of the  $K_1$  footprints of  $R_1$  have had an opportunity to communicate with each of the  $K_1$  footprints of  $S_1$ . The time allotted on transponder No. 1 for communication between  $R_1$  and  $S_1$  is precisely equal to the time needed to interconnect the footprints of each region as based upon the footprint-to-footprint demand for service of matrix (1).

This process is repeated for all other zonal interconnections. Thus, we have presented an assignment technique which satisfies the traffic requirements of the original traffic matrix  $\mathbf{T}$  on a noninterfering basis and with 100 percent transponder utilization efficiency.

A block diagram of the satellite repeater for this scheme appears in Figure 29. Here, one up-link antenna port is dedicated to each of the  $N$  up-link zones  $R_1$  through  $R_N$ , and one down-link antenna port is dedicated to each of the down-link zones  $S_1$  through  $S_N$ . An on-board  $N \times N$  switch allows the zonal interconnections displayed in the TDMA frames of Figure 28. Each antenna port can be rapidly scanned over the footprints spanning the associated zone to permit the footprint interconnections illustrated in Figure 28.

### e. Antenna Design for Limited Scanning

This antenna consists of a set of linear array feeds located in the focal plane of a parabolic cylinder reflector oriented parallel to the linear array feeds. Each row acts essentially as a line source radiating a cylindrical wave which is transformed by the reflector into a spot beam. Each element in the array illuminates a strip of the parabolic reflector, as shown, which in turn illuminates a strip in the far-field, also shown. The height  $h$  of each element in the array controls the corresponding width  $w$  of the far-field strip. Adjacent strips of the reflector surface illuminated by adjacent array elements from a common row in the array feed illuminate the same far field strip but with different phase. The superposition of all such images forms a spot beam within the far field. Thus, by linearly varying the phase across the elements of one row, a spot beam can be formed anywhere within the far field strip of that row. Elements from an adjacent row in the array feed illuminate the same strips upon the reflector surface, but with a constant phase offset relative to the neighboring rows. This corresponds to a linear translation of the strip formed in the far field. By properly phasing the elements of  $N$  rows in the array feed,  $N$  independent spot beams are formed, one in each of  $N$  strips of the far field.

In the next section a method is described where the aperture of a relatively small array is magnified, inside a satellite, using an arrangement of several reflectors. Because of imaging by the reflectors, the field distribution over the array aperture was reproduced faithfully over the much larger aperture of the main reflector. Thus, a narrow beam which may be directed efficiently towards any location in USA was obtained. We now present a practical antenna design also using imaging techniques. Each linear array feed for this antenna is capable of scanning a beam over a rectangular strip of width typically  $0.4^\circ$  to  $0.6^\circ$  and length  $5^\circ$  as seen from synchronous orbit. Within each strip, the beam formed has a typical  $-3$  dB contour of  $0.4^\circ$  to  $0.6^\circ$ .

We wish to produce several spot beams, each scannable over a narrow strip. To this purpose, we propose use in the satellite of an off-set Cassegrain arrangement of two reflectors, so as to form on the focal plane  $\Sigma_f$  a small image of the USA as shown in Fig. 30. Then, for each ground station  $S_\infty$  on the earth there will be a corresponding image  $S_1$  and  $\Sigma_f$ . In order to form a beam radiated in the direction of  $S_\infty$ , a feed acting as a point source  $S_1$  must be placed on the focal plane. One can show that the angle  $\theta$  specifying the direction of  $S_\infty$  in Fig. 30 is related to the displacement  $\ell = |S_1 F_1|$  through the relation

$$\theta \sim \frac{\ell}{f} , \quad (5)$$

where  $f$  is the equivalent focal length of the Cassegrain arrangement.

As shown in Fig. 30, the hyperboloid forms on a plane  $\Sigma_1$  at a distance  $d = |S_1 C_1|$  from  $S_1$  a virtual image of the paraboloid. This image is centered at  $C_1$ , and its diameter  $D_1$  is related to the diameter  $D_p$  of the paraboloid by:

$$D_p \sim D_1 M_1 , \quad (6a)$$

where



$$M_1 = \frac{|C_p C_h|}{|C_b C_1|} \quad (6b)$$

Thus, in order to maximize aperture efficiency, the spherical wave radiated by the point source  $S_1$  must efficiently illuminate this image and, therefore, it must satisfy the following requirements:

- 1) The illuminated area on  $\Sigma_1$  must have diameter approximately equal to  $D_1$ .
- 2) The spherical wave from  $S_1$  must be centered around the ray proceeding in Fig. 30 from  $S_1$  towards  $C_1$ .

The above ray will be called the principle ray and,  $S_1$  the feed phase center. We now draw a straight line through  $S_1$  and, in addition to the above two requirements, we require that by varying the feed excitation, the location of  $S_1$  be movable continuously on this line.

A feed satisfying the above requirements can be realized as shown in Fig. 31. A linear array with its aperture centered at  $C_0$  radiates a wave which is guided between two parallel plates. This wave propagates in the direction of the ray which originates at  $C_0$ , is reflected at I, and then passes through the phase center  $S_1$ . This ray is the principle ray defined earlier and, in order to satisfy conditions 2), the curve defined by the cylinder on the plane  $y = 0$  must be an ellipse with foci  $C_0$  and  $C_1$ .

To determine the illumination over the plane  $z = d$ , we now assume that this plane is in the far-field of the feed. It has been assumed, so far, that the wave radiated by the feed is a spherical wave. In general, if this condition is not satisfied, the wave-fronts illuminating the plane  $z = d$  will have different curvature in the two principle planes and, therefore, the phase centers in the two planes will be different. In Fig. 31, the phase center in the principle plane orthogonal to the plates is located on the feed aperture and is given by  $S_1$ . The other phase center is a focal point determined on the principle ray by the wave reflected by the cylinder. We conclude that, if the plane  $z = d$  is to be illuminated by a spherical wave from  $S_1$ , the above focal point must coincide with  $S_1$ . The array excitation must be chosen so as to satisfy this requirement. In the particular case where

$$\frac{1}{|IS_1|} = \frac{1}{|C_0I|} + \frac{1}{|IC_1|} ,$$

one can show that the required array excitation is a plane wave. We now consider the amplitude distribution over the plane  $z = d$ . It can be shown to be the product of two functions,  $F(x)$  and  $G(y)$ , related respectively to the Fourier transforms of the field distributions along the  $x$ - and  $y$ -axes on the feed aperture. Taking this into account, one finds that  $G(y)$  is independent of the feed excitation, and it is determined only by the separation  $t$  of the plates and the polarization of the array. If one requires at the edge of the paraboloid for  $x = 0$  and  $y = D_1/2$ , an illumination of  $-10$  dB with respect to the center  $x = y = 0$ , one finds that  $t$  must be given by

$$t_1 = 1.48\lambda \frac{f}{D_p}, \text{ or } t_2 = 2.12\lambda \frac{f}{D_p}, \quad (7)$$

depending on whether the electric field polarization inside the feed is orthogonal or parallel to the plates. For the other distribution  $F(x)$ , on the other hand, one has that it is determined by the array excitation and, since  $C_0$  and  $C_1$  are conjugate points,  $F(x)$  is the image of the array distribution  $A(u)$ ,

$$|F(x)|^2 \cong \frac{1}{M_2} \left| A \left( \frac{x}{M_2} \right) \right|^2,$$

$M_2$  being the magnification. Thus,

$$M_2 \cong \frac{|C_1 I|}{|C_0 I|}$$

if both the array aperture and the plane  $z = d$  are orthogonal to the principle ray.

We conclude that by properly choosing the array amplitude distribution  $A$  and the spacing  $t$  of the plates, efficient illumination of the paraboloid aperture will be obtained. By changing the array phase distribution, the phase center  $S_1$  will move along a straight line, as indicated in Fig. 28. The corresponding beam direction, given by  $S_\infty$ , will describe on the earth a curve given by the projection of this line.

We have seen that for efficient illumination of the paraboloid a different value of  $t$  must be used depending on whether the feed polarization is parallel or orthogonal to the plates. It is thus convenient to use two separate feeds for the two polarizations. A grid of straight wires is then required between the hyperboloid and the focus  $F_1$ . Signals with polarization orthogonal to the wires will pass through the wires, whereas total reflection will occur for the parallel polarization. Two separate focal planes are thus obtained for the two polarizations.

The two beams of Fig. 32 centered at  $\theta = 0$  and  $\theta = \theta_1$  are produced by adjacent feeds with polarization orthogonal to the plane of the plates and correspond to the minimum separation between simultaneous uses of that polarization. However, by subdividing the array width  $t$  of Fig. 31 into  $N$  equal parts and assigning a separate array to each, we can now form a beam by exciting any  $N$  adjacent feeds, thereby allowing a beam to be produced at  $\theta = k\theta_1/N$ ,  $0 \leq k \leq 1$ . Of course, no such beam can simultaneously be produced with either of the beams at  $\theta = 0$  or  $\theta = \theta_1$  shown in Figure 32. Similarly, the minimum separation between simultaneous beams of polarization parallel to the plates is  $\theta_2$ , although beams can be formed, in different time slots, at  $\theta = k\theta_2/N$ .

## VI. Multireflector Arrays

Normally, the use of arrays in a satellite antenna of very large aperture is difficult because they are heavy, and difficult to realize because of the long interconnections required between the array elements. Using multiple reflectors to produce a magnified image of the array over the antenna aperture array size simplifies many of these problems.

The reflectors are arranged so that a magnified image of the array  $S_0$  is formed over the aperture of the main reflector. The magnification  $M$  relating the diameters  $D_0$  and  $D_1$  of the main reflector and the array, respectively, is chosen much greater than unity, i.e.,

$$M = \frac{D_0}{D_1} \gg 1, \quad (1)$$

so that the array is much smaller than the main reflector.

An important property of these arrangements is that the transformation relating the field over the array aperture to the field over the main reflector aperture is essentially frequency independent, and therefore it can be approximated by its asymptotic behavior at high frequency. That is, the transformation can be determined accurately using the laws of geometric optics.

In Fig. 33, the first paraboloid,  $S_0$ , transforms a plane wave, propagating in the direction of the paraboloid axis, into a spherical wave converging toward the focus  $F$ . This spherical wave is then transformed into a plane wave, by the second paraboloid  $S_1$ , which is large enough to intercept all incident rays. After the second reflection, the reflected rays illuminate the array plane  $\Sigma_1$ . Since the illuminated area corresponds to the projection of the first paraboloid, its diameter  $D_1$  is determined by  $D_0$ , and from Fig. 33,

$$M = \frac{D_0}{D_1} = \frac{f_0}{f_1}, \quad (2)$$

where  $f_1$  and  $f_0$  are the axial focal lengths of the two paraboloids. Thus, by choosing

$$\frac{f_0}{f_1} \gg 1,$$

a small array diameter  $D_1$  is sufficient to intercept all the incident rays. Notice on  $\Sigma_1$  the center of illumination is determined by the ray corresponding to the center  $C_0$  of the paraboloid. The center  $C_1$  of the array must therefore be placed on this ray, which will be called the central ray.

Now suppose in Fig. 33 the direction of the incident wave is changed so that the ray incident at  $C_0$  makes a small angle  $\delta\theta_0$  with respect to the central ray. The center of illumination will then vary with  $\delta\theta_0$ , unless  $C_0$  and  $C_1$  are conjugate points, as in Fig. 33. In this case, for small  $\delta\theta_0$ , all rays reflected at  $C_0$  pass through  $C_1$  after the second reflection. We thus conclude that, for maximum efficiency of illumination, the following condition must be satisfied:

The center of the main reflector and the center of the array must be conjugate points.\* (3)

When this condition is satisfied, the field in the vicinity of  $C_1$  is the image of the field in the vicinity of  $C_0$ . More precisely, let  $\Sigma_0$  and  $\Sigma_1$  be the two planes orthogonal to the central ray, through  $C_0$  and  $C_1$ . Then  $\Sigma_0$  and  $\Sigma_1$  are conjugate planes, in the vicinity of  $C_0$  and  $C_1$ , and therefore the field  $E_1$  on  $\Sigma_1$  is the image of the field  $E_0$  on  $\Sigma_0$ .

The consequences of this basic condition are now discussed. The transformation which relates the input field  $E_0$  to the output field  $E_1$  in Fig. 33 involves several reflections and, because of diffraction, the field propagating from one reflector to the next cannot be determined accurately using the laws of geometric optics. Thus, suppose Fresnel's diffraction formula is used to determine the transformation from one reflector to the other, or from the reflector to the array in Fig. 33. When the input and output planes are conjugate planes of the optical system, the output field  $E_1$  is simply the image of the input field  $E_0$ , and it can be calculated using the laws of geometric optics. This result is quite remarkable for, in general, the laws of geometric optics give correctly only the field in the output plane, not the field inside the optical system.

The location of  $C_1$  is now determined. The ray reflected in Fig. 33 at  $C_0$  for  $\delta\theta_0 \neq 0$  will be called the principal ray. Let  $\delta\theta_1$  be the angle this ray makes with the central ray at  $C_1$ . Then, since  $M$  is the magnification of the two conjugate planes  $\Sigma_0$  and  $\Sigma_1$ , the angles  $\delta\theta_0$  and  $\delta\theta_1$  must satisfy the well-known relation

$$\delta\theta_1 = M\delta\theta_0 .$$

Now, from Fig. 33,

$$d_1\delta\theta_1 = d_0\delta\theta_0 , \quad (4)$$

$d_1$  and  $d_0$  being the distances of  $C_1$  and  $C_0$ , respectively, from the center  $B_1$  of the subreflector. One can show that

$$d_0 = \frac{f_1 + f_0}{\cos^2 i} , \quad (5)$$

$i$  being the angle of incidence at  $C_0$  (or  $B_1$ ) for the central ray. From the above relations one

---

\* Conjugate elements in an optical system have the property that the rays originating from a point of one element are transformed, by the optical system, into rays which pass through a corresponding point of the other element. Two such corresponding points are called conjugate points.

obtains

$$d_1 = \frac{f_1 + f_0}{\cos^2 i} \frac{1}{M} \quad (6)$$

or

$$d_1 = \frac{f_1}{\cos^2 i} \frac{M + 1}{M} = |FB_1| \frac{M + 1}{M} \quad (7)$$

In Fig. 33, the array is relatively close to the subreflector  $S_1$ , and this may be a disadvantage for some applications. In some applications, a greater distance  $d_1$  will be needed to place a grid between the array and the subreflector for polarization or frequency diplexing. In this case, it is advantageous to use three reflectors  $S_0$ ,  $S'_0$  and  $S_1$ ; details of this arrangement are given in [47].

#### *Acknowledgments*

The author wishes to thank Messrs A. S. Acampora, H. W. Arnold, D. C. Cox, C. Dragone, M. J. Gans, and Y. S. Yeh for graciously allowing me to incorporate generous portions of their original work in this manuscript.

## REFERENCES

- [1] Pierce, J. R., "Orbital Radio Relays", *Jet Propulsion*, April, 1955.
- [2] Oliver, B. M., Pierce, J. R. and Shannon, C. E., "The Philosophy of PCM", *Proc. IRE*, Vol. 36, November, 1948.
- [3] Pierce, J. R., and Kompfner, R., "Transoceanic Communication by Means of Satellite", *Proc. IRE*, Vol. 47, March, 1959.
- [4] Jakes, W. C., Jr., "Participation of Bell Telephone Laboratories in Project Echo and Experimental Results", *BSTJ*, July, 1961, p. 975.
- [5] Crawford, A. B., Hogg, D. C., Hunt, L. E., "A Horn-Reflector Antenna for Space Communication", *BSTJ*, July, 1961, p. 1095.
- [6] Crawford, A. B., Cutler, C. C., Kompfner, R., and Tillotson, L. C., "The Research Background of the Telstar Experiment", *BSTJ*, Vol. 42, July, 1963.
- [7] Tillotson, L. C., "A Model of a Domestic Satellite System", *BSTJ*, Vol. 47, December, 1968.
- [8] Ohm, E. A., "Systems Aspects of a Multibeam Antenna for Full U.S. Coverage", *ICC'79 Conf. Rec.*, Vol. 3, Paper 49.2, Boston, June 1979.
- [9] Reudink, D. O. and Yeh, Y. S., "A Scanning Spot Beam Satellite System", *BSTJ*, Vol. 56, October, 1977.
- [10] Reudink, D. O. and Yeh, Y. S., "A Rapid Scan Area-Coverage Communication Satellite", *Journal Spacecraft and Rockets*, Vol. 17, No. 1, January-February 1980, p. 9-14.
- [11] D. C. Hogg and T. S. Chu, "The Role of Rain in Satellite Communications", *Proc. IEEE*, 63, September 1975.
- [12] T. Oguchi, "Scattering from Hydrometeors — A Survey", *URSI Comm. F Symp. on "Effects of the Lower Atmosphere on Radio Wave Propagation Above 1 GHz"*, Lennoxville, Canada, May 26-30, 1980 and *Radio Science*, September-October 1981, pp. 691-730.
- [13] R. K. Crane, "Propagation Phenomena Affecting Satellite Communication Systems Operating in the Centimeter and Millimeter Wavelength Band", *Proc. IEEE*, Vol. 59, February 1971, pp. 173-188.
- [14] D. C. Cox, H. W. Arnold, H. H. Hoffman, "Depolarization of 19 and 28 GHz Earth-Space Signals by Ice Particles", *Radio Science*, 13, May-June, 1978, pp. 511-517.
- [15] T. S. Chu, "Rain Induced Cross-Polarization at Centimeter and Millimeter Wavelengths", *BSTJ*, 53, October, 1974, pp. 1557-1579.
- [16] T. S. Chu, "Microwave Depolarization of an Earth-Space Path", *BSTJ*, 59, July-August 1980, pp. 987-1007.
- [17] S. H. Lin, H. J. Bergmann, and M. V. Pursely, "Rain Attenuation on Earth-Satellite Paths - Summary of 10-Year Experiments and Studies", *BSTJ*, 59, February 1980, pp. 183-228.
- [18] R. W. Wilson, "Sun Tracker Measurements of Attenuation by Rain at 16 and 30 GHz", *BSTJ*, 48, No. 5, May-June 1969, pp. 1383-1404.
- [19] P. S. Henry, "Measurement and Frequency Extrapolation of Microwave Attenuation Statistics on the Earth-Space Path at 13, 19 and 30 GHz", *IEEE Trans. on Ant. and Prop.*, March 1975, pp. 271-274.
- [20] R. W. Wilson, "A Three-Radiometer Path-Diversity Experiment", *BSTJ*, 49, No. 6, July-August 1970, pp. 1239-1242.

- [21] D. A. Gray, "Earth-Space Path Diversity; Dependence on Base Line Orientation", IEEE *G-AP* symposium, August 22-24, 1973, Boulder, Colorado, pp. 366-369.
- [22] D. C. Cox, "Design of the Bell Laboratories 19 and 28 GHz Satellite Beacon Propagation Experiment", IEEE ICC, June 17-19, 1974, Minneapolis, Minnesota, pp. 27E1-27E5.
- [23] D. C. Cox, "An Overview of the Bell Laboratories 19 and 28 GHz COMSTAR Beacon Propagation Experiments", *BSTJ*, 57, May-June, 1978, pp. 1231-1255.
- [24] L. Pollack, "Centimeter Wave Beacons for the COMSTAR Satellites", *COMSAT Tech. Rev.*, Spring 1977, pp. 103-108.
- [25] W. J. Getsinger, "Centimeter Wave beacon Transmitter Design", *COMSAT Tech. Rev.*, Spring 1977, pp. 109-128.
- [26] M. J. Barrett, "19- and 28-GHz IMPATT Amplifiers", *COMSAT Tech. Rev.*, Spring 1977, pp. 129-152.
- [27] R. E. Stegens, "Low-Jitter Oscillator Source for the COMSTAR Beacons", *COMSAT Tech. Rev.*, Spring 1977, pp. 153-169.
- [28] R. B. Briskman, R. F. Latter and E. E. Muller, "Call for Help", *IEEE Spectrum*, 11, October 1974, pp. 35-36.
- [29] E. E. Muller, "Notes on the COMSTAR Experiment", *BSTJ*, 57, May-June, 1978, pp. 1369-1370.
- [30] L. J. Ippolito, "Radio Propagation for Space Communications Systems", *Proc. IEEE*, Vol. 69, June 1981, pp. 697-727.
- [31] G. Brussaard, "Prediction of Attenuation Due to Rainfall on Earth-Space Links", *URSI Comm. F Symp. on "Effects of the Lower Atmosphere on Radio Wave Propagation above 1 GHz"*, Lennoxville, Canada, May 26-30, 1980 and *Radio Science*, September-October 1981, pp. 745-760.
- [32] D. C. Cox, "Depolarization of Radio Waves by Atmospheric Hydrometers in Earth-Space Paths: A Review", *URSI Comm. F Symp. on "Effects of the Lower Atmosphere on Radio Propagation Above 1 GHz"*, Lennoxville, Canada, May 26-30, 1980 and *Radio Science*, September-October, 1981, pp. 781-812.
- [33] D. C. Cox, H. W. Arnold, H. H. Hoffman, "Measured Bounds on Rain-Scatter Coupling Between Space-Earth Radio Paths", *IEEE Trans. on Ant. and Prop.*
- [34] H. W. Arnold, D. C. Cox and H. H. Hoffman, "Antenna Beamwidth Independence of Measured Rain Attenuation on a 28 GHz Earth-Space Path", *IEEE Trans. on Ant. and Prop.*
- [35] D. C. Cox, H. W. Arnold and H. H. Hoffman, "Observations of Cloud-Produced Amplitude Scintillation on 19 and 28 GHz Earth-Space Paths", *IEE 2nd International Conf. on Ant. and Prop.*, April 13-16, 1981, York, England and *Radio Science*, September-October 1981, pp. 885-907.
- [36] D. C. Cox and H. W. Arnold, "Results from the 19 and 28 GHz COMSTAR Satellite Propagation Experiments at Crawford Hill", to be published in *IEEE Proceedings*, May 1982.
- [37] Arnold, H. W., "Measurement-Based Estimates of Outage on Earth-Space RF Links from Attenuation and Depolarization", *ICC*, June 1982, Philadelphia, Pennsylvania.
- [38] V. K. Prabhu, "The Detection Efficiency of 16-ary QAM", *BSTJ*, 59, No. 4, April 1980, pp. 639-666.

- [39] V. K. Prabhu, "Error Probability Performance of  $M$ -ary CPSK Systems with Intersymbol Interference", IEEE Trans. Comm., COM-21, No. 2, February 1973, pp. 97-109.
- [40] R. E. Freeland, "Industry capability for large space antenna structures", Jet Propulsion Lab., Rep. 710-12, May 25, 1978.
- [41] T. S. Chu, R. W. Wilson, R. W. England, D. A. Gray, W. E. Legg, "The Crawford Hill 7-Meter Millimeter Wave Antenna", BSTJ, 57, May-June 1978, pp. 1257-1288.
- [42] Ohm, E. A., "A Proposed Multiple-Beam Microwave Antenna for Earth Stations and Satellites", BSTJ, 53, No. 8 (October 1974), pp. 1657-1666.
- [43] Ohm, E. A. and Gans, M. J., "Numerical Analysis of Multiple-Beam Offset Cassegrainian Antennas", AIAA Paper, No. 76-301, AIAA/CASI 6th Communication Satellite Systems Conference, Montreal, Canada, April 5-8, 1976.
- [44] Dragone, C., "An Improved Antenna for Microwave radio Systems Consisting of Two Cylindrical Reflectors and a Corrugated Horn", BSTJ, 53, No. 7 (September 1974), pp. 1351-1377.
- [45] Turrin, R. H., "A Multibeam, Spherical Reflector Satellite Antenna for the 20- and 30-GHz Bands", BSTJ, July-August 1975, Vol. 54, No. 6, pp. 1011-1027.
- [46] Semplak, R. A., "100-GHz Measurements on a Multiple-Beam Offset Antenna", BSTJ, Vol. 56, No. 3, March 1977, pp. 385-397.
- [47] Dragone, C. and Gans, M. J., "Imaging Reflector Arrangements to Form a Scanning Beam Using a Small Array", BSTJ, Vol. 58, No. 2, (February 1979) pp. 501-515.
- [48] Dragone, C. and Gans, M. J., "Satellite Phased Arrays: Use of Imaging Reflectors with Spatial Filtering in the Focal Plane to Reduce Grating Lobes", BSTJ, Vol. 59, No. 3 (March 1980), pp. 449-461.
- [49] Ed. by S. Silver, "Microwave Antenna Theory and Design", Vol. 12, MIT Rad. Lab. Series, McGraw-Hill Book Company, New York, 1949, p. 187.
- [50] D. O. Reudink, A. S. Acampora, Y. S. Yeh, "Methods for Achieving High Capacity Universal Service Satellites", Nat'l Telecomm. Conf., Birmingham, Ala., December, 1978.



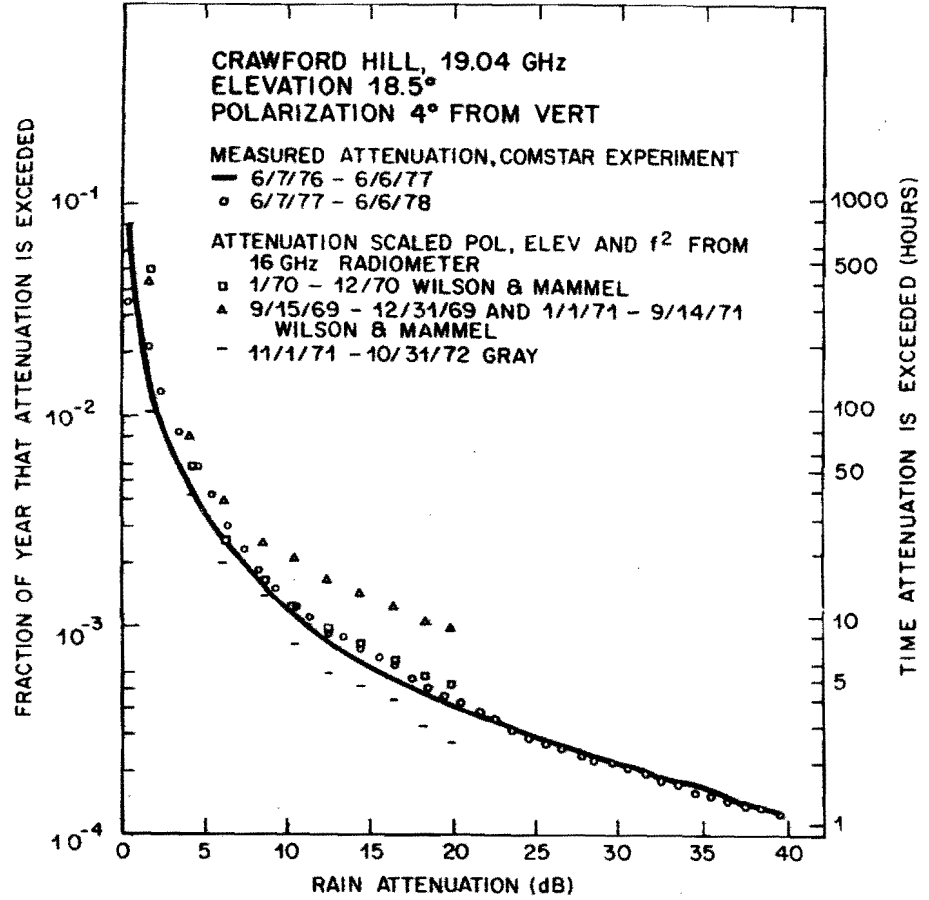
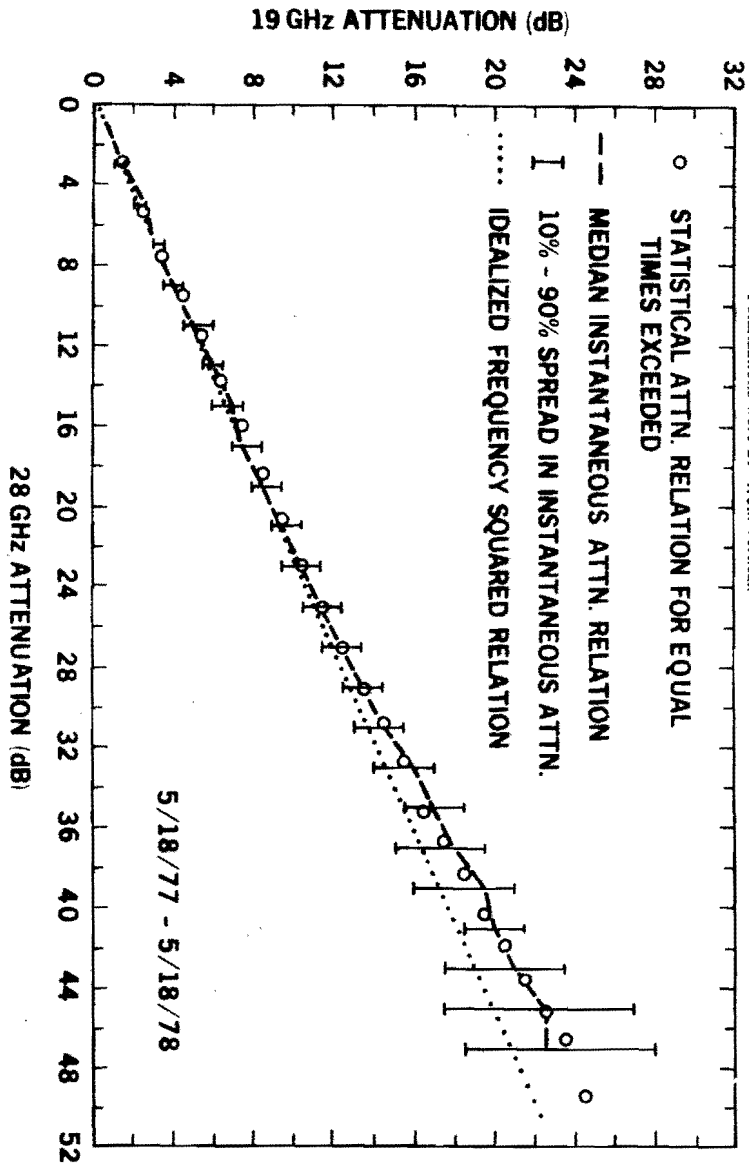


Figure 1 Cumulative distributions of 19 GHz rain attenuation showing yearly variation. The scaled data are from earlier 16 GHz radiometer measurements. Right and left ordinates are the time during the year and the fraction of the year that the attenuation of the abscissa was exceeded.

Figure 2 Relationships between measured attenuations at 28.56 GHz and 19.04 GHz. The open circles show the statistical relationship between pairs of attenuation values that are exceeded for the same amount of time on the attenuation distributions in Figure 3. The dashed line connects median values of the instantaneous 19 GHz attenuation for each 2 dB increment of 28 GHz attenuation. The 10% to 90% spread in instantaneous 19 GHz attenuation is indicated by the vertical bars. The path elevation angle was 38.6°. Polarizations were 21° from vertical.



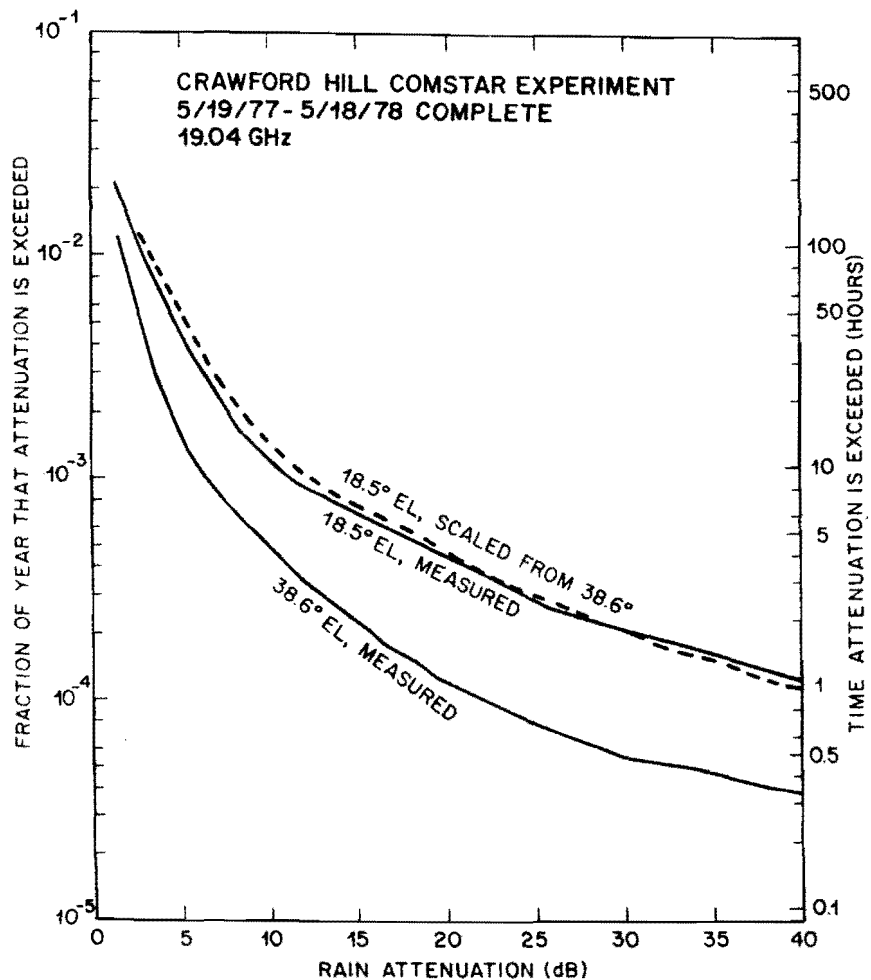


Figure 4 Cumulative distributions of 19 GHz rain attenuation showing elevation-angle scaling from 38.6° to 18.5°.

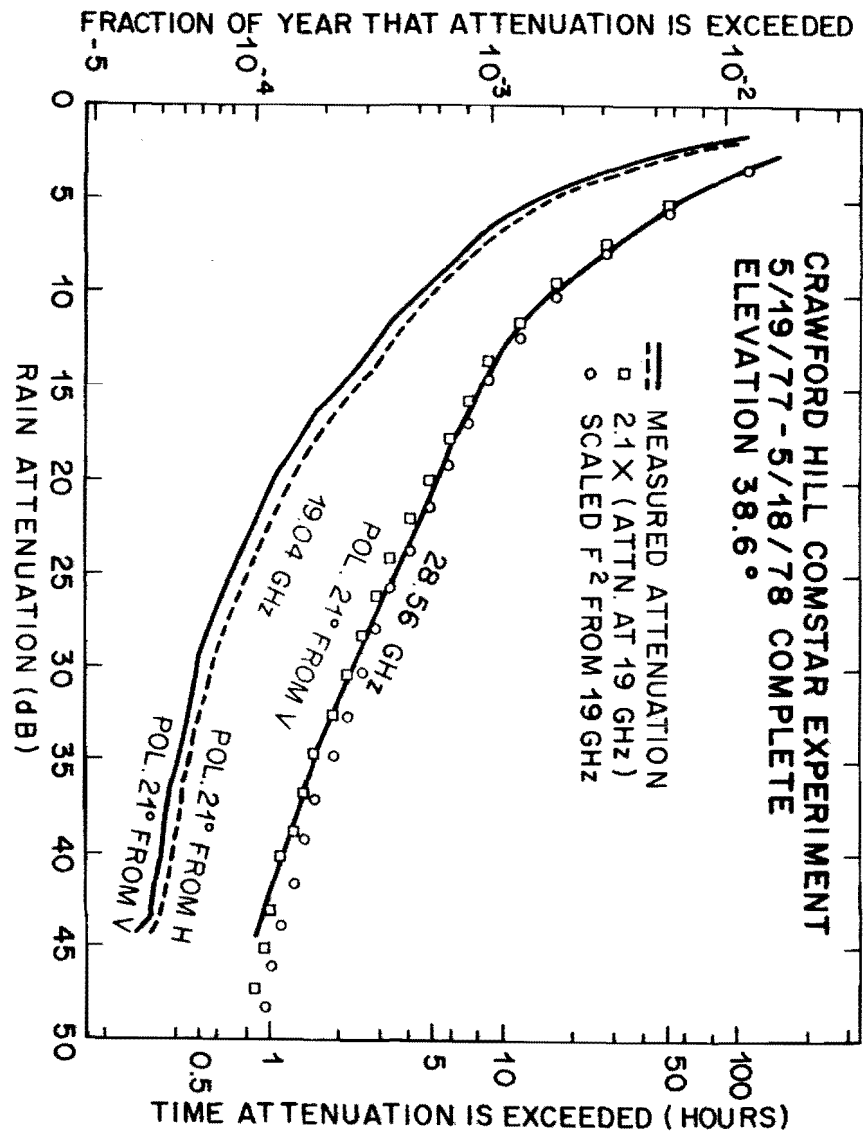


Figure 3 Cumulative distributions of rain attenuation showing frequency scaling from 19.04 GHz to 28.56 GHz.

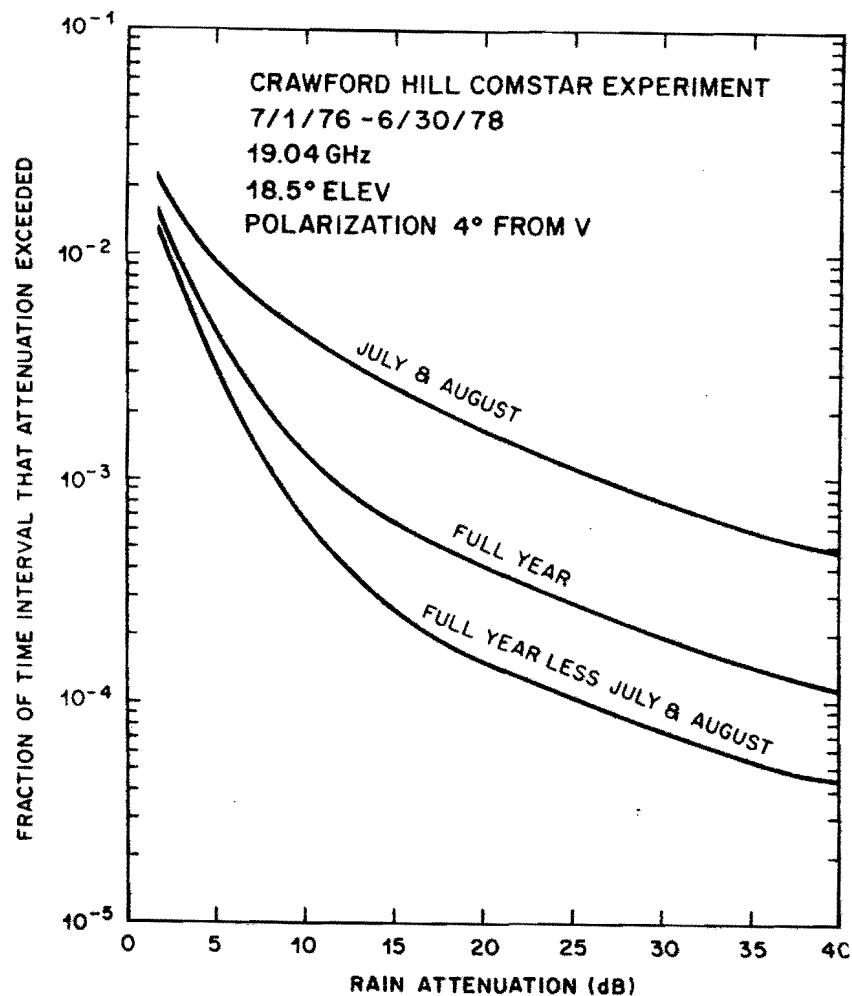


Figure 5 Cumulative distributions showing seasonal variation of 19 GHz rain attenuation.

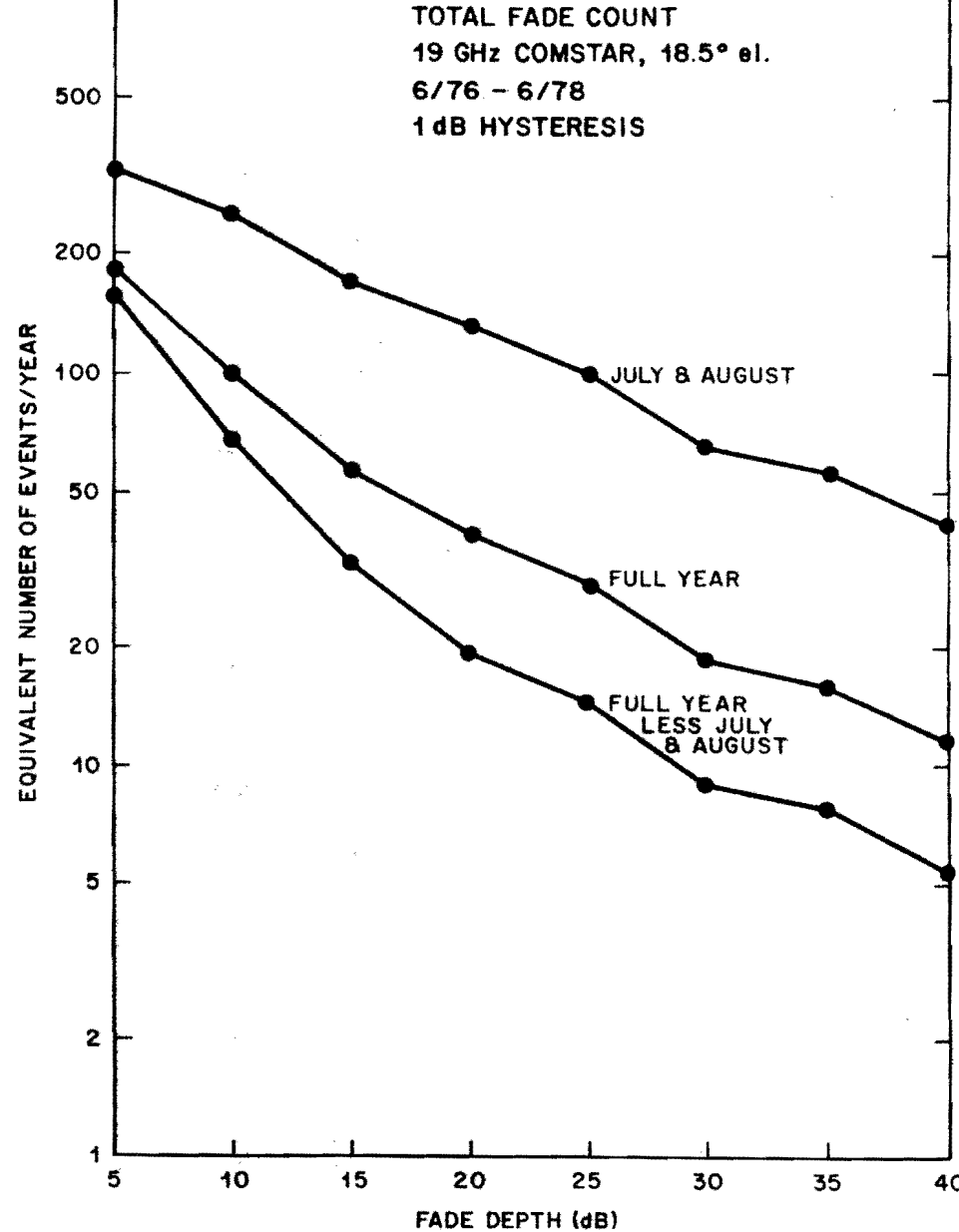


Figure 6 Loci of measured times and fractional times of one-hour intervals that specific 19 GHz attenuation levels are exceeded. These data show the diurnal variation of rain attenuation.

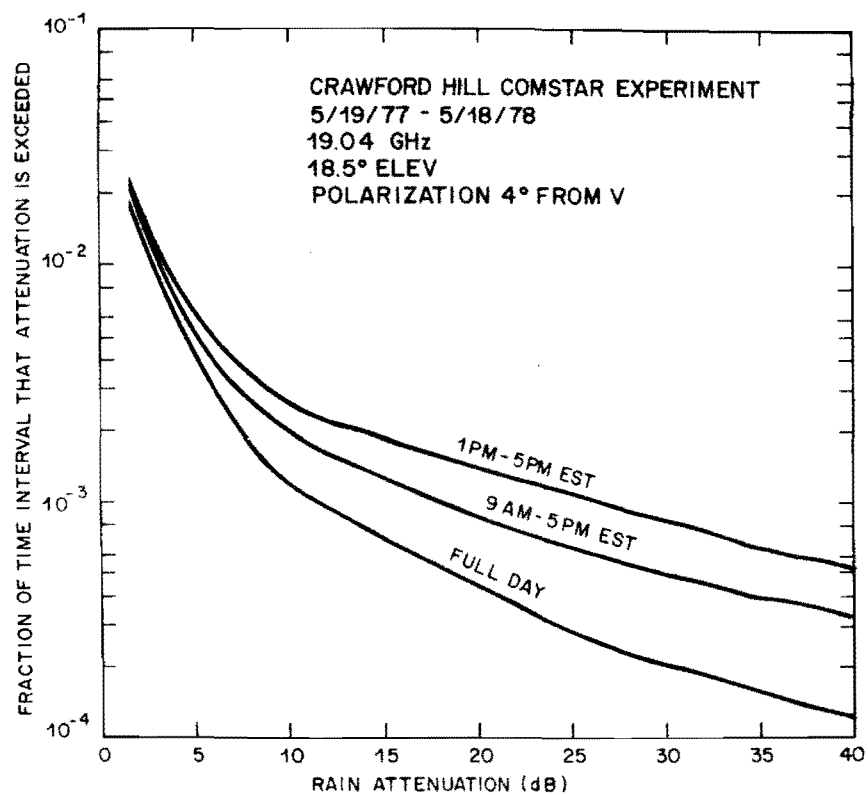


Figure 7 Cumulative distributions showing diurnal variation of 19 GHz rain attenuation.

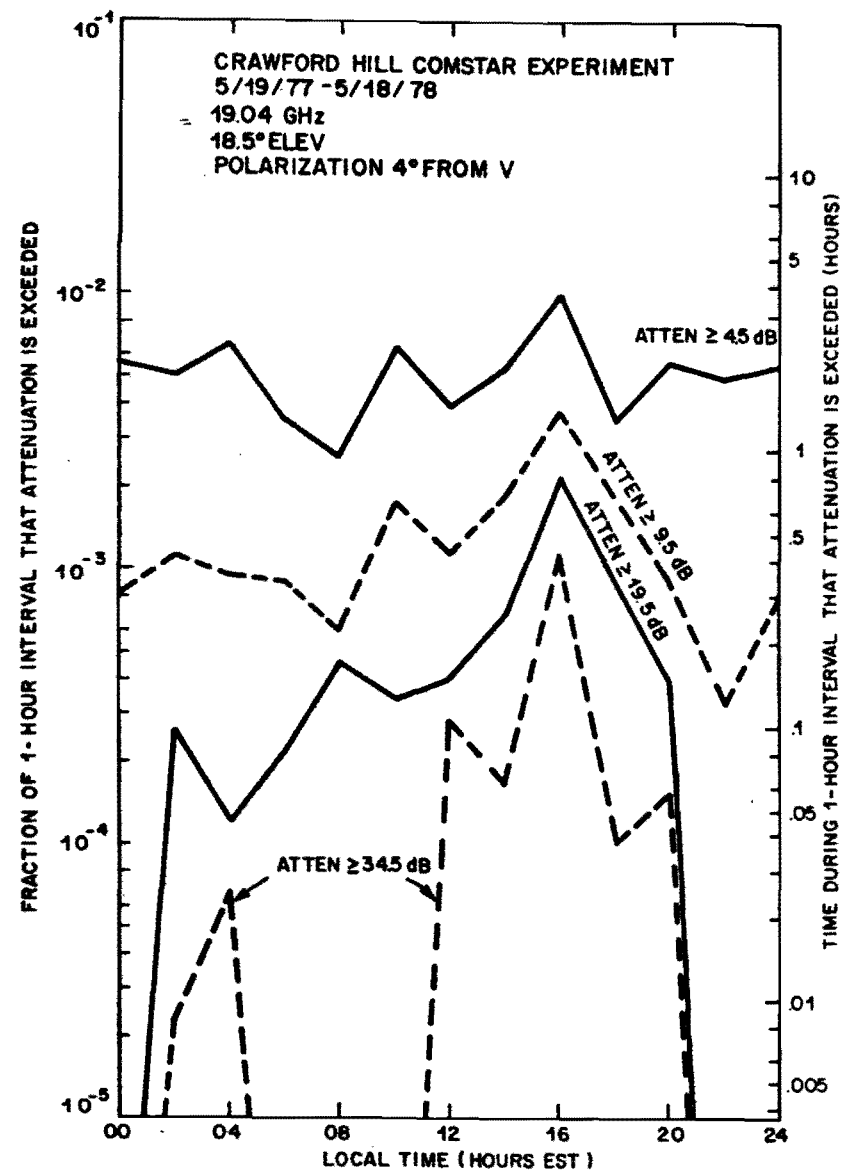


Figure 8 Cumulative distributions of fade durations showing the average number of fade events in a year with fade durations equal to or greater than the abscissa.

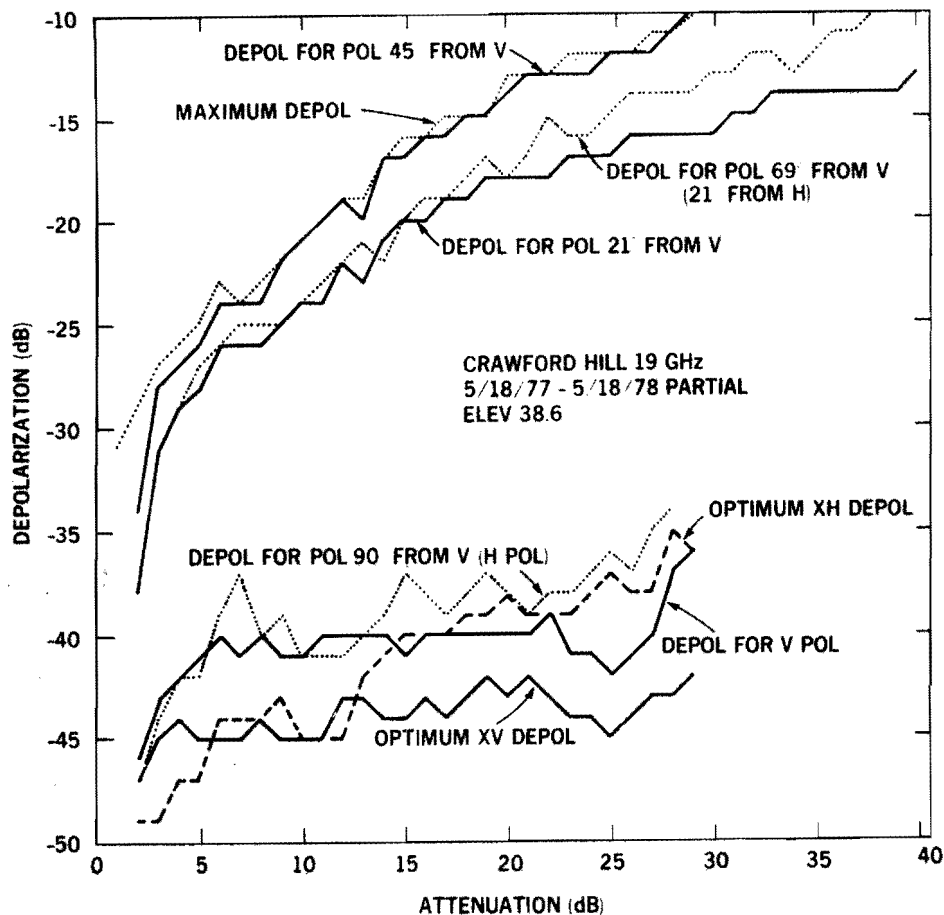


Figure 9 Relationships between median depolarization and corresponding copolarized signal attenuation for fixed linear polarizations oriented 90°, 69°, 45°, 21°, and 0° from vertical and for the varying linear polarizations that produce the instantaneous minimum and maximum depolarization values. The accuracy of the very low depolarization values ( $\leq -35$  dB) is limited by measurement uncertainties.

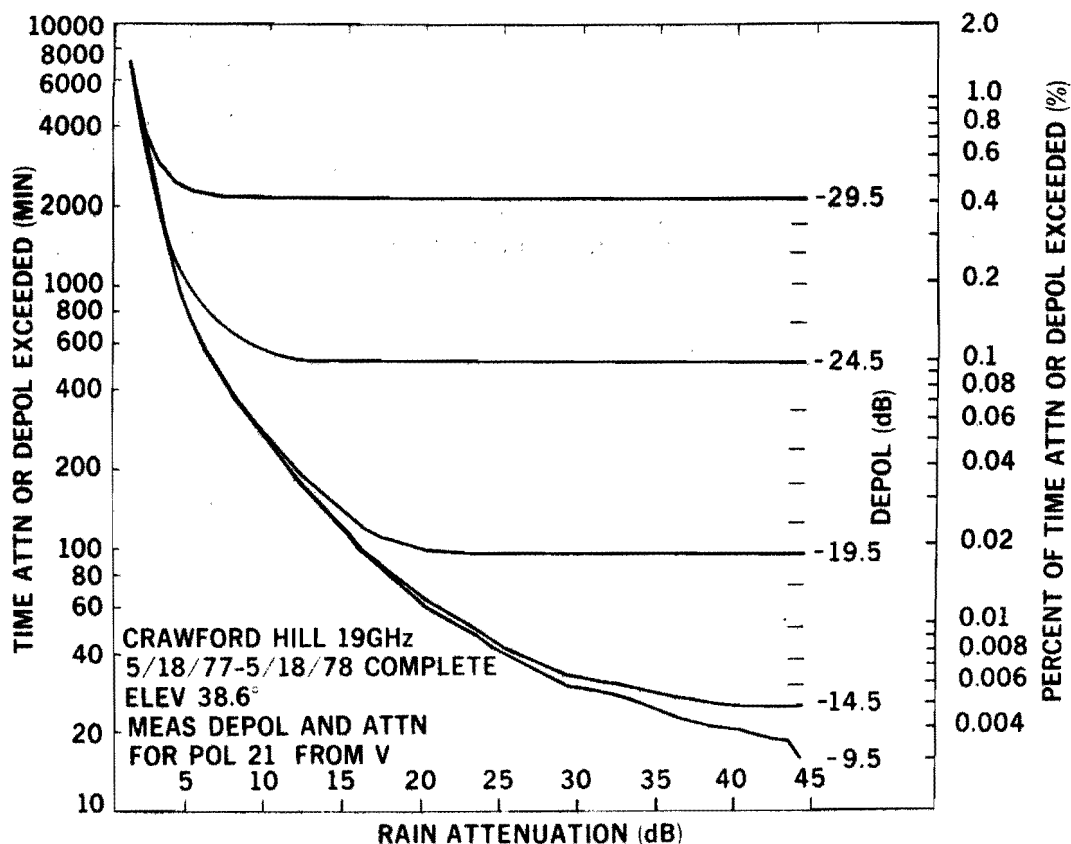


Figure 10

Cumulative distributions showing the amount of time and percentage of time of a year that either the depolarization indicated as a parameter beside each curve or the copolarized signal attenuation on the abscissa is exceeded. Lowest curve is the cumulative distribution for attenuation only.

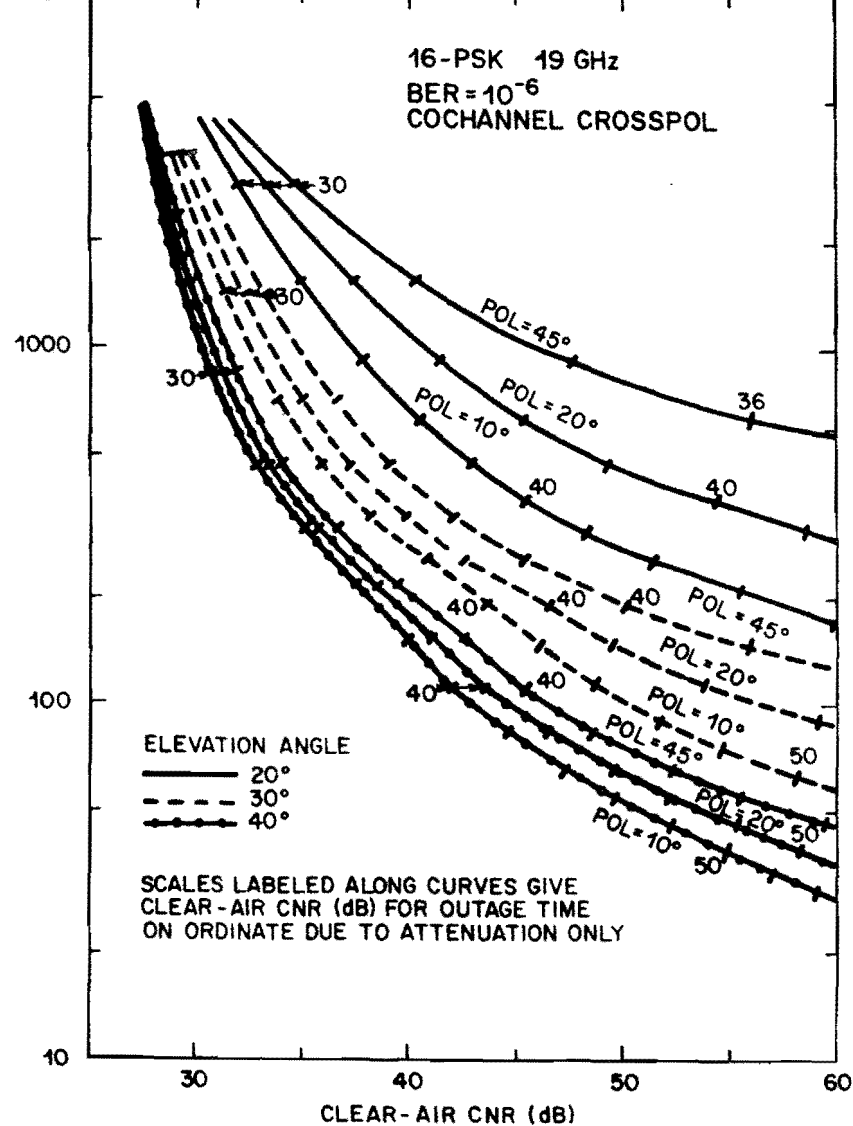
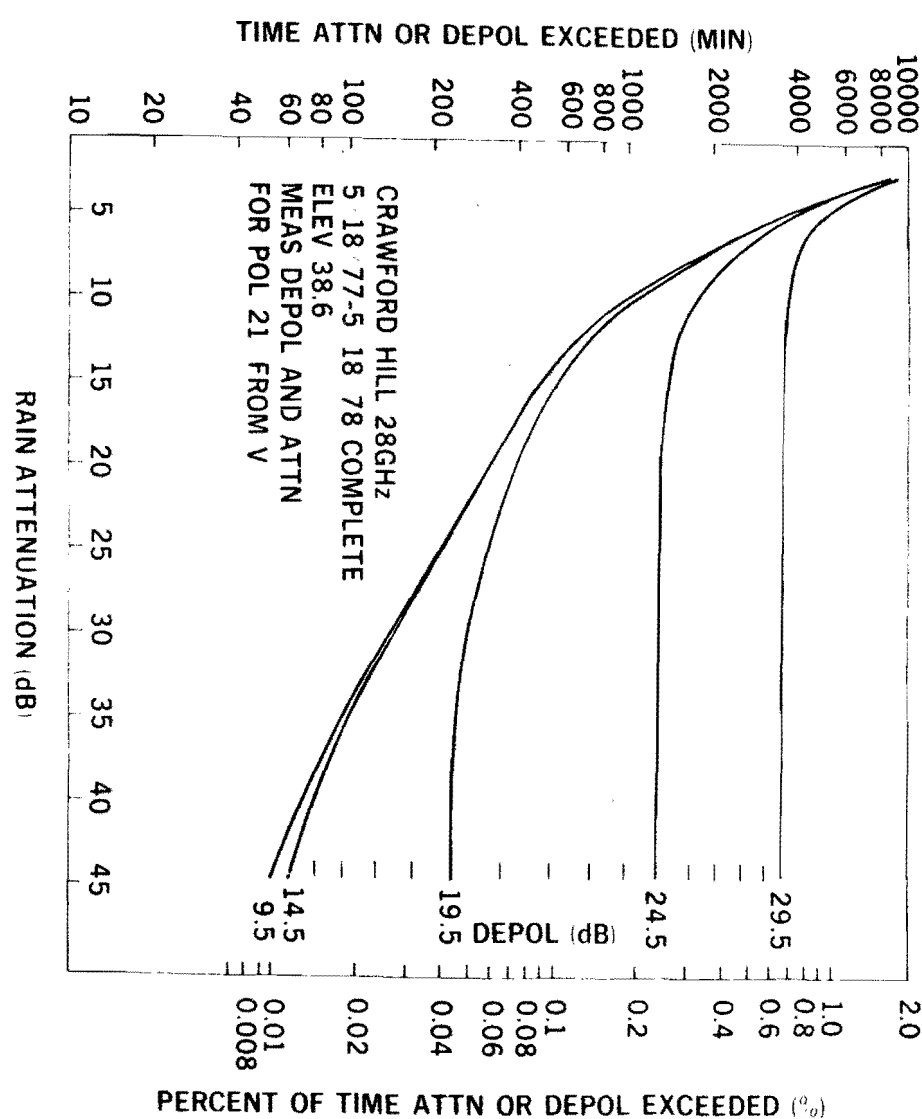


Figure 12 Attenuation-depolarization outage time vs. clear-air CNR for 19 GHz 16-PSK link with elevation angle and polarization angle as parameters. Scales along curves give CNR for equivalent outage from attenuation alone

Figure 11 Cumulative distributions similar to those in Figure 10 but for 28 GHz.



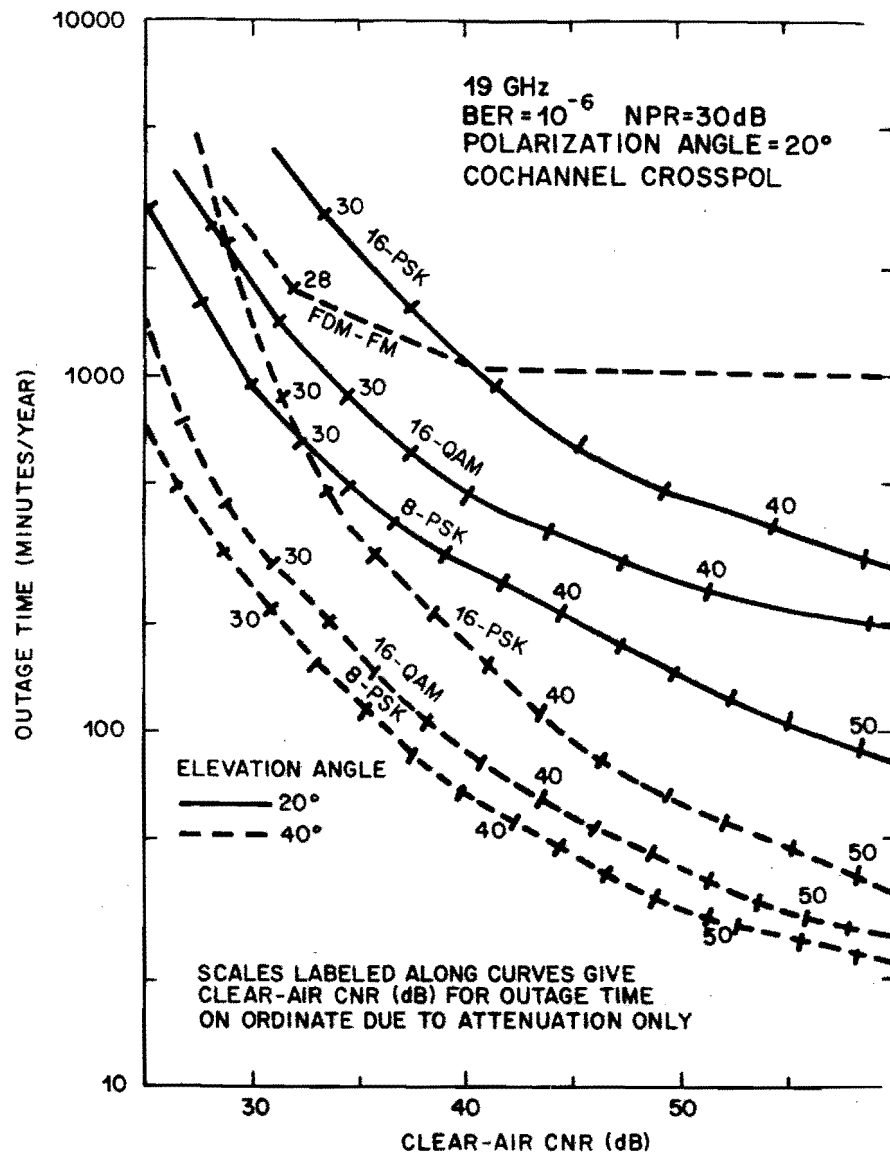


Figure 13 Attenuation-depolarization outage time vs. clear-air SNR at GHz with elevation angle an modulation type as parameters. Scales along curves give CNR for equivalent outage from attenuation alone.

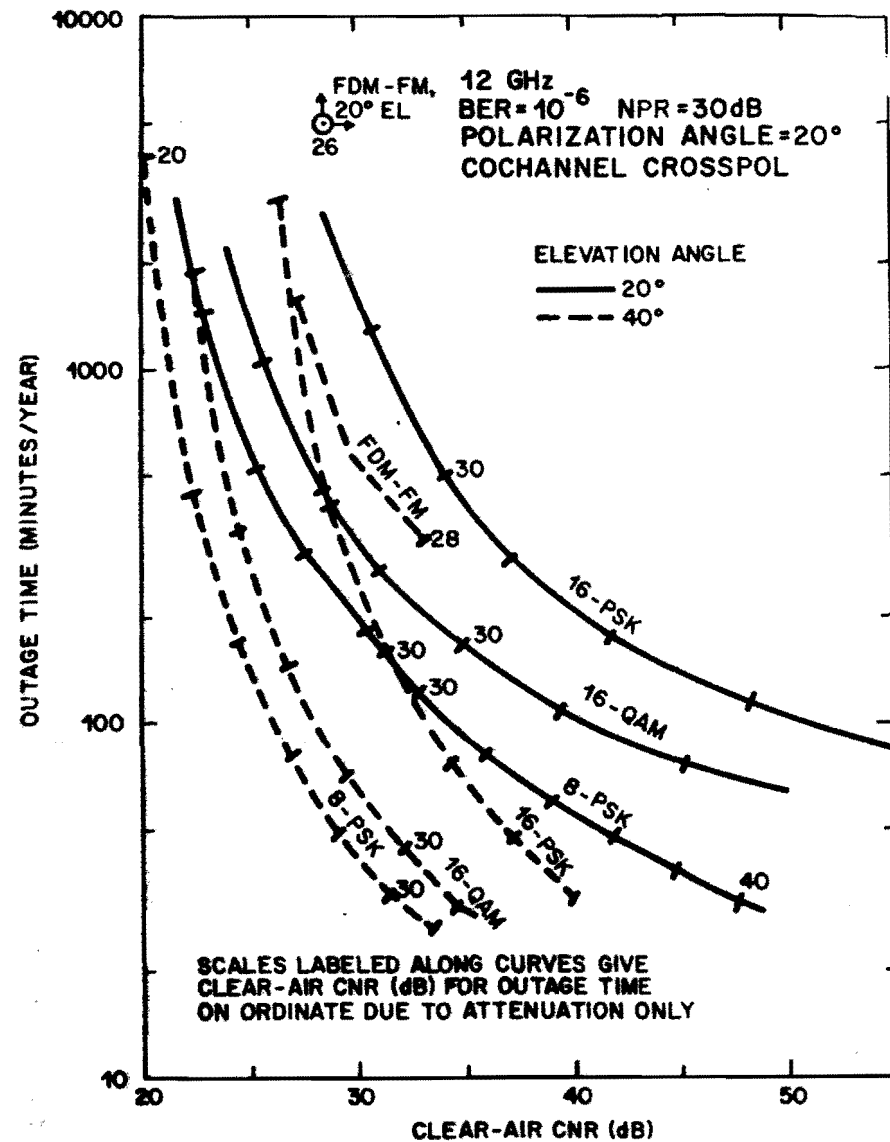


Figure 14 Attenuation-depolarization outage time vs. clear-air CNR at 12 GHz.

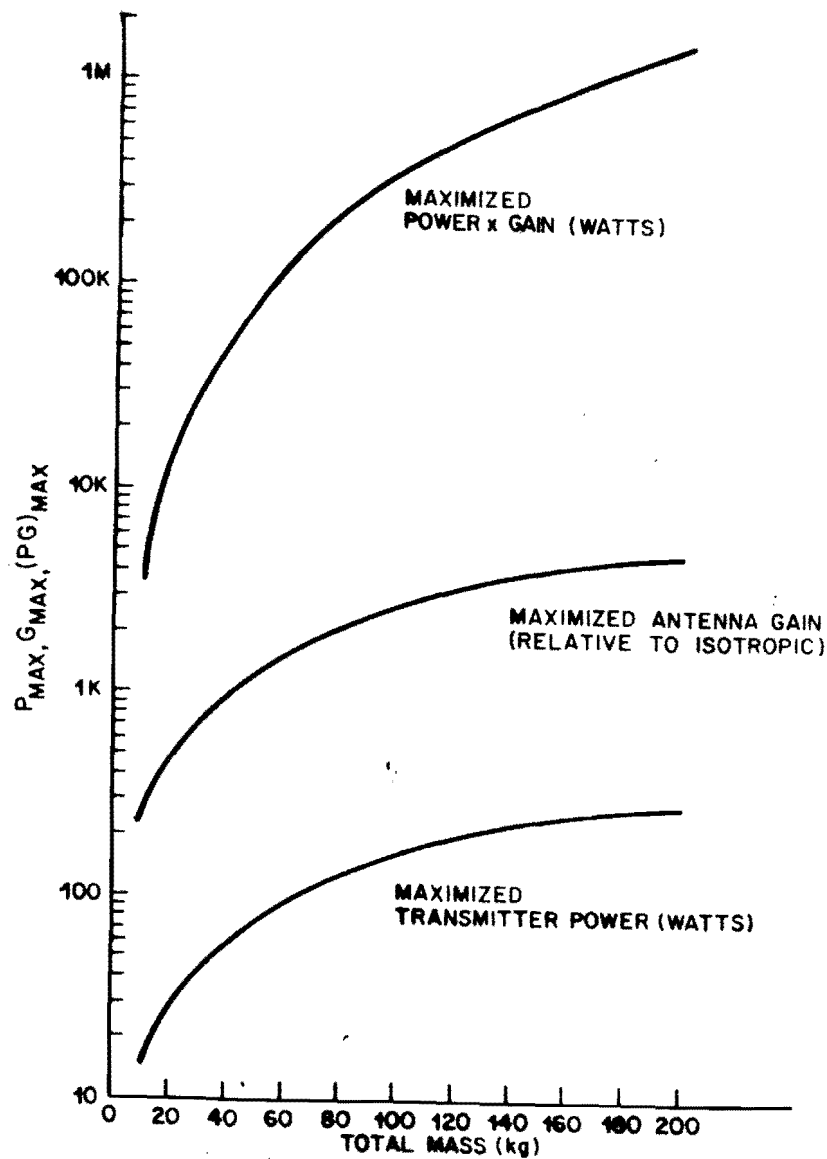


Figure 14 Transmitted power and antenna gain for maximum effective radiated power.

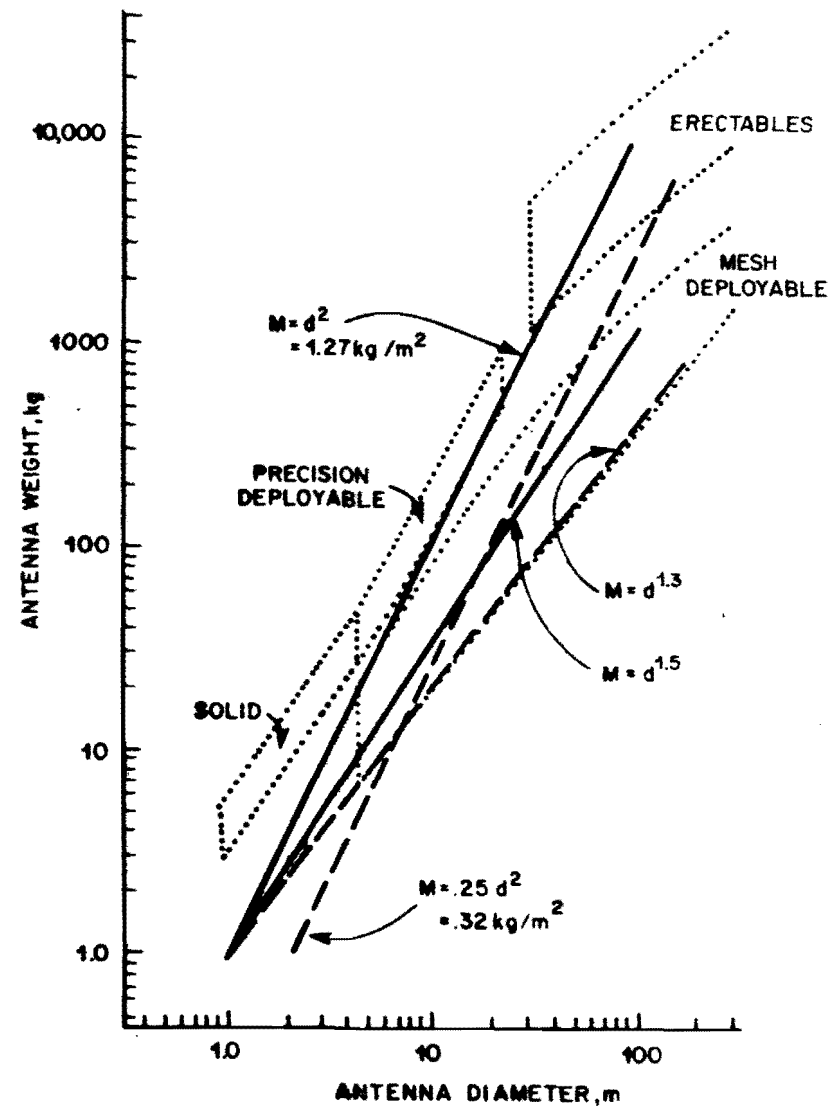


Figure 15 Estimates of antenna weight as a function of antenna size.



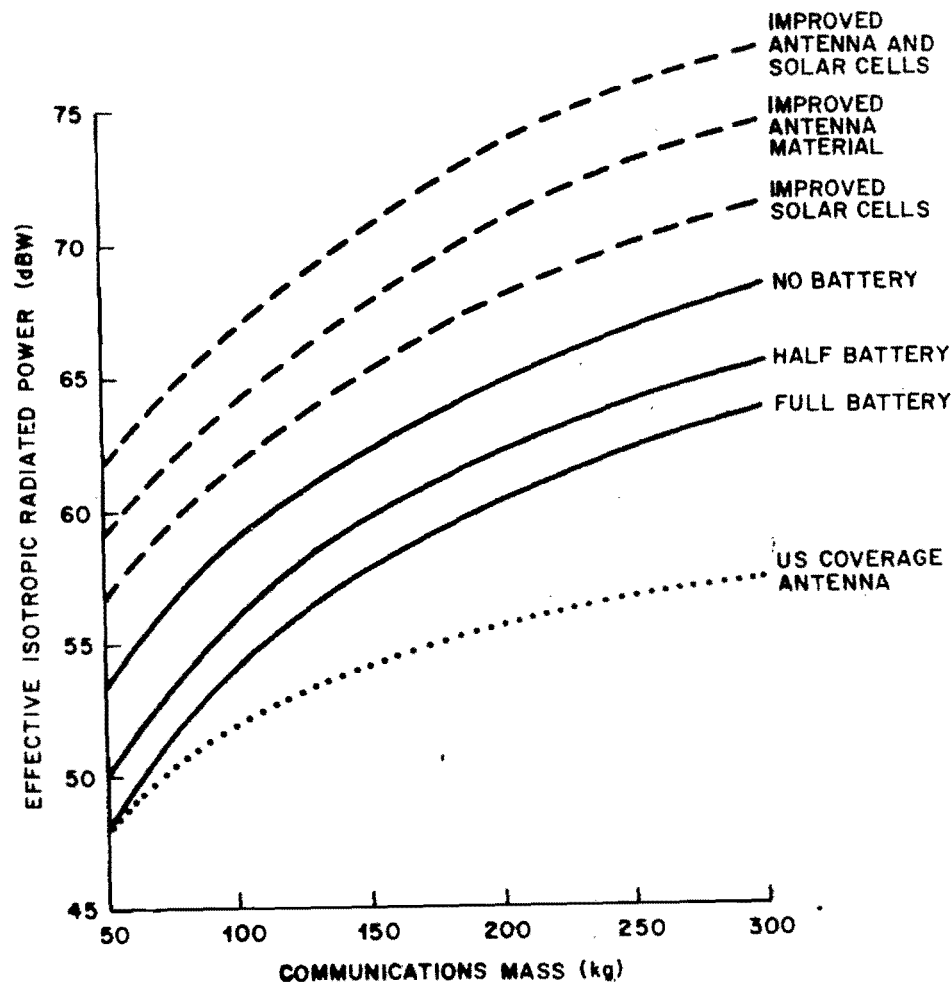


Figure 17 Effective radiated power for optimized antenna and transmitter mass distribution at 900 MHz.

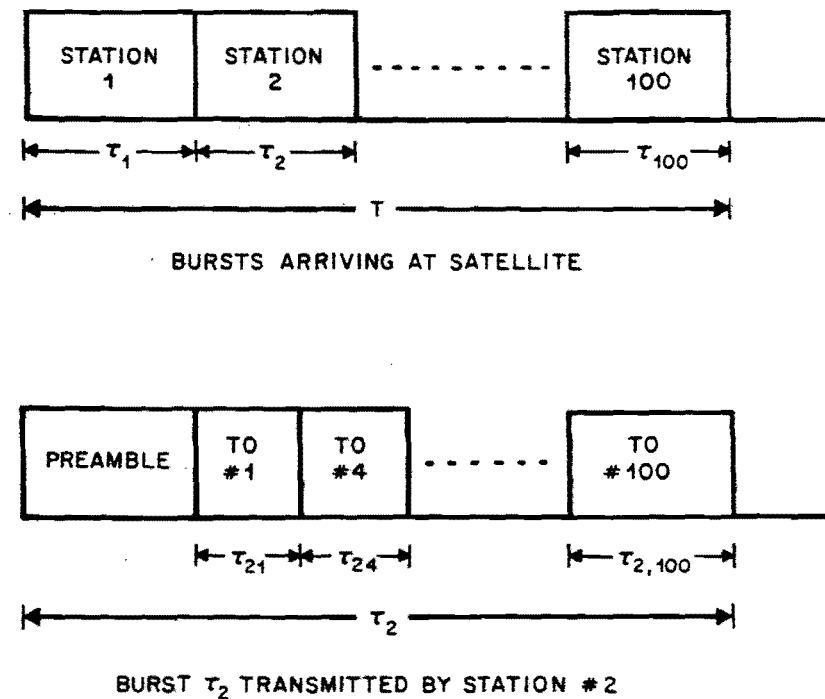
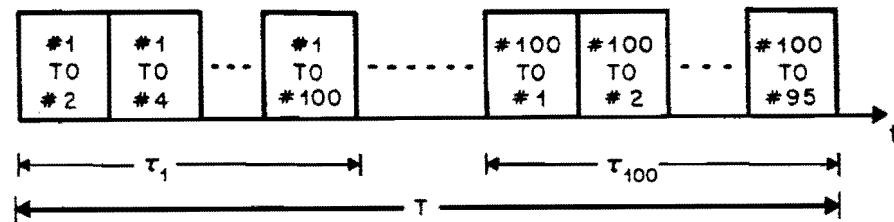
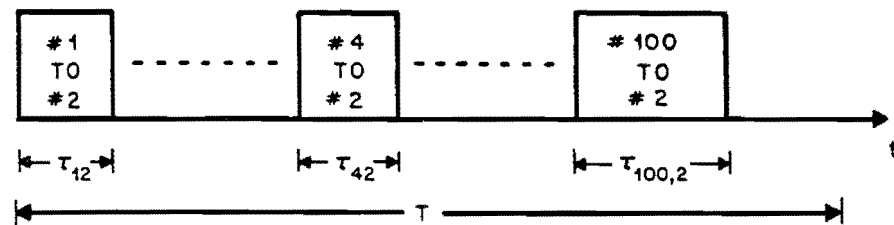


Figure 18 Uplink frame and burst format. Frame length  $T$ , burst length  $\tau_k$ , sub-burst length  $\tau_{ij}$ .

FIGURE 18



a. DOWNLINK BURSTS



b. DOWNLINK BURSTS INTENDED FOR GROUND STATION #2

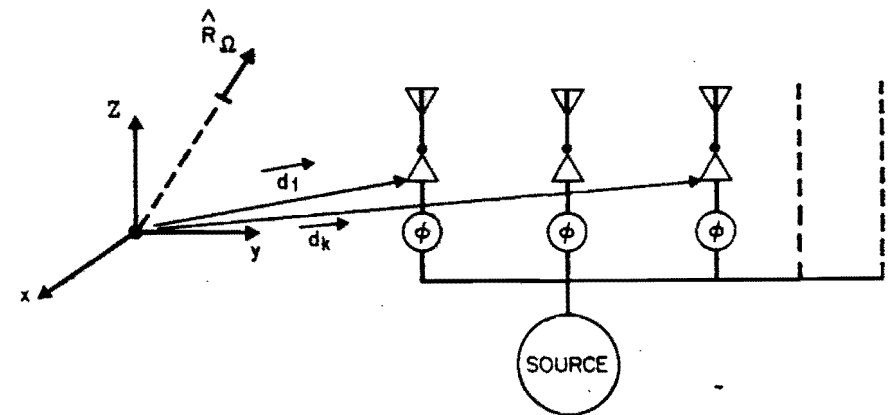


Figure 20 The orientation of a phased array.

Figure 19 Downlink burst formats.

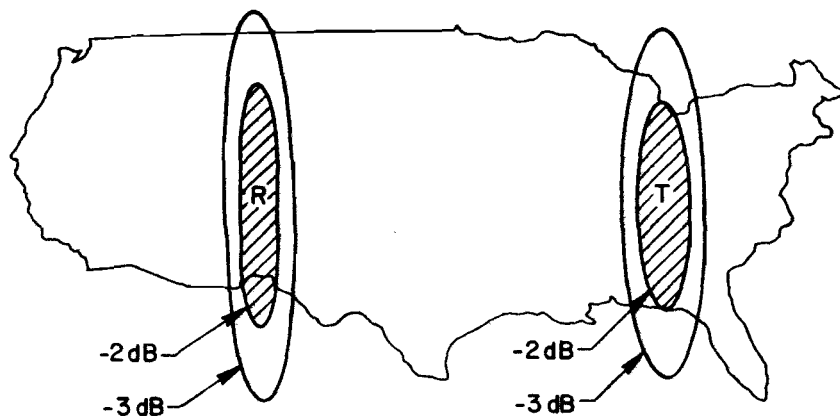


Figure 21 Fan beams transmission at 12 GHz and receiving at 14 GHz.

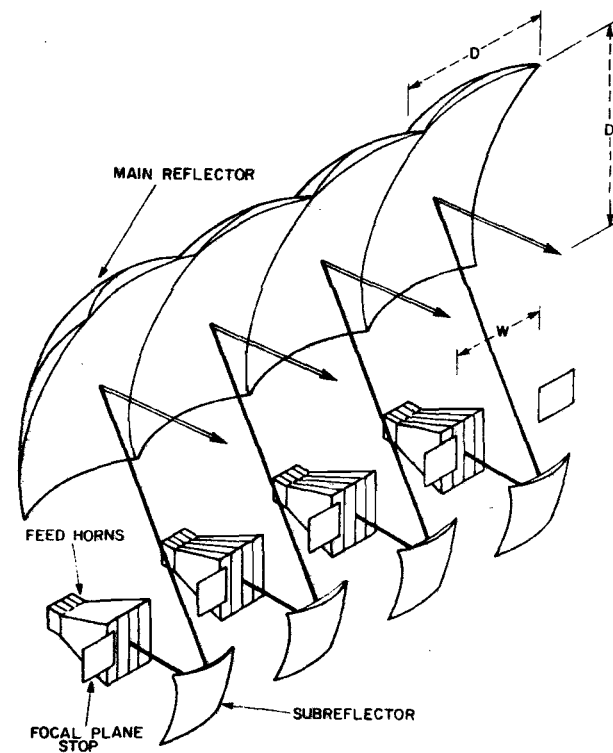


Figure 22 Compact scanning array antenna.

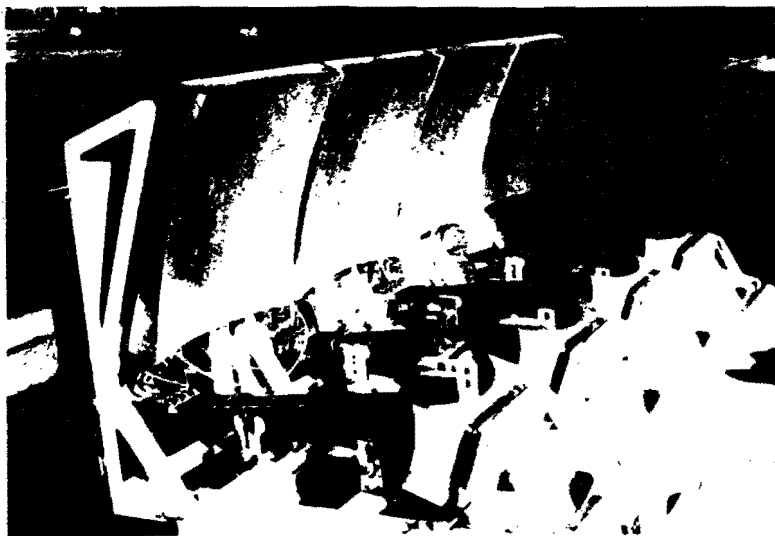


Figure 24 Full size RF model.

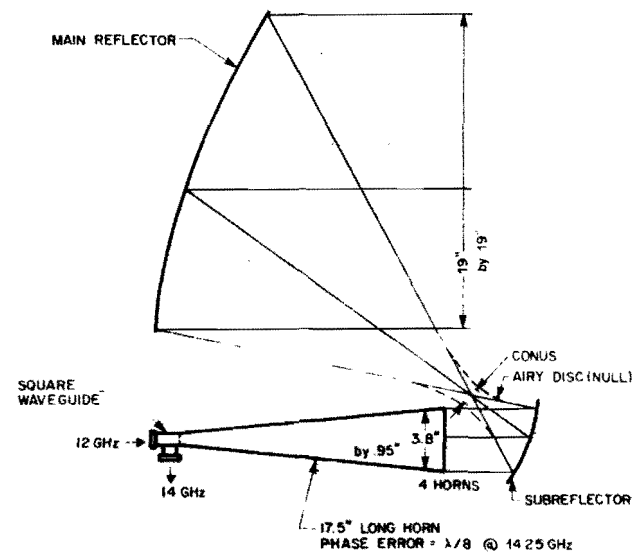


Figure 25 Antenna side view.

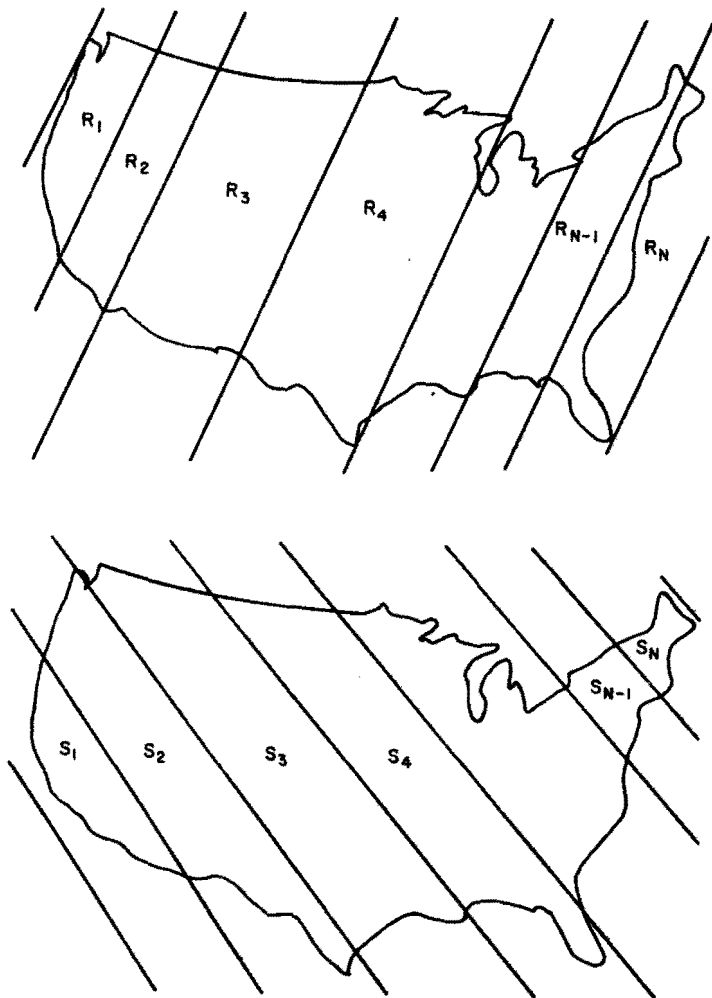


Figure 24. Transmit,  $R_i$ , and received zones,  $S_i$ , for limited scan concept.

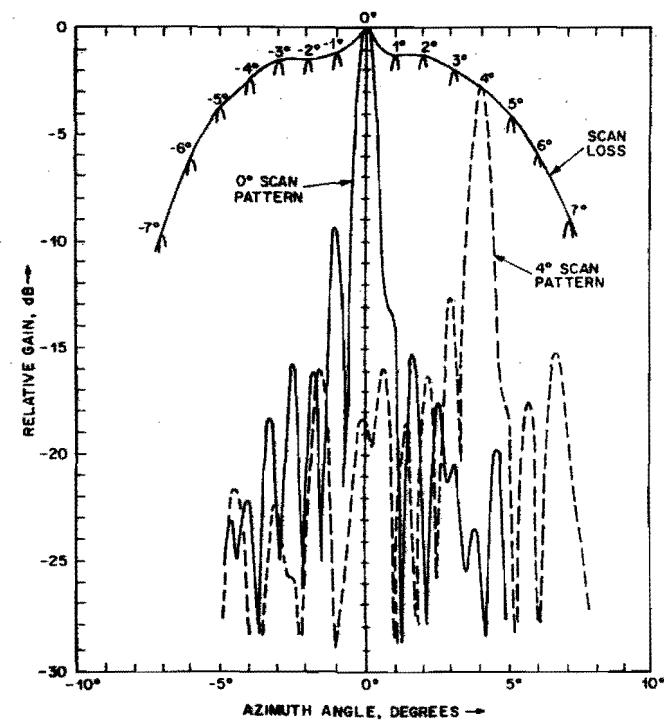


Figure 25. Measured scan patterns of RF model at 11.95 GHz.

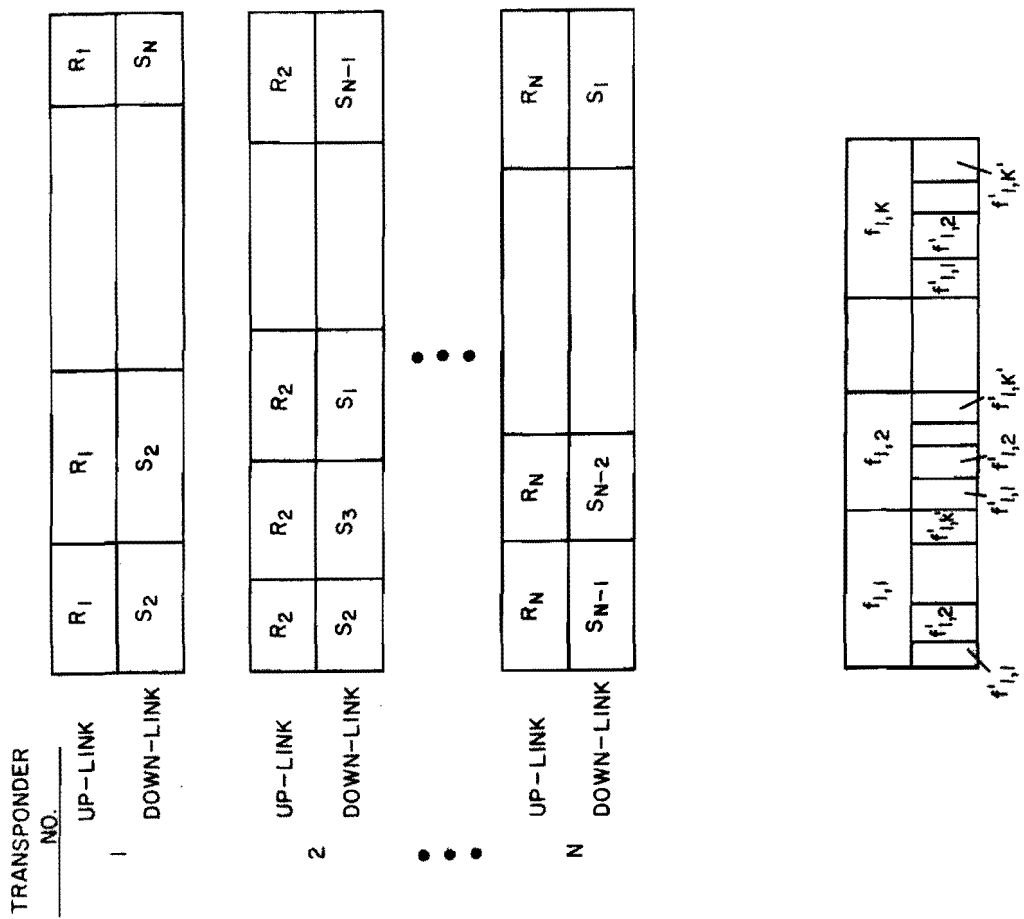


Figure 27

a) Nonconflicting traffic assignment to the TDMA switching frames of transponders 1 through N. b) Expanded view of switching frame for transponder 1 during the time interval when  $R_1$  is connected to  $S_1$  showing transmit and receive footprint interconnections.

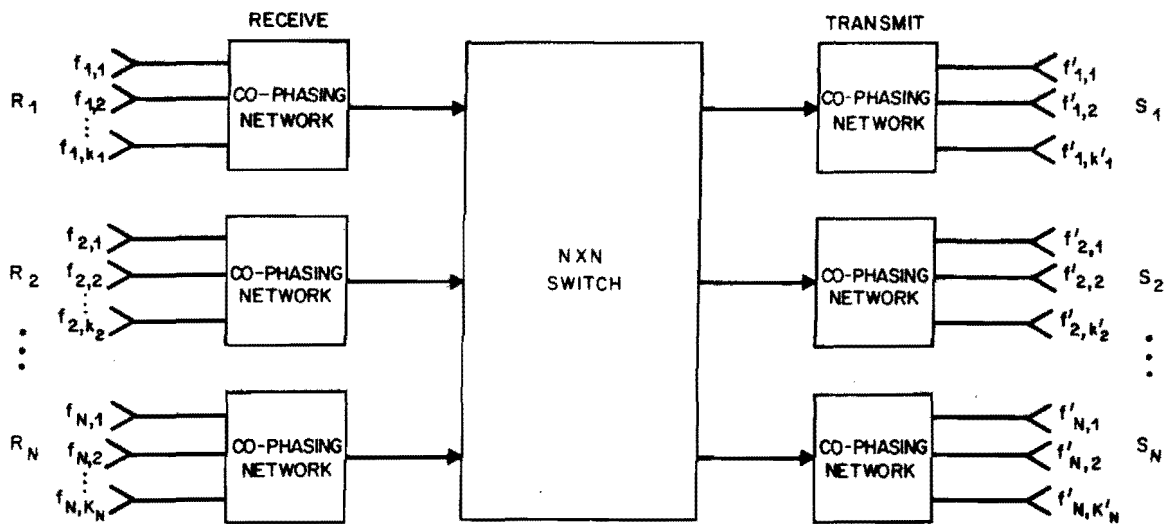


Figure 23

Satellite switching network. The cophasing networks focus beams to the appropriate footprint within each receive and transmit zone.

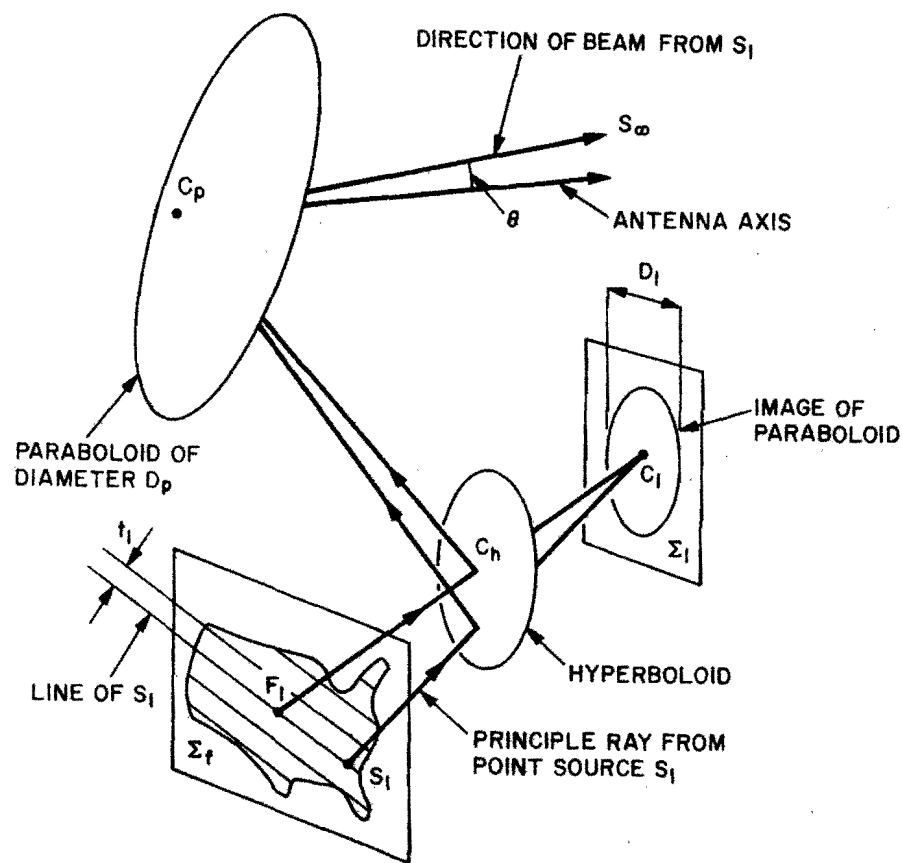
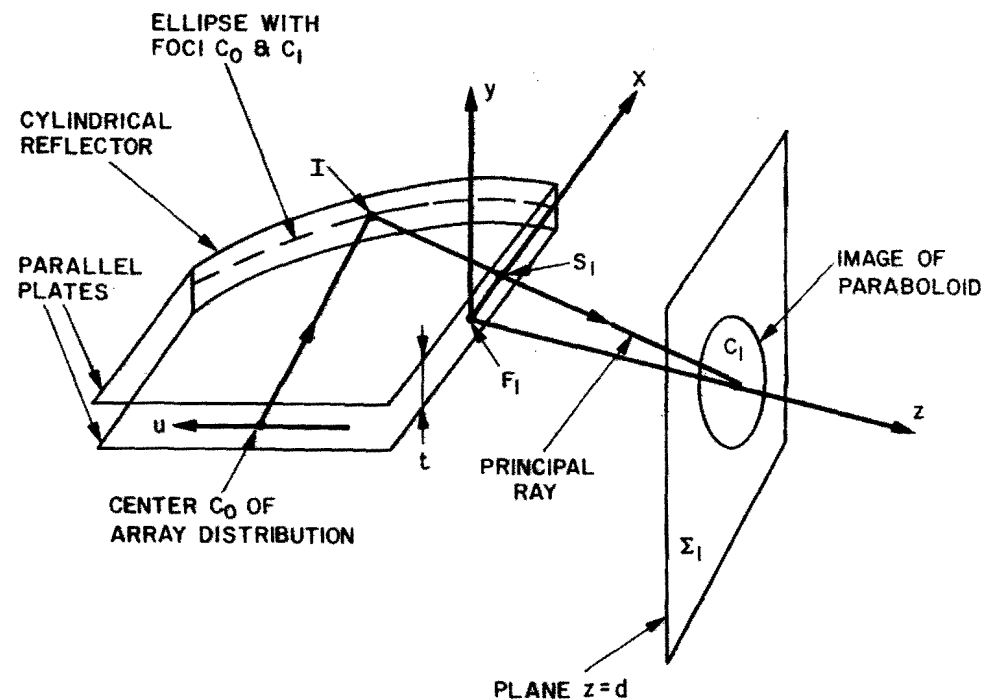


Figure 29 An offset cassegrain arrangement is used aboard the satellite to form a small U.S. image.



NOTICE: THE ARRAY ELEMENTS  
ARE PLACED ON THE  $u$ -AXIS

Figure 30 To produce a movable phase center  $S_I$ , a linear array is combined with two metal plates and a cylinder. The array elements are placed on the  $u$ -axis, with distribution centered at  $C_0$ .

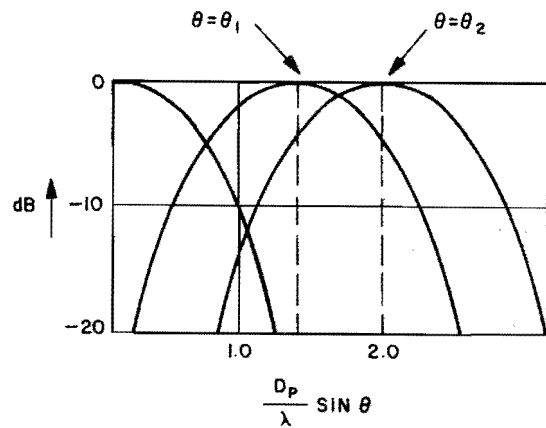


Figure 31 Beams radiated from a circular aperture with edge illumination of  $-10$  dB.

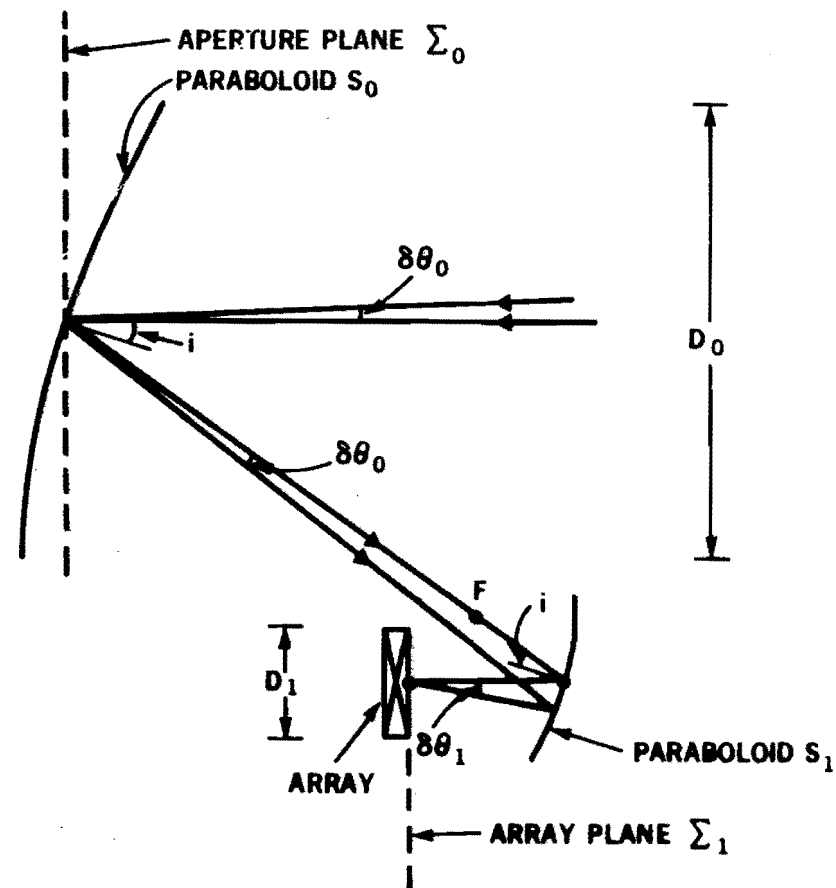


Figure 32 A Gregorian arrangement of two confocal paraboloids magnifying a small array. The main reflector  $S_0$  and the array are conjugate elements.



## 9. Antenna Measurements

### 9.1. Spherical near-field scanning

by F. Holm Larsen

#### 9.1.1. Introduction

Methods for measuring antennas at reduced distances have been the subject of a substantial amount of research and development during the last twenty years. It can be foreseen that this effort will greatly influence the testing of satellite antennas in the future. Satellite antennas are designed to transmit or receive over long distances and accordingly the requirements to beam pointing accuracy can be severe. The power limitation of the signal source in the satellite together with limitations on the size and weight of the antenna itself often makes it necessary to optimize the design of the antenna to fulfill the specifications on the radiation pattern. In such a case, a small degradation in antenna performance can affect the overall performance of the system, and therefore a high measurement accuracy is required to verify that the antenna fulfills the specifications. The launch cost of a satellite and the lack of repair possibilities also justifies a careful test program for the antennas.

The advantages of near-field measurements in this context can be exemplified as follows

Indoor measurements. Measurements can be done indoors under laboratory conditions which can improve the stability and accuracy of the instrumentation. Clean room conditions can be obtained to a certain extent. A measurement program can be carried out independently of the weather and is therefore more likely to be completed as scheduled - a point which is often crucial in satellite flight hardware development.

No far-field approximations. Assumption of far-field conditions for measurements carried out at a finite distance implies some uncertainties in the measurements. In most near-field measurement methods, such

approximations are eliminated. In fact, the optimum distance will be determined by considerations quite different from those in a far-field measurement.

Suppressed ground reflection. The short distance between the antenna under test and the measuring antenna implies that the angle between the direct signal and the specular ground reflection is large compared to a far-field measurement. Accordingly, the reflected signal will be weak because it is transmitted and received through far-out sidelobes. Furthermore, the angle of incidence will be such that absorbers at the ground or the floor will be more efficient than for the grazing incidence in a far-field measurement.

Extended information. Processing of near-field measurements into far-field patterns requires the phase of the field to be determined in one way or the other. Also, the field must be sampled and digitized for computer processing. However, once the data are in the computer, not only the far-field amplitude pattern but also the phase pattern and field in the vicinity of the antenna can be found. If, for example, a large feed system has been measured, the field at the surface of the reflector can be calculated. In many cases, the aperture field of the antenna can be determined and used for diagnostics of errors in the antenna, e.g. faulty elements in an array or surface errors in a reflector antenna.

An excellent survey of methods for measurement of antenna patterns at reduced distances has been given by Johnson, Ecker and Hollis [1]. The methods are divided into three categories:

The probe scanning techniques, where the near field of the antenna is sampled on a suitable surface and the far field is found by computer processing.

The compact ranges, where the antenna is illuminated by an approximate plane wave in front of a large reflector or lens.

The focusing technique which can be used if the antenna can be focused at a finite distance where patterns can be measured. These patterns are similar to the far-field patterns when the antenna has been re-focused to infinity.

The present subchapter 9.1 deals with one of the probe scanning techniques, while subchapter 9.3 treats the compact range method. The planar and the cylindrical measurement surfaces will only be discussed briefly, and the reader is referred to [2], [3] and [4] for a description of these methods. The spherical scanning surface is the one which has been developed at the latest, and the spherical modal expansion technique for near-field to far-field transformation will be outlined in section 9.1.3. An alternative formulation of the near-field to far-field transformation, namely plane wave synthesis, is presented in the following section and compared to the modal expansion technique. Finally, some actual spherical near-field measurements are demonstrated.

#### 9.1.2. Near-field effects

Before turning to the near-field methods, we shall briefly examine how a finite distance can influence antenna measurements in practice. Because most antennas are reciprocal, the measured amplitude and phase will be independent of whether the antenna under test transmits or receives. Therefore, we shall allow ourselves to switch freely between the two cases in the discussion.

Phase error. A source at infinity would create a plane wave field incident upon the test antenna. In order to measure the far-field pattern of the test antenna, it should accordingly be illuminated by a plane wave. However, the phase front of the field from a source antenna at a finite distance will be rather spherical, as illustrated in fig. 9.1.1. For many applications, a phase error of  $\pi/8$  is accepted at the edge of the aperture leading to the Rayleigh criterion for the measurement distance

$$R > \frac{2D^2}{\lambda}$$

where  $D$  is the diameter of the antenna aperture and  $\lambda$  is the wavelength.

For an antenna with a constant phase in the aperture, the phase error will tend to make the received signal lower than given by the far-field transmission formula

$$P_{\text{received}} = G_1 G_2 \frac{\lambda^2}{(4\pi R)^2} P_{\text{in}} \quad (9.1.1)$$

where  $G_1$  and  $G_2$  are the far-field gain values of the two antennas. If the phase and amplitude distribution of the antennas are well known, one might compute a near-field correction to eq. 9.1.1. This can be done for horn antennas [5]. However, a reflector antenna under test might have a quadratic phase distribution which fits the spherical phase front of the source antenna or probe, and in that case the received signal will be higher than indicated by eq. 9.1.1. The focused aperture treated in Collin and Zucker [6] is a good illustration of this.

Therefore, in general, one cannot calculate near-field corrections to eq. 9.1.1 for gain measurements, and the same goes for other parameters like beam width, sidelobe levels, null depth etc. A near-field to far-field transformation, however, rigorously corrects for the spherical phase front.

Transverse amplitude taper. A common problem in the near-field scanning methods is that the probe antenna does not measure the field at a single point but rather a weighted average value over the aperture plane. If the test antenna is in the far field of the probe, the problem can be described as a weighting of the contributions from the various current elements on the test antenna with the amplitude and phase pattern of the probe. The correction in the far-field calculation for this phenomenon is called probe correction or probe compensation.

It should be noted that weighting or amplitude taper over the test aperture is not confined to near-field measurements. In a far-field measurement, one will often use a directive source antenna with a zero in the direction of the specular reflection. This will lead to an amplitude taper over the test aperture and a resulting error in a gain measurement.

Longitudinal amplitude taper. The power density in the incident field will decay with the distance  $R$  from the source antenna as  $R^{-2}$ . Ideally,  $R$  should be large compared to the size of the test antenna such that the gain determined by eq. 9.1.1 is independent of from which point inside the antenna the distance is measured. If not, one has an uncertainty in the gain measurement. In a near-field measurement this problem is solved by assigning a coordinate system to each antenna. The characteristics of each antenna are then referred to its coordinate system and the distance in the measurement is rigorously defined as the distance between the centers of the two coordinate systems.

### 9.1.3. Modal expansion techniques

A common way of transforming measured near-field data into far-field patterns is to use an expansion of the field of the unknown antenna in terms of modes. The modes are basic solutions to the vector wave equation outside the antenna, and they can be plane, cylindrical or spherical waves. If the transformation involves probe correction, a modal expansion is used for the probe field also.

The three types of modes mentioned here are not the only ones which can be used, but they are advantageous in the way that the wave equation separates in their respective coordinate systems. This implies that each component of the mode functions can be written as a product of functions, where each function depends on one coordinate only, see for example equation 9.1.2. for the spherical modes. Accordingly, the mode functions are simple to compute everywhere outside the antenna.

The near-field to far-field transformation consists in principle of two steps. First, the coefficients in the modal expansion are determined by use of orthogonality integrals over the scanning surface and secondly, the expansion is evaluated in the far field. Efficient and accurate computer programs exist for planar, cylindrical and spherical scanning, and therefore the antenna engineer does not have to deal with all the mathematical details in order to apply the near-field measurement methods. However, in order to illustrate some of the concepts, we shall present some of the mathematics

for the spherical method.

### Spherical waves

First, a coordinate system is introduced for description of the field of the test antenna. A field point is specified by spherical coordinates  $r$ ,  $\theta$ ,  $\phi$  and in each point unit vectors  $\hat{r}$ ,  $\hat{\theta}$  and  $\hat{\phi}$  are defined as illustrated in fig. 9.1.2. The spherical vector wave functions can then be written in the form

$$\begin{aligned} F_{1mn}(r, \theta, \phi) = & \frac{k}{\sqrt{n}} \left( -\frac{m}{|m|} \right)^m \sqrt{\frac{2n+1}{4\pi n(n+1)}} \sqrt{\frac{(n-|m|)!}{(n+|m|)!}} \left[ 0 \hat{r} \right. \\ & + \frac{im}{\sin\theta} P_n^{|m|}(\cos\theta) e^{im\phi} h_n^{(1)}(kr) \hat{\theta} \\ & \left. - \frac{d}{d\theta} P_n^{|m|}(\cos\theta) e^{im\phi} h_n^{(1)}(kr) \hat{\phi} \right] \end{aligned} \quad (9.1.2a)$$

$$\begin{aligned} F_{2mn}(r, \theta, \phi) = & \frac{k}{\sqrt{n}} \left( -\frac{m}{|m|} \right)^m \sqrt{\frac{2n+1}{4\pi n(n+1)}} \sqrt{\frac{(n-|m|)!}{(n+|m|)!}} \\ & \cdot \left[ \frac{n(n+1)}{kr} P_n^{|m|}(\cos\theta) e^{im\phi} h_n^{(1)}(kr) \hat{r} \right. \\ & + \frac{d}{d\theta} P_n^{|m|}(\cos\theta) e^{im\phi} \frac{1}{kr} \frac{d(kr h_n^{(1)}(kr))}{d(kr)} \hat{\theta} \\ & \left. + \frac{im}{\sin\theta} P_n^{|m|}(\cos\theta) e^{im\phi} \frac{1}{kr} \frac{d(kr h_n^{(1)}(kr))}{d(kr)} \hat{\phi} \right] \end{aligned} \quad (9.1.2b)$$

where the  $P_n^{|m|}(\cos\theta)$ 's are associated Legendre functions and the  $h_n^{(1)}(kr)$ 's are spherical Hankel functions.  $\eta$  is the free space admittance. Since the time dependence  $e^{-i\omega t}$  is assumed, the Hankel functions of the first kind are chosen corresponding to outward propagation. The functions 9.1.2a and b are solutions to the vector wave equation outside a sphere enclosing the antenna. They form a discrete set of functions and they are numbered by the polar index  $n$  and the azimuth index  $m$ , where

$$1 < n < \infty$$

and

$$-n \leq m \leq n.$$

The set of functions 9.1.2a and b is complete for the electromagnetic field such that the electric field radiated by the antenna into free space can be expanded as

$$\underline{E}(r, \theta, \phi) = \sum_{smn} Q_{smn} \underline{F}_{smn}(r, \theta, \phi) \quad (9.1.3)$$

The limits on the summations are

$$\sum_{smn} \equiv \sum_{s=1}^2 \sum_{n=1}^{\infty} \sum_{m=-n}^n$$

and the  $Q_{smn}$ 's are complex expansion coefficients. The magnetic field corresponding to eq. 9.1.3 is

$$\underline{H}(r, \theta, \phi) = -i\eta \sum_{smn} Q_{smn} \underline{F}_{s+1,m,n}(r, \theta, \phi) \quad (9.1.4)$$

The spherical waves have many similarities with ordinary waveguide modes. Each field component is an oscillating function of  $\theta$  and  $\phi$  as illustrated in fig. 9.1.3, and the modes propagate in the  $\hat{r}$  direction. Since the radial component of  $\underline{F}_{lmn}$  is zero, one can compare eqs. 9.1.3 and 9.1.4 and define that

$$s = 1 \quad \text{for TE-waves}$$

$$s = 2 \quad \text{for TM-waves}$$

The mode functions 9.1.2a and b are normalized such that the power radiated

by the test antenna is

$$\text{POWER} = \frac{1}{2} \sum_{smn} |Q_{smn}|^2 \quad (9.1.5)$$

Usually only relative field values are measured, and in that case eq. 9.1.5 can be used to normalize the field expansion such that far-field directivities are given in dBi.

In practice the mode sum in eq. 9.1.3 can be truncated at a point

$$N = \max n \approx kr_0 + 10 \quad (9.1.6)$$

where  $r_0$  is radius in the smallest sphere centered at the origin and surrounding the antenna. The argumentation for the criterion 9.1.6 goes as follows. At the surface of the minimum sphere no high order mode can be excited much stronger than all the low order modes because this would imply a wildly oscillating current distribution which could not be obtained in practice. Going radially outward from the minimum sphere, all modes with  $n > kr_0$  are heavily attenuated and from a few wavelengths outside the minimum sphere all modes with  $n > kr_0 + 10$  are much smaller than the measurement error.

#### Transmission formula

The coordinates involved in a spherical near-field measurement are shown in fig. 9.1.4. The distance  $A$  is constant and the coordinates  $\theta$  and  $\phi$  determine the position of the probe. The  $\chi$  angle determines the polarization of the probe such that  $\chi = 0^\circ$  means that the  $X'$ -axis is parallel to  $\hat{\theta}$ . In order to correct for the probe pattern a spherical expansion is used for the probe. In the probe coordinate system indices  $\sigma\mu\nu$  are used in the same manner as  $smn$  in the test antenna coordinate system. We introduce receiving scattering matrix elements  $P_{\sigma\mu\nu}$  for the probe defined such that if  $a_{\sigma\mu\nu}$  are coefficients of the incoming modes centered at the probe and the load on the probe is matched, then the received signal (in complex value) is

$$W = \sum_{\sigma\mu\nu} a_{\sigma\mu\nu} P_{\sigma\mu\nu} \quad (9.1.7)$$



By application of mathematical coefficients of the spherical vector waves under rotation and translation of the coordinate system, one can write the field radiated by the test antenna in terms of modes incident on and centered at the probe. The field of a test antenna mode can be expressed in terms of modes belonging to a coordinate system rotated the three Eulerian angles  $\phi$ ,  $\theta$  and  $\chi$ .

$$\underline{F}_{smn} = \sum_{\mu} e^{im\phi} d_{\mu m}^n(\theta) e^{i\mu\chi} \underline{F}_{s\mu n} \quad (9.1.8)$$

Each of the "rotated" modes  $\underline{F}_{s\mu n}$  can then be expanded in modes centered at the probe coordinate system

$$\underline{F}_{s\mu n} = \sum_{\sigma\nu} C_{\sigma\mu\nu}^{sn}(A) \underline{F}_{\sigma\mu\nu} \quad (9.1.9)$$

Eqs. 9.1.8 and 9.1.9 define the rotation and the translation coefficients, respectively. These are quite complicated functions of  $\theta$  and  $A$ . Details are given in [7]. They are inserted in eq. 9.1.3 which then gives the incident field in the probe coordinate system (with the probe absent). The mode functions  $\underline{F}_{\sigma\mu\nu}$  have Bessel function dependence since the field is finite at the origin. As  $j_n(kr) = \frac{1}{2} (h_n^{(1)} + h_n^{(2)}(kr))$ , one must include a factor of  $\frac{1}{2}$  to get the coefficients of the incoming modes. Under the assumption that multiple reflections between the test antenna and the probe are neglected, insertion of the probe into the field will not change the coefficients of the incoming modes. This is because the field scattered by the probe contributes to the outward propagation only. The signal received by the probe antenna is then found by eq. (9.1.7) and has the form

$$W(A, \phi, \theta, \chi) = \sum_{smn\mu} Q_{smn} e^{im\phi} d_{\mu m}^n(\theta) e^{i\mu\chi} P_{s\mu n}(A) \quad (9.1.10)$$

where

$$P_{s\mu n}(A) = \frac{1}{2} \sum_{\sigma\nu} C_{\sigma\mu\nu}^{sn}(A) P_{\sigma\mu\nu} \quad (9.1.11)$$

This transmission formula is the basic formula for spherical near-field measurements with probe correction. It can also be derived by use of the Lorentz reciprocity theorem [8], but the present derivation, originally proposed at NBS [2] and [9], is more direct.

### Computation of spherical wave coefficients

The input data for the computations are  $W(A, \phi, \theta, \chi)$  sampled on a full sphere with radius  $A$  in points spaced equidistantly in  $\theta$  and  $\phi$  with two polarization orientations of the probe,  $\chi = 0^\circ$  and  $\chi = 90^\circ$ , applied in each point. The probe coefficients  $P_{\sigma\mu\nu}$  are assumed to have been determined by measurement of the probe pattern and application of the same algorithm as will be derived now. The  $Q_{smn}$ 's are the unknown coefficients to be determined. The computations are based on the orthogonality integral

$$\int_{\chi=0}^{2\pi} \int_{\phi=0}^{2\pi} \int_{\theta=0}^{\pi} e^{im\phi} d_{\mu m}^n(\theta) e^{i\mu\chi} \cdot e^{-im'\phi} d_{\mu' m'}^{n'}(\theta) e^{-i\mu'\chi} \sin\theta d\theta d\phi d\chi$$

$$= \frac{8\pi^2}{2n+1} \delta_{nn'} \delta_{mm'} \delta_{\mu\mu'} \quad (9.1.12)$$

which can be applied on both sides of eq. 9.1.10 to yield

$$Q_{1mn} P_{1\mu n} + Q_{2mn} P_{2\mu n} = \quad (9.1.13)$$

$$\frac{n + \frac{1}{2}}{4\pi^2} \int_{\chi=0}^{2\pi} \int_{\phi=0}^{2\pi} \int_{\theta=0}^{\pi} W(A, \phi, \theta, \chi) d_{\mu m}^n(\theta) \sin\theta d\theta e^{-im\phi} d\phi e^{-i\mu\chi} d\chi$$

The  $P_{1\mu m}$ 's and  $P_{2\mu n}$ 's can be calculated in advance from the probe coefficients and the translation coefficients as indicated in eq. 9.1.11. For each  $m$  and  $n$  the integral on the right-hand side is calculated for  $\mu = +1$  and  $\mu = -1$ . In this way two equations with two unknowns  $Q_{1mn}$  and  $Q_{2mn}$  are established and the  $Q$ 's can be found.

The values  $\mu = +1$  and  $-1$  are chosen because they correspond to a probe pattern of the form

$$\underline{E}_{\text{probe}}(\theta, \phi) = \underline{a}_1(\theta) \cos\phi + \underline{a}_2(\theta) \sin\phi \quad (9.1.14)$$

and this can be realized with a conical horn excited by the fundamental mode in a circular waveguide. In fact, we impose the condition that

$$P_{\sigma\mu\nu} \text{ must be } 0 \quad \text{for } \mu \neq \pm 1$$

(9.1.15)

on the probe pattern such that the measured signal  $W$  will have an  $e^{+i\chi}$  and  $e^{-i\chi}$  dependence only as can be seen from eq. 9.1.10. This means that the  $\chi$ -integral in eq. 9.1.13 can be calculated from only two measurements at each point  $(\theta, \phi)$ , namely  $\chi = 0^0$  and  $\chi = 90^0$ . A probe containing modes with more  $\mu$ 's than  $+1$  and  $-1$  would require measurements for the same number of  $\chi$  values in each point  $(\theta, \phi)$  as the number of  $\mu$ -values present in the probe pattern.

The  $\phi$ -integral in eq. 9.1.13 is a Fourier integral of a periodic function and accordingly it can be computed by the Fast Fourier Transform (FFT) and we can define

$$W_{\mu m}(\theta) = \frac{1}{4\pi^2} \int_0^{2\pi} \int_0^{2\pi} W(A, \phi, \theta, \chi) e^{-im\phi} e^{-i\mu\chi} d\phi d\chi \quad (9.1.16)$$

The  $\theta$  integral in eq. 9.1.13 is not a Fourier integral but using a special trick, FFT in  $\theta$  is possible and facilitates the integration. The  $W_{\mu m}(\theta)$  is actually measured for  $0 \leq \theta < \pi$  only, but they can be extended analytically into the range  $-\pi < \theta \leq 0$ . One can convince oneself that  $W(A, \phi, -\theta, \chi)$  is exactly the same probe position as  $W(A, \phi + \pi, \theta, \chi + \pi)$ , and therefore

$$W_{\mu m}(-\theta) = (-1)^{\mu+m} W_{\mu m}(\theta) \quad (9.1.17)$$

Having defined  $W_{\mu m}(\theta)$  for  $-\pi \leq \theta \leq 0$  one can Fourier transform the data in  $\theta$  and perform the  $\theta$  integration in equation (9.1.13) by insertion of

$$W_{\mu m}(\theta) = \sum_{m''} W_{\mu m}^{m''} e^{im''\theta} \quad (9.1.18)$$

and the exact Fourier expansion of  $d_{\mu m}^n(\theta)$ , [7]

$$d_{\mu m}^n(\theta) = i^{\mu-m} \sum_{m'=-n}^n \Delta_{m', \mu}^n \Delta_{m', m}^n e^{-im'\theta} \quad (9.1.19)$$

which gives

$$Q_{1mn}P_{1\mu n} + Q_{2mn}P_{2\mu n} = (n + \frac{1}{2}) i^{\mu-m} \sum_{m'm''} \Delta_{m',\mu}^n \Delta_{m',m}^n \left( \int_0^\pi e^{i(m''-m')\theta} \sin\theta d\theta \right) W_{\mu m}^{m''} \quad (9.1.20)$$

The integrals in this equation are simple, and efficient recurrence formulas exist for the deltas [7]. The right-hand sides of eq. 9.1.20 can thus be computed and the Q's can be found.

The far field of the test antenna could now be found by eq. 9.1.3, but since the rotation coefficients have already been computed, it is more convenient to use eqs. 9.1.10 and 9.1.11 with  $A = \infty$ .

The algorithm outlined here builds on the work by Jensen [8] and Wacker [9], and it has been implemented in a computer program SNIFTC [10]. The measurements in section 9.1.5 have been processed by this computer program.

### Sampling

The sampling intervals required in  $\theta$  and  $\phi$  can be derived from the truncation criteria for the spherical wave expansions. If the expansion of the test antenna can be truncated at  $\max n = N$ , then the Fourier expansion (9.1.19) implies that the probe signal is band limited to  $e^{\pm iN\theta}$ , and accordingly

$$\Delta\theta = \frac{\pi}{N} \quad (9.1.21)$$

or less is sufficient to calculate the  $\theta$ -integrals by FFT. Since  $\max |m| \leq N$ ,  $\Delta\phi = \Delta\theta$  will always be sufficient for the  $\phi$ -integrals to be computed. However, in many situations larger  $\Delta\phi$  can be chosen, for instance if the field is sampled in a region around  $\theta = 0$  only, or if the antenna possesses some degree of symmetry [7].

For a directive antenna pointing towards the equator of the sampling grid, i.e.  $\theta = 90^\circ$ ,  $\Delta\phi = \Delta\theta$  must be used. However, if the near-field measurement can be truncated, one can assume the field to be periodic in  $\phi$  with a period of  $2\pi$  divided by an integer repetition number. The computation time can in this way be reduced by the repetition factor [11].

The sampling interval 9.1.21 derived from the truncation criteria (9.1.6) corresponds to roughly half a wavelength on the minimum sphere with radius  $r_0$ . Close to the minimum sphere 9.1.21 is in agreement with the sampling criterion for planar near-field measurements by Joy and Paris [3].

#### Numerical test case

The preceding algorithm for near-field to far-field transformation is exact except for the truncation of the wave expansions. The potential accuracy is therefore much better than for methods like physical optics or GTD usually applied in antenna analysis. A numerical antenna model based on these methods cannot be used to demonstrate the full capability of the algorithm. Accordingly, the numerical test case illustrated in fig. 9.1.5 have been chosen. In this model both the test antenna and the probe consist of Hertzian dipoles, and the near field received by the two-dipole probe as well as the far field can be computed exactly.

For a test antenna  $50\lambda$  in diameter, sampled in 65160 points ( $\Delta\theta = \Delta\phi = 1^\circ$ ), the maximum error in the far field was more than 80 dB below the isotropic level of the antenna [10]. This error level is much lower than what can be obtained for the measured near-field data. The computation time for this case is 3 min. CPU-time on an IBM 3033 or 60 min. on a HP 1000 minicomputer. Antennas up to  $D = 120\lambda$  can be treated at present.

#### 9.1.4. Plane wave synthesis

An alternative method for near-field to far-field transformation with probe correction has been devised by Bennett and Schoessow [12]. Suppose a spherical array of probes were built and excited such that a plane wave were generated around the antenna as illustrated in fig. 9.1.6. Then the far field could be measured directly. However, one can also measure the response from one probe at the time and then multiply by the excitation factors and sum over the probe positions in the computer. A summation must be carried out for each far-field direction. The excitation factors are in [12] found by an iterative procedure. An advantage of the method is that in the calculation of the excitations one can compensate for a truncation of the

surface on which the scanning is done.

The modal expansion method involving Fourier transformations and matrix multiplications can, however, also be viewed as a far-field computation by weighting of near-field data. In [13] the equivalent weights for a full spherical array have been calculated and when the field from the array is evaluated around the center of the array, one finds that a plane wave is generated. In fig. 9.1.7, phase error contours for a field propagating in the Z direction are shown. It has been found that the plane wave zone is approximately spherical and the size is determined by the probe spacing, in accordance with the sampling theorem. In fig. 9.1.7, a spacing of  $\Delta\theta = 6^\circ$  has been chosen and a plane wave zone with a radius of  $5\lambda$  is formed. The deviations from a plane wave with the inner sphere in the figure are less than  $0.1^\circ$  and 0.001 dB illustrating the accuracy of the numerical processing. Of course such accuracies cannot be obtained for the measured near field.

In order to complete the picture of spherical scanning, we shall mention that approximate methods for transforming measurements made in the Fresnel region into far fields have been developed in the USSR. Reference [14] gives an excellent review of this work. Also, the holographic metrology method for large reflectors [15] is a kind of spherical Fresnel zone scanning. Here the field is measured in amplitude and phase at a distance much closer than the Rayleigh distance. Only the mainlobe and a few sidelobes are measured. By taking the Fourier transform of the measurements an aperture field is obtained. However, this contains a quadratic phase deviation corresponding to the finite measurement distance. The quadratic phase deviation is subtracted in the computer and a second Fourier transform yields the far field. Since the aperture field is obtained in both amplitude and phase, it can be used for diagnostics of both feed position errors and surface deformation of the reflector.

#### 9.1.5. Measurement example

An accurate spherical scanner has been developed for the European Space Agency in the radio anechoic chamber at the Technical University of Denmark. The system contains a two-axes positioner with high resolution

angular encoders ( $0.001^\circ$ ). A block diagram of the system is shown in fig. 9.1.8. A dual polarized probe is used such that two polarization components are measured simultaneously. The near-field scanning is supervised by a HP 1000 minicomputer which also computes the far field when the near-field data have been recorded.

The measurements presented here were taken on a duplicate of the spotbeam antenna on the OTS satellite. The frequency was 11.7 GHz where the antenna is  $30\lambda$  in diameter. Near-field measurements were taken at three distances 1.5 m, 2.5 m and 5.0 m with sample spacings of  $\Delta\theta = \Delta\phi = 1.5^\circ$ . A part of the sampling points is shown in fig. 9.1.9 in scale with the antenna. Each of the three near fields were transformed to far fields using probe data for probe correction. The boresight of the antenna is close to  $\theta = 0^\circ$  and fig. 9.1.11 shows the three near-field amplitudes in the interval  $-10^\circ \leq \theta \leq 10^\circ$  in a cut perpendicular to the  $\hat{z}$ -axis. The corresponding far fields are shown in fig. 9.1.12.

Since a full sphere of near-field data is taken for each of the three distances, three values for the peak directivity can be found as described in section 9.1.3. Table 9.1.1 contains these values. Also shown are the results of computations without probe correction. In this case, an ideal dipole pattern is assumed for the probe. It can be seen that the directivities with probe correction agree within 0.03 dB. Later measurements on the same antenna have also fallen within this error interval [16].

The error from omitting probe correction is 0.35 dB for the closest distance. The influence of probe correction can be understood from fig. 9.1.10. The field in front of the antenna is essentially a plane wave with a certain amplitude taper. As the probe scans the aperture of the reflector, it is somewhat rotated relative to the plane wave, and it therefore measures the aperture field to be more tapered than it actually is. If there is not corrected for this effect one obtains a broader mainlobe and lower sidelobes. This can be seen in fig. 9.1.13 showing the co-polar far field transformed from the 1.5 m distance both with and without probe correction.

measurement distance	without probe corr.	with probe corr.
1.5 m	36.50 dBi	36.85 dBi
2.5 m	36.76 dBi	36.88 dBi
5.0 m	36.82 dBi	36.85 dBi

Table 9.1.1 Peak directivity for OTS spotbeam antenna.

Probe correction has been found to have an effect on the cross-polar field also, as can be seen in fig. 9.1.14. The relation between the E-plane and the H-plane pattern of the present horn probe is different from that of an ideal dipole. In the measurements, the E- and H-plane distributions of the aperture field are modified by the respective probe patterns, and if there is not corrected for this, cross-polar lobes are generated in the  $\phi = 45^\circ$  and  $\phi = 135^\circ$  planes. The cross-polar field at the electrical bore-sight is not affected, however. The accuracy of the cross-polar component is affected by many other error sources, e.g. phase drift, and work is still going on in order to improve the accuracy of the cross-polarization measurements. More information on this point can be found in [16].

#### 9.1.6. Conclusion

Near-field methods offer the possibility of very accurate indoor testing of antennas. In the present subchapter, the spherical modal expansion technique has been described and illustrated by some measurement results. Equally accurate results have been obtained with planar and cylindrical near-field scanning. The following statements can be made regarding the probe scanning techniques

- No assumptions about the test antenna are involved except for the size.
- The computation time is always much smaller than the time required to measure the near-field data. This is true even on a minicomputer.
- Reliable computer programs exist for near-field to far-field transformation.



- Probe correction can be used to increase the accuracy.
- Complete far-field information can be obtained in a two-dimensional grid consistent with the sampling theorem.
- Data from near-field probe scanning can be used for error diagnostics.

#### References

- 1) Johnson, R.C., Ecker, H.A., and Hollis, J.S., "Determination of far-field patterns from near-field measurements", Proc. IEEE, Vol. 61, No. 12, pp. 1668-1694, December 1973.
- 2) Kerns, D.M., "Plane-wave scattering-matrix theory of antennas and antenna-antenna interactions", NBS monograph 162, National Bureau of Standards, June 1981.
- 3) Paris, D.M., Leach, W.M., and Joy, E.B., "Basic theory of probe compensated near-field measurements", IEEE Trans. Antennas Propagation, Vol. AP-26, No. 3, pp. 373-379, May 1978.
- 4) Joy, E.B., Leach, W.M., Rodrigue, G.P., and Paris, D.T., "Applications of probe-compensated near-field measurements", IEEE Trans. Antennas Propagation, Vol. AP-26, No. 3, pp. 379-389, May 1978.
- 5) Chu, T.S. and Samplak, R.A., "Gain of electromagnetic horns", Bell Syst. Tech. J., Vol. 44, pp. 527-537, March 1965.
- 6) Collin, R.E. and Zucker, F.J., "Antenna theory", Chapter 3, McGraw-Hill, New York 1969.
- 7) Larsen, F.H., "Probe-corrected spherical near-field antenna measurements", Ph.D. Thesis, Electromagnetics Institute, Technical University of Denmark, Report LD 36, December 1980.
- 8) Jensen, F., "Electromagnetic near-field - far-field correlations", Ph.D. Thesis, Laboratory of Electromagnetic Theory, Technical University of Denmark, Report LD 15, July 1970.
- 9) Wacker, P.F., "Non-planar near-field measurements: Spherical scanning", Report NBSIR 75-809, Electromagnetics Division, Institute for Basic Standards, Nat. Bur. Stds., Boulder, Colorado, June 1975.
- 10) Larsen, F.H., "Spherical near-field transformation program with probe correction", Report R 201, Electromagnetics Institute, Technical Univ. of Denmark, October 1978.

- 11) Hess, D.W. and Tavormina, J.J., "An algorithm with enhanced efficiency for computing the far-field from near-field data on a partial spherical surface", URSI meeting, p. 185, Boulder, Colorado, January 1982.
- 12) Bennett, J.C. and Schoessow, E.P., "Antenna near-field/far-field transformation using a plane-wave synthesis technique", Proceedings of IEE, Vol. 125, No. 3, pp. 179-184, March 1978.
- 13) Ludwig, A.C. and Larsen, F.H., "Spherical near-field measurements from a "compact-range" viewpoint", IEE Conference Publication No. 195, pp. 274-277, York, April 1981.
- 14) Turchin V.I. and Tseytlin, N.M., "Antenna testing based on near-field measurements", Radio Engineering and Electronic Physics, Vol. 24, pp. 1-26, December 1979.
- 15) Bennett, J.C., Anderson, A.P., McInnes, P.A., and Whitaker, J.T., "Microwave holographic metrology of large reflector antennas", IEEE Trans. Antennas Propagation, Vol. AP-24, No. 3, pp. 295-303, May 1976.
- 16) Christensen, E.L., Hansen, J.E., Hansen, C.K., Hansen, S.B., Larsen, F.H., and Lemanczyk, G.H., "Experimental spherical near-field antenna test facility, phase 2," Final report on ESA contract No. 3916/79/NL/DG, Electromagnetics Institute, Technical University of Denmark, R 248, December 1981.

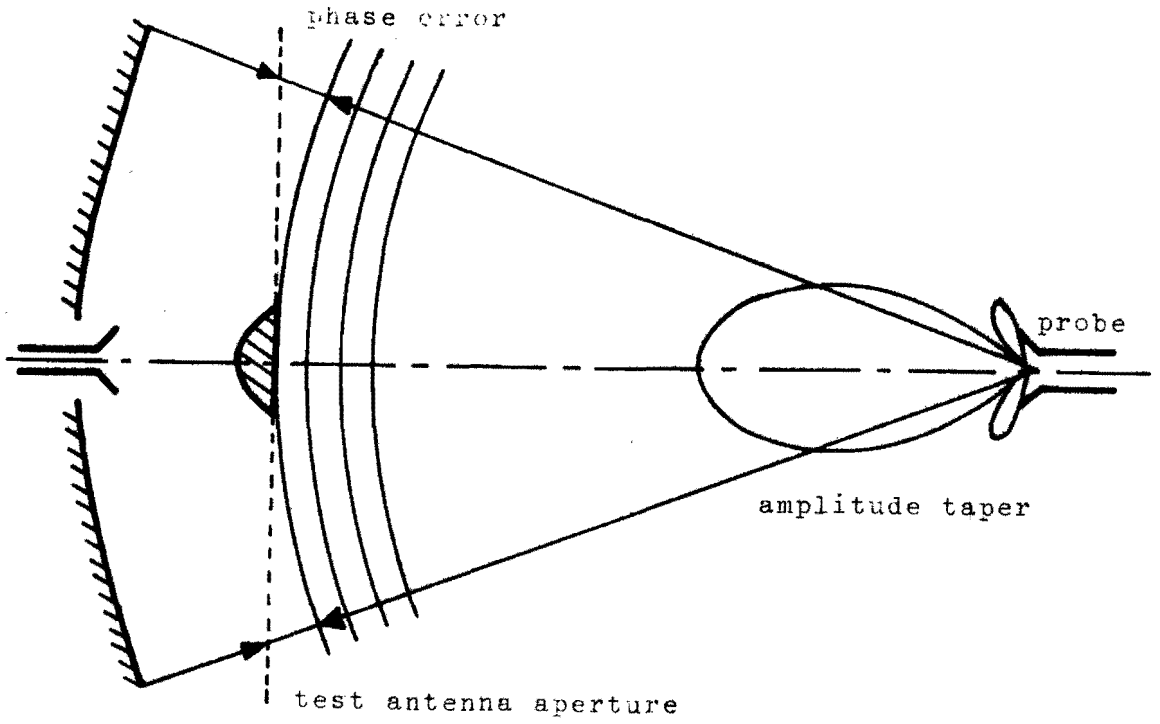


Fig. 9.1.1. The phase error and proximity effect associated with a finite range length in antenna measurements.

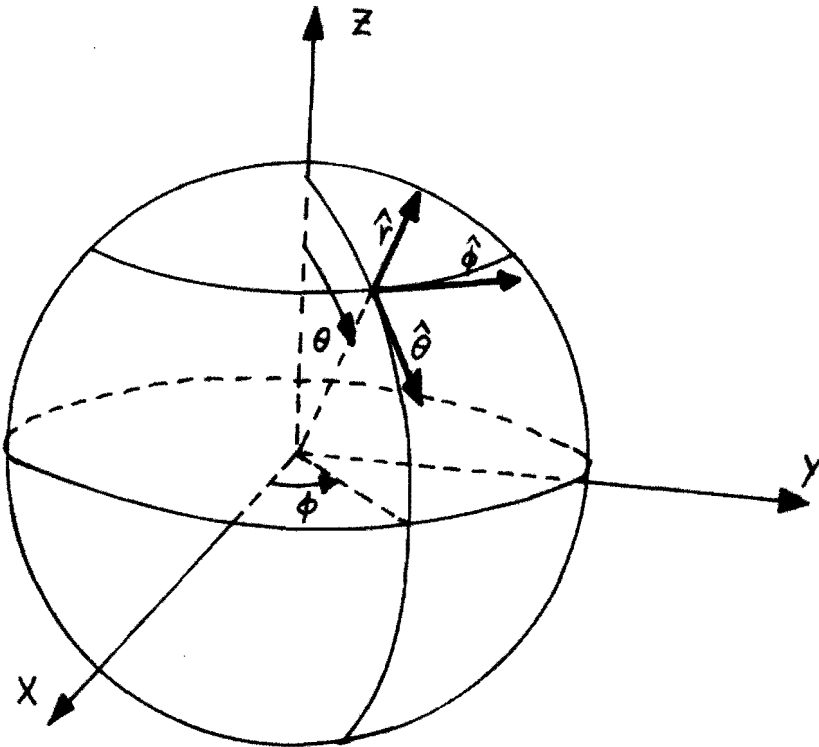


Fig. 9.1.2. Spherical coordinate system with the unit vectors  $\hat{r}$ ,  $\hat{\theta}$ ,  $\hat{\phi}$  shown in a field point  $(r, \theta, \phi)$ .

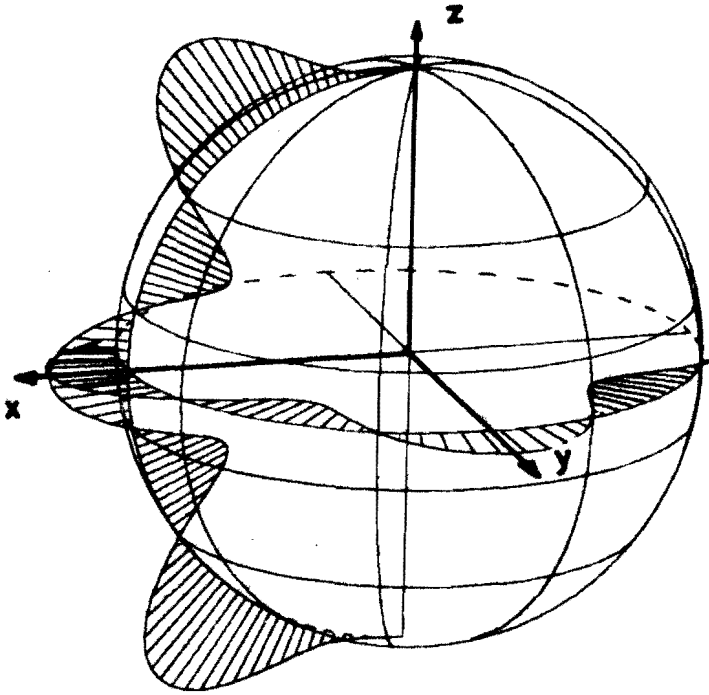


Fig. 9.1.3. Sketch of the radial component  $E_{248}(r, \theta, \phi)$ .

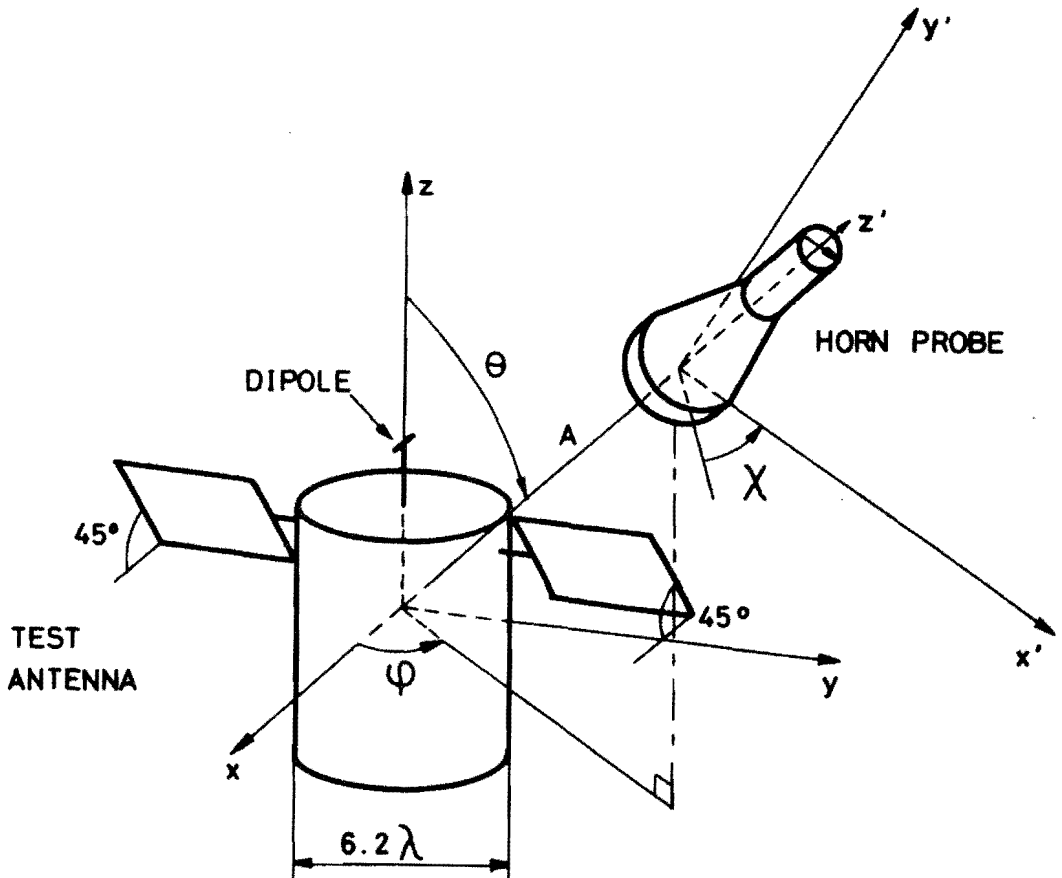


Fig. 9.1.4. The geometry of spherical near-field measurements.

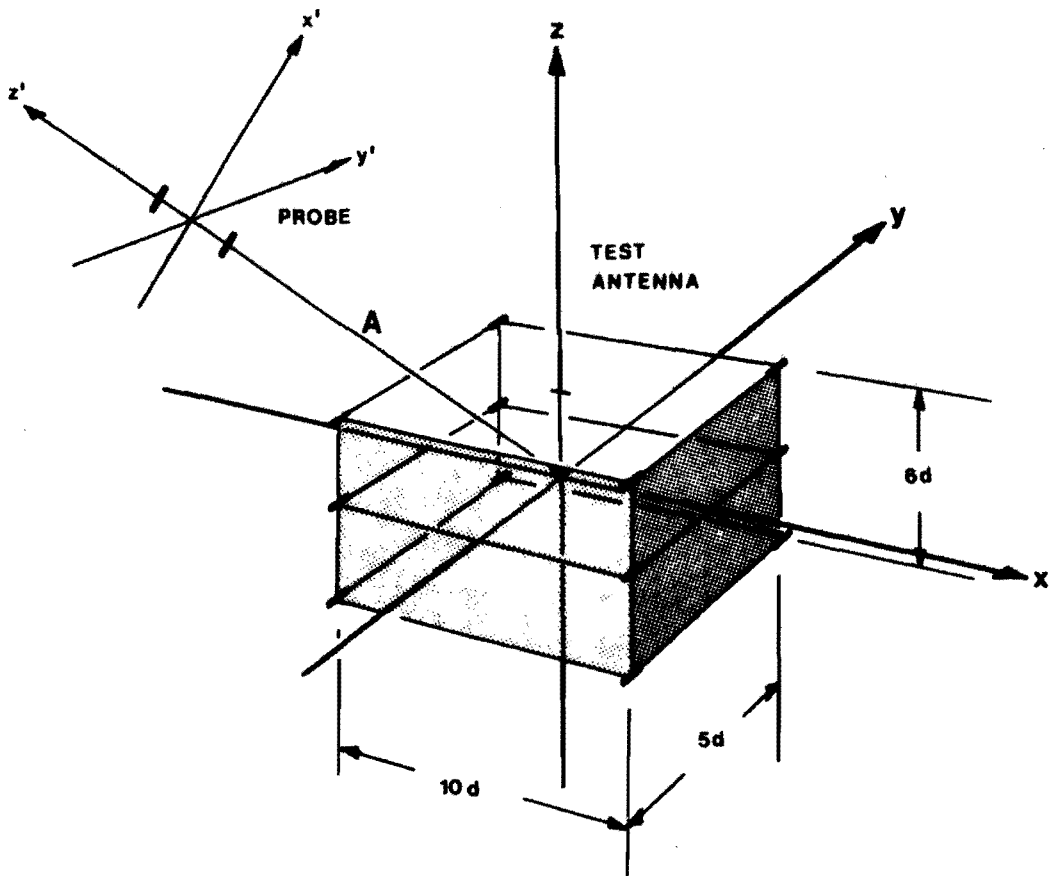


Fig. 9.1.5. Numerical test care. The test antenna consists of 12 dipoles and the probe of two dipoles.

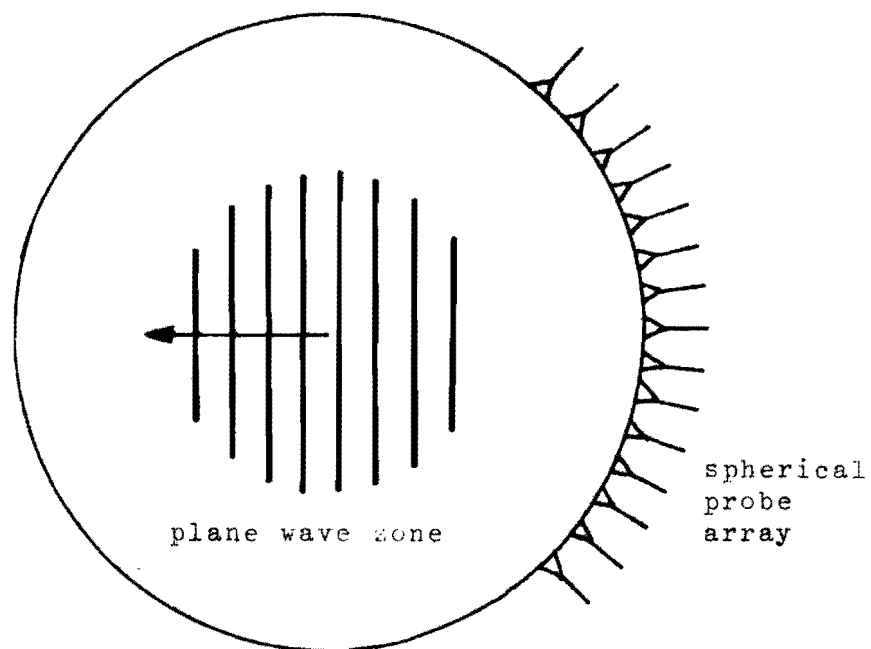


Fig. 9.1.6. Plane wave synthesis.

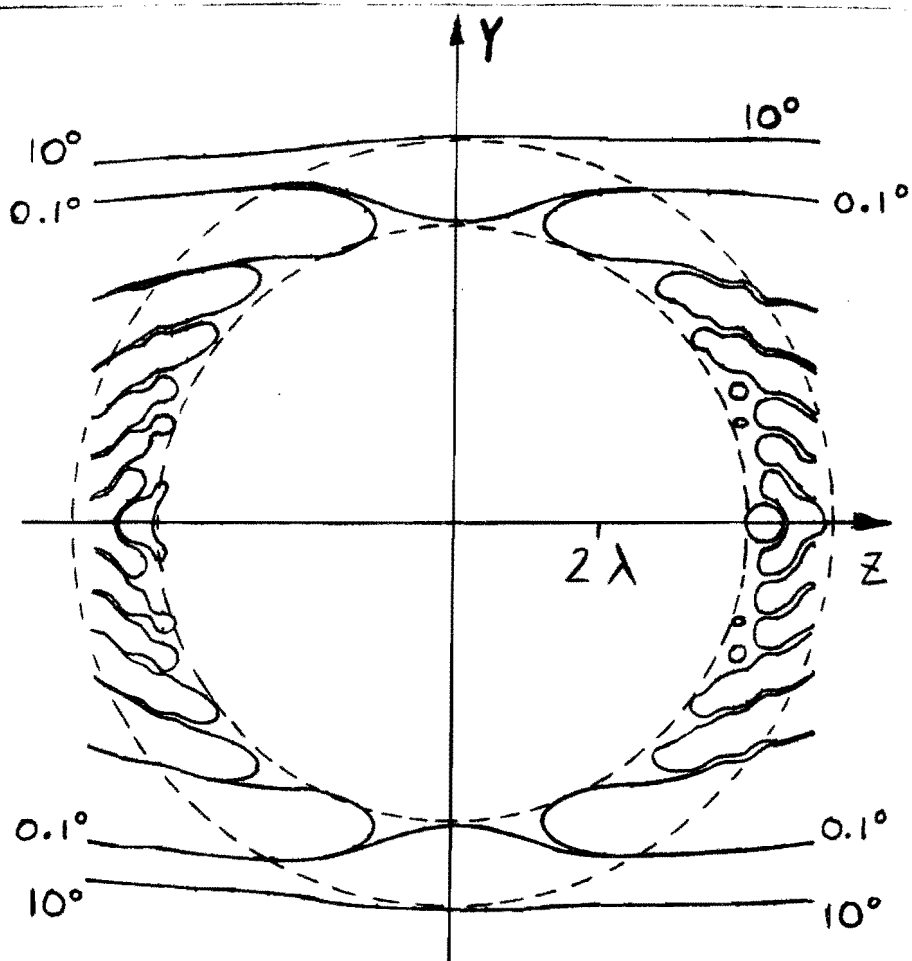


Fig. 9.1.7. Phase error contour plot.

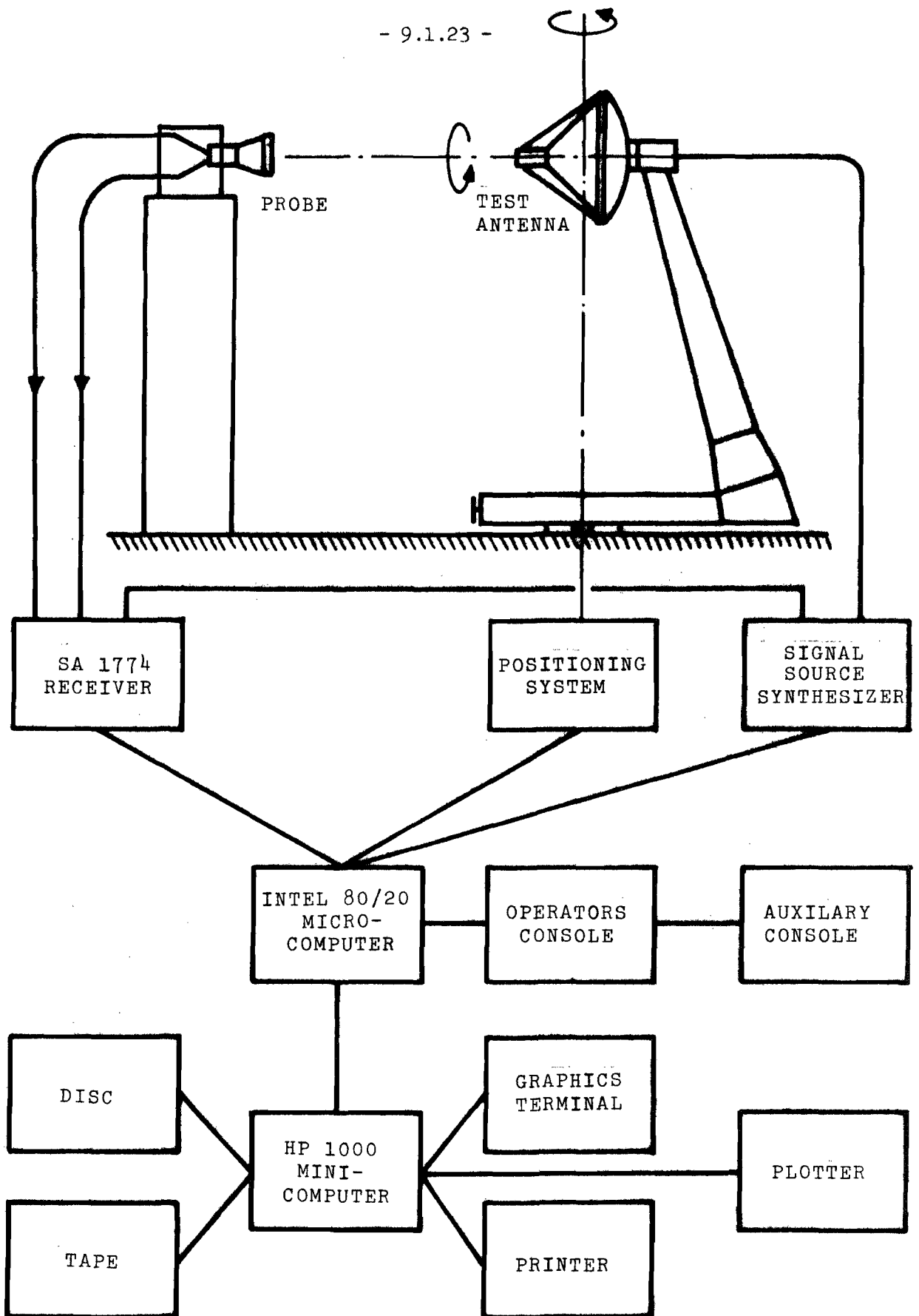
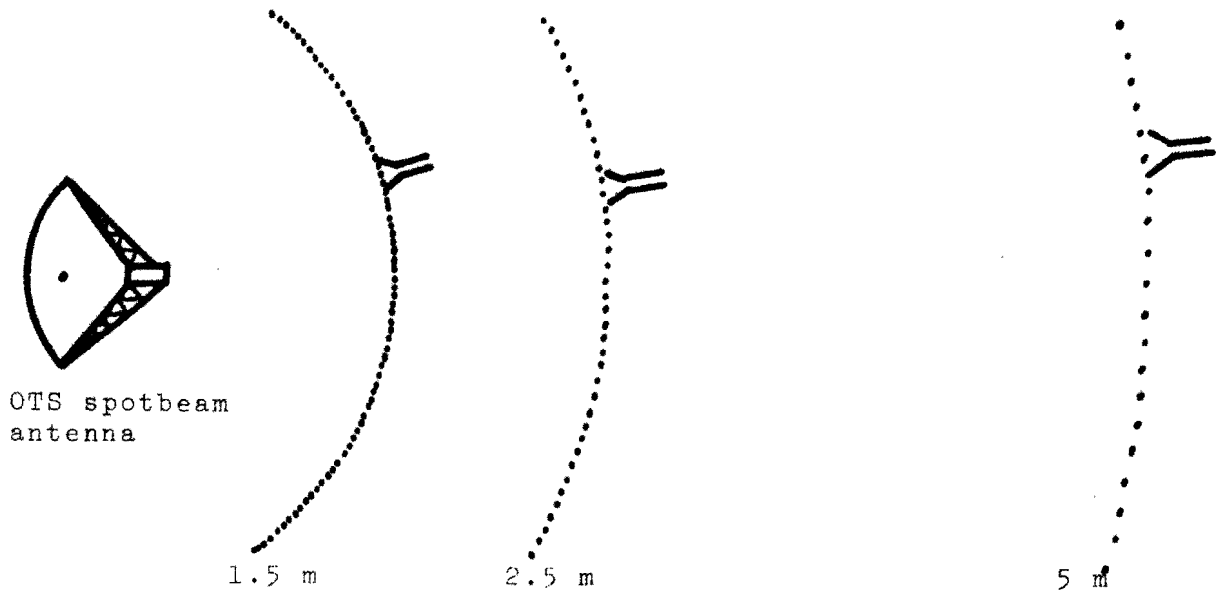
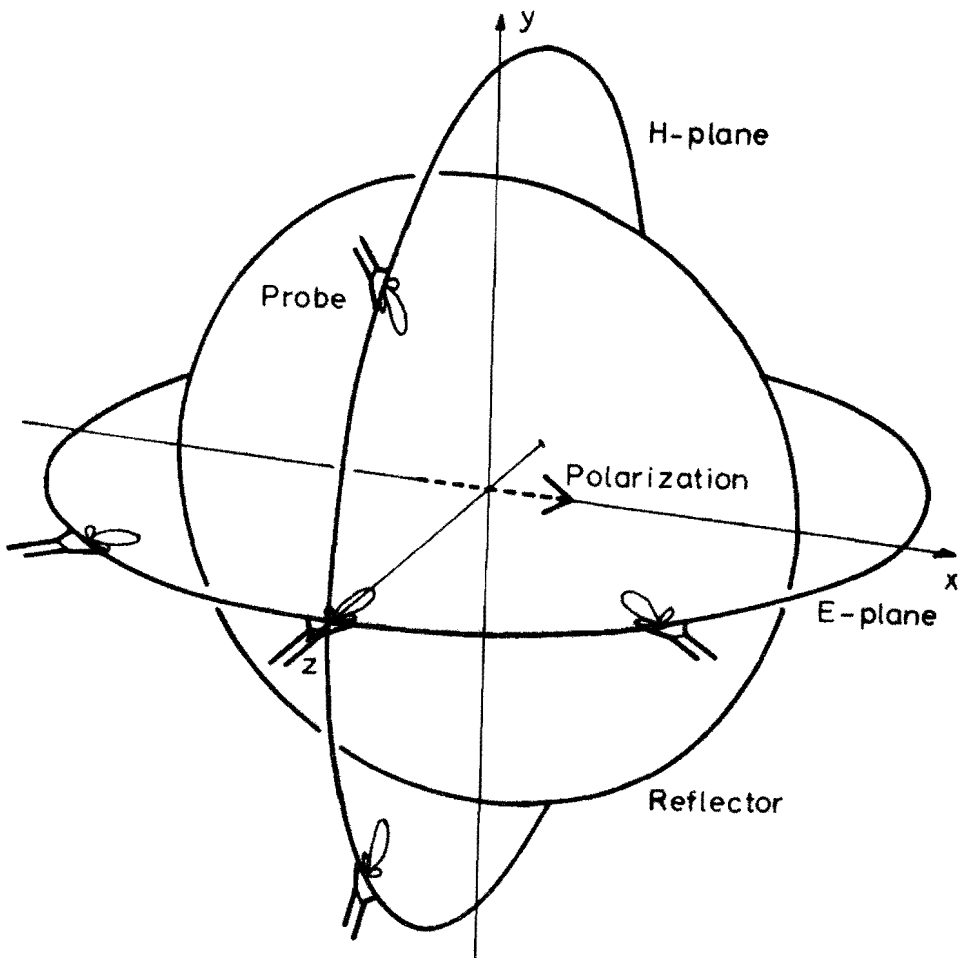


Fig. 9.1.8. Schematic diagram of the spherical near-field antenna test facility at the Technical University of Denmark.



*Fig. 9.1.9. The three measurement distances shown in scale with the antenna.*



*Fig. 9.1.10. The orientation of the probe while scanning the aperture field in the E-plane and the H-plane.*



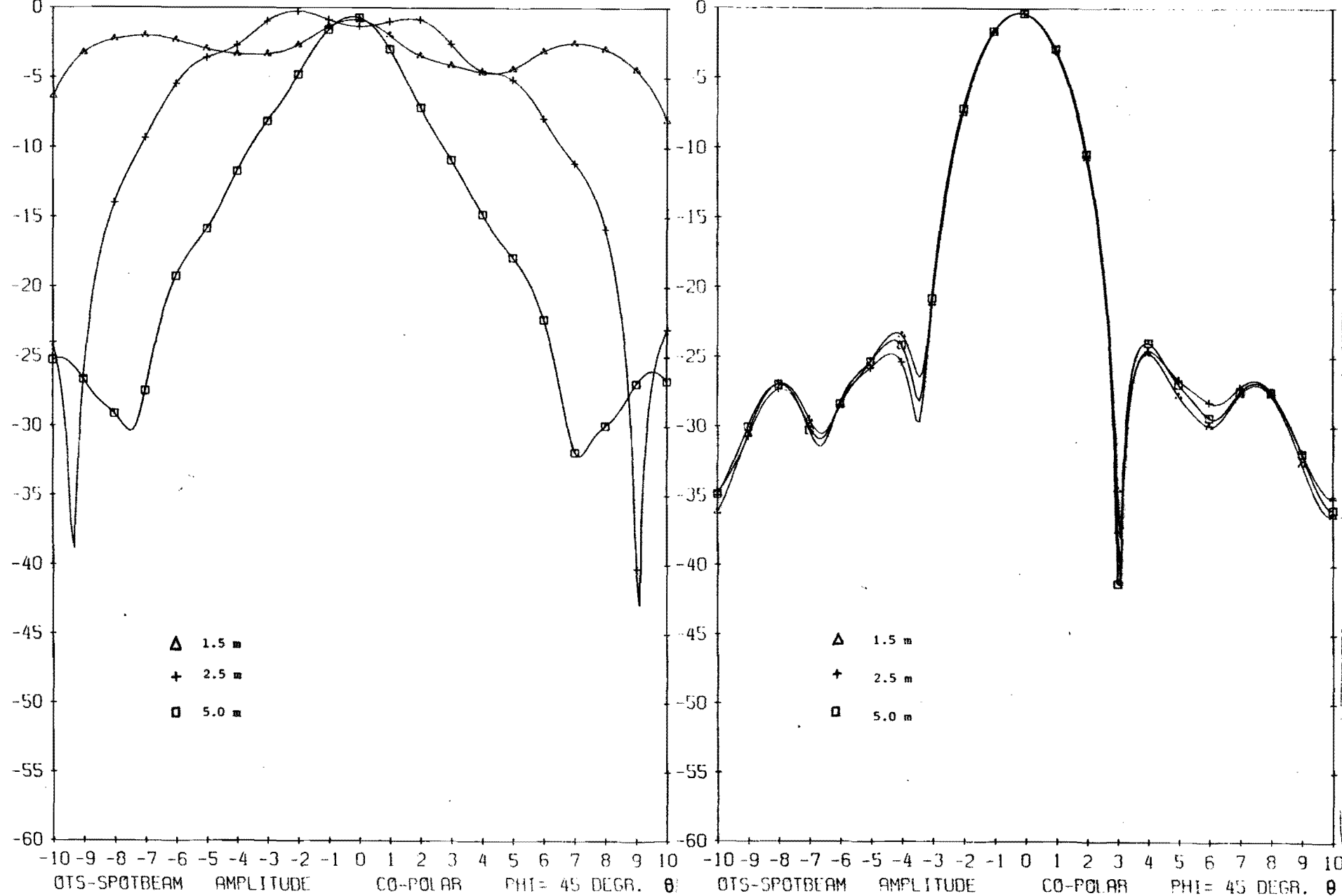


Fig. 9.1.11. Copolar near fields at  $\phi = 45^\circ$  at three measurement distances.

Fig. 9.1.12. Copolar far fields at  $\phi = 45^\circ$  transformed from measurements at three distances.

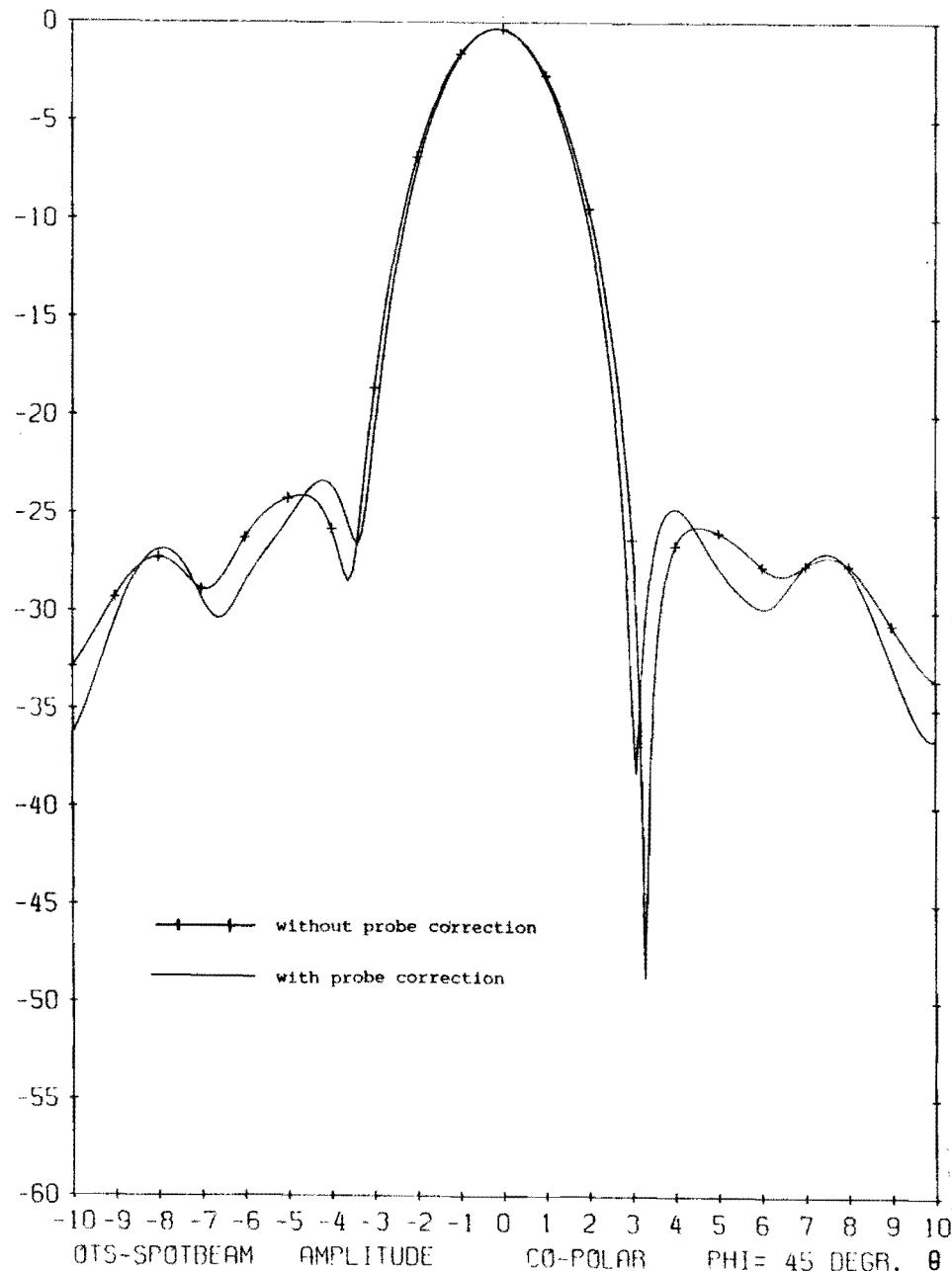


Fig. 9.1.13. Copolar far fields at  $\phi = 45^\circ$  calculated with and without probe correction.

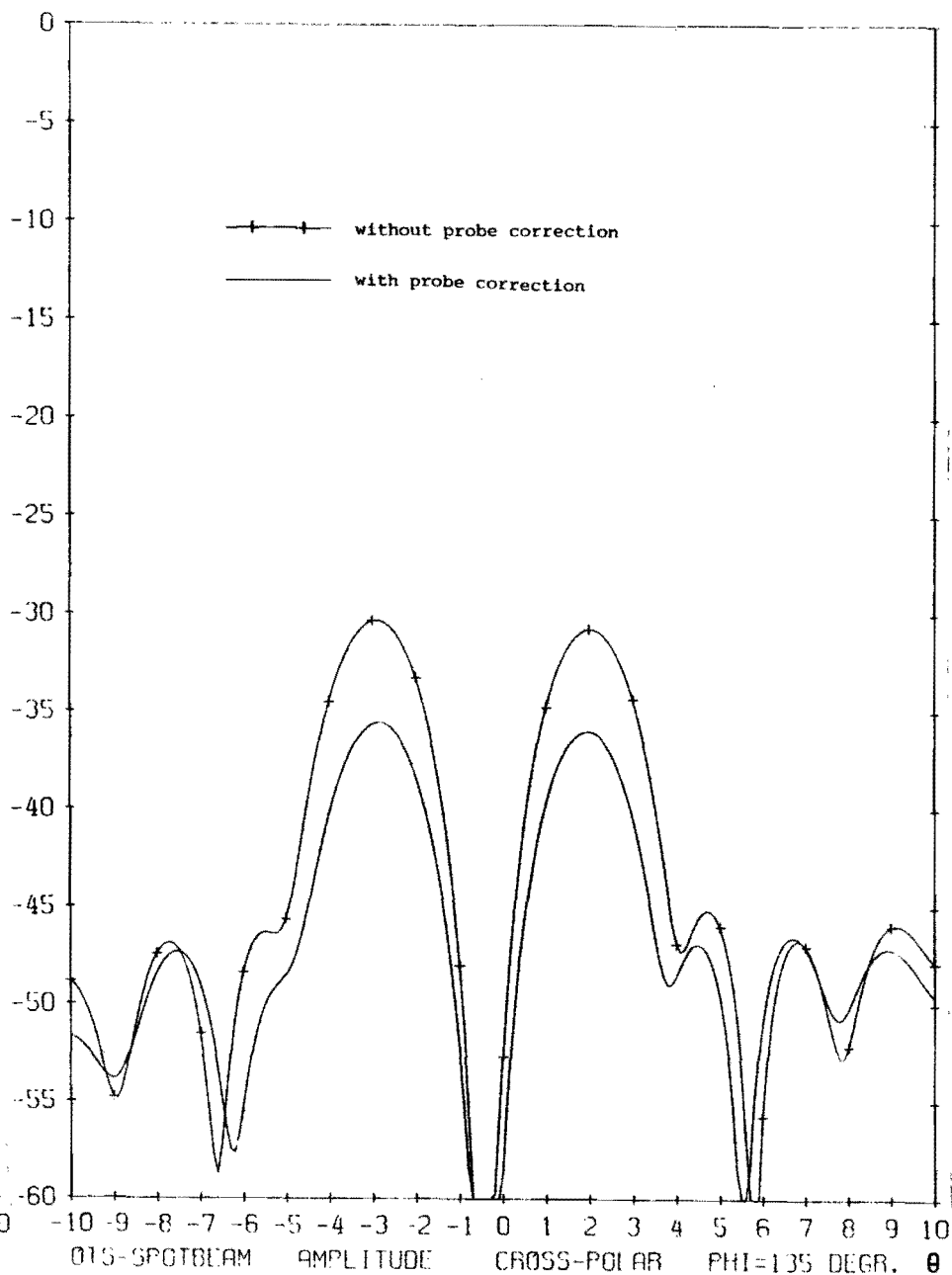


Fig. 9.1.14. Crosspolar far fields at  $\phi = 135^\circ$  calculated with and without probe correction.

## 9.2. The role of sampling techniques in antenna measurements

by Giorgio Franceschetti

### 9.2.1. Introduction

These notes have been especially prepared for the Eindhoven Summer School on Satellite Communication Antenna Technology, August 23-27, 1982. The material is a part of the topic: "Some Aspects of Antenna Measurements" and is intended to introduce the Reader to the sampling theory applied to antenna problems.

The use of sampling theorem for computing the radiation diagram of antennas is now a rather mature technique. Used in optics since 1955 [23] and for the synthesis of the current distribution on linear antennas since 1947 [33], has been recently extended to cover practically any type of antenna [41, 44, 47], although the emphasis has been put on parabolic reflectors. Conversely, the use of sampling theorem in antenna measurements, particularly near field/far field transformation, has not been so popular till now. Nevertheless, it is likely that sampling techniques can be successfully adopted in the field of antenna measurements, leading to unexpected results.

Accordingly, a broad overview of sampling techniques is presented in Sect. 9.2.2, just to introduce the Reader to the main points. Then, the extension of sampling, in its various forms, to near fields is given in Sect. 9.2.3 and 4. Finally some few suggestions of possible applications to antenna measurement processing is given in Sect. 9.2.5.

### 9.2.2. The sampling idea. Historical background

The sampling theorem was developed in the frame of information and communication theory by Kotel'nikov [1] in the East and by Shannon [2] in the West, respectively. Its mathematical content can be traced down to the original work by C.E. and J.M. Whittaker [3-4] on cardinal series. In its simplest form the theorem can be stated as follows:

Any square-integrable (finite energy) function  $f(t)$  whose Fourier transform (spectrum) is almost everywhere zero outside the finite interval  $(-\Omega, \Omega)$  is completely determined by its values at a series of points spaced  $\pi/\Omega$  apart:

$$f(t) = \sum_{-\infty}^{\infty} f(t_0 + \frac{n\pi}{\Omega}) \frac{\sin[\Omega(t - t_0) - n\pi]}{[\Omega(t - t_0) - n\pi]} \quad (9.2.1)$$

wherein  $t_0$  is an (arbitrary) value of  $t$ . The right hand side member of (9.2.1) is called the "cardinal series" of the function  $f(t)$ . The converse is also true:

Given a square-summable sequence  $f_n$ , the corresponding cardinal series converges to a function bandlimited to  $(-\Omega, \Omega)$  [4].

Furthermore, the Paley-Wiener theorem [5] characterizes the square-integrable bandlimited functions  $f(t)$  as the class of the entire functions of exponential type  $\Omega$ , i.e., such that

$$|f(z)| < C \exp(\Omega|\tau|) \quad , \quad z = t + j\tau \quad (9.2.2)$$

for some (real) constant  $C$ .

Since its early days, the sampling theorem underwent a large number of generalizations and extensions: sampling representations of integral transforms more general than the truncated Fourier transform [6-8]; recon-

struction of the function  $f(t)$  starting from more general elements of information than the values of the function at prescribed points [9-17]; use of different sampling functions, e.g., the self-truncating functions [18]; extension to the multi-dimensional case [19-22], the two-dimensional one being of particular interest for our applications.

As far as electromagnetics is concerned, sampling theory has been rather widely applied in the field of optics. Since 1955 Toraldo di Francia [23] used sampling theorem to define the degrees of freedom of an optical image, in connection with the problem of resolving power. Since then, several papers on this argument have been published [24-28]. Sampling theory has been also applied to the analysis of holographic restoration, optical processing and Fourier spectroscopy [29-31], as well as a computational tool for an efficient evaluation of the optical field diffracted by an aperture [32].

Coming to antenna problems, first applications of sampling theory have been made in the synthesis field. Since 1947 Woodward [33] and then Woodward and Laws [34] utilized the sampling theorem for synthesizing the current distribution on a linear antenna such to produce a radiated field matching a desired pattern at a certain number of points. A different procedure is used by Zelkin [35]. Woodward procedure has been extended to two-dimensional apertures by Ruze [36] and Borgiotti [37].

The application of signal theory concepts to antennas has been reported in a tutorial paper by Drabowich [38]. In particular, sampling theorem is used to define the degrees of freedom of the field of a linear antenna, as it was already done in optics since 1955 [23]. The degree of freedom concept has been used to evaluate the spacing of the grid points on a reflector antenna for the numerical computation of the radiation integral [39-40].

The application of the sampling series as computational tool for the radiation diagram of a reflector antenna has appeared for the first time in 1980 [41] and further developed in the following years [42-54].

In order to simply understand how sampling theorem can be applied to antenna analysis, let us consider the communication experiment depicted under Figure 9.2.1. If the signal is bandlimited - being filtered by an ideal band pass filter - sampling theorem can be applied exactly. If not, an equivalent bandwidth,  $\bar{B} > B$ , should be defined, accordingly to a convenient measure of the signal itself. It follows that the sampling reconstruction algorithm can be (approximately) used at a sampling rate  $\pi/\bar{B}$  higher than the Nyquist rate  $\pi/B$ .

In antenna applications (see Figure 9.2.2, a one dimensional case, for the sake of simplicity), the aperture in a ground plane produces a far field  $E$  which is proportional to the Fourier Transform (FT) of the aperture distribution  $E_0$ :

$$E(u) = K \int_{-a}^a E_0(y) \exp(juy) dy = K \int_{-\infty}^{+\infty} E_0(y) \exp(juy) dy . \quad (9.2.3)$$

Since the latter is space limited between  $(-a, a)$ , the sampling theorem can be used for the exact reconstruction of the far field:

$$E(u) = \sum_{n=-\infty}^{+\infty} E(u_0 + \frac{n\pi}{a}) \frac{\sin[a(u - u_0) - n\pi]}{[a(u - u_0) - n\pi]} \quad (9.2.4)$$

$u_0$  being a convenient value of  $u$  (e.g., the direction of the maximum).

Since the sample's spacing is given by

$$\Delta u = \pi/a \quad (9.2.5)$$

it follows that reconstruction is possible by using just one sample per lobe. Note that each sample is the FT of the aperture distribution at

$$u = u_n = u_0 + n\pi \quad (9.2.6)$$

For a reflector antenna (still, a one dimensional case), the far-field is no more a FT of the induced current distribution. Accordingly, two possibilities can be considered.

- (i) An equivalent aperture is defined, larger than the physical one,

$$a' = \chi a, \chi > 1 \quad (9.2.7)$$

and sampling theorem is applied with reference to  $a'$ . This just implies sampling at a rate higher than the Nyquist rate:

$$\Delta u = \pi/a' . \quad (9.2.8)$$

The samples are no more FT, and the sampling functions are sinc(x) functions. Summarising:

Samples  $\neq$  FT and correspond to measurable fields  
interpolating functions = sinc(x), for any type of antenna.

- (ii) We can force the samples to be FT, properly matching the interpolating functions to the particular considered antenna. Summarising:

Samples = FT and different from measurable fields  
interpolating functions  $\neq$  sinc(x) and dependent on the considered antenna.

In the case of a radiating reflector (two-dimensional case, more interesting from the application viewpoint), we consider the geometry depicted in the Figure 9.2.3. The far-field associated to the reflector is given by

$$\underline{E}(R, \theta, \phi) = - \frac{j\omega\mu}{4\pi R} \exp(-jkR) \left[ \underline{\underline{I}} - \underline{\hat{R}} \underline{\hat{R}} \right] \cdot \underline{\underline{I}} \quad (9.2.9)$$

wherein the radiation integral  $\underline{\underline{I}}$  is given by:

$$\begin{aligned}
 \underline{I} &= \iint_{S_0} \underline{J}_S \exp(jk\underline{\rho} \cdot \hat{\underline{R}}) dS_0 = \\
 &= \iint_S \underline{J}_S \left( \frac{\partial S_0}{\partial S} \right) \exp(jk\underline{\rho} \cdot \hat{\underline{R}}) dS = \\
 &= \iint_S \underline{J} \exp(jk\underline{\rho} \cdot \hat{\underline{R}}) dS \quad , \quad \underline{J} = \underline{J}_S \left( \frac{\partial S_0}{\partial S} \right) \quad (9.2.10)
 \end{aligned}$$

where  $\underline{J}_S$  are the currents induced on the reflector and  $(\partial S_0/\partial S)$  is the jacobian of the transformation from  $S_0$  to  $S$ . In the very important case of a parabolic reflector,

$$\left( \frac{\partial S_0}{\partial S} \right) = \sqrt{1 + \left( \frac{r}{2f} \right)^2} \quad . \quad (9.2.11)$$

Computation of the far field is thus reduced to the computation of the radiation integral  $\underline{I}$ . Note that (9.2.10) is not a FT. Again, we can follow two ways, which are summarized under Figure 9.2.4.

The first possibility is to use as samples  $\underline{I}_{nm}$  the values of the radiation integral computed at

$$u = u_n = n\pi \quad ; \quad v = v_m = m\pi \quad (9.2.12)$$

$$u = ka' \sin\theta \cos\phi \quad ; \quad v = ka' \sin\theta \sin\phi \quad , \quad a' = \chi a \quad ,$$

namely

$$\underline{I}_{nm} = \underline{I}(n\pi, m\pi) \quad . \quad (9.2.13)$$

Note that  $\underline{I}_{nm}$  are not FT, and should be computed using any available standard method (Ludwig integration algorithm, geometrical theory of



diffraction if applicable, etc.). The interpolating functions are, in this case, the sinc functions, for any type of reflector antennas, hence:

$$\underline{I}(u,v) = \sum_n \sum_m \underline{I}(n\pi, m\pi) \frac{\sin(u-n\pi)}{u-n\pi} \frac{\sin(v-m\pi)}{v-m\pi} . \quad (9.2.14)$$

The second possibility is to force the samples to be FT, hence:

$$\underline{I}_{nm} = \frac{1}{4ab} \iint_S \underline{J} \exp(jn\pi x + jm\pi y) dx dy \neq \underline{I}(n\pi, m\pi) \quad (9.2.15)$$

(2a and 2b being normalizing dimensions of a rectangle circumscribing S) properly modifying the interpolating functions, which will be dependent on the geometry of the reflector only, and not on the excitation. Accordingly,

$$\underline{I}(u,v) = \sum_n \sum_m \underline{I}_{nm} \psi_{nm}(u,v) \quad (9.2.16)$$

wherein the  $\psi_{nm}$  are appropriate functions which may be considered as a convenient spectral representation of the integral operator appearing in (9.2.10):

$$\psi_{nm}(u,v) = \iint_S \exp(jk_{\underline{g}} \cdot \hat{\underline{R}}) \exp(-jn\pi x - jm\pi y) dx dy \quad (9.2.17)$$

In the following, we call sampling interpolation the reconstruction technique which leads to (9.2.14); while we call pseudo-sampling expansion the radiation integral representation (9.2.17).

In all practical uses of (9.2.14) and/or (9.2.17), truncation of the series is necessary. Numerical experiments (as well as theoretical analysis, at least in the one dimensional case) provided a very simple rule. Assume that  $2N \times 2M$  samples fall within the angular range in which the field is

computed. Then, the series can be safely truncated at  $N_{\max} = N + (1 \div 2)$ ,  $N_{\max} = M + (1 \div 2)$ , i.e., a belt of one, two guard samples around the angular range of interest should be included in the summation. Above rule is valid provided that the neglected samples fall in the region when the asymptotic expansion of the radiation integral (9.2.10) is valid.

Some few examples of sampling application for the reconstruction of the far field are given in Figures 9.2.6 and 9.2.7, the geometry of the reflector being depicted in Figure 9.2.5. An application of the pseudo-sampling expansion is shown in Figure 9.2.8. The parabolic dish is illuminated by 5 feeds and the (far field) explored area is of  $10 \times 10$  beam-widths. Overall computer time has been 75 sec. on an UNIVAC 1100/80 computer.

### 9.2.3. Sampling reconstruction of near field

We have shown under Sect. 9.2.2 that the far field associated to an electromagnetic source can be produced, to a prescribed degree of approximation, by an equivalent finite aperture distribution. Hence, the sampling theorem can be used for reconstructing the far field from a limited number of samples.

In order to extend the sampling reconstruction algorithm also to the near field, we have to prove that these fields are (approximately) equal (or proportional) to the FT of an equivalent finite aperture distribution.

With reference to Figure 9.2.9, let us consider a source  $Q$  which produces a field distribution on the plane  $S$ ; and this field distribution can be used - via the equivalence theorem - for computing the field radiated in  $P$ . It is intuitive that the integration along  $S$  can be truncated to a finite portion of the plane. But, once the truncation has been performed, we still have to establish a FT relationship between near field and some equivalent source distribution on  $S$ . We have, in the two-dimensional case,

$$\begin{aligned}
 r' &= \sqrt{r^2 + x^2 - 2rx \sin\theta} = \\
 &= \sqrt{r^2 + x^2} \left[ 1 - \frac{rx}{r^2 + x^2} \sin\theta - \frac{1}{2} \frac{r^2 x^2}{(r^2 + x^2)} \sin^2\theta + \dots \right] \quad (9.2.18)
 \end{aligned}$$

so that the phase term of the integral on S is given by

$$\begin{aligned}
 \exp(-jkr') &= \exp(-jk\sqrt{r^2 + x^2} + j \frac{r}{\sqrt{r^2 + x^2}} ux + j \frac{1}{2k\sqrt{r^2 + x^2}} u^2 x^2 + \dots) \\
 &= \exp(-jk\sqrt{r^2 + x^2} + j \frac{r}{\sqrt{r^2 + x^2}} ux) \left[ 1 + j \frac{1}{2k\sqrt{r^2 + x^2}} u^2 x^2 + \dots \right] \\
 &= \exp(-jk\sqrt{r^2 + x^2}) \left\{ 1 - j \frac{1}{2k\sqrt{r^2 + x^2}} \frac{1}{r^2} \frac{\partial^2}{\partial u^2} + \dots \right\} \exp(j \frac{r}{\sqrt{r^2 + x^2}} ux) \quad (9.2.19)
 \end{aligned}$$

The near field is now given as a series of terms. When the integration is limited to a finite segment  $2a'$ , and

$$\frac{1}{2} ua' \left( \frac{a'}{r} \right)^2 < 1 \quad (9.2.20)$$

then we can put

$$\exp(j \frac{r}{\sqrt{r^2 + x^2}} ux) \approx \exp(jux) \quad (9.2.21)$$

and each term becomes a FT of a finite aperture distribution. Sampling theorem can be applied again, and the sampling functions are successive derivatives of the  $\text{sinc}(u)$  function, but for the first term. Since the second term is of order  $(a'/r)^2/2kr$ , it follows that can be neglected, under the same approximation (9.2.20), so that the reconstruction can be essentially obtained using only the  $\text{sinc}(u)$  function. Numerical results relative to a square aperture with uniform current distribution along the  $x$  - axis are given in Figure 9.2.10.

#### 9.2.4. Pseudo-sampling representation of Fresnel zone field

Let us now discuss how the pseudo sampling representation (9.2.16) can be applied in the Fresnel zone region. With reference to the parabolic dish represented in Figure 9.2.11, it can be easily shown that the factor  $\underline{k}_\rho \cdot \underline{\hat{R}}$  appearing in (9.2.17) becomes

$$\begin{aligned} \underline{k}_\rho \cdot \underline{\hat{R}} = (u\xi + v\eta) \left[ 1 + \frac{1}{2kR} (u\xi + v\eta) + \frac{a^2}{8fR} (\xi^2 + \eta^2) \cos\theta \right] + \\ + \frac{ka^2}{4f} (\xi^2 + \eta^2) \left[ \cos\theta - \frac{2f}{R} + \frac{a^2}{8fR} (\xi^2 + \eta^2) \sin^2\theta \right] \end{aligned} \quad (9.2.22)$$

wherein

$$u = ka \sin\theta \cos\phi ; v = ka \sin\theta \sin\phi \quad (9.2.23)$$

$$\xi = x/a ; \eta = y/a \quad (9.2.24)$$

and are the normalized coordinates of the projected aperture of the dish.

If the geometry is such that we can neglect the last two terms in the first bracket and the last term in the second, then

$$\underline{k}_\rho \cdot \underline{\hat{R}} \approx (u\xi + v\eta) + \frac{ka^2}{4f} (\xi^2 + \eta^2) \left[ \cos\theta - \frac{2f}{R} \right] . \quad (9.2.25)$$

Above assumption is referred to as Fresnel small angle approximation [55]. If (9.2.25) is valid, then the radiation integral (9.2.10) can be expanded (save a proportionality factor) as

$$\underline{I} = \sum_n \sum_m \underline{I}_{nm} \psi_n(u - n\pi, \Delta) \psi_m(v - m\pi, \Delta) \quad (9.2.26)$$

wherein the samples  $I_{nm}$  are the Fourier Transforms (9.2.15) of the surface current induced on the reflector and the pseudo-sampling functions are given by:

$$\psi(z, \Delta) = \frac{\exp(-j\Delta/8)}{\sqrt{\Delta}} \left\{ \exp(jz) S \left[ \frac{z - \frac{\Delta}{2}}{\sqrt{\Delta}} \right] - \exp(-jz) S \left[ \frac{z + \frac{\Delta}{2}}{\sqrt{\Delta}} \right] \right\} ; \quad (9.2.27)$$

$$S(\gamma) = \exp(j\gamma^2) \int_z^\infty \exp(-jt^2) dt ; \quad (9.2.28)$$

$$\Delta = ka \left[ \frac{a}{2f} \cos \theta - \frac{a}{R} \right] . \quad (9.2.29)$$

A better approximation can be obtained by using the transformation of coordinates

$$\begin{cases} \xi = \xi' \cos \phi + \eta' \sin \phi \\ \eta = -\xi' \sin \phi + \eta' \cos \phi \end{cases} \quad (9.2.30)$$

which corresponds to a  $\phi$  - rotation of the axes around Z. Neglecting only the last terms in the two brackets of (9.2.22), we get:

$$\underline{k}_\rho \cdot \underline{\hat{R}} \approx \xi' u' + \eta' v' + \xi'^2 \frac{\Delta_1}{2} + \eta'^2 \frac{\Delta_2}{2} \quad (9.2.31)$$

wherein:

$$\begin{cases} u' = u \cos \phi - v \sin \phi \\ v' = v \cos \phi + u \sin \phi \\ \Delta_1 = ka \left[ \frac{a}{2f} \cos \theta - \frac{a}{R} (1 - \sin^2 \theta \cos^2 \phi + \sin^2 \theta \sin \phi \cos \phi) \right] \\ \Delta_2 = ka \left[ \frac{a}{2f} \cos \theta - \frac{a}{R} (1 - \sin^2 \theta \sin^2 \phi - \sin^2 \theta \sin \phi \cos \phi) \right] . \end{cases} \quad (9.2.32)$$

Again, the representation (9.2.26) can be used with:

$$\psi_n \rightarrow \psi_n(u' - n\pi, \Delta_1) ; \psi_m \rightarrow \psi_m(v' - m\pi, \Delta_2) \quad (9.2.33)$$

An example of reconstruction of the Fresnel field using the series representation (9.2.26) is given in Figure 9.2.12, which is relative to a uniformly illuminated circular aperture with  $2a/\lambda = 15$ . Note that those terms in (9.2.22) containing the factor  $1/f$  are exactly zero in this case, so that relation (9.2.31), at variance of (9.2.25), is exact.

The representation (9.2.22) allows a smooth transition from the Fresnel to the Fraunhofer zone just changing the parameter  $a/R$  in the pseudo-sampling functions  $\psi_n, \psi_m$ , while the coefficients of the expansion  $I_{nm}$  remain the same. The pseudo sampling functions can be easily computed using the following series representation:

$$S(\gamma) = \frac{\sqrt{\pi}}{2} \exp \left[ j(\gamma^2 - \frac{\pi}{4}) \right] - \sum_0^{\infty} \frac{(2j)^n \gamma^{2n+1}}{(2n+1)!!} ; \quad (9.2.34)$$

$$\frac{S(\gamma)}{|\gamma|} \underset{|\gamma| \rightarrow \infty}{\sim} \frac{1}{2j\gamma} \sum_0^{\infty} (-)^n \frac{(2n-1)!!}{(2j\gamma^2)^n} \quad (9.2.35)$$

for  $-\pi < \arg \gamma < \pi/2$ . Furthermore,

$$\psi(z, \Delta) = \psi(-z, \Delta) ; \psi(z, -\Delta) = \psi^*(z^*, \Delta^*) ; \quad (9.2.36)$$

$$S(\gamma) + S(-\gamma) = \pi \exp \left[ j(\gamma^2 - \frac{\pi}{4}) \right] ; \quad (9.2.37)$$

$$S(-j\gamma) = -j S^*(\gamma^*) . \quad (9.2.38)$$

An alternative series representation for  $\psi(z, \Delta)$  is:

$$\exp(j \frac{\pi}{8}) \psi(z, \Delta) = \sum_0^{\infty} \left( \frac{j\Delta}{2x} \right)^n j_n(z) - \quad (9.2.39)$$

wherein  $j_n(x)$  is the spherical Bessel function of first kind.

The representation (9.2.39) is particularly useful inasmuch it expresses  $\psi(Z, \Delta)$  as a series of trigonometric functions. It is an absolutely convergent series in both the variables  $Z$  and  $\Delta$ ; and, also, an asymptotic representation for  $Z \rightarrow \infty$ .

#### 9.2.5. Application of sampling representation to measurements. A research program

In the previous sections, two series representations of the field associate to a radiating structure have been presented: the sampling interpolation and the pseudo-sampling representation. Both series are valid not only in the far but also in the near field.

The validity of such series is well established in the contest of antenna pattern calculations. Their relevance to measurements is still to be proved, comparing accuracy, simplicity and computational time with those other techniques based upon plane, cylindrical and spherical wave expansions. Possible applications that are worthy of being explored are listed hereafter.

The sampling interpolation provides a rigorous frame for reducing the redundancy of measurements. Once the field has been measured at  $u_n = n\pi$ ,  $v_m = m\pi$ , then it can be reconstructed for any couple  $(u, v)$  by using (9.2.14). It can be noted that this expression is really proportional to the vector potential, and not to the field itself. However, numerical experiments have shown that it is valid also for any component of the field. If only the module of the field is of interest, it is sufficient to measure it at

$$u_n = \frac{n\pi}{2} \quad ; \quad v_m = \frac{m\pi}{2} \quad , \quad (9.2.40)$$

i.e., using a sampling rate double with respect to the conventional one. The reason is that the module of the field,

$$|E(u,v)|^2 = \underline{E}(u,v) \cdot \underline{E}^*(u,v) \quad (9.2.41)$$

has a FT which is the convolution of the FT of  $\underline{E}(u,v)$  and  $\underline{E}^*(u,v)$ , respectively. Accordingly, the (spatial) bandwidth associate to (9.2.41) is twice as large as that of  $\underline{E}(u,v)$ .

The sampling interpolation can probably be used as a convenient tool for phase retrieval. If this proves to be valid, that near field measurements can be limited to the module, with a tremendous simplification in the hardware of the system.

The pseudo-sampling series (9.2.16) provides a smooth representation of the field from the near to the far regions. If the field is measured on a plane area, and it is assumed negligible outside, than the pseudo-samples  $\underline{I}_{nm}$  are vectors parallel to the area itself and FT of the measured field. Then, the series (9.2.16) allows the reconstruction of the field at any distance. In particular, in the Fresnel region the pseudo-sampling functions are those indicated in (9.2.33), and the reconstruction is exact.



## References

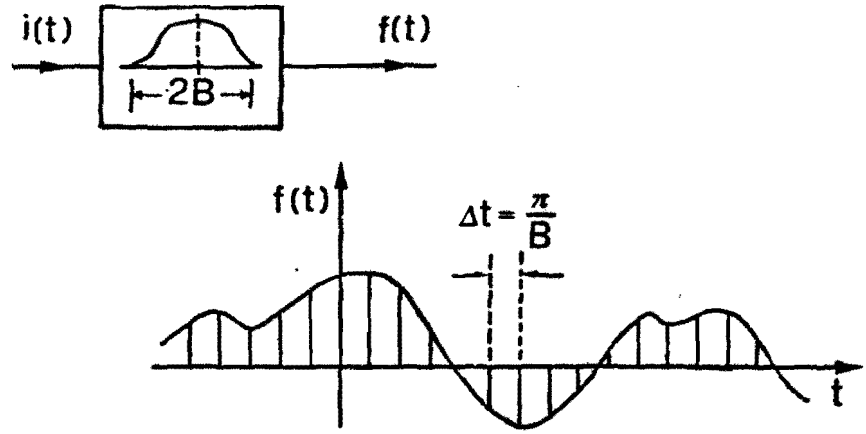
- [ 1 ] Kotel'nikov V.A., "O propusknoi sposobnosti "efira" i provoloki v elektrosviazi (On the transmission capacity of "ether" and wire in electrocommunications)" Izd. Red. Upr. Suyazi RKKA (Moscow), 1933.
- [ 2 ] Shannon C.E., "Communications in presence of noise", Proc. IRE, Vol. 37, pp. 10-71, 1949.
- [ 3 ] Whittaker E.T., "On the functions which are represented by the expansion of interpolating theory", Proc. Roy. Soc. Edinburgh, Vol. 35, pp. 181-194, 1915.
- [ 4 ] Whittaker J.M., "The Fourier theory of the cardinal functions", Proc. Math. Soc. Edinburgh, Vol. 1, pp. 169-176, 1929.
- [ 5 ] Paley R.E.A. C. and Wiener N., "Fourier transforms in the complex domain", Am. Math. Soc., Colloquium Publications, Vol. 19, 1934.
- [ 6 ] Kramer H.P., "A generalized sampling theorem", J. Math. Phys., Vol. 38, pp. 68-72, 1959.
- [ 7 ] Haddad A.H., Yao K. and Thomas J.B., "General methods for the derivation of sampling theorems", IEEE Trans. Inf. Theory, Vol. IT-13, pp. 227-230, 1967.
- [ 8 ] Jerri A.J., "Sampling expansion for the  $L_Y^\alpha$ -Laguerre integral transform", J. Res. NBS, Sect. B: Math. Sciences, Vol. 80B, pp. 415-418, 1976.
- [ 9 ] Beutler F.J., "Error-free recovery of signals from irregularly spaced samples", SIAM Review, Vol. 8, pp. 328-335, 1966.
- [ 10 ] Yao K. and Thomas J.B., "On some stability and interpolation properties of nonuniform sampling expansions", IEEE Trans. Circuit Theory, Vol. CT-14, pp. 404-408, 1967.
- [ 11 ] Landau H.J., "Sampling data transmission, and the Nyquist rate", Proc. IEEE, Vol. 55, pp. 1701-1706, 1967.
- [ 12 ] Brown J.L. Jr., "Uniform linear prediction of bandlimited processes from past samples", IEEE Trans. Inf. Theory, Vol. IT-18, pp. 662-664, 1972.

- [13] Yen J.L., "On nonuniform sampling of bandwidth-limited signals", IEEE Trans. Circuit Theory, Vol. CT-3, pp. 251-257, 1956.
- [14] Papoulis A., "Signal analysis", McGraw-Hill, New York, 1977.
- [15] Linden D.A. and Abramson N.M., "A generalization of the sampling theorem", Inform. Contr., Vol. 3, pp. 26-31, 1960. Correction: ibidem, Vol. 4, pp. 95-96, 1961.
- [16] McNamee J., Stenger F. and Whitney E.L., "Whittaker cardinal functions in retrospect", Math. of Comput., Vol. 25, pp. 141-154, 1971.
- [17] Jerri A.J. and Kreisler D.W., "Sampling expansion with derivatives for finite Hankel and other transforms", SIAM J. Math. Anal., Vol. 6, pp. 262-267, 1975.
- [18] Helms H.D. and Thomas J.B., "Truncation error of sampling theorem expansion", Proc. IRE, Vol. 50, pp. 179-184, 1962.
- [19] Papoulis A., "Systems and transforms with application in optics", McGraw-Hill, New York, 1968.
- [20] Peterson D.P. and Middleton D., "Sampling and reconstruction of wave-number-limited functions in N-dimensional Euclidean space", Informat. Contr., Vol. 5, pp. 279-323, 1962.
- [21] Montgomery W.D., "K-order sampling of N-dimensional bandlimited functions", Int. J. Contr., Vol. 1, pp. 7-12, 1965.
- [22] Garder N.T., "A note on multidimensional sampling theorem", Proc. IEEE, Vol. 60, pp. 247-248, 1972.
- [23] Toraldo di Francia G., "Resolving power and information", J. Opt. Soc. Am., Vol. 45, pp. 497-501, 1955.
- [24] Miyamoto K., "On Gabor's expansion theorem", J. Opt. Soc. Am., Vol. 50, pp. 856-858, 1960.
- [25] Gabor D., "Progress in Optics", Ed.: E. Wolf, North-Holland, Amsterdam, 1961.

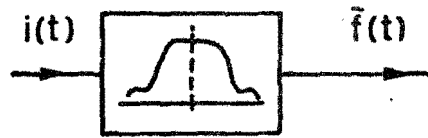
- [26] Toraldo di Francia G., "Degrees of freedom of an image", J. Opt. Soc. Am., Vol. 59, pp. 799-804, 1969.
- [27] Gori F. and Guattari G., "Shannon number and degrees of freedom of an image", Opt. Commun., Vol. 7, pp. 163-165, 1973.
- [28] Blazek V., "Sampling theorem and the number of degrees of freedom of an image", Opt. Commun., Vol. 11, pp. 144-147, 1974.
- [29] Som S.C., "Simultaneous multiple reproduction of space-limited functions by sampling of spatial frequencies", J. Opt. Soc. Am., Vol. 60, pp. 1628-1634, 1970.
- [30] Gori F. and Guattari G., "Holographic restoration of nonuniformly sampled band-limited function", Opt. Commun., Vol. 3, pp. 147-149, 1971.
- [31] Vanasse G.A. and Sakai H., "Fourier spectroscopy" in "Progress in Optics", Ed.: E. Wolf, North-Holland, 1971.
- [32] Barakat R., "Application of the sampling theorem to optical diffraction theory", J. Opt. Soc. Am., Vol. 54, pp. 920-930, 1964.
- [33] Woodward P.M., "A method of calculating the field over a plane aperture required to produce a given polar diagram", Jour. IEEE, Vol. 93, Part. III A, pp. 1554-1558, 1974.
- [34] Woodward P.N. and Lawson J.D., "The theoretical precision with which an arbitrary radiation pattern may be obtained from a source of finite size", Proc. IEEE, Vol. 95, Part. III A, pp. 363-370, 1948.
- [35] Zalkin E.G., "Design of an emitting system by the directional pattern" (in Russian), Gostekhizdat, 1963. See, also, D.E. Vakman, "Sophisticated signals and the uncertainty principle in radar", Springer-Verlag, Berlin, pp. 140-142, 1968.
- [36] Ruze J., "Circular aperture synthesis", IEEE Trans. Antennas Propagat., Vol. AP-12, pp. 691-694, 1964.

- [37] Borgiotti G.V., "A synthesis method for bidimensional apertures", IEEE Trans. Antennas Propagat., Vol. AP-16, pp. 188-193, 1968.
- [38] Drabowich S., "Application aux antennes de la théorie du signal", L'Onde Electrique, Vol. 45, pp. 550-560, 1965.
- [39] Ksienki A., "Equivalence between continuos and discrete radiating arrays", Canad. J. Phys., Vol. 35, pp. 335-349, 1961.
- [40] Carberry T.F., "Optimum computer methods for large aperture antenna problems", Symposium on Electromagnetic Waves, Stresa, Italy, 1968.
- [41] Bucci O.M., Franceschetti G. and D'Elia G., "Fast analysis of large antennas. A new computational philosophy", IEEE Trans. Antennas Propagat., Vol. AP-28, pp. 306-310, 1980.
- [42] Bucci O.M., D'Elia G. and Pierri R., "Fast analysis of reflector antennas using sampling expansion", Terza Riunione Nazionale Elettromagnetismo Applicato, Bari, Italy, June 1980.
- [43] Bucci O.M., D'Elia G. and Franceschetti G., "Computation of radiation from reflector antennas. An optimal strategy", Alta Frequenza, Vol. 49, pp. 390-399, 1980.
- [44] Bucci O.M. and Franceschetti G., "Radiation from reflector antennas. Exact aperture and aperture-like approaches", International URSI Symposium, München, 1980.
- [45] D'Elia G., Marinoni G.L., Pierri R., "A generalized sampling-like technique for fast analysis of reflector antennas", ICAP, York, Great Britain, April 1981, IEE Conf. Publ. n. 195, pp. 486-490.
- [46] Bucci O.M., D'Elia G. and Pierri R., "Numerical evaluation of antennas field using a new aperture like expansion", 10<sup>th</sup> European Microwave Conference, Warszawa, 1980; also in "Advanced Antenna Technology", Ed. by P.J.B. Clarricoats, MEPL - London, 1981.
- [47] Bucci O.M., Franceschetti G. and Pierri R., "Reflector antennas fields. An exact aperture-like approach", IEEE Trans. Antennas Propagat., Vol. AP-29, pp. 580-586, 1981.

- [48] D'Elia G. and Pierri R., "Iterative method and sampling technique in the analysis of shaped reflectors", 11<sup>th</sup> European Microwave Conference, Amsterdam, September 1981.
- [49] Bencini F., D'Elia G. and Pierri R., "Numerical evaluation of Fresnel zone fields by sampling like techniques", URSI/AP-S Symposium, Albuquerque, May 1982.
- [50] Bucci O.M., D'Elia G., Franceschetti G. and Pierri R., "The effectiveness of the sampling-like technique in reflector antenna analysis", 12<sup>th</sup> European Microwave Conference, Helsinki, September 1982.
- [51] Bucci O.M., Franceschetti G., D'Elia G. and Pierri R., "Use of sampling functions for the analysis of radiating structures", Final Report, ESTEC Contract no. 4380/80/NL/DG, European Space Agency, January 1982.
- [52] D'Elia G., Pierri R. and Scafuro N., "Analysis of a strip in Fresnel zone using the pseudo-sampling technique", 7<sup>th</sup> Colloquium on Microwave Communication, Budapest, September 1982.
- [53] Barbato R., D'Elia G. and Pierri R., "Analysis of reflector antennas with elliptical aperture", 7<sup>th</sup> Colloquium on Microwave Communication, Budapest, September 1982.
- [54] Bucci O.M., D'Elia G. and Pierri R., "The sampling-like and the Jacobi-Bessel techniques in the analysis of reflector antennas", IV Riunione Nazionale di Elettromagnetismo, Firenze, Ottobre 1982.
- [55] Galindo-Israel V. and Rahmat-Samii Y., "A new look at Fresnel field computation using the Jacobi-Bessel series", IEEE Trans. Antennas Propagat., Vol. AP-29, pp. 885-898, 1981.



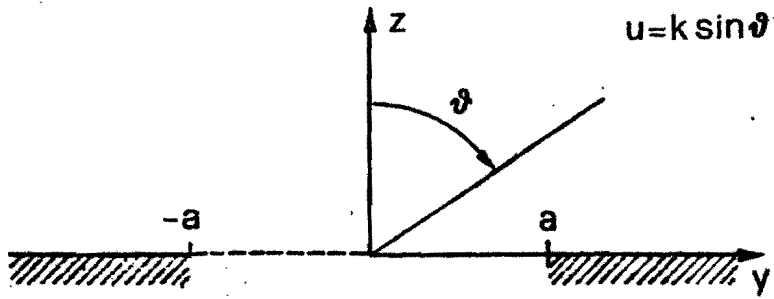
$$f(t) = \sum_{-\infty}^{+\infty} f\left(\frac{n\pi}{B}\right) \frac{\sin(Bt - n\pi)}{Bt - n\pi}$$



$$\bar{f}(t) = \sum_{-\infty}^{+\infty} \bar{f}\left(\frac{n\pi}{\bar{B}}\right) \frac{\sin(\bar{B}t - n\pi)}{\bar{B}t - n\pi}, \quad \bar{B} > B$$

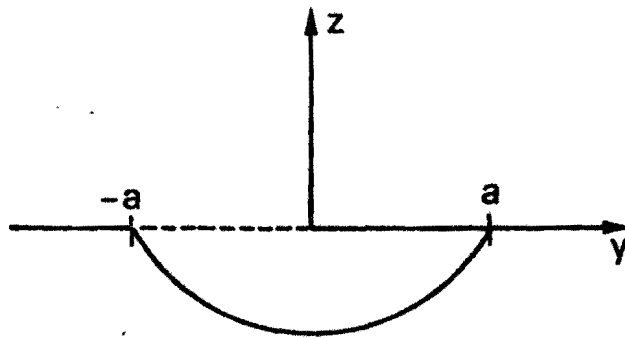
$$\Delta \bar{t} = \frac{\pi}{\bar{B}} < \frac{\pi}{B} = \Delta t$$

Fig. 9.2.1 - A communication experiment for understanding sampling idea.



$$E(u) = K \int_{-a}^a E_d(y) \exp[juy] dy$$

$$E(u) = \sum_{-\infty}^{\infty} E\left(u_0 + \frac{n\pi}{a}\right) \frac{\sin[a(u-u_0)-n\pi]}{a(u-u_0) - n\pi}$$



$$E(u) = \sum_{-\infty}^{+\infty} E\left(u_0 + \frac{n\pi}{a'}\right) \frac{\sin[a'(u-u_0)-n\pi]}{a'(u-u_0) - n\pi}$$

Fig. 9.2.2 - Sampling theory applied to antenna radiation analysis.

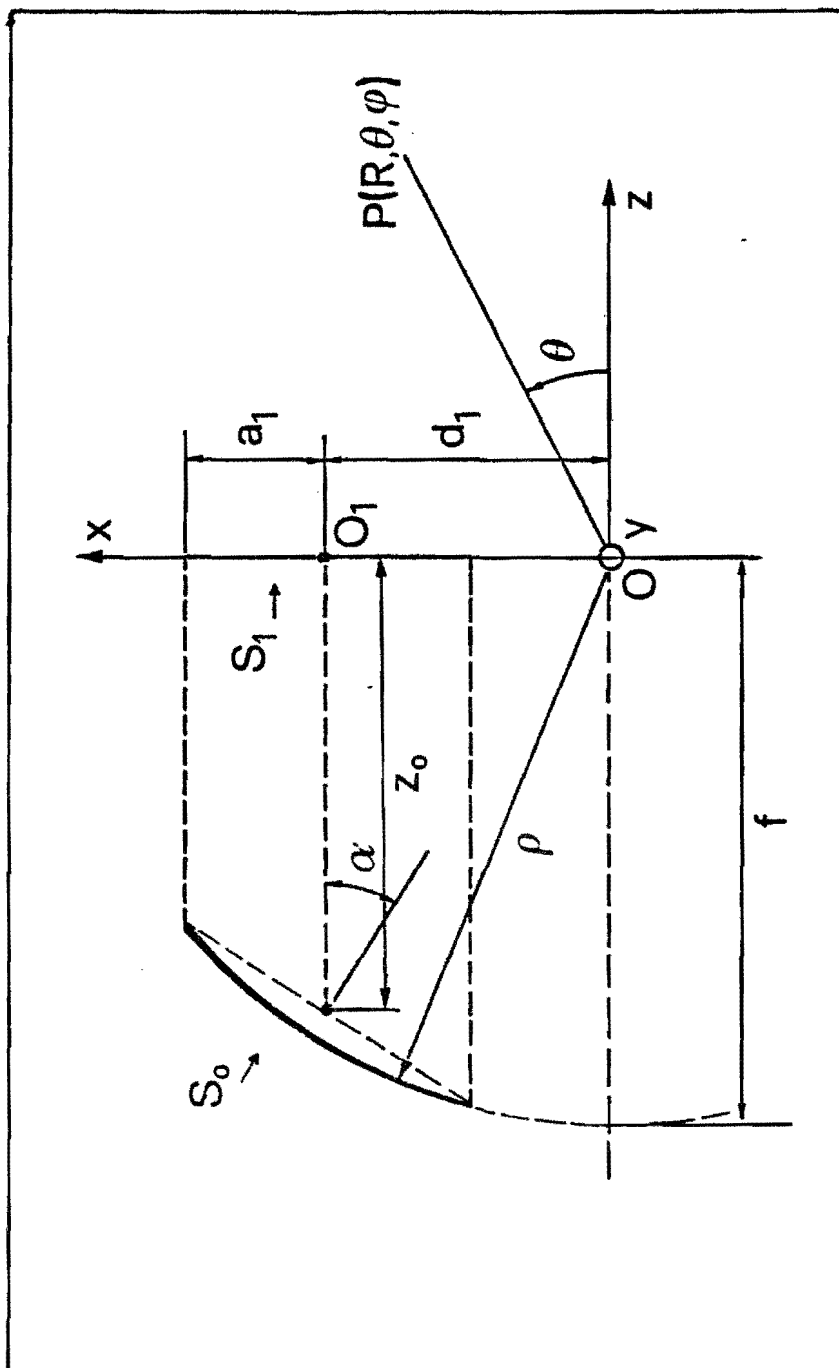


Fig. 9.2.3 - Geometry of the radiating structure.



$$\underline{I}(u,v) = \sum_{nm} \underline{I}_{nm} \varphi_{nm}(u,v)$$

$$u = k \sin \vartheta \cos \varphi \quad ; \quad v = k \sin \vartheta \sin \varphi$$

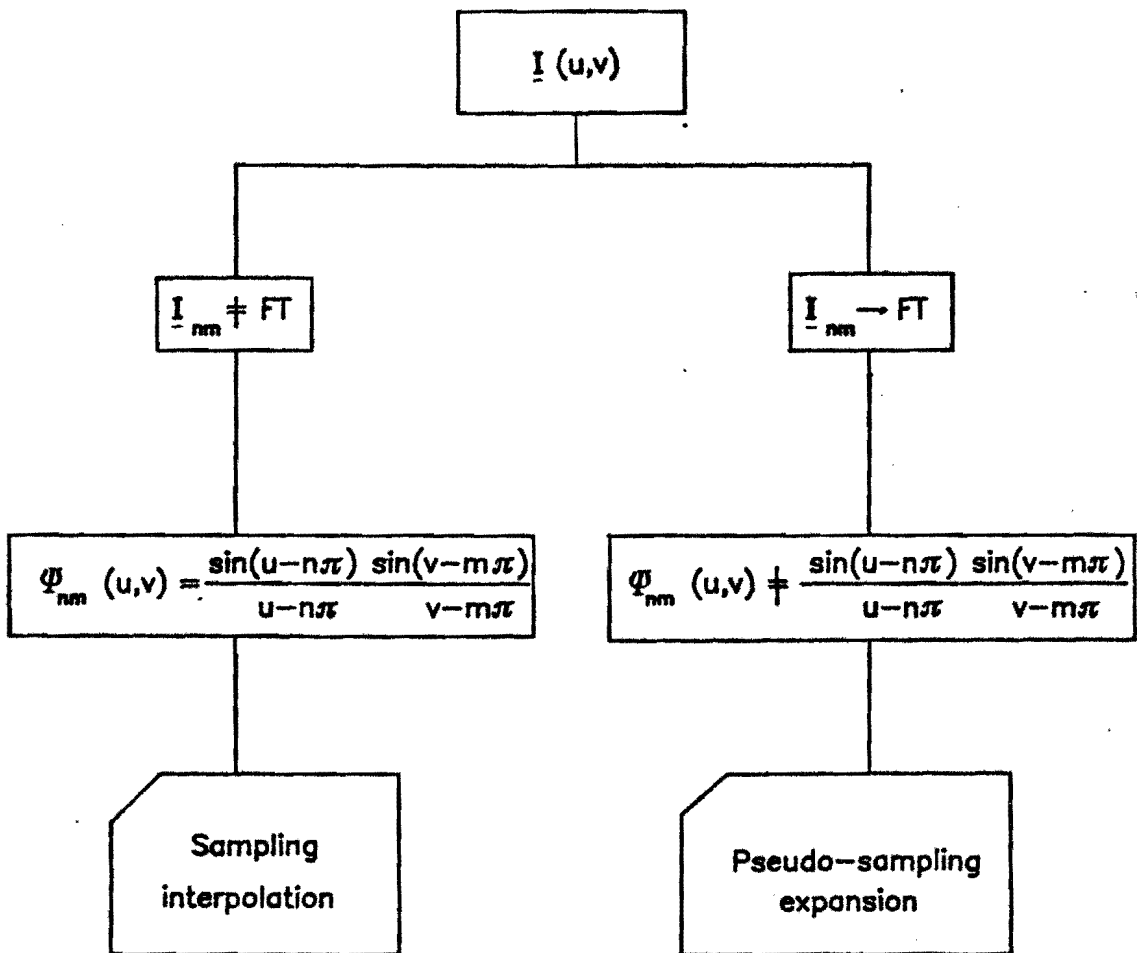
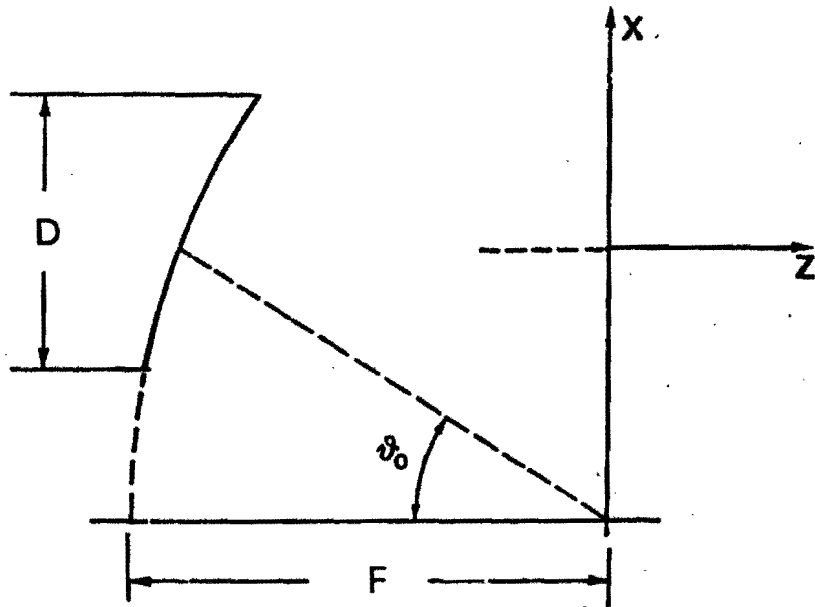


Fig. 9.2.4 - Use of sampling algorithm for computing the radiated field.



INTELSAT V

$\vartheta_0 = 31^\circ$        $D = 1120 \text{ mm}$

$F/D = 1$        $f = 9.5 \text{ GHz}$

$D/\lambda = 35.5$

Feed : Potter horn

Fig. 9.2.5 - Intelsat V reflector antenna geometry.

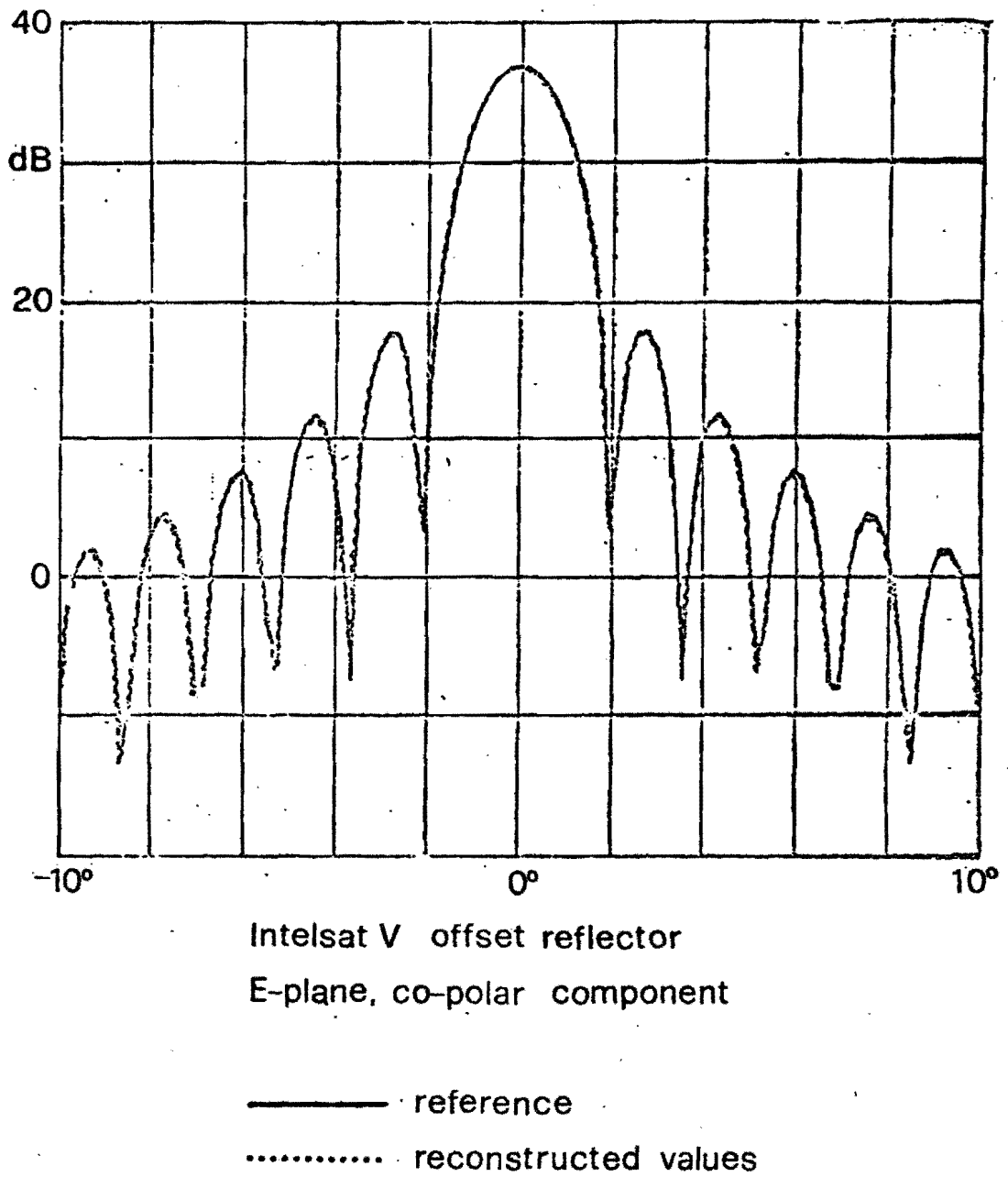


Fig. 9.2.6 - E - plane cut.

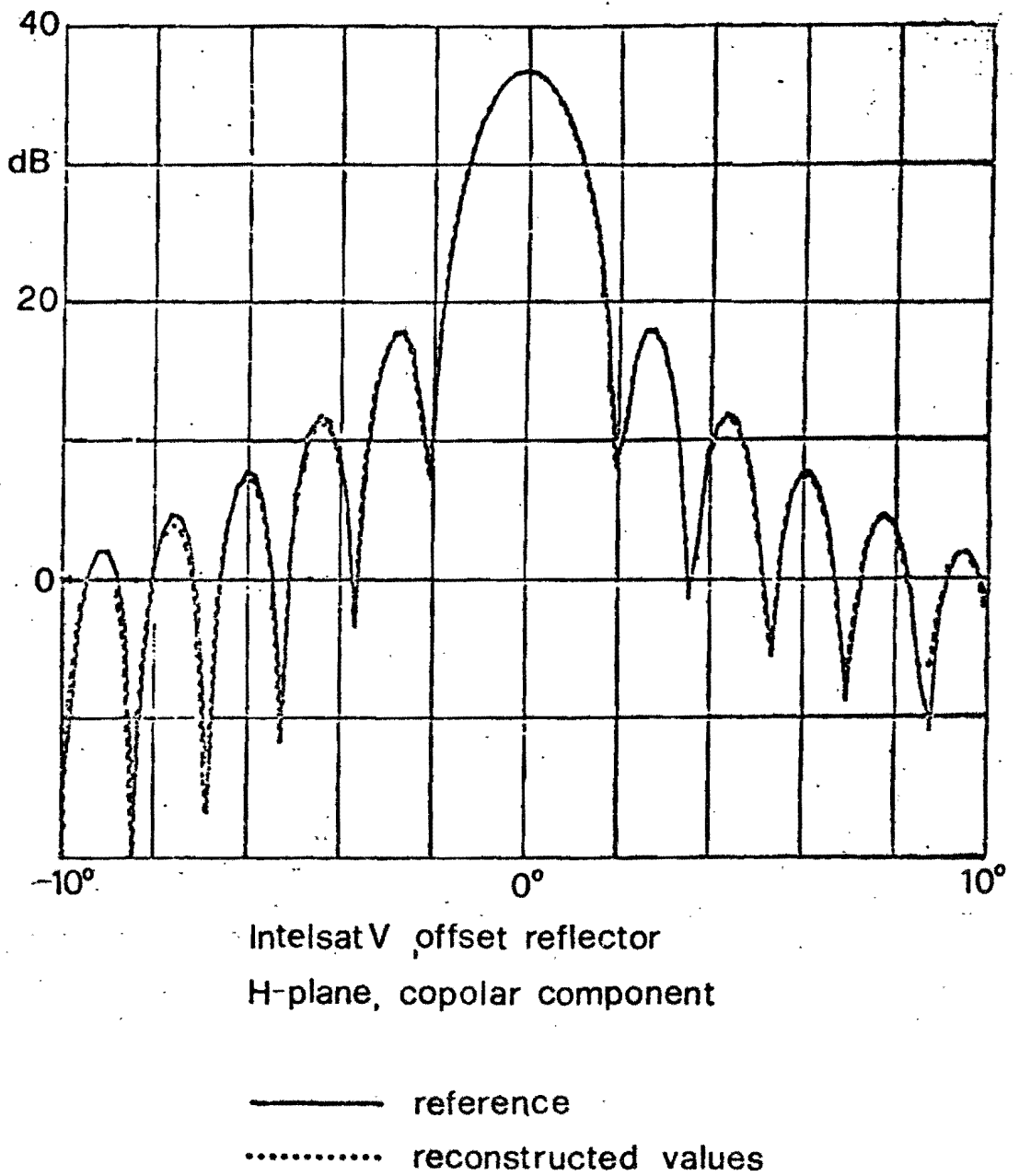


Fig. 9.2.7 - H - plane cut.

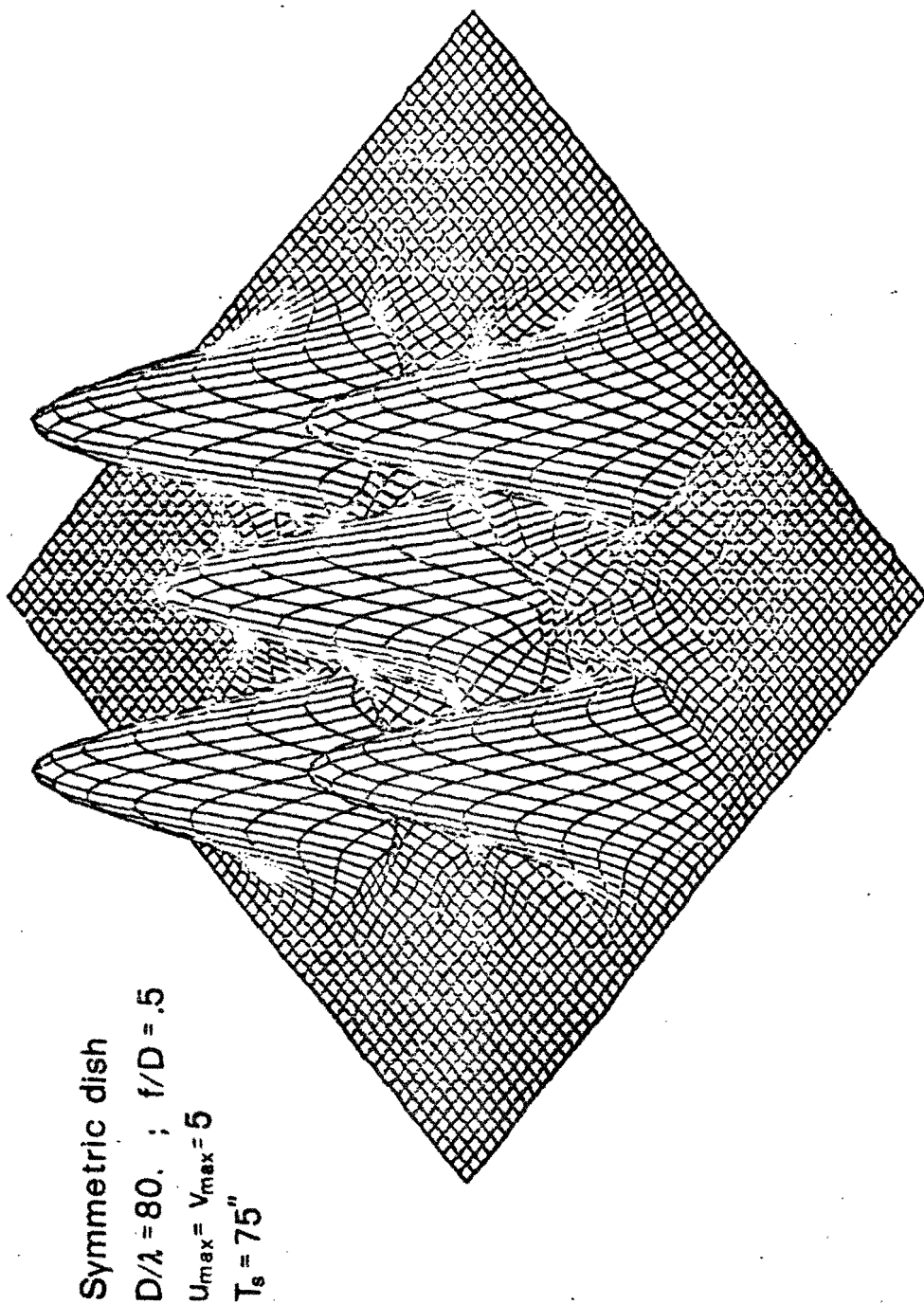
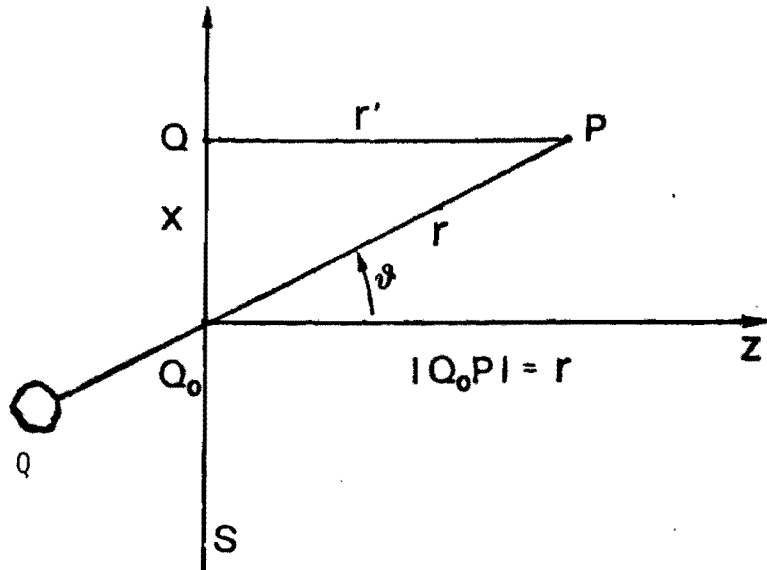


Fig. 9.2.8 - Stereographic plot of the radiation diagram.



$$\exp(-jkr') = \exp(-jk\sqrt{r^2 + x^2}).$$

$$\cdot \left\{ 1 - i \frac{1}{2k\sqrt{r^2 + x^2}} - \frac{1}{r^2} \frac{\partial^2}{\partial u^2} + \dots \right\} \exp\left(i \frac{r}{\sqrt{r^2 + x^2}} ux\right)$$

$$\frac{1}{2} ua' \left( \frac{a'}{r} \right)^2 < 1$$

Fig. 9.2.9 - Relevant to sampling interpolation of near field.

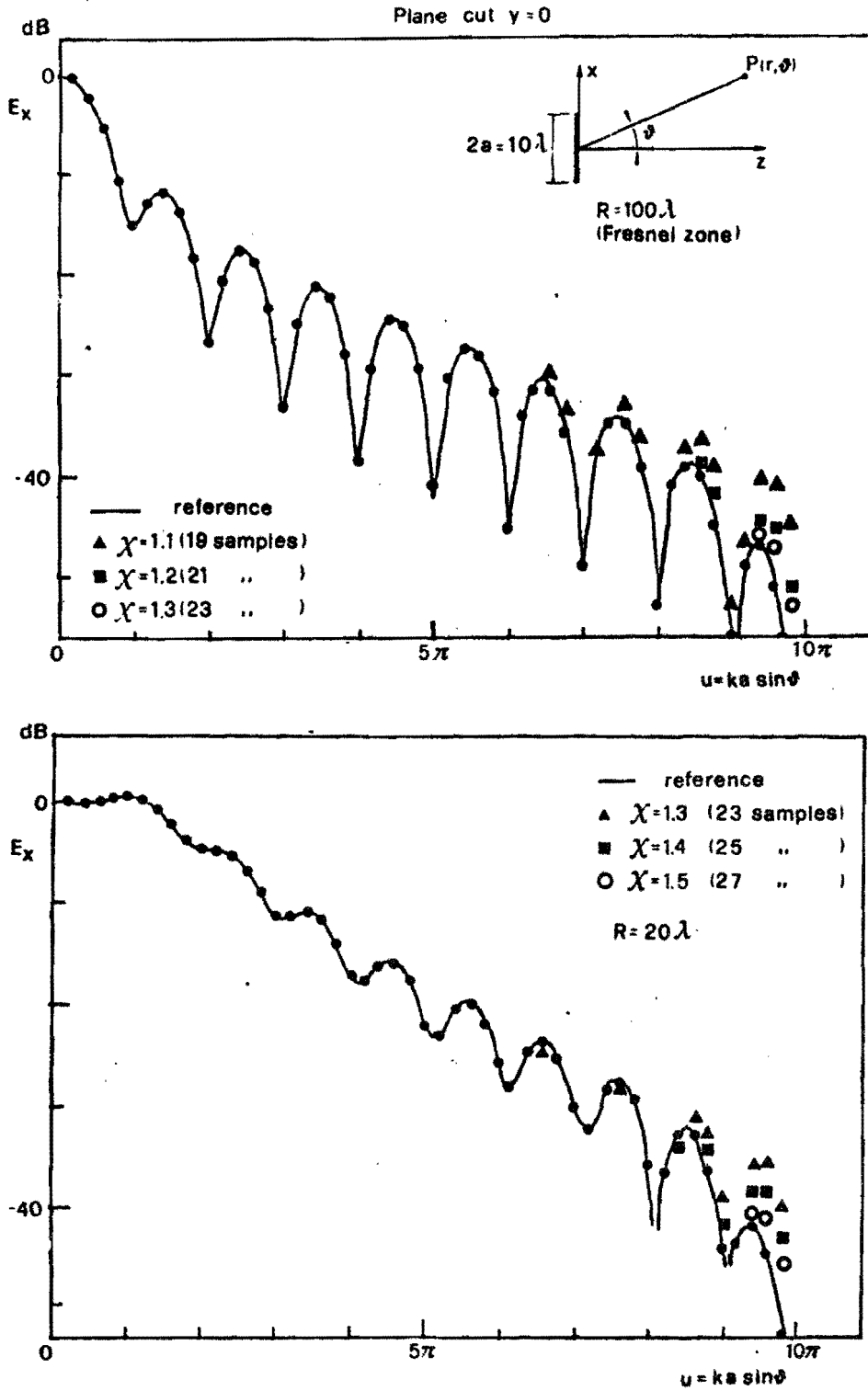


Fig. 9.2.10 - Sampling reconstruction of near field.  $\chi = a'/a$ .

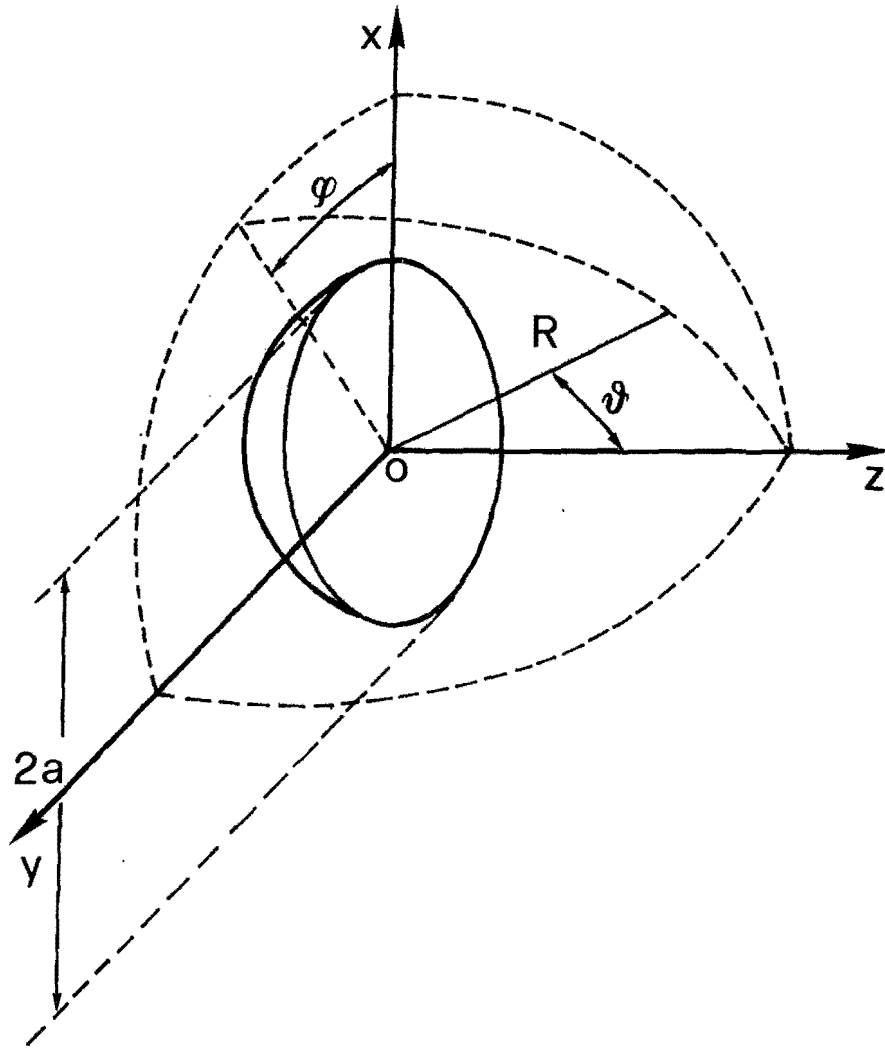


Fig. 9.2.11 - Relevant to the Fresnel zone of parabolic dish.



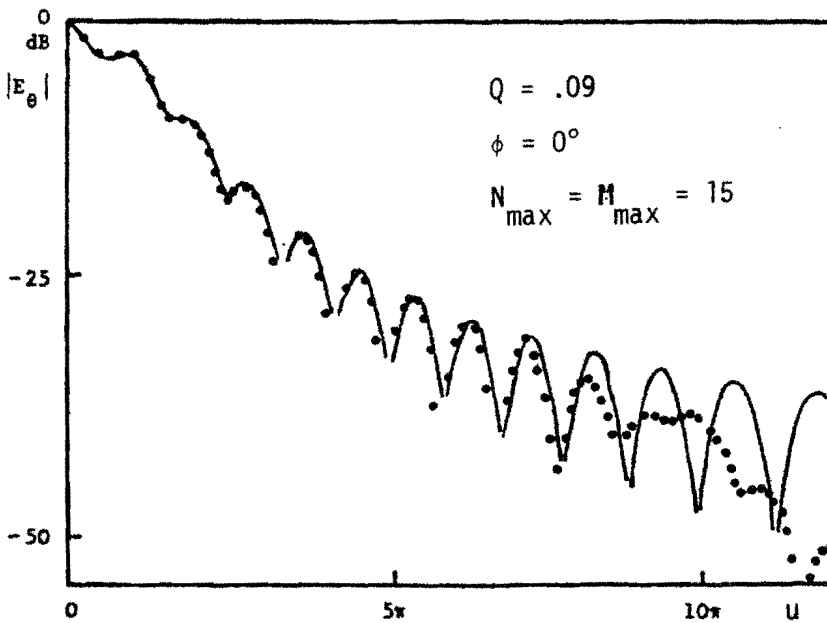
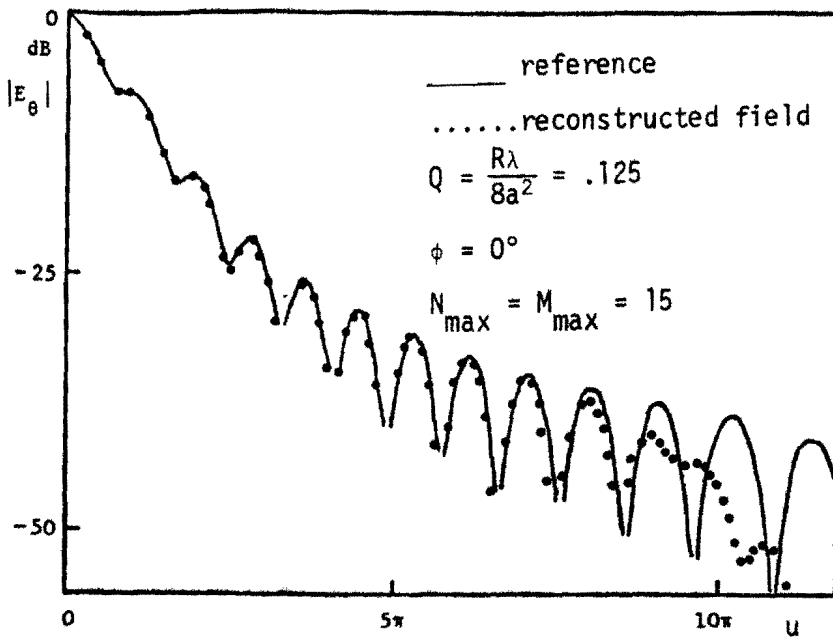


Fig. 9.2.12 - Pseudo-sampling series reconstruction of Fresnel zone field.

## 9. Antenna Measurements

### 9.3. Compact Antenna Range

by V.J. Vokurka

#### 9.3.1 Introduction

Measurements on microwave antennas are based on electromagnetic environment simulation so that the errors between the measured and true radiation behaviour of a test antenna are minimal. The importance of high-quality measuring ranges is evident; even slight errors between the measured and real radiation patterns could raise doubts as to the design technique or the theoretical approach used in predicting the radiation properties of the test antenna.

Most antenna measurements have to be carried out in the far-field, i.e. the test antenna should be illuminated by a plane wave. The oldest and most frequently used technique is based on sufficient separation between the transmitter and the receiver so that part of a spherical wave approaching the test antenna has almost a plane-wave character. However, the common far-field criterion  $R > 2D^2/\lambda$  gives a phase deviation of  $22.5^\circ$  at the edge of the test antenna, which results in errors in the recorded pattern. For instance, for shaped-beam antennas the separation between the transmitter and the receiver should be greater, typically  $4D^2/\lambda$  or  $8D^2/\lambda$ . For electrically large antennas, operating at frequencies between 4 and 30 GHz, the range length could be several kilometres. Ground reflections, high towers, high powers needed and the dependance on weather conditions are the disadvantages.

For indoor measurements the far-field technique is often used in anechoic chambers. Electrically small antennas (feeds, small reflectors) can be measured directly at these ranges. These measurements are, however, often less accurate than is assumed [1].

There is, however, another method which allows indoor measurements under far-field conditions. The Compact Antenna Range (often C.R., short for Compact Range) collimates the radiation from a point or line source by means of a lens or a parabolic reflector. The test antenna located close to the latter is then illuminated by a wave front which is approximately uniform in amplitude and phase. Let us, for example, assume that we are able to collimate the beam within a cone  $2\theta_0 = 20^\circ$ , having a uniform amplitude distribution across the latter. According to GO we find a "plane-wave zone" with a diameter of 2 metres, provided the collimation takes place at a distance of 5 metres from the source. The amplitude taper due to the space loss is about 0.07 dB. Since GO is used in this consideration, such design is basically independent of frequency. It should be noted that the effect of diffraction at the edges of the collimator are not considered here.

Although some attempts have been made using a lens for Compact Range design, reflectors are preferred for practical applications (Fig. 1).

Theoretical and experimental investigations into Compact Ranges have been carried out by several authors. Johnson [2] has described two such ranges. The point-source range consists of a reflector of revolution and a spherical source. The feed illuminates the upper half of the reflector (a conventional dish may be used). The line-source range consists of a parabolic cylindrical reflector and a line feed (hophorn type). Such a range possesses some mechanical advantages, but is unsuitable for wide-band operation. Moreover, the polarisation of this C.R. is fixed. The application of the C.R. to measurements of tracking antennas has been described by Hansen [3]. Results of experimental investigations of a Scientific Atlanta Compact Range are given by Johnson and Hess [4].

However, it is known that this solution has certain disadvantages. High system cost and limited physical dimensions of the test area ( $d=120\text{cm}$ ) are seen to be the main obstacles to wide use of these devices. Further increase of the test-area dimension would require a very large reflector,

while higher upper frequency limit can only be achieved by improving the reflector surface accuracy. On the other hand, low reflectivity and very low variations in phase make high performance measurements possible.

A new class of Compact Ranges has been described by Vokurka [5], [6], [8]. This system consists of two parabolic cylinders positioned perpendicular to each other (Fig. 2). When illuminated by a spherical source the resulting wave front in the aperture of the main reflector will have a plane-wave character. Such a system is very suitable for the offset arrangement which is required in our case. First, primary source may be pointed in any direction fixed by angles  $\theta$  and  $\phi$ . Further, the subreflector and the feed can both be rotated about the focal line  $F_2$ , which is identical with the image focal line  $F'_1$ . Due to the increased focal length the uniformity of the amplitude distribution across the final aperture is increased considerably compared to conventional design (Fig. 3). According to the reflector geometry, the cross-polarization is to be expected at very low levels ( $<-35\text{dB}$ ); naturally the latter depends also on the feed characteristics. It may, therefore, be possible to use this C.R. for accurate cross-polar measurements.

Due to the fact that this design is based on geometrical optics, operation in a very wide band may be expected. The upper frequency limit depends on the reflector surface accuracy. Recently, experimental measurements have been carried out at 70 GHz. The reflector surface accuracy realized in this case was 0,03 mm. Therefore, it is expected that such a range will operate up to 90 GHz without performance degradation.

Although the measured pattern agrees very well with that which could occur at infinite distance, further improvement is possible since the phase and amplitude of the antenna response, as well as of the wave front illuminating the test antenna, are known.

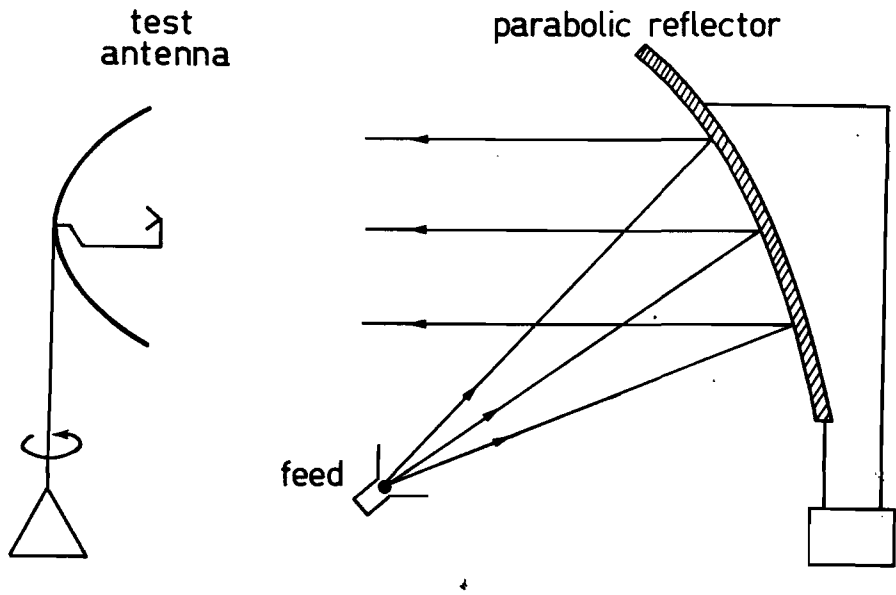


Fig. 1: Single-reflector Compact Antenna Range.

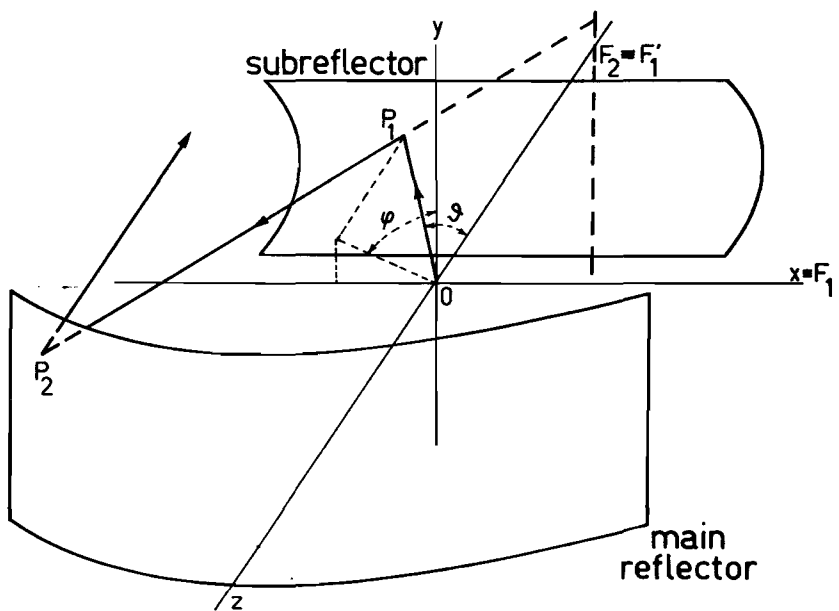


Fig. 2: Double-crossed parabolic cylinders, basic geometry.

An asymmetrical "plane-wave zone" can be created owing to the reflector geometry. The range can be thus tailored to some particular application. Reflectivity below -60 dB has been measured with the first experimental model.

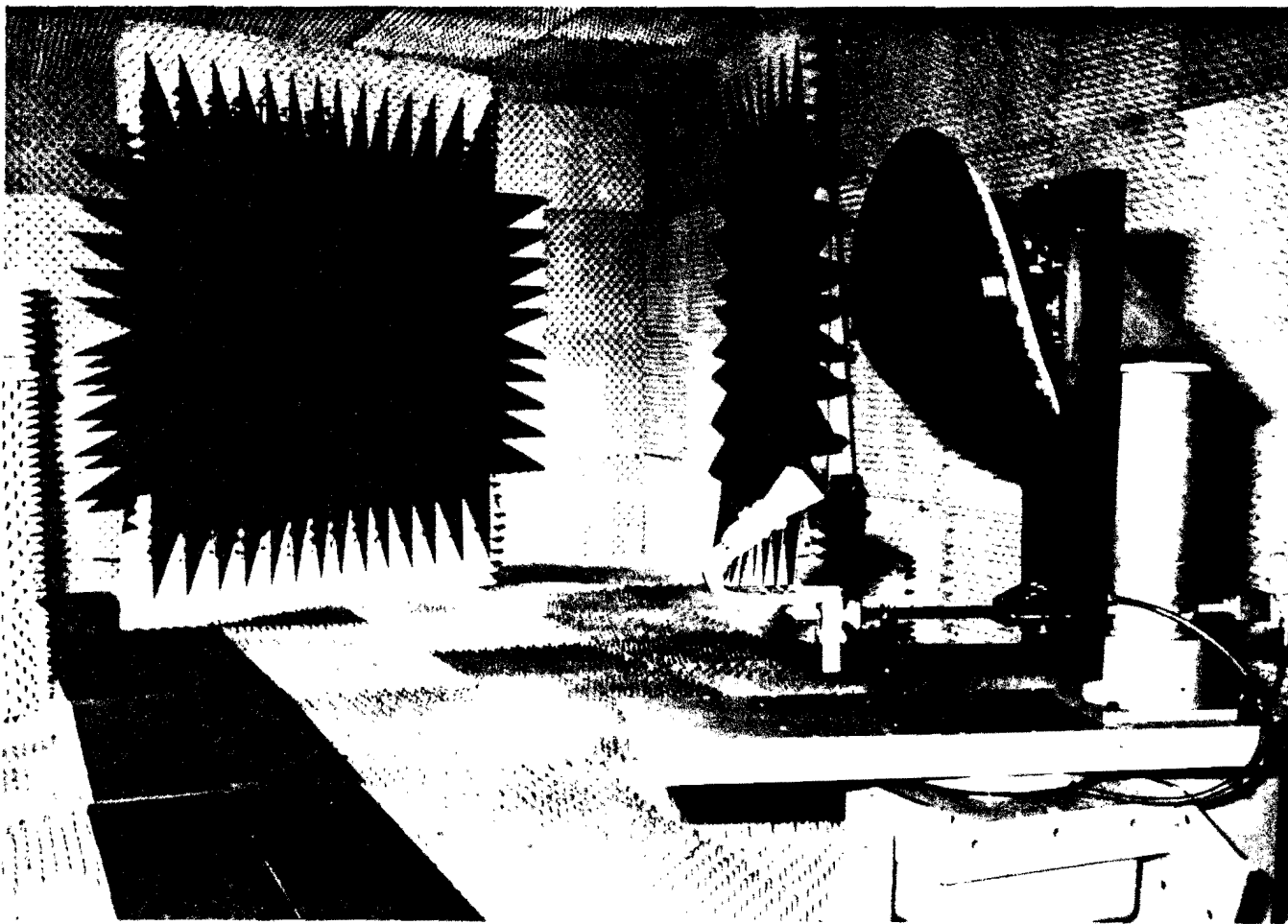
Summarizing, Compact Ranges are eminently suitable in indoor antenna measurements for various applications (photograph 1). The measurements are carried out directly under similar conditions as in the far-field. High performance measurements are possible mainly due to low phase variations (typically  $\pm 2^\circ$ ) over the test area and very low reflectivity level. Applying the concept of two crossed parabolic cylinders, considerable improvements may be achieved for cross-polarisation and compactness of the range. For the same size of plane-wave zone, the compact range reflector will be approximately half (in linear dimension) of the corresponding design with a single offset reflector. The manufacture of cylindrical reflectors is also simpler than that of double-curved surfaces.

Another technique for determining the far-field radiation characteristics indoors is that of near-field scanning. The far-field characteristics are then determined numerically. These techniques have been developed over the past 15 years and in some particular cases they offer important advantages when compared with the classical far-field approach [9]. Planar, cylindrical and spherical scanning are three possible arrangements. A comparison of the techniques is given, for instance in [1]. A choice of one of these methods will mainly depend on the geometry of the test antenna. However, both the mechanical stability and alignment could cause serious problems, in particular at higher frequencies (above 10 GHz). Moreover, due to the main disadvantage of these methods, namely the long time needed for scanning and computing the radiation pattern, their suitability for development testing (which is usually time-consuming) is questionable.

In Table 1. the methods mentioned above are compared. We observe that no

CHARACTERISTICS	FAR FIELD	NEAR FIELD	NEAR FIELD		
	OUTDOOR	COMPACT RANGE	PLANAR	CYLINDRICAL	SPHERICAL
Real Estate/Structures	Range length $2D^2/\lambda < R < 10D^2/\lambda$ Towers 3 axis precision positioner	Anechoic room RF Absorber (100 %) 3 axis precision positioner	----- Anechoic room ----- RF Absorber (15 %)	RF Absorber (20 %)	RF-Absorber (20-100 %)
Instrumentation/software	Weatherized test terminal Broadband radome Data collection system	C.R. Reflector(s) Error analysis(optional) Data collection system	2-dim scanner ----- ----- ----- -----	1-dim scanner 2 axis positioner Control software Error analysis Data collection system Analysis software	3 axis precision positioner ----- ----- ----- -----
Operational Constraints	Wind & Weather Safety Security Logistics	None	----- Large scan times -----		
Performance Constraints	Ground reflections Rain attenuation	Reflector tolerances Quality of feed pattern	----- Scanner and/or positioner tolerances -- (static & dynamic) --- Inefficient for early development tests -----		
Overall Relative Cost Estimate	5 (Highest)	1 (Lowest)	2	3	4

Table 1: Comparison of near-field and far-field techniques.



*Photograph 1: C.A.R. with two crossed-parabolic cylindrical reflectors. Antenna under test is a contoured-beam antenna for satellite applications (courtesy of MBB, Munich).*



single measurement technique will be ideal for general use. For instance, for measurements on large-phased arrays [9] planar scanning has proved its suitability and it saves a considerable amount of time. In other applications, the same technique might be unsuitable just because of its time-consuming character, for instance on account of the large number of repeated measurements during development test on satellite antennas. In the case of the latter, direct indoor measurements under the far-field conditions are probably most attractive. Compact Range arrangement consisting of reflectors with a very high degree of surface accuracy and improved cross-polarisation will be needed in view of the wide frequency range and the antenna characteristics.

### 9.3.2. General Design Considerations

In developing new Compact Ranges, a number of aspects are to be considered. The following are the most important:

- a) stray radiation level,
- b) efficiency factor,
- c) shape and dimensions of the plane-wave zone,
- d) cross-polarisation level,
- e) optimum feed design,
- f) reflector surface accuracy,
- g) operational frequency range.

Stray radiation - which is unwanted radiation that reaches the test area, is the most important of the effects with an influence on C.R. performance. In conventional far-field outdoor ranges the reflections from the ground and direct test-area environment play a significant role. In the Compact Range, however, more effects have to be eliminated. Diffraction at the feed, its supports and reflector edges are of primary interest. Other sources of unwanted radiation, such as the multiple reflections within the room or direct radiation from the feed are important for high-performance ranges. Most of these effects can be successfully eliminated. Proper use of absorbent material, rolled edges or serrations significantly improves range performance. The geometry of the system, primary feed-radiation pattern and the amount of spill-over energy will also affect the performance of the Compact Range since unwanted stray radiation cannot be fully eliminated. These aspects will therefore determine theoretical performance of a particular C.R. design.

The efficiency factor, which is the ratio of the test-area diameters to C.R. reflector diameter will determine the physical size of the Compact Range for the required test-area dimension. The axial location of the test area is important for the performance and compactness of the system. The application of long focal distances to present single-reflector C.R. does not seem possible, since the test antenna cannot be located between

the feed and C.R. dish. On the other hand, short focal distance (low F/D ratio) causes a relatively strong amplitude taper across the C.R. aperture due to the space attenuation and tapered feed pattern. The only possible correction of this effect, namely a modified feed pattern, is difficult to realise and would result in narrowing of the applicable frequency band.

Due to the fact that the dual-cylindrical reflector C.R. has a relatively large focal length, it is possible to illuminate the reflector edges at about -1dB. Consequently, this will result in a larger test-zone area (up to 2x) for the same C.R. dimension.

Shape and dimensions of the plane-wave zone will depend on particular applications. Existing Compact Ranges are mainly suitable for measurements on antennas with a circular aperture. For other applications, where an asymmetrical plane-wave zone could be preferred, for instance radar antennas, arrays or antennas including the direct environment (satellite body, etc.), the present design of the Compact Range with circular plane-wave zone cannot operate efficiently. An increase in size of the plane-wave zone will bring a rapid rise in cost, given that the upper frequency limit and the efficiency factor remain unchanged.

As already mentioned, dual-cylindrical reflector geometry is eminently suitable for producing of symmetrical as well as asymmetrical aperture images. Therefore, the range can be tailored to some particular application.

Cross-polarisation level across the test zone plays a very important part, for instance in satellite-antenna design where a very low cross-polar is required. For accurate cross-polar measurements a high polarisation purity of the incident field will be needed. The (unwanted) cross-polar component can be caused by:

1. feed characteristics,
2. diffraction effects,

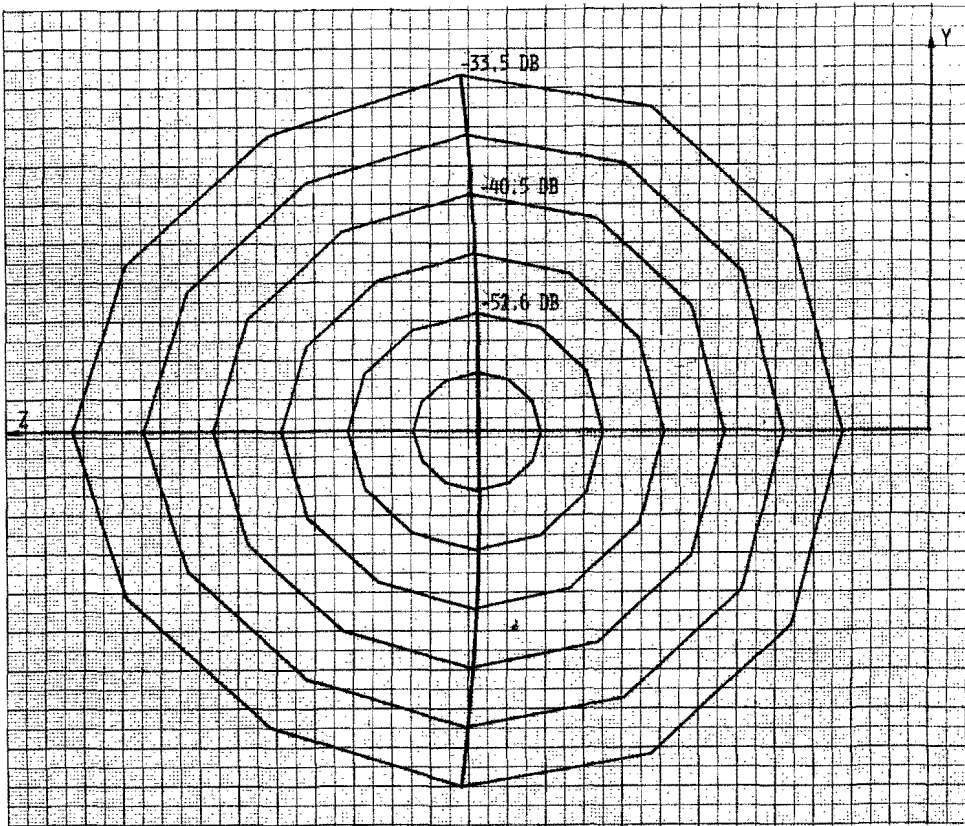


Fig. 3: Aperture-plane images, crosspolar below copolar.  
Present design.

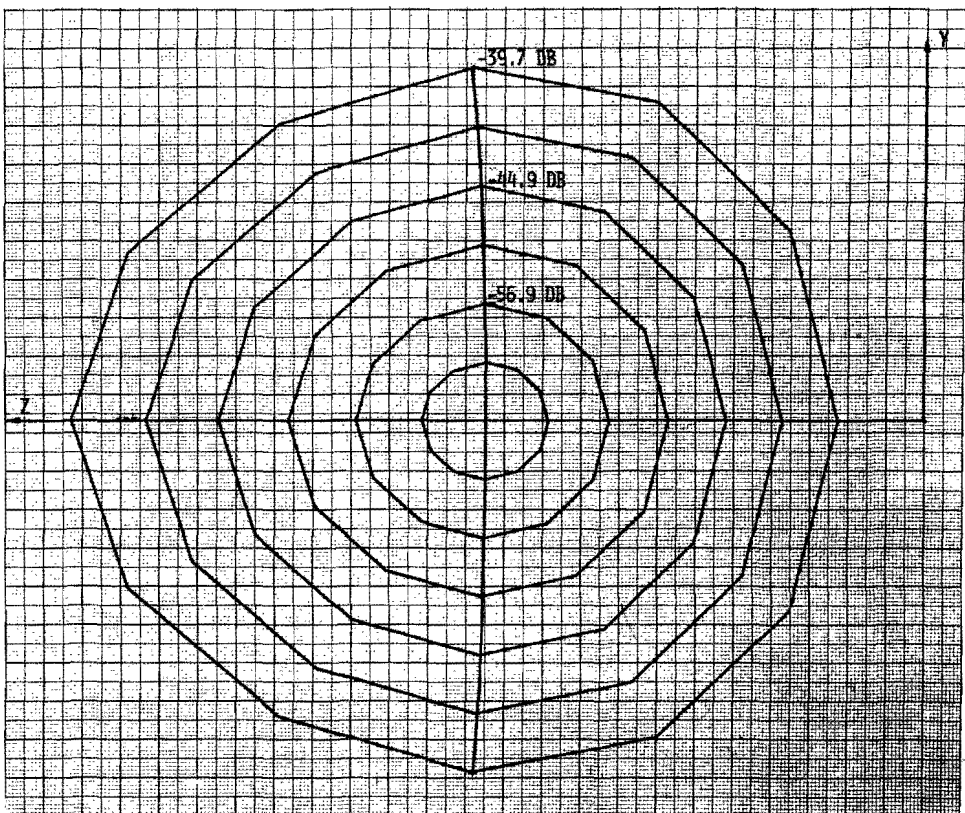


Fig. 4: Aperture-plane images, crosspolar below copolar.  
Proposed geometry.

### 3. off-set reflector geometry.

The first-mentioned contribution can be eliminated by a properly designed feed, having very good characteristics close to the boresight. Since the reflector edges are seen at angles corresponding to about -1dB beamwidth, the cross-polar maximum will occur outside the test zone.

Possible depolarisation due to the diffraction can be minimized in a similar way as for the co-polar component, i.e. carefully designed serrations, proper use of absorber etc.

Finally, the cross-polar contribution due to the off-set geometry cannot be eliminated in a simple way. However, due to the fact that both the off-set angle and the cone illuminating the subreflector are small, the cross-polar component can be kept below -50dB, which is acceptable for most application. Computed aperture images and corresponding cross-polar maxima are shown in Figs. 3 and 4, respectively.

Optimum feed design is one of the most important design aspects due to its direct influence on the reflectivity, cross-polar and the field uniformity (in phase and amplitude) across the test zone. According to the range geometry, we would require a feed pattern which is almost uniform within a cone of about 20 degrees and having low spill-over outside this region. In particular, the radiation beyond  $80^\circ$  should be kept as low as possible, in order to minimize the direct radiation into the test zone. A corrugated conical horn with flare angle of about  $20^\circ$  seems to be the best candidate. A typical radiation pattern is shown in Fig. 5. We observe that the power pattern shows a high degree of uniformity within approximately  $20^\circ$ . At  $90^\circ$  the power level drops to about -40dB which is acceptable for our application. The phase deviations are less than 2 degrees in the central region.

Finally, low V.S.W.R. is of great importance due to possible interaction between the test antenna and C.R.

Reflector surface accuracy. It has been pointed out in [14] that the fractional change in amplitude at the observation point will be  $8\Delta/\lambda$ ,

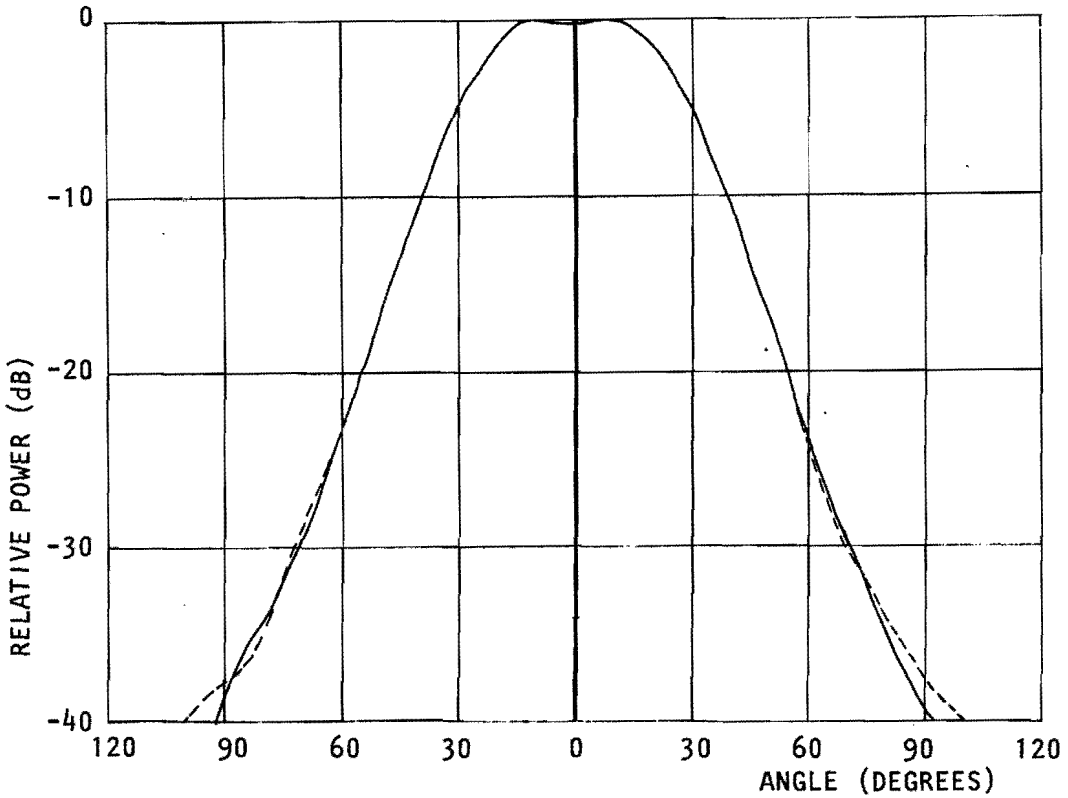


*Fig. 5: Typical far-field pattern of corrugated conical horn for C.A.R. application.*

where  $\Delta$  is the maximum deviation of the reflector and  $\lambda$  is the wavelength. For a maximum deviation of  $0.007\lambda$ , variations of approximately 0.5dB are found across the test area. At 30 GHz, for instance, the reflector surface accuracy should be better than 0.07 mm. A more complete analysis of the effects of reflector surface distortions are given in [17]. In general, distortions which are large in terms of wavelength will have a greater effect on the C.R. performance. Cylindrical surfaces used here have an advantage of easier and cheaper manufacture than double-curved surfaces. Deviations of the reflector profile from a true parabolic cylinder are less than 0.02 mm. Consequently, the upper frequency limit is about 100 GHz.

Operational frequency range. Although the Compact Range is basically frequency independent device, there is a number of limitations which are to be taken into account. First, the feed will be frequency dependent (co- and cross-polar performance). In cases where very accurate measure-

ments are required, the useful bandwidth of a single feed will be limited to about 20%. For less accurate measurements the useful bandwidth could be approx. 50%. The lower frequency limit will be determined by the size of the serrations. It has been proved by experiments that the serrations which are approximately 3-4 wavelength long give a very good protection against unwanted diffraction effects. On the other hand, the upper frequency limit will depend mainly on the reflector surface accuracy. Finally, the absorber which is used will be a limiting factor for wide-band operation.

### 9.3.3. Experimental Investigation

In order to determine the suitability of the Compact Antenna Range for various applications, an experimental study for three different reflector antennas (highly-shaped, shaped and a contoured-beam antenna) has been carried out.

The test procedure reads as follows:

- a) Calibrating of the Compact Range with a planar scanner. The following characteristics are recorded: copolar, crosspolar and phase patterns. In most cases these measurements are carried out with an open waveguide (O.W.) and a standard gain horn (S.G.H.).
- b) The far-field characteristics of the test antenna are measured on the Compact Range. For determining the reflectivity level, the pattern comparison method is applied, i.e. the measurements are repeated at different axial distances.
- c) Reference measurements are taken on the outdoor range with  $R = 180\text{m}$ .

#### A. HIGHLY-SHAPED BEAM ANTENNA

This antenna produces a highly-shaped beam with a maximum at about  $65^\circ$  off axis.

##### Technical data:

Circularly symmetrical reflector, two feed supports.

Diameter: 42 cm ,

Frequency: 12.05 GHz,

Feed: corrugated horn,

Polarisation: LHC.

Some of the experimental data are shown in Figs. 6 and 7, respectively. We observe that there is an excellent agreement in copolar characteristics in the angular region  $-108^\circ < \theta < 108^\circ$ . The copolar measurements are repeated at 7 different axial distances. Variations in the copolar patterns indicate that the reflectivity level is below -50dB. Accurate





Fig. 6: Highly-shaped beam antenna, LHCP,  $f = 12.05$  GHz, feed supports in horizontal position, azimuth pattern.

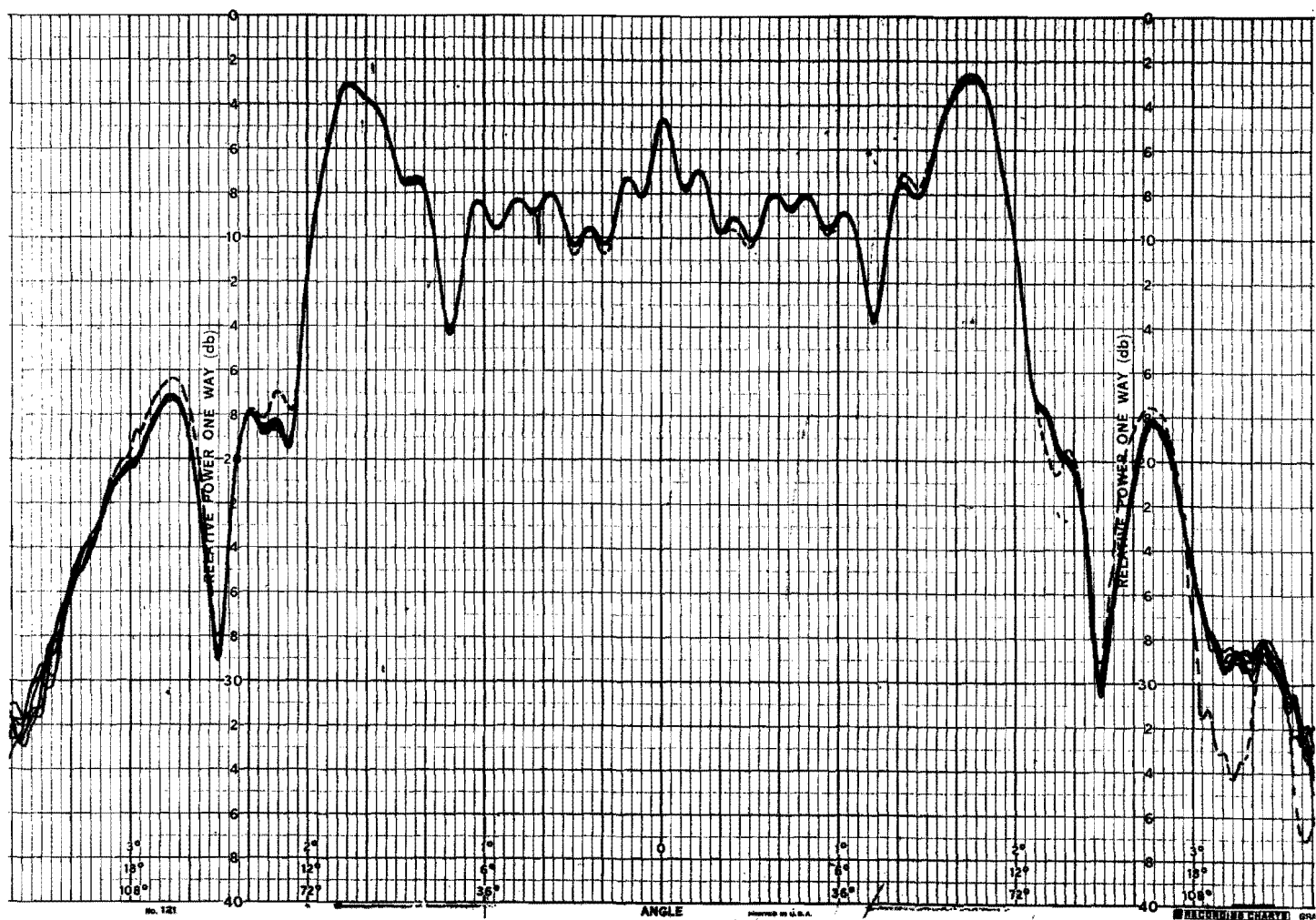


Fig. 7: Highly-shaped beam antenna, LHCP,  $f = 12.05$  GHz, feed supports in vertical position, azimuth pattern.

measurements of the crosspolar performance were not possible in this case due to the quality of the polarizer. Although the common far-field criterion  $2D^2/\lambda$  corresponds to about 14 metres and the antenna could thus be measured on some indoor far-field ranges, the advantages in using a Compact Range are evident. Better reflectivity and a more accurate pattern prediction over a wide angular range are of great importance for this particular type of reflector antennas.

#### B. CONTOURED BEAM ANTENNA

##### Technical data:

Off-set reflector, elliptical aperture

Dimensions: 85 x 46cm,

Frequency: 12.0 GHz,

Feed: four-horn type,  $\Sigma$  and  $\Delta$  channels,

Polarisation: linear.

For this antenna,  $2D^2/\lambda$  corresponds to approximately 60 metres. For accurate pattern prediction, however, a larger distance will be required, for instance  $6D^2/\lambda$ . Naturally, an outdoor range will be needed for measurements of the far-field characteristics. In Fig. 8 the C.R. characteristics are shown. We observe that both amplitude and phase have a high degree of uniformity across the test antenna. Also shown are the differences when O.W. or S.G.H. are used as probes. In Figs. 9 and 10 azimuth patterns for the sum and difference patterns are given. The agreement with outdoor data is excellent for both co- and cross-polar patterns. For the elevation pattern (Fig. 11) a small disagreement was found between 4 and 6 degrees. This error is caused by mechanical instability of the feed tower. The outdoor range is slightly elevated ( $4^\circ$ ) and the boresight measurements are carried out in a different antenna position when compared to C.R. measurements. By the pattern comparison method a reflectivity level below -65dB has been measured.

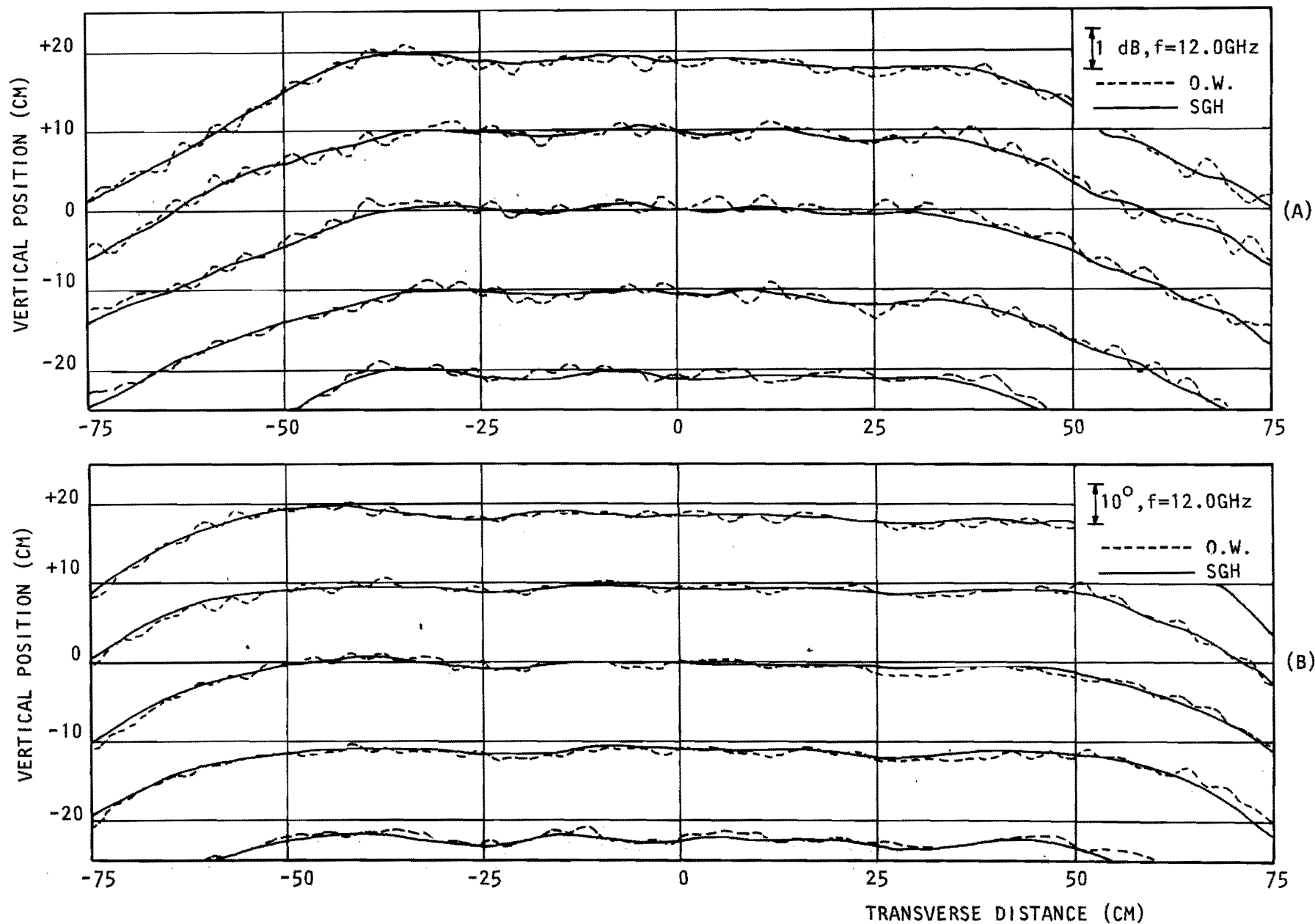


Fig. 8: Compact Range characteristics, (A) amplitude, (B) phase.

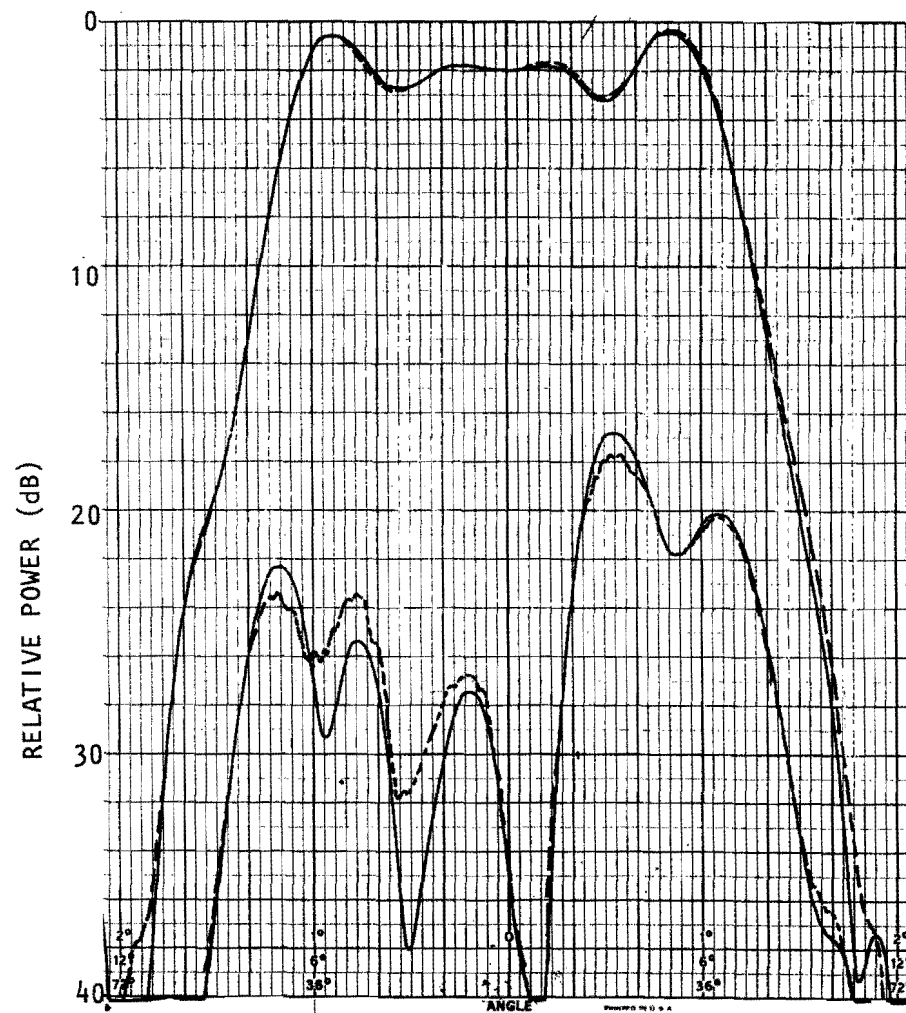


Fig. 9: Contoured-beam antenna, sum pattern,  
 $f = 12.0$  GHz, — CR, --- FF, hor. polarisation, azimuth pattern.

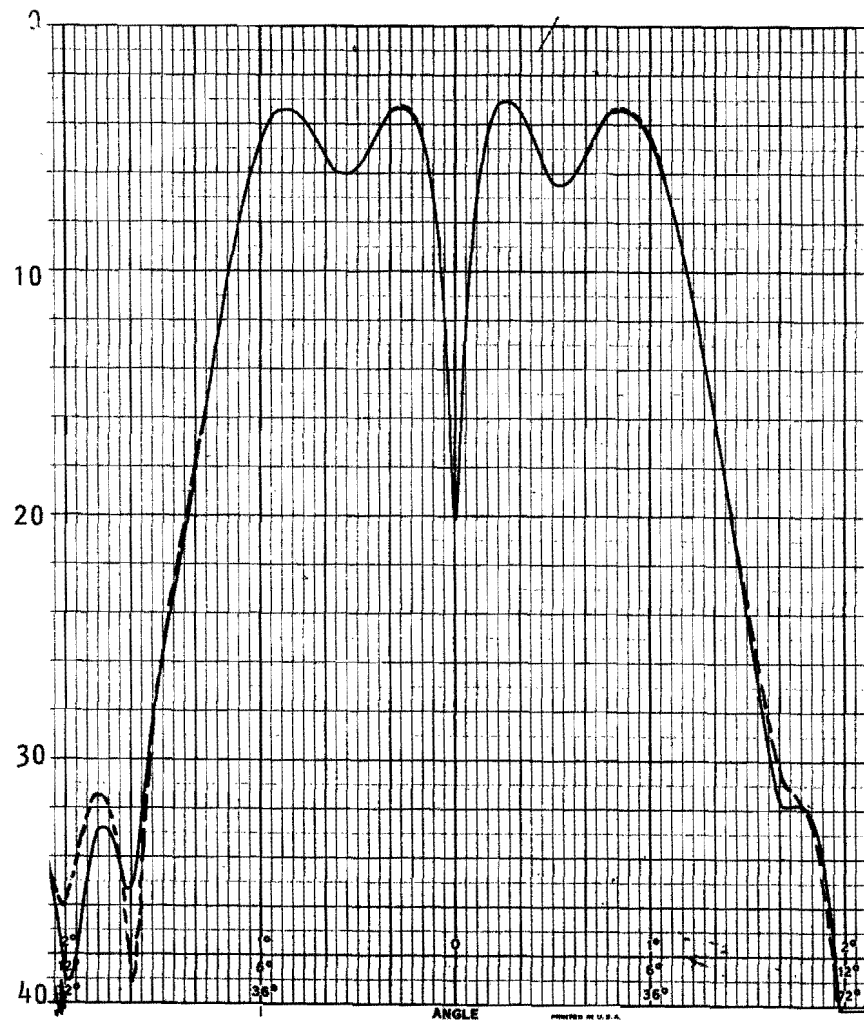


Fig. 10: Contoured-beam antenna, diff. pattern,  
 $f = 12.05$  GHz, — CR, --- FF, hor. polarisation, azimuth pattern.

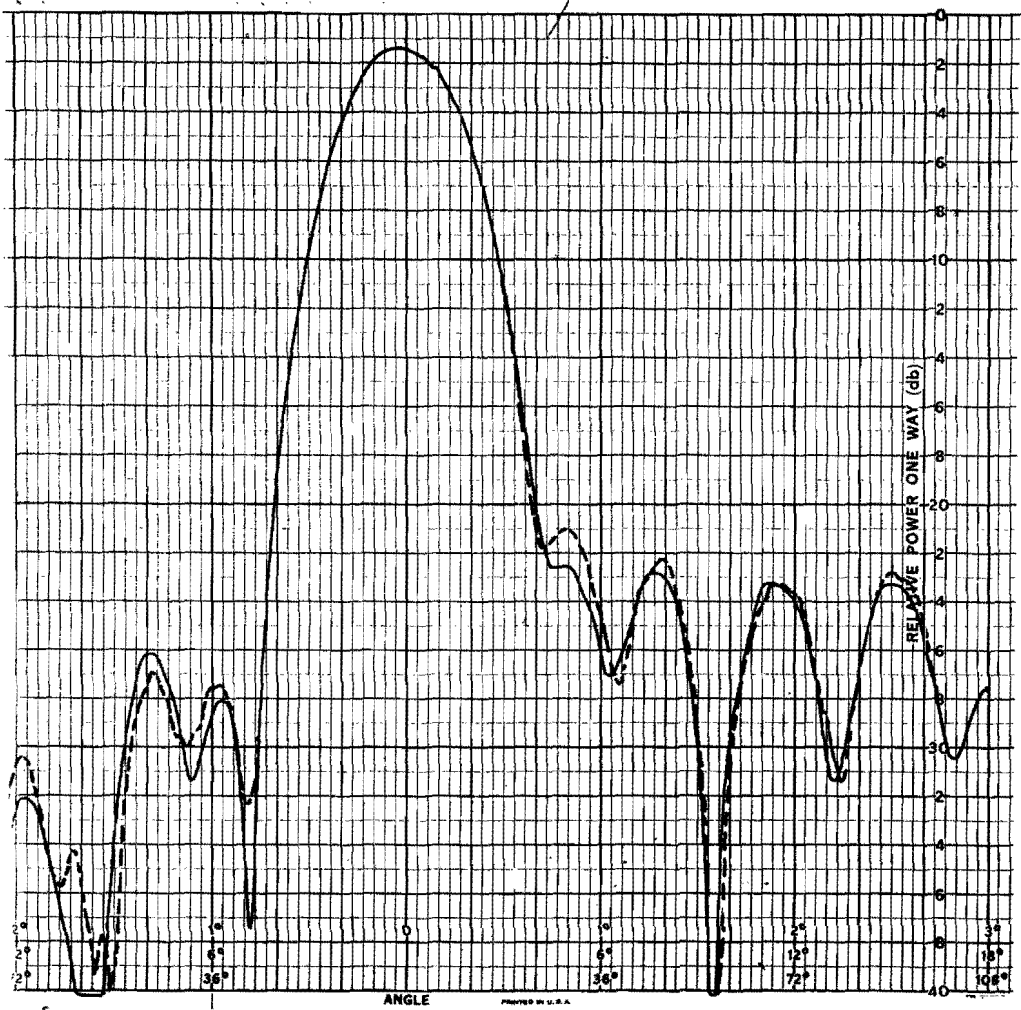


Fig. 11: Contoured-beam antenna, sum pattern,  $f = 12.05$  GHz,  
— CR, --- FF, hor. polarisation, elevation pattern.

### C. OTS-TX ANTENNA

#### Technical data:

Front-fed shaped reflector,

Diameter: 32cm,

Frequency: 14.0 - 14.5 GHz,

Polarisation: dual-linear, two orthogonal ports.

This antenna has been chosen because of its very good cross-polarisation performance. In Figs. 12 and 13 characteristics of the Compact Range are shown. Far-field characteristics of the test antenna (at 14.25 GHz) are given in Figs. 14 to 19. We conclude that there is an excellent agreement in co-polar as well as cross-polar patterns. Small errors in the cross-polarisation (at levels between -30 and -60dB) are caused by dis-alignment. As in the previous case, the reflectivity is found below -65dB.

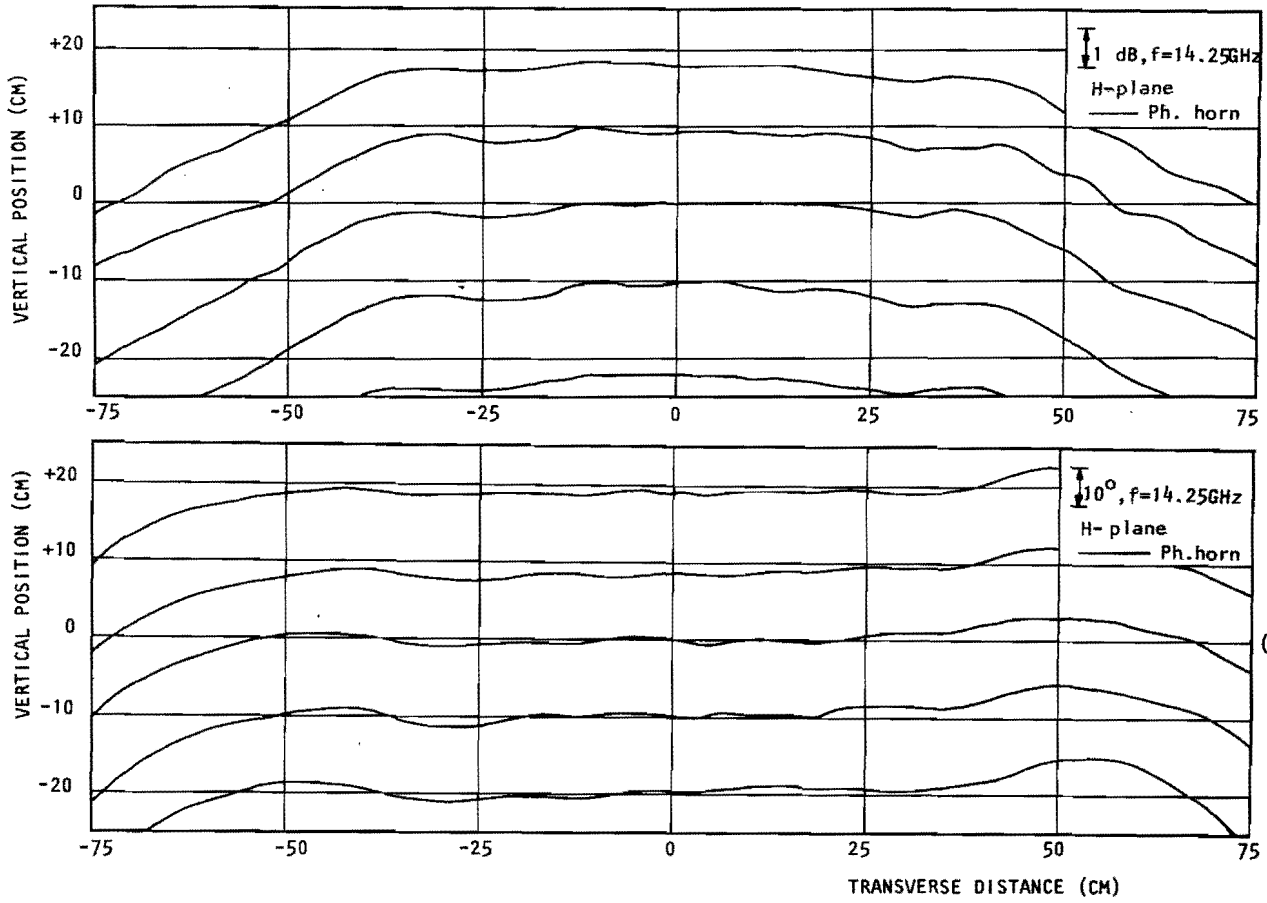


Fig. 12: C.R. characteristics, (A) amplitude, (B) phase.

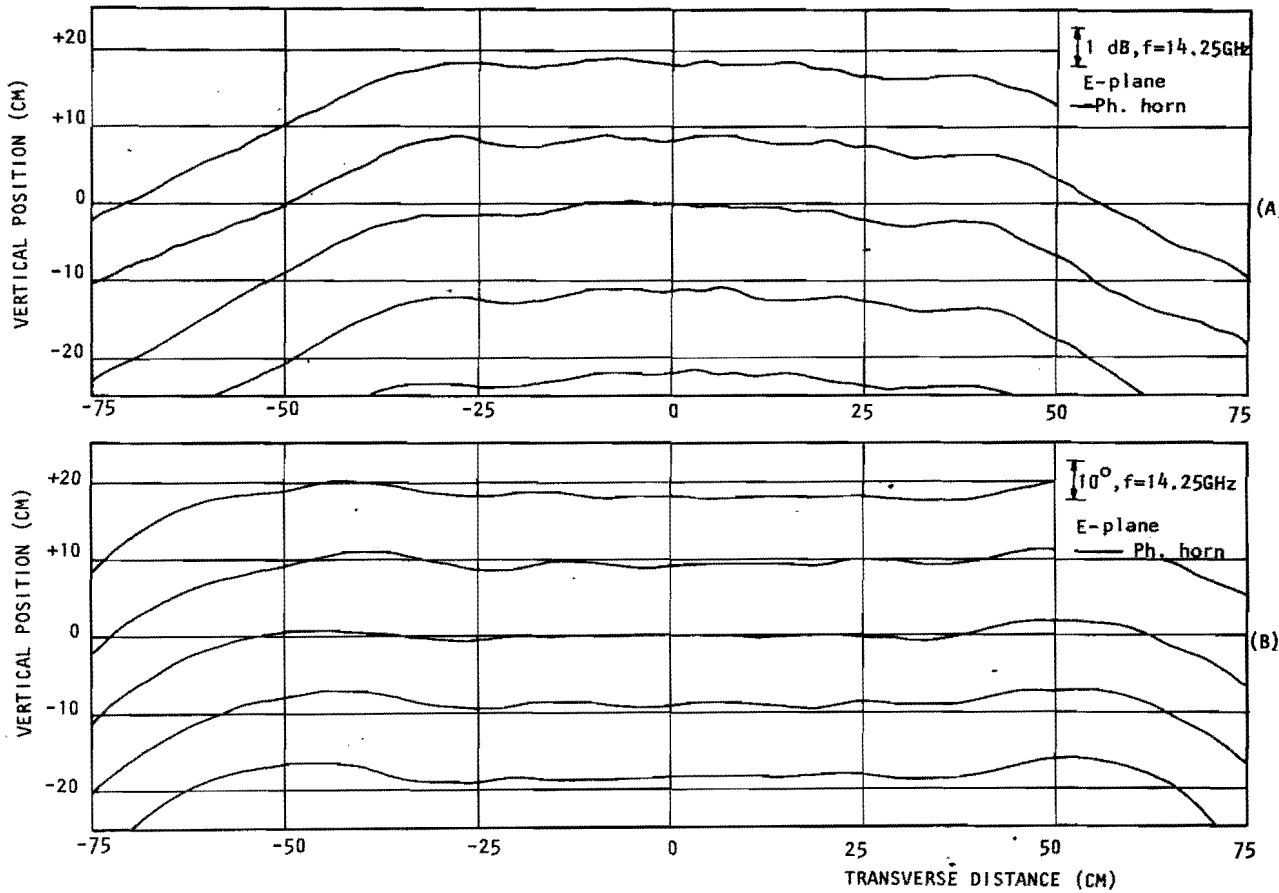


Fig. 13: C.R. characteristics, (A) amplitude, (B) phase.

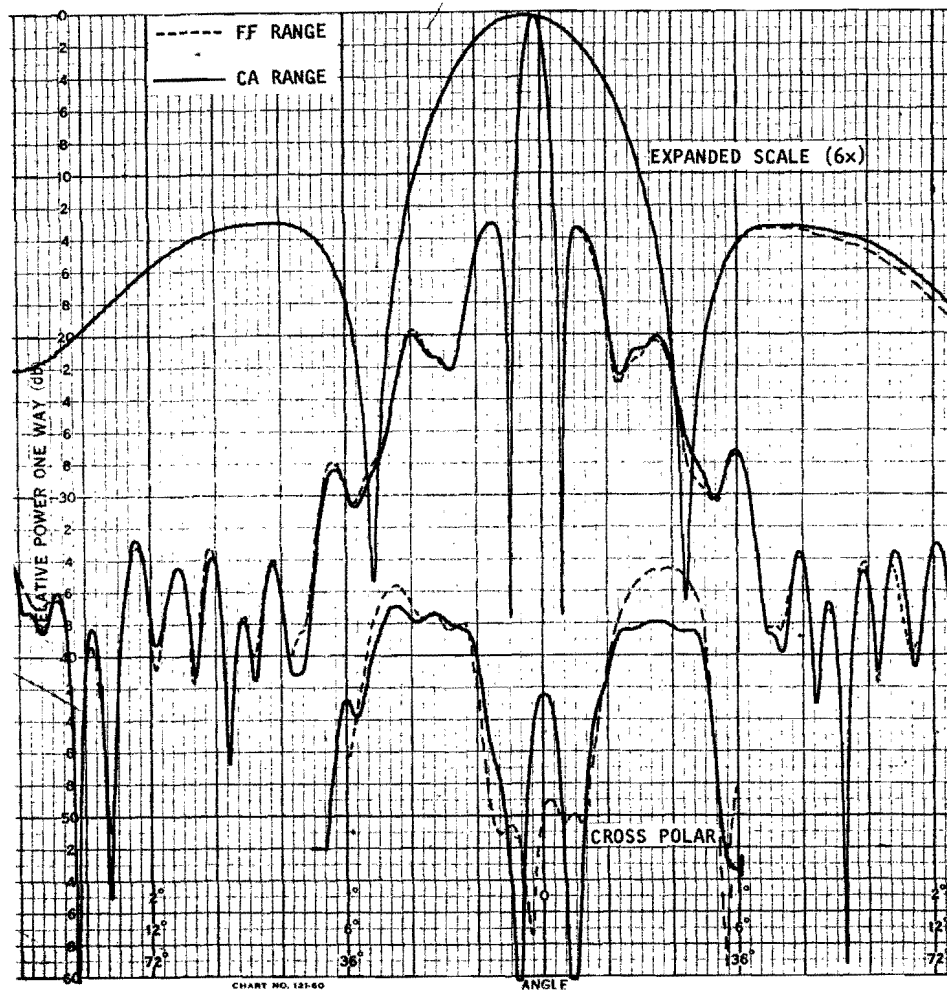


Fig. 14: OTS antenna pattern,  $f=14.25$  GHz, feed support vertical position, parallel polarisation.

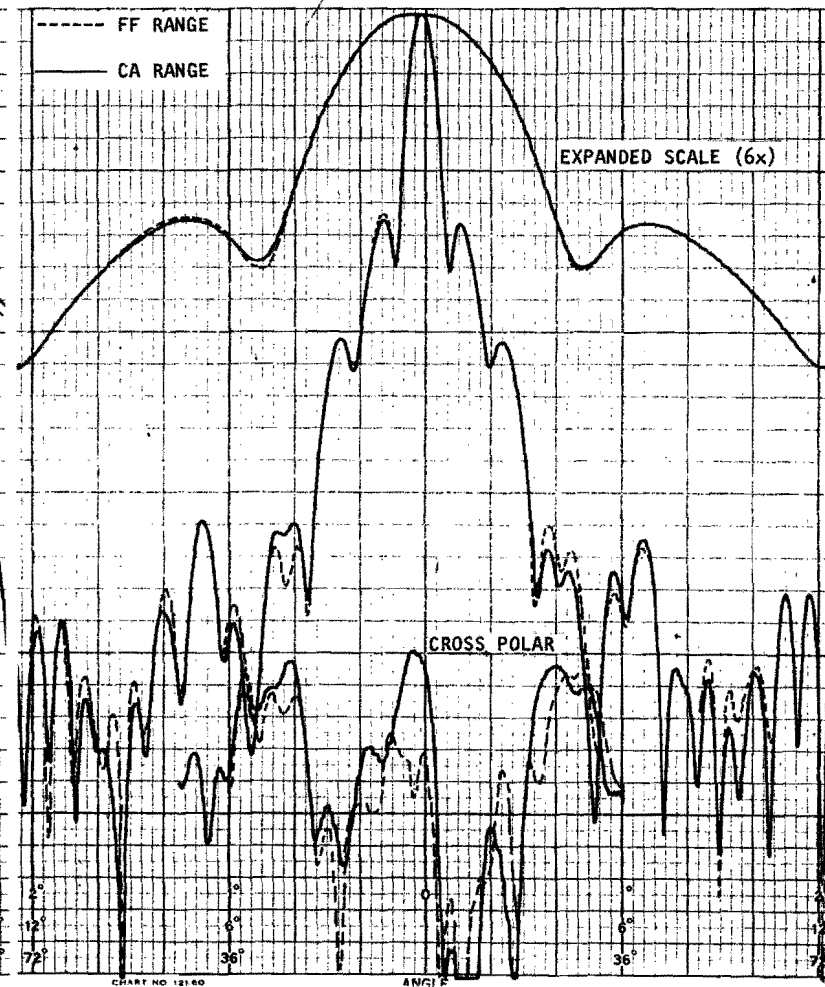


Fig. 15: OTS antenna pattern,  $f=14.25$  GHz, feed support vertical position, perp. polarisation.



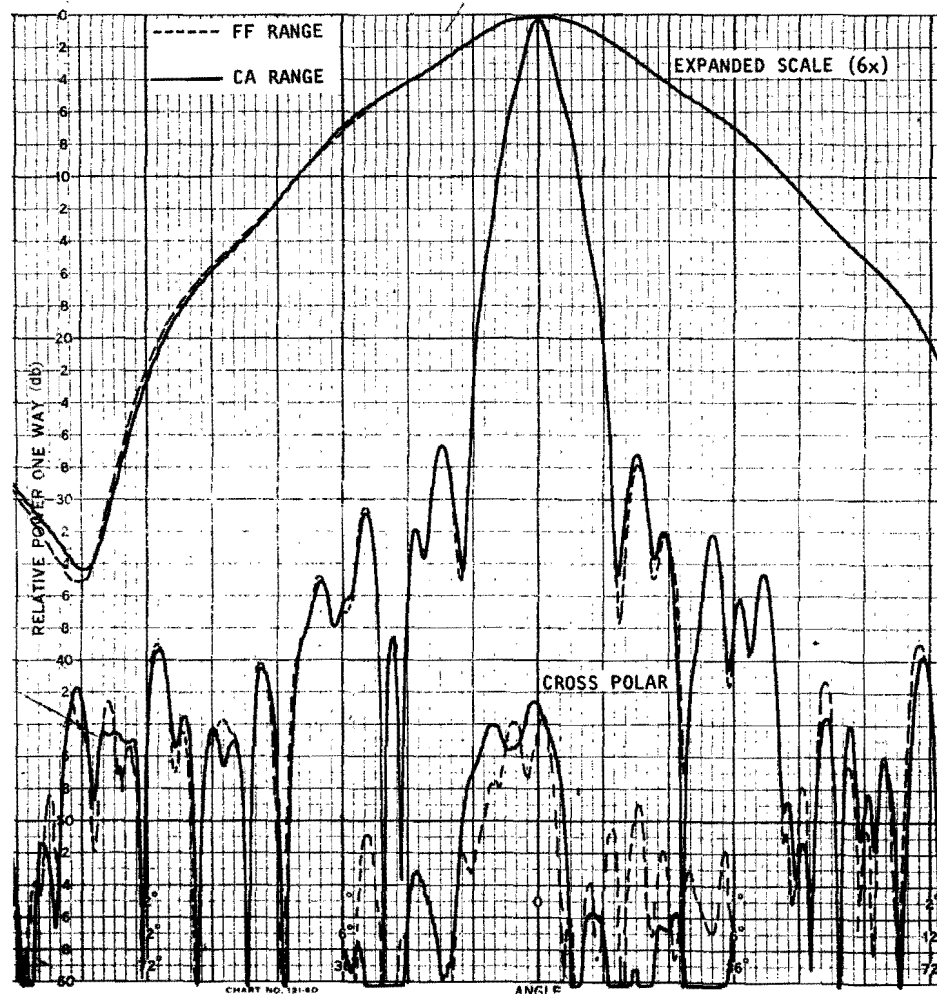


Fig. 16: OTS antenna pattern,  $f=14.25$  GHz, feed support horizontal position, parallel polarisation.

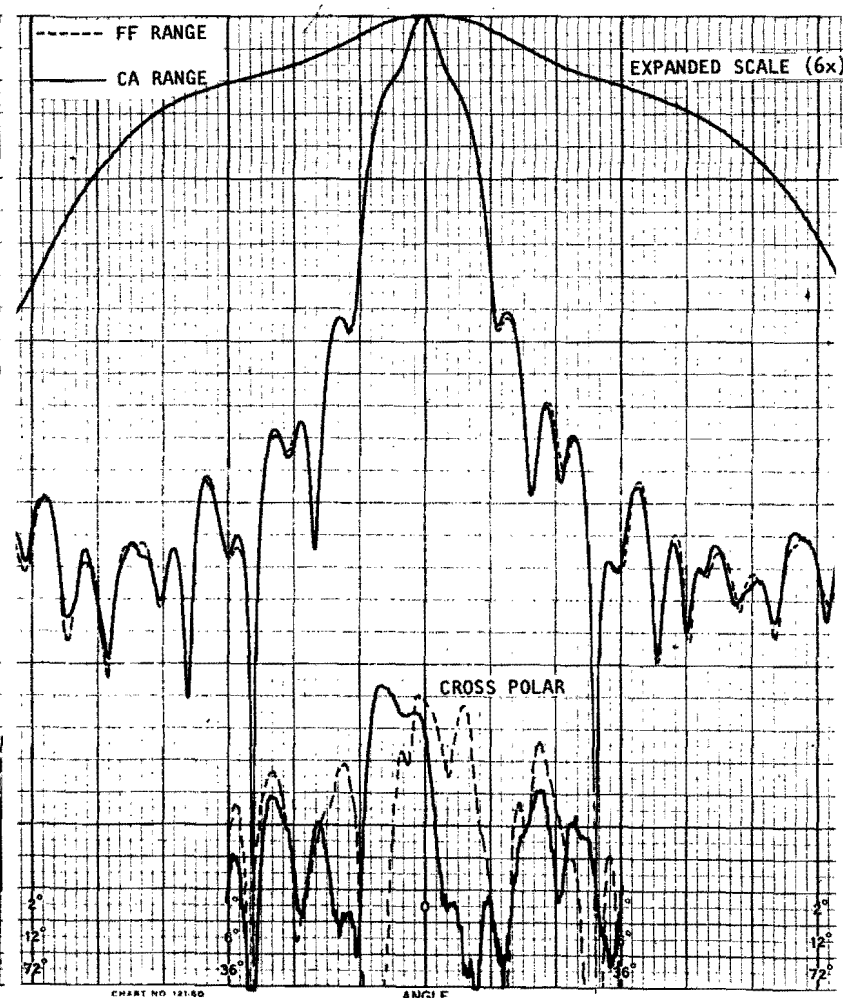


Fig. 17: OTS antenna pattern,  $f=14.25$  GHz, feed support hor. position, perp. polarisation.

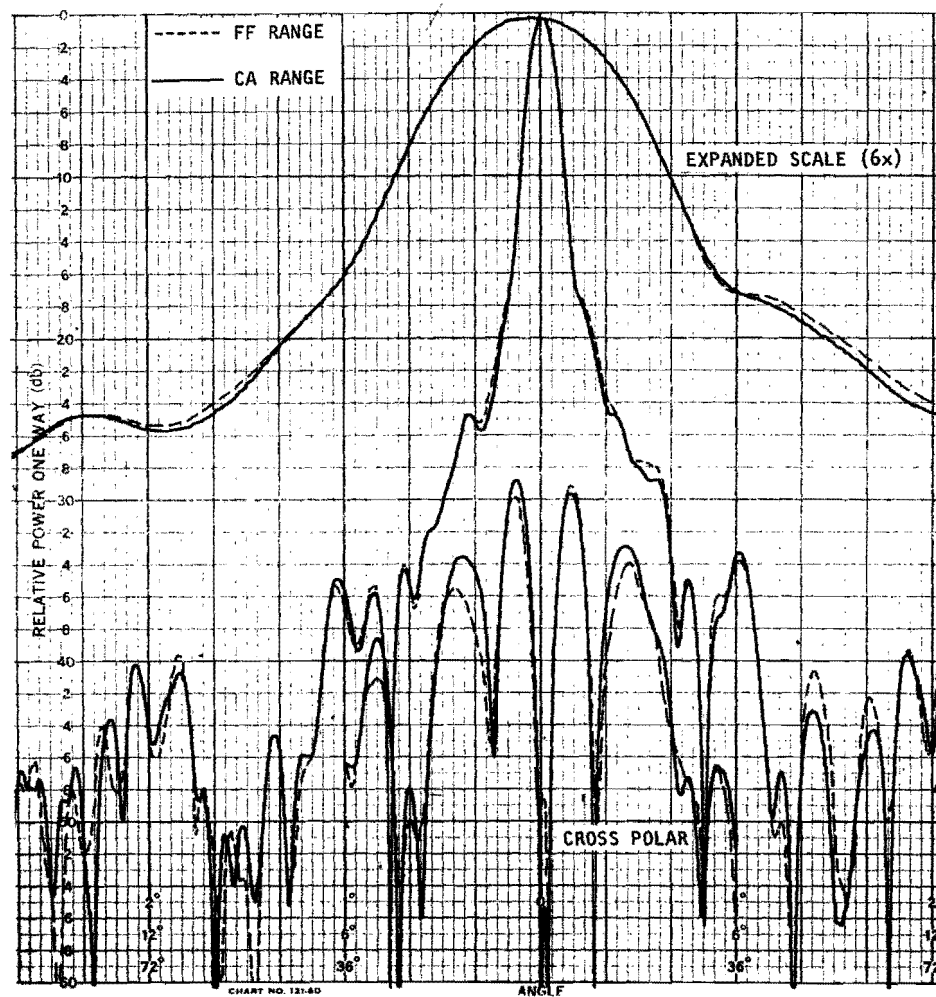


Fig. 18: OTS antenna pattern,  $f=14.25$  GHz, feed support  $45^\circ$ , parallel polarisation.

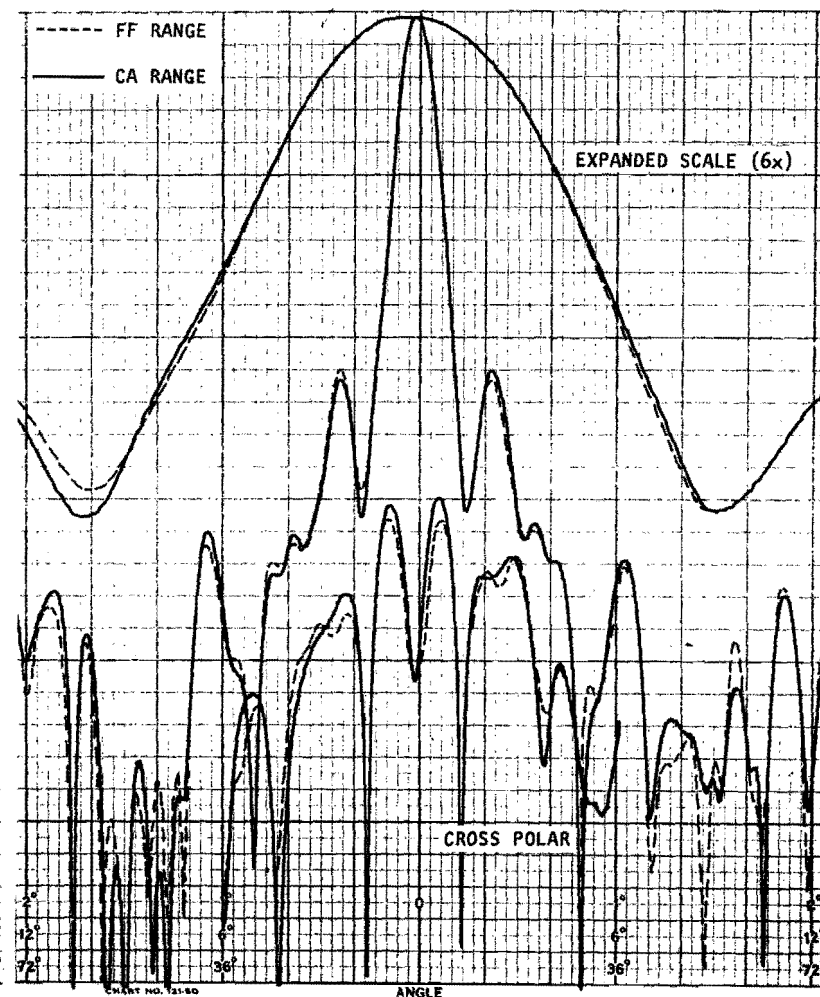


Fig. 19: OTS antenna pattern;  $f=14.25$  GHz, feed support  $45^\circ$ , perpendicular polarisation.

#### 9.3.4. Performance Comparison of Two Compact Ranges with Different Geometry.

At present, a Compact Antenna Range consisting of a single parabolic reflector is commercially available (Scientific Atlanta). Its performance, in particular at frequencies below 18 GHz is very good and such a range is suitable for a large number of applications. On the other hand, limited dimensions of the plane-wave zone (120 cm), large C.R. reflector (4.9 x 4.7 m) and a decreasing performance at higher frequencies are the main disadvantages, As already mentioned, most of these disadvantages can be eliminated by applying a dual-reflector geometry.

In Table 2 a performance comparison is given for the two above-mentioned ranges. We conclude that for all critical parameters the dual-cylindrical reflector C.A.R. is superior to the single-reflector design. For purpose of illustration, a front view of both ranges is shown in Fig. 20. We observe that for the same test antenna diameter (120 cm) the C.R. with two cylindrical reflectors is considerably smaller (approx. 2x in linear dimension). Consequently, considerable savings will be achieved as to the cost of the test facility. Furthermore, increasing the size of this C.R. will be possible; indoor measurements on large antennas up to about 3 metres in diameter (or even larger) may be seen as realistic for the near future.

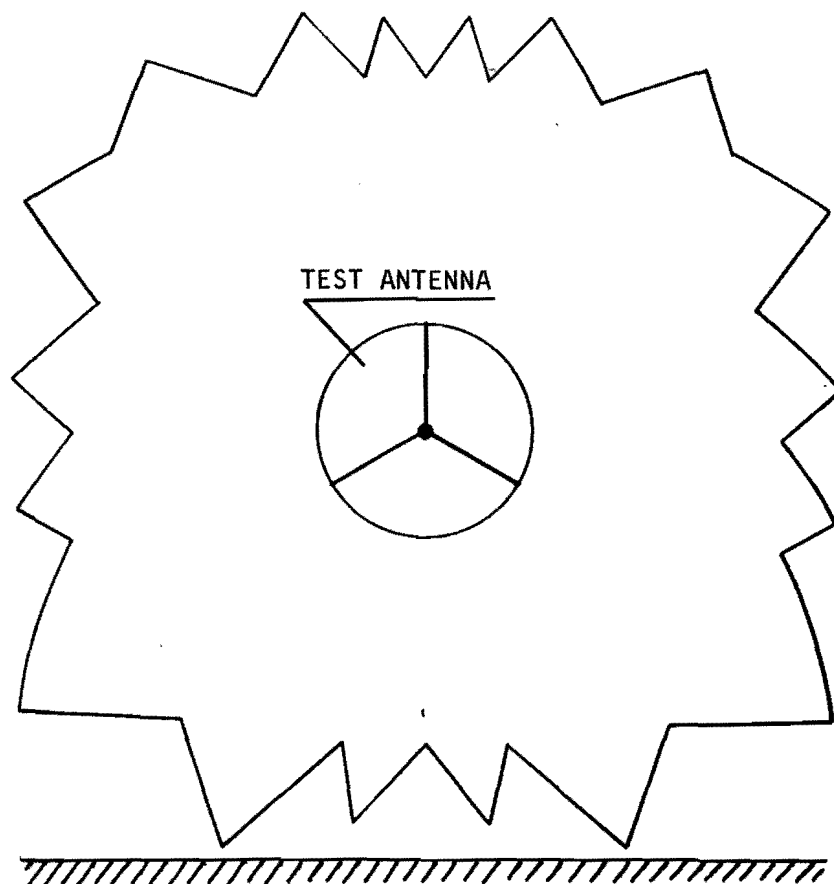
In conclusion, the Compact Antenna Range with two cylindrical reflectors is eminently suitable for applications where direct measurements of far-field antenna patterns are preferred. High degree of accuracy can be realized for various antenna types, including those for space applications.

Table 2. Comparison of two Compact Ranges.

	Scientific-Atlanta C.A.R.	<sup>1</sup> Dual-cylindrical reflector C.A.R.
Test antenna diameter	1.22m	1.22m
Frequency range	4-18 GHz	4-18 GHz
Amplitude taper	0.5dB typical	0.25dB max.
Total variation about the overall taper	4-8 GHz $\leq$ 1dB	4-8 GHz $\leq$ 0.3dB
	8-12 GHz $\leq$ 0.5dB	8-12 GHz $\leq$ 0.5dB
	12-18 GHz $\leq$ 0.3dB	12-18 GHz $\leq$ 0.3dB
Total phase variation	<10 degr. (max.)	<4 degr. (max.)
	<5 degr. (typical)	
Maximum extraneous signal level	3.9 - 5.8 GHz, -25dB <sup>2</sup>	4-8 GHz, -50dB
	5.8 - 8.2 GHz, -30dB <sup>2</sup>	8-12 GHz, -50dB
	8.2 - 18 GHz, -35dB <sup>2</sup>	12-18 GHz, -55dB
Cross polarisation	-25dB (-35dB typical)	-35dB max.
Overall dimensions	4.9m (H) x 4.7m (W)	2.5m (H) x 2.7m (W) <sup>3</sup>
		2.5m (H) x 2.4m (W) <sup>4</sup>
Weight	2270 kg	580 kg
Anechoic chamber dimension	6m(H) x 6m(W) x 12m(L)	3.0m(H)x3.6m(W)x8m(L)

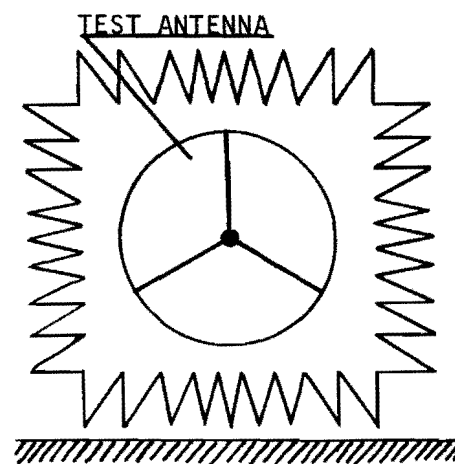
*Note: Data shown above have been recorded with a standard gain horn (S-A range); in case of the dual-cylindrical reflector C.A.R. an open waveguide was used as probe. Consequently, differences in performance might be greater than shown.*

- <sup>1</sup>. Data are based on experiments with a 2-metre range. Scaling 1:1.25 is applied.
- <sup>2</sup>. Maximum values. Typical extraneous signal level is 5-10dB lower.
- <sup>3</sup>. Main reflector.
- <sup>4</sup>. Subreflector.



(A)

1.22 m



(B)

Fig. 20: Comparison of two Compact Ranges for a test antenna with  $d=122\text{cm}$ .  
(A) Scientific-Atlanta C.R., (B) C.R. with two cylindrical reflectors.

### 9.3.5 References

- [1] E.F. Wacker and A.C. Newell - Advantages and disadvantages of planar,, circular and spherical scanning, Proc. ESA workshop on Antenna Testing Techniques, pp. 115-121,, 1977..
- [2] R.C. Johnson et al. - Compact range techniques and measurements,, IEEE Trans. Ant. Propagat. Vol.. AP-17,, pp. 568-576,, 1969..
- [3] R.C. Hansen - Evaluation of near-field compact ranges for measurements of tracking antennas,, IEEE Trans. Ant. Propagat. Vol.. AP-23,, no. 3,, pp. 329-334,, 1975..
- [4] R.C. Johnson and D.W. Hess - Performance of a compact antenna range,, Proc. AP-S Symposium, pp. 349-352,, 1975..
- [5] V.J. Vokurka - New compact range with cylindrical reflectors and high efficiency factor,, Proc. Electronica 76 Conf., München, Germany 1976..
- [6] V.J. Vokurka - Feeds and reflector antennas for shaped beams,, Dr.. Thesis,, Eindhoven, 1977..
- [7] M.J. Gans -Cross polarisation in reflector type beam waveguides and antennas,, BSTJ,, Vol.. 55,, no. 3,, pp. 289-316,, 1976..
- [8] V.J. Vokurka - Compact antenna range performance at 70 GHz,, Proc.. AP-S Symposium, pp. 260-263,, 1980..
- [9] Aegis near-field antenna test system, Final report NAVSEA MT S-475-77,, NOSC TR 499,, June 1980..

### Other related references

- [10] T.G. Hickman and R.C. Johnson - Boresight measurements utilizing a compact range, Abstract 1972 Spring USNC/URSI Meet. Washington D.C., April 13-15,, p. 111,, 1972..
- [11] H.L. Basset and H.A. Ecker and R.C. Johnson and A.P. Sheppard - New Techniques for implementing microwave biological-exposure systems,, IEEE Trans. Microwave Theory Tech., Vol.. MTT-19,, pp. 197-205,, 1971..
- [12] R.C. Spencer et al. - Double parabolic cylinder pencil beam antenna,, IRE Trans. Ant. Propagat., pp. 4-8, 1955..
- [13] C. Dragon - An improved antenna for microwave radio systems consisting of two cylindrical reflectors and corrugated horn,, BSTJ,, Vol.. 53,, no. 7,, pp. 1351-1377,, 1974..
- [14] R.C. Johnson, H.A. Ecker and J.S. Hollis - Determination of far-field antenna pattern from near-field measurements, Proc. IEEE, Vol.. 61,, no. 12, pp. 1668-1694,, 1973..

- [15] W.H. Kummer and E.S. Gillespie - Antenna Measurements, Proc. IEEE, Vol. 66, no. 4, pp. 483-507, 1978.
- [16] L.D. Bakhrakh et al. - Determination of Parameters of Antennas Illuminated by a Nonplanar Wave, Radio Eng. and Elec. Physics, no. 12, pp. 1-8, 1975.
- [17] K. Bhan and A.D. Olver - Influence of Reflector Surface Distortions on the Performance of a Compact Antenna Range, Final Report no. 2042/061/RL, Queen Mary College, 1979.